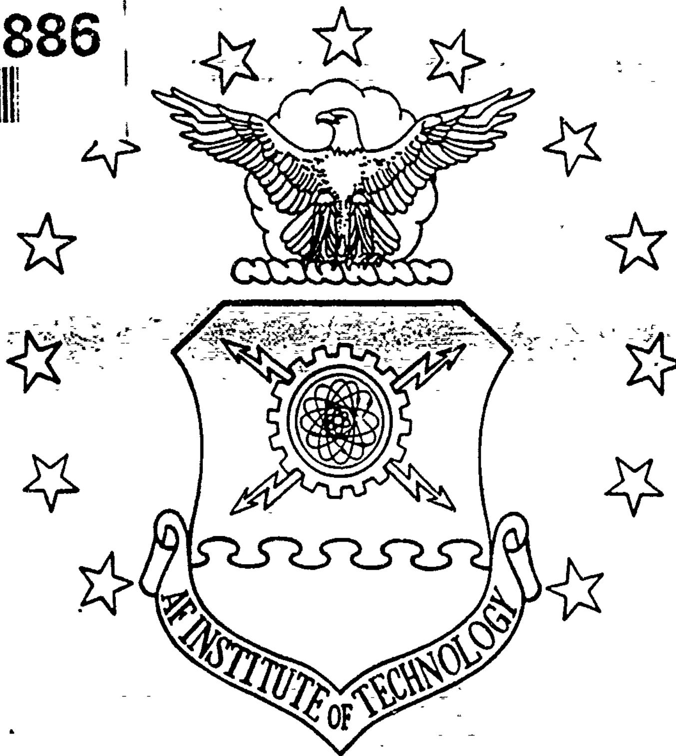

DTIC
ELECTE
JAN 0 6 1992
S D D

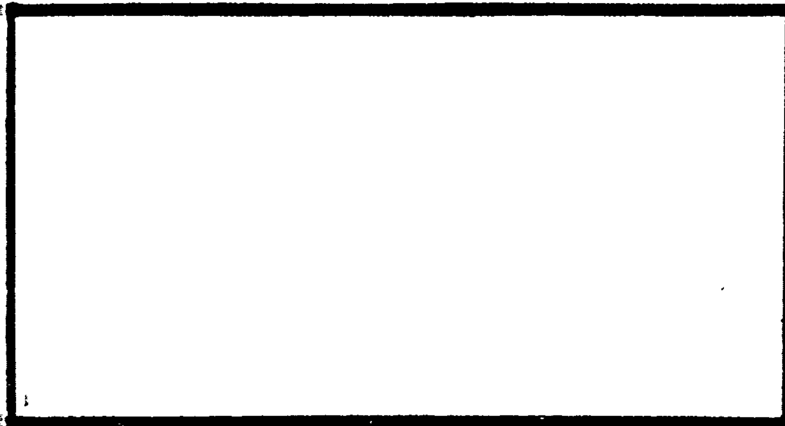

This document has been approved for public release and sale; its distribution is unlimited.

DEPARTMENT OF THE AIR FORCE

AIR UNIVERSITY

AIR FORCE INSTITUTE OF TECHNOLOGY

92 1 2 134

Wright-Patterson Air Force Base, Ohio

92 1 2 134

DISCLAIMER NOTICE

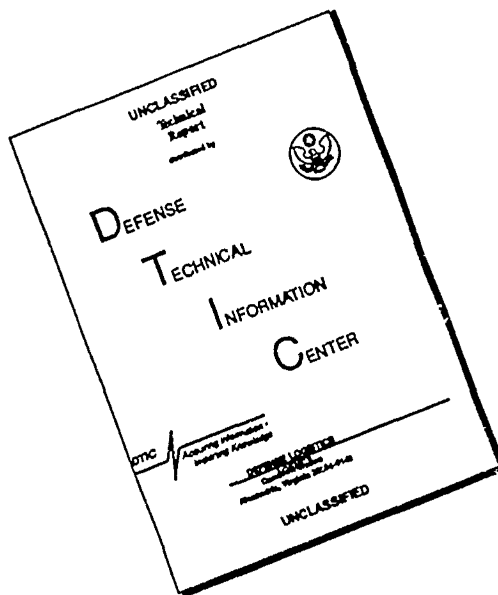

THIS DOCUMENT IS BEST QUALITY AVAILABLE. THE COPY FURNISHED TO DTIC CONTAINED A SIGNIFICANT NUMBER OF PAGES WHICH DO NOT REPRODUCE LEGIBLY.

AFIT/GE/ENG/91D-16

DTIC
ELECTE
JAN 06 1992
S D
D

ROBOTIC TACTILE SENSOR FABRICATED FROM A MONOLITHIC SILICON INTEGRATED CIRCUIT AND A PIEZOELECTRIC POLYVINYLIDENE FLUORIDE THIN FILM

THESIS

Craig Stephen Dyson
Captain, USAF

AFIT/GE/ENG/91D-16

Approved for public release: distribution unlimited

AFIT/GE/ENG/91D-16

ROBOTIC TACTILE SENSOR FABRICATED FROM A MONOLITHIC SILICON INTEGRATED CIRCUIT AND A PIEZOELECTRIC POLYVINYLIDENE FLUORIDE THIN FILM

THESIS

Presented to the Faculty of the School of Engineering

of the Air Force Institute of Technology

Air University

In Partial Fulfillment of the

Requirements for the Degree of

Master of Science in Electrical Engineering

Accesion For		
NTIS CRA&I		☑
DTIC TAB		☐
Unannounced		☐
Justification		
By		
Distribution /		
Availability Codes		
Dist	Avail and / or Special	
A-1		23

Craig Stephen Dyson, BSEE

Captain, USAF

December 1991

Approved for public release; distribution unlimited

Acknowledgments

Throughout this effort, many people have provided invaluable assistance to me. First and foremost, I would like to thank my thesis advisor, Lt Col Edward Kolesar. His technical expertise, motivation, and philosophy were a great source of inspiration. I would also like to thank the members of my thesis committee, Dr. Matthew Kabrisky, Capt Mark Mehalic, and Capt Michael Leahy for their support. I owe special thanks to Capt Bob Fitch for showing me the ropes early. Additionally, I would like to thank the members of the devices sequence for their emotional support.

Most of all, I would like to thank my beautiful wife, Terry, for her undying devotion, understanding, and support throughout this challenging effort, and my two daughters, Amanda and Brooke, for their unconditional love.

Craig Stephen Dyson

Table of Contents

Page

Acknowledgments ii

Table of Contents iii

List of Figures ix

List of Tables xxxi

Abstract xxxii

I. Introduction 1-1

Background 1-1

Problem Statement 1-3

Integrated Circuit Dimensions 1-3

Output Amplification 1-4

Transducing via Piezoelectricity 1-4

Adhesives 1-4

Sensor Biasing 1-4

Output Multiplexing 1-5

Minimization of the Pyroelectric Effect 1-5

Scope of the Effort 1-5

Amplifier Design/Revised Performance Characteristics 1-5

Adhesive Evaluation 1-6

Charge Leakage 1-6

Electrode Array Initial Bias State 1-6

Pyroelectric Effect Minimization 1-7

		Page
	Assumptions	1-7
	Approach	1-9
	Order of Presentation	1-9
II.	Robotic Tactile Sensors	2-1
	Introduction	2-1
	Robotic Sensors	2-1
	Human Touch Sensing	2-2
	Tactile Sensor Definition	2-5
	Types of Tactile Sensors	2-7
	Magnetostrictive Tactile Sensors	2-7
	Piezoresistive Tactile Sensors	2-9
	Capacitive Tactile Sensors	2-10
	Optical Tactile Sensors	2-12
	Ultrasonic Tactile Sensors	2-16
	Piezoelectric Tactile Sensors	2-18
	Conclusion	2-20
III.	Piezoelectric and Pyroelectric Phenomena	3-1
	Introduction	3-1
	Definition of Piezoelectricity and Pyroelectricity	3-1
	Scope	3-2
	History of Piezoelectricity	3-2
	Microscopic Description of Piezo- and Pyroelectricity	3-5
	Macroscopic Description of Piezo- and Pyroelectricity	3-13
	Stress and Strain	3-14
	Piezoelectric Equations	3-22
	Pyroelectric Equations	3-26

Page

Generalized Polarization Equations 3-27

Piezoelectric Materials 3-28

Rochelle Salt 3-28

Quartz 3-30

Ceramics 3-33

Polymers 3-33

Conclusion 3-41

IV. Design of the Tactile Sensor and the Supporting Experimental Performance Evaluation Hardware Configuration 4-1

Introduction 4-1

Integrated Circuit Design 4-1

Electrode Array Pattern Design 4-3

Charge Amplifier Design 4-4

Piezoelectric PVDF Film 4-10

PVDF Film Adhesive Performance Comparative Investigation 4-10

Tactile Sensor Configuration 4-10

Component Design 4-12

Bias Voltage Circuit Configuration 4-12

Multiplexer Circuit Configuration 4-15

Pyroelectric Effect Limitation Chamber 4-15

Test-Load Shapes 4-17

Conclusion 4-21

V. Fabrication and Evaluation Procedures 5-1

Introduction 5-1

Component Testing 5-1

Piezoelectric PVDF Film Characterization 5-1

Page

Tactile Sensor's Bias Circuit Evaluation 5-5

Multiplexer Circuit Evaluation 5-5

Electrode Array Integrated Circuit Evaluation 5-6

Evaluation of the Tactile Sensor Bias Circuit, Multiplexer Circuit and Tactile Sensor Protoboard System 5-7

Tactile Sensor Fabrication 5-7

Adhesive Evaluation 5-10

Tactile Sensor Evaluation 5-10

Individual Taxel Performance 5-11

Taxel Array Evaluation 5-11

Conclusion 5-13

VI. Evaluation Results 6-1

Introduction 6-1

Component Testing 6-1

Piezoelectric PVDF Film Characterization Results . 6-2

Tactile Sensor Bias Circuit Evaluation 6-5

Multiplexer Circuit Evaluation 6-6

Electrode Array Integrated Circuit Evaluation 6-7

Tactile Sensor Protoboard, Bias Circuit, and Multiplexer System Evaluation Results 6-16

Adhesive Evaluation 6-21

Tactile Sensor Evaluation 6-22

Individual Taxel Verification 6-24

Taxel Array Evaluation 6-26

Conclusion 6-66

		Page
VII.	Conclusions and Recommendations	7-1
	Conclusions	7-1
	Recommendations	7-2
Appendix A.	Materials and Equipment	A-1
Appendix B.	Test Load Shape Designs	B-1
Appendix C.	SPICE Deck Files	C-1
	Charge Amplifier SPICE Deck	C-1
	SPICE Model Parameters	C-2
	Multiplexer Inverter SPICE Deck	C-4
Appendix D.	Piezoelectric PVDF Film Characterization Procedure	D-1
Appendix E.	BASIC Data Acquisition Programs	E-1
	Keithley Model 617 Electrometer Data Acquisition Program	E-1
	LeCroy Model 9400A Digital Storage Oscilloscope Data Acquisition Program	E-7
	Hewlett-Packard Model 54100A Digital Storage Oscilloscope Data Acquisition Program	E-21
Appendix F.	Procedure for Fabricating the Tactile Sensor	F-1
Appendix G.	Adhesive Study Photographs	G-1
Appendix H.	Tactile Sensor Evaluation Procedures	H-1
Appendix I.	Three-dimensional Tactile Sensor Shape Information	I-1
Appendix J.	Contour and Threshold Plots	J-1

		Page
Appendix K.	Response of the Sensor to Several Different Weights . .	K-1
Appendix L.	Tactile Sensor Shape Plots in Several Different Locations	L-1
Appendix M.	Potential T-Gate Multiplexer Design	M-1
	T-Gate Array Design	M-1
	Control Scheme	M-3
	Suggested T-Gate Multiplexer Evaluation	M-3
Bibliography		BIB-1
Vita		VITA-1

List of Figures

Figure | Page

1.1. Fixture For Applying The Test Load Shapes 1-8

2.1. Neuromuscular Spindle 2-3

2.2. Neurotendinous Spindle 2-3

2.3. Nerve Supply To The Skin Of The Hand 2-4

2.4. Nerve Supply To The Hair Follicle 2-5

2.5. Magnetostrictive Tactile Sensor 2-8

2.6. Tactile Sensor Utilizing Polysilicon As The Piezoresistive Element 2-10

2.7. Side View Of A Capacitive Tactile Sensor Fabricated On A Silicon Substrate 2-12

2.8. Schematic Of The Internal Reflection Tactile Sensor 2-14

2.9. Cross-Sectional View Of The Fingertip Shaped, Internal Reflection Tactile Sensor 2-15

2.10. Cross-Sectional View Of An Ultrasonic Tactile Sensor Utilizing A Piezoelectric PVDF Film 2-17

2.11. Tactile Sensor Utilizing Layered Piezoelectric PVDF Films 2-19

2.12. Piezoelectric Tactile Sensor Utilizing ZnO 2-20

3.1. Spatial Configuration Of A Generalized Electric Dipole 3-5

3.2. Model Of An Atom: (a) Without An External Electric Field Present, And (b) The Resulting Atomic Dipole After An External Electric Field **E** Is Applied 3-8

3.3. Crystal With A Center Of Inversion (a) Before The Application Of A Force And (b) After The Application Of A Force 3-11

3.4. Crystal Without A Center Of Inversion (a) Before The Application Of A Force And (b) After The Application Of A Force 3-12

Figure		Page

3.5. Example Of A Crystal With Trigonal Symmetry (a) Before The Application Of A Force And (b) After The Application Of A Force . . . 3-12

3.6. Stress System: (a) Compressional Stress, (b) Extensional Stress, And (c) Shear Stress . . . 3-14

3.7. Stress Directions . . . 3-15

3.8. Small Parallelepiped Used To Establish The Equations Of Equilibrium . . . 3-16

3.9. Two Types Of Strain: (a) Normal, And (b) Shear . . . 3-19

3.10. Strains In The x-, y-, And z-Directions . . . 3-20

3.11. Chemical Structure Of Rochelle Salt . . . 3-29

3.12. Distortion Caused By A Shear Strain Applied To A Square Crystal And A Method For Obtaining A Longitudinal Mode . . . 3-31

3.13. Typical Quartz Crystal Cuts . . . 3-32

3.14. Perovskite Crystalline Structure - Barium Titanate ($BaTiO_3$) Crystal 3-34

3.15. Molecular Structure Of α-Phase PVDF . . . 3-36

3.16. Molecular Structure Of β-Phase PVDF . . . 3-37

3.17. Unit Cells Of α-, β-, $\alpha_p(\delta)$-, And γ-Phases Of PVDF Projected Perpendicular Onto The Molecular Chains . . . 3-38

3.18. Schematic Illustrating The Conventional Identification Of Axes . 3-40

4.1. Essential Components Required For The Tactile Sensor System . 4-2

4.2. Floorplan Of The Robotic Tactile Sensor Integrated Circuit Showing 16 Electrical Connections Between One Bank Of The MOSFET Amplifiers And Their Corresponding Electrodes . . . 4-3

4.3. Photograph Of The Robotic Tactile Sensor Integrated Circuit Without The Piezoelectric PVDF Film (12.5 ×) . . . 4-5

4.4. Tactile Sensor Charge Amplifier Schematic . . . 4-7

4.5. Characteristic Transfer Function Plot Of The Tactile Sensor Charge Amplifier Predicted By A SPICE Analysis . . . 4-8

Figure		Page

4.6. Robotic Tactile Sensor Charge Amplifier Caltech Intermediate Format (CIF) Plot (380×) 4-11

4.7. Cross-Sectional View Of The Robotic Tactile Sensor Configuration 4-13

4.8. High Impedance Switch Configuration Connected With The Input Of The Taxel Amplifier 4-14

4.9. Off-Chip Tactile Sensor Multiplexer Configuration 4-16

4.10. Adjustable Chamber Frame Design For Minimizing Pyroelectric Effects 4-18

4.11. Representative Test-Load Shape - A Sharp Edge 4-19

4.12. Fixture For Applying The Test Load Shapes 4-20

5.1. Fabrication And Evaluation Flow Diagram 5-2

5.2. Bulk Piezoelectric PVDF Film Characterization Scheme Using A Glass Microscope Slide Substrate 5-3

5.3. Piezoelectric PVDF Film Characterization Instrumentation Configuration 5-4

5.4. Amplifier Test Configuration 5-6

5.5. Fabrication Configuration Of The Tactile Sensor 5-9

5.6. Taxel Array Evaluation Instrumentation Arrangement 5-12

6.1. Output Response Of A 100 g Load Applied To A Piece Of Piezoelectric PVDF Film Attached To A Glass Microscope Slide . . . 6-3

6.2. Output Response Of Heat (135°C) Applied To A Piece Of Piezoelectric PVDF Film Attached To A Glass Microscope Slide . . . 6-4

6.3. Output Response Of A 100 g Load And Heat (135°C) Applied To A Piece Of Piezoelectric PVDF Film Attached To A Glass Microscope Slide 6-5

6.4. Arithmetic Average Time Response Of 10 High Impedance Reed Switches 6-7

6.5. Multiplexer Circuit Response To A 5.8-V Bias Voltage Input Applied At A 20 kHz Rate 6-8

Figure		Page

6.6. Taxel Numbering Scheme 6-9

6.7. Characteristic Transfer Function Curve For The Charge Signal Amplifier Generated Using SPICE With 7.34 kΩ And 5.28 kΩ Resistors And A 15-V V_{dd} Bias 6-11

6.8. Measured Transfer Function Response For The Charge Signal Amplifier Operated With A 15-V V_{dd} Bias 6-11

6.9. Characteristic Transfer Function Curve For The Charge Signal Amplifier Generated Using SPICE With 7.34 kΩ And 5.28 kΩ Resistors And A 14-V V_{dd} Bias 6-12

6.10. Measured Transfer Function Response For The Charge Signal Amplifier Operated With A 14-V V_{dd} Bias 6-12

6.11. Output Of A New (< 1 Hour Use) Tactile Sensor IC Without The Piezoelectric PVDF Film Attached 6-14

6.12. Output Of A Tactile Sensor IC Without The Piezoelectric PVDF Film After 12 Hours Of Operation 6-14

6.13. Schematic Representation Of The Signal Charge Amplifier Test Probe Pad Locations 6-15

6.14. Schematic Of The Bias Switch Network, The Multiplexer, And The Tactile Sensor Protoboard System Evaluation Configuration . . . 6-17

6.15. The Output Of The Wavetek Signal Switcher Connected To The Reed Switch Control Line 6-18

6.16. Reed Switch Characteristic Response Possessing A Large Voltage Transient 6-18

6.17. Reed Switch Characteristic Response After The Wavetek Signal Switcher Used To Switch All The Reed Switches Simultaneously Was Removed 6-19

6.18. Multiplexed Output Of An 8.1-V Bias Applied To The Tactile Sensor Protoboard Clocked At 14 kHz 6-20

6.19. The Multiplexed Output Of Taxel 11 Biased At 5-V 6-20

6.20. Crosstalk Of The Nearest-Neighbor Taxels When A 6.21-V Bias Was Applied To Taxel Number 27 6-21

Figure	Page

6.21. Example Of The Conformal Coverage Existing Over The Entire Electrode Array Using The Urethane Adhesive (75 ×) 6-23

6.22. Example Of The Non-Conformal Coverage Existing Over Most Of The Electrode Array Using The *Loctite* Adhesive (75 ×) 6-23

6.23. Output Of A Charge Signal Amplifier When A 135 g Load Was Repeatedly Applied To A Discrete Electrode 6-24

6.24. Characteristic Voltage Versus Load Functional Relationship For The Tactile Sensor 6-25

6.25. Response Of The Charge Signal Amplifier For A 135 g Load Over A Long Period Of Time 6-27

6.26. Pre-load, Load, And Post-load Measurements Of A 100 g Small Circle Shape Load (Taxel 1-16 Responses Are Shown) 6-29

6.27. Pre-load, Load, And Post-load Measurements Of A 100 g Small Circle Shape Load (Taxel 17-32 Responses Are Shown) 6-29

6.28. Pre-load, Load, And Post-load Measurements Of A 100 g Small Circle Shape Load (Taxel 33-48 Responses Are Shown) 6-30

6.29. Pre-load, Load, And Post-load Measurements Of A 100 g Small Circle Shape Load (Taxel 49-64 Responses Are Shown) 6-30

6.30. Shape Information For The Small Circle Applied To The Upper Right Hand Corner Of The Electrode Array 6-31

6.31. Three-Dimensional Representation Of A Sharp Edge Shaped Load Applied To The Surface Of The Electrode Array. The z-Axis Corresponds To The Normalized Difference Between The Sensor's Loaded And Unloaded States, And The x- And y-Axes Correspond To The Electrode Columns And Rows, Respectively 6-33

6.32. 0.4-V Equipotential Contour Plot For A 100 g Sharp Edge Shaped Load Applied To The Surface Of The Electrode Array 6-34

6.33. 0.4-V Threshold Plot Of A 100 g Sharp Edge Shaped Load – Taxels With An Output Level Above This Threshold Level Are Displayed As Black And Taxels With An Output Level Below This Threshold Level Are Displayed As White 6-35

Figure | Page

6.34. Three-Dimensional Representation Of A Small Square Shaped Load Applied To The Surface Of The Electrode Array. The z-Axis Corresponds To The Normalized Difference Between The Sensor's Loaded And Unloaded States, And The x- And y-Axes Correspond To The Electrode Columns And Rows, Respectively 6-36

6.35. 0.35-V Equipotential Contour Plot For A 100 g Small Square Shaped Load Applied To The Surface Of The Electrode Array 6-37

6.36. 0.35-V Threshold Plot Of A 100 g Small Square Shaped Load – Taxels With An Output Level Above This Threshold Level Are Displayed As Black And Taxels With An Output Level Below This Threshold Level Are Displayed As White 6-38

6.37. Three-Dimensional Representation Of A Small Circularly Shaped Load Applied To The Surface Of The Electrode Array. The z-Axis Corresponds To The Normalized Difference Between The Sensor's Loaded And Unloaded States, And The x- And y-Axes Correspond To The Electrode Columns And Rows, Respectively 6-39

6.38. 0.7-V Equipotential Contour Plot For A 100 g Small Circularly Shaped Load Applied To The Surface Of The Electrode Array . . 6-40

6.39. 0.7-V Threshold Plot Of A 100 g Small Circularly Shaped Load – Taxels With An Output Level Above This Threshold Level Are Displayed As Black And Taxels With An Output Level Below This Threshold Level Are Displayed As White 6-41

6.40. Three-Dimensional Representation Of A Polygon Shaped Load Applied To The Surface Of The Electrode Array. The z-Axis Corresponds To The Normalized Difference Between The Sensor's Loaded And Unloaded States, And The x- And y-Axes Correspond To The Electrode Columns And Rows, Respectively 6-42

6.41. 0.4-V Equipotential Contour Plot For A 100 g Polygon Shaped Load Applied To The Surface Of The Electrode Array 6-43

6.42. 0.4-V Threshold Plot Of A 100 g Polygon Shaped Load – Taxels With An Output Level Above This Threshold Level Are Displayed As Black And Taxels With An Output Level Below This Threshold Level Are Displayed As White 6-44

Figure Page

6.43. Three-Dimensional Representation Of A Slotted Screw Shaped Load Applied To The Surface Of The Electrode Array. The z-Axis Corresponds To The Normalized Difference Between The Sensor's Loaded And Unloaded States, And The x- And y-Axes Correspond To The Electrode Columns And Rows, Respectively 6-45

6.44. 0.51-V Equipotential Contour Plot For A 100 g Slotted Screw Shaped Load Applied To The Surface Of The Electrode Array 6-46

6.45. 0.51-V Threshold Plot Of A 100 g Slotted Screw Shaped Load - Taxels With An Output Level Above This Threshold Level Are Displayed As Black And Taxels With An Output Level Below This Threshold Level Are Displayed As White 6-47

6.46. Three-Dimensional Representation Of A Cross Slotted Screw Shaped Load Applied To The Surface Of The Electrode Array. The z-Axis Corresponds To The Normalized Difference Between The Sensor's Loaded And Unloaded States. And The x- And y-Axes Correspond To The Electrode Columns And Rows, Respectively 6-48

6.47. 0.15-V Equipotential Contour Plot For A 100 g Cross-Slotted Screw Shaped Load Applied To The Surface Of The Electrode Array . . 6-49

6.48. 0.15-V Threshold Plot Of A 100 g Cross-Slotted Screw Shaped Load - Taxels With An Output Level Above This Threshold Level Are Displayed As Black And Taxels With An Output Level Below This Threshold Level Are Displayed As White 6-50

6.49. Three-Dimensional Representation Of A Large Solid Circularly Shaped Load Applied To The Surface Of The Electrode Array. The z-Axis Corresponds To The Normalized Difference Between The Sensor's Loaded And Unloaded States. And The x- And y-Axes Correspond To The Electrode Columns And Rows, Respectively 6-51

6.50. 0.5-V Equipotential Contour Plot For A 100 g Large Solid Circularly Shaped Load Applied To The Surface Of The Electrode Array . . 6-52

6.51. 0.5-V Threshold Plot Of A 100 g Large Solid Circularly Shaped Load - Taxels With An Output Level Above This Threshold Level Are Displayed As Black And Taxels With An Output Level Below This Threshold Level Are Displayed As White 6-53

Figure | Page

6.52. Three-Dimensional Representation Of A Toroid Shaped Load Applied To The Surface Of The Electrode Array. The z-Axis Corresponds To The Normalized Difference Between The Sensor's Loaded And Unloaded States, And The x- And y-Axes Correspond To The Electrode Columns And Rows, Respectively 6-54

6.53. 0.5-V Equipotential Contour Plot For A 100 g Toroid Shaped Load Applied To The Surface Of The Electrode Array 6-55

6.54. 0.5-V Threshold Plot Of A 100 g Toroid Shaped Load - Taxels With An Output Level Above This Threshold Level Are Displayed As Black And Taxels With An Output Level Below This Threshold Level Are Displayed As White 6-56

6.55. Three-Dimensional Representation Of A Sharp Edge Shaped Load Applied To The Surface Of The Electrode Array. The z-Axis Corresponds To The Normalized Difference Between The Sensor's Loaded And Unloaded States. And The x- And y-Axes Correspond To The Electrode Columns And Rows. Respectively - The Sensor Was Fabricated Using A Polyimide Adhesive 6-57

6.56. 0.58-V Equipotential Contour Plot For A 100 g Sharp Edge Shaped Load Applied To The Surface Of The Electrode Array - The Sensor Was Fabricated Using A Polyimide Adhesive 6-58

6.57. 0.58-V Threshold Plot Of A 100 g Sharp Edge Shaped Load - Taxels With An Output Level Above This Threshold Level Are Displayed As Black And Taxels With An Output Level Below This Threshold Level Are Displayed As White The Sensor Was Fabricated Using A Polyimide Adhesive 6-59

6.58. Three-Dimensional Representation Of A Small Square Shaped Load Applied To The Surface Of The Electrode Array. The z-Axis Corresponds To The Normalized Difference Between The Sensor's Loaded And Unloaded States, And The x- And y-Axes Correspond To The Electrode Columns And Rows. Respectively - The Sensor Was Fabricated Using A Polyimide Adhesive 6-60

Figure		Page

6.59. 0.55-V Equipotential Contour Plot For A 100 g Small Square Shaped Load Applied To The Surface Of The Electrode Array - The Sensor Was Fabricated Using A Polyimide Adhesive 6-61

6.60. 0.55-V Threshold Plot Of A 100 g Small Square Shaped Load - Taxels With An Output Level Above This Threshold Level Are Displayed As Black And Taxels With An Output Level Below This Threshold Level Are Displayed As White - The Sensor Was Fabricated Using A Polyimide Adhesive 6-62

6.61. Three-Dimensional Representation Of A Small Circularly Shaped Load Applied To The Surface Of The Electrode Array. The z-Axis Corresponds To The Normalized Difference Between The Sensor's Loaded And Unloaded States. And The x- And y-Axes Correspond To The Electrode Columns And Rows. Respectively - The Sensor Was Fabricated Using A Polyimide Adhesive 6-63

6.62. 0.8-V Equipotential Contour Plot For A 100 g Small Circularly Shaped Load Applied To The Surface Of The Electrode Array - The Sensor Was Fabricated Using A Polyimide Adhesive 6-64

6.63. 0.8-V Threshold Plot Of A 10 g Small Circularly Shaped Load - Taxels With An Output Level Above This Threshold Level Are Displayed As Black And Taxels With An Output Level Below This Threshold Level Are Displayed As White - The Sensor Was Fabricated Using A Polyimide Adhesive 6-65

7.1. Modification Of The Fixture For Applying The Test Load Shapes Incorporating Micrometer Adjustment Screws 7-1

B.1. Sharp-Edge Test Load Shape B-1

B.2. Small Square Shaped Test Load B-2

B.3. Small Solid Circle Test Load Shape B-3

B.4. Polygon Shaped Test Load B-4

B.5. Slotted Screw Test Load Shape B-5

B.6. Cross-Slot Screw Test Load Shape B-6

Figure		Page

B.7. Large Solid Circle Test Load Shape B-7

B.8. Toroid Test Load Shape B-8

D.1. Bulk Piezoelectric PVDF Film Characterization Scheme Using A Glass Microscope Slide Substrate D-2

D.2. Piezoelectric PVDF Film Characterization Instrumentation Configuration D-3

F.1. Fabrication Configuration Of The Tactile Sensor F-2

G.1. Electrode Coverage With A 40 μm Thick Piezoelectric PVDF Film Attached With The Urethane Adhesive – Initial Photo (75 ×) . . G-1

G.2. Electrode Coverage With A 40 μm Thick Piezoelectric PVDF Film Attached With The Urethane Adhesive – Initial Photo (75 ×) . . G-2

G.3. Corner Of The 40 μm Thick Piezoelectric PVDF Film Attached With The Urethane Adhesive – Initial Photo (75 ×) G-2

G.4. Electrode Coverage With A 40 μm Thick Piezoelectric PVDF Film Attached With The Urethane Adhesive – Final Photo (75 ×) . . G-3

G.5. Electrode Coverage With A 40 μm Thick Piezoelectric PVDF Film Attached With The Urethane Adhesive – Final Photo (75 ×) . . G-3

G.6. Corner Of The 40 μm Thick Piezoelectric PVDF Film Attached With The Urethane Adhesive – Final Photo (75 ×) G-4

G.7. Electrode Coverage With A 40 μm Thick Piezoelectric PVDF Film Attached With The Polyimide Adhesive – Initial Photo (75 ×) . G-4

G.8. Electrode Coverage With A 40 μm Thick Piezoelectric PVDF Film Attached With The Polyimide Adhesive – Initial Photo (75 ×) . G-5

G.9. Corner Of The 40 μm Thick Piezoelectric PVDF Film Attached With The Polyimide Adhesive – Initial Photo (75 ×) G-5

G.10. Electrode Coverage With A 40 μm Thick Piezoelectric PVDF Film Attached With The Polyimide Adhesive – Final Photo (75 ×) . . G-6

G.11 Electrode Coverage With A 40 μm Thick Piezoelectric PVDF Film Attached With The Polyimide Adhesive – Final Photo (75 ×) . . G-6

Figure | Page

G.12. Corner Of The 40 μm Thick Piezoelectric PVDF Film Attached With The Polyimide Adhesive - Final Photo (75 ×) G-7

G.13. Electrode Coverage With A 40 μm Thick Piezoelectric PVDF Film Attached With The *Loctite* Adhesive - Initial Photo (75 ×) . . . G-7

G.14. Electrode Coverage With A 40 μm Thick Piezoelectric PVDF Film Attached With The *Loctite* Adhesive - Initial Photo (75 ×) . . . G-8

G.15. Corner Of The 40 μm Thick Piezoelectric PVDF Film Attached With The *Loctite* Adhesive - Initial Photo (75 ×) G-8

G.16. Electrode Coverage With A 40 μm Thick Piezoelectric PVDF Film Attached With The *Loctite* Adhesive - Final Photo (75 ×) G-9

G.17. Electrode Coverage With A 40 μm Thick Piezoelectric PVDF Film Attached With The *Loctite* Adhesive - Final Photo (75 ×) G-9

G.18. Corner Of The 40 μm Thick Piezoelectric PVDF Film Attached With The *Loctite* Adhesive - Final Photo (75 ×) G-10

H.1. Tactile Sensor Array Performance Evaluation Instrumentation Configuration H-2

J.1. 0.3-V Equipotential Contour Plot For A 100 g Sharp Edge Shaped Load Applied To The Surface Of The Electrode Array J-2

J.2. 0.3-V Threshold Plot Of A 100 g Sharp Edge Shaped Load - Taxels With An Output Level Above This Threshold Level Are Displayed As Black And Taxels With An Output Level Below This Threshold Level Are Displayed As White J-3

J.3. 0.5-V Equipotential Contour Plot For A 100 g Sharp Edge Shaped Load Applied To The Surface Of The Electrode Array J-4

J.4. 0.5-V Threshold Plot Of A 100 g Sharp Edge Shaped Load - Taxels With An Output Level Above This Threshold Level Are Displayed As Black And Taxels With An Output Level Below This Threshold Level Are Displayed As White J-5

J.5. 0.3-V Equipotential Contour Plot For A 100 g Small Square Shaped Load Applied To The Surface Of The Electrode Array J-6

Figure		Page

J.6. 0.3-V Threshold Plot Of A 100 g Small Square Shaped Load - Taxels With An Output Level Above This Threshold Level Are Displayed As Black And Taxels With An Output Level Below This Threshold Level Are Displayed As White J-7

J.7. 0.4-V Equipotential Contour Plot For A 100 g Small Square Shaped Load Applied To The Surface Of The Electrode Array J-8

J.8. 0.4-V Threshold Plot Of A 100 g Small Square Shaped Load - Taxels With An Output Level Above This Threshold Level Are Displayed As Black And Taxels With An Output Level Below This Threshold Level Are Displayed As White J-9

J.9. 0.6-V Equipotential Contour Plot For A 100 g Small Circularly Shaped Load Applied To The Surface Of The Electrode Array . . J-10

J.10. 0.6-V Threshold Plot Of A 100 g Small Circularly Shaped Load - Taxels With An Output Level Above This Threshold Level Are Displayed As Black And Taxels With An Output Level Below This Threshold Level Are Displayed As White J-11

J.11. 0.8-V Equipotential Contour Plot For A 100 g Small Circularly Shaped Load Applied To The Surface Of The Electrode Array . . J-12

J.12. 0.8-V Threshold Plot Of A 100 g Small Circularly Shaped Load - Taxels With An Output Level Above This Threshold Level Are Displayed As Black And Taxels With An Output Level Below This Threshold Level Are Displayed As White J-13

J.13. 0.3-V Equipotential Contour Plot For A 100 g Polygon Shaped Load Applied To The Surface Of The Electrode Array J-14

J.14. 0.3-V Threshold Plot Of A 100 g Polygon Shaped Load - Taxels With An Output Level Above This Threshold Level Are Displayed As Black And Taxels With An Output Level Below This Threshold Level Are Displayed As White J-15

J.15. 0.5-V Equipotential Contour Plot For A 100 g Polygon Shaped Load Applied To The Surface Of The Electrode Array J-16

Figure | Page

J.16. 0.5-V Threshold Plot Of A 100 g Polygon Shaped Load – Taxels With An Output Level Above This Threshold Level Are Displayed As Black And Taxels With An Output Level Below This Threshold Level Are Displayed As White J-17

J.17. 0.5-V Equipotential Contour Plot For A 100 g Slotted Screw Shaped Load Applied To The Surface Of The Electrode Array J-18

J.18. 0.5-V Threshold Plot Of A 100 g Slotted Screw Shaped Load – Taxels With An Output Level Above This Threshold Level Are Displayed As Black And Taxels With An Output Level Below This Threshold Level Are Displayed As White J-19

J.19. 0.56-V Equipotential Contour Plot For A 100 g Slotted Screw Shaped Load Applied To The Surface Of The Electrode Array J-20

J.20. 0.56-V Threshold Plot Of A 100 g Slotted Screw Shaped Load – Taxels With An Output Level Above This Threshold Level Are Displayed As Black And Taxels With An Output Level Below This Threshold Level Are Displayed As White J-21

J.21. 0.4-V Equipotential Contour Plot For A 100 g Cross-Slotted Screw Shaped Load Applied To The Surface Of The Electrode Array . . J-22

J.22. 0.4-V Threshold Plot Of A 100 g Cross-Slotted Screw Shaped Load – Taxels With An Output Level Above This Threshold Level Are Displayed As Black And Taxels With An Output Level Below This Threshold Level Are Displayed As White J-23

J.23. 0.5-V Equipotential Contour Plot For A 100 g Cross-Slotted Screw Shaped Load Applied To The Surface Of The Electrode Array . . J-24

J.24. 0.5-V Threshold Plot Of A 100 g Cross-Slotted Screw Shaped Load – Taxels With An Output Level Above This Threshold Level Are Displayed As Black And Taxels With An Output Level Below This Threshold Level Are Displayed As White J-25

J.25. 0.48-V Equipotential Contour Plot For A 100 g Large Solid Circularly Shaped Load Applied To The Surface Of The Electrode Array J-26

Figure | Page

J.26. 0.48-V Threshold Plot Of A 100 g Large Solid Circularly Shaped Load - Taxels With An Output Level Above This Threshold Level Are Displayed As Black And Taxels With An Output Level Below This Threshold Level Are Displayed As White J-27

J.27. 0.55-V Equipotential Contour Plot For A 100 g Large Solid Circularly Shaped Load Applied To The Surface Of The Electrode Array J-28

J.28. 0.55-V Threshold Plot Of A 100 g Large Solid Circularly Shaped Load - Taxels With An Output Level Above This Threshold Level Are Displayed As Black And Taxels With An Output Level Below This Threshold Level Are Displayed As White J-29

J.29. 0.45-V Equipotential Contour Plot For A 100 g Toroid Shaped Load Applied To The Surface Of The Electrode Array J-30

J.30. 0.45-V Threshold Plot Of A 100 g Toroid Shaped Load - Taxels With An Output Level Above This Threshold Level Are Displayed As Black And Taxels With An Output Level Below This Threshold Level Are Displayed As White J-31

J.31. 0.55-V Equipotential Contour Plot For A 100 g Toroid Shaped Load Applied To The Surface Of The Electrode Array J-32

J.32. 0.55-V Threshold Plot Of A 100 g Toroid Shaped Load - Taxels With An Output Level Above This Threshold Level Are Displayed As Black And Taxels With An Output Level Below This Threshold Level Are Displayed As White J-33

J.33. 0.54-V Equipotential Contour Plot For A 100 g Sharp Edge Shaped Load Applied To The Surface Of The Electrode Array - The Sensor Was Fabricated Using A Polyimide Adhesive J-34

J.34. 0.54-V Threshold Plot Of A 100 g Sharp Edge Shaped Load - Taxels With An Output Level Above This Threshold Level Are Displayed As Black And Taxels With An Output Level Below This Threshold Level Are Displayed As White - The Sensor Was Fabricated Using A Polyimide Adhesive J-35

J.35. 0.6-V Equipotential Contour Plot For A 100 g Sharp Edge Shaped Load Applied To The Surface Of The Electrode Array - The Sensor Was Fabricated Using A Polyimide Adhesive J-36

Figure	Page

J.36. 0.6-V Threshold Plot Of A 100 g Sharp Edge Shaped Load - Taxels With An Output Level Above This Threshold Level Are Displayed As Black And Taxels With An Output Level Below This Threshold Level Are Displayed As White - The Sensor Was Fabricated Using A Polyimide Adhesive J-37

J.37. 0.55-V Equipotential Contour Plot For A 100 g Small Square Shaped Load Applied To The Surface Of The Electrode Array - The Sensor Was Fabricated Using A Polyimide Adhesive J-38

J.38. 0.55-V Threshold Plot Of A 100 g Small Square Shaped Load - Taxels With An Output Level Above This Threshold Level Are Displayed As Black And Taxels With An Output Level Below This Threshold Level Are Displayed As White - The Sensor Was Fabricated Using A Polyimide Adhesive J-39

J.39. 0.58-V Equipotential Contour Plot For A 100 g Small Square Shaped Load Applied To The Surface Of The Electrode Array - The Sensor Was Fabricated Using A Polyimide Adhesive J-40

J.40. 0.58-V Threshold Plot Of A 100 g Small Square Shaped Load - Taxels With An Output Level Above This Threshold Level Are Displayed As Black And Taxels With An Output Level Below This Threshold Level Are Displayed As White - The Sensor Was Fabricated Using A Polyimide Adhesive J-41

J.41. 0.76-V Equipotential Contour Plot For A 100 g Small Circularly Shaped Load Applied To The Surface Of The Electrode Array - The Sensor Was Fabricated Using A Polyimide Adhesive J-42

J.42. 0.76-V Threshold Plot Of A 100 g Small Circularly Shaped Load - Taxels With An Output Level Above This Threshold Level Are Displayed As Black And Taxels With An Output Level Below This Threshold Level Are Displayed As White - The Sensor Was Fabricated Using A Polyimide Adhesive J-43

J.43. 0.84-V Equipotential Contour Plot For A 100 g Small Circularly Shaped Load Applied To The Surface Of The Electrode Array - The Sensor Was Fabricated Using A Polyimide Adhesive J-44

Figure Page

J.44. 0.84-V Threshold Plot Of A 100 g Small Circularly Shaped Load – Taxels With An Output Level Above This Threshold Level Are Displayed As Black And Taxels With An Output Level Below This Threshold Level Are Displayed As White – The Sensor Was Fabricated Using A Polyimide Adhesive J-45

K.1. Three-Dimensional Representation Of A Sharp Edge Shaped Load Applied To The Surface Of The Electrode Array. The z-Axis Corresponds To The Normalized Difference Between The Sensor's Loaded And Unloaded States. And The x- And y-Axes Correspond To the Electrode Columns And Rows. Respectively K-2

K.2. 0.47-V Equipotential Contour Plot For A 75 g Sharp Edge Shaped Load Applied To The Surface Of The Electrode Array K-3

K.3. 0.47-V Threshold Plot Of A 75 g Sharp Edge Shaped Load - Taxels With An Output Level Above This Threshold Level Are Displayed As Black And Taxels With An Output Level Below This Threshold Level Are Displayed As White K-4

K.4. Three-Dimensional Representation Of A Sharp Edge Shaped Load Applied To The Surface Of The Electrode Array. The z-Axis Corresponds To The Normalized Difference Between The Sensor's Loaded And Unloaded States. And The x- And y-Axes Correspond To the Electrode Columns And Rows, Respectively K-5

K.5. 0.52-V Equipotential Contour Plot For A 50 g Sharp Edge Shaped Load Applied To The Surface Of The Electrode Array K-6

K.6. 0.52-V Threshold Plot Of A 50 g Sharp Edge Shaped Load - Taxels With An Output Level Above This Threshold Level Are Displayed As Black And Taxels With An Output Level Below This Threshold Level Are Displayed As White K-7

K.7. Three-Dimensional Representation Of A Sharp Edge Shaped Load Applied To The Surface Of The Electrode Array. The z-Axis Corresponds To The Normalized Difference Between The Sensor's Loaded And Unloaded States. And The x- And y-Axes Correspond To the Electrode Columns And Rows. Respectively K-8

Figure		Page
K.8.	0.5-V Equipotential Contour Plot For A 10 g Sharp Edge Shaped Load Applied To The Surface Of The Electrode Array	K-9
K.9.	0.5-V Threshold Plot Of A 10 g Sharp Edge Shaped Load – Taxels With An Output Level Above This Threshold Level Are Displayed As Black And Taxels With An Output Level Below This Threshold Level Are Displayed As White	K-10
K.10.	Three-Dimensional Representation Of A Small Square Shaped Load Applied To The Surface Of The Electrode Array. The z-Axis Corresponds To The Normalized Difference Between The Sensor's Loaded And Unloaded States. And The x- And y-Axes Correspond To the Electrode Columns And Rows. Respectively	K-11
K.11.	0.39-V Equipotential Contour Plot For A 75 g Small Square Shaped Load Applied To The Surface Of The Electrode Array	K-12
K.12.	0.39-V Threshold Plot Of A 75 g Small Square Shaped Load – Taxels With An Output Level Above This Threshold Level Are Displayed As Black And Taxels With An Output Level Below This Threshold Level Are Displayed As White	K-13
K.13.	Three-Dimensional Representation Of A Small Square Shaped Load Applied To The Surface Of The Electrode Array. The z-Axis Corresponds To The Normalized Difference Between The Sensor's Loaded And Unloaded States. And The x- And y-Axes Correspond To the Electrode Columns And Rows. Respectively	K-14
K.14.	0.51-V Equipotential Contour Plot For A 50 g Small Square Shaped Load Applied To The Surface Of The Electrode Array	K-15
K.15.	0.51-V Threshold Plot Of A 50 g Small Square Shaped Load – Taxels With An Output Level Above This Threshold Level Are Displayed As Black And Taxels With An Output Level Below This Threshold Level Are Displayed As White	K-16
K.16.	Three-Dimensional Representation Of A Small Square Shaped Load Applied To The Surface Of The Electrode Array. The z-Axis Corresponds To The Normalized Difference Between The Sensor's Loaded And Unloaded States. And The x- And y-Axes Correspond To the Electrode Columns And Rows. Respectively	K-17

Figure		Page

K.17. 0.5-V Equipotential Contour Plot For A 10 g Small Square Shaped Load Applied To The Surface Of The Electrode Array K-18

K.18. 0.5-V Threshold Plot Of A 10 g Small Square Shaped Load – Taxels With An Output Level Above This Threshold Level Are Displayed As Black And Taxels With An Output Level Below This Threshold Level Are Displayed As White K-19

K.19. Three-Dimensional Representation Of A Small Circularly Shaped Load Applied To The Surface Of The Electrode Array. The z-Axis Corresponds To The Normalized Difference Between The Sensor's Loaded And Unloaded States. And The x- And y-Axes Correspond To the Electrode Columns And Rows, Respectively K-20

K.20. 0.68-V Equipotential Contour Plot For A 75 g Small Circularly Shaped Load Applied To The Surface Of The Electrode Array . . K-21

K.21. 0.68-V Threshold Plot Of A 75 g Small Circularly Shaped Load – Taxels With An Output Level Above This Threshold Level Are Displayed As Black And Taxels With An Output Level Below This Threshold Level Are Displayed As White K-22

K.22. Three-Dimensional Representation Of A Small Circularly Shaped Load Applied To The Surface Of The Electrode Array. The z-Axis Corresponds To The Normalized Difference Between The Sensor's Loaded And Unloaded States, And The x- And y-Axes Correspond To the Electrode Columns And Rows, Respectively K-23

K.23. 0.67-V Equipotential Contour Plot For A 50 g Small Circularly Shaped Load Applied To The Surface Of The Electrode Array . . K-24

K.24. 0.67-V Threshold Plot Of A 50 g Small Circularly Shaped Load – Taxels With An Output Level Above This Threshold Level Are Displayed As Black And Taxels With An Output Level Below This Threshold Level Are Displayed As White K-25

K.25. Three-Dimensional Representation Of A Small Circularly Shaped Load Applied To The Surface Of The Electrode Array. The z-Axis Corresponds To The Normalized Difference Between The Sensor's Loaded And Unloaded States. And The x- And y-Axes Correspond To the Electrode Columns And Rows. Respectively K-26

Figure | Page

K.26. 0.78-V Equipotential Contour Plot For A 10 g Small Circularly Shaped Load Applied To The Surface Of The Electrode Array . . K-27

K.27. 0.78-V Threshold Plot Of A 10 g Small Circularly Shaped Load – Taxels With An Output Level Above This Threshold Level Are Displayed As Black And Taxels With An Output Level Below This Threshold Level Are Displayed As White K-28

K.28. Three-Dimensional Representation Of A Polygon Shaped Load Applied To The Surface Of The Electrode Array. The z-Axis Corresponds To The Normalized Difference Between The Sensor's Loaded And Unloaded States, And The x- And y-Axes Correspond To the Electrode Columns And Rows, Respectively K-29

K.29. 0.51-V Equipotential Contour Plot For A 75 g Polygon Shaped Load Applied To The Surface Of The Electrode Array K-30

K.30. 0.51-V Threshold Plot Of A 75 g Polygon Shaped Load – Taxels With An Output Level Above This Threshold Level Are Displayed As Black And Taxels With An Output Level Below This Threshold Level Are Displayed As White K-31

K.31. Three-Dimensional Representation Of A Polygon Shaped Load Applied To The Surface Of The Electrode Array. The z-Axis Corresponds To The Normalized Difference Between The Sensor's Loaded And Unloaded States, And The x- And y-Axes Correspond To the Electrode Columns And Rows, Respectively K-32

K.32. 0.5-V Equipotential Contour Plot For A 50 g Polygon Shaped Load Applied To The Surface Of The Electrode Array K-33

K.33. 0.5-V Threshold Plot Of A 50 g Polygon Shaped Load – Taxels With An Output Level Above This Threshold Level Are Displayed As Black And Taxels With An Output Level Below This Threshold Level Are Displayed As White K-34

K.34. Three-Dimensional Representation Of A Polygon Shaped Load Applied To The Surface Of The Electrode Array. The z-Axis Corresponds To The Normalized Difference Between The Sensor's Loaded And Unloaded States, And The x- And y-Axes Correspond To the Electrode Columns And Rows, Respectively K-35

Figure		Page

K.35. 0.6-V Equipotential Contour Plot For A 10 g Polygon Shaped Load Applied To The Surface Of The Electrode Array K-36

K.36. 0.6-V Threshold Plot Of A 10 g Polygon Shaped Load – Taxels With An Output Level Above This Threshold Level Are Displayed As Black And Taxels With An Output Level Below This Threshold Level Are Displayed As White K-37

L.1. Three-Dimensional Representation Of A 100 g Sharp Edge Shaped Load Applied To The Surface Of The Electrode Array. The z-Axis Corresponds To The Normalized Difference Between The Sensor's Loaded And Unloaded States. And The x- And y-Axes Correspond To The Electrode Columns And Rows. Respectively L-2

L.2. 0.36-V Equipotential Contour Plot For A 100 g Sharp Edge Shaped Load Applied To The Surface Of The Electrode Array L-3

L.3. 0.36-V Threshold Plot Of A 100 g Sharp Edge Shaped Load – Taxels With An Output Level Above This Threshold Level Are Displayed As Black And Taxels With An Output Level Below This Threshold Level Are Displayed As White L-4

L.4. Three-Dimensional Representation Of A 100 g Sharp Edge Shaped Load Applied To The Surface Of The Electrode Array. The z-Axis Corresponds To The Normalized Difference Between The Sensor's Loaded And Unloaded States. And The x- And y-Axes Correspond To The Electrode Columns And Rows. Respectively L-5

L.5. 0.35-V Equipotential Contour Plot For A 100 g Sharp Edge Shaped Load Applied To The Surface Of The Electrode Array L-6

L.6. 0.35-V Threshold Plot Of A 100 g Sharp Edge Shaped Load – Taxels With An Output Level Above This Threshold Level Are Displayed As Black And Taxels With An Output Level Below This Threshold Level Are Displayed As White L-7

L.7. Three-Dimensional Representation Of A 100 g Sharp Edge Shaped Load Applied To The Surface Of The Electrode Array. The z-Axis Corresponds To The Normalized Difference Between The Sensor's Loaded And Unloaded States. And The x- And y-Axes Correspond To The Electrode Columns And Rows. Respectively L-8

Figure		Page

L.8 0.35-V Equipotential Contour Plot For A 100 g Sharp Edge Shaped Load Applied To The Surface Of The Electrode Array L-9

L.9. 0.35-V Threshold Plot Of A 100 g Sharp Edge Shaped Load – Taxels With An Output Level Above This Threshold Level Are Displayed As Black And Taxels With An Output Level Below This Threshold Level Are Displayed As White L-10

L.10. Three-Dimensional Representation Of A 100 g Small Square Shaped Load Applied To The Surface Of The Electrode Array. The z-Axis Corresponds To The Normalized Difference Between The Sensor's Loaded And Unloaded States, And The x- And y-Axes Correspond To The Electrode Columns And Rows, Respectively L-11

L.11. 0.5-V Equipotential Contour Plot For A 100 g Small Square Shaped Load Applied To The Surface Of The Electrode Array L-12

L.12. 0.5-V Threshold Plot Of A 100 g Small Square Shaped Load – Taxels With An Output Level Above This Threshold Level Are Displayed As Black And Taxels With An Output Level Below This Threshold Level Are Displayed As White L-13

L.13. Three-Dimensional Representation Of A 100 g Small Square Shaped Load Applied To The Surface Of The Electrode Array. The z-Axis Corresponds To The Normalized Difference Between The Sensor's Loaded And Unloaded States, And The x- And y-Axes Correspond To The Electrode Columns And Rows, Respectively L-14

L.14. 0.46-V Equipotential Contour Plot For A 100 g Small Square Shaped Load Applied To The Surface Of The Electrode Array L-15

L.15. 0.46-V Threshold Plot Of A 100 g Small Square Shaped Load – Taxels With An Output Level Above This Threshold Level Are Displayed As Black And Taxels With An Output Level Below This Threshold Level Are Displayed As White L-16

L.16. Three-Dimensional Representation Of A 100 g Small Circularly Shaped Load Applied To The Surface Of The Electrode Array. The z-Axis Corresponds To The Normalized Difference Between The Sensor's Loaded And Unloaded States, And The x- And y-Axes Correspond To The Electrode Columns And Rows, Respectively . L-17

Figure	Page

L.17. 0.7-V Equipotential Contour Plot For A 100 g Small Circularly Shaped Load Applied To The Surface Of The Electrode Array . . . L-18

L.18. 0.7-V Threshold Plot Of A 100 g Small Circularly Shaped Load - Taxels With An Output Level Above This Threshold Level Are Displayed As Black And Taxels With An Output Level Below This Threshold Level Are Displayed As White L-19

L.19. Three-Dimensional Representation Of A 100 g Small Circularly Shaped Load Applied To The Surface Of The Electrode Array. The z-Axis Corresponds To The Normalized Difference Between The Sensor's Loaded And Unloaded States, And The x- And y-Axes Correspond To The Electrode Columns And Rows, Respectively . L-20

L.20. 0.7-V Equipotential Contour Plot For A 100 g Small Circularly Shaped Load Applied To The Surface Of The Electrode Array . . L-21

L.21. 0.7-V Threshold Plot Of A 100 g Small Circularly Shaped Load - Taxels With An Output Level Above This Threshold Level Are Displayed As Black And Taxels With An Output Level Below This Threshold Level Are Displayed As White L-22

M.1. T-gate Multiplexer Caltech Intermediate Format (CIF) File (40×) M-2

M.2. Schematic Diagram Of The Test Probe Pad Locations In One Element Of The 16-to-1 Multiplexer T-gate M-3

List of Tables

Table | Page

2.1. Characteristics Of Human Nerve Endings 2-6

4.1. Tactile Sensor Amplifier Characteristics With Different Supply Voltages 4-9

4.2. Tactile Sensor Amplifier Characteristics For A 10-V And 15-V Bias Supply And The Expected Sheet Resistance Values 4-9

6.1. Optimum Threshold Levels For Each Load Shape 6-32

A.1. Materials And Equipment A-1

AFIT/GE/ENG/91D-16

Abstract

The purpose of this research effort was to design, fabricate, and test a tactile sensor system consisting of an external high impedance switch circuit, an external multiplexing circuit, and a tactile sensor IC. In order to accomplish this objective, a hardware design and selection process was implemented along with a logical test methodology. The hardware included an electrode array IC containing an 8 x 8 array of equally space aluminum electrodes (each electrode measured 400 x 400 μm and they were spaced 300 μm apart), and 64 high input impedance MOSFET amplifiers (each possessing a gain of 1.25). Also included were supporting component hardware sub-systems consisting of a high impedance reed switch network and a multiplexer circuit, both of which were realized from commercially available components. The test methodology developed ensured that any problems associated with either the supporting component hardware or the integrated circuit could be identified early in the test phase, and thus, their effects could be accounted for.

A high impedance switch network resulted in the ability to externally apply a fixed bias the entire electrode array structure and the attached piezoelectric PVDF film to achieve a uniform initial condition state. The external multiplexer circuit facilitated sampling the array elements without degrading any taxel's electrical charge. The response of the tactile sensor fabricated using a 40 μm thick square of piezoelectric PVDF film indicated linearity spanning loads of 0.8 g to 135 g, a load resolution of 20 g, and a maximum bandwidth of 25 Hz. Using an elementary shape recognition algorithm that was implemented by mathematically manipulating the pre-load, load, and post-load measurements of the tactile sensor electrode array, it was discovered that the tactile sensor could detect the shape of a load in contact with its surface with a spatial resolution on the order of 700 μm.

The considerable crosstalk (between 35% and 75% resulting from the IC layout design combined with the coupling effects due to the adhesives used for fabricating the tactile sensor) slightly affected the operation of the sensor: however, shape and load information could be readily extracted. The charge signal amplifiers exhibited breakdown over time due to the magnitude of the operating power supply voltage used to achieve the desired operating characteristics of the amplifier.

The adhesive study revealed that the urethane adhesive possessed the best electrical characteristics and physical robustness compared to either a plastic type of adhesive, *Loctite*, or a polyimide used as an adhesive. The plastic dielectric adhesive tended to cure extremely quickly, resulting in poor adhesion and physical coupling to the electrode array. While the polyimide possessed bonding characteristics similar to the urethane, its electrical characteristics exhibited an increase in taxel crosstalk level much larger than that observed with the urethane adhesive.

ROBOTIC TACTILE SENSOR FABRICATED FROM A MONOLITHIC SILICON INTEGRATED CIRCUIT AND A PIEZOELECTRIC POLYVINYLIDENE FLUORIDE THIN FILM

I. Introduction

Background

Computer controlled robots are programmed to move in predetermined patterns with minimal or no feedback from their environment. In the future, however, robots will need to autonomously adapt quickly to changes in their surroundings. Toward this end, robots will need to possess senses, principally, vision and touch (90:177). When designing a sensing system which will enable robots to augment a human worker, inspiration from physiological processes have frequently been investigated (7:18-46). The sense of touch is necessary for robots which must perform intricate manipulations where pressure sensitivity and movement within tightly controlled spaces is critical. Equipped with a taction capability, robots will be able to directly measure the physical properties of unknown objects, such as their position, orientation, shape, and texture (90:177).

Robotic tactile sensing has been defined as the continuous sensing of variable contact forces (55:3). Consequently, a distinction is made between this definition and simple (binary) contact or force sensing. Tactile sensing refers to skin-like properties, where localized regions of force-sensitive surfaces are capable of reporting quantized signals and parallel patterns of touch (55:3). From a design perspective, robotic tactile sensing can be thought of as a two-step process, transduction and data processing (90:178).

The typical tactile sensor should possess skin-like properties, including high sensitivity, fast response time, and continuously variable signal output. Additionally, the sensor should consume low power. The tactile sensor should

discriminate objects as well or better than a human adult, who is capable of discriminating two points 1.5 mm apart when contacting their fingertip (7:18-47). The sensor should have a dynamic sensitivity spanning 1 g to 1000 g with no hysteresis, and the corresponding outputs should be stable and reproducible (90:178). Finally, the sensor transducer should have a minimum bandwidth of 100 Hz (90:178).

Although there are various types of tactile sensors, including those utilizing magnetostrictive, piezoresistive, capacitive, optical, ultrasonic, and piezoelectric techniques, research at the Air Force Institute of Technology (AFIT) has concentrated on the piezoelectric tactile sensing concept which uses a piezoelectric polyvinylidene fluoride (PVDF) film and a monolithic silicon integrated circuit (IC). A summary of this research can be found in a paper authored by Kolesar, and others (63:280–283).

Research conducted by Capt David Pirolo (GE-87D) investigated various sensor electrode array configurations coupled to piezoelectric PVDF film. The tactile sensor was fabricated from printed circuit boards with the hope of determining an optimum electrode configuration. His investigation concluded that a matrix of square electrodes was the optimum taxel configuration, and that a 10 μm thick PVDF film was the optimum film thickness for a tactile sensing device (91).

Capt Rocky Reston (GE-88D) designed, fabricated and characterized a tactile sensor configured as a silicon integrated circuit that contained a 5 x 5 matrix of electrodes coupled to a piezoelectric PVDF film. He concluded that a 25 μm thick PVDF film manifested the most promising results, and that the *in situ* charge amplifiers provided an adequate linear response for loads spanning 0.8 g to 78 g (100).

Capt Douglas Ford (GE-89D) incorporated a multiplexer into the integrated circuit design. Unfortunately, incompatibilities between the RC time constants of the piezoelectric polyvinylidene fluoride (PVDF) film and the input impedance of each taxel electrode amplifier compromised the sensor's operation (46). Nevertheless, he successfully utilized Capt Reston's sensor with an off-chip commercial analog multiplexer to demonstrate the feasibility and advantages of automating the data collection process. His research also established the desirability of attaining a uniform charge state over the entire array by contacting

each MOSFET amplifier's gate electrode with a Micromanipulator probe which was biased at a desired voltage level (46).

Capt Robert Fitch (GE-90D) increased the density of the electrode configuration to a 7 x 7 matrix of electrodes and incorporated a multiplexer element in the integrated circuit which serialized the output data (45). However, he discovered that charge-leakage compromised the sensor's performance, and it was caused by two phenomena. The first cause was attributed to a low impedance path through the T-gate electrode selection circuitry which was part of the on-chip multiplexer circuit. To solve the leakage problem associated with the multiplexer circuit, it was totally isolated from the electrode array elements. Subsequently, a successful 3 x 3 sub-array of taxels was shown to function properly. The second charge-leakage problem was attributed to a low resistance path between the gold wire bond pads on the IC package. This path was subsequently identified to have been caused by residual traces of acetone which was used to remove excess adhesive when applying the PVDF film. This charge-leakage limitation did not negate the successful operation of the sensor; however, it did reduce the time the sensor was able to operate. To solve this problem, he recommended using a silicon rubber coating to cover the bond pads before fabricating the tactile sensor (45).

Problem Statement

This thesis will investigate a method for continuously sensing the shape and weight of an applied load using a sensor whose active area is on the order of that of a human adult's fingertip. This research effort should satisfy several requirements.

Integrated Circuit Dimensions. In future robotic applications, the size of the tactile sensor should be on the order of the adult human's fingertip to facilitate its integration with a robotic manipulator. If, for example, these sensors are mounted on a robot's fingertips, the force feedback from the sensors would indicate how tightly an object has been grasped. Additionally, the tactile sensor should have the ability to distinguish spatial resolution as well, or better, than a human. This level of performance requires a high density of closely spaced taxels. A sensor composed of a two-dimensional array of closely spaced taxels should be capable of fundamental image sensing, and thus, render the robot with the ability to identify the shape of an object in its grasp.

Output Amplification. The voltage generated by the piezoelectric film selected for this application is extremely small (typically a few mV). Therefore, the electrical signals generated must be amplified. The amplifier circuitry must also possess a large linear region to facilitate accurate detection and amplification of a taxel's response voltage, a large bandwidth to enable detection of the changes in the charge relative to small increments of time, and sufficient gain to provide an adequate output signal level for off-chip signal processing.

Transducing via Piezoelectricity. Since the purpose of the tactile sensor is to detect whether it is in contact with an object and the resulting applied force, the sensor must be able to transduce the mechanical forces into useful electrical signals. Although there are several transducing techniques available, piezoelectric technology will be investigated in this thesis. The piezoelectric material selected for this research effort was a polyvinylidene fluoride (PVDF) polymeric film. The PVDF polymeri lm possesses several advantages relative to other transducing materials, including a wide frequency range of operation (DC to approximately 10 MHz), a large dielectric strength compared to conventional piezoceramic materials (30-V/micron versus 1.5-V/micron) and a relatively large electrical impedance (this is an advantage which allows the film to provide a complimentary match to high-input impedance devices; for example, CMOS integrated circuits). Since the film is thin and flexible, it can be laminated to a vibrating structure without significantly dampening the motion of the structure, and the film can be cut and formed into complex shapes or prepared as a large transducer area. Additionally, the PVDF polymer's fabrication costs are generally lower than those of other piezoelectric materials (21:55).

Adhesives. A robust adhesive for bonding the piezoelectric thin film to the IC's electrode array is required for long-term research applications and potential use of the sensor in different environments.

Sensor Biasing. The piezoelectric PVDF polymeric film, which will be used in this investigation, must be stabilized (or biased) prior to the application of a load. Previous research efforts discovered that the piezoelectric PVDF film requires an initial bias voltage be applied across the film to induce a uniform polarized

state. This enables the film to generate an adequate amount of charge which is proportional to an applied load (45:6-1; 46:VI-1; 100:6-1). This initial biasing requirement will be satisfied by establishing a uniform initial condition across the film's surface; it also tends to compensate for any inherent stress in the PVDF film resulting from the sensor's fabrication and film adherence process.

Output Multiplexing. The tactile sensor's output will consist of several simultaneous output lines of information. To be able to process the information rapidly, the outputs will be multiplexed. The sampled output voltage can be processed by comparing the results before, during, and after a load is applied to the sensor's surface.

Minimization of the Pyroelectric Effect. The piezoelectric PVDF film is also pyroelectric (the electrical characteristics vary according to temperature) (68:17). To accurately obtain test data which corresponds to the PVDF's piezoelectric effect, the pyroelectric effects must be minimized or otherwise compensated for.

Scope of the Effort

A tactile sensor will be designed, fabricated, and characterized with respect to its ability to detect the weight and shape of an applied load. A piece of piezoelectric PVDF film will act as the charge generating polymer which will be attached to the surface of the integrated circuit electrode array. The integrated circuit will be fabricated using silicon planar technology, and it will contain a two-dimensional aluminum electrode array and associated voltage amplifiers. Once the piezoelectric PVDF film is coupled to the electrode array, the tactile sensor is realized.

Off-chip biasing circuitry, realized with a high output impedance switch, will be used to establish a uniform initial condition. Off-chip multiplexing circuitry, configured from commercially available IC's, will be used to serially output the taxel data for subsequent signal processing. This research effort will focus on the following critical issues:

Amplifier Design/Revised Performance Characteristics. The voltage amplifiers on the integrated circuit will be designed to provide an adequate signal

level which can be multiplexed with a separate circuit. The MOSFET amplifiers designed and fabricated in Capt Reston's research possessed a linear region which extended from 3.5-V to 5-V, and the corresponding gain was 6.7 (100:4-2). In Capt Fitch's research, the *in situ* MOSFET amplifiers possessed a linear region which extended from 3.5-V to 6.2-V, and the corresponding gain was 4 (45:5.8). A goal in this research effort was to design a MOSFET amplifier which would provide a larger linear operating region (ideally, extending from 0-V to 15-V) compared to the previous designs. Because the linear region was extended, the gain was reduced to approximately 1.25.

Adhesive Evaluation. Urethane, a polyimide dielectric, and a plastic dielectric, typically used to bond and conformally passivate printed circuit boards and electrical components, were evaluated as potential PVDF film adhesives. The ability of these three adhesives to couple charge to the MOSFET gate electrodes and to establish a robust mechanical bond to the electrode array was evaluated.

Charge Leakage. Previous research (45:6-2; 46:VI-3) has indicated that charge leakage was prevalent in the integrated circuit package. In an effort to resolve this issue, a conservative design based upon Capt Reston's successful tactile sensor was implemented. To minimize charge leakage through the IC package, two procedures were used during the fabrication of the tactile sensor to minimize the charge leakage effects. Initially, plasma ashing was used to remove the residual acetone contamination which remains as a result of attaching the piezoelectric PVDF film with an adhesive. Should the DC resistance between the gold bond pads be degraded, this IC and all subsequent IC's will be fabricated by coating the gold bond pads and leads with a silicone rubber membrane or an alternative low-loss dielectric thin film before the piezoelectric PVDF film attachment adhesive is applied.

Electrode Array Initial Bias State. The previous research efforts revealed that biasing the input electrodes, which are directly coupled to the charge amplifiers, is a difficult problem (45:6-1; 46:VI-1; 100:6-1). Nevertheless, this bias feature is critical for establishing a homogeneous initial charge state condition throughout the two-dimensional array of sensing elements. Any stress in the PVDF film, due to its adherence to the array structure or which is attributable to a prior

loading condition, may cause the pre-loaded initial condition potential to differ among the electrodes. This variation must be minimized and controlled, and this requirement can be achieved by biasing each MOSFET amplifier to establish a pseudo-linear and time-invariant direct current (DC) operating point.

Pyroelectric Effect Minimization. Because the piezoelectric PVDF film is also a pyroelectric material, the pyroelectric effects from external light sources, the surrounding equipment, and human contact should be minimized. Pyroelectric effects will be measured relative to a bulk piezoelectric PVDF film sample and for an assembled tactile sensor. An attempt to minimize these pyroelectric effects will be pursued by using a light-tight chamber to isolate the tactile sensor, the associated circuits, and test probe during the sensor testing phase.

Assumptions

1. The piezoelectric PVDF film will isolate and minimize crosstalk between nearest-neighbor taxels. Any measurable crosstalk attributed to the fringing field or leakage current between adjacent electrodes will be quantified experimentally to determine its effect on the sensor's performance.

2. The adhesive which bonds the piezoelectric PVDF film to the array will have electrical characteristics that do not compromise the charge generating properties of the PVDF film. That is, the piezoelectric PVDF film will generate a sufficient quantity of charge which can be detected by the charge signal amplifiers.

3. The 132-pin integrated circuit packages fabricated by the Metal-Oxide-Semiconductor Implementation System (MOSIS) will function according to the Computer Aided Design (CAD) tool Simulation Program, Integrated Circuit Emphasis (SPICE) analyses performed during the IC design process.

4. The test fixture (designed by Capt Fitch and illustrated in Figure 1.1) will be capable of applying the test load shapes (for example, an edge, a small square, a small circle, a polygon, a slotted screw, a cross-slotted screw, a large solid circle, and a toroid) spanning in weight from 1 g to 100 g. The contacting planar surface of each load shape will form a uniform interface with the IC array upon their initial contact and throughout the full application of the test load.

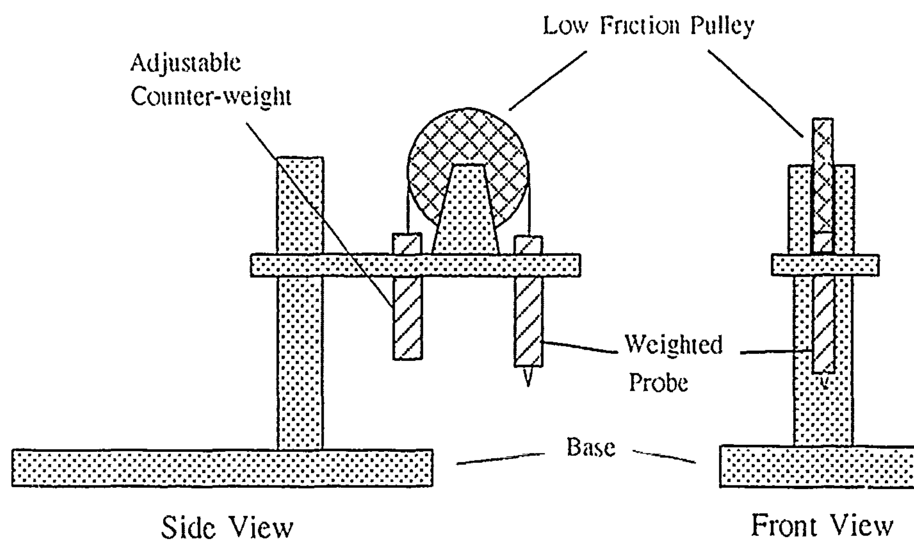

Figure 1.1. Fixture For Applying The Test Load Shapes (45:4-18).

Approach

This investigation consisted of three critical objectives: first, the design of the integrated circuit and associated support equipment configurations; second, the fabrication of the tactile sensor and assembly of the support equipment; and third, the performance evaluation of the sensor.

The integrated circuit was designed using the Very Large Scale Integrated Circuit (VLSI) Computer Aided Design (CAD) tools known as MAGIC (a graphical integrated circuit layout editor) and SPICE. The IC size was limited to an area measuring 7.9 mm by 9.2 mm. The center of the IC die contained an 8 x 8 array of equally spaced and sized aluminum electrodes surrounded by charge signal amplifiers. To minimize leakage between bond pads, all input bond pads were be placed along one edge of the IC, and all output bond pads were located on the opposite edge. An over-glass cut was used to facilitate the uniform adherence of the PVDF film to the electrode array.

The Metal-Oxide-Semiconductor Implementation System (MOSIS) fabricated the integrated circuit. During this fabrication period, the test equipment, including the external bias and multiplexer circuit, was configured and tested in the Cooperative Electronics and Materials Processing Laboratory. Also, preliminary tests were performed on the PVDF film to evaluate its charge generating capabilities. When the IC was received from MOSIS, its electrical properties were evaluated. Once its operation is characterized, a tactile sensor was realized by attaching the PVDF film to the IC's electrode array.

The tactile sensor performance tests began with individual electrode response tests designed to characterize electrode performance and to determine if inter-electrode crosstalk exists. Next, several load shapes were placed on the electrode array to establish the sensor's capability to detect the load's shape and weight. Throughout the performance evaluation phase, the effects of temperature on the electrical performance of the device were measured, and the adhesives used to attach the PVDF film to the IC were evaluated relative to their electrical and physical performance over time.

Order of Presentation

Chapter II establishes a definition of tactile sensing and includes a brief literature review of tactile sensor research efforts. The definition, history and

theory of piezoelectric and pyroelectric phenomena are presented in Chapter III. Chapter IV describes the integrated circuit and support component design. Chapter V outlines the tactile sensor fabrication process and general test procedures required to evaluate the electrical characteristics of the tactile sensor as well as the electrical and physical characteristics of the different adhesives. Chapter VI contains the test results and subsequent analysis. A summary of the pertinent conclusions and recommendations is presented in Chapter VII. The appendices include listings of the materials and equipment required for this thesis, test data and graphs acquired during the evaluation of the tactile sensor, and the computer code listings used to extract data from the test equipment.

II. Robotic Tactile Sensors

Introduction

Tactile sensing depends significantly upon the ability of its material characteristics to transduce externally applied forces into electrical signals. The problem of transducing externally applied forces into electrical signals possesses several solutions. Many material properties lend themselves well to the transduction process; typically, the effects of external pressure on the material's inherent properties are determined by measuring the changes in one of its electrical characteristics. such as capacitance. induction. or resistance. Light, for example, can be used in the transduction process by determining the affects of the applied pressure on the transmission of the light in its transmission media.

In this chapter, a definition and description of tactile sensing will be presented. Next, a basic review of the human tactile ability will be discussed, providing a background which relates this ability to the design requirements of robotic tactile sensors. Finally, current literature concerning tactile sensor research will be reviewed. This review will describe several categories which correspond to the particular technology being exploited. Initially, piezoresistive tactile sensors will be discussed. followed by those sensors utilizing a magnetostrictive transducing technique. Next, capacitive tactile sensors will be discussed. The use of ultrasonics in sensors will then be developed. followed by a review of several optical techniques currently being pursued. Finally. to provide insight into this research investigation. piezoelectric tactile sensor technology will be presented. From this literature review. the reader will understand that the solution to the tactile sensor transducing problem does not possess only one solution. but rather. many solution opportunities exist each with their own set of advantages and disadvantages. This chapter will provide the reader with the foundation to appreciate and understand this research effort.

Robotic Sensors

The first robots were designed for the repeated execution of preprogrammed sequences of motion, and they did not require any external sensing capabilities (9:17). However. if robots are to be utilized autonomously, they must possess

certain qualities which will enable them to interact with their environment (42:35). To realize this type of autonomy, robots must possess senses, and this need will place an increased demand on the performance requirements of new tactile imaging sensors, image processing and control systems (136:141).

The two most critical robotic senses are vision and touch, both of which are generally considered complementary for most future applications (55:4). Vision systems, perhaps the most developed robotic technology, enable a robot to identify an object, determine its location, and avoid it, if necessary (90:177). Unfortunately, vision systems require structured lighting, multiple cameras, and complex computational assets to provide depth perception, and they can frequently be obstructed by the robot itself or other objects (42:35).

On the other hand, touch is unaffected by shadows, and it can distinguish objects relative to their backgrounds. Obviously, when a touch sensing system is designed for a robotic manipulator, the touch sensor must be able to sense contact with an object. However, the sensor must also be capable of sensing a range of contact forces to perform manipulative tasks. That is, the robot must be capable of grasping an object and determining its physical characteristics - weight, size, temperature, thermal conductivity, hardness, surface texture, and spatial displacement (9:19). Additionally, a robot must regulate the amount of force required to grasp an object without having it slip during handling; for example, carefully holding an egg without breaking it, or firmly grasping a hammer without dropping it (9:18). To implement these required tasks, a feedback mechanism must be incorporated to supply force information back to the robot's control system. The feedback mechanism is considered essential to successfully manipulate a robot's manipulator (39:3).

Human Touch Sensing

The human is quite good at grasping and manipulating objects, using touch as the feedback mechanism for holding the object (104:5). To provide a basis for tactile sensor requirements and designs, a brief description of a human's ability to sense touch will be discussed.

The human skin possesses nine different touch sensors, each responding to particular external stimuli, such as heat or pressure. Of these nine touch sensor

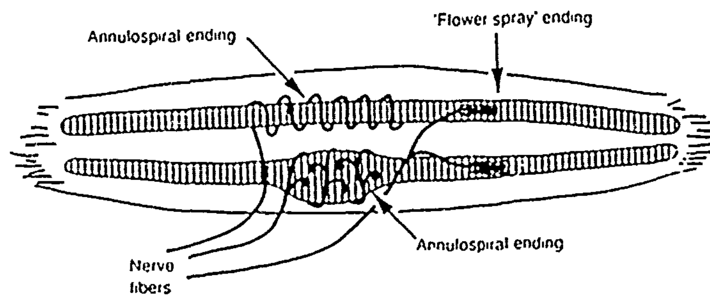

Figure 2.1. Neuromuscular Spindle (104:6).

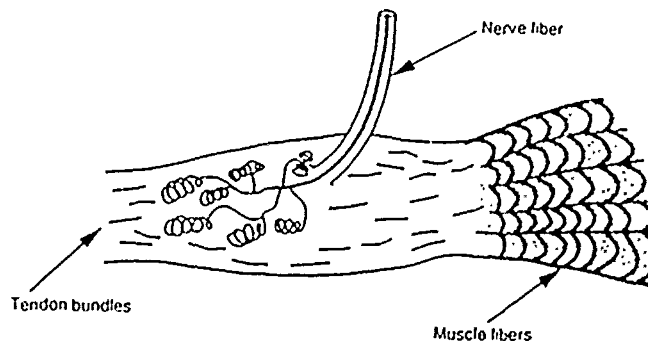

Figure 2.2. Neurotendinous Spindle (104:6).

types, two variants of sensors, or nerve endings, sense the activity of the muscles (the neuromuscular spindle, as depicted in Figure 2.1) and the tendons (the neurotendinous spindle, as depicted in Figure 2.2), providing information concerning the spatial location and movement of these areas of the body. The seven other types of sensors can be regarded as the human skin's touch sensors, and they include free nerve endings, Merkel's disks, Ruffini end-organs, Meissner's corpuscles, Pacinian corpuscles, Kraus's corpuscles, and hair end-organs. All of these touch sensors are located within three layers of the skin: the epidermis (or outermost layer), the dermis, and the subcutaneous fat (the innermost layer) (45:2-2). All of the sensors act together to provide a direct response to contact pressure, texture, temperature and pain. Figure 2.3 illustrates a schematic representation of the nerve supply to the outer layers of the hair-free skin covering

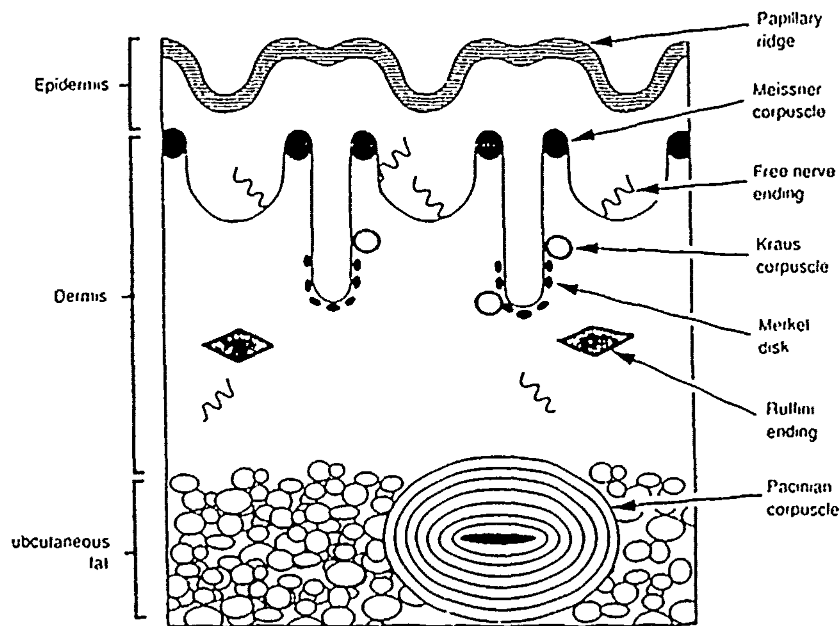

Figure 2.3. Nerve Supply To The Skin Of The Hand (104:8).

the fingers and palm, while Figure 2.4 depicts a schematic representation of the hair-end organ.

When the human skin makes contact with an object, the free nerve endings in the outer epidermal layer detect simple touch along with heat flow to and from the object. The Meissner corpuscles detect normal force and textural detail of the object's surface: the Merkel disks detect shape, edges, and texture (104:8). The Kraus corpuscles and Ruffini endings respond to temperature changes (104:9), while the Ruffini endings also sense lateral skin stretching and the continual deformation of the skin (45:2-3). The Pacinian corpuscles detect minimal vibrations, and they provide the hand with an added advantage in determining the object's identity (104:8). Table 2.1 provides specific information regarding several nerve endings.

The spatial arrangement of the skin's touch sensors varies over the surface of the skin, and as a result, the human can typically sense a minimum spatial separation between two distinct points of approximately 2 mm on the fingertip, to nearly 20 mm on the back of the fingertip. Unfortunately, the human's touch sensing capability is poor at determining absolute quantities, but it is very sensitive to changing quantities (104:10). For example, by simply pressing the

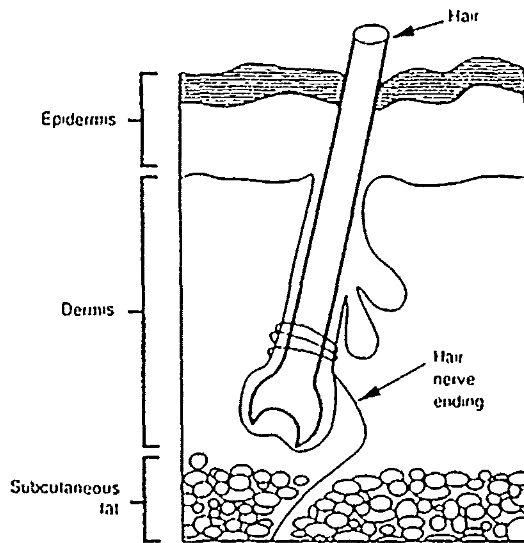

Figure 2.4. Nerve Supply To The Hair Follicle (104:9).

fingertip onto the edge of a piece of paper lying on a table, it cannot be felt; however, if the finger moves across the edge, the edge is easily detected.

In simulating the human's ability to touch, a robot should possess similar characteristics in its touch sensing mechanism. The specific definition of a tactile sensor and the requirements, which ensure that the sensor possesses at least the sensing performance of the human, will be described next.

Tactile Sensor Definition

The ability to continuously sense the contacting forces exerted on an object with an array of sensors can be defined as tactile sensing (55:3). Tactile sensing refers to skin-like properties where areas of force-sensitive surfaces are capable of reporting discrete signals in a parallel fashion to a processing system (55:3). Typically, tactile sensor surfaces consist of two-dimensional distributed arrays which are incorporated on thin, flexible substrates that are durable and compliant (55:4).

When designing a tactile sensing system which will enable robots to augment the human worker, inspiration from physiological processes are frequently investigated (7:18-16). In human tactile perception, the ability to discriminate two

Table 2.1. Characteristics Of Human Nerve Endings (104:8).

Nerve Ending	Receptive Field (mm)	Vibration Response (Hz)	Temperature Range (°C)	Stimulus
Meissner	3 - 4	8 - 14	-	Texture, Normal Force
Merkel	3 - 4	2 - 32	-	Shape, Edges. Texture
Pacinian	10	64 - 400	-	Vibration
Ruffini	-	1 - 16	40 +	Skin Stretch & Warmth
Kraus	-	-	18 - 40	Cold

simultaneous indentations with the fingertip is seriously degraded when the interpoint distance becomes less than 2 mm. and it worsens to more than 20 mm with respect to areas located on the back of the fingertip (55:10). To realize a similar resolution, each tactile sensor should incorporate a dense array composed of discrete sensor elements, or taxels, which typically number from 25 (5 x 5) to 1024 (32 x 32), and are spaced less than 2 mm center-to-center. The surface configuration of the array should best mimic the human touch sensing mechanism. being limited only by the particular geometric constraints offered by the particular design and fabrication tools used to realize the tactile sensor. The array configuration will help minimize tactile imaging time and enable the robot to determine object orientation by detecting flat-surfaces. rounded corners. sharp edges. etc. (55:11).

Observations of how humans recognize objects suggests that it may be useful to sense other variables in addition to the force which is perpendicularly directed relative to the sensor's surface (28:46). That is. a tactile sensor should possess the ability to conform to a "fingertip" surface and sense both shear forces (slippage) and temperature (9:18). The determination of slippage will enable a robot to handle flexible materials (wires or cloth) or grasp small conventional tools designed for human use (screw drivers. hammers. pliers. wrenches. etc.) (55:7.11).

The requirements for designing and building a tactile sensor correspond directly to the intended application of the tactile sensor (9:18). As such. the following requirements are the "ideal" requirements for a tactile sensor. and best approximate or improve its touch sensing ability when compared to the human. A robot's tactile sensitivity should ideally span 1 g to 1000 g with respect to each array element. and a 1 g difference should be resolvable (9:18). Also. the sensor

should be able to tolerate excess force without suffering permanent damage. It should also possess a fast response time (wide bandwidth), on the order of 100 Hz (9:18). The sensor should manifest low hysteresis to facilitate correlating the output responses with the applied forces in a reproducible manner which is independent of any pre-load conditions (9:18). The touch sensor should be able to pre-process collected data to relieve the central processing unit (CPU) of massive data manipulations. This feature can be accomplished with distributed-logic arrays and multiplexers (55:4).

There are several excellent books which describe the tactile sensing concept. including the books by Staugaard (114). Coiffet (26). Russell (104). and Brady (16). which can be supplemented with articles by Harmon (55: 56: 57). Regtien (97), Barth (9). Dario (27). Fearing (39: 40; 41), Zheng and Fan (140). Rooks (103), P. Allen (2: 3), Pennywitt (90) and Arbib (4).

To realize a tactile sensor. a selection from a multitude of transduction technologies must be accomplished. Research into the various sensor technologies. specifically. magnetostrictive, piezoresistive, capacitive, optical, ultrasonic. and piezoelectric. continues.

Types of Tactile Sensors

There are two general types of tactile sensors: pure force sensors. which transduce the direct application of a force into an electrically measureable quantity (for example. the piezoelectric and piezoresistive effects) and deflection sensors. which measure a force-related dis lacement (for example. magnetic. capacitive. ultrasonic. and optical effects) (97:94). In this section. several types of tactile sensors will be discussed. First. magnetostrictive tactile sensors will be presented. Next. piezoresistive tactile sensors will be described. The research on capacitive tactile sensors will be presented. next followed by a description of the research regarding optical tactile sensors. Finally. the principles of ultrasonic tactile sensing and piezoelectric tactile sensing will be developed.

Magnetostrictive Tactile Sensors. A magnetostrictive material is a material which exhibits a change in its magnetic field as a result of being influenced by external forces. Several magnetostrictive sensors have been developed exploiting this material property. including research conducted by Checinski (22). Clark (21).

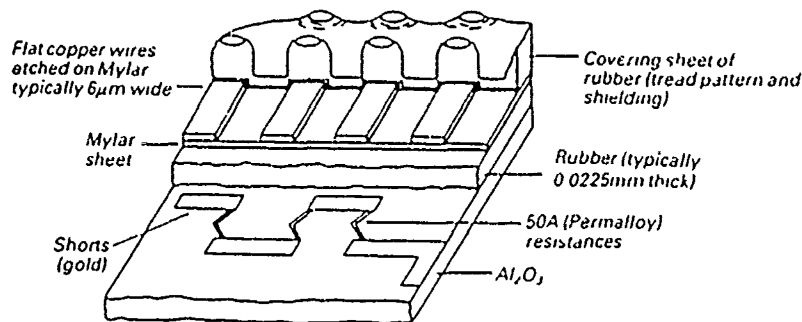

Figure 2.5. Magnetostrictive Tactile Sensor (129:100).

Vranish (129), Luo (70), and Hackwood (54). To demonstrate magnetostrictive devices, a typical magnetostrictive tactile sensor will be discussed.

J. M. Vranish of the National Bureau of Standards designed a magnetostrictive tactile sensor consisting of a thin-film magnetoresistive array with a 64 element sensor covering a 25 mm by 25 mm square, where the taxel spacing was 2.5 mm (129:110). All of the taxels were covered with a thin rubber sheet containing a row of flat wires which were etched on a Mylar film. Figure 2.5 illustrates the magnetostrictive sensor configuration. The distance between the wires and the taxels determined the ability to sense the deformation of the rubber, and thus, a load's shape and weight. By using the magnetoresistive material, the taxel detected small changes in the magnetic field surrounding the wires directly above it (129:100). Any deformation of the rubber sheet which caused a wire to move towards its corresponding taxel produced a change in the magnetic field at the taxel. Thus, the magnitude of the load applied was proportional to the magnetic field being measured (129:100).

This tactile sensor possessed characteristics which included a linear region of operation which spanned 30 N/m^2 to 3000 N/m^2 (or equivalent loads spanning 2 g to 200 g), and a resolution of 2.5 mm (129:108). The pressure range could be shifted to a higher operating range by increasing the rubber's stiffness, producing a pressure range spanning 2×10^4 N/m^2 to 2×10^6 N/m^2 (or equivalently 1.27 kg to 127 kg)(129:108).

By utilizing special coatings, such as the rubber sheets discussed above, magnetostrictive tactile sensors possess highly compliant properties, enabling the sensor to operate over a wide range of forces. Unfortunately, the membranes which provide this compliant property tend to diffuse the load shape's image, and this feature tends to reduce the sensor's overall shape resolution. Additionally, magnetostrictive taxels could potentially detect stray magnetic fields surrounding the tactile sensor, interfering with its operation (129:111).

Piezoresistive Tactile Sensors. A material which exhibits a change in electrical conductivity (or resistivity) based upon the amount of pressure applied to its surface is said to be piezoresistive. Piezoresistive tactile sensors incorporate this principle in the design of the sensor as the transducing material. Several piezoresistive designs have been pursued by Hillis (60), Eckerle (36), Podoloff (92: 93). Severwright (111), Sugiyama (115), Knittel (65), H. Allen (1), Roberston (102), and Tise (120).

Typically, piezoresistive tactile sensors are composed of a grid of piezoresistive components (92:42; 111:27). In some designs, the rows and columns themselves are fabricated from these elastic conductors, while in others, the piezoresistive material is incorporated into the substrate of the tactile sensor (92:42; 115:397). When an external force is applied to the grid, the resistance of the crosspoints in the array changes as a result of the deformation of the sensor's surface. By sequentially applying a voltage to each row and measuring the current output of each column. the resistance between the row trace and the column trace can be measured and related to the applied force (92:43; 115:397).

The piezoresistive tactile sensor illustrated in Figure 2.6 was fabricated by Susumu Sugiyama. Ken Kawahata. Masakazu Yoneda. and Isemi Igarashi of the Toyota Central Research and Development Laboratories, using a single-sided silicon processing technique to produce microdiaphragm pressure transducers on a silicon substrate (115:397). Since the entire structure of the sensor was planar. MOSFETs were incorporated into the integrated circuit design to provide taxel output selection along with an *in situ* multiplexer (115:397). This sensor incorporated a 32 by 32 element array of polysilicon piezoresistors. which had a spacing of 250 μm between discrete taxels. Each microdiaphragm size was 50 μm by 50 μm (115:398). This sensor possessed characteristics which included a

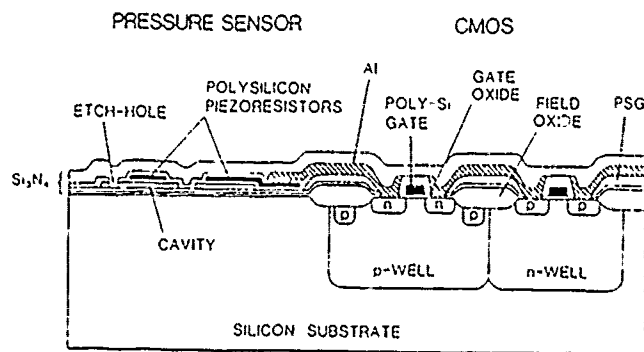

Figure 2.6. Tactile Sensor Utilizing Polysilicon As The Piezoresistive Element (115:397).

pressure sensitivity of 2 mV/kg $\cdot$ cm^2 (or an equivalent load sensitivity of 0.025 g), a resolution of 250 μm, and a 60 Hz bandwidth (115:399-400).

Piezoresistive tactile sensors have promise; however, they suffer from several problems which are inherent to piezoresistive materials. In particular, the transducer could exhibit fatigue due to stresses, which occur at material crosspoints where the piezoresistiv- material is located. (102:91-92).

Capacitive Tactile Sensors. Another technique which is useful for converting force information into an electrical signal is the measurement of the changes in capacitance across an electrode array. There are several research efforts in this particular field, including designs by Chun (25), Wolffenbuttel and Regtien (135; 136; 137), Seekircher (109), Boie (13; 14), Muller (81), and Suzuki (116; 117).

To construct a capacitive tactile sensor, the initial (undeflected) displacement between two parallel capacitor plates is measured, along with its corresponding capacitance. A sinusoidal driving voltage is then applied to the sensor, and it is switched to the appropriately selected, aluminum upper surface electrode. Then, the change in capacitance is measured after a load is applied. This information facilitates determining the degree of deflection bet een the parallel capacitor plates, and it can correspondingly be related to the applied force (109:317). Using a matrix electrode structure, the array can be scanned, permitting the arrangement of many capacitive taxels in a small area, because a capacitive transducer is formed at the intersections of the striped electrodes (109:317).

The capacitance, C_o, of a single element with no mechanical load (undeflected) will be equal to (136:144):

$$C_o = \frac{\epsilon_r \epsilon_0 A}{d_o} \qquad (2.1)$$

where ϵ_r is the relative permittivity of the dielectric material.
ϵ_0 is the permittivity of free space.
A is the electrode's area, and
d_o is the distance (undeflected) between the electrodes with no externally applied mechanical load.

With an applied load, the local deformation, $d_o - d = \Delta d$, will cause a change in capacitance equal to (136:144):

$$\Delta C = \epsilon_r \epsilon_0 A\left(\frac{1}{d_o - d} - \frac{1}{d_o}\right) = C_o\left(\frac{\Delta d}{d_o - \Delta d}\right) \qquad (2.2)$$

where C_o is the capacitance with no externally applied mechanical load,
ϵ_r is the relative permittivity of the dielectric material,
ϵ_0 is the permittivity of free space,
A is the electrode's area,
d_o is the distance (undeflected) between the electrodes with no externally applied mechanical load,
d is the distance between the electrodes with an externally applied mechanical load, and
Δd is $d_o - d$.

When $d \ll d_o$, Equation 2.2 becomes (136:144):

$$\Delta C \simeq \left(\frac{C_o}{d_o}\right)\Delta d \qquad (2.3)$$

where C_o is the capacitance with no externally applied mechanical load,
d_o is the distance (undeflected) between the electrodes with no externally applied mechanical load, and
Δd is $d_o - d$.

To illustrate a typical capacitive type tactile sensor, a design by K. Suzuki, N. Najafi, and K. D. Wise from the University of Michigan will be presented. Their

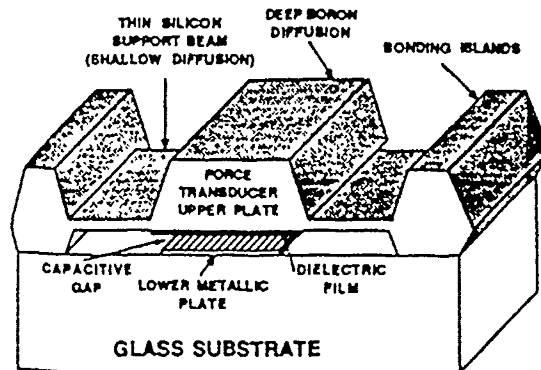

Figure 2.7. Side View Of A Capacitive Tactile Sensor Fabricated On A Silicon Substrate (116:675).

design consisted of a 32 by 32 element array configured on a silicon integrated circuit (116:674). The integrated circuit included *in situ* CMOS circuitry which provided a data acquisition system. The force-sensing capacitors are formed at the intersections of the etched metal lines arranged on a glass substrate in conjunction with highly doped (boron) silicon stripes. The glass substrate and each silicon strip were electrostatically bonded. Each silicon strip was physically isolated from adjacent rows of doped silicon to reduce coupling (116:674). Figure 2.7 illustrates the cross-section of one of the imaging cells.

Each of the transducer elements in the array possessed a capacitance of 0.22 pF when unloaded. This particular sensor was linear over a relatively small operating range from 0.025 g to a maximum load of 1 g. The taxel arrangement enabled this sensor to possess a resolution of 0.5 mm (116:676).

Capacitive tactile sensors can exploit current silicon IC fabrication processing technologies to incorporate large arrays on silicon substrates. They provide high resolution and typically operate over large load ranges; however, several problems, such as dielectric loss, dielectric stress due to overpressure, and parasitic capacitance effects must be solved before a completely successful capacitive tactile sensor is realized.

Optical Tactile Sensors. Optical tactile sensors utilize several transduction techniques to convert applied force into an electrical response. Typically, they

accomplish this by transducing force-induced variations in a propagating light's path into an electrical signal. For example, a change in the detected light after the application of a load corresponds to the strength of the electrical response. Several optical tactile sensor research efforts include those by Regtien and Wolffenbuttel (98), White (132; 133), Tsujimura (124), Schneiter (105), Rebman and Morris (96). Jenstrom, Emge and Chen (37; 61), Begej (10; 11), Kanade (62). Togai and Wang (121), Schoenwald (106). Tanie (119), Mott (80), and Winger (134).

One type of optical sensor design has been patented by Richard M. White. and it relies upon the frustration of internal reflections at a surface, which are caused by the contact between an object and an opaque elastic film which rests on the optical surface (133). A transparent plate is illuminated from one of its edges. and as much light as possible is confined in the interior of the plate using reflecting surfaces on the top and bottom surfaces. A thin elastic membrane is placed close to, but not touching the with the transparent surface (illustrated in Figure 2.8). When an object is pressed against the top of the elastic membrane, the membrane comes into contact with the transducing surface of the transparent plate and frustrates the internal reflections at the sites where contact has occurred. The degree of frustration can be detected by an array of optical sensors located next to the plate (133). The signals detected, correlated with their spatial location. provides information concerning the shape and size of the applied load. A similar effect may be observed by looking vertically into a glass of water and noting the disappearance of the "silver lining" wherever the outer surface of the glass is touched (133).

This concept has been incorporated into a tactile sensor developed by Stefan Begej of the Begej Corporation. The design consists of a fingertip shaped sensor and is illustrated in Figure 2.9 (11:481). The fingertip configuration possesses an optical array of 256 image detecting taxels. This sensor is able to detect normal forces between 0 and 400 g. has a resolution of 1 mm. possesses a frequency response up to 200 Hz, and is virtually immune to all electrical interference (11:481).

While optical transducers are impervious to electromagnetic interference. the optical detectors possess the potential for coupling between taxel signals. Also. extensive support and data processing resource requirements must be reduced to allow incorporation of this type of sensor into robotic technologies.

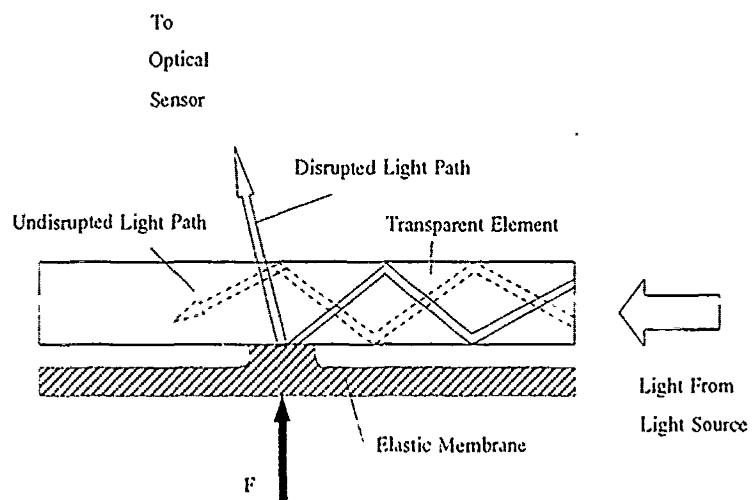

Figure 2.8. Schematic Of The Internal Reflection Tactile Sensor (133).

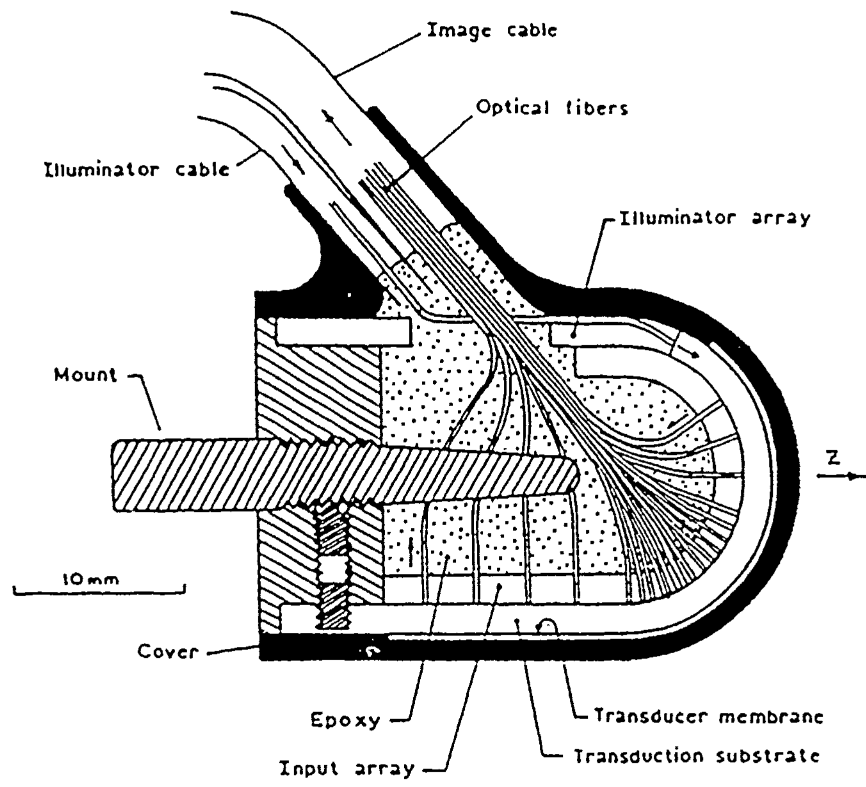

Figure 2.9. Cross-Sectional View Of The Fingertip Shaped, Internal Reflection Tactile Sensor (11:481).

Ultrasonic Tactile Sensors. Ultrasonic technology has been adapted to tactile sensing in a variety of ways. The study of object recognition and proximity sensing using ultrasonic waves provides a link in robotics between macroscopic motion and microscopic motion by providing essential feedback to the control system concerning the distance from an object and its size and shape. This method typically uses ultrasonic acoustic ranging with pulse-echo detection in air, with each object's echo being unique with respect to its shape, distance, and size. Proximity sensing has been studied by Kleinschmidt and Magori (64), Regtien and Hakkestaeegt (99), Borenstein (15), Moravec (79), Ueda (127), Marsh (74), M. Brown (18), Kuroda (67), Gehlbach (49), Miller (78), Tsujimura (124), Tone (122), Higuchi (59), and Schoenwald (107; 108). While proximity sensing is not direct touch sensing, it does represent a unique technology which has been adapted to the tactile sensing application.

Grahn (52), Fiorillo (44), Squire (113), Ermert (38), and Park (86) have developed methods for using piezoelectric materials in tactile sensors which utilize ultrasonic means to detect object size, shape, and weight information. These sensors typically use a pulse-echo ranging method to measure the change in the thickness of a compliant, elastic pad whose surface is deformed when an object is contacted (52:21-1). To demonstrate a typical ultrasonic tactile sensor, a design by Allen R. Grahn and Lynn Astle from Bonneville Scientific will be discussed (52:21-1).

The design consists of a metallized piezoelectric PVDF thin film material which has been etched on one surface to allow intimate contact between it and a metal electrode array (52:21-4). Figure 2.10 illustrates an early version of this sensor configuration. The array consists of a 4 by 4 matrix of metal electrodes. The most recent configuration of the sensor includes the 16-element array coupled to the piezoelectric PVDF film which is protected by a silicone rubber coating. The silicone rubber also acts as the ultrasonic wave transmission medium. This particular device possessed a resolution less than 0.5 mm, and a linear pressure range spanning 0.15 psi (0.013 g) to 300 psi (25 kg) (52:21-17).

The ultrasonic tactile sensors provide a robust and rugged device: however, the protective coating typically used to passivate the sensor and provide the transmission media for the ultrasonic waves deforms rapidly, resulting in unreliable responses to large loads. Also, the sensor possesses some degree of hysteresis as a

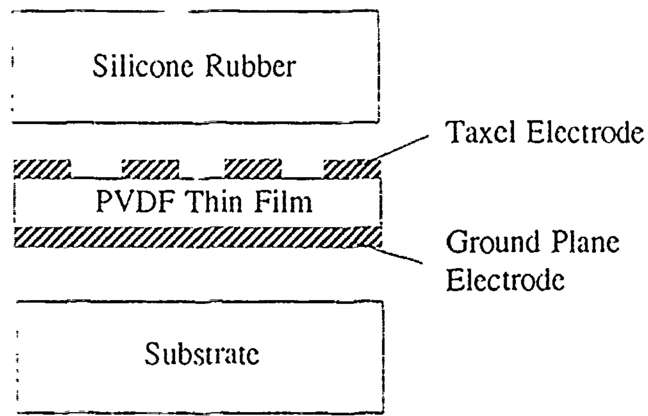

Figure 2.10. Cross-Sectional View Of An Ultrasonic Tactile Sensor Utilizing A Piezoelectric PVDF Film (52:21-5).

result of the material deformation recovery properties inherent in the silicone rubber used.

Piezoelectric Tactile Sensors. A piezoelectric tactile sensor is a device which detects the electrical charge generated by a piezoelectric material under pressure. When the geometry and material properties are considered, the resulting electrical signal can be related to the magnitude of the applied force. To implement a piezoelectric tactile sensor, a piezoelectric material is required to serve as the charge source; the specific material selection should be made to facilitate cost-effective sensor fabrication (55:4).

One of the first piezoelectric tactile sensors utilizing a semiconductor substrate was designed and patented by R. S. Muller in November 1967 (82). Several piezoelectric tactile sensors have since been developed including those by Dario (27; 28; 29; 30; 31), Lerch (69), Polla (94), Muller ((82; 83), Gao (47), Chen (23), Bardelli (7), Kolesar, Reston, Ford and Fitch (63), Patterson (87), Pedotti (89), Park (86), Brown (19), Ben'kova (12), Reston and Kolesar (101), Finch (43), Tzou (126), De Rossi (33; 34), Swartz (118), Barsky (8), Greeneich (53), Voorthuyzen (128) Assente (6), and Gerliczy (50). Related investigations of pyroelectric material properties and sensors include those by Muller (84), Münch (85), Mader (71), and Meixner (77).

One classic example of a piezoelectric tactile sensor developed by Paolo Dario and Danilo De Rossi at the University of Pisa incorporates the piezoelectric transducing properties of a polyvinylidene fluoride (PVDF) film. The piezoelectric PVDF thin film is used as the transducing mechanism by attaching it to a metal electrode array used to sample the charge generated on the surface of the sensor. The sensor replicates the human skin by incorporating epidermal and dermal layers of piezoelectric PVDF film, as illustrated in Figure 2.11. The authors indicate that this particular tactile sensor design can be adapted for use in either flat grippers or curved artificial fingers (28:50).

The sensor utilizes the epidermal layer to replicate the human skin receptor's ability to distinguish between cold and warm objects. The epidermal sensing elements are backed by a thin layer of flexible, resistive paint connected to a regulated power supply to raise the sensor's temperature to 37°C. When the tactile sensor contacts an object, heat flows from the resistive layer through the PVDF

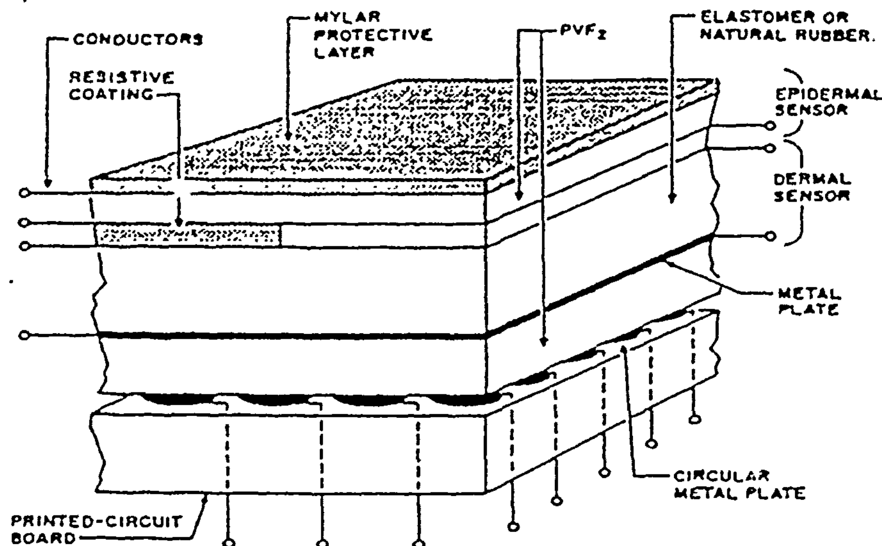

Figure 2.11. Tactile Sensor Utilizing Layered Piezoelectric PVDF Films (28:50).

epidermal layer to the object, which changes the temperature of the epidermal surface. The PVDF film, being a pyroelectric material, as well as a piezoelectric material, generates charge proportional to the change in temperature, enabling the sensor to detect the temperature of the object (28:50).

The dermal sensor array continuously measures the contact forces which are distributed over a relatively dense array of taxels. Its electrode array is configured to detect the geometrical features of objects, such as edges, corners, and depressions. Moreover, due to its location deep beneath the surface of the sensor, it possesses a small sensitivity to temperature variations, which establishes a temperature reference signal and enables the sensor to distinguish between thermal variations and pressure variations in the epidermal layer (28:51).

Another piezoelectric tactile sensor design exploits the piezoelectric properties of zinc oxide (ZnO) on a silicon substrate. The concept of utilizing materials which can be directly incorporated into the fabrication process of silicon integrated circuits is being pursued by D. L. Polla, W. T. Chang, R. S. Muller, and R. M. White at the University of California at Berkeley (94:133). The design consists of a

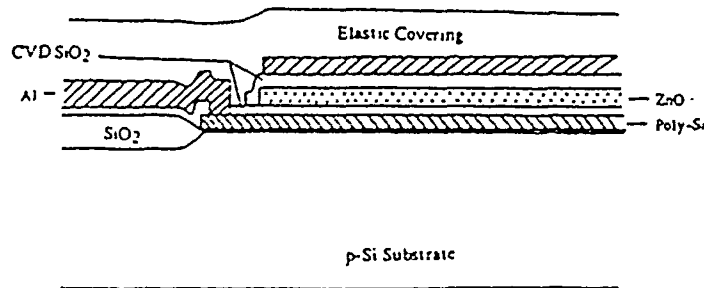

Figure 2.12. Piezoelectric Tactile Sensor Utilizing ZnO (94:135).

64-element tactile sensor array composed of 1.0 μm thick sputtered ZnO piezoelectric capacitors, each measuring 70 x 70 μm (Figure 2.12) (94:133). The entire array is protected with a 5 μm thick silicone elastic membrane coating. The charge generated by the piezoelectric effect in the ZnO is detected by MOSFET amplifiers. The amplifiers are NMOS transistors whose gate width is 66 μm, the gate length is 2 μm, and the resistive load is 1 kΩ (94:134).

This sensor detects a linear response range spanning 5 g to 100 g with little or no hysteresis; the output saturates at 350 g, and the surface of the sensor was damaged for loads exceeding 500 g (94:134). The resolution of the sensor was 70 μm.

Advantages of the piezoelectric tactile sensor include high durability, conformity, linearity, low hysteresis relative to a wide range of load forces (0.8 g to 76 g (100:6-1)), and high resolution (less than 1 mm) (90:185). However, some disadvantages include susceptibility to electromechanical interference, and rapid charge dissipation inhibiting the response of the sensor to static loads (90:185).

Conclusion

The wide variety of transducing techniques used for tactile sensors have been reviewed. Piezoresistive tactile sensors illustrated a technique for measuring differences in a material's resistance which correspond directly with the magnitude of an externally applied force. Unfortunately, the piezoresistive material's response is typically limited by the magnitude of the applied loads, restricting this transducing technology to a limited set of applications. Magnetostrictive

transducing was a novel way to determine changes in applied loads by measuring the change in a magnetic field using an electrode array: however, the magnetic membrane typically used in the tactile sensor diffuses and dampens the shape and weight of the applied load which results in lower resolution. Capacitive tactile sensors are easily incorporated into large arrays on silicon integrated circuits. but stray capacitance limits the reliability of the output signals. Optical tactile sensing methods are impervious to external electrical interference: however, the external instrumentation required to support the tactile sensors is extensive and will likely limit this technology in robotic applications. Ultrasonic tactile sensors are indeed rugged and robust devices. but the elastic membrane used to transmit the ultrasonic waves typically deforms under large stresses. thus compromising its sensing performance. The piezoelectric tactile sensor technology provides both an electrical force sensitive response and a temperature response. Admittedly. the susceptibility of piezoelectric tactile sensors to electrical interference and charge leakage potentially restricts this transduction design technique, but the advantages of simplicity in design, flexibility of material construction, and the ability to incorporate the design onto a silicon integrated circuit, all combined with temperature sensitivity, outweigh the disadvantages.

Before a detailed description of a piezoelectric tactile sensor can be developed. a theoretical background of the piezoelectric effect will be presented. In the next chapter. the piezoelectric theory. along with its interaction with the pyroelectric effect. will be discussed. Different piezoelectric materials will also be presented. illustrating the advances in material technology over the course of time.

III. Piezoelectric and Pyroelectric Phenomena

Introduction

Definition of Piezoelectricity and Pyroelectricity. Before a description of the piezoelectric phenomenon is developed, a definition of piezoelectricity is presented, along with a discussion of the various piezoelectric material properties. Walter Cady defined piezoelectricity as follows (20:1):

> A piezoelectric crystal may be defined as a crystal in which "electricity" or "electric polarity" is produced by pressure (more briefly, as one that becomes electrified on squeezing) or as one that becomes deformed when in an electric field. The first two definitions express the direct effect, while the third expresses the converse effect.

This definition states that piezoelectricity has two properties, the direct effect, that of transducing mechanical stress into an electric field, and the converse effect, that of transducing an electric field into a mechanical deformation of the material. For a material to be piezoelectric, the substance must exhibit both of these properties. Within a piezoelectric material, the polarity of the surface charge can be changed if the external force is applied in the opposite direction (76:14). For example, if the initial charge on the surface is positive while the external force is applied to "push on" the surface, a negative charge will be generated when the external force "pulls on" the surface. Similarly, the deformation of a piezoelectric material will occur with an externally applied electric field. If, for example, the material contracts under the application of an external electric field, it will expand correspondingly when the polarity of the electric field is reversed.

Piezoelectric materials exhibit various, interrelated phenomena occurring together or selectively in a material. One of these properties is called the pyroelectric effect. Pyroelectricity, as the name suggests, describes the ability of the material to generate charge on specific crystal surfaces in direct proportion to the external temperature (20:4). When the material is subjected to temperature variations, the internal strain of the material induces charge (and thus, a voltage potential) between its surfaces. Many piezoelectric materials exhibit significant pyroelectric effects.

Scope. To appreciate piezoelectric tactile sensors, the piezoelectric effect will be developed to include the inherent pyroelectric properties. To begin the discussion, a brief history of piezo- and pyroelectricity will be provided, beginning with the discovery of piezoelectricity in 1880, and its continued evolution which has resulted in new piezoelectric polymers that are being applied in a variety of practical technologies. Next, the critical theoretical issues will be developed, starting with a microscopic description of piezoelectricity using the dipole theory to illustrate how external forces affect the polarization of a piezoelectric material. Since the piezo- and pyroelectric properties of bulk materials are difficult to describe using a microscopic theory, a macroscopic description of the piezoelectric and pyroelectric effects will be presented, and the emphasis in this approach will focus on the concepts of stress and strain. An explanation describing how these two quantities interact to generate the charge within a piezoelectric material due to both an applied force and an external temperature gradient will be presented. Finally, a brief discussion of various piezoelectric materials will be presented, including Rochelle salt, quartz, barium titanate ($BaTiO_3$), and polyvinylidene fluoride (PVDF).

History of Piezoelectricity

In the early 18th century, Dutch merchants purchased tourmaline crystals from Ceylon. Europeans noticed a peculiar phenomenon associated with these crystals – when placed in hot ashes, the crystals attracted the ashes, and, as the crystals cooled, they repelled the ashes. This crystal was nicknamed the "Ceylon Magnet". In 1759, Lord Kelvin postulated the first scientific theory for this effect, and in 1824, Brewster experimented with tourmaline and Rochelle salt, which both exhibit this phenomenon, and he described them as *pyroelectric* (20:1).

In 1880, Jacques and Pierre Curie suspected a relationship between the pyroelectric phenomena and piezoelectricity. Several pyroelectric materials were selected as candidate piezoelectric specimens, and each material's piezoelectric properties were investigated. The Curies discovered that each crystal, when compressed in specific directions, generated a positive and negative charge on particular surfaces. They noticed that the amount of charge was proportional to the pressure, and that it dissipated when the pressure was removed. Also, they were able to predict the specific direction the pressure should be applied to

generate the charge, and to which crystal classes the effect was anticipated (20:2). In their paper describing the piezoelectric phenomenon, they stated (20:2-3):

> Those crystals having one or more axes whose ends are unlike have the special physical property of giving rise to two electric poles of opposite signs at the extremities of the axes when they are subjected to a change in temperature: this phenomena known under the name of *pyroelectricity*. We have found a new method for the development of polar electricity in these same crystals, which consists of subjecting them to variations in pressure along their hemihedral axes.

The converse piezoelectric effect was not observed by the Curie brothers: however, in the following year, Lippmann published a paper describing the application of thermodynamic principles to reversible processes involving electric quantities (20:4). He treated the special cases of pyroelectricity and piezoelectricity, asserting there should exist a converse phenomenon corresponding to each of these effects (20:4). The Curies experimentally verified the converse effect that same year (20:4).

Many theories developed during the ensuing years, and in 1910, a German crystallographer, Woldemar Voigt, wrote *Lehrbuch der Kristallphysik* (20:5). This monumental book developed a piezoelectric effect theory which combined the elements of crystallographic symmetry with elastic tensors and electric vectors. He clarified which of the 32 classes of crystals were piezoelectric, and he defined the piezoelectric constants for each of these classes (20:5). Subsequently, this book became the "bible" for scientists in this field, and today, it is recognized as the foundation of the macroscopic description of piezoelectricity (20:5).

During World War I, Langevin conceived the idea of electrically exciting a piece of quartz which was plated with electrodes to serve as an underwater acoustic wave emitter (20:5-6). When excited with a high frequency (HF) electric field, the quartz crystal generated HF sound waves (via the converse piezoelectric effect). The quartz could also be used (via the direct piezoelectric effect) to detect the reflected HF sound waves. This technology soon emerged as the method for locating immersed objects, such as submarines, and for exploring the ocean's

bottom. For the development of this application, Langevin became the founder of the field of *ultrasonics* (20:5).

Other piezoelectric experiments were undertaken during WWI. In 1918. Walter Cady used Rochelle salt crystal plates in underwater signaling. and examined the electrical behavior at frequencies close to the piezoelectric material's mechanical resonance (20:6). As a result of these experiments, Cady was able to develop the piezoelectric resonator. studying its various uses as a frequency stabilizer, oscillator, and filter. Cady first experimented with Rochelle salt; however, its material properties did not lend themselves well to a changing environment (hygroscopic effect). and quartz was soon found to be the most suitable material (20:6).

By World War II, quartz resonators revolutionized communications equipment. During the war, over 30 million quartz crystals were used in communications equipment. Because of the potential to deplete this natural resource, new piezoelectric materials were studied and developed. One of the materials discovered was barium titanate ($BaTiO_3$). This material was fabricated as a ceramic, rather than as a crystal. To make this ceramic piezoelectric, it was polled with a large electric field at a temperature just less than the material's Curie temperature. This process induced a change in the molecular structure's orientation such that the material formed macrosopic dipoles, and a subsequent macroscopic polarization when stressed (58:93). Other materials were developed during the 1950's in an effort to replace quartz in communications equipment. including synthetic crystals, such as ethylene diamine tartrate (EDT). lead zirconate titanate (PZT) and dipotassium tartrate (DKT) (75:78). The piezoelectric. as well as the pyroelectric. characteristics of each of these materials has been thoroughly exploited. enabling researchers to develop new transducers. including temperature. pressure. and chemical sensors.

Over the next few decades. several new materials were developed as cost effective alternatives to $BaTiO_3$, and in 1969. a radically new technology was discovered (51:1). That is. Kawai discovered and measured the piezoelectric effect in a polymer called polyvinylidene fluoride (PVDF). The prospect of using a thin polymer film as a piezoelectric or pyroelectric transducing material appealed to many scientists and engineers. In the past two decades, the ability to apply this polymer to numerous engineering applications has slowly increased; however. one

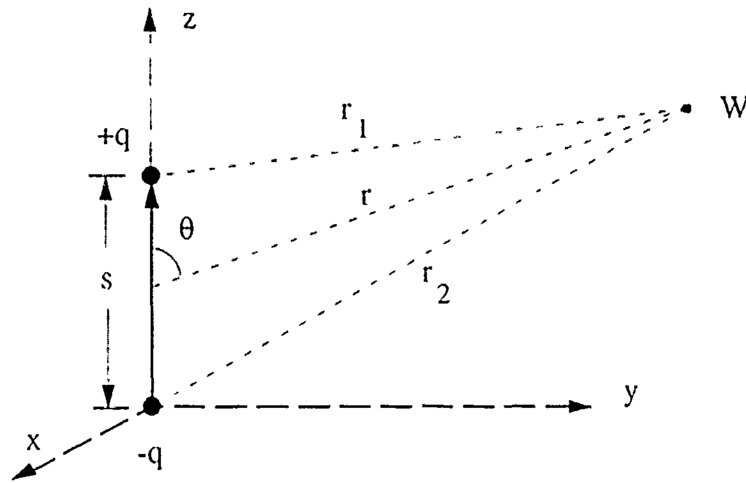

Figure 3.1. Spatial Configuration Of A Generalized Electric Dipole.

limitation associated with this particular piezoelectric polymer is its inability to generate and maintain sufficient charge when stressed (95:119). As a result of this limitation, thicker films have been developed which provide sufficient charge generation. These advances have made the piezoelectric PVDF thin films cost effective competitors with the piezoceramics as transducing materials (48:208).

Microscopic Description of Piezo- and Pyroelectricity

For simplicity, the piezoelectric and pyroelectric phenomena can initially be modelled by considering a microscopic-level dipole arrangement. The strain induced by an external force or a temperature gradient changes the orientation of the microscopic atomic dipoles within the material, and thus, the internal polarization of the material. This theoretical development will provide a background for the concepts of dielectric polarization and its relationship to polarization and piezo- and pyroelectric effects.

From fundamental electromagnetic theory, an electric dipole is an entity composed of two oppositely charged regions of equal magnitude (+q and -q) separated by a distance, s (Figure 3.1) (66:35). The potential (V_1) of the positive

charge (+q) measured at an arbitrary reference point W is (66:35):

$$V_1 = \frac{+qs}{4\pi\epsilon_r\epsilon_0 r_1^2} \tag{3.1}$$

where qs is the magnitude of the electric dipole moment (C-m).
ϵ_r is the relative permittivity of the medium (dimensionless).
ϵ_0 is the permittivity of free space (F/m), and
r_1 is the distance measured from the positive charge to point W (m).

The potential (V_2) of the negative charge (-q) at point W is (66:35):

$$V_2 = \frac{-qs}{4\pi\epsilon_r\epsilon_0 r_2^2} \tag{3.2}$$

where qs is the magnitude of the electric dipole moment (C-m).
ϵ_r is the relative permittivity of the medium (dimensionless),
ϵ_0 is the permittivity of free space (F/m), and
r_2 is the distance measured from the negative charge to point W (m).

The net potential (V) at point W is the linear superposition of the two potentials or (66:35):

$$V = \frac{qs}{4\pi\epsilon_r\epsilon_0}\left(\frac{1}{r_1} - \frac{1}{r_2}\right) \tag{3.3}$$

where qs is the magnitude of the electric dipole moment (C-m).
ϵ_r is the relative permittivity of the medium (dimensionless).
ϵ_0 is the permittivity of free space (F/m), and
r_1 and r_2 are the distances measured from the positive and negative charge, respectively, to point W (m).

If r is defined to be the distance measured from the center of the dipole to point W, then (66:36):

$$r_1 = r - \frac{s\cos\theta}{2} \tag{3.4}$$

and

$$r_2 = r + \frac{s\cos\theta}{2} \tag{3.5}$$

where r is the distance measured from the center of the dipole to point W (m).
s is the distance between charged particles (m), and
θ is the angle between the axis of the dipole and r.

Therefore, if point W is located a large distance away from the dipole (compared to the charge separation distance, s). then r is nearly parallel to r_1 and r_2, and the potential (V) at point W due to the dipole is (66:36):

$$V = \frac{qs}{4\pi\epsilon_r\epsilon_0 r^2}\cos\theta \qquad (3.6)$$

where qs is the magnitude of the electric dipole moment (C-m),
θ is the angle measured with respect to the z axis (degrees),
ϵ_r is the relative permittivity of the medium (dimensionless),
ϵ_0 is the permittivity of free space (F/m). and
r is the distance measured from the center of the dipole to point W (m).

By using the spherical coordinate system. a simple description of the electric field generated by the dipole arrangement can be developed. Using the center of the dipole as the center of the spherical coordinate system, the electric field can be found using $\mathbf{E} = -\nabla V$ or (66:35):

$$\mathbf{E} = \left(\frac{qs}{4\pi\epsilon_r\epsilon_0 r^3}\right)[\hat{r}2\cos\theta + \hat{\theta}\sin\theta] \qquad (3.7)$$

where qs is the magnitude of the electric dipole moment (C-m),
θ is the angle measured with respect to the z axis (degrees).
ϵ_r is the relative permittivity of the medium (dimensionless).
ϵ_0 is the permittivity of free space (F/m). and
r is the distance measured from the center of the dipole to point W (m).

However, many of the equations which describe piezoelectric materials use the rectangular coordinate system. Using the spherical coordinate system described in Figure 3.1. the electric field in rectangular coordinates is (91:2.6):

$$\mathbf{E} = \left(\frac{qs}{4\pi\epsilon_r\epsilon_0 r^3}\right)[\hat{x}3\cos\theta\sin\theta\sin\phi + \hat{y}3\cos\theta\sin\theta\cos\phi + \hat{z}3\cos^2\theta] \qquad (3.8)$$

where qs is the magnitude of the electric dipole moment (C-m).
θ is the angle measured with respect to the z-axis (degrees).
ϕ is the angle measured with respect to the x-axis (degrees).
ϵ_r is the relative permittivity of the medium (dimensionless).
ϵ_0 is the permittivity of free space (F/m). and
r is the distance measured from the center of the dipole to point W (m).

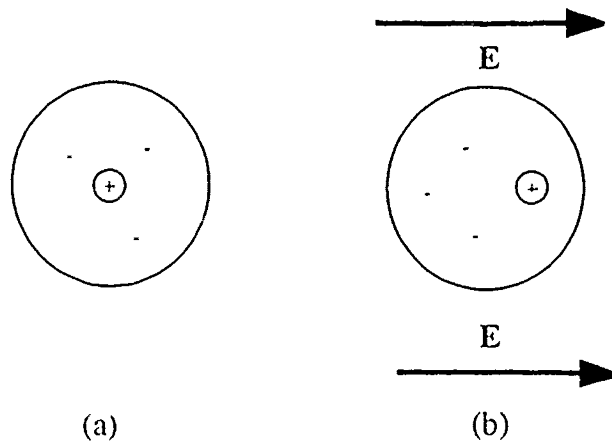

Figure 3.2. Model Of An Atom: (a) Without An External Electric Field Present. And (b) The Resulting Atomic Dipole After An External Electric Field E Is Applied (66:60).

When an ideal dielectric material is positioned in an externally applied electric field, there is no migration of charge; however, there is a slight displacement of the negative and positive charges in the atoms composing the dielectric material (66:59). As illustrated in Figure 3.2, each polarized atom can be modelled as an electric dipole, where the positive point charge represents the nucleus of the atom, and the negative point charge represents the electron cloud (66:59). In the absence of an externally applied electric field, the point charges do not form a dipole (Figure 3.2a); however, under the influence of an externally applied electric field, the positive and negative charges migrate slightly to form a dipole arrangement (Figure 3.2b).

An electric dipole moment vector, p, can be defined as the vector pointing from the negative to the positive charge with magnitude qs and in the direction of s (Figure 3.1). A polarization vector, P, can then correspondingly be defined as the dipole moment per unit volume (88:106):

$$\mathbf{P} = \lim_{\Delta v \to 0} \frac{\sum_i \mathbf{p}_i}{\Delta v} = \frac{\partial \mathbf{p}_i}{\partial v} \qquad (3.9)$$

where v is the volume, and
p is the dipole moment.

The polarization vector (P) and the externally applied electric field vector (E) can be related by the following Equation (88:111):

$$P = \epsilon_0 \chi_e E \tag{3.10}$$

where ϵ_0 is the permittivity of free space.
χ_e is the electric susceptibility (a scalar quantity), and
E is the externally applied electric field vector.

Unfortunately, since χ_e is a scalar quantity, Equation 3.10 is only true for homogeneous, isotropic, and linear materials. Piezoelectric materials are anisotropic, and consequently, the electric susceptibility is a tensor quantity. This tensor quantity will be referred to as χ_{es} to distinguish it from the scalar electric susceptibility χ_e. χ_{es} possesses nine terms which relate the three electric field vector components to the polarization vector components. Therefore, for piezoelectric materials, the polarization vector and the externally applied electric field vector are related as follows (131:178):

$$\begin{bmatrix} P_1 \\ P_2 \\ P_3 \end{bmatrix} = \epsilon_0 \begin{bmatrix} \chi_{11} & \chi_{12} & \chi_{13} \\ \chi_{21} & \chi_{22} & \chi_{23} \\ \chi_{31} & \chi_{32} & \chi_{33} \end{bmatrix} \begin{bmatrix} E_1 \\ E_2 \\ E_3 \end{bmatrix} . \tag{3.11}$$

In this format, P_1, P_2, and P_3 represent the polarization vector components in the x-, y-, and z-directions, respectively. The first subscript on the electric susceptibility tensor, χ_{es}, indicates the resulting polarization's direction, and the second subscript corresponds to the externally applied electric field vector's direction. Finally, E_1, E_2, and E_3 represent the electric field vector components in the x-, y-, and z-directions, respectively. A more compact representation can be expressed as:

$$P_E = \epsilon_0 \chi_{es} E \tag{3.12}$$

where P_E is the polarization vector resulting from an externally applied electric field vector.
ϵ_0 is the permittivity of free space.
χ_{es} is the electric susceptibility tensor, and
E is the externally applied electric field vector.

Piezoelectric materials, being dielectrics themselves, can be described by the above equations; additionally, they possess properties which can be related to the external forces applied to them. According to Walter Cady, if a crystal is not piezoelectric, the crystal possesses a center of inversion which maintains a symmetrical charge distribution even under stress, and hence, a net polarization state is not produced (20:11). Figure 3.3 illustrates a planar distribution of charges where, in the plane, the polarization is equal to zero. If a force, **F**, is applied in this plane, the crystal distorts, but the charges within the crystal maintain a symmetrical physical arrangement, and thus do not produce a polarization. However, if the material is piezoelectric, the crystal develops an internal polarization state because its crystal class lacks a center of inversion, and consequently, the external forces distort the crystal symmetry (Figure 3.4) (20:11). To illustrate the generation of a polarization vector resulting from an externally applied force, a crystal with trigonal symmetry will be analyzed (Figure 3.5). With no external forces applied, the net polarization within the structure is zero, and it is illustrated in Figure 3.5a. However, as illustrated in Figure 3.5b, when a sufficiently large force is applied to the external surface of the crystal, it causes a slight distortion of the crystal lattice. This distortion changes the angle between the charges, creating a net polarization in the y-direction, such that:

$$\mathbf{P} = \mathbf{p}_1 + \mathbf{p}_2 + \mathbf{p}_3. \tag{3.13}$$

Using rectangular coordinates, and with the distance between charges (l) defined as one unit length, then:

$$\mathbf{p}_1 = q(0.0\hat{x} + 1.0\hat{y}) \tag{3.14}$$

$$\mathbf{p}_2 = q(0.91\hat{x} - 0.42\hat{y}) \tag{3.15}$$

$$\mathbf{p}_3 = q(-0.91\hat{x} - 0.42\hat{y}). \tag{3.16}$$

yielding a net polarization of:

$$\mathbf{P} = q(0.0\hat{x} + 0.16\hat{y}). \tag{3.17}$$

A similar distorting effect occurs when the piezoelectric material is subjected to an externally applied electric field.

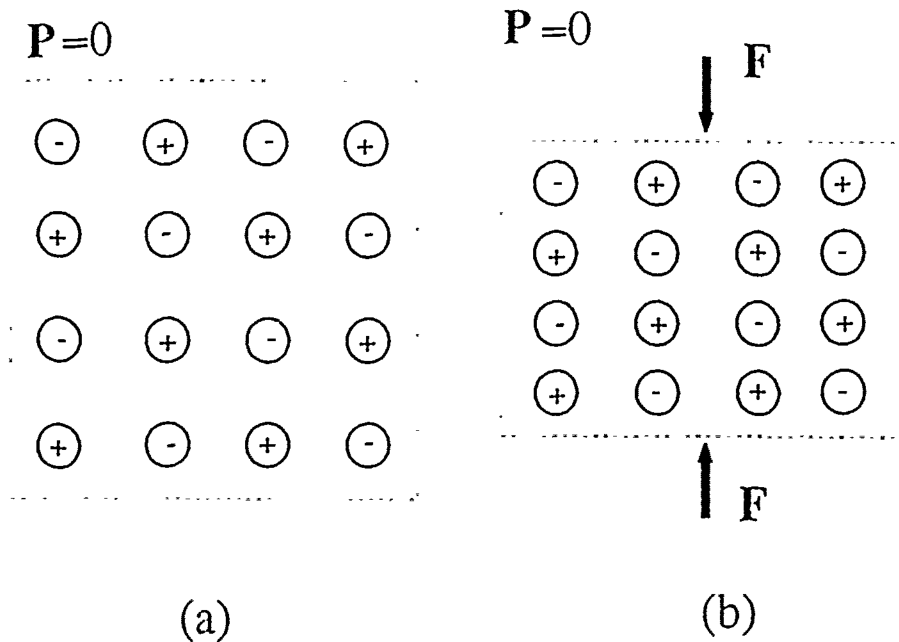

Figure 3.3. Crystal With A Center Of Inversion (a) Before The Application Of A Force And (b) After The Application Of A Force.

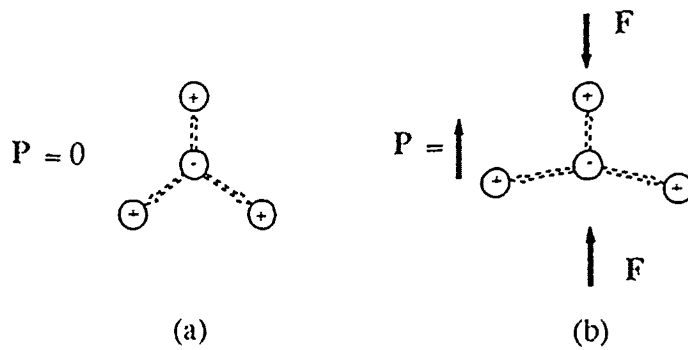

Figure 3.4. Crystal Without A Center Of Inversion (a) Before The Application Of A Force And (b) After The Application Of A Force.

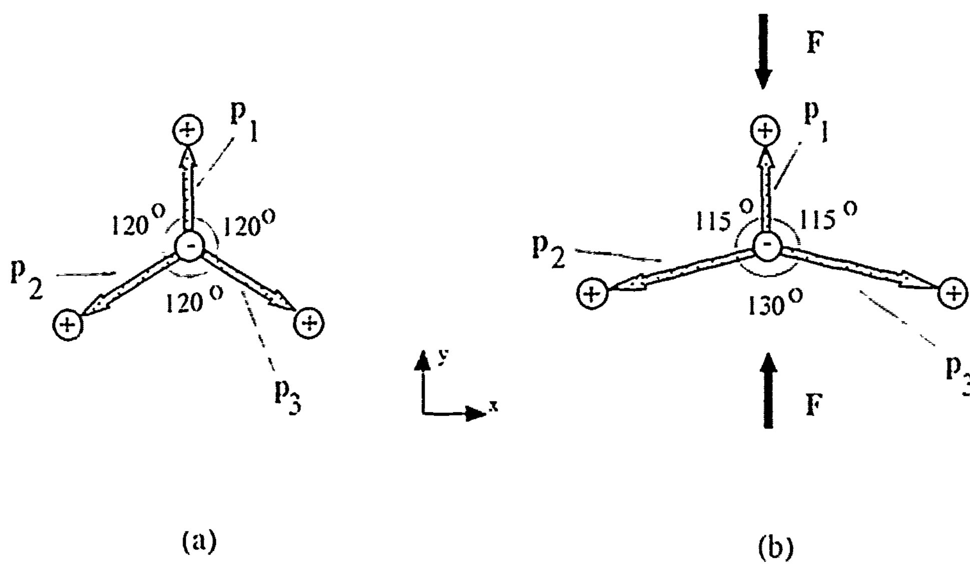

Figure 3.5. Example Of A Crystal With Trigonal Symmetry (a) Before The Application Of A Force And (b) After The Application Of A Force.

Unfortunately, the microscopic dipole theory tends to be unwieldy when an attempt is made to describe macroscopic piezoelectric crystals and their relationship to externally applied forces. Therefore, the development of an alternative description of the piezoelectric phenomenon is in order – the macroscopic description. In the textbook *Piezoelectricity*, Walter Cady illustrated the difficulty in using the microscopic theory to describe the piezoelectric phenomenon (20:731):

> In spite of the fact that molecular or atomic theories of piezoelectricity began to appear very soon after the Curies discovery, a satisfactory theoretical treatment of the phenomenon can hardly be said to have passed the initial stages. The resources of modern lattice dynamics are still unequal to the task of predicting anything better than a rough approach to the order of magnitude of the piezoelectric effect, even for the simplest structures.

Macroscopic Description of Piezo- and Pyroelectricity

In 1910, Woldemar Voigt developed a method for describing and analyzing piezo- and pyroelectricity (20:4). This method depends signincantly upon the mechanical engineering concepts of stress and strain, and relates them to the material's internal polarization. These relationships form the foundation for a macroscopic description of the piezo- and pyroelectric phenomena. To develop this theory, a brief review of stress and strain will be presented, and then, the evolution of the piezo- and pyroelectric equations will be discussed. The direct piezoelectric effect requires that mechanical energy can be proportionately converted to electrical energy, and the converse piezoelectric effect describes the inverse process (20:4). Stresses, strains, and piezoelectric constants determine how the energy is converted.

Voigt's system of designation relates the electric field and polarization vectors to stress and strain vectors. His system uses a rectangular coordinate system where the x-, y-, and z-directions are designated by the digits 1, 2, and 3, respectively. Elastic compliance coefficients, stiffness coefficients, electric susceptibilities, and piezoelectric constants are double subscripted to indicate directions, where the first subscript identifies the resulting direction, and the second subscript identifies the

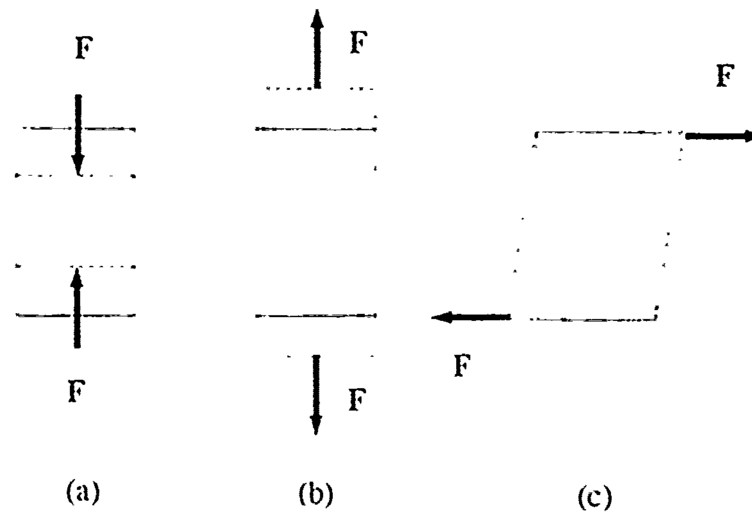

Figure 3.6. Stress System: (a) Compressional Stress. (b) Extensional Stress. And (c) Shear Stress.

impressed force's direction. Stresses. strains. electric fields and polarizations are identified with a single numerical subscript to identify the applicable rectangular coordinate system axis (91:2.11).

Stress and Strain. Stress is defined as the force per unit area or the change in force per unit area change (5:2). and it is a tensor quantity composed of one or more pairs of equal and opposite forces per unit area (20:45). Stress consists of two components: normal stress. which acts perpendicular to a given surface (also referred to as extensional and compressional). and shear stress. which acts parallel to a given surface (5:2). Each of these stresses is illustrated in Figure 3.6. The notation used to describe the stress system can be conveniently depicted using the rectangular coordinate system in Figure 3.7. compressional and extensional stress. and X_y. X_z. Y_x. Y_z. Z_x. and Z_y are used to denote the shear stresses. where the direction of the applied force is identified by the upper case letter. and the subscript defines the direction of the normal to the surface upon which the force acts (20:47).

Consider an infinitesimally small rectangular parallelepiped with edges dx. dy. and dz parallel to the coordinate axes. and depicted in Figure 3.8. Since the parallelepiped is small. the forces acting on it can be thought of as uniform. and

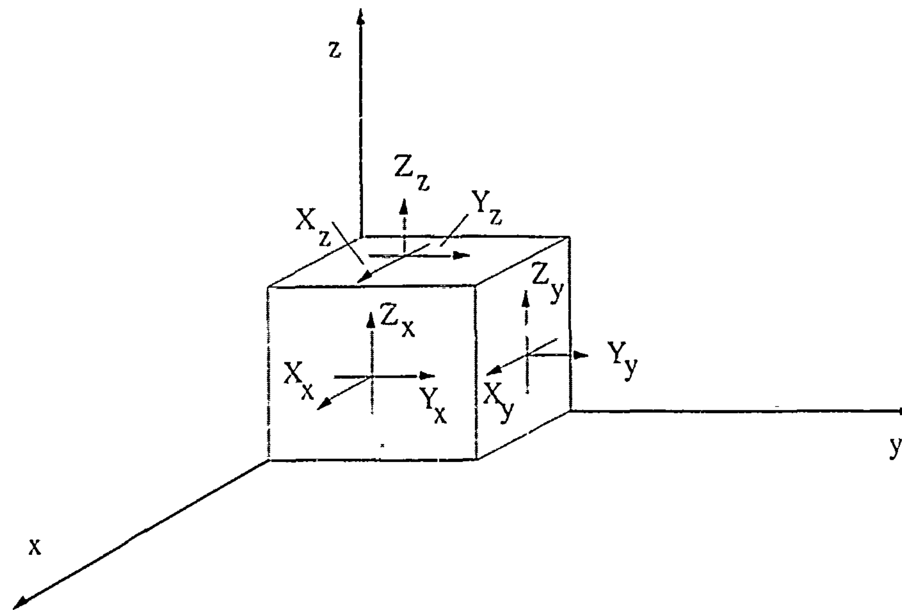

Figure 3.7. Stress Directions.

represented as the average of the loads applied in the center of their areas of application (35:12). If the forces per unit volume resisting the external application of force are designated by R, S, and T (and correspond to the forces per unit volume in the x-, y-, and z-directions, respectively), then the following equations apply (35:12):

$$\sum F_x = 0 \tag{3.18}$$

$$\sum F_y = 0 \tag{3.19}$$

$$\sum F_z = 0 \tag{3.20}$$

$$\sum M_x = 0 \tag{3.21}$$

$$\sum M_y = 0 \tag{3.22}$$

$$\sum M_z = 0 \tag{3.23}$$

where F_x are the forces in the x-direction,
F_y are the forces in the y-direction,
F_z are the forces in the z-direction,

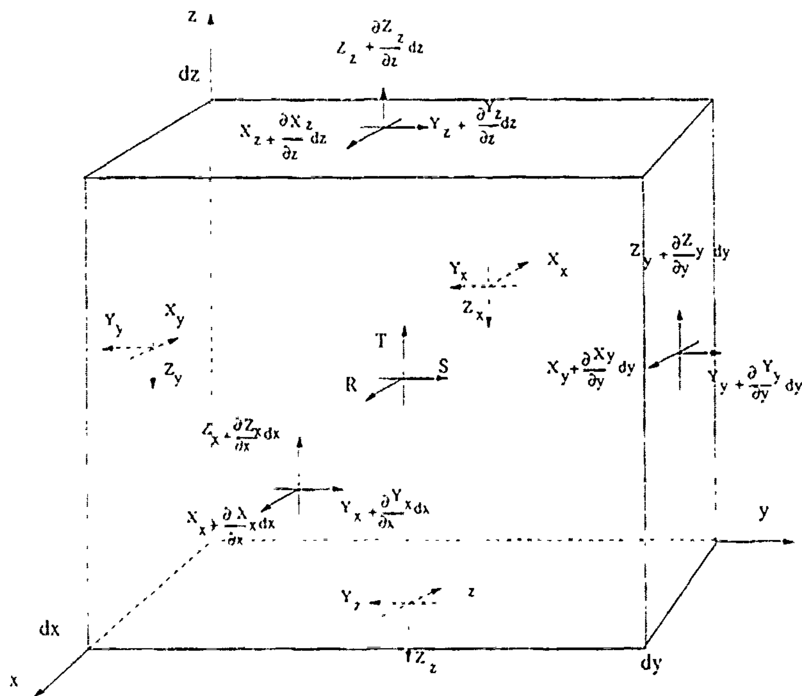

Figure 3.8. Small Parallelepiped Used To Establish The Equations Of Equilibrium.

M_x are the moments whose axis is parallel to the x-direction,
M_y are the moments whose axis is parallel to the y-direction, and
M_z are the moments whose axis is parallel to the z-direction.

(35:12):

$$\begin{aligned}\sum F_x &= (X_x + \frac{\partial X_x}{\partial x} dx)\,dz - X_x\,dy\,dz \\ &+(X_y + \frac{\partial X_y}{\partial y} dy)\,dx\,dz - X_y\,dx\,dz \\ &+(X_z + \frac{\partial X_z}{\partial z} dz)\,dx\,dy - X_z\,dx\,dy \\ &+R\,dx\,dy\,dz = 0.\end{aligned} \tag{3.24}$$

Equations for F_y and F_z can be found in a similar manner. After canceling terms and dividing by dx dy dz, the following equations are found (35:13):

$$\frac{\partial X_x}{\partial x} + \frac{\partial X_y}{\partial y} + \frac{\partial X_z}{\partial z} + R = 0 \tag{3.25}$$

$$\frac{\partial Y_x}{\partial x} + \frac{\partial Y_y}{\partial y} + \frac{\partial Y_z}{\partial z} + S = 0 \tag{3.26}$$

$$\frac{\partial Z_x}{\partial x} + \frac{\partial Z_y}{\partial y} + \frac{\partial Z_z}{\partial z} + T = 0. \tag{3.27}$$

These equations describe the applied forces per unit area of the parallelepiped. and they apply throughout the entire structure of the material (35:13).

Since the parallelepiped is in equilibrium, then Equation 3.21 becomes (35:13):

$$\begin{aligned}\sum M_x &= Z_y\,dx\,dz\,dy/2 + (Z_y + \frac{\partial Z_y}{\partial y} dy)\,dx\,dz\,dy/2 \\ &-Y_z\,dx\,dy\,dz/2 - (Y_z + \frac{\partial Y_z}{\partial z} dz)\,dx\,dy\,dz/2 = 0.\end{aligned} \tag{3.28}$$

The equations for the moments about the y- and z-axes can be found in a similar manner. Equation 3.28 becomes (35:13):

$$Z_y + \frac{\partial Z_y}{\partial y} dy/2 - Y_z - \frac{\partial Y_z}{\partial z} dz/2 = 0. \qquad (3.29)$$

Since the parallelepiped is small, the terms involving the differentials can be neglected as compared to the terms Z_y and Y_z, and (35:13):

$$Z_y = Y_z \qquad (3.30)$$

where Z_y is the shear stress in the z-direction along the plane whose normal is in the y-direction, and
Y_z is the shear stress in the y-direction along the plane whose normal is in the z-direction.

In a similar manner, the remaining moment equations give the following results: $X_y = Y_x$, and $X_z = Z_x$, which simplify the mathematical representation that describes the stress system (35:14). A common way to represent the six remaining stress components is to use the X_i notation, where i is an integer ranging from 1 to 6. Hence, $X_1 = X_x$ is the normal stress in the x-direction; $X_2 = Y_y$ is the normal stress in the y-direction; $X_3 = Z_z$ is the normal stress in the z-direction. Since the shear stresses are in equilibrium, $X_4 = Y_z = Z_y$, $X_5 = X_z = Z_x$, and $X_6 = X_y = Y_x$ (20:47).

Strain is defined as the deformation which a body undergoes during stress (5:8). For example, if a block is acted upon by a force (**F**), any subsequent deformation is regarded as the induced strain. Similar to stress, there are two types of strain, normal and shear. Normal strain is defined as the ratio of the deformation of the material, δ, to the original length of the material, L, or $\frac{\delta}{L}$, as illustrated in Figure 3.9a (5:9). Shear strain is defined as a force acting parallel to the surface of the object. For example, during the application of a shearing force, a small angle of deflection, denoted by γ, is formed. The shear strain, at small deflection angles, can be approximated by $\gamma = \tan\gamma = \frac{\delta}{L}$ (Figure 3.9b) (5:9).

Similar to the stress system, the strain system is described by six components, x_x, y_y, z_z, y_z, z_x, and x_y (20:47). In this notation, x_x, y_y, and z_z are the extensional or compressional strain components (positive for extensional and negative for

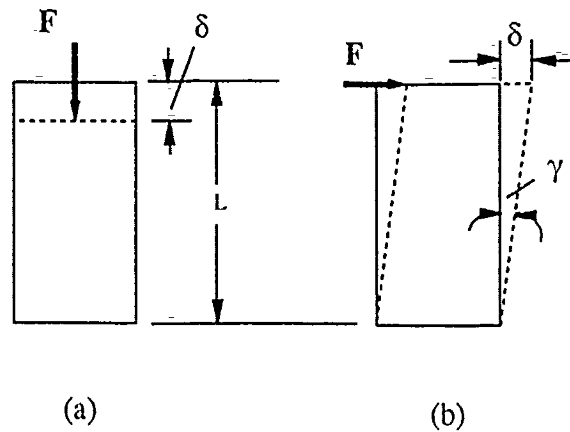

Figure 3.9. Two Types Of Strain: (a) Normal, And (b) Shear (5:9).

compressional), and y_z, z_x, and x_y are the shearing strain components (20:47). To simplify the mathematical representation of strain, the x_i notation is commonly used, where i is an integer ranging from 1 to 6, and hence $x_1 = x_x$, $x_2 = y_y$, $x_3 = z_z$, $x_4 = y_z$, $x_5 = z_x$, and $x_6 = x_y$ (20:47). Strains can be related to displacements as follows: if the undisturbed coordinates of a point are x, y, and z, and u, v, and w describe the displacement of this point as the result of strain, the new coordinates of the point are (x + u), (y + v), and (z + w). Figure 3.10 illustrates the effect of positive strains occurring in the x-, y-, and z-directions. Consequently (20:273):

$$x_1 = \frac{\partial u}{\partial x} \tag{3.31}$$

$$x_2 = \frac{\partial v}{\partial y} \tag{3.32}$$

$$x_3 = \frac{\partial w}{\partial z} \tag{3.33}$$

$$x_4 = \frac{\partial w}{\partial y} + \frac{\partial v}{\partial z} \tag{3.34}$$

$$x_5 = \frac{\partial u}{\partial z} + \frac{\partial w}{\partial x} \tag{3.35}$$

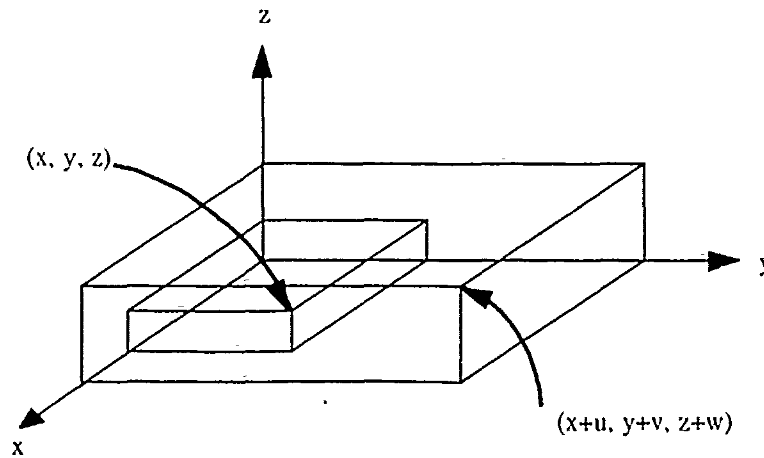

Figure 3.10. Strains In The x-, y-, And z-Directions (91:2.16).

$$x_6 = \frac{\partial v}{\partial x} + \frac{\partial u}{\partial y}. \tag{3.36}$$

Stress and strain can be related by Hooke's Law. That is (20:49):

$$X_1 = c_{11}x_1 + c_{12}x_2 + c_{13}x_3 + c_{14}x_4 + c_{15}x_5 + c_{16}x_6 \tag{3.37}$$
$$X_2 = c_{21}x_1 + c_{22}x_2 + c_{23}x_3 + c_{24}x_4 + c_{25}x_5 + c_{26}x_6 \tag{3.38}$$
$$X_3 = c_{31}x_1 + c_{32}x_2 + c_{33}x_3 + c_{34}x_4 + c_{35}x_5 + c_{36}x_6 \tag{3.39}$$
$$X_4 = c_{41}x_1 + c_{42}x_2 + c_{43}x_3 + c_{44}x_4 + c_{45}x_5 + c_{46}x_6 \tag{3.40}$$
$$X_5 = c_{51}x_1 + c_{52}x_2 + c_{53}x_3 + c_{54}x_4 + c_{55}x_5 + c_{56}x_6 \tag{3.41}$$
$$X_6 = c_{61}x_1 + c_{62}x_2 + c_{63}x_3 + c_{64}x_4 + c_{65}x_5 + c_{66}x_6. \tag{3.42}$$

where c_{11}, c_{12}, etc. are the stiffness coefficients, and the first subscript corresponds to the resulting stress component's direction, and the second subscript corresponds to the induced strain component's direction. In equivalent matrix notation,

$$\begin{bmatrix} X_1 \\ X_2 \\ X_3 \\ X_4 \\ X_5 \\ X_6 \end{bmatrix} = \begin{bmatrix} c_{11} & c_{12} & c_{13} & c_{14} & c_{15} & c_{16} \\ c_{21} & c_{22} & c_{23} & c_{24} & c_{25} & c_{26} \\ c_{31} & c_{32} & c_{33} & c_{34} & c_{35} & c_{36} \\ c_{41} & c_{42} & c_{43} & c_{44} & c_{45} & c_{46} \\ c_{51} & c_{52} & c_{53} & c_{54} & c_{55} & c_{56} \\ c_{61} & c_{62} & c_{63} & c_{64} & c_{65} & c_{66} \end{bmatrix} \begin{bmatrix} x_1 \\ x_2 \\ x_3 \\ x_4 \\ x_5 \\ x_6 \end{bmatrix} . \tag{3.43}$$

In vector notation, equation 3.43 becomes:

$$X_{strain} = cx \tag{3.44}$$

where X_{strain} is the stress vector resulting from an applied strain vector,
c is the stiffness coefficient, and
x is the strain vector.

Similarly, strain can be defined as (20:49):

$$x_1 = s_{11}X_1 + s_{12}X_2 + s_{13}X_3 + s_{14}X_4 + s_{15}X_5 + s_{16}X_6 \tag{3.45}$$
$$x_2 = s_{21}X_1 + s_{22}X_2 + s_{23}X_3 + s_{24}X_4 + s_{25}X_5 + s_{26}X_6 \tag{3.46}$$
$$x_3 = s_{31}X_1 + s_{32}X_2 + s_{33}X_3 + s_{34}X_4 + s_{35}X_5 + s_{36}X_6 \tag{3.47}$$
$$x_4 = s_{41}X_1 + s_{42}X_2 + s_{43}X_3 + s_{44}X_4 + s_{45}X_5 + s_{46}X_6 \tag{3.48}$$
$$x_5 = s_{51}X_1 + s_{52}X_2 + s_{53}X_3 + s_{54}X_4 + s_{55}X_5 + s_{56}X_6 \tag{3.49}$$
$$x_6 = s_{61}X_1 + s_{62}X_2 + s_{63}X_3 + s_{64}X_4 + s_{65}X_5 + s_{66}X_6 \tag{3.50}$$

where s_{11}, s_{12}, etc. are the compliance coefficients, and each provide a relationship between an imposed stress vector, X, and the resulting strain vector, x. The first subscript corresponds to the resulting strain component's direction, and the second subscript corresponds to the applied stress component's direction. In vector notation,

$$x_{stress} = sX \tag{3.51}$$

where x_{stress} is the strain vector resulting from an applied stress vector,
s is the compliance coefficient, and
X is the applied stress vector.

Piezoelectric Equations. While the stress and strain relationships developed above are valid for both piezoelectric and non-piezoelectric materials, piezo- and pyroelectric effects must be modelled using additional relationships. These equations will describe the generation of the polarization, strain, or electric field induced within a piezoelectric material due to an externally applied stress or electric field.

The converse piezoelectric effect can be described by considering a material which is positioned in an externally applied **E** field (with the applied strain equal to zero) and developing a relation to express the resulting stress. That is (20:187):

$$X_1 = e_{11}E_1 + e_{12}E_2 + e_{13}E_3 \quad (3.52)$$
$$X_2 = e_{21}E_1 + e_{22}E_2 + e_{23}E_3 \quad (3.53)$$
$$X_3 = e_{31}E_1 + e_{32}E_2 + e_{33}E_3 \quad (3.54)$$
$$X_4 = e_{41}E_1 + e_{42}E_2 + e_{43}E_3 \quad (3.55)$$
$$X_5 = e_{51}E_1 + e_{52}E_2 + e_{53}E_3 \quad (3.56)$$
$$X_6 = e_{61}E_1 + e_{62}E_2 + e_{63}E_3. \quad (3.57)$$

The electric field components E_1, E_2, and E_3 only possesses three degrees of freedom and correspond to the x-, y-, and z-directions, respectively. Correspondingly, e_{11}, e_{12}, etc. are the piezoelectric stress coefficients, where the first subscript corresponds to the resulting stress component's direction, and the second subscript corresponds to the induced electric field component's direction. In vector notation,

$$X_{E-field} = eE \quad (3.58)$$

where $X_{E-field}$ is the resulting stress vector when the applied strain vector equals zero,
e is the piezoelectric stress coefficient, and
E is the applied electric field vector.

The strain resulting from an externally applied electric field can be described by (20:188):

$$x_1 = d_{11}E_1 + d_{12}E_2 + d_{13}E_3 \quad (3.59)$$
$$x_2 = d_{21}E_1 + d_{22}E_2 + d_{23}E_3 \quad (3.60)$$
$$x_3 = d_{31}E_1 + d_{32}E_2 + d_{33}E_3 \quad (3.61)$$
$$x_4 = d_{41}E_1 + d_{42}E_2 + d_{43}E_3 \quad (3.62)$$
$$x_5 = d_{51}E_1 + d_{52}E_2 + d_{53}E_3 \quad (3.63)$$
$$x_6 = d_{61}E_1 + d_{62}E_2 + d_{63}E_3. \quad (3.64)$$

where d_{11}, d_{12}, etc. are called piezoelectric strain coefficients, and the first subscript corresponds to the resulting strain component's direction, and the second subscript corresponds to the induced electric field component's direction. In vector notation,

$$x_{E-field} = dE \quad (3.65)$$

where $x_{E-field}$ is the resulting strain vector when the applied stress vector equals zero,
d is the piezoelectric strain coefficient, and
E is the externally applied electric field vector.

To determine the overall stress resulting from both a strain and an electric field, the linear superposition of Equation 3.44 and Equation 3.58 becomes (20:185):

$$X = X_{strain} + X_{E-field} \quad (3.66)$$

or

$$X = cx - eE \quad (3.67)$$

where X is the resulting stress vector.
c is the stiffness coefficient.
x is the applied strain vector.
e is the piezoelectric stress coefficient, and
E is the externally applied electric field vector.

The overall strain can be found from the linear superposition of Equations 3.51 and 3.65 (20:185):

$$x = x_{stress} + x_{E-field} \quad (3.68)$$

or

$$x = sX + dE \tag{3.69}$$

where x is the resulting strain vector,
s is the compliance coefficient,
X is the applied stress vector,
d is the piezoelectric strain coefficient, and
E is the externally applied electric field vector.

To describe the direct effect, the polarization due to an externally applied stress or strain will be discussed. When an external stress is applied to the piezoelectric material (assuming the electric field is zero), the following scalar equations describe the system (20:187):

$$P_1 = d_{11}X_1 + d_{12}X_2 + d_{13}X_3 + d_{14}X_4 + d_{15}X_5 + d_{16}X_6 \tag{3.70}$$
$$P_2 = d_{21}X_1 + d_{22}X_2 + d_{23}X_3 + d_{24}X_4 + d_{25}X_5 + d_{26}X_6 \tag{3.71}$$
$$P_3 = d_{31}X_1 + d_{32}X_2 + d_{33}X_3 + d_{34}X_4 + d_{35}X_5 + d_{36}X_6. \tag{3.72}$$

The polarization, P_1, P_2, and P_3 only possesses three degrees of freedom, and they correspond to the x-, y-, and z-directions, respectively. In vector notation,

$$P_{stress} = dX, \tag{3.73}$$

where P_{stress} is the polarization vector due to stress when the externally applied electric field vector is zero,
d is the piezoelectric strain coefficient, and
X is the applied stress vector.

The polarization vector resulting from an applied strain, in the absence an externally applied electric field, is (20:187):

$$P_1 = e_{11}x_1 + e_{12}x_2 + e_{13}x_3 + e_{14}x_4 + e_{15}x_5 + e_{16}x_6 \tag{3.74}$$
$$P_2 = e_{21}x_1 + e_{22}x_2 + e_{23}x_3 + e_{24}x_4 + e_{25}x_5 + e_{26}x_6 \tag{3.75}$$
$$P_3 = e_{31}x_1 + e_{32}x_2 + e_{33}x_3 + e_{34}x_4 + e_{35}x_5 + e_{36}x_6. \tag{3.76}$$

In vector notation,

$$\mathbf{P}_{\mathbf{strain}} = \mathbf{e}\mathbf{x}, \tag{3.77}$$

where $\mathbf{P}_{\mathbf{strain}}$ is the polarization vector due to an applied strain when the externally applied electric field vector is zero,
e is the piezoelectric stress coefficient, and
$\mathbf{x}$ is the applied strain vector.

As a result of an externally applied electric field and an externally applied stress, the polarization becomes (using Equations 3.12 and 3.73) (20:183):

$$\mathbf{P}_{\mathbf{piezo-1}} = \mathbf{P}_{\mathbf{E-field}} + \mathbf{P}_{\mathbf{stress}} \tag{3.78}$$

or

$$\mathbf{P}_{\mathbf{piezo-1}} = \chi_{\mathbf{stress}}\mathbf{E} + \mathbf{d}\mathbf{X} \tag{3.79}$$

where $\mathbf{P}_{\mathbf{piezo-1}}$ is the resulting polarization vector due to an externally applied electric field vector and an applied stress,
$\chi_{\mathbf{stress}}$ is the dielectric susceptibility tensor neglecting effects of the applied stress,
$\mathbf{E}$ is the externally applied electric field vector,
d is the piezoelectric strain coefficient, and
$\mathbf{X}$ is the applied stress vector.

The direct effect can also be described by relating an externally applied electric field and strain (defined by Equations 3.12 and 3.77) (20:183):

$$\mathbf{P}_{\mathbf{piezo-2}} = \mathbf{P}_{\mathbf{E-field}} + \mathbf{P}_{\mathbf{strain}} \tag{3.80}$$

or

$$\mathbf{P}_{\mathbf{piezo-2}} = \chi_{\mathbf{strain}}\mathbf{E} + \mathbf{e}\mathbf{x} \tag{3.81}$$

where $\mathbf{P}_{\mathbf{piezo-2}}$ is the resulting polarization vector due to an externally applied electric field vector and an applied strain vector,
$\chi_{\mathbf{strain}}$ is the dielectric susceptibility tensor neglecting effects of the applied

strain,

E is the externally applied electric field vector,

e is the piezoelectric stress coefficient, and

x is the applied strain vector.

To find the electric field, strain, or stress generated by an applied strain, stress, or polarization, the following equations are used (20:258):

$$\mathbf{E} = -g\mathbf{X} + \frac{\mathbf{P}}{\chi_{stress}} \tag{3.82}$$

$$\mathbf{E} = -h\mathrm{x} + \frac{\mathbf{P}}{\chi_{strain}} \tag{3.83}$$

$$\mathrm{x} = s\mathbf{X} + g\mathbf{P} \tag{3.84}$$

$$\mathbf{X} = c\mathrm{x} - h\mathbf{P} \tag{3.85}$$

where **E** is the resulting electric field vector,

g is the piezoelectric strain (or voltage) constant,

h is the piezoelectric stress (or voltage) constant,

X is the stress vector,

P is the polarization vector,

χ_{stress} is the dielectric susceptibility tensor neglecting the effects of the applied stress,

χ_{strain} is the dielectric susceptibility tensor neglecting the effects of the applied strain,

s is the compliance coefficient,

c is the stiffness coefficient, and

x is the strain vector.

Pyroelectric Equations. For pyroelectric materials, an externally applied temperature gradient can be related to the resulting polarization by a pyroelectric constant, p (130:2041). This constant (actually a vector with one component in the 3-direction or z-direction) relates the scalar quantity of temperature (T), to a vector quantity, the polarization (**P**) (20:701). Unlike thermocouples, pyroelectric materials exhibit a response which corresponds to the rate of change of the external temperature rather than the ambient temperature itself (68:44). The temperature increase of the material, $T - T_0$ (where T is the final temperature and T_0 is the initial temperature), produces an electric charge (q) due to the pyroelectric effect

(neglecting any secondary pyroelectric effects due to strains developed as the crystal distorts). That is (68:47):

$$q = pA(T - T_0) \tag{3.86}$$

where q is the generated charge,
p is the pyroelectric coefficient, and
A is the surface area of the piezoelectric material.

Subsequently, the polarization which results due to pyroelectric effects is (20:701):

$$\mathbf{P}_{\mathbf{pyro-}} = p(T - T_0) \tag{3.87}$$

where $\mathbf{P}_{\mathbf{pyro-}}$ is the polarization vector due to a thermal gradient,
p is the pyroelectric coefficient,
T is the final temperature, and
T_0 is the initial temperature.

Generalized Polarization Equations. A material which is both piezoelectric and pyroelectric exhibits an electrical response that can be characterized by the linear superposition of the dielectric relationship between polarization and an external electric field, Hooke's Law, and the pyroelectric effect. Two cases follow: the first equation describes the resulting polarization found by relating the combined effects of the electric field, stress and the temperature (Equations 3.79 and 3.87). That is (20:701):

$$\mathbf{P} = \mathbf{P}_{\mathbf{piezo-1}} + \mathbf{P}_{\mathbf{pyro-}} \tag{3.88}$$

or

$$\mathbf{P} = \chi_{\mathbf{stressT}}\mathbf{E} + d\mathbf{X} + p(T - T_0) \tag{3.89}$$

where $\mathbf{P}$ is the resulting polarization vector,
$\chi_{\mathbf{stressT}}$ is the dielectric susceptibility tensor neglecting the effects of strain or temperature,
$\mathbf{E}$ is the externally applied electric field vector,
d is the piezoelectric strain constant,

X is the applied stress vector.
p is the pyroelectric constant.
T is the final temperature, and
T_0 is the initial temperature of the material.

The second case uses Equations 3.81 and 3.87 to describe the polarization due to the combined effects of electric field, strain, and temperature. That is (20:701):

$$P = P_{piezo-2} + P_{pyro-} \tag{3.90}$$

or

$$P = \backslash_{strainT} E + ex + p(T - T_0) \tag{3.91}$$

where P is the resulting polarization vector.
$\backslash_{strainT}$ is the dielectric susceptibility tensor neglecting the effects of strain or temperature.
E is the externally applied electric field vector.
e is the piezoelectric stress constant.
x is the applied strain vector.
p is the pyroelectric constant.
T is the final temperature, and
T_0 is the initial temperature of the material.

One additional term which deserves mention is the coupling factor, k. This factor represents the ability of the piezoelectric material to transduce electrical and mechanical energy or vice versa. Additionally, k^2 is equal to the transformed energy divided by the total input energy (68:44).

Piezoelectric Materials

Woldemar Voigt demonstrated that 20 of the 32 crystal classes exhibit piezoelectric properties due to their lack of a center of symmetry (20:5). Therefore, many materials are potentially piezoelectric; however, only a few materials, which have been primarily used in engineering applications, will be discussed.

Rochelle Salt. Rochelle salt was first produced in 1672 by an apothecary, Pierre de la Seignette, in LaRochelle, France (75:114). Rochelle salt was originally

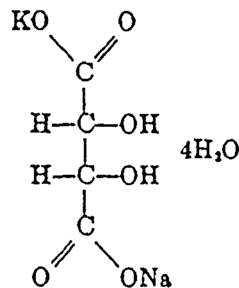

Figure 3.11. Chemical Structure Of Rochelle Salt (20:516).

used as a drug; however, its strong pyroelectric effect was quickly noticed. In 1824, Brewster studied this property in both Rochelle salt and tourmaline, and termed their effects *pyroelectric*. In 1880, the Curie brothers discovered piezoelectricity using this crystal (20:6).

Rochelle salt, or sodium potassium tartrate tetrahydrate, consists of a crystal structure whose formula is $NaKC_4H_4O_6(4H_2O)$, and its chemical structure is illustrated in Figure 3.11 (20:516). Because a large portion of the chemical structure of Rochelle salt is water, the water molecules evaporate into the atmosphere if the relative humidity is less than 35%. Additionally, Rochelle salt dissolves when the relative humidity is above 85%, because water is absorbed into its structure. At 55°C, the crystalline structure disintegrates. Rochelle salt is a very unstable material at room temperature, exhibiting highly pyroelectric and piezoelectric properties between the temperature extremes of −18°C and 24°C. Even though the material requires a restricted temperature and relative humidity range to behave as a piezo- and pyroelectric transducer, early engineering applications using Rochelle salt were successful due to its large piezoelectric constant. Rochelle salt's piezoelectric strain constant ($d_{14} = 2300 \times 10^{-12}$ C/N) is one of the largest constants of any known piezoelectric material (58:398).

Even with its environmental limitations, one of the first engineering applications of Rochelle salt was as a low frequency oscillator (20:7). To obtain select oscillation frequencies, Rochelle salt is cut into specific lengths relative to the appropriate crystal orientation. As a result, the crystal's oscillation stabilizes at its

natural resonant frequency which can be used to control electrical instrumentation. However, the oscillators made from Rochelle salt required extensive environmental controls to stabilize their operating points, and consequently, this limitation forced scientists and researchers to find new, more stable materials. As a result, quartz was discovered to be a more suitable piezoelectric material that could be configured as an oscillator, even though its largest piezoelectric constant is a mere fraction of that of Rochelle salt.

Quartz. Quartz is a crystalline form of silicon dioxide (SiO_2), and it can be found throughout the earth. The crystal exists in several forms, of which α-quartz is the most extensively used variety (139:46). This crystal was found to be piezoelectric soon after the discovery of piezoelectricity, and it was first used by Walter Cady of Wesleyan University in oscillator circuits as a replacement for Rochelle salt (20:6). Even though the largest piezoelectric constant (d_{11}) in quartz is 2.3×10^{-12} C/N ($\frac{1}{1000}$ that of the d_{14} piezoelectric constant in Rochelle salt), its low internal losses and stability at all ordinary temperatures established it as the first piezoelectric crystal suitable for precise control of electric oscillator frequencies (20:6).

To illustrate how piezoelectricity is harnessed in quartz, an example of a typical quartz crystal cut will be described. According to Mason, when an electric field is applied to a y-cut crystal, two types of shear strains develop, X_5 and X_6 (75:97). Assuming a square shaped crystal cut, both of these shear strains would distort the square into a rhombus as shown in Figure 3.12. The longitudinal mode can thus be obtained by properly cutting the specimen into a size where the length corresponds to the direction in which the material distorts (the dotted rectangle in Figure 3.12).

To obtain select resonant frequencies from quartz, the crystal must be cut along special planes which maximize the direct and converse piezoelectric effects at a specific frequency. According to Cady, the directions in a specimen of quartz can be found by observing specific faces of the bulk crystal and assigning directions according to the orientation of the naturally occurring external faces (Figure 3.13) (20:406–410). Once the x-, y-, and z-directions have been determined, crystallographers designate the crystal cut by the direction normal to the plane of the cut (for example, a cut whose face is parallel to the yz-plane would be

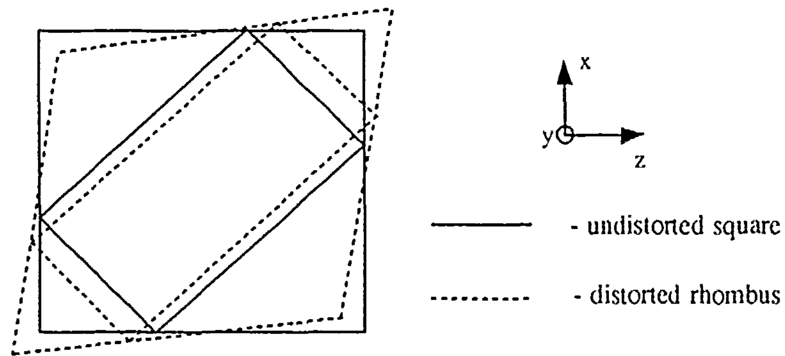

Figure 3.12. Distortion Caused By A Shear Strain Applied To A Square Crystal And A Method For Obtaining A Longitudinal Mode (75:86).

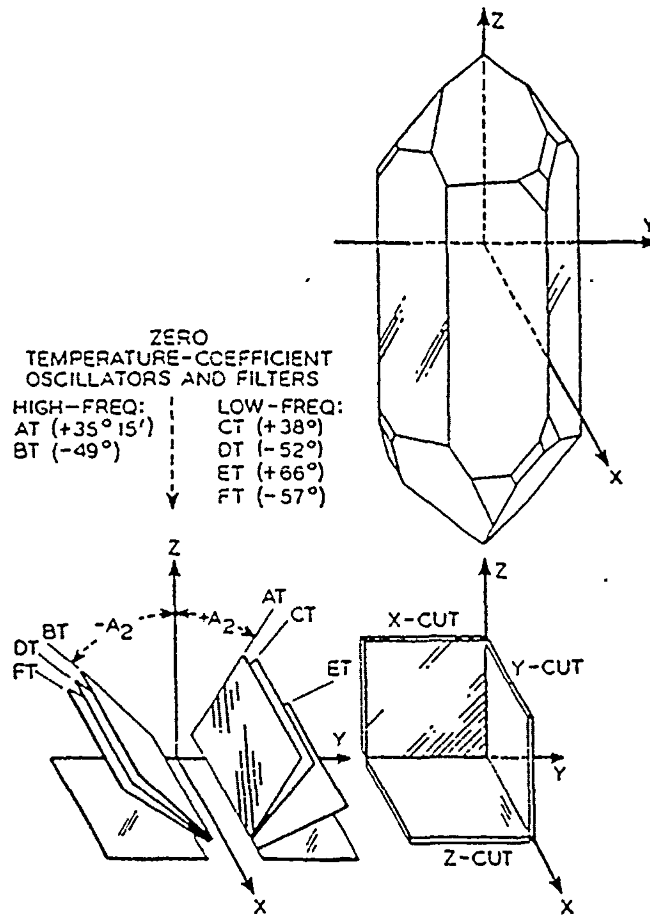

Figure 3.13. Typical Quartz Crystal Cuts (75:86).

designated as an x-cut) (75:83). Since quartz is used to control electric oscillator frequencies, considerable study has been accomplished to determine resonant frequencies with low temperature coefficients (20:435–468). Many cuts possess these properties; however, those which possess the optimum characteristics are illustrated in Figure 3.13. For example, the AT-cut corresponds to a high-frequency oscillator with a low temperature coefficient, and it can be cut from a slice whose face is located 39°15′ as measured with respect to the positive z-direction (75:83). Unfortunately, the crystal cut designations correspond to the frequency characteristics along with their associated temperature coefficients; a direct correlation to just one of the piezoelectric coefficients cannot be made. Due to the angle of the cut with respect to the x-, y-, and z-axes (the 1, 2, and 3

subscripts of the piezoelectric constants) several piezoelectric coefficients contribute the material's bulk piezoelectric effects (75:84).

The most significant use of quartz crystals has been in the communications industry, where the crystals were used in very selective band-pass filters in broad-band carrier frequency systems (75:111). However, new materials, like barium titanate, were discovered to possess significantly enhanced piezoelectric properties compared to quartz; they have since replaced quartz in communications equipment (75:111).

Ceramics. During World War II, over 30 million quartz crystals were used in communications equipment (20:6). Because of the magnitude of the requirements for physically large piezoelectric crystals which oscillate at specific frequencies, new materials were investigated with properties similar to quartz. One of the materials discovered was barium titanate ($BaTiO_3$), which possesses the perovskite crystalline structure (see Figure 3.14) (139:60). $BaTiO_3$ is a unique piezoelectric material because it is a ceramic. This ceramic is fabricated similar to ordinary ceramics; however, after fabrication, it is placed between metal plate electrodes connected to a large DC voltage which polarizes the polycrystalline $BaTiO_3$ into a crystalline piezoelectric material (58:114). A distinct advantage of ceramics relative to the natural piezoelectric materials is the ceramic's ability to be molded into various shapes, including cylinders, bowls, and disks (123:147). Following the development of the poling fabrication technology, several other synthetic piezoelectric materials were developed and classified into this same crystalline structure, including lead zirconate titanate ($PbZrO_3$ or PZT). The large piezoelectric constant found in (d_{33} equal to 450×10^{-12} C/N), coupled with its ability to be fabricated into various shapes, has enabled it to dominate transducer applications, such as hydrophones, sonar, and audio tone generators, for more than 40 years (123:147).

Polymers. The piezo- and pyroelectric effects traditionally encountered in ceramics and polar single crystals were also discovered in certain polymers (73:724). In 1969, Kawai discovered piezoelectric properties in a polymer called polyvinylidene fluoride (PVDF) (51:1). Since that time, many studies have verified that PVDF has the largest piezoelectric and pyroelectric coefficients of any known polymers (73:724). The largest PVDF piezoelectric coefficient is d_{33} which has a

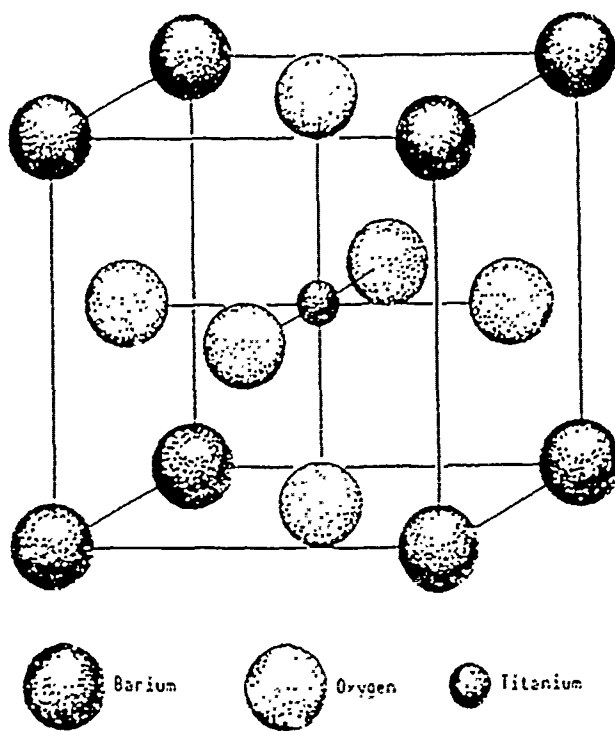

Figure 3.14. Perovskite Crystalline Structure - Barium Titanate ($BaTiO_3$) Crystal (100:2-16).

value of -33×10^{-12} C/N (68:49). PVDF possesses a pyroelectric coefficient (p) which spans 24 to 26 C/m^2 °K (112:2).

PVDF is fabricated from $(CH_2CF_2)_n$, and it consists of long molecular chains (110:1596). Presently, four crystalline forms of PVDF are known: the β-phase, α-phase, $\alpha_p(\delta)$-phase, and γ-phase (also represented in the literature as Form I, Form II, Form II_p, and Form III, respectively) (110:1596). Figure 3.15 illustrates the molecular chains of α-phase PVDF, Figure 3.16 illustrates the β-phase PVDF, and Figure 3.17 shows the unit cells of the crystalline structure formed by projections of the molecular chains into the ab-plane.

The α-phase is the naturally occurring phase found just after the film is cooled during its synthesis. The individual chains arrange themselves to form a centrosymmetric unit cell, producing an unpolarized polymer crystal (110:1597). In the β-phase, all chains are oriented essentially parallel to the c-axis of the unit cell with all its dipoles pointing in the same direction. This structure results in a noncentrosymmetric, polarized crystal (110:1597). Similar to the β-phase, the γ-phase occurs when the molecular chains are packed in a parallel arrangement, forming a noncentrosymmetric polar crystal; however, this phase is difficult to retain (stabilize) (32:49; 110:1597). The $\alpha_p(\delta)$-phase has the same molecular chain structure as the α-phase, except that the chains rotate every second chain such that all chains are aligned, making this form noncentrosymmetric and polar (110:1597).

Commercially available PVDF films usually consist of the unpolarized α-phase material (110:1598). To form a piezoelectric material, the film sheet must be uniaxially stretched (typically at temperatures between 60°C to 65°C) 3 to 5 times its original length (110:1598). This stretching forces the long polymer chains to become aligned in the stretched direction, forming a β-phase PVDF film. Poling is then performed on the film, either with a thermal or corona poling process. In thermal poling, the sample is first sandwiched between electrodes and then subjected to an electric field spanning 500 to 800 kV/cm at 90°C to 110°C for one hour. The dipoles in the film will partially align in the crystalline regions in the electric field's direction. Subsequent cooling to room temperature under the influence of the applied electric field stabilizes the polar alignment which results in permanent polarization (110:1598). In corona poling, a non-metallized polymer sample is subjected to a corona discharge from a needle electrode positioned a few centimeters above the film. As the charge accumulates on the film, it causes a high

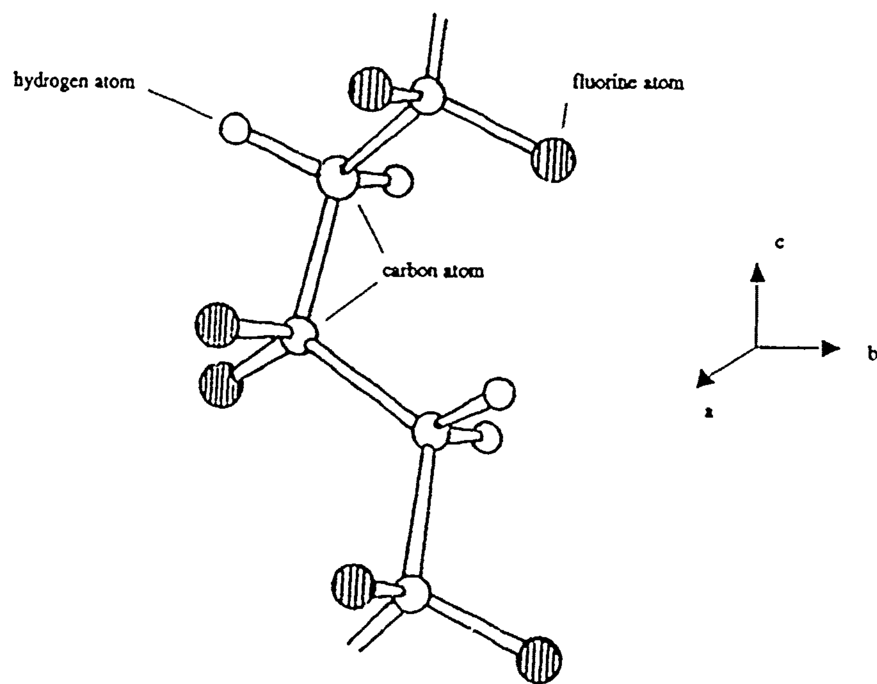

Figure 3.15. Molecular Structure Of α-Phase PVDF (68:27).

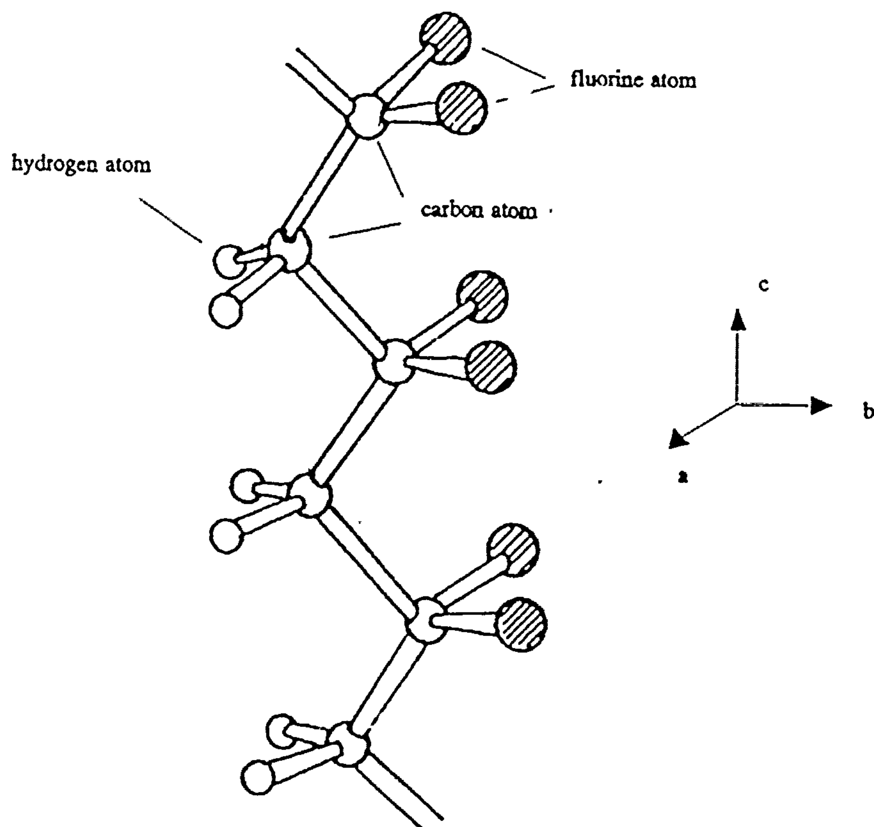

Figure 3.16. Molecular Structure Of β-Phase PVDF (68:28).

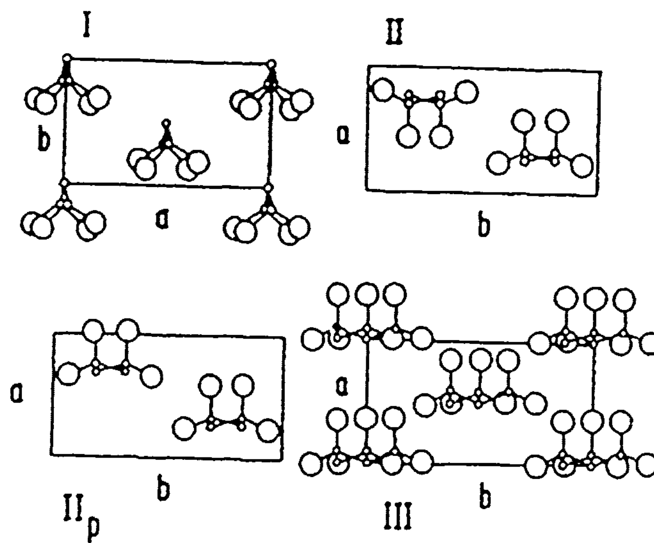

Figure 3.17. Unit Cells Of α-, β-, $\alpha_p(\delta)$-, And γ-phases Of PVDF Projected Perpendicular Onto The Molecular Chains (17:6).

electric field condition to exist across the film. This condition aligns the polymer chains within the film, even at room temperature (110:1598).

PVDF thin films can be characterized by their piezoelectric coefficient matrix, d, with the directions corresponding to Figure 3.18 and the notation described in Equations 3.70, 3.71, and 3.72. A generic d matrix has been found, which after uniaxial stretching and poling, is (110:1599):

$$\mathrm{d} = \begin{bmatrix} 0 & 0 & 0 & 0 & d_{15} & 0 \\ 0 & 0 & 0 & d_{24} & 0 & 0 \\ d_{31} & d_{32} & d_{33} & 0 & 0 & 0 \end{bmatrix}. \qquad (3.92)$$

Typical values for the d_{31}, d_{32}, and d_{33} piezoelectric constants range from 6 to 10 pC/N, 6 to 10 pC/N, and -33 to -13 pC/N, respectively. Additionally, a typical pyroelectric constant, p, for PVDF films spans from 24 to 26 $C/m^2 \cdot {}^{\circ}K$ (112:2).

While PVDF film does not possess a strong piezoelectric constant relative to the synthetic piezoelectric materials developed, PVDF film does possess several distinct advantages, including (21:55):

1. The ability to function over an extremely wide frequency range (DC to approximately 10 MHz).

2. A low acoustic impedance, making it a good impedance match for medical ultrasound and hydrophone applications.

3. A larger dielectric strength compared to piezoceramic materials (30-V/micron versus 1.5-V/micron) and, therefore, the ability to withstand larger electric fields.

4. A relatively large electrical impedance, an advantage which allows the film to provide a match to high-impedance devices, like complimentary metal-oxide-semiconductor (CMOS) transistors.

5. A structure which facilitates its synthesis as a thin and flexible sheet, which can be laminated to a vibrating structure without significantly destroying the motion of the structure.

6. A large molecular weight, which makes it mechanically strong and resistant to extreme environmental conditions (most solvents, acids, oxidants, and ultraviolet radiation).

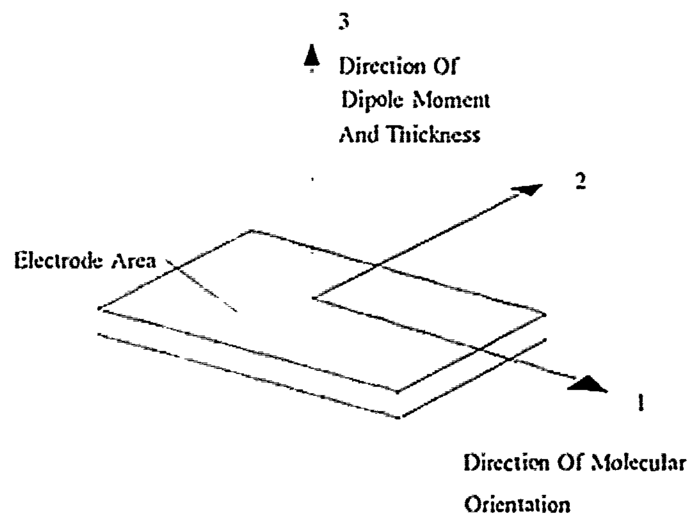

Figure 3.18. Schematic Illustrating The Conventional Identification Of Axes (17:8).

7. The ability to be cut and formed into complex shapes or prepared as a large transducer area.

8. Generally lower material and fabrication costs compared to those associated with other piezoelectric materials.

Conclusion

Piezoelectricity can be defined as the generation of a net polarization state, and subsequently an electric field, within a crystal when an external force is applied. Conversely, the mechanical distortion of the material occurs when an external electric field is applied. Additionally, pyroelectric effects must be considered when a piezoelectric material is subjected to temperature gradients. This latter situation results in the generation of a net polarization state, and a subsequent electric field within the crystal.

With the fundamental atomic view of piezoelectricity described by the electric dipole, scientists have developed equations to describe piezo- and pyroelectricity in terms of stress, strain, electric fields, and temperature gradients. Subsequent research into materials possessing these properties has led to the development of man-made materials, such as ceramics and polymers.

With the fundamental characteristics of piezo- and pyroelectric effects of PVDF film explained, the operating principle of a piezoelectric tactile sensor fabricated with PVDF film as the charge generating polymer can be fully appreciated. The next few chapters describe the design, test, and performance of a candidate tactile sensor.

IV. Design of the Tactile Sensor and the Supporting Experimental Performance Evaluation Hardware Configuration

Introduction

In a successful research effort, advanced planning is required to develop and solidify the intended research objectives and to ensure access to the critical equipment and instrumentation used to support the test and performance evaluation of a specific piece of hardware. To design such a system, a "requirements evaluation" of each fundamental component is necessary. Usually, this process motivates the consideration of several alternatives, and trade-offs must be performed between the options, selecting the best alternative for the particular device to be tested. In this chapter, the design of each component utilized in this research effort is presented, along with the rationale behind the specific design parameters (Figure 4.1 illustrates the essential components of the tactile sensor system). The chapter begins by presenting the design of the tactile sensor integrated circuit (IC), followed by a description of the piezoelectric PVDF film being used in this research effort. Next, a description of the adhesives that were used to bond the PVDF film to the IC are discussed, followed by a description of the final tactile sensor configuration. Finally, each component which supports the operation of the tactile sensor is presented.

Integrated Circuit Design

To fabricate a tactile sensor that will functionally mimic a human's tactile ability, the design of the sensor should ideally correspond to the layout of the human skin and the associated nerve endings (9:18). Unfortunately, the integrated circuit design tools (specifically MAGIC) associated with this research effort could not provide a tactile sensor possessing the equivalent characteristics of the human fingertip. That is, right angle corners are required in all IC designs. Considering this limitation in determining the best possible electrode array pattern geometry, previous research by Capt Pirolo included an investigation of two types of electrode array layout configurations: a striped pattern and an array of square electrodes (91). His research concluded that the square electrode array pattern would best

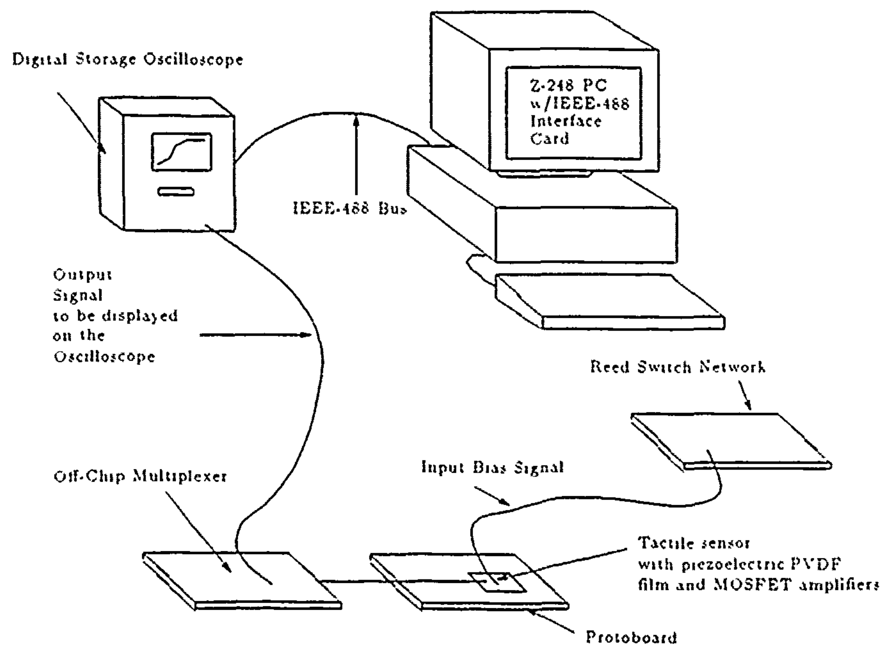

Figure 4.1. Essential Components Required For The Tactile Sensor System.

facilitate the sensor's performance (91:6.1). Following this recommended design approach and understanding that the design of the tactile sensor was limited by the tools used to design and fabricate the sensor, the tactile sensor was designed using a two-dimensional array of electrodes.

The revised tactile sensor integrated circuit (IC) design used in this research effort was based upon a previous configuration (100:2-16). To maximize the density of the two-dimensional taxel array pattern, the number of electrodes were limited based upon the geometrical constraints of the IC package. The amplifier circuit was revised to include a more extensive linear region (which would ideally span 15-V), and a gain of at least 1.25. VLSI CAD tools (MAGIC and SPICE) were utilized to accomplish the IC design phase. The overall dimensions of the IC were 7.9 mm by 9.2 mm. A floorplan of the tactile sensor integrated circuit is illustrated in Figure 4.2.

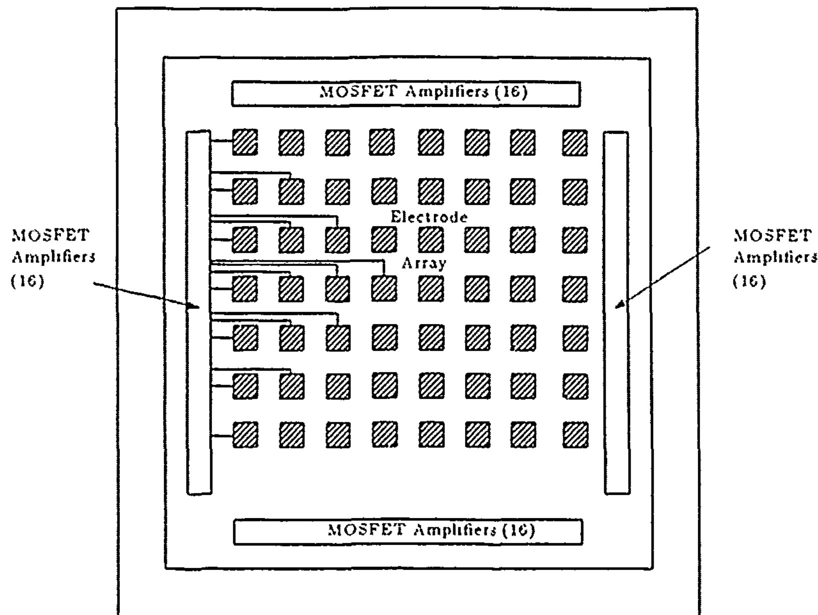

Figure 4.2. Floorplan Of The Robotic Tactile Sensor Integrated Circuit Showing 16 Electrical Connections Between One Bank Of The MOSFET Amplifiers And Their Corresponding Electrodes.

Electrode Array Pattern Design. The tactile sensor was designed using a two-dimensional planar electrode array. Without significantly changing the physical size and arrangement of the electrode array relative to the previous design (45:4-5), and by maximizing the number of electrodes to correspond with the limited number of input/output pins (132 pins) in the MOSIS package, electrodes measuring 400 μm by 400 μm that were separated from their nearest-neighbor by 300 μm were designed. A glass-cut was used to expose the electrode array and to facilitate the intimate coupling of the piezoelectric PVDF film with the array. With these constraints, the number of taxel electrodes was configured as an 8 x 8 electrode matrix measuring 5.3 mm by 5.3 mm, subject to the following pin assignments:

1. 64 input lines for the bias voltage input.
2. 64 output lines for the amplifier outputs.
3. 2 ground lines,
4. 2 supply (V_{dd}) lines.

In the previous research effort, Capt Fitch discovered a potential charge leakage path between nearest-neighbor gold bond pads on the IC package (45:6-1):

therefore, all input wirebond pads were located on the left and right sides of the integrated circuit, and all output wirebond pads were positioned on the top and bottom edges of the IC (when the IC is viewed with respect to its upper (top) surface). A photograph of an actual IC die without the piezoelectric PVDF film is shown in Figure 4.3.

Charge Amplifier Design. The amplifier functions as a buffer between the high impedance of the piezoelectric PVDF film and the relatively low impedance of the multiplexer circuit which is connected to the outputs of the amplifiers. The gate region of the MOSFET has a floating gate input with a near infinite input resistance ($> 10^{12}\ \Omega$) and a capacitance on the order of 10^{-12} farads (46). The RC time constant of this amplifier should be compatible with the RC time constant of the piezoelectric PVDF film (typically between 1 and 100 seconds) (46).

The electrode size was determined to be compatible with the anticipated input voltage generated by the piezoelectric PVDF film while it is under a practical mechanical load. That is, the theoretical charge generated by the piezoelectric PVDF film (q_F) due to an externally applied force (F) is given by (68:43):

$$q_F = d_{33}|F| = d_{33}m|g| \tag{4.1}$$

where d_{33} is the piezoelectric charge constant, relating the externally applied force, which is in a direction perpendicular to the surface of the film, to the resulting charge, which accumulates between the top and bottom surfaces of the film.
|F| is the magnitude of the externally applied force,
m is the mass of the externally applied load, and
|g| is the magnitude of the acceleration due to gravity.

Also, the charge generated by the pyroelectric effect of the PVDF film (q_T) is (68:47):

$$q_T = pA(T - T_0) \tag{4.2}$$

where p is the pyroelectric constant of the PVDF film,
A is the area of the PVDF film,
T is the final temperature of the system, and
T_0 is the initial temperature of the system.

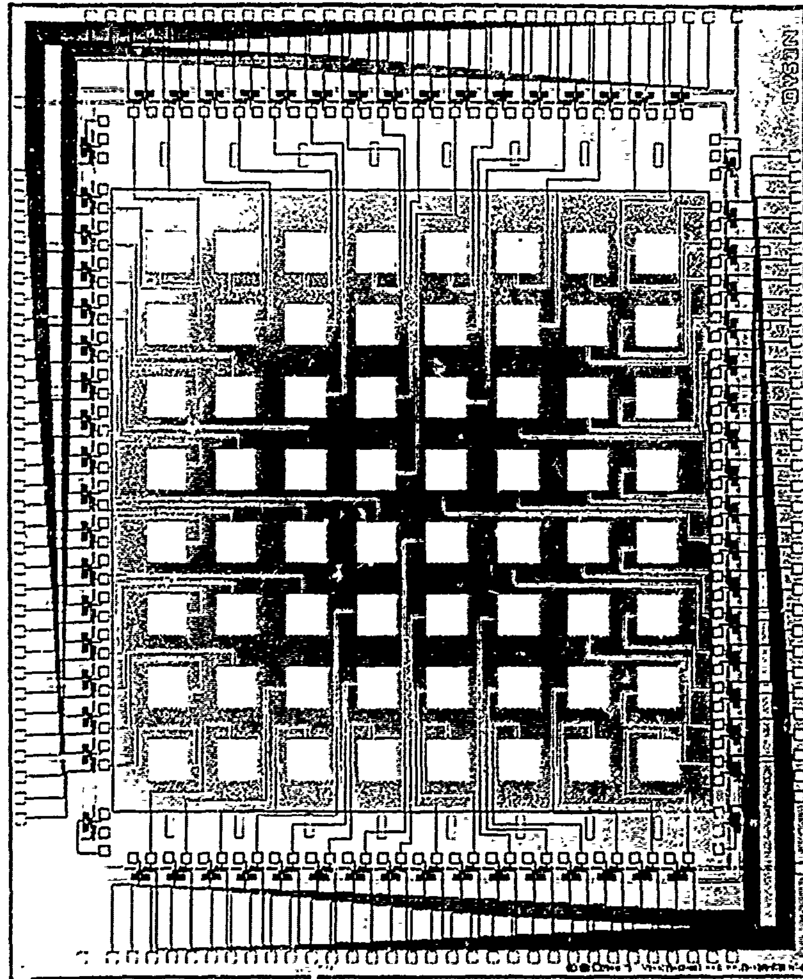

Figure 4.3. Photograph Of The Robotic Tactile Sensor Integrated Circuit Without The Piezoelectric PVDF Film (12.5 ×).

Therefore, the total voltage (V) generated in the piezoelectric PVDF film is (68:47):

$$V = \frac{d_{33} t m |g|}{\epsilon_r \epsilon_0 A} + \frac{p t (T - T_0)}{\epsilon_r \epsilon_0} \tag{4.3}$$

where, for example, the values of the constants are:

d_{33} is the piezoelectric charge constant (-16 pC/N) (112:2),
t is the thickness of the PVDF film (40×10^{-6} m),
m is the mass of the externally applied load (kg),
$|g|$ is the magnitude of the acceleration due to gravity (9.81 m/s^2)
ϵ_0 is the electrical permittivity of free space (8.85×10^{-12} F/m) (66:57),
ϵ_r is the relative permittivity of the PVDF film (12 dimensionless) (68:50),
A is the area of the electrode (0.16×10^{-6} m^2),
p is the pyroelectric constant (24×10^{-6} C/m^{2}K), (68:50)
T is the final temperature of the system (K), and
T_0 is the initial temperature of the system (typically, 300K).

Hence, for loads spanning 1 g to 100 g with no temperature change, a piezoelectric PVDF film should generate voltages that span 0.37 V to 37-V. On the other hand, if the temperature changes 1°K (or 1°C) the film should generate -9-V. The ideal amplifier should possess a linear output region for input levels spanning -8.63-V to 37-V.

One objective in the design of the amplifiers was to minimize variations between the performance of this tactile sensor and the previous sensor configurations. To achieve this goal, the value of the load resistors and gate sizes on each of the amplifier MOSFETs were systematically varied to extend the linear region of the amplifier, yet still maintain a voltage gain of at least 1.25. The VLSI CAD tool SPICE was used to model the amplifier. Appendix C contains the SPICE code used in this design effort. To enhance the range of the linear region of the amplifier without degrading the operation of each MOSFET or deviating significantly from the previous designs, the amplifier was designed to be compatible with a 15-V power supply. According to the ideal SPICE response, the amplifier should possess a linear region spanning from just less than 2-V to greater than 8-V. The schematic of the amplifier and its associated physical dimensions are illustrated in Figure 4.4, and Figure 4.5 depicts the SPICE-predicted characteristic transfer function of this amplifier design.

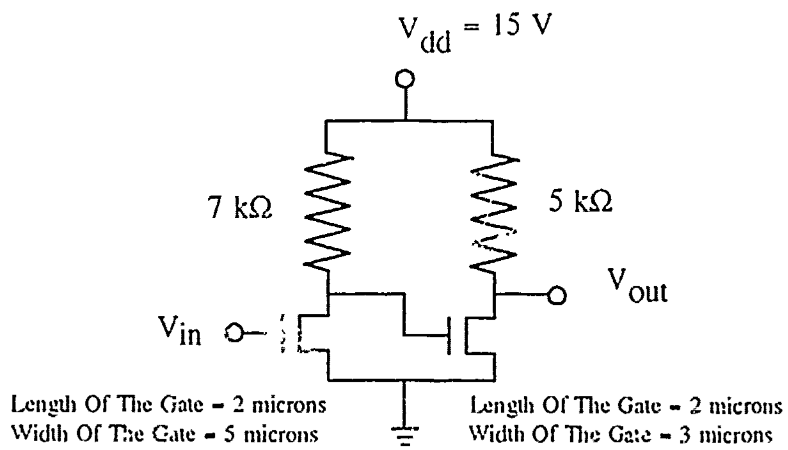

Figure 4.4. Tactile Sensor Charge Amplifier Schematic.

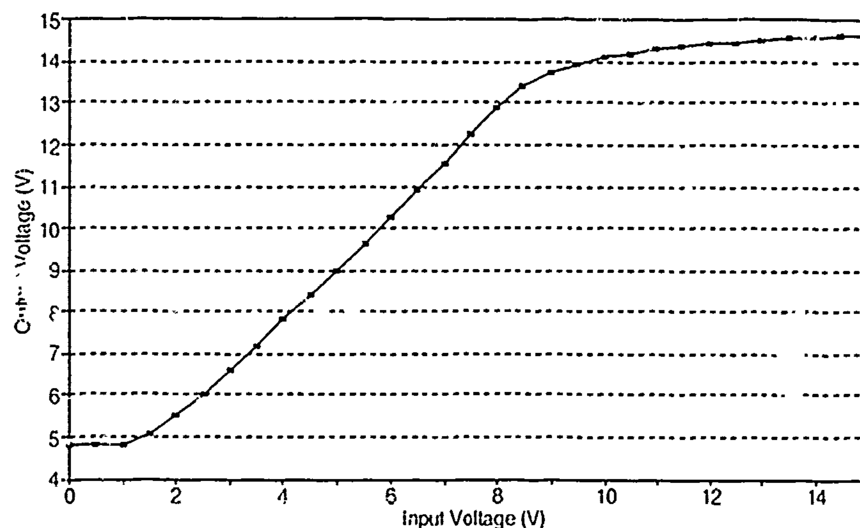

Figure 4.5. Characteristic Transfer Function Plot Of The Tactile Sensor Charge Amplifier Predicted By A SPICE Analysis.

To analyze the characteristics of the amplifier relative to a range of supply voltages (V_{dd}), different supply voltages were used as inputs in the SPICE simulation. Table 4.1 lists the characteristic linear ranges and the expected gains relative to a span of supply voltages. The MOSIS fabrication process guarantees sheet resistance values to within a given tolerance (for the 2 μm, n-well fabrication process the sheet resistance values span $\pm$ 20%). Obviously, the amplifier's response will change due to variations in resistor values; consequently, the ideal response of the amplifier, relative to a range of sheet resistance values (hence resistor values), was calculated. Table 4.2 illustrates the effects of the variations in sheet resistance relative to the amplifier's performance. In each case, the linear region of the amplifier spans a range of input and output voltages whose gain at a specific input voltage is within 10% of the amplifier's gain within the linear region.

Test probe pads were incorporated at the amplifier's input gate contact to facilitate biasing, should the bias configuration fail to operate, and to also verify proper operation of the amplifier during the integrated circuit evaluation process. Additionally, one isolated amplifier was placed on each corner of the array to evaluate deviations from the expected amplifier characteristics across the entire IC.

Table 4.1. Tactile Sensor Amplifier Characteristics With Different Supply Voltages.

Supply Voltage	Linear Range (Input)	Linear Range (Output)	Voltage Gain
10 V	1.6 V - 6.15 V	3.5 V - 9.2 V	1.32
11 V	1.8 V - 6.5 V	4.0 V - 9.8 V	1.32
12 V	2.0 V - 7.0 V	4.1 V - 10.5 V	1.31
13 V	2.1 V - 7.5 V	4.75 V - 11.5 V	1.31
14 V	2.1 V - 7.9 V	4.9 V - 12.2 V	1.28
15 V	2.3 V - 8.1 V	5.0 V - 13.5 V	1.27
16 V	2.5 V - 8.7 V	5.7 V - 13.5 V	1.20
17 V	2.6 V - 9.5 V	6.0 V - 14.5 V	1.18
18 V	2.7 V - 10.0 V	6.5 V - 16.0 V	1.14
19 V	2.9 V - 10.4 V	7.0 V - 16.5 V	1.05
20 V	3.0 V - 11.0 V	7.7 V - 17.3 V	1.00

Table 4.2. Tactile Sensor Amplifier Characteristics For A 10-V And 15-V Bias Supply And The Expected Sheet Resistance Values.

Supply Voltage	Sheet Resistance	Linear Range (Input)	Linear Range (Output)
10.0 V	20 Ω/□	2.2 V - 6.8 V	5.0 V - 9.0 V
	22 Ω/□	2.2 V - 6.4 V	4.7 V - 9.0 V
	24 Ω/□	2.2 V - 5.7 V	4.3 V - 8.3 V
	25 Ω/□	2.4 V - 5.6 V	4.2 V - 8.2 V
	26 Ω/□	2.4 V - 5.2 V	4.3 V - 8.3 V
	28 Ω/□	2.4 V - 5.0 V	4.0 V - 8.2 V
	30 Ω/□	2.6 V - 5.0 V	3.9 V - 8.3 V
15.0 V	20 Ω/□	2.6 V - 10.0 V	8.0 V - 13.2 V
	22 Ω/□	2.5 V - 9.0 V	7.0 V - 13.2 V
	24 Ω/□	2.4 V - 8.3 V	5.5 V - 13.0 V
	25 Ω/□	2.3 V - 8.1 V	5.0 V - 12.5 V
	26 Ω/□	2.0 V - 7.9 V	4.7 V - 12.5 V
	28 Ω/□	2.1 V - 7.6 V	4.5 V - 12.5 V
	30 Ω/□	2.1 V - 7.3 V	4.2 V - 12.5 V

The final amplifier's Caltech Intermediate Format (CIF) plot is depicted in Figure 4.6.

Piezoelectric PVDF Film

The principle of tactile sensing utilized in this research is based upon the deformation of a planar piezoelectric polymer film while it is under the influence of an externally applied stress. Since the charge generated in the film is directly proportional to the PVDF film's thickness, and a more robust output signal is desired, a film thicker than that used in previous research has recently been evaluated. Several piezoelectric PVDF film thicknesses were investigated in Capt Pirolo's research, including the 25 μm and 40 μm thick films. His research concluded that the 40 μm thick PVDF film possessed a more useful piezoelectric activity compared to the 25 μm thick film (91:6.1). Additionally, the piezoelectric PVDF film can be cut to practical sizes and shapes, and it can be readily coupled to the planar electrode array on the sensor's integrated circuit.

PVDF Film Adhesive Performance Comparative Investigation

Last year, Capt Fitch reported that a urethane adhesive (Miller-Stephenson Chemical Co., MS-470/22, George Washington Highway, Danbury, CT. 06810) was the most robust adhesive evaluated (45). To establish a baseline and to minimize deviation from previous research findings, urethane was used as the baseline adhesive material. To evaluate the relative adhesive robustness of several adhesives, two other adhesives were evaluated as potential candidates for coupling the piezoelectric PVDF film to the electrode array. Besides bonding the PVDF film to the electrode array, the adhesive must act as a non-conducting (low-loss) dielectric. The two candidate dielectrics selected include representative samples of dielectrics used in electronic device fabrication: a polyimide dielectric (Ultradel Polyimide Dielectric, AMOCO Chemical Co., Chicago, IL 60601), and a plastic dielectric (*Loctite* Tak Pak, Number 7586A21, Loctite Corporation, Newington, CT 06111).

Tactile Sensor Configuration

The final tactile sensor configuration included a planar electrode array which measured 5.3 mm by 5.3 mm, and it was surrounded by MOSFET charge amplifiers. The piezoelectric PVDF film was attached to the integrated circuit, and

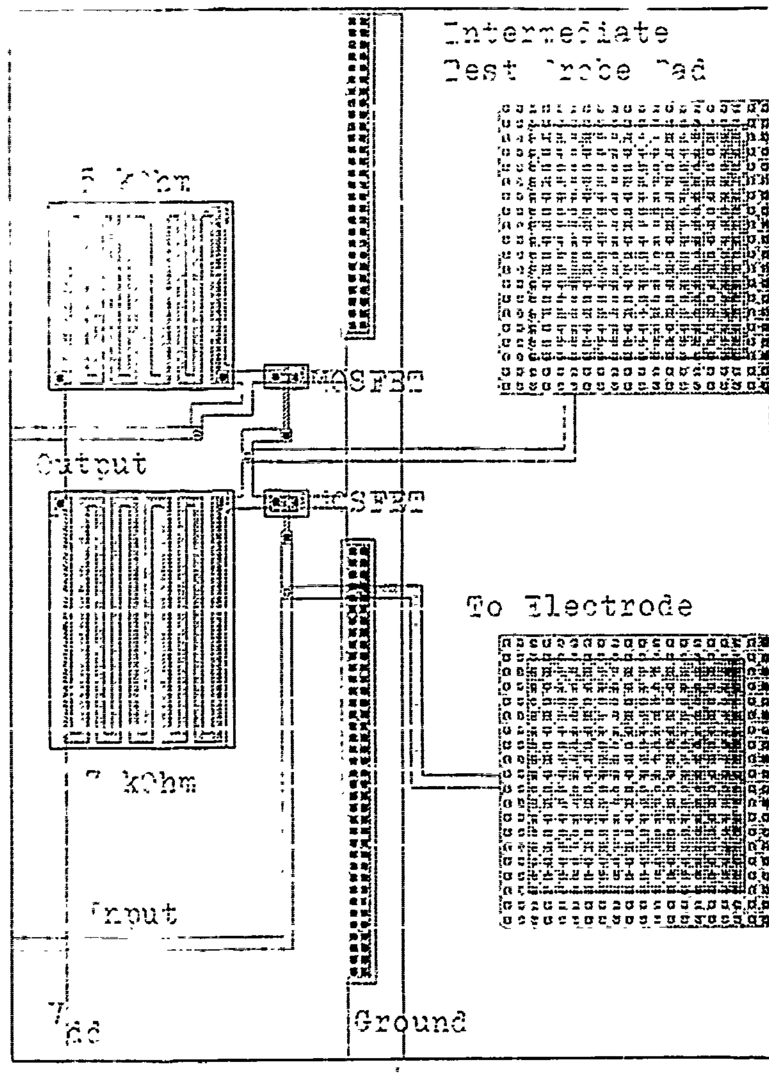

Figure 4.6. Robotic Tactile Sensor Charge Amplifier Caltech Intermediate Format (CIF) Plot (380×).

the charge generated by the stressed polymer was accumulated between the metal electrodes. This small voltage was then amplified by the MOSFET amplifiers which are connected to the lower electrodes via a Metal-1 line. The Metal-1 conductor is isolated from the piezoelectric PVDF film with a 3 μm thick dielectric passivation layer of silicon dioxide (SiO_2). A cross-sectional view of a small section of the completed tactile sensor is shown in Figure 4.7.

Component Design

This thesis effort consists of several critical phases. Each component design phase must be considered individually, and the particular design parameters must be calculated to ensure proper integration into the system and successful operation of the tactile sensor. The support components of the effort include the bias voltage circuit configuration, the multiplexer circuit, the pyroelectric effect minimization chamber, the load shapes, and the test fixture for applying the load shapes.

Bias Voltage Circuit Configuration. To provide a uniform bias condition across the surface of th entire tactile sensor array, an off-chip bias circuit configuration was designed. This functionality was intended to eliminate the requirement for separately biasing each taxel amplifier using the Micromanipulator probe station (as was utilized in Capt Fitch's research (45:5-25)). The specific configuration adapted in this research consisted of high impedance (10^{12} Ω when open circuited) switches which, when simultaneously activated, uniformly biased the entire electrode array. Figure 4.8 illustrates how a high impedance switch is connected to the input of the taxel amplifier. Once the tactile sensor's MOSFET amplifiers were biased, the switches were opened to isolate the bias voltage from the tactile sensor circuitry.

To ensure minimum charge leakage during the off-state of the bias circuit, a switch was required that possessed an impedance greater than or equal to that of the PVDF film and the MOSFETs gate contact. After a review of several commercially available switches, high impedance, miniature reed switches were selected. The reed switches selected were fabricated by Potter and Brumfield (Potter and Brumfield Relay Specialties, Inc., model JWD-171-21, Oakland, NJ 07436). Each reed switch contains two independent switches with an off impedance on the order of 10^{12} Ω. Thirty-two high impedance switches were assembled on a

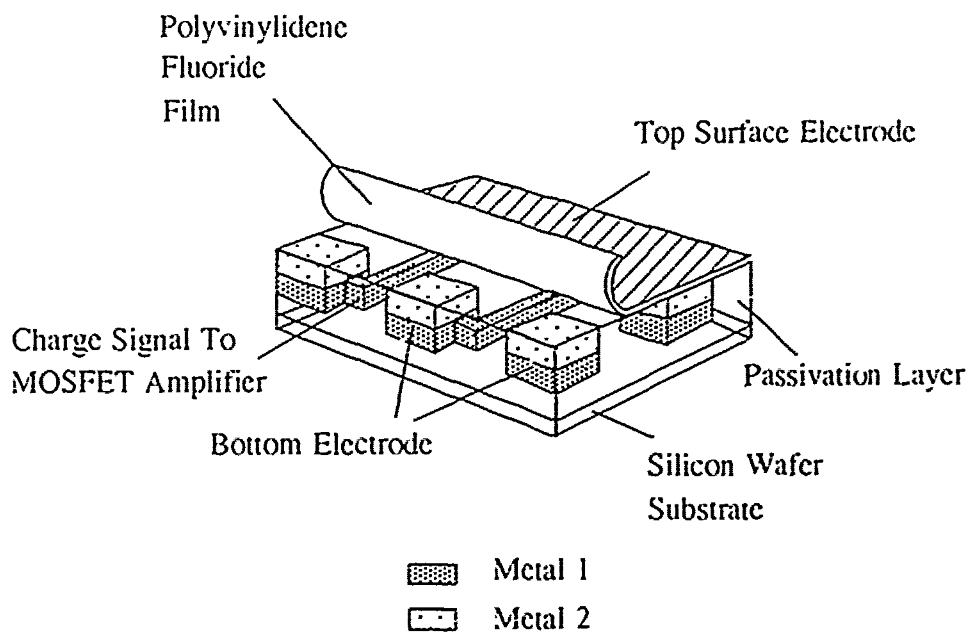

Figure 1.7. Cross-Sectional View Of The Robotic Tactile Sensor Configuration.

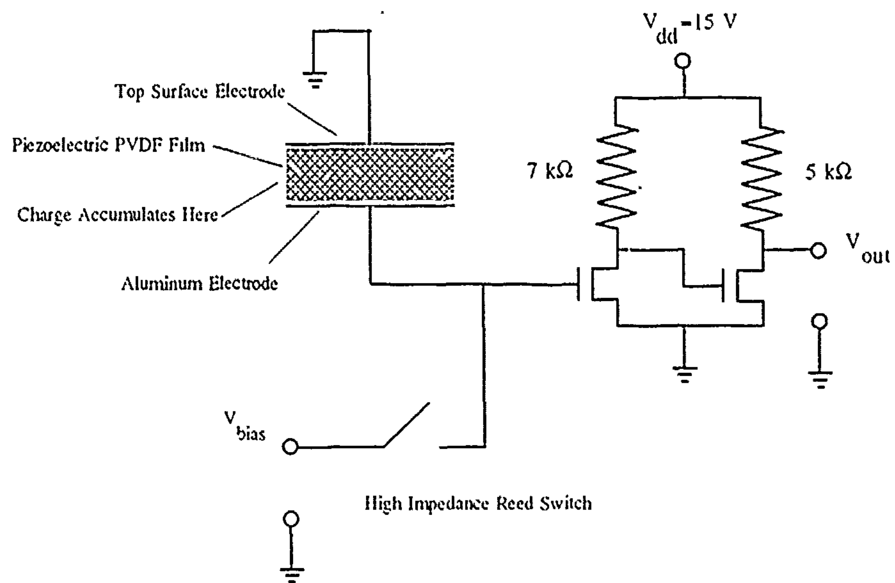

Figure 4.8. High Impedance Switch Configuration Connected With The Input Of The Taxel Amplifier.

solderless protoboard (E&L Instruments, Inc., Elite-1 Circuit Design System Protoboard, New Haven, CT 06512), to realize the required bias voltage switch network.

Multiplexer Circuit Configuration. To eliminate the charge-leakage problems found in the previous research due to the on-chip multiplexing circuitry (45:6-1), an off-chip multiplexer circuit configuration was designed. The multiplexer must support 64 channels because the tactile sensor electrode array contains 64 taxels. The multiplexer was designed to sample each taxel's response and generate a serial stream of data as its output. The multiplexer circuit configuration consisted of nine 8-to-1 multiplexers (Maxim Integrated Products, number MAX328, Sunnyvale, CA 94086). To control the multiplexer, several other devices were selected, including a counter to control the decoder (consisting of two counter chips - Texas Instruments, number SN74161, Dallas, TX 75265), a decoder which selects a particular multiplexer IC (assembled from a 3-to-8 decoder chip - Texas Instruments, number SN74156, Dallas, TX 75265), and a combinational circuit used to reset the counter and trigger the Digital Storage Oscilloscope (assembled from an AND gate - Texas Instruments, number SN7421, Dallas, TX 75265). All of the chips were configured on an Elite-1 Circuit Design System Protoboard. Figure 4.9 illustrates the configuration of the multiplexer.

Pyroelectric Effect Limitation Chamber. Since the piezoelectric PVDF film is also a pyroelectric material (68:17), the pyroelectric effects of the film could potentially perturb the expected tactile sensor performance results of the piezoelectric PVDF film. Therefore, minimizing the pyroelectric effects is essential. To satisfy this requirement, effects from overhead lights, external test equipment, and human contact was minimized by placing the tactile sensor IC, bias circuit, and test load shape application fixture in a chamber. This ensured all connections to the floating gate of the electrode array were enclosed by the chamber.

To determine the physical size and shape of the chamber, the specific performance features of the chamber were established. Initially, the PVDF film, tactile sensor IC, and related support circuitry required the use of the Micromanipulator probe station (Micromanipulator Company, Inc., model 6200 Probe Station, Carson , NV 89701). To minimize the pyroelectric effects, the chamber must cover the Micromanipulator probe station. After the initial testing

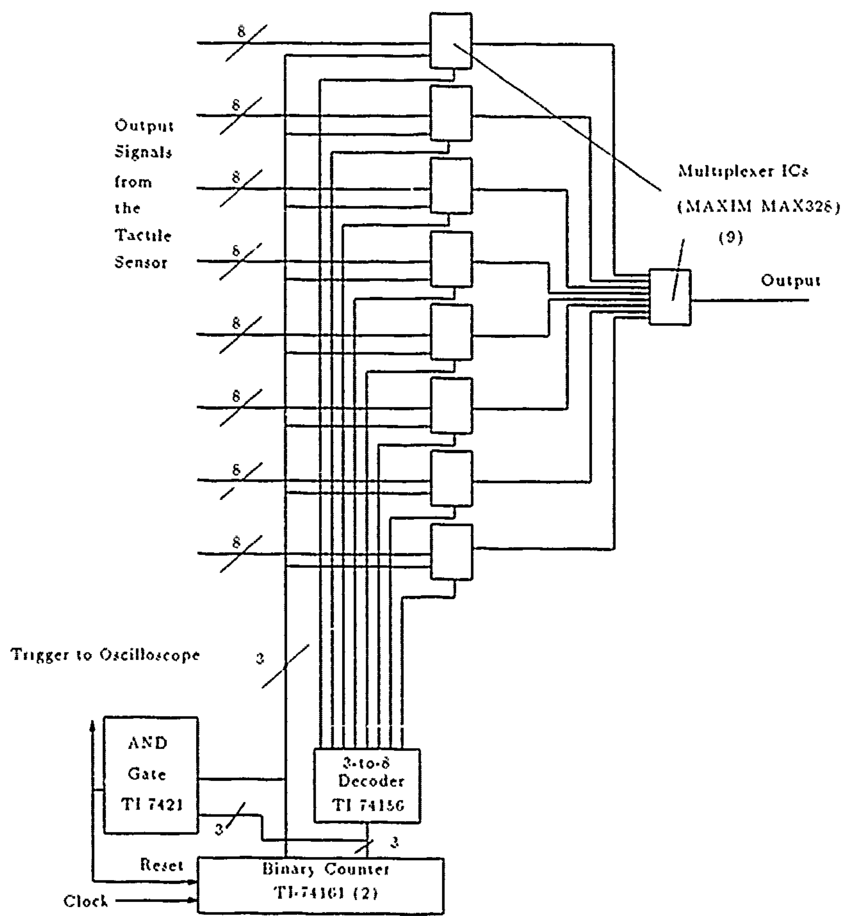

Figure 4.9. Off-Chip Tactile Sensor Multiplexer Configuration.

was completed, the tactile sensor system was moved to a test bench and the system's performance was evaluated. To minimize the pyroelectric effects under these new operating conditions, the chamber must physically cover the sensor system, bias circuit, and test load shape application fixture.

Two alternatives were considered for realizing this chamber. One option required the design of two separate chambers, one to cover the Micromanipulator probe station, and one to cover the tactile sensor system on the test bench. The other alternative considered was an adjustable-size chamber which could be used in either instrument configuration. The adjustable-size chamber was the option selected because of its design simplicity, physical weight, and flexibility.

The chamber was fabricated from PVC pipe, and it was fitted with a cloth cover. The legs can be adjusted to two positions: a maximum height of 36 inches and a minimum height 18 inches. The support beams of the container were adjustable over a range of widths and depths: a minimum width of 18 inches, and a maximum width of 36 inches; a minimum depth of 15 inches, and a maximum depth of 31 inches (Figure 4.10).

Test-Load Shapes. In this research, smaller test-load shapes were designed to evaluate the sensor's ability to image different shapes and recognize them when applied to different areas of the electrode array. To implement this objective, several shapes were designed, including a sharp edge (designed to activate one row of taxels), a small solid square (each side 1/2 the length of the sensor's electrode array edge), a small solid circle (radius less than 1/4 that of the sensor's array size), and a small polygon (one side as long as that of the sensor's array edge, and the other side 1/2 the length of the sensor's array edge). Additionally, to illustrate the ability of the tactile sensor to detect industrial type of shapes, two additional designs were implemented: a slotted screw head and a cross-slot screw head. In previous research, the test-load shapes typically contacted virtually all the taxels in the electrode array. Two load shapes, a large solid circle and a toroid, designed and fabricated previously, were also utilized. A representative sample of the load shape geometries is included in Figure 4.11, and each load shape is presented in more detail in Appendix B. The test fixture used to apply the load shapes was designed and fabricated by Capt Fitch. Figure 4.12 illustrates this test fixture.

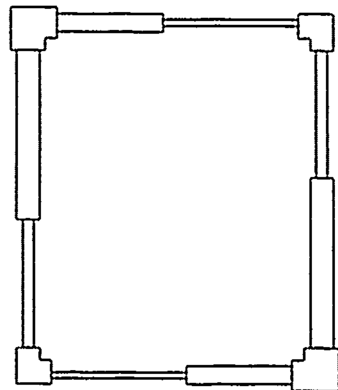

Material PVC Pipe and Connectors

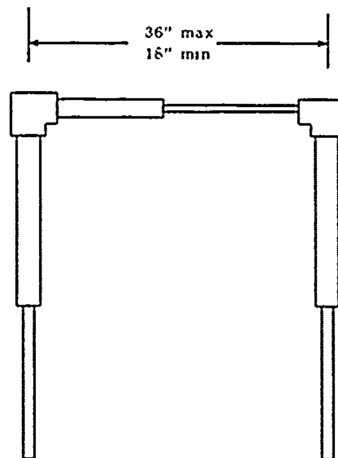

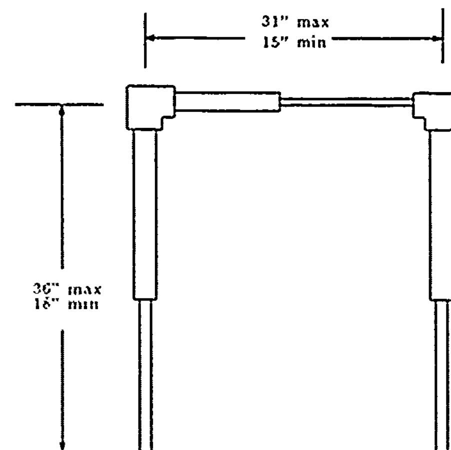

Figure 4.10. Adjustable Chamber Frame Design For Minimizing Pyroelectric Effects.

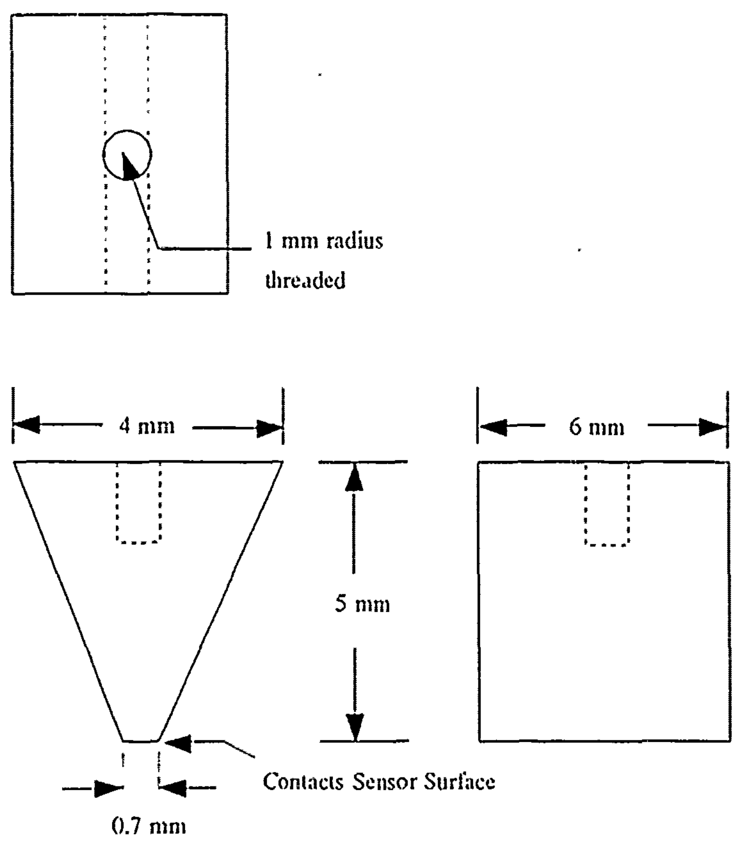

Figure 4.11. Representative Test-Load Shape - A Sharp Edge.

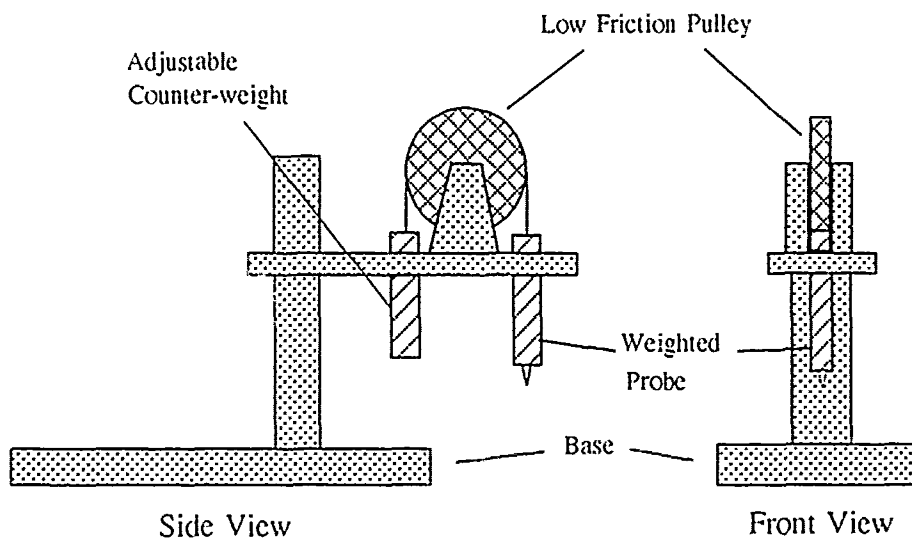

Figure 4.12. Fixture For Applying The Test Load Shapes (45:4-18).

Conclusion

A tactile sensor system comprised of several essential components was designed. The primary component, the electrode array IC maximized the number of allowable pin assignments, resulting in an 8 x 8 electrode array. To provide charge signal amplification, 64 MOSFET amplifiers were incorporated into the IC. each possessing a gain of 1.25 from 2.3-V to 8.1-V. To couple a 40 μm thick piece of piezoelectric PVDF film to the IC surface. three potential adhesives were selected for an adhesive study. These adhesives included a urethane adhesive. a polyimide dielectric and a plastic dielectric (*Loctite*). The results of this adhesive study determined which adhesive possessed the best physical and electrical characteristics for use in a piezoelectric tactile sensor. Several additional components were designed to support the operation of the tactile sensor IC. To apply a uniform initial voltage to all taxel electrodes, a high impedance bias network was designed using reed switches possessing an off-impedance of 10^{13} Ω. A 64-to-1 multiplexer used to serialize the 64 output lines was designed using commercially available components. Also, to minimize any pyroelectric effects during the operation of the sensor, a chamber fabricated from PVC pipe was designed to enclose the tactile sensor IC and support equipment. Finally, several shapes were designed in an effort to characterize the tactile sensor's ability to detect the shape of the load in contact with the taxel array.

To ensure successful operation of the tactile sensor. all components in this research effort were designed with the overall system operation in mind. To verify whether the individual components. as well as the integrated system. operated as designed. a comprehensive evaluation program was implemented. The next chapter discusses the test and evaluation procedures implemented in this research effort.

V. Fabrication and Evaluation Procedures

Introduction

In any successful experimental endeavor, not only does the critical item have to perform properly, but all supporting equipment must also perform as intended. To enhance the probability of success, each component in this research effort was tested individually to characterize its performance before assembling the components together to realize the tactile sensor test configuration. This chapter presents, in chronological order, the fabrication and evaluation procedures accomplished to realize an operational tactile sensor (Figure 5.1 illustrates the evaluation increments). The presentation begins with a description of each component's test methodology, including the piezoelectric PVDF film characterization, the tactile sensor bias circuit evaluation, and multiplexer circuit evaluation. Next, the evaluation of the tactile sensor support system will be presented, and it consists of the tactile sensor bias circuit, the multiplexer circuit, and tactile sensor protoboard configured together. Then, the fabrication of the tactile sensor will be described, along with a presentation of the adhesive study procedures. Finally, the tactile sensor evaluation procedures will be presented, including both the individual electrode tests and the electrode array tests.

Component Testing

To provide a baseline response of the test configuration supporting the tactile sensor IC, a performance evaluation characterized each fundamental component before it was integrated into the final test configuration. The components tested included the piezoelectric PVDF film, the tactile sensor bias circuit, the multiplexer circuit, and the electrode array IC.

Piezoelectric PVDF Film Characterization. Concurrent with the IC fabrication process, the piezoelectric PVDF film was characterized to determine its polarization (68:29). The surface of the film which developed a positive charge when the film was contacted with an externally applied force was identified as the surface that was subsequently attached to the electrode array (this side was also identified as having a negative voltage response due to a positive change in

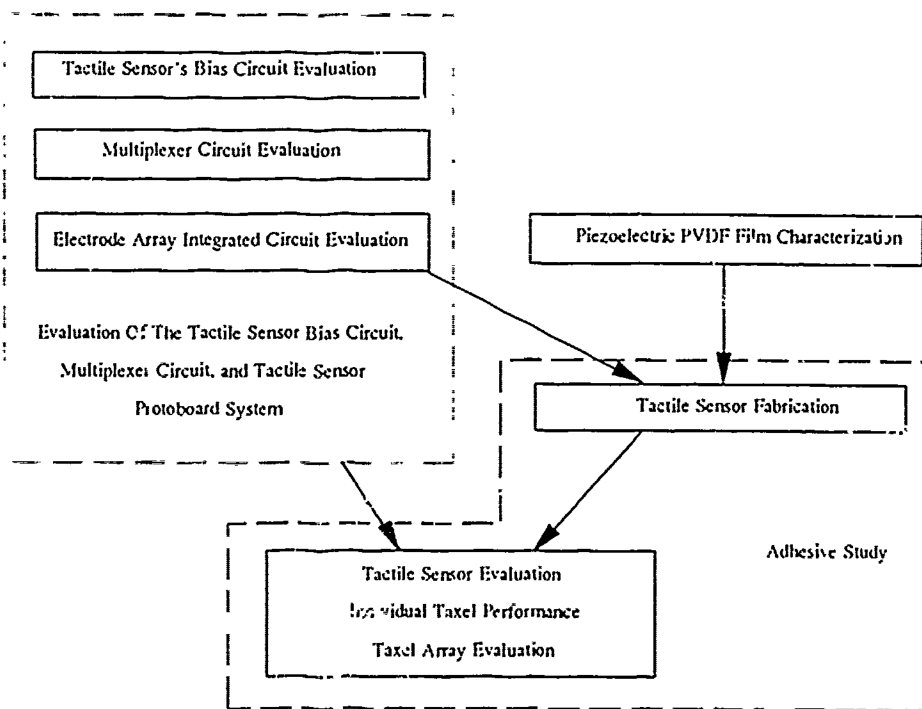

Figure 5.1. Fabrication And Evaluation Flow Diagram.

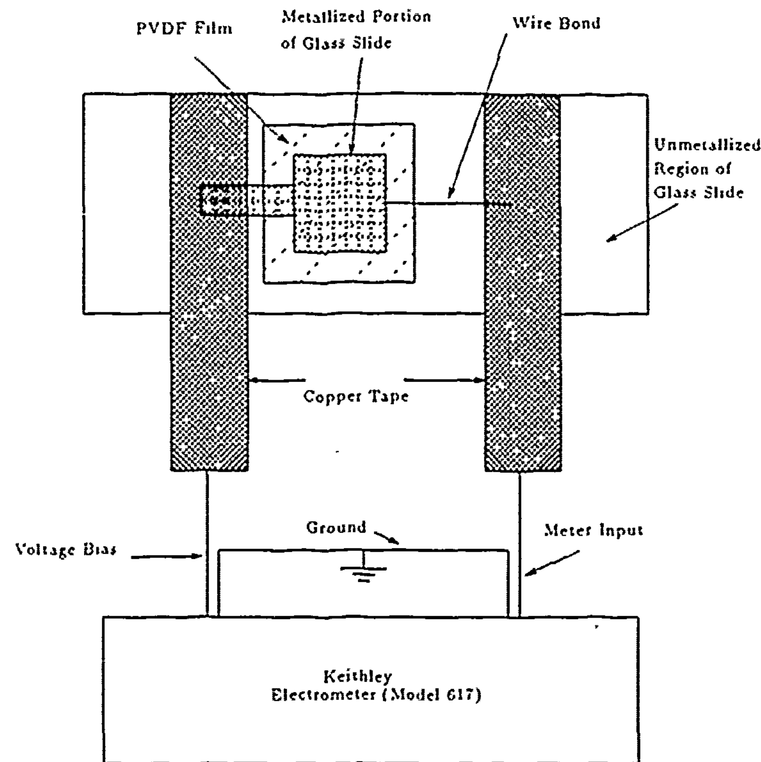

Figure 5.2. Bulk Piezoelectric PVDF Film Characterization Scheme Using A Glass Microscope Slide Substrate.

temperature). This surface was not metallized, and this feature facilitated coupling the charge generated in the PVDF film with the gate contacts of the *in situ* MOSFETs. The detailed procedures for performing the piezoelectric PVDF film characterization process are discussed in Appendix D, and a summary follows.

To determine the polarity of the film, it was attached to a partially metallized glass microscope slide. A metallization process (either thermal evaporation or sputtering) was used to partially cover the glass microscope slide to realize the electrode configuration shown in Figure 5.2. This configuration was also used to simulate the electrode array pattern and the subsequent piezoelectric PVDF film coverage of the electrode on the tactile sensor integrated circuit. One strip of the conductive copper tape was also attached to the deposited electrode.

A piece of the piezoelectric PVDF film was attached to the glass slide using the urethane adhesive. Once the piezoelectric PVDF film was attached to the glass

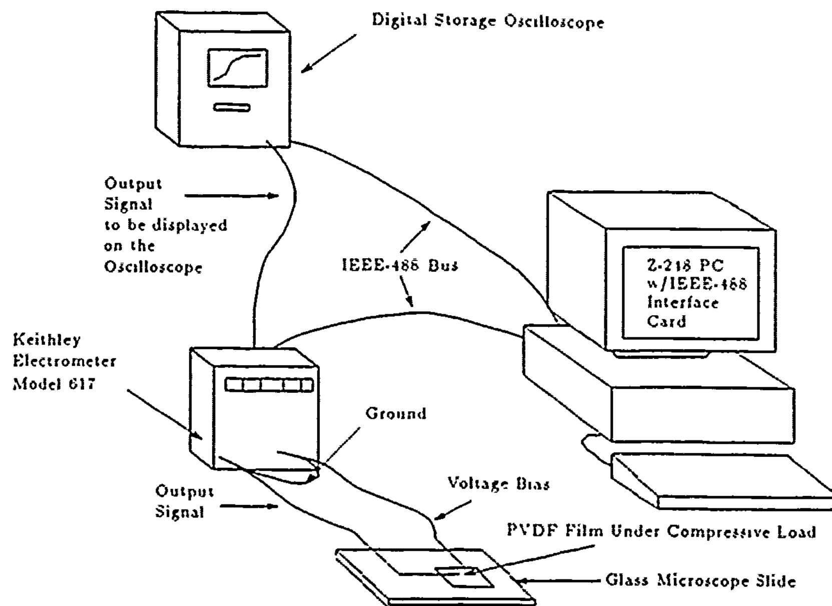

Figure 5.3. Piezoelectric PVDF Film Characterization Instrumentation Configuration.

slide, a bias voltage from the electrometer (Keithley Instruments, model 617, Cleveland, OH 44139) was impressed across the film to simulate the bias voltage required to operate the tactile sensor's IC amplifier. To observe any potential pyroelectric effects, a heat source was brought close to the surface of the piezoelectric PVDF film, and the voltage detected by the electrometer was recorded on a floppy diskette using a personal computer (Zenith Data Systems Corporation. model Z-248, St. Joseph, MI 49085) equipped with an IEEE-488 interface card (Capital Equipment Corporation. model 01000-60300. Burlington. MA 01730) in conjunction with the BASIC program whose listing is provided in Appendix E.

Next, a fixed load was applied to the film, and the voltage detected by the electrometer was recorded on floppy diskette using a Z-248 personal computer in conjunction with the BASIC program. The equipment configuration is illustrated in Figure 5.3. Also, the pyroelectric effects were evaluated by placing a heat source close to the piezoelectric PVDF film while it was under a loaded condition.

If the signal was positive, the top surface of the film was marked to indicate that the metal on that surface would be removed with a wet chemical etchant (ferric chloride); if the signal detected was negative. the film orientation was

reversed, and the load was reapplied. The electrometer then detected a positive response signal. The newly oriented film's surface was then marked for the subsequent metal etch process.

The proper side of a large sheet of the piezoelectric PVDF film was then etched with ferric chloride, rinsed in deionized water, and dried with nitrogen. Next, 6 mm by 6 mm pieces of the piezoelectric PVDf film were cut from the etched sheet and stored for the subsequent fabrication of the tactile sensor.

Tactile Sensor's Bias Circuit Evaluation. The high impedance reed switches (Potter and Brumfield Relay Specialties, Inc., model JWD-171-21, Oakland, NJ 07436) were placed on a solderless test protoboard (E&L Instruments, Inc., Elite-1 Circuit Design System, New Haven, CT 06512). The Keithley electrometer (model 617) was used to evaluate the commercial high impedance switches by measuring both off- and on-impedances. Next, a constant voltage source supplied by a battery was connected to one side of the switch. An oscilloscope was then used to verify that the outputs produced a voltage bias when the switch was activated. The characteristic response of each switch was measured to determine the maximum switching speed of the network. The data acquired during this evaluation was stored on a floppy diskette using a Z-248 personal computer in conjunction with a BASIC program. The BASIC program listing is provided in Appendix E.

Multiplexer Circuit Evaluation. The multiplexer ICs were inserted into an Elite-1 circuit design system protoboard. To evaluate the multiplexer circuit, a random selection subset of 12 inputs were connected to a bias voltage supplied by a battery, and the remaining inputs were connected to a common ground. To evaluate the circuit's ability to multiplex and pass the input voltage provided by the tactile sensor's amplifiers to the output of the circuit, the input provided by the battery varied between 0-V and 15-V using a voltage divider network. Next, a function generator (Hewlett-Packard, Inc., model 3314, Palo Alto, CA 94304) was used to produce a range of frequencies (500 Hz to 100 kHz) to clock the multiplexer circuitry. A digital storage oscilloscope (either a Hewlett-Packard, Inc., model 54100, Palo Alto, CA 94304, or a LeCroy Corporation, model 9400, Chestnut Ridge, NY 10977) was used to display the output of the multiplexer and to store the data. The data was transferred to a Z-248 personal computer for subsequent data processing using the BASIC programs whose listings appear in Appendix E.

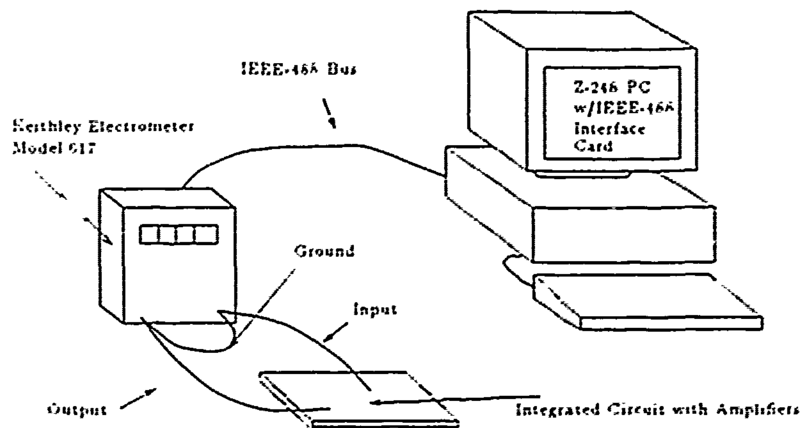

Figure 5.4. Amplifier Test Configuration.

Electrode Array Integrated Circuit Evaluation. Once the integrated circuit was received from MOSIS, the critical elements of the IC were tested. To verify that the integrated circuit had no fabrication defects, a comprehensive visual inspection of the IC was performed using an optical microscope. Next, the DC resistance between adjacent gold wire bond pads in the IC package were measured using the Keithley electrometer (model 617). Finally, the amplifier circuit was evaluated utilizing the following procedure:

1. The expected theoretical DC operating point of the amplifier was determined using a Multimeter (John Fluke Manufacturing Co., model 77/AN, Everett, WA) to measure the amplifier's resistor values. The resistance measurements of several resistors were recorded, and their fundamental statistics (arithmetic average, standard deviation, etc.) were computed.

2. The Keithley electrometer (model 617) was used to apply a linear input signal (increasing from 0-V to 20-V) to one of the amplifiers, and its output characteristics were measured. The results were recorded on a computer diskette using the test configuration shown in Figure 5.4. The data was acquired using a BASIC computer program on a Zenith Model 248 personal computer. This BASIC program listing is provided in Appendix E.

3. An average set of amplifier characteristics was then compared to the SPICE analysis performed during the sensor's design phase.

Evaluation of the Tactile Sensor Bias Circuit, Multiplexer Circuit and Tactile Sensor Protoboard System

The bias, multiplexer, and protoboard circuits comprise a system which provides the bias voltage to the tactile sensor and interrogates response signals from the tactile sensor, and it must be thoroughly characterized. This intensive characterization will ensure that the system operates as intended, and that any deviations from the designed parameters are accounted for.

The sixty-four outputs from the high impedance bias switch network were connected to the input connections of the tactile sensor's protoboard. Several random input connections were tied to ground using a capacitor (165 picofarads), which simulated the piezoelectric PVDF film. The bias voltage was then switched on and off repetitively, and the response was recorded on a digital storage oscilloscope. A characteristic response t me of this configuration was then calculated to ermine its maximum operating speed.

Next, the sixty-four output connections of the tactile sensor protoboard were connected to the input connections of the multiplexer circuit. Similar to the multiplexer's evaluation, several output connections with voltage signals supplied by a battery were routed from the tactile sensor protoboard to the multiplexer inputs. These output channels were displayed and stored on a digital storage oscilloscope, and the data was retrieved using a Z-248 personal computer with a BASIC program. A characteristic response time of this output configuration was then calculated to determine its maximum operating speed.

Finally, an electrode array IC was placed into the tactile sensor protoboard, and select electrodes were activated using a Micromanipulator test probe. The multiplexed output of this condition was recorded using a Z-248 personal computer with a BASIC program. This arrangement provided an operating condition close to the sensor's final operating condition, and it was used to determine the optimum operating speed of the multiplexer during the tactile sensor array evaluation. Also, the effects of this voltage input on neighboring taxels was evaluated before attaching the piezoelectric PVDF film.

Tactile Sensor Fabrication

The physical size of the IC was intentionally limited to an area measuring 7.9 mm by 9.2 mm, and the associated electrode array measured 5.3 mm by

5.3 mm. To fabricate the tactile sensor, the piezoelectric PVDF film was attached to the surface of the IC. Three different adhesives (urethane, polyimide, and *Loctite*) were used to couple the piezoelectric PVDF film to the surface of the IC. The detailed procedures used to fabricate the tactile sensor are presented in Appendix F, and a summary follows.

To fabricate the sensor, the charge on the piezoelectric PVDF film was charge-neutralized by immersing it in a grounded solution of deionized water and HCl. Next, adhesive was dispensed from a syringe onto the center of the piezoelectric PVDF film and spread as a thin layer with a glass slide. The piezoelectric PVDF film was then transferred to and properly centered on the taxel array. A small piece of cellophane was then placed over the piezoelectric PVDF film to prevent the adhesive from bonding with the glass microscope slide. Then, a 6 mm by 6 mm glass microscope slide substrate was properly centered over the piezoelectric PVDF film. A uniform force was then applied to the ensemble with several paper binder clips. The fabrication configuration is illustrated in Figure 5.5. The entire package was then transferred to a vacuum system and exposed to a pressure of 100 microns of mercury for 15 minutes. This cure process was utilized to eliminate trapped gas (solvent) molecules beneath the piezoelectric PVDF film, and it caused the film to be snugly drawn against the electrodes in the IC. Finally, the ensemble was cured at 65°C for 1 hour.

Once the fabrication process was complete, the tactile sensor was visually inspected under an optical microscope to discern the overall quality of the bonded piezoelectric PVDF film. Should the piezoelectric PVDF film not adhere properly, the film was removed, the adhesive was removed with acetone, and the IC was placed in the plasma asher (SPI Supplies, SPI Plasma Prep II, West Chester, PA 19380) to remove residual acetone. The DC resistance between adjacent gold bond pads was then measured using the Keithley electrometer (model 617). (If the DC resistance between adjacent gold bond pads degraded, the gold bond pads of this and subsequent ICs were coated with silicone rubber and the DC resistance was again measured with the Keithley electrometer (model 617)).

For each fabricated tactile sensor, a 1-mil diameter wire was connected to the top electrode surface of the piezoelectric PVDF film, and the other end was attached to a gold wire bond pad on the IC's ceramic package. Conductive silver

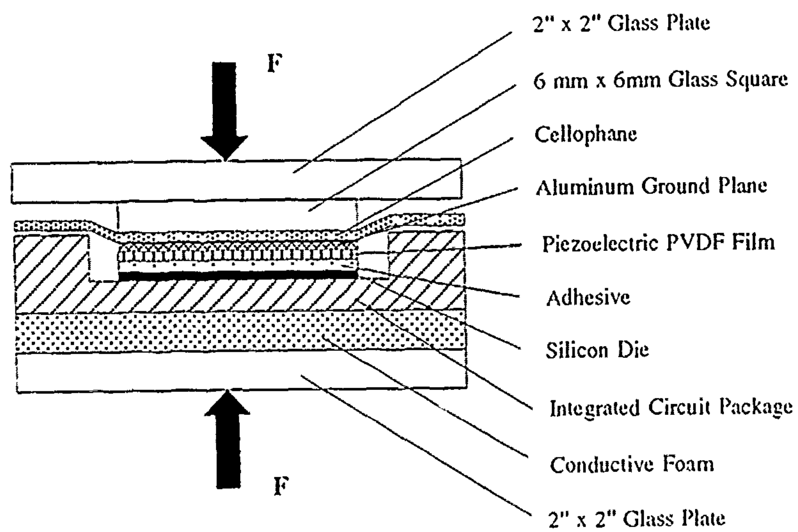

Figure 5.5. Fabrication Configuration Of The Tactile Sensor.

paint was used to attach the wire to the polymer's top surface electrode. This connection serves to electrically ground the top surface electrode.

Adhesive Evaluation

A piezoelectric tactile sensor which is fabricated in the manner described above must possess robust mechanical characteristics. A critical element in the fabrication process is the adhesive used to bond the piezoelectric PVDF film to the electrode array. The adhesive evaluation consisted of two basic components, which included an evaluation of the aging characteristics of the three adhesives, and an evaluation of the electrical properties of the three adhesives.

To evaluate the aging qualities of the adhesives, spare ICs from the previous research efforts were utilized. The spare ICs do not possess the proper electrical characteristics; however, their electrode array pattern is similar to the present design, and they adequately simulate the desired configuration. This technique reduced the number of functioning ICs needed to perform this portion of the research effort. Three sensors using each of the three adhesives (a total of nine) were inspected every seven days over a total duration of two months. Should the properties of one of the adhesives be unacceptable (for example, cracking), the adhesive was not evaluated in the subsequent electrical performance tests.

Using the IC designed during this research effort, the first tactile sensor was fabricated using the urethane adhesive. Capt Fitch reported that the urethane adhesive possessed robust adhesive mechanical characteristics (45:6-1). Using the urethane based adhesive, the tactile sensor was subjected to the individual taxel performance tests and the taxel array performance tests described above. These test results served as a baseline, relative to which the other adhesives were compared. The second and third adhesives were then used to fabricate two other tactile sensors, and their performance measurements were collected. The three tactile sensors were evaluated to provide reproducibility information relative to time, facilitating a comparison of the electrical qualities of the different adhesives.

Tactile Sensor Evaluation

Once the tactile sensor was fabricated, its performance was evaluated in two phases: the discrete taxel response verification test, and the entire taxel array's

response test. These diagnostics were performed for the adhesives which revealed promising results during the initial portion of the adhesive evaluation. To conduct the performance evaluation phases, the tactile sensor IC, tactile sensor protoboard, multiplexer circuit, bias circuit, and test probe were placed in a chamber designed to minimize pyroelectric effects (Figure 4.10). Then, the following tests were performed.

Individual Taxel Performance. Individual taxels were randomly selected for the discrete taxel performance evaluation phase. The top surface of the PVDF film covering the aluminum electrode of the taxel was grounded. The selected taxel was biased with the high impedance reed switch network. The charge correspondingly generated was trapped between the high impedance of the amplifier's gate input and the large impedance of the piezoelectric PVDF film. The output of the *in situ* amplifier was connected to the digital storage oscilloscope and the time rate of change of the charge was measured. An average decay time was calculated, and graphical plots were generated to evaluate whether the output variation possessed a linear, exponential, or some other functional dependency. Next, the bias voltage was reapplied and the response of the taxel was measured for several loads applied using the Micromanipulator probe station. An IEEE-488 bus was used to transmit the data to the Z-248 personal computer where it was recorded on floppy diskettes. A BASIC computer program was used to process this data, and it is listed in Appendix E.

Electrode crosstalk effects were also evaluated. Several taxels were biased using the high impedance reed switch network. Then, the Micromanipulator probe station was used to apply the load to a taxel. Using the output of the tactile sensor protoboard, the output responses of the nearest-neighbor taxels were displayed on the digital storage oscilloscope. As loads were applied to the selected taxel, the response from the neighboring taxels were measured and recorded using an IEEE-488 bus connected to a Z-248 personal computer. A BASIC computer program, whose listing is provided in Appendix E, was used to process the data.

Taxel Array Evaluation. The tactile sensor was inserted into its protoboard and connected to the bias circuit and multiplexer configuration. The entire system (Figure 5.6) was evaluated using the step-by-step procedures listed in Appendix H. A summary of the taxel array evaluation procedures follows.

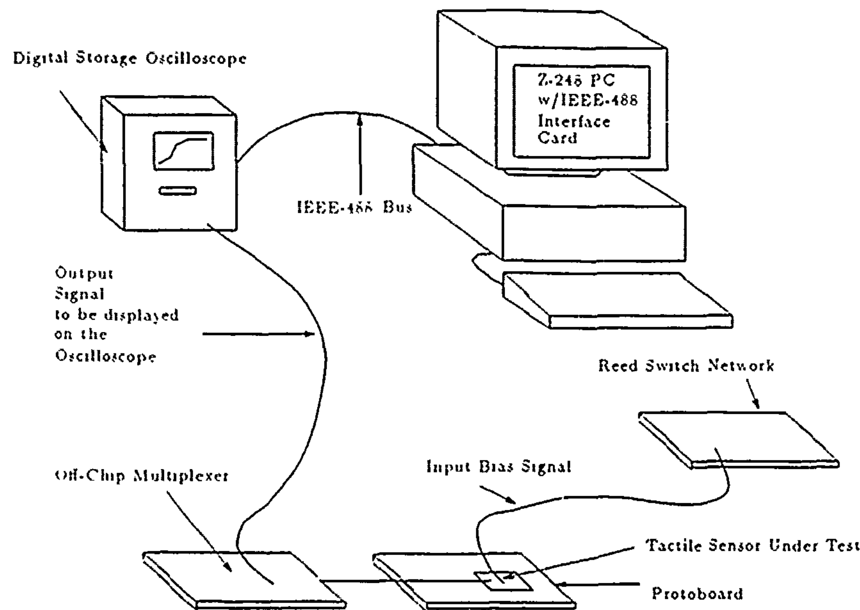

Figure 5.6. Taxel Array Evaluation Instrumentation Arrangement.

Initially, the bias circuit configuration was switched-on to provide a uniform initial condition of the piezoelectric PVDF film. Then, the bias circuit configuration was switched-off, and a pre-load condition was recorded using the digital storage oscilloscope and a Z-248 personal computer equipped with a BASIC program (listed in Appendix E). Next, the test fixture, configured with one of the various load shapes (for example. a sharp edge, small solid square, small solid circle, small polygon. slotted screw head, cross-slot screw head, large solid circle. or toroid) was lowered onto the surface of the tactile sensor IC. and the subsequent output condition was recorded from the digital storage oscilloscope. Finally. the load was removed. and the post-load response was recorded. This procedure was repeated for each load shape.

To analyze the data. an arithmetic average of the pre-load and post-load measurements was used to produce a baseline response indicative of the unloaded state of the sensor. This baseline response was then subtracted from the load measurement. Once the algorithm was performed. the magnitude of the difference values should correspond to the weight of the applied load. Additionally. these difference values were then mapped to their respective locations on a computer generated 8 x 8 array to reconstruct the response of the IC's electrode array. This

process resulted in a three-dimensional plot of the data. In an effort to verify whether the sensor actually detected the shape, several equipotential contours were evaluated to determine which contour most closely resembled the shape of the applied load. The value of this equipotential contour was then used to determine which taxels possessed output responses above or below this threshold contour level. On a two-dimensional representation of the 8 x 8 electrode array, the taxels which possess output values above this threshold level were displayed as black, and the taxels which possess output values below this threshold level were displayed as white. The ensemble of three-dimensional plot, best-fit contour level, and two-dimensional threshold taxel representation should depict the sensor's ability to detect shapes.

Conclusion

The procedures enumerated in this chapter have provided a means to systematically ensure that the entire tactile sensor configuration performs as intended. Any deviations from the designed operating parameters associated with each individual component relative to the actual operating characteristics could be discerned early in this testing phase, and then corrected or compensated to minimize their impact on the overall test program. The data collected from the component tests, the adhesive evaluation study, and the tactile sensor tests will be presented in the next chapter.

VI. Evaluation Results

Introduction

Critical to the evaluation of a research effort is the analysis of the acquired data results. Since the evaluation portion of this research effort was constructed around an incremental test approach, each component was thoroughly evaluated and analyzed before proceeding to the next higher-level evaluation phase. In this fashion, unexpected results led to a better understanding of how each component contributed to the overall performance of the tactile sensor.

This chapter will present, in the chronological order accomplished, the performance evaluation results for each supporting component, the adhesive study, and the tactile sensor. Initially, each component which supported the final performance evaluation configuration was thoroughly tested and evaluated to determine its measured performance relative to its anticipated performance specified in Chapter IV. Next, an intermediate evaluation of the combination of support components without the tactile sensor IC was evaluated to determine the effects, if any, of integrating the support components together. Then, in an effort to evaluate the performance of three adhesives, several non-functioning tactile sensors were fabricated and their adhesive properties evaluated. Finally, an operational tactile sensor was fabricated and inserted into the performance evaluation equipment configuration, where both individual taxel response and the array response were evaluated.

Component Testing

The evaluation of each fundamental component was used to characterize its operation before it was integrated into the final test configuration. The results of this portion of the test program include those from the piezoelectric PVDF film characterization, the tactile bias circuit evaluation, and the multiplexer circuit evaluation. Also included are the electrode array IC evaluation results, and the evaluation results of the tactile sensor protoboard, bias circuit, and multiplexer system.

Piezoelectric PVDF Film Characterization Results. Concurrent with the fabrication of the tactile sensor IC, the piezoelectric PVDF film was characterized to determine its polarity. The surface of the piezoelectric film which develops a positive charge when contacted with an externally applied force was determined, to ensure proper operation of the *in situ* amplifiers after attachment of the piezoelectric film to the surface of the electrode array IC.

To implement this evaluation, a glass microscope slide was placed into the sputter system (SPI Supplies, SPI Sputter Coater, P. O. Box 342, West Chester, PA 19380), and a 3000 Å thick gold film was sputtered onto its surface. Once the small piece of piezoelectric PVDF film was attached to the slide, the copper tape leads were connected to the electrometer (Keithley Instruments, model 617, Cleveland, OH 44139) as described in Chapter V. Several tests were then performed to determine the polarity of the film and the effects of a temperature gradient.

To determine the polarity of the film, the first test implemented was to evaluate the response of the film under the influence of an externally applied load. Figure 6.1 illustrates the response of the film, initially biased at 2-V, to a 100 g load. While this test confirmed the proper polarity of the film, it revealed the fragility of the test configuration. The performance of the glass microscope slide configuration tended to decay quite rapidly, as indicated by a voltage smaller than the 2-V level appearing across the film. This attenuated voltage level was caused by poor adhesion of the gold metal to the glass microscope slide surface, and poor uniformity of the urethane adhesive. Since each glass microscope configuration could typically be utilized for 4 or 5 tests before any film adhesion problems became apparent, 10 glass microscope slide configurations were fabricated, and data was collected before the configuration performance degraded.

To experimentally measure the effects of a temperature gradient and record a baseline response of the piezoelectric PVDF film to heat, a heat source was placed near the film. As discussed in Chapter III, the piezoelectric constant of the piezoelectric PVDF film and its pyroelectric constant possess opposite signs, potentially resulting in charge signal amplifier output signals which do not necessarily correspond to the amplifier output when simply a load is applied. The temperature change resulting from the application of heat from a soldering iron (135°C) placed 3 cm from the surface of the PVDF film produced a negative voltage response illustrated in Figure 6.2.

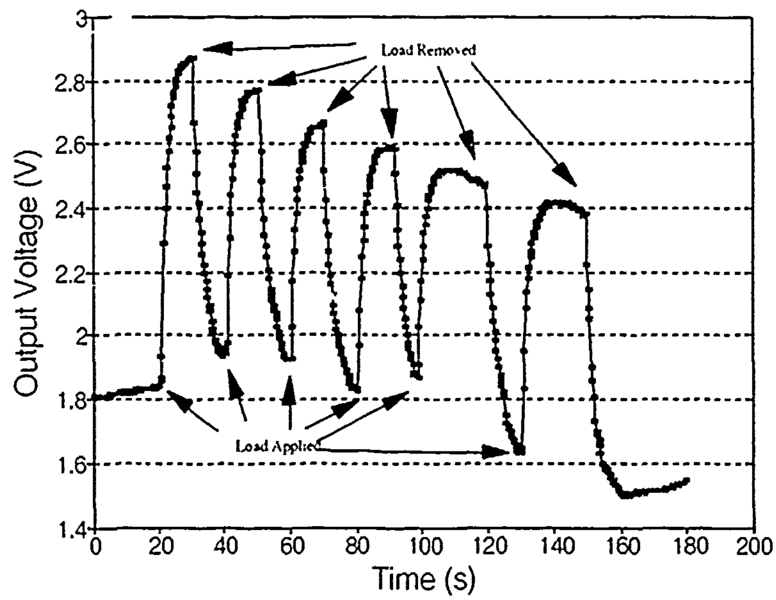

Figure 6.1. Output Response Of A 100 g Load Applied To A Piece Of Piezoelectric PVDF Film Attached To A Glass Microscope Slide.

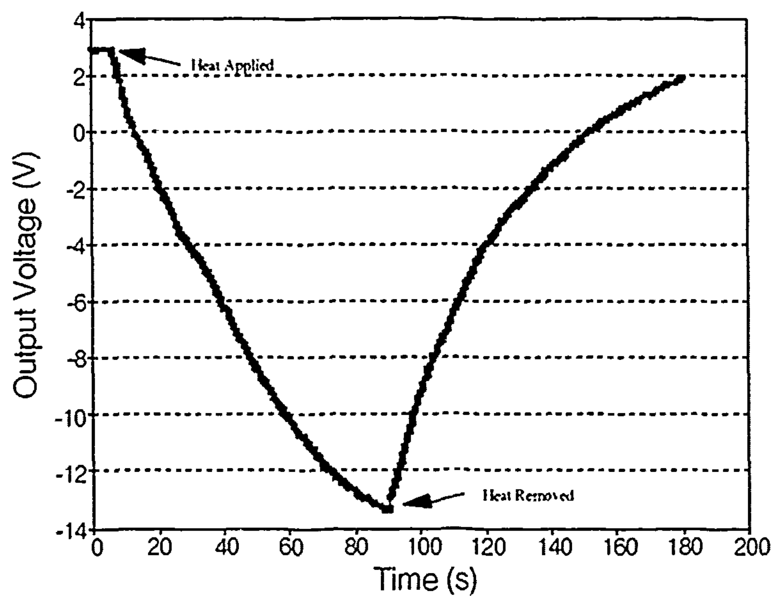

Figure 6.2. Output Response Of Heat (135°C) Applied To A Piece Of Piezoelectric PVDF Film Attached To A Glass Microscope Slide.

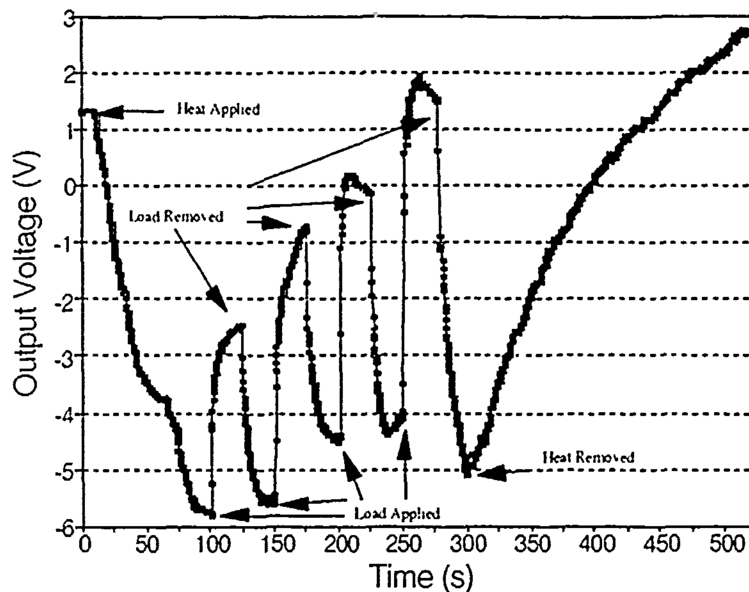

Figure 6.3. Output Response Of A 100 g Load And Heat (135°C) Applied To A Piece Of Piezoelectric PVDF Film Attached To A Glass Microscope Slide.

To evaluate the effects of both the application of heat and the application of an externally applied load, a temperature gradient and a load were simultaneously applied to the glass microscope slide configuration. The results of a 100 g load and a 135°C temperature gradient are illustrated in Figure 6.3. Unfortunately, a voltage generated by a large temperature gradient applied to the completed tactile sensor configuration could potentially drive the floating electrode potential negative and out of the linear region of the amplifier. With the charge amplifier output at zero, no output changes resulting from the application of an externally applied load would be measured. In an effort to eliminate or minimize temperature gradients of this magnitude, the test configuration was placed within the pyroelectric effect minimization chamber. Unfortunately, this chamber was unable to protect the system from external variations in temperature.

Tactile Sensor Bias Circuit Evaluation. The tactile sensor bias circuit was designed to apply a uniform voltage to the electrode array and the piezoelectric

PVDF film, and then to disengage itself from the taxel array. To perform this function, each reed switch in the circuit must possess a high off-impedance as well as a low on-impedance. Therefore, the impedance of each reed switch was measured using the electrometer configured with a 70-V bias voltage. Four measurements of the 64 reed switches indicated an average off-impedance of $2.05 \times 10^{13}\ \Omega$ and an average on-impedance of $0.1\ \Omega$. Over the course of this entire research effort, several subsequent measurements of the reed switches were performed. If the off-impedance of one of the reed switches fell below $10^{12}\ \Omega$, it was replaced with a new switch.

To simultaneously switch the high impedance switches from an off-state to an on-state, a signal switcher (Wavetek, Inc., Wavetek Programmable Signal Switcher, model 604, 9045 Balboa Ave., San Diego, CA 92123) was connected to the reed switch control line. This allowed immediate switching of the reed switch control line using a single switch button. If the reed switch control line was biased to a level larger than the switch threshold level of 3.5-V, then the reed switches turned on, and if the control line was biased to a level less than 3.5-V, the reed switches turned off.

To determine the timing characteristics of the switch, the high impedance switch was configured with an input bias voltage of 5-V. To simulate the capacitive load of the piezoelectric PVDF film over the tactile sensor electrode, a 4 pF capacitor was inserted into the protoboard (E&L Instruments, Inc., Elite-1 Circuit Design System, New Haven, CT 06512), and the timing response recorded. However, due to parasitic capacitances within the protoboard, the response of a switch with a 4 pF capacitive load was identical to the response of a switch without any capacitive load. Therefore, in an effort to produce an output which was different from the no load response, a 165 pF capacitor was chosen. The characteristic worst-case response time is displayed in Figure 6.4, indicating a 0.4 ms decay time constant.

Multiplexer Circuit Evaluation. The function of the multiplexer circuit was to convert simultaneous voltage outputs from the tactile sensor IC into a serial stream of information which was displayed on the digital storage oscilloscope. To ensure that the multiplexer utilized in this research effort would pass the data unaffected from its input to its output, at a sufficient speed to sample the entire

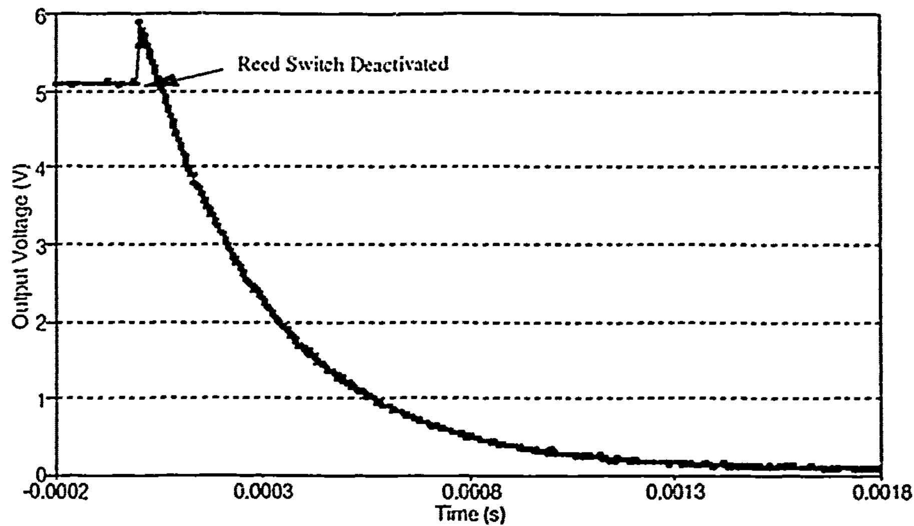

Figure 6.4. Arithmetic Average Time Response Of 10 High Impedance Reed Switches.

array before the state of the array changed, a range of voltage values corresponding to the output of the charge signal amplifier linear region was used. Additionally, the clock frequency was varied over a range spanning 500 Hz to 100 kHz. As an example of data extracted during this testing phase, Figure 6.5 illustrates the response of the multiplexer to a 5.8 V input voltage applied directly to the inputs of the multiplexer ICs. No adverse operating affects (for example, abnormally long switching times) could be discerned.

Electrode Array Integrated Circuit Evaluation. When the electrode array integrated circuit was received from MOSIS, an extensive visual inspection of the IC using an optical microscope concluded that no fabrication defects were visible. Next, the DC resistance between the gold bond pads of the IC measured with the electrometer confirmed high impedance (10^{13} Ω), and potentially no charge leakage between the pads. Once this initial device verification was complete, an evaluation of the IC components ensued. To illustrate the physical arrangement of the electrodes and their corresponding taxel numbers, Figure 6.6 is provided.

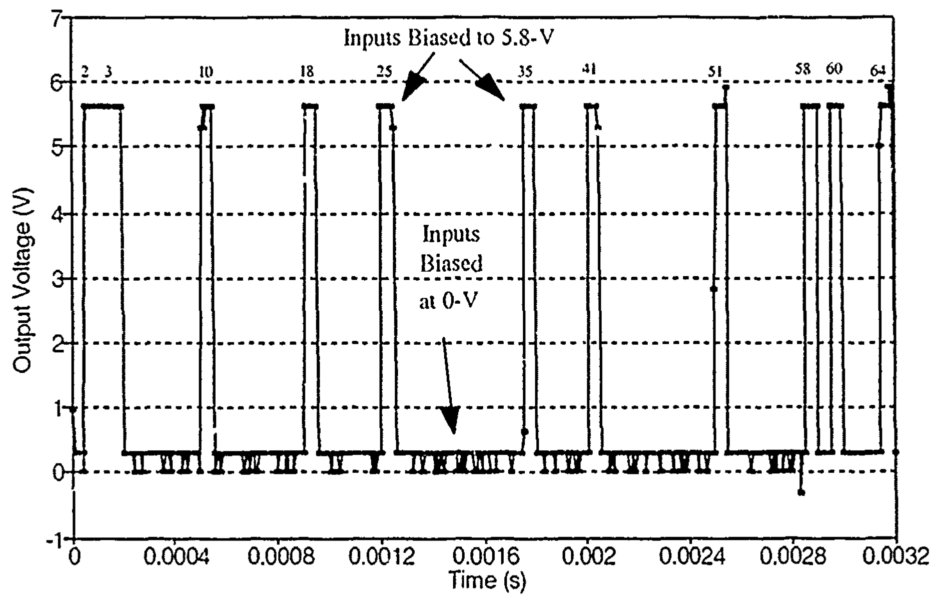

Figure 6.5. Multiplexer Circuit Response To A 5.8-V Bias Voltage Input Applied At A 20 kHz Rate.

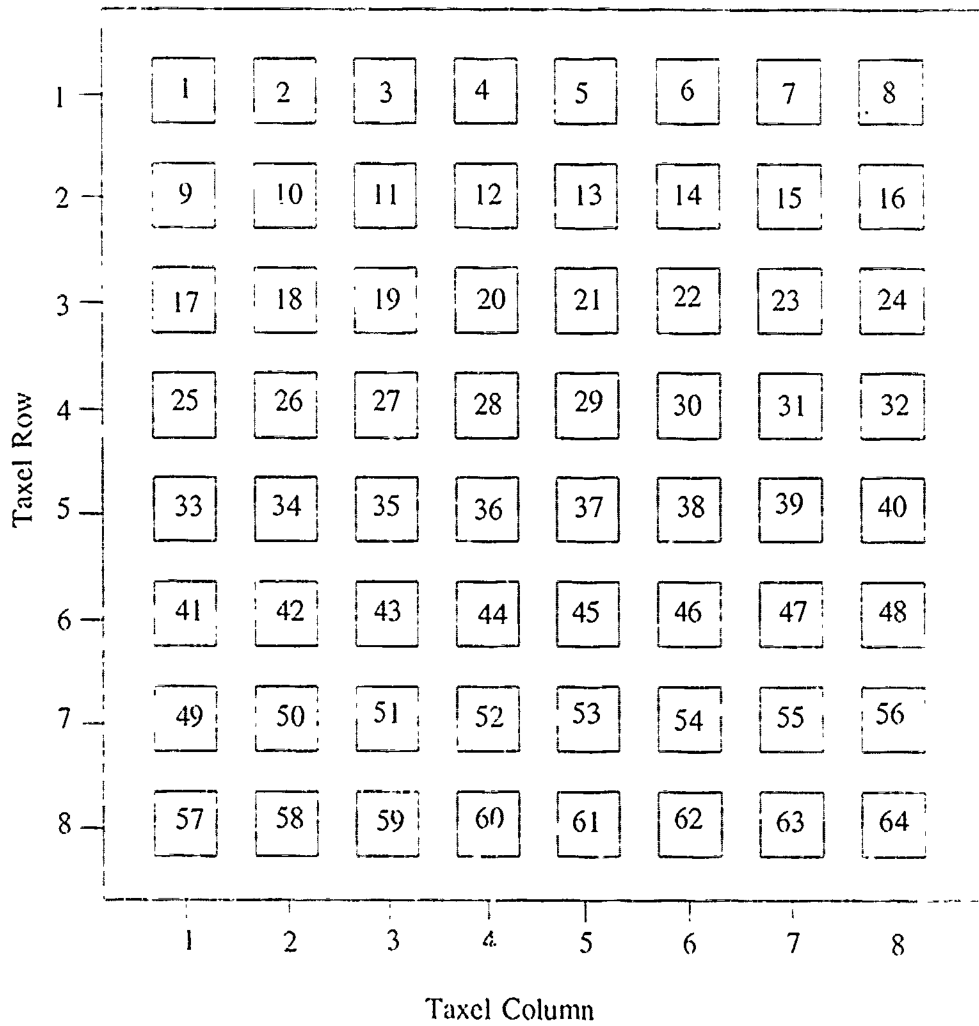

Figure 6.6. Taxel Numbering Scheme.

Charge Signal Amplifier Performance Results. To ensure the charge signal amplifier would perform as designed, the two resistors contained in the amplifier were measured to determine whether they were fabricated within the tolerances specified by MOSIS. Two hundred twenty-four amplifiers on seven ICs were characterized, resulting in average resistor values of 7.34 kΩ and 5.28 kΩ for the two resistors. Subsequently, the resistor parameters were updated in the SPICE simulation program, resulting in the expected characteristic transfer function curve for a 15-V supply bias (V_{dd}) illustrated in Figure 6.7.

The IC was then inserted into the tactile sensor protoboard, and a supply voltage (V_{dd}) applied (Hewlett-Packard Co., Power Supply, model HP6205B, 3155 Porter Dr., Palo Alto, CA 94304). A Keithley electrometer (model 617) provided a bias voltage, which spanned 0-V to 20-V in 0.5-V steps, to the input of a randomly selected amplifier. Simultaneously, the electrometer measured the output of this amplifier. Several amplifiers were tested using different V_{dd} values spanning 10-V to 20-V, in 2-V increments. To produce a measured charge signal amplifier transfer function curve for each V_{dd}, 11 measured transfer function responses were arithmetically averaged. The resulting transfer function curve for a 15-V Vdd is illustrated in Figure 6.8. Unfortunately, the measured operating performance of the amplifier was not acceptable because the range of output voltages was not as large as expected. To find a supply voltage which produced a range of output voltages similar to the SPICE simulated amplifier output range, V_{dd} was reduced incrementally. A 14-V V_{dd} resulted in amplifiers which perform similar to the SPICE simulated circuit. Figure 6.9 and 6.10 present the expected transfer function calculated by SPICE for a 14-V V_{dd} and the measured charge signal amplifier transfer function, respectively.

In an effort to determine the minimum input voltage variation detected on the output, the linear region of the amplifier was analyzed. The measured linear region of the amplifier when operating with a 14-V V_{dd} spanned 2.5-V to 7-V. The gain over this region averaged 0.98, so a a 0.1-V change in the input voltage would cause a 0.098-V change on the output. The gain of the amplifier was less than the expected gain derived from the SPICE analysis; however, an extended linear region resulting from using this V_{dd} level was desired. Using the Keithley electrometer (model 617), a voltage was applied to the input of the charge signal amplifier. The output signal was also measured using the electrometer. The smallest detectable

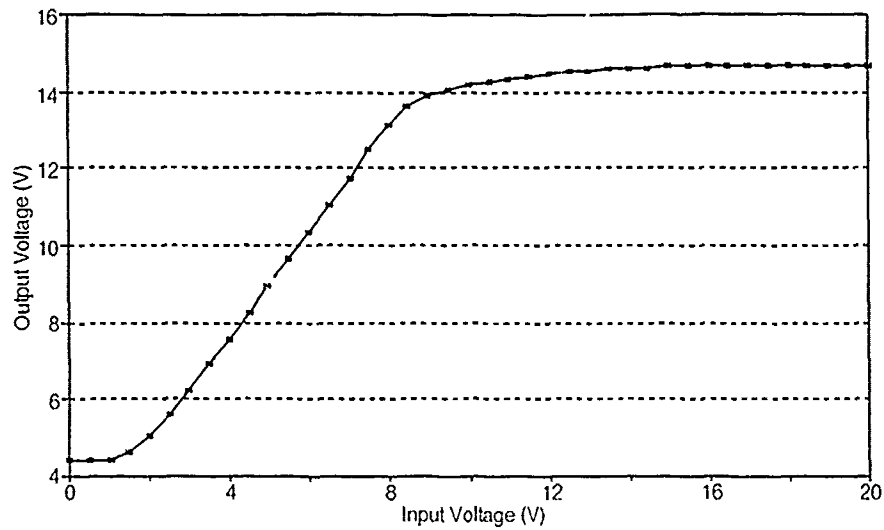

Figure 6.7. Characteristic Transfer Function Curve For The Charge Signal Amplifier Generated Using SPICE With 7.34 kΩ and 5.28 kΩ Resistors And A 15-V V_{dd} Bias.

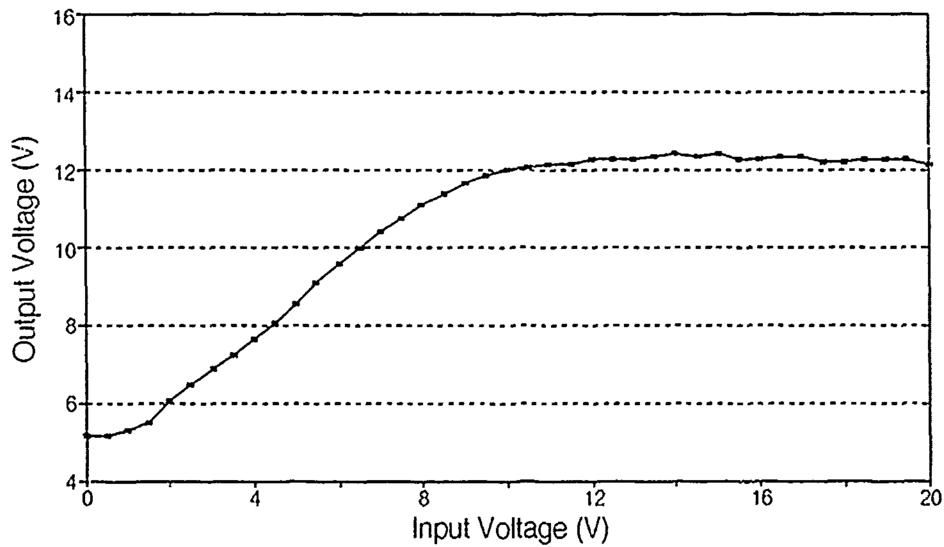

Figure 6.8. Measured Transfer Function Response For The Charge Signal Amplifier Operated With A 15-V V_{dd} Bias.

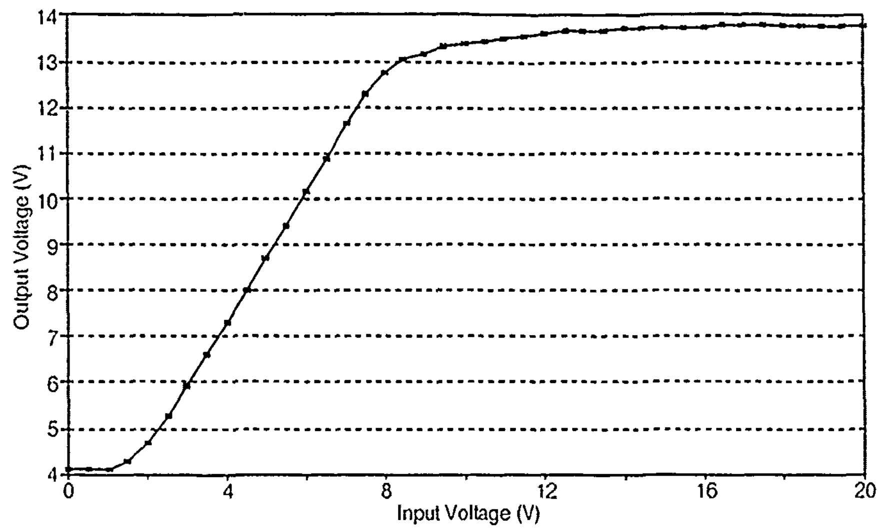

Figure 6.9. Characteristic Transfer Function Curve For The Charge Signal Amplifier Generated Using SPICE With 7.34 kΩ And 5.28 kΩ Resistors And A 14-V V_{dd} Bias.

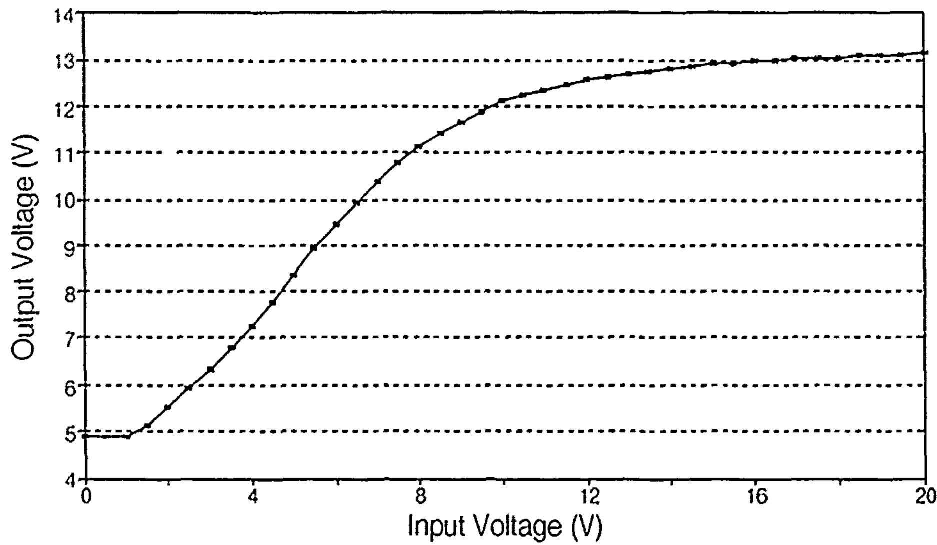

Figure 6.10. Measured Transfer Function Response For The Charge Signal Amplifier Operated With A 14-V V_{dd} Bias.

output signal was a 0.041-V change in the input level, corresponding to a 0.04-V change in the output level. If the operating point of the amplifier was below the linear region of the amplifier, the gain dropped from 0.8 at the 2-V input level to 0.003 at the 0.5-V input level. For an input above the linear region of the amplifier, the gain drops from 0.8 at the 7.5-V input level to 0.1 at the 14-V input level. Consequently, any change in input voltage was extremely difficult to detect and record.

Charge Signal Amplifier Problem. While operating the electrode array IC over time, a phenomenon developed which manifested itself as one or more "stuck" outputs. Always initially occurring on the same taxel amplifier output (taxel number 49), the outputs were either stuck at ground, or stuck at V_{dd}. Figure 6.11 illustrates each taxel output when a new tactile sensor IC, with no piezoelectric film attached, was inserted into the tactile sensor protoboard and the inputs biased to 3-V. Figure 6.12 represents the same IC after more than 12 hours of operation with a 14-V V_{dd}. To determine the cause of this phenomenon, the impedance was measured between several points on the charge signal amplifier (Figure 6.13 provides a schematic representation of the measurement locations).

For an amplifier with its output stuck at V_{dd}, two causes were found. In the first case, impedance measurements between the aluminum electrode and the intermediate test probe pad indicated a reduction in value with respect to time. Initially, the resistance between the electrode gate and the test probe pad located within the amplifier measured $> 10^{13}$ Ω, as expected. However, after several hours, this resistance slowly decreased (as time increased) to less than 200 Ω. Apparently, this shorting effect between the electrode and the intermediate amplifier node caused the electrode to be biased at a level different from the external bias level. This manifested itself as a "stuck-high" output. In the second case, impedance measurements between the intermediate node and ground indicated that the drain of the amplifier first MOSFET was shorted to ground, which also manifested itself as a "stuck-high" output. For charge amplifiers whose outputs were stuck at ground, the impedance measurements between the output and ground confirmed the drain of the second MOSFET was shorted to ground, resulting in the "stuck-low" output.

To determine whether the 14-V V_{dd} was an excessive supply voltage which caused the MOSFETs to breakdown, several additional tests were performed on a

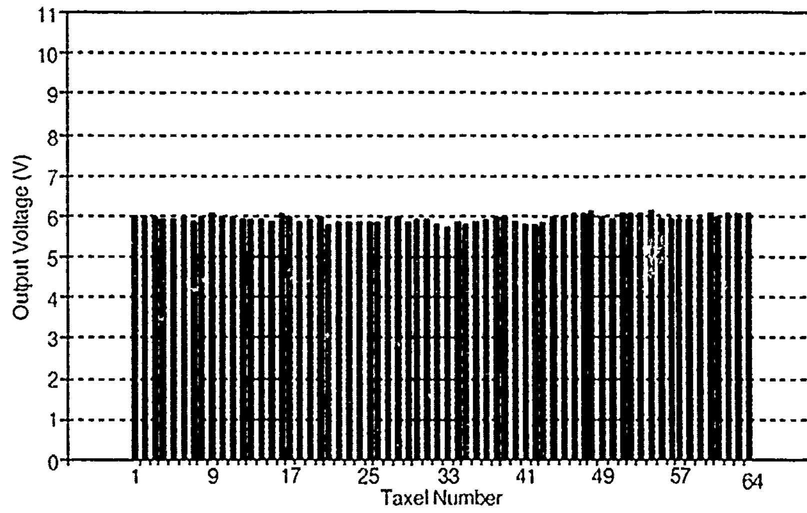

Figure 6.11. Output Of A New (< 1 Hour Use) Tactile Sensor IC Without The Piezoelectric PVDF Film Attached.

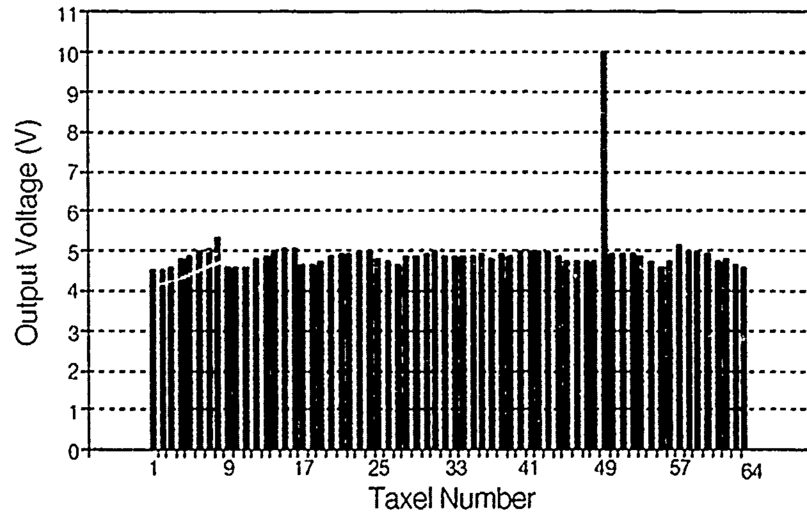

Figure 6.12. Output Of A Tactile Sensor IC Without The Piezoelectric PVDF Film After 12 Hours Of Operation.

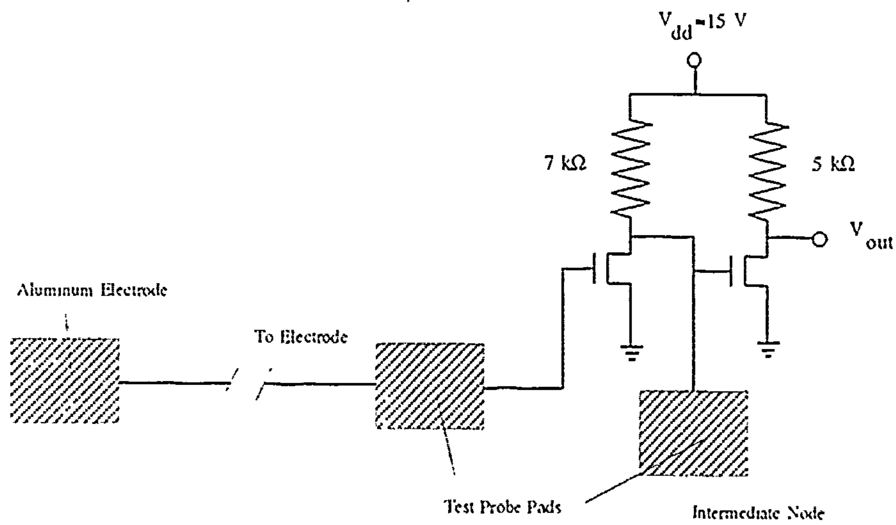

Figure 6.13. Schematic Representation Of The Signal Charge Amplifier Test Probe Pad Locations.

new IC. The V_{dd} was incrementally varied from 10-V to 14-V in 1-V steps. For each value of V_{dd}, all of the charge signal amplifier outputs were monitored and recorded during a 36 hour period. The evaluation results indicated that a V_{dd} of 10-V, 11-V, and 12-V did not damage the MOSFETs within this period of time. However, for a V_{dd} above 12-V, the MOSFET breakdown problem manifested itself. One contributing factor could have been the size of the MOSFETs used in this effort. These MOSFETs were designed using minimum feature size, and a physically larger amplifier possessing similar characteristics could potentially resolve this problem.

Tactile Sensor Protoboard, Bias Circuit, and Multiplexer System Evaluation Results

Before an operational sensor was inserted into the tactile sensor evaluation configuration, the system used to support the sensor operation was characterized. This evaluation consisted of integrating three components: the bias circuit, the multiplexer, the tactile sensor protoboard, and the electrode array IC (without the piezoelectric PVDF film attached). The tactile sensor protoboard was connected to the bias circuit and multiplexer circuit via 3 foot long ribbon cables. These tests were designed to evaluate whether any signal degradation occurred when the system integration was implemented. Figure 6.14 illustrates a schematic representation of the system configuration.

The initial test performed in this evaluation phase verified whether the reed switches possessed similar characteristics after the integration step. To implement the test, a 165 pF capacitor was inserted in the protoboard between an input line and ground, and the response was measured and compared to the initial reed switch tests. The Wavetek Signal Switcher produced a voltage transient on the reed switch control line (illustrated in Figure 6.15) which caused the reed switch output to fluctuate. Figure 6.16 illustrates a transient voltage peak which appeared after the reed switch was turned off. The additional capacitance due to the long ribbon cables connecting the tactile sensor protoboard and the reed switch bias circuit could have potentially held this large voltage peak at a high level, biasing the operational tactile sensor electrode to an unknown value. To eliminate this peak, the Wavetek signal switcher was removed. A voltage source was connected to the reed switch control line, and the voltage level control knob was used to switch the reed switches simultaneously using their threshold voltage (3.5-V) as the switching point. Figure 6.17 illustrates their characteristic response.

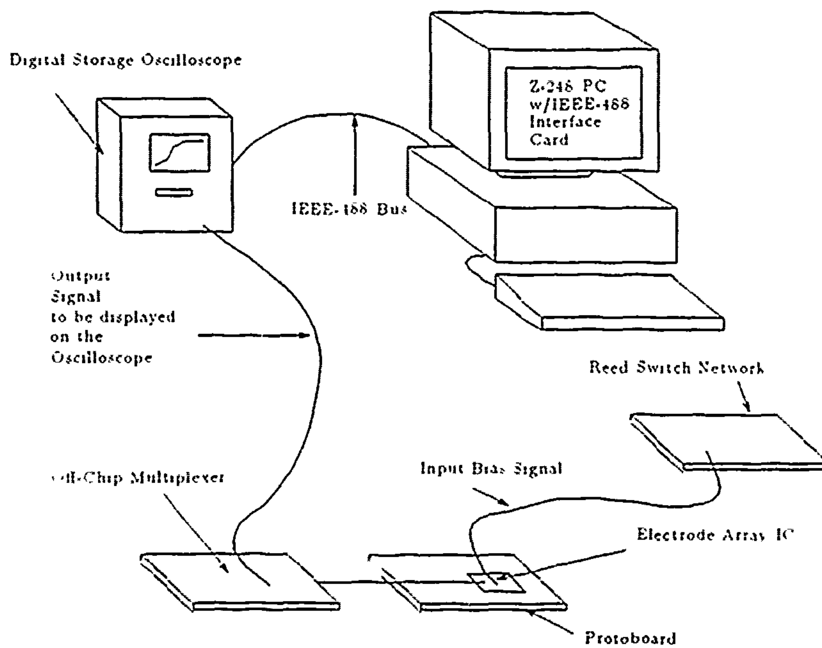

Figure 6.14. Schematic Of The Bias Switch Network, The Multiplexer. And The Tactile Sensor Protoboard System Evaluation Configuration.

Next. the multiplexer output response was measured over a frequency range spanning 355 Hz to 14 kHz with input voltages spanning 1-V to 14-V applied directly to the test protoboard. The response over this range illustrates a reduction in multiplexer performance when compared to the initial multiplexer tests. and it was caused by the addition of the long ribbon cables to the system. Figure 6.18 illustrates a sample multiplexed output while the multiplexer was clocked at 14.2 kHz. The results showed that the switching time from a high level to a low level increased. Consequently. the multiplexer was operated at a lower frequency.

To verify whether this degradation would potentially affect the multiplexed tactile sensor output, and to determine an adequate operating clock frequency for the system. an electrode array IC with no piezoelectric PVDF film attached was inserted into the tactile sensor protoboard. The Micromanipulator probe station was used to apply a voltage bias (spanning 0-V to 14-V) directly to an electrode. in an effort to simulate the voltage generated by the application of a load. The individual taxel output was then multiplexed over a range of frequencies spanning 160 Hz to 10.4 kHz. and the rise and fall times of the taxel output were measured.

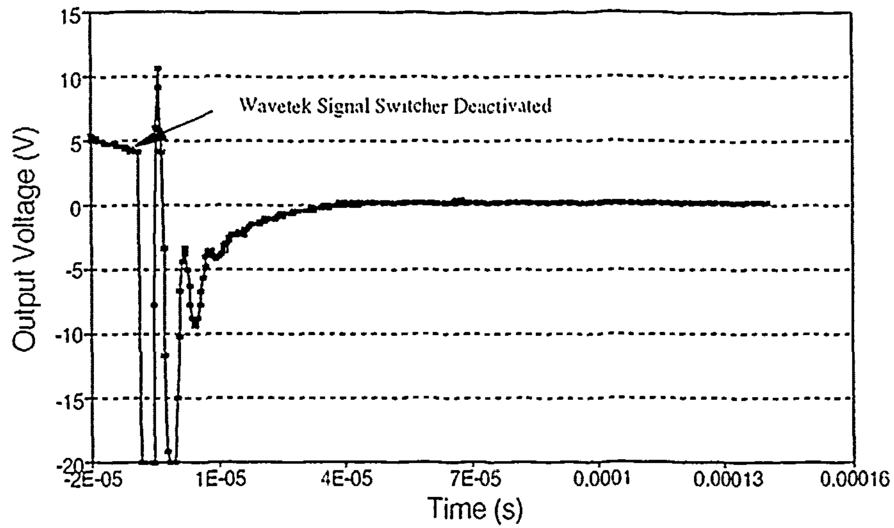

Figure 6.15. The Output Of The Wavetek Signal Switcher Connected To The Reed Switch Control Line.

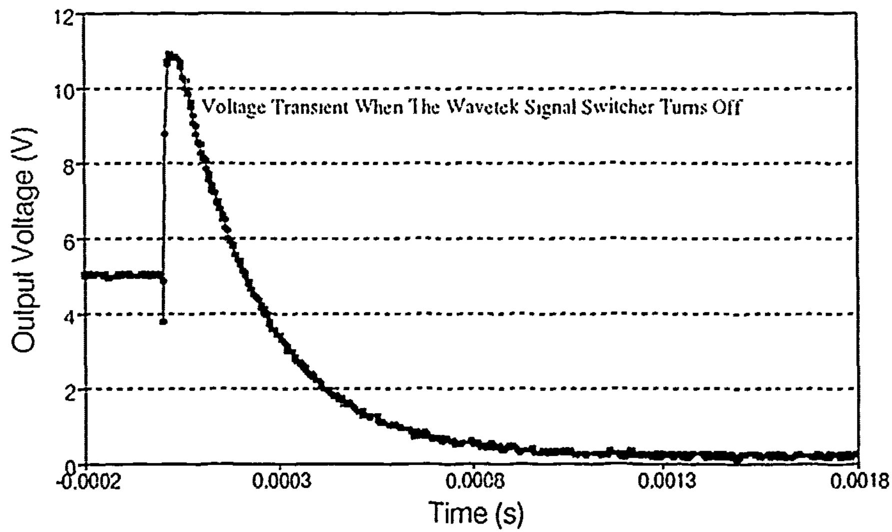

Figure 6.16. Reed Switch Characteristic Response Possessing A Large Voltage Transient.

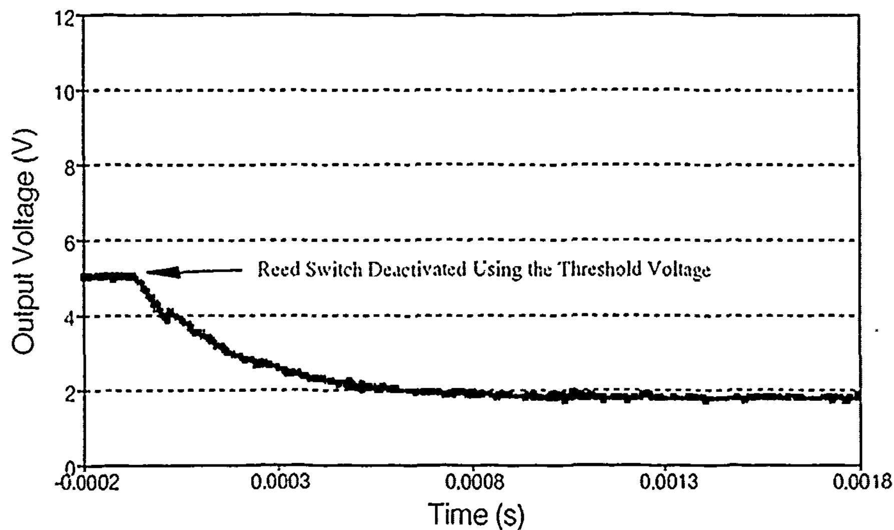

Figure 6.17. Reed Switch Characteristic Response After The Wavetek Signal Switcher Used To Switch All The Reed Switches Simultaneously Was Removed.

Figure 6.19 illustrates the multiplexed output of taxel number 11 biased at 5-V. with the multiplexer clocked at 320 Hz. Under these test conditions, the multiplexer possessed a characteristic rise time of 14 μs and a fall time of 140 μs for all frequencies. Since the multiplexer could operate between 500 Hz and 2 kHz without significant input to output signal degradation, a compromise between speed of the multiplexed output and width of each individual input signal contained in the overall output signal stream resulted in an optimum operating frequency of 1.28 kHz. This allowed all 64 taxels to be displayed on the digital storage oscilloscope at one time, with each input signal possessing a 781 μs width. The array was scanned every 50 ms, which was sufficient time to sample the array before its surface potential state changed.

The final test performed in the support component evaluation phase consisted of an electrode crosstalk evaluation. A voltage bias was applied directly to a taxel on the electrode array IC using the Micromanipalator probe station. This voltage bias spanned 0-V to 14-V. The multiplexed output revealed crosstalk between taxels whose signal lines were placed next to each other. An example of the taxel

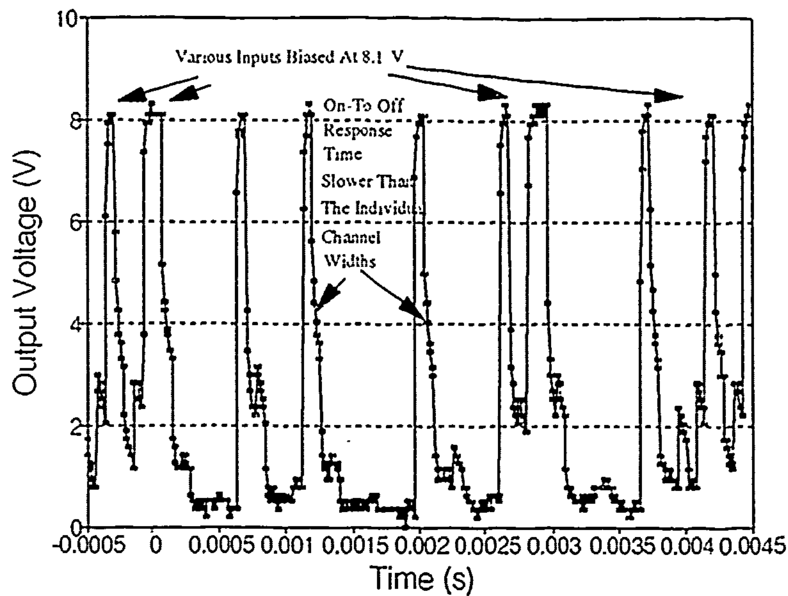

Figure 6.18. Multiplexed Output Of An 8.1-V Bias Applied To The Tactile Sensor Protoboard Clocked At 14 kHz.

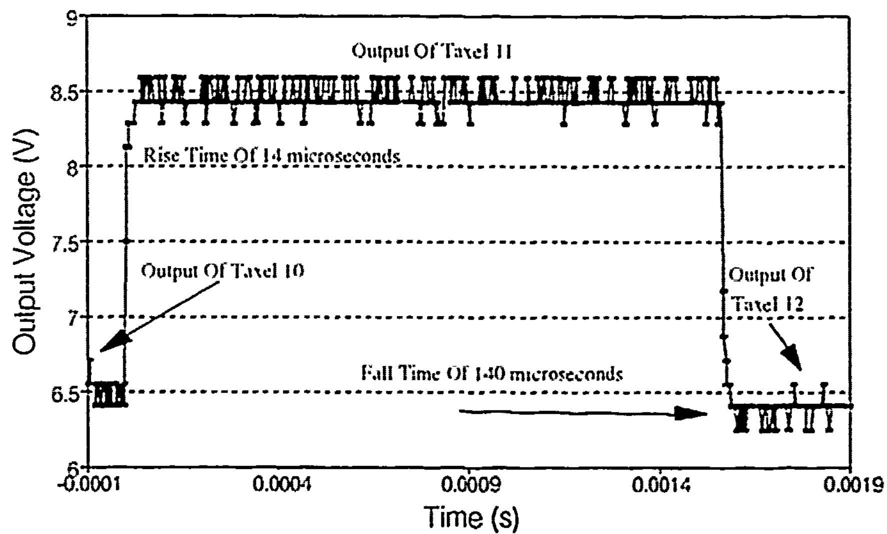

Figure 6.19. The Multiplexed Output Of Taxel 11 Biased At 5-V.

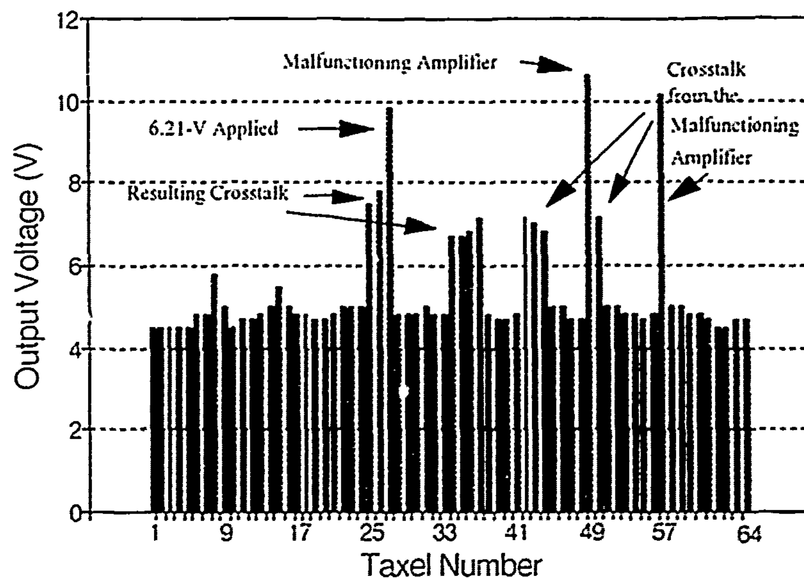

Figure 6.20. Crosstalk Of The Nearest-Neighbor Taxels When A 6.21-V Bias Was Applied To Taxel Number 27.

outputs is displayed in Figure 6.20. Because the crosstalk between taxels was not detected until the electrode array IC was inserted into the equipment configuration, crosstalk was determined to be inherent in the IC layout. The crosstalk values depended on the location of the taxel and its associated signal line routing. the results of the nearest-neighbor output voltage responses indicate a range from 20% to 67% of the applied voltage value on the neighboring taxel.

Adhesive Evaluation

In an effort to find a robust adhesive for attaching the piezoelectric PVDF film to the surface of the IC, three adhesives were used to fabricate 10 non-functioning tactile sensors. The adhesives used were urethane (Miller-Stephenson Chemical Co., Urethane (MS 470/22) Aerosol, George Washington Highway, Danbury, CT 06180), polyimide (AMOCO Chemical Co., 200 E. Randolph Dr., Chicago, IL 60601), and a plastic dielectric (Loctite Corporation, *Loctite* Tak Pak number 7586A21, Newington, CT 06111). To provide

a sample size sufficiently large to draw conclusions concerning the adhesive's properties, three sensors were fabricated from the urethane, three from the polyimide, and four from the plastic dielectric (each fabricated using the adhesive stored at different temperatures).

The urethane and polyimide adhesives possessed similar physical adhesive properties, for example conformal electrode coverage over the entire array (Figure 6.21), and adequate edge adhesion. On the other hand, at room temperature, the *Loctite* tended to cure extremely fast, before proper application of force from the compression sandwich configuration could be implemented, resulting in poor adhesion. In an effort to change the cure time of the adhesive, three other attempts were made to fabricate a sensor using this adhesive stored at three different temperatures. One sensor was fabricated using the adhesive stored at −15°C, one was fabricated using the adhesive stored at −8°C, and one was fabricated using the adhesive stored at 40°C. The only relatively successful sensor fabricated was the one which used the adhesive stored at −8°C. A small portion of the electrode array possessed conformal coverage (illustrated in Figure 6.22); however, the film sample did not adhere to most of the array, and one of the corners did not adhere properly.

These 10 sensors were monitored for a period of two months to record any deviations and defects which occurred over time. It appeared that no visible degradation of the adhesive properties for any of the adhesive samples developed during this period of time. Appendix G contains several photographs comparing the initial and final conditions of sensors fabricated with urethane, polyimide, and *Loctite* adhesive.

Tactile Sensor Evaluation

Once an operational tactile sensor was fabricated, its performance was evaluated in two phases, including discrete taxel response verification tests, and the evaluation of the entire taxel array response tests. Also performed was a comparison of the electrical characteristics resulting from the polyimide and urethane adhesives (the *Loctite* candidate did not produce a functional tactile sensor). Additionally, the tactile sensor IC, multiplexer circuit, bias circuit, and test probe were placed in the pyroelectric effects minimization chamber.

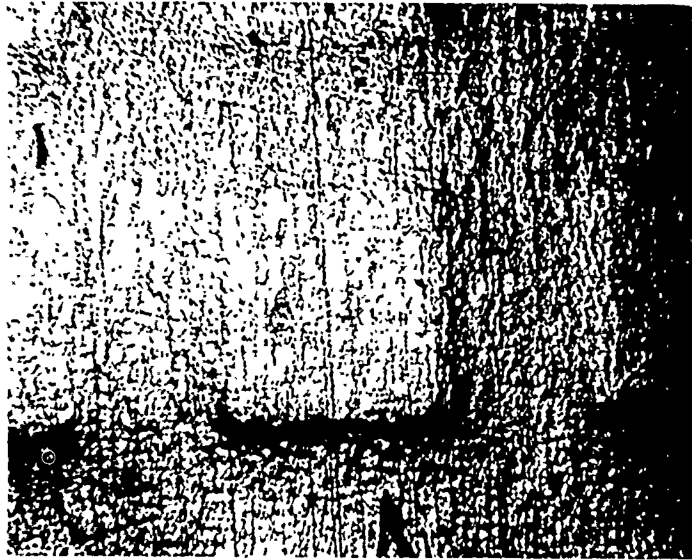

Figure 6.21. Example Of The Conformal Coverage Existing Over The Entire Electrode Array Using The Urethane Adhesive (75 ×).

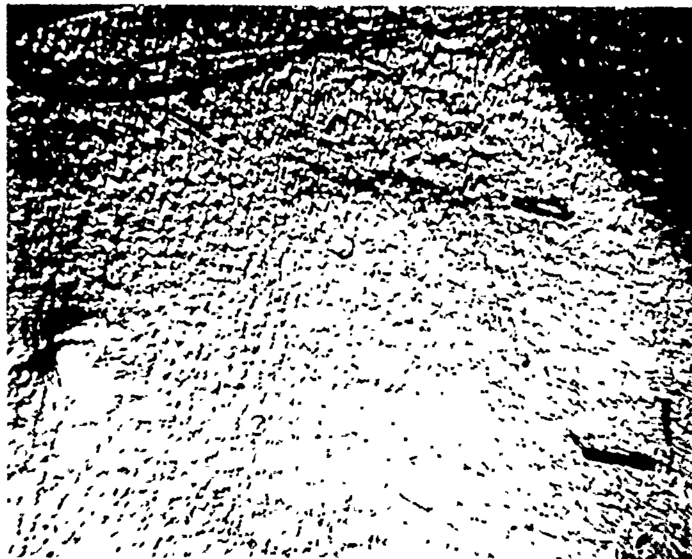

Figure 6.22. Example Of The Non-Conformal Coverage Existing Over Most Of The Electrode Array Using The *Loctite* Adhesive (75 ×).

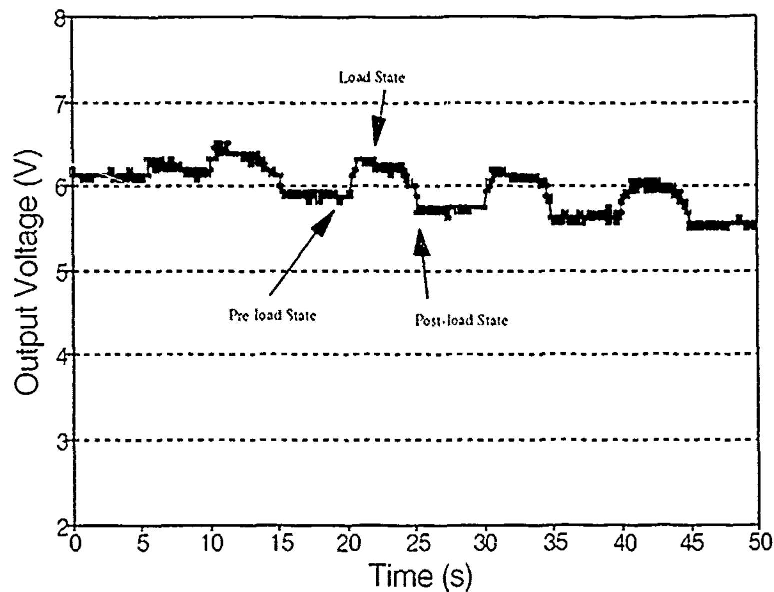

Figure 6.23. Output Of A Charge Signal Amplifier When A 135 g Load Was Repeatedly Applied To A Discrete Electrode.

Individual Taxel Verification. To measure the response of an individual taxel, a load was placed on a single taxel using the Micromanipulator probe station. Figure 6.23 illustrates the output of the charge signal amplifier when the load was repeatedly applied to the taxel. Using these measurements, the sensor bandwidth could be determined. The taxel electrode response from the unloaded state to a loaded state indicated a bandwidth of 25 Hz (0.04 s rise time), and the loaded to unloaded state bandwidth of 20 Hz (0.05 s fall time). In an effort to determine the relationship between the externally applied load weight and the corresponding change in output voltage values, the weight of the applied load was varied from 0.8 g to 135 g. The load weight and its corresponding change in output voltage of the taxel was then plotted. Figure 6.24 illustrates the voltage versus load functional relationship. Using a linear least squares curve fitting routine, the resulting line possesses a slope of 2 mV/g. To adequately resolve weight increments, the change in output voltage due to a load must be greater than the change in output voltage due to noise within the system. The amplifier performance evaluation revealed that while operating in the linear region of the

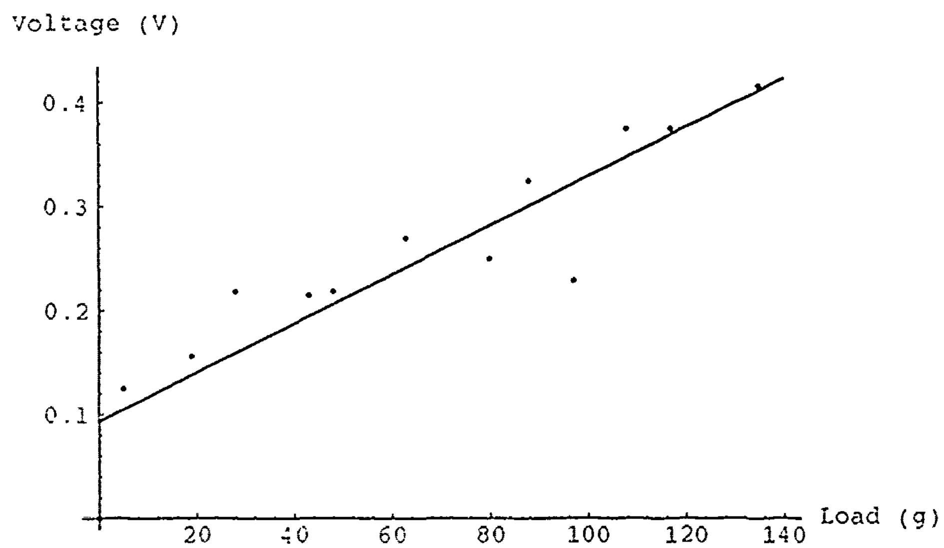

Figure 6.24. Characteristic Voltage Versus Load Functional Relationship For The Tactile Sensor.

amplifier, the sensor and supporting equipment configuration allows reliable detection of a 0.04-V increment. Since the sensor possesses a voltage versus load function slope of 2 mV/g, this 0.04-V increment corresponded to a weight change of 20 g. Any weight increment less than 20 g could not be reliably detected.

To determine how long the sensor would operate before the electrode array required re-biasing, several long-term taxel response tests were performed. While each taxel possesses an average charge decay with respect to time of approximately 50 s, the taxel response tests indicated that not all of the charge dissipated after this characteristic time. These tests revealed the ability of the sensor to maintain sufficient charge over an extended period of time to generate repeatable load responses (maximum of 200 seconds). Figure 6.25 illustrates the output when a load is applied, and demonstrates that the change in voltage due to the application of the load remains constant over the length of the test. However, minute changes in temperature and slow charge leakage across the array changed the initial state of the sensor surface, and it caused the sensor to require re-biasing just before any measurement was made.

Next, crosstalk between taxels was evaluated for each of the adhesives utilized in fabricating the tactile sensor. The urethane adhesive possessed crosstalk between 35% and 75% of the nearest-neighbor voltage value, while the polyimide adhesive exhibited a larger coupling (between 10% and 80%). This indicates an increase of 10% over the inherent IC crosstalk for a tactile sensor utilizing the urethane adhesive, and an increase of 15% for tactile sensor fabricated using the polyimide adhesive.

Taxel Array Evaluation. The final evaluation performed consisted of placing several load shapes onto the surface of the tactile sensor IC, and determining if the corresponding output response was indicative of the shape and weight of the load applied. Several load shapes were fitted to the test load fixture, and the high impedance bias network was switched on, biasing the electrode array to an operating point at the lower end of the charge signal amplifier linear region. Next, the bias network was switched off, and sufficient time was allowed for the system to equilibrate. When a taxel was not under the influence of crosstalk, the corresponding taxel output exhibited an exponential decay of approximately 50 s; however, when crosstalk existed between two taxels, the nearest-neighbor taxel

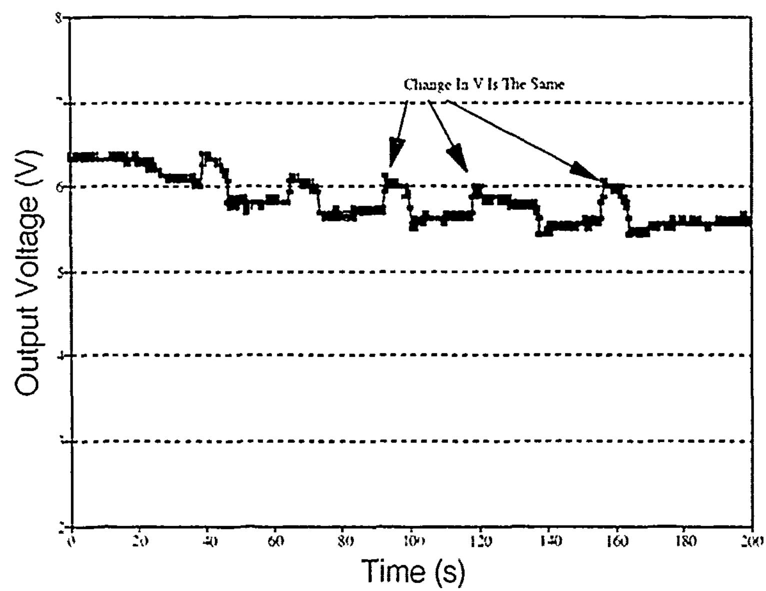

Figure 6.25. Response Of The Charge Signal Amplifier For A 135 g Load Over A Long Period Of Time.

output increased to a stable bias voltage other than the externally applied bias voltage applied, but still within the linear region of the amplifier. Since the amplifiers were linear for input levels between 2.5-V and 7-V, the taxels which were affected by the crosstalk did not suffer performance degradation. A pre-load measurement was recorded. A load was applied to the surface of the sensor, and a loaded-state measurement of the sensor electrode array was recorded. Finally, when the load was removed, a post-load measurement was recorded. To illustrate this process, the results of a small circularly shaped load applied to the surface of the tactile sensor will be presented. The application of the small circle resulted in the pre-load, load, and post-load measurements compiled in Figures 6.26, 6.27, 6.28, and 6.29.

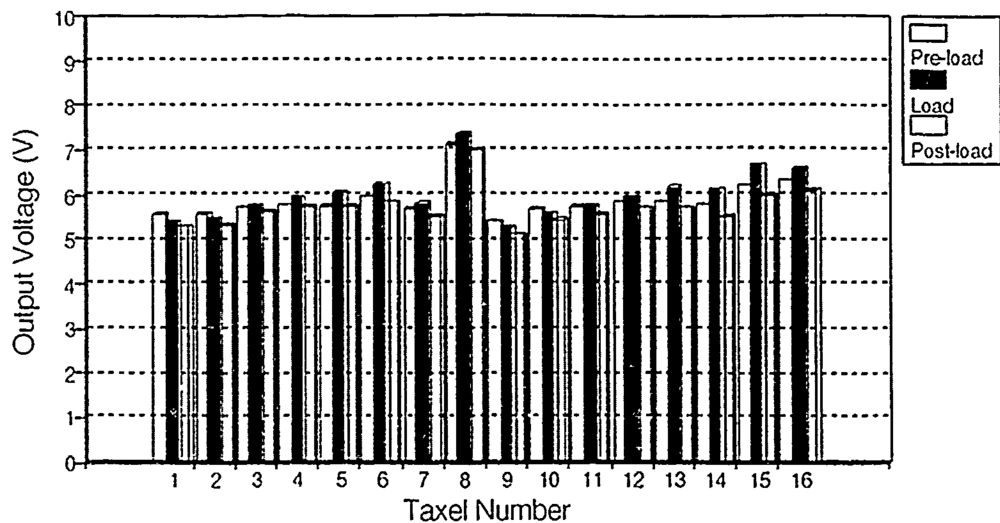

Figure 6.26. Pre-load, Load, And Post-load Measurements Of A 100 g Small Circle Shape Load (Taxel 1-16 Responses Are Shown).

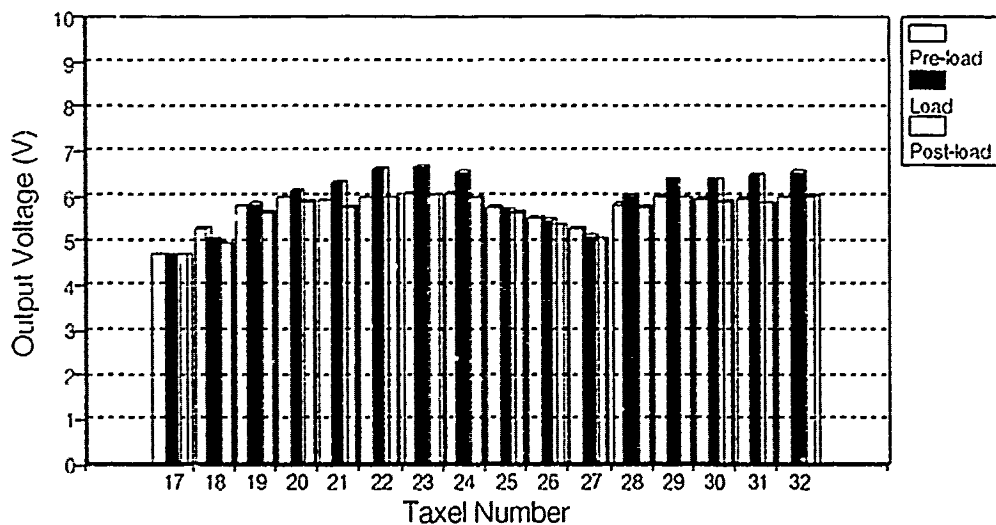

Figure 6.27. Pre-load, Load, And Post-load Measurements Of A 100 g Small Circle Shape Load (Taxel 17-32 Responses Are Shown).

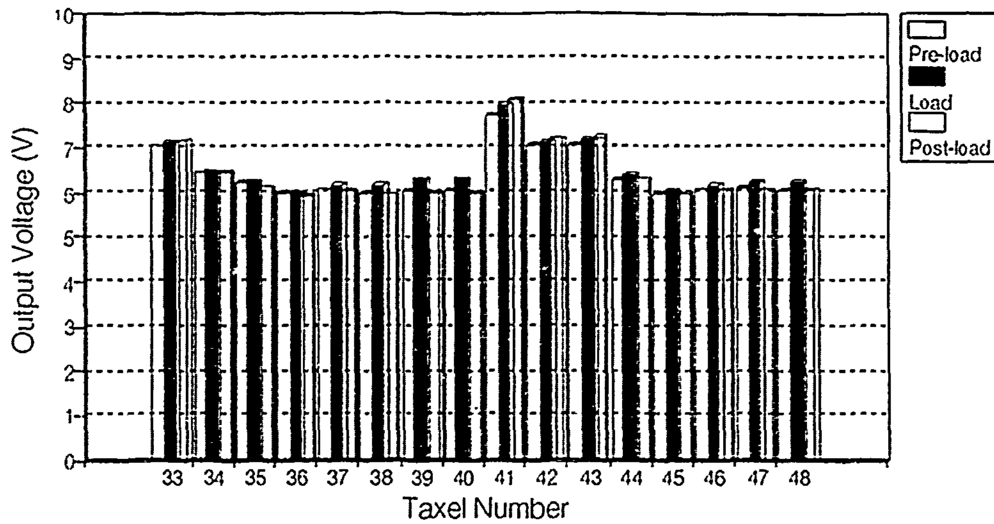

Figure 6.28. Pre-load, Load, And Post-load Measurements Of A 100 g Small Circle Shape Load (Taxel 33-48 Responses Are Shown).

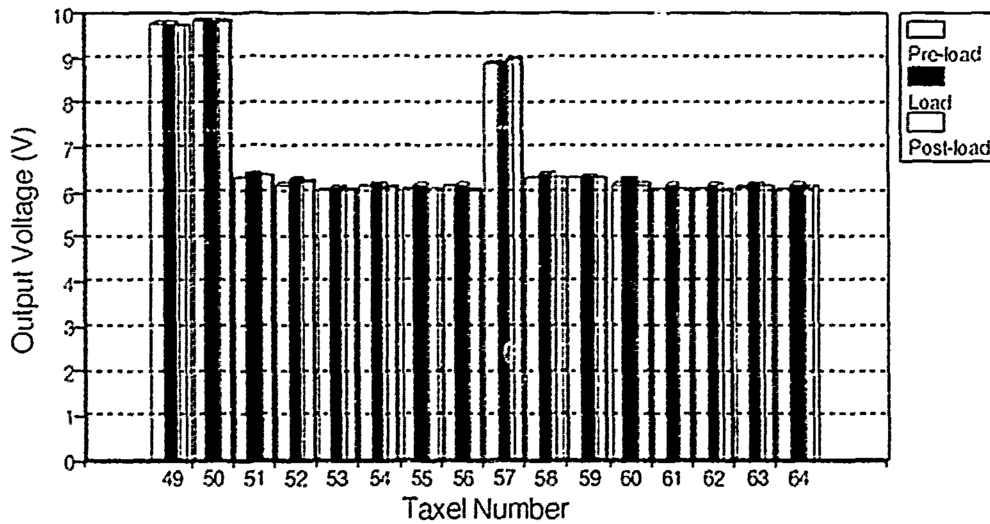

Figure 6.29. Pre-load, Load, And Post-load Measurements Of A 100 g Small Circle Shape Load (Taxel 49-64 Responses Are Shown).

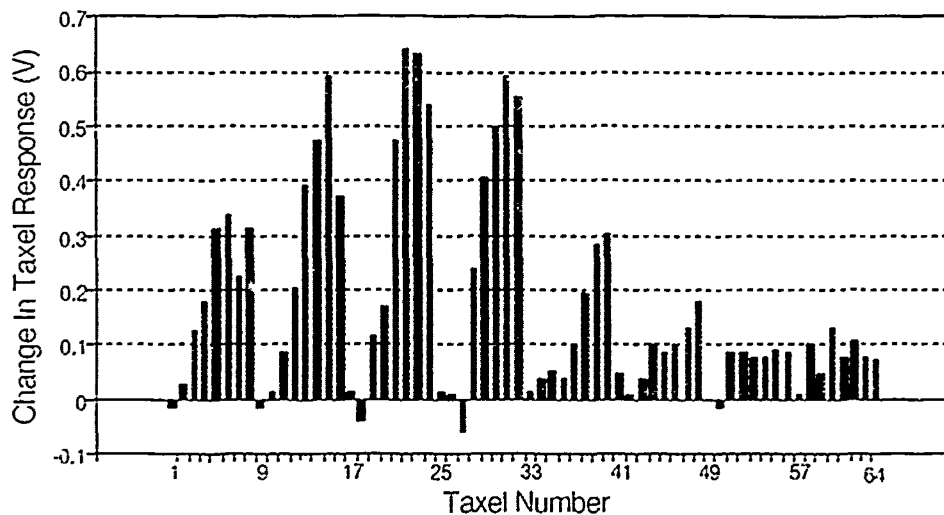

Figure 6.30. Shape Information For The Small Circle Applied To The Upper Right Hand Corner Of The Electrode Array.

From these pre-load, load, and post-load measurements, shapes could potentially be discerned by using the algorithm provided in Chapter V. The first step in the algorithm results in the change in output voltage level for a given taxel. Figure 6.30 illustrates the results after applying a 100 g small circularly shaped load to the surface of the tactile sensor, arithmetically averaging the pre- and post load measurements, and subtracting the result from the load measurement. Next, the taxel responses were mapped to their corresponding locations in an 8 x 8 arrangement, producing a three-dimensional plot of the data. Several equipotential contours were analyzed using the criteria provided in Chapter V to determine the "best-fit" contour corresponding to the shape of the applied load. On a two-dimensional 8 x 8 array diagram, the taxels which possessed output responses above this "best-fit" threshold level were displayed as black, and the taxels below this threshold equipotential were displayed as white.

To demonstrate the ability of this sensor to detect shapes, the figures provided on the following pages illustrate the sensor's responses to a sharp edge, a small square, a small circle, a polygon, a slotted screw, a cross-slotted screw, a large solid circle, and a toroid. Each shape is presented using three figures: the

Table 6.1. Optimum Threshold Levels For Each Load Shape.

Shape	Threshold Level (V)
Sharp Edge	0.4
Small Square	0.35
Small Circle	0.7
Polygon	0.4
Slotted Screw	0.51
Cross-Slotted Screw	0.45
Large Solid Circle	0.5
Toroid	0.5

three-dimensional plot, the contour plot, and the threshold plot. The plots were generated using a program called *Mathematica*: a sample data file and program is included in Appendix I. The threshold analysis results are provided in Table 6.1, indicating the threshold level which corresponds to the contour level that "best-fits" the shape of the applied load. The smallest feature size of all of the shapes was the sharp edge measuring 700μm wide, and it was easily detected by the sensor (Figure 6.31). However, the sensor's ability to resolve the separation distance between two points was evaluated using the screw shaped load, successfully distinguishing the 1.5 mm wide feature (Figure 6.43 illustrates how well the tactile sensor could resolve this distance). Figures 6.55 through 6.63 demonstrate the increased crosstalk due to the polyimide adhesive. Appendix J provides contour and threshold plots which helped determine the "best-fit" contour and threshold plots contained in this chapter. Appendix K contains plots of the sharp edge, small square, small circle, and polygon applied to the surface of the tactile sensor using 75 g, 50 g, and 10 g weighted shapes. Additionally, Appendix L contains data for the sharp edge, small square, and small circle when they were applied to different locations on the surface of the tactile sensor.

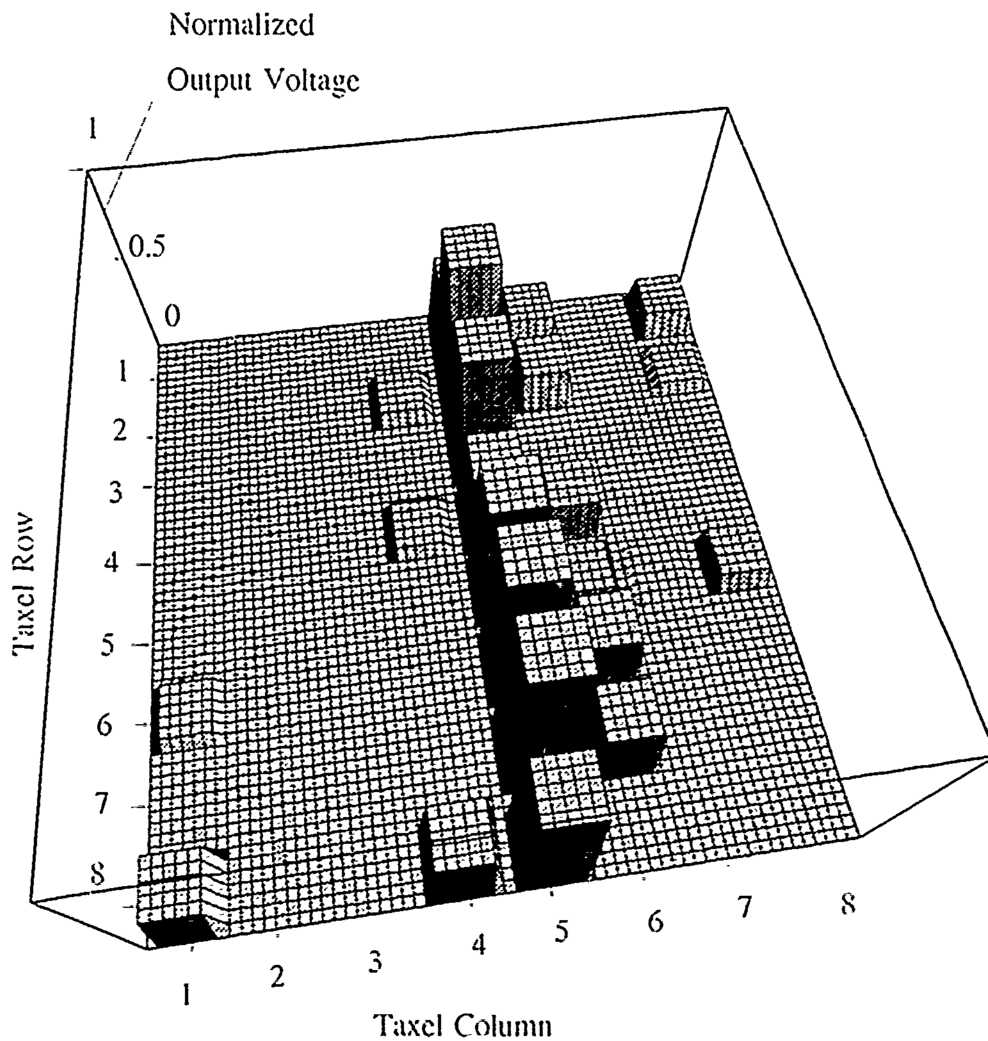

Figure 6.31. Three-Dimensional Representation Of A Sharp Edge Shaped Load Applied To The Surface Of The Electrode Array. The z-Axis Corresponds To The Normalized Difference Between The Sensor's Loaded And Unloaded States, And The x- And y-Axes Correspond To The Electrode Columns And Rows, Respectively.

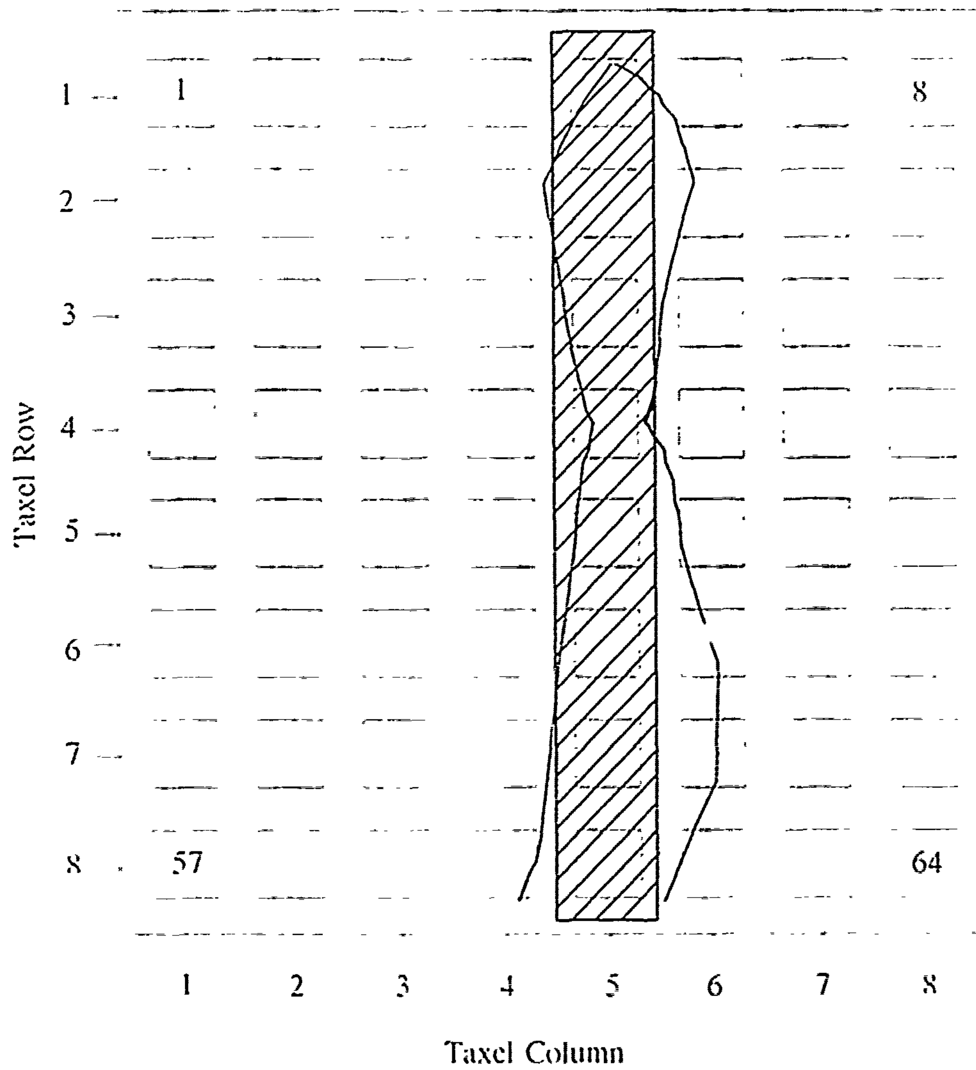

Figure 6.32. 0.4-V Equipotential Contour Plot For A 100 g Sharp Edge Shaped Load Applied To The Surface Of The Electrode Array.

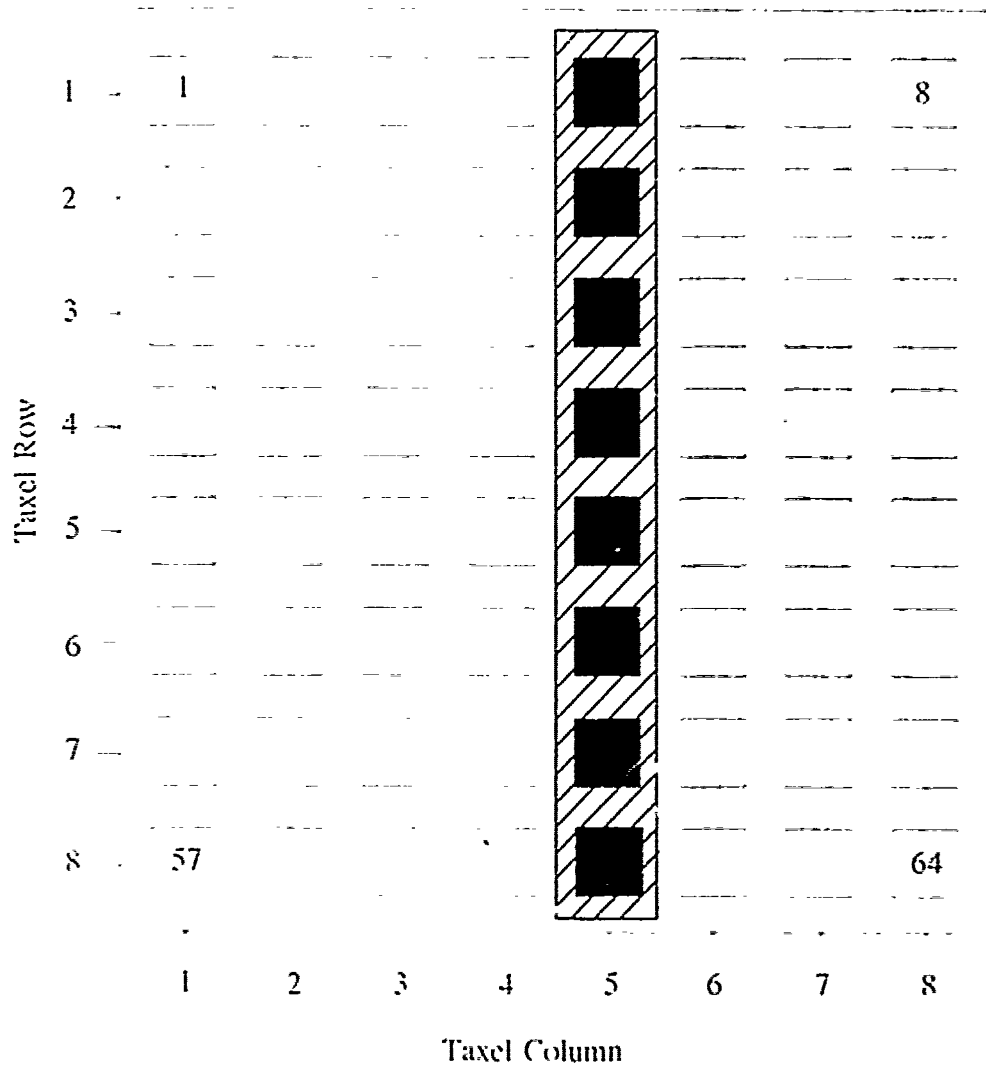

Figure 6.33. 0.4-V Threshold Plot Of A 100 g Sharp Edge Shaped Load – Taxels With An Output Level Above This Threshold Level Are Displayed As Black And Taxels With An Output Level Below This Threshold Level Are Displayed As White.

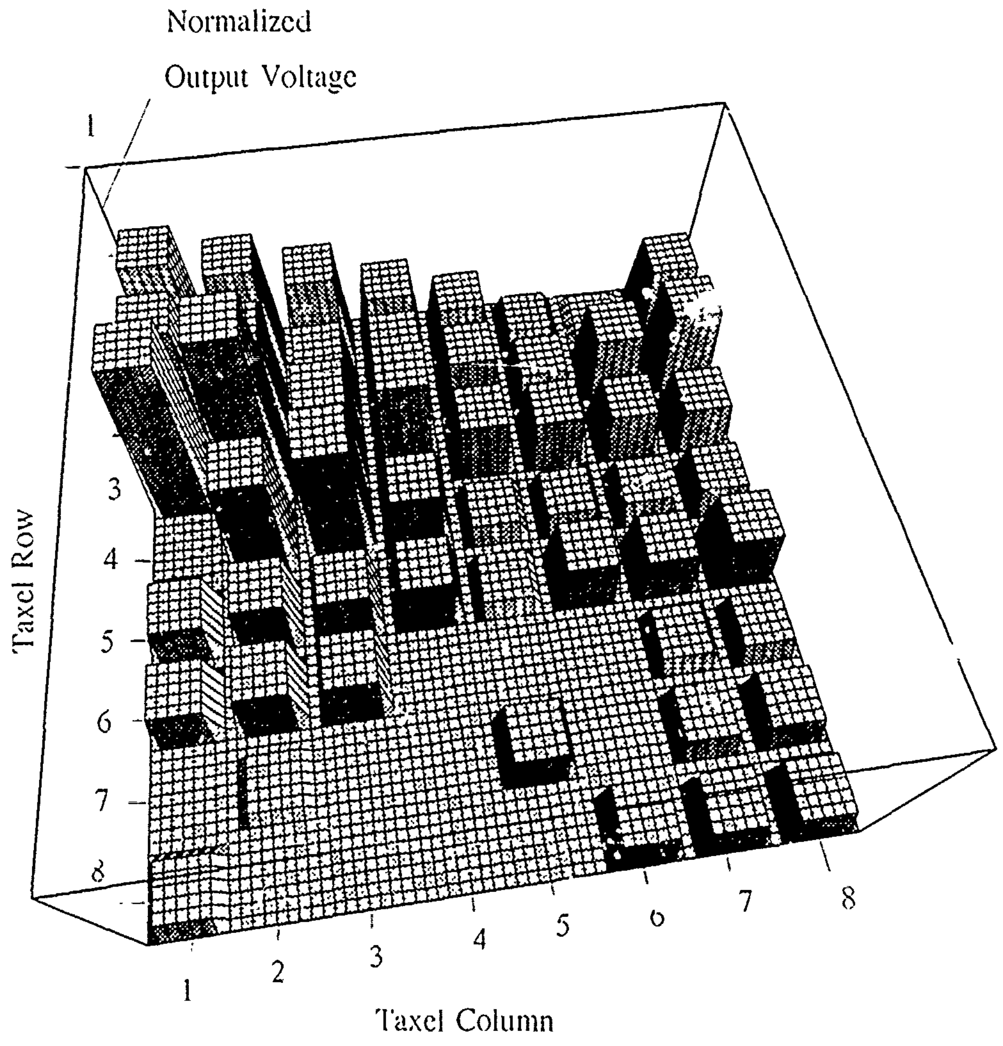

Figure 6.34. Three-Dimensional Representation Between A Small Square Shaped Load Applied To The Surface Of The Electrode Array. The z-Axis Corresponds To The Normalized Difference Between The Sensor's Loaded And Unloaded States. And The x- And y-Axes Correspond To The Electrode Columns And Rows, Respectively.

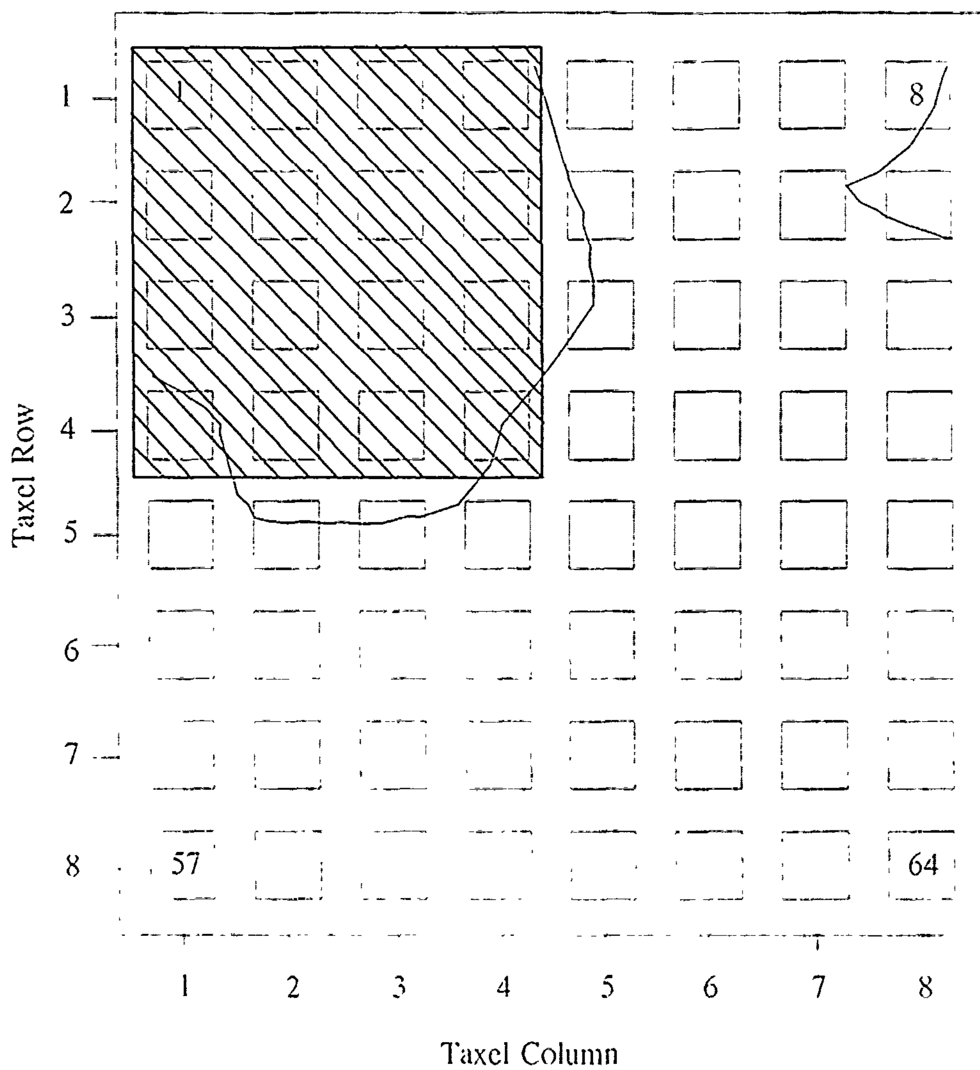

Figure 6.35. 0.35-V Equipotential Contour Plot For A 100 g Small Square Shaped Load Applied To The Surface Of The Electrode Array.

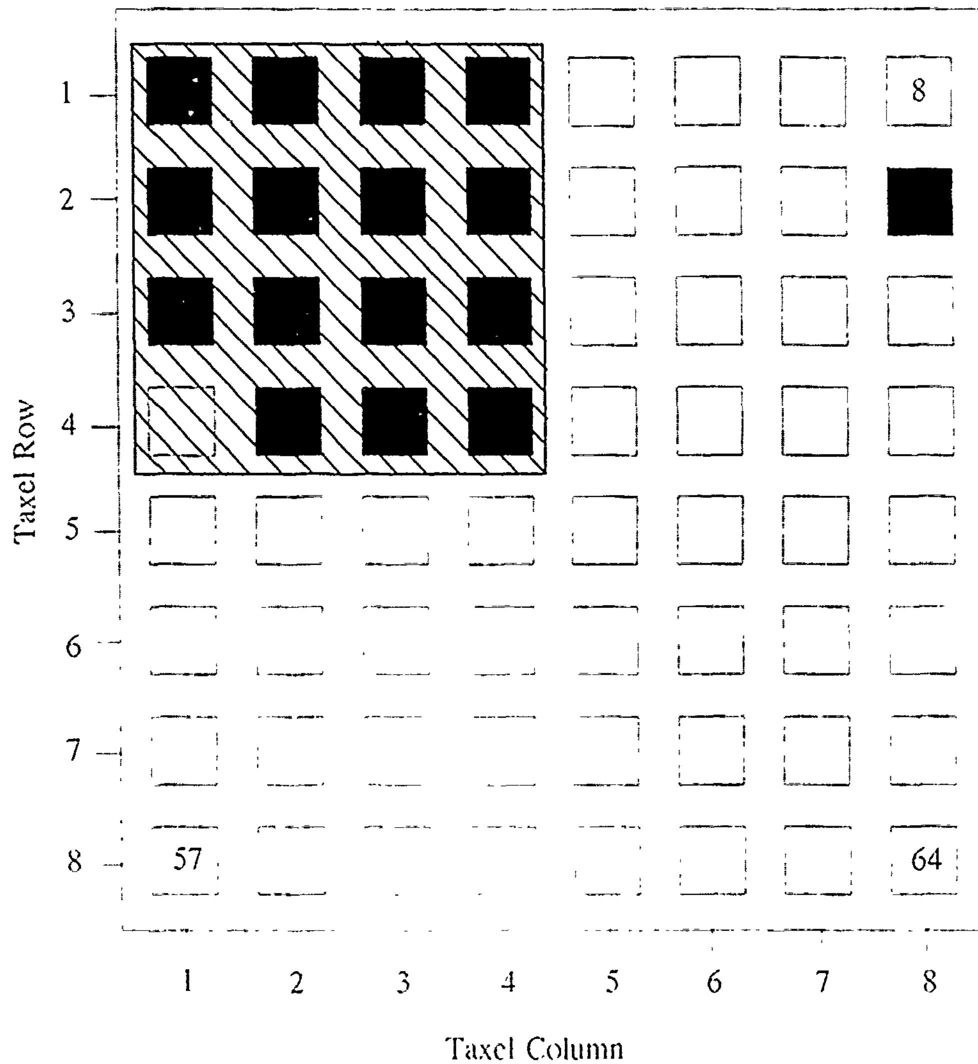

Figure 6.36. 0.35-V Threshold Plot Of A 100 g Small Square Shaped Load - Taxels With An Output Level Above This Threshold Level Are Displayed As Black And Taxels With An Output Level Below This Threshold Level Are Displayed As White.

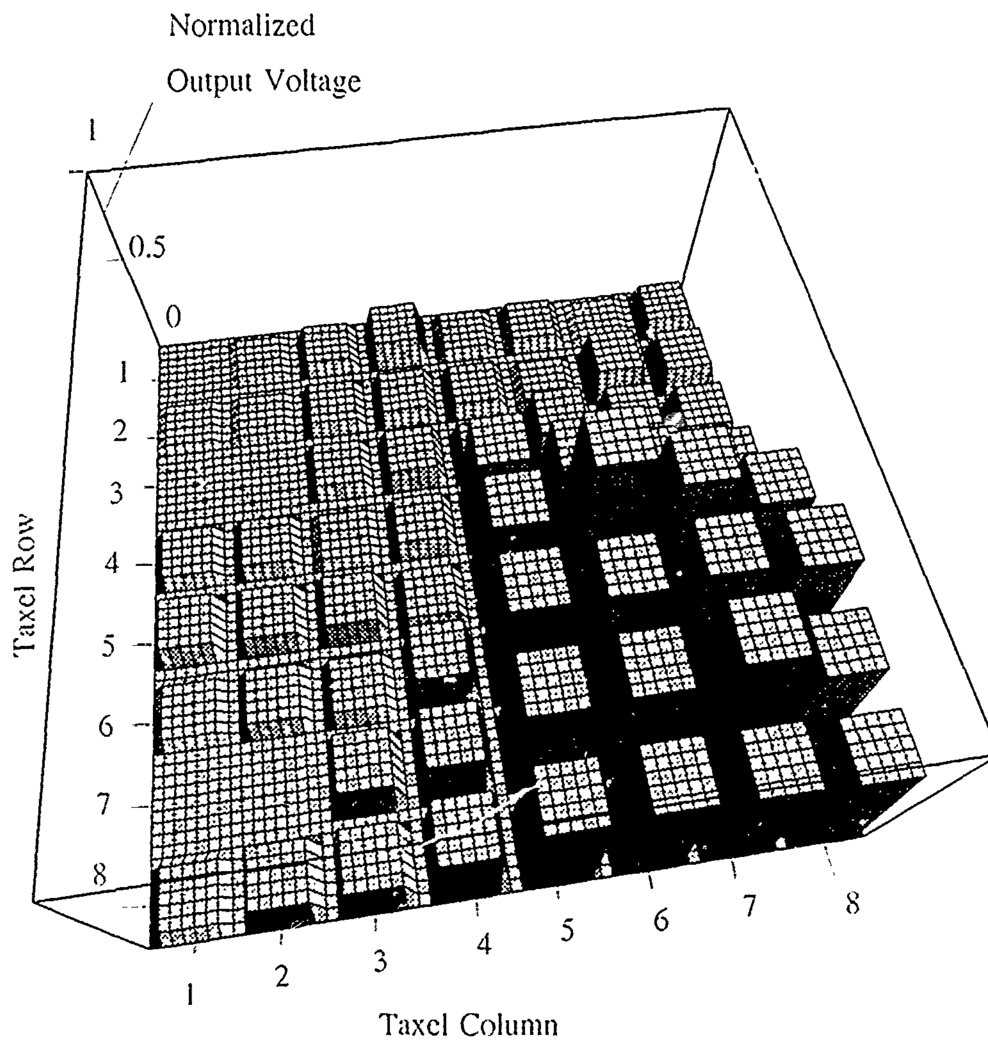

Figure 6.37. Three-Dimensional Representation Of A Small Circularly Shaped Load Applied To The Surface Of The Electrode Array. The z-Axis Corresponds To The Normalized Difference Between The Sensor's Loaded And Unloaded States, And The x- And y-Axes Correspond To The Electrode Columns And Rows, Respectively.

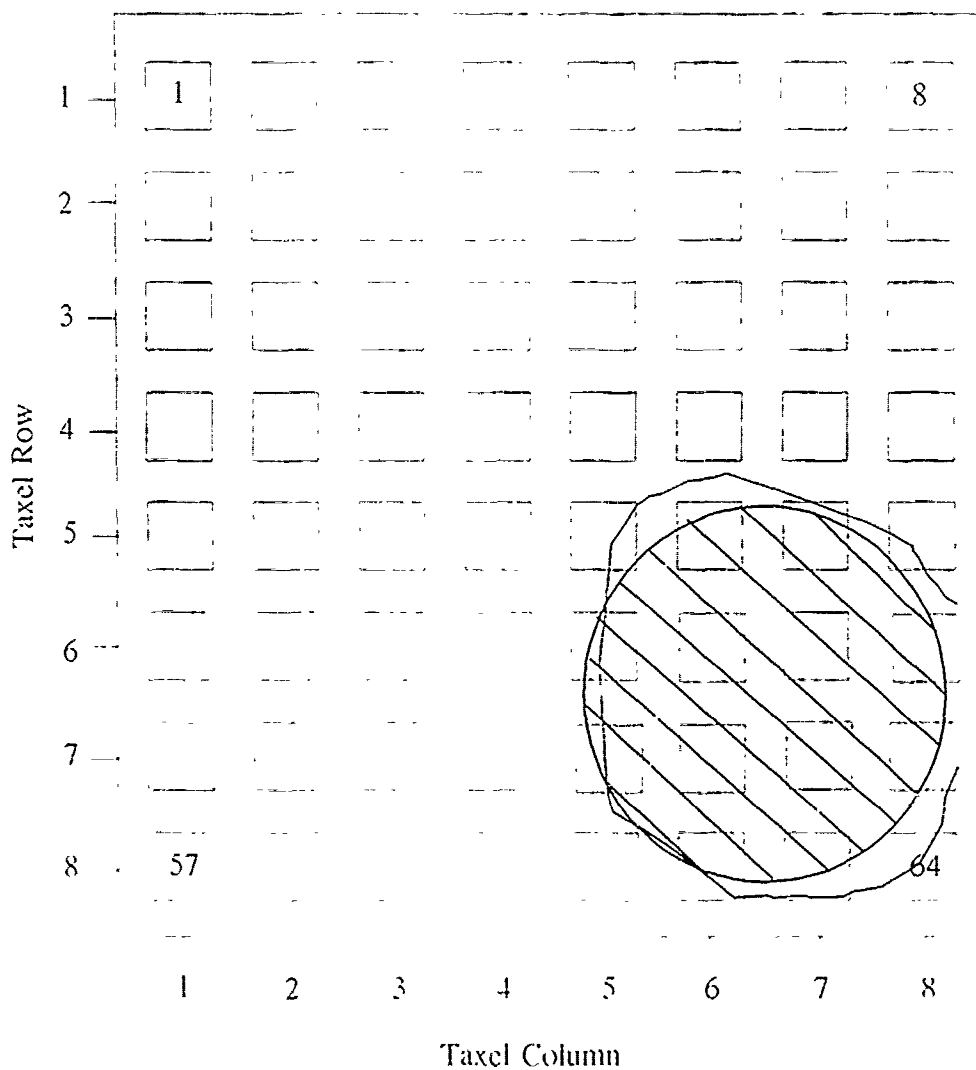

Figure 6.38. 0.7-V Equipotencial Contour Plot For A 100 g Small Circularly Shaped Load Applied To The Surface Of The Electrode Array.

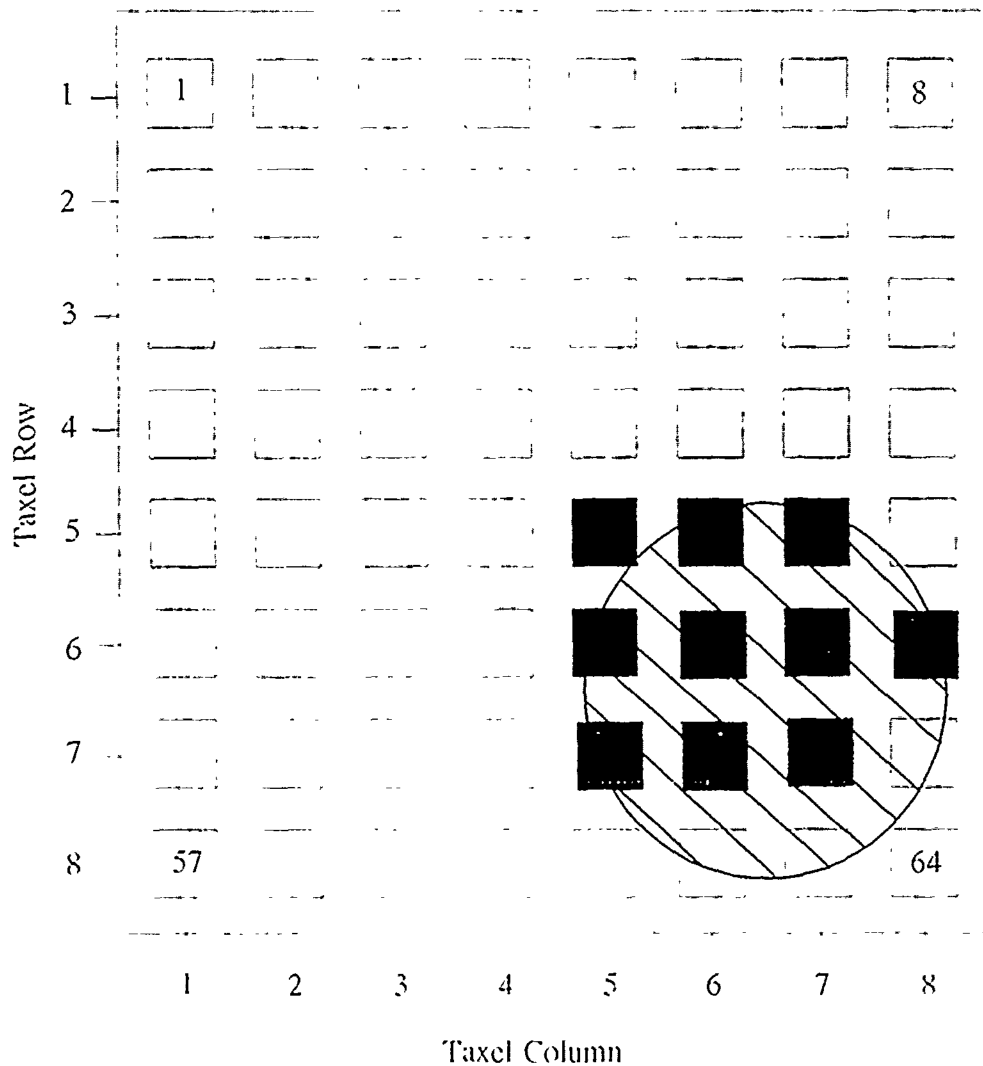

Figure 6.39. 0.7-V Threshold Plot Of A 100 g Small Circularly Shaped Load - Taxels With An Output Level Above This Threshold Level Are Displayed As Black And Taxels With An Output Level Below This Threshold Level Are Displayed As White.

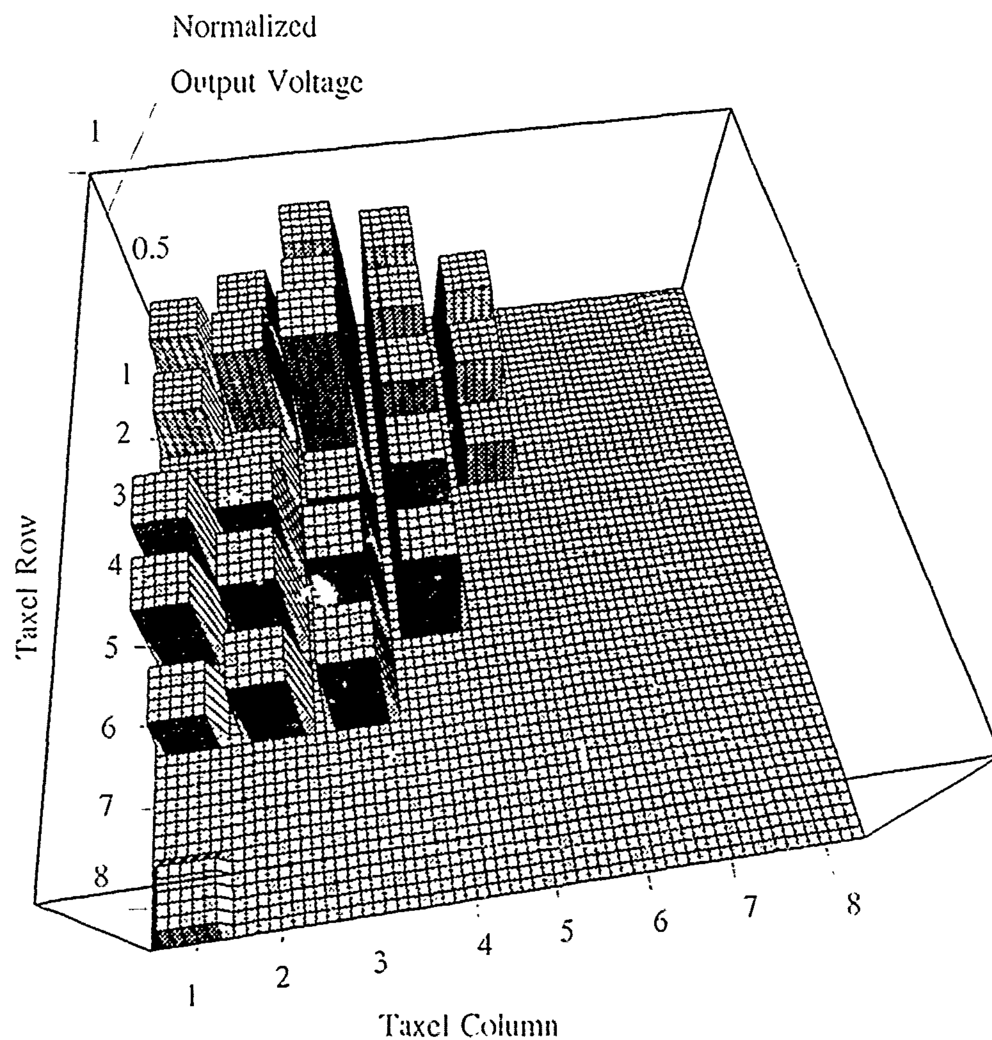

Figure 6.40. Three-Dimensional Representation Of A Polygon Shaped Load Applied To The Surface Of The Electrode Array. The z-Axis Corresponds To The Normalized Difference Between The Sensor's Loaded And Unloaded States, And The x- And y-Axes Correspond To The Electrode Columns And Rows, Respectively.

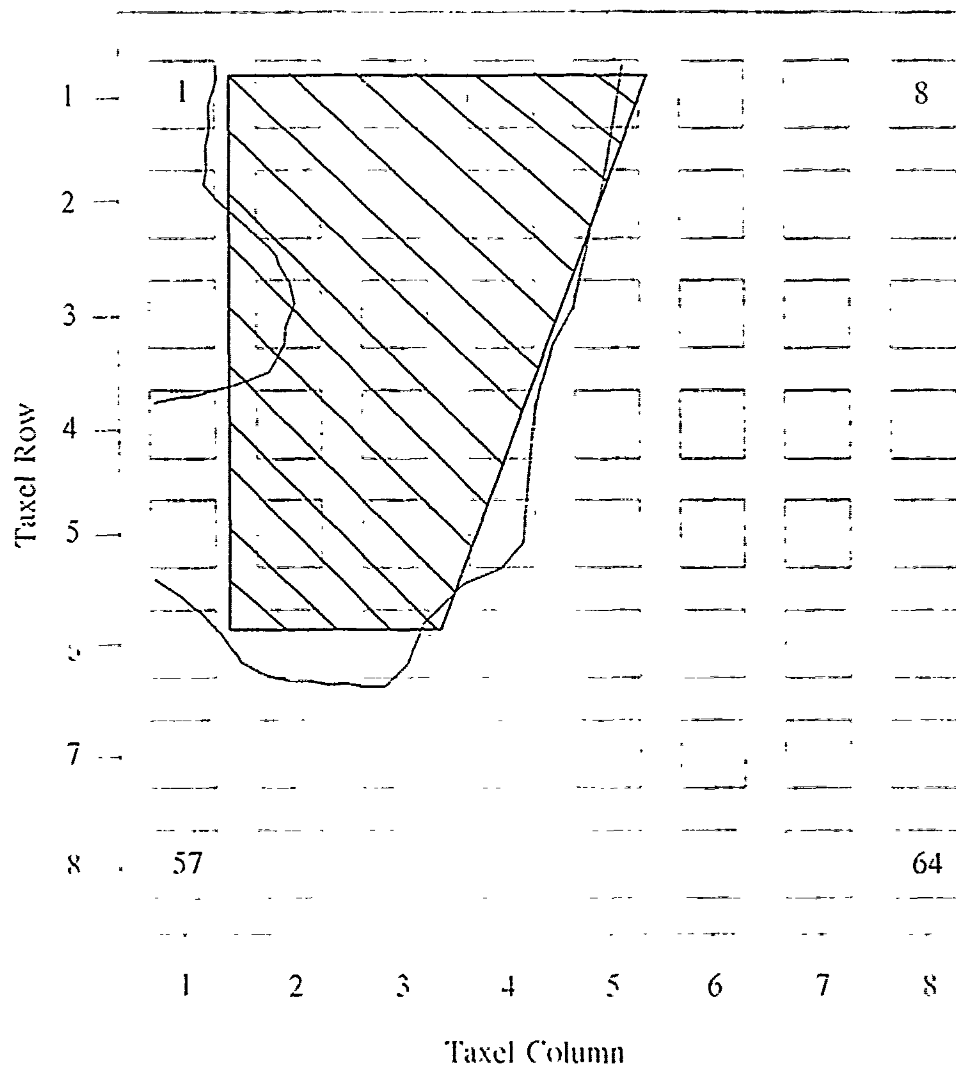

Figure 6.11. 0.4-V Equipotential Contour Plot For A 100 g Polygon Shaped Load Applied To The Surface Of The Electrode Array.

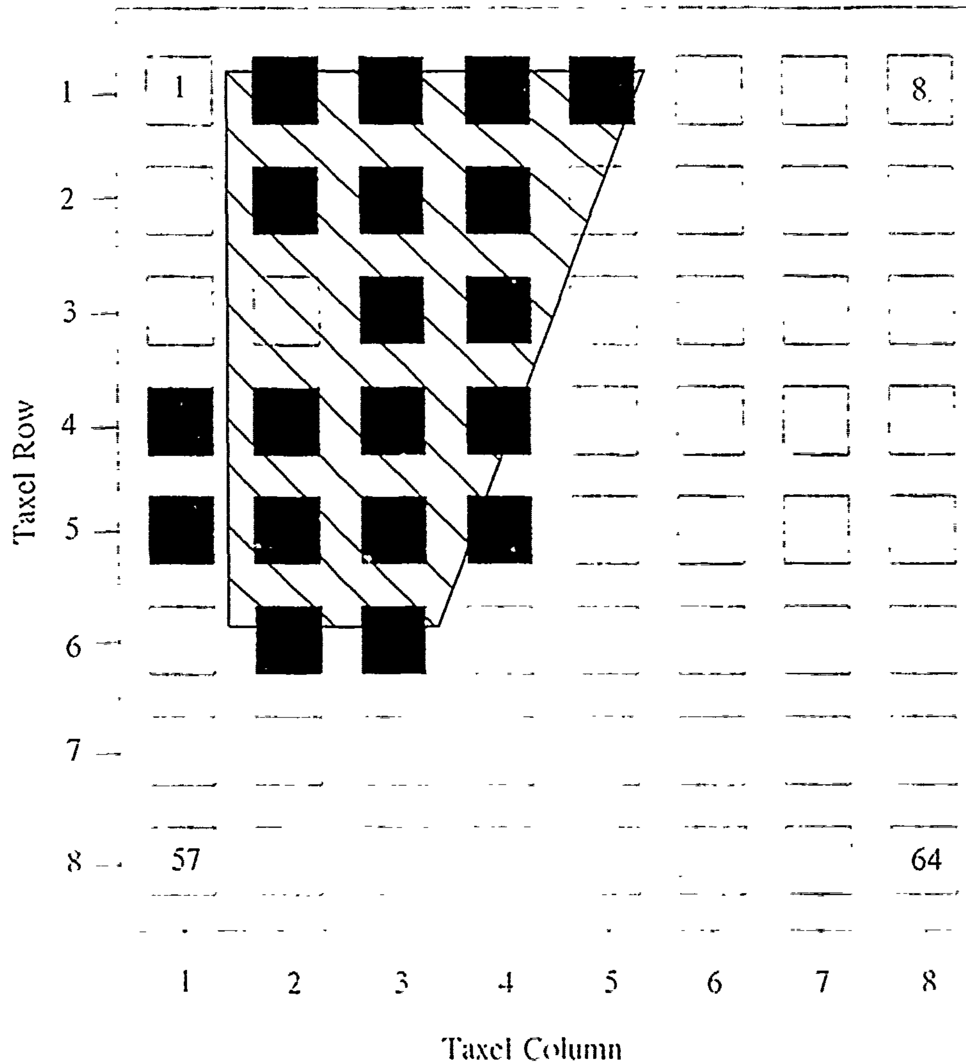

Figure 6.42. 0.4-V Threshold Plot Of A 100 g Polygon Shaped Load - Taxels With An Output Level Above This Threshold Level Are Displayed As Black And Taxels With An Output Level Below This Threshold Level Are Displayed As White.

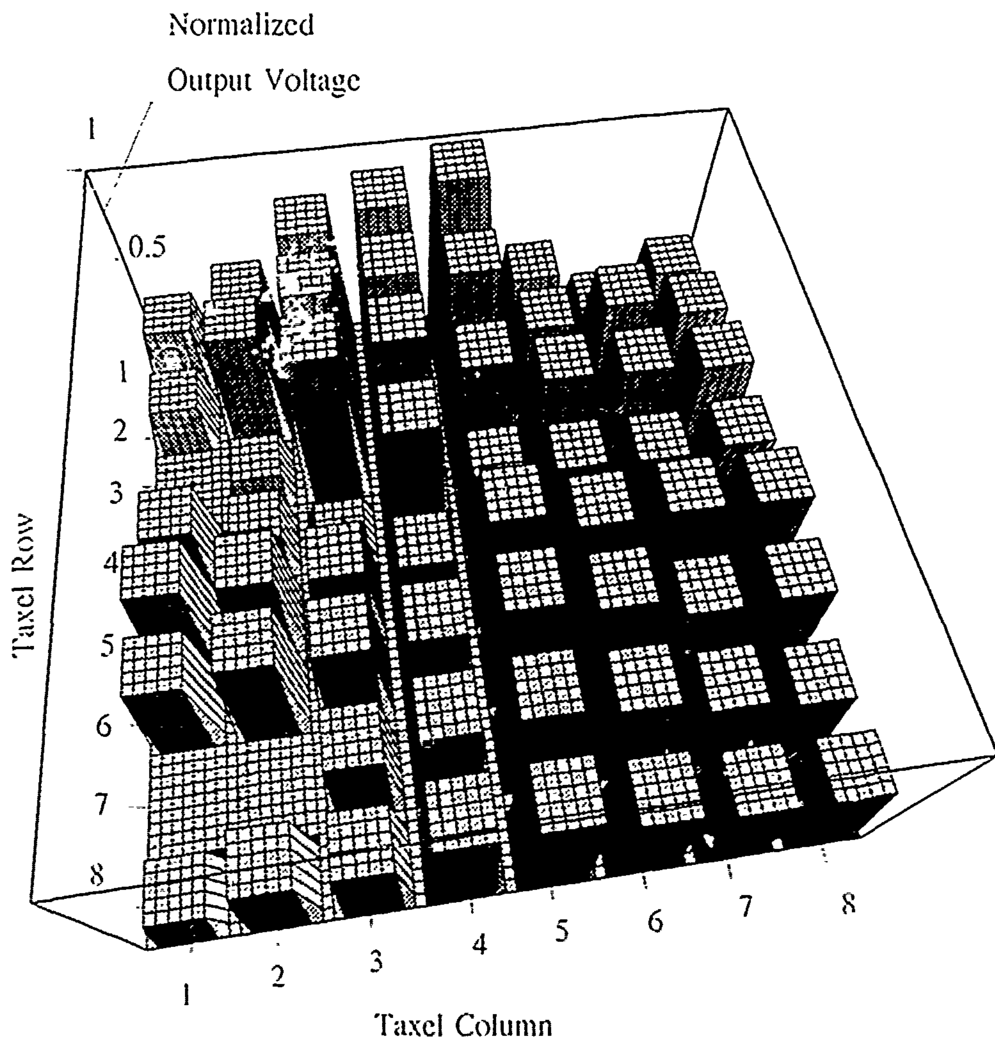

Figure 6.13. Three-Dimensional Representation Of A Slotted Screw Shaped Load Applied To The Surface Of The Electrode Array. The z-Axis Corresponds To The Normalized Difference Between The Sensor's Loaded And Unloaded States. And The x- And y-Axes Correspond To The Electrode Columns And Rows. Respectively.

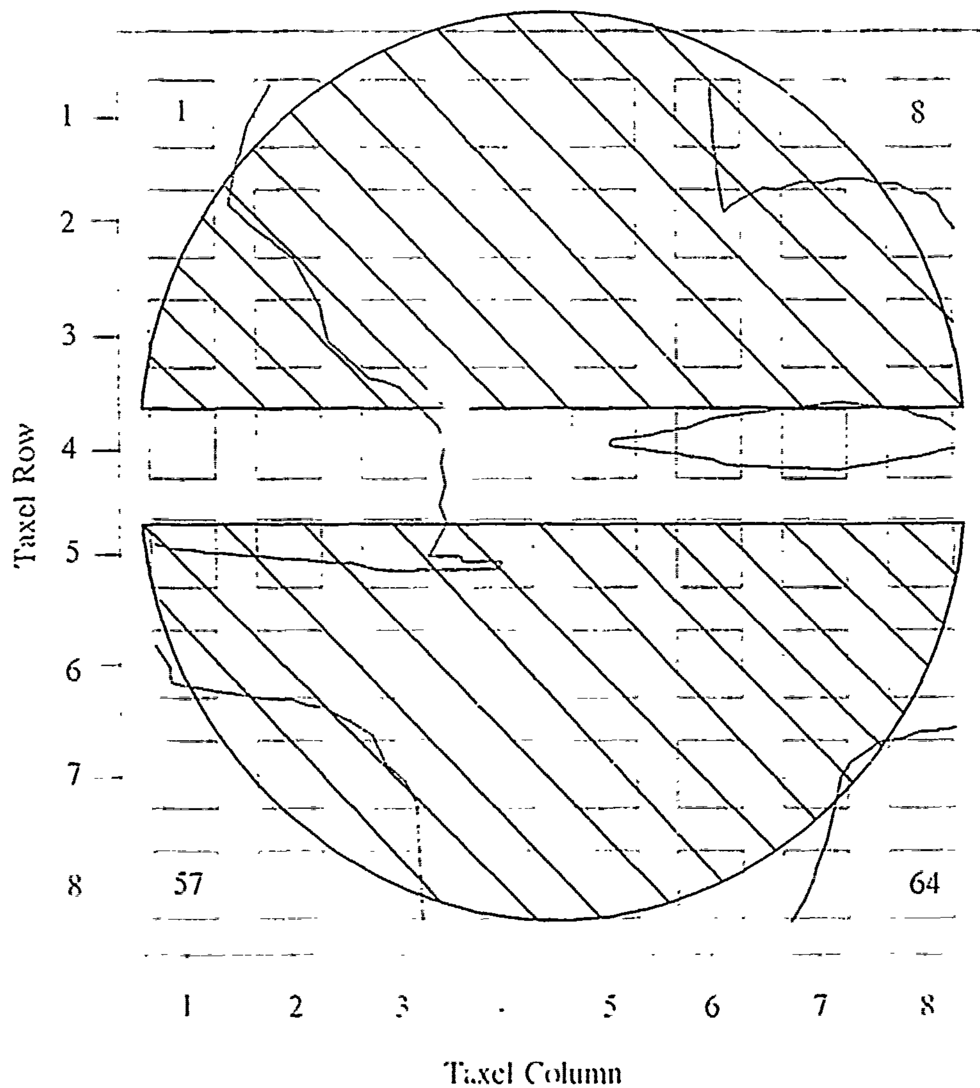

Figure 6.44. 0.51-V Equipotential Contour Plot For A 100 g Slotted Screw Shaped Load Applied To The Surface Of The Electrode Array.

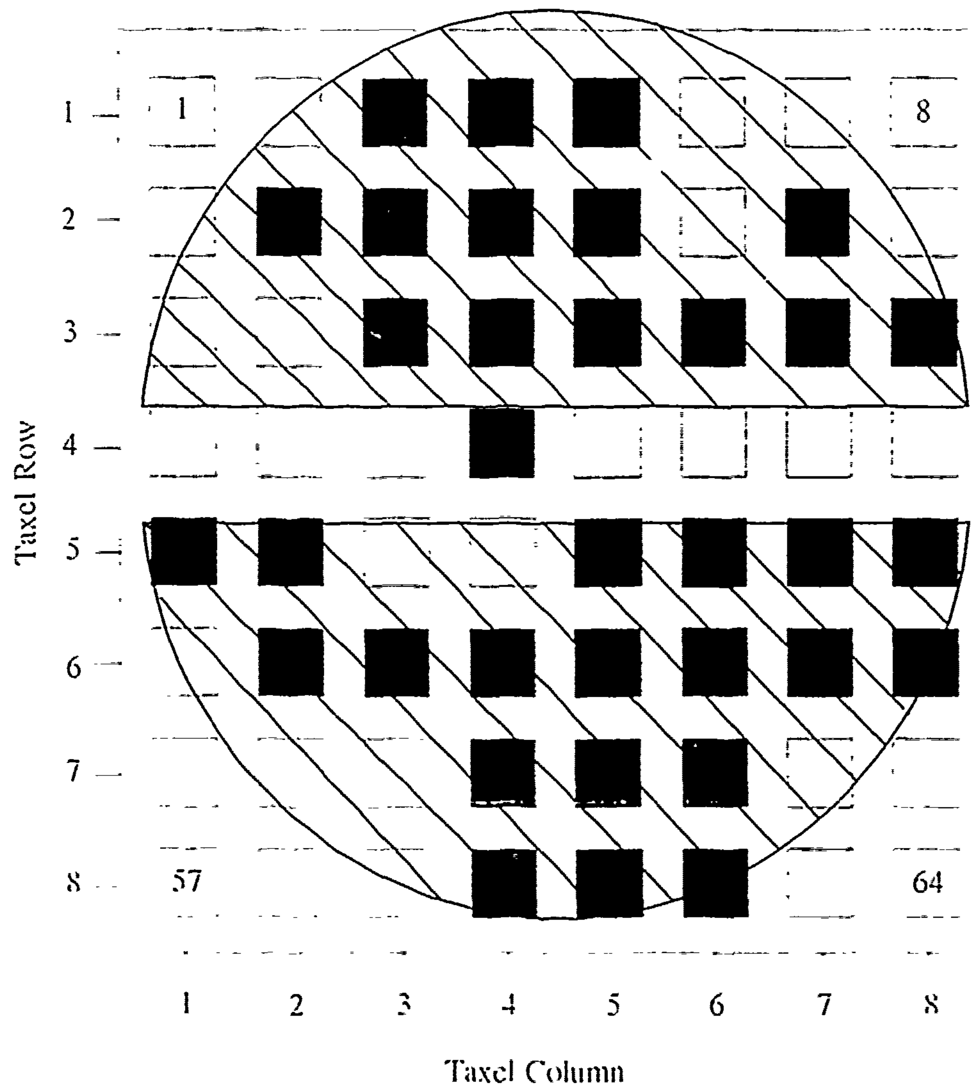

Figure 6.45. 0.51-V Threshold Plot Of A 100 g Slotted Screw Shaped Load - Taxels With An Output Level Above This Threshold Level Are Displayed As Black And Taxels With An Output Level Below This Threshold Level Are Displayed As White.

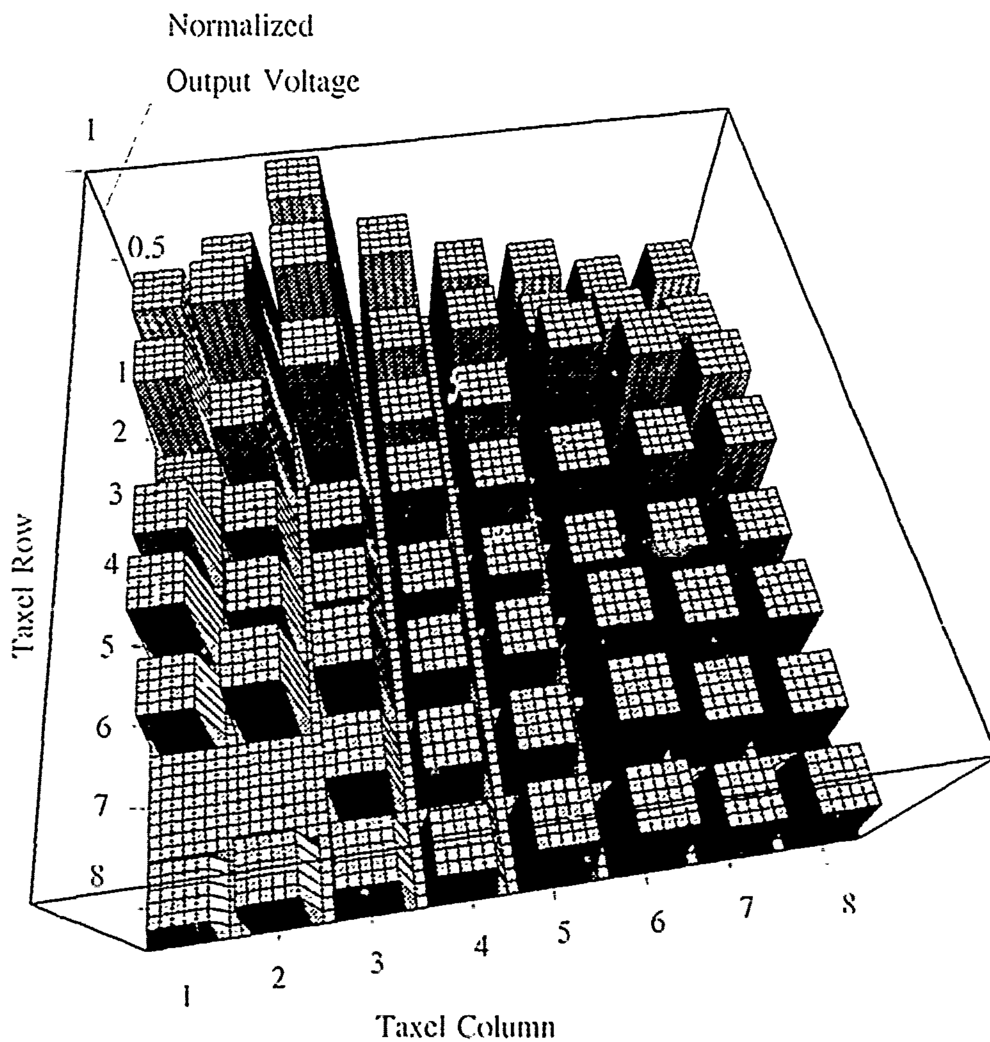

Figure 6.16. Three-Dimensional Representation Of A Cross-Slotted Screw Shaped Load Applied To The Surface Of The Electrode Array. The z-Axis Corresponds To The Normalized Difference Between The Sensor's Loaded And Unloaded States, And The x- And y-Axes Correspond To The Electrode Columns And Rows, Respectively.

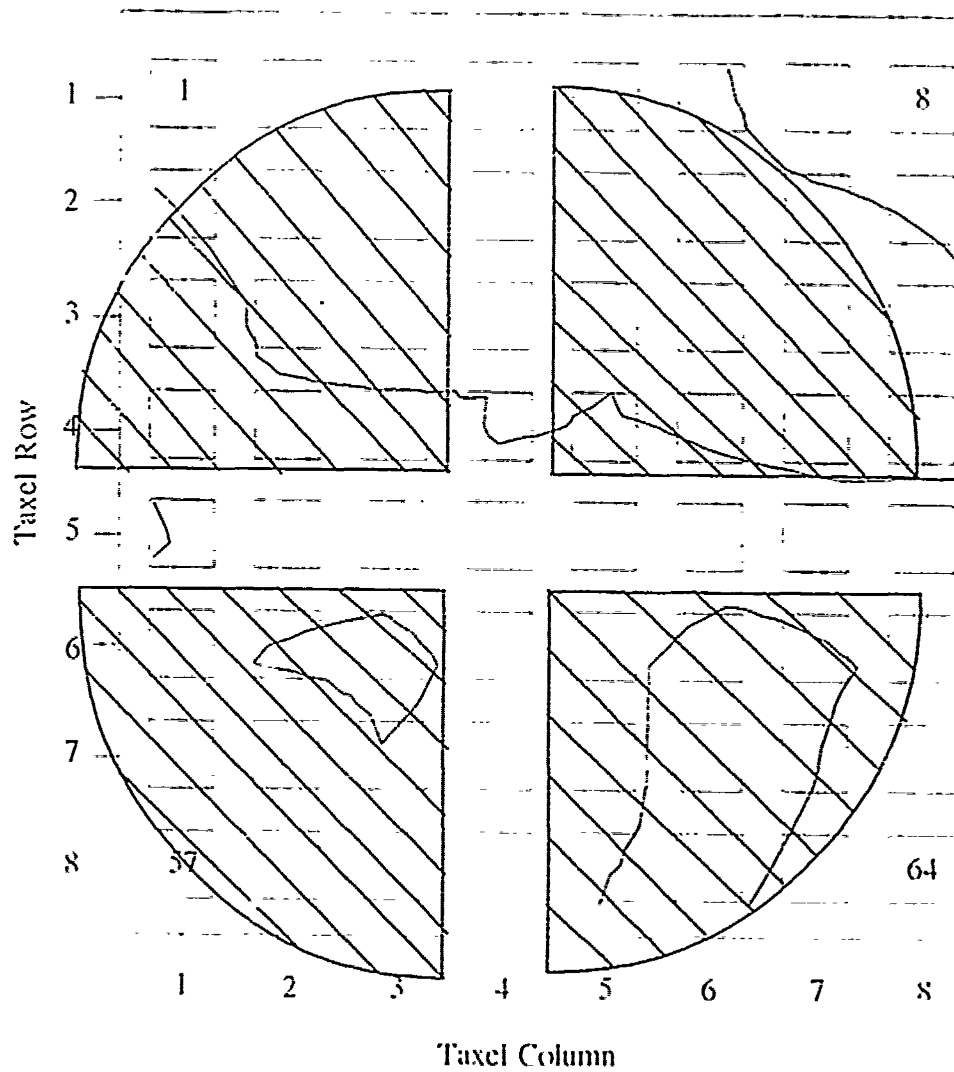

Figure 6.17. 0.45-V Equipotential Contour Plot For A 100 g Cross-Slotted Screw Shaped Load Applied To The Surface Of The Electrode Array.

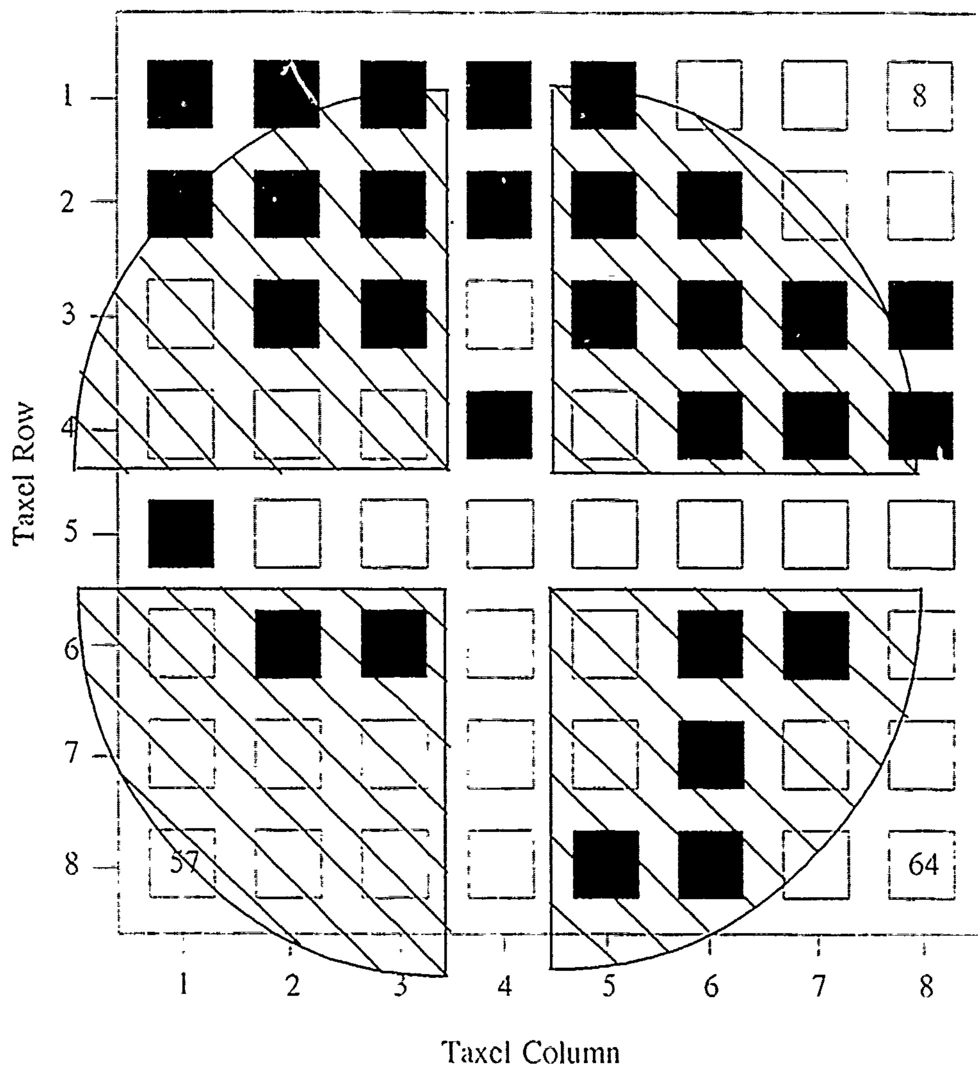

Figure 6.48. 0.45-V Threshold Plot Of A 100 g Cross-Slotted Screw Shaped Load - Taxels With An Output Level Above This Threshold Level Are Displayed As Black And Taxels With An Output Level Below This Threshold Level Are Displayed As White.

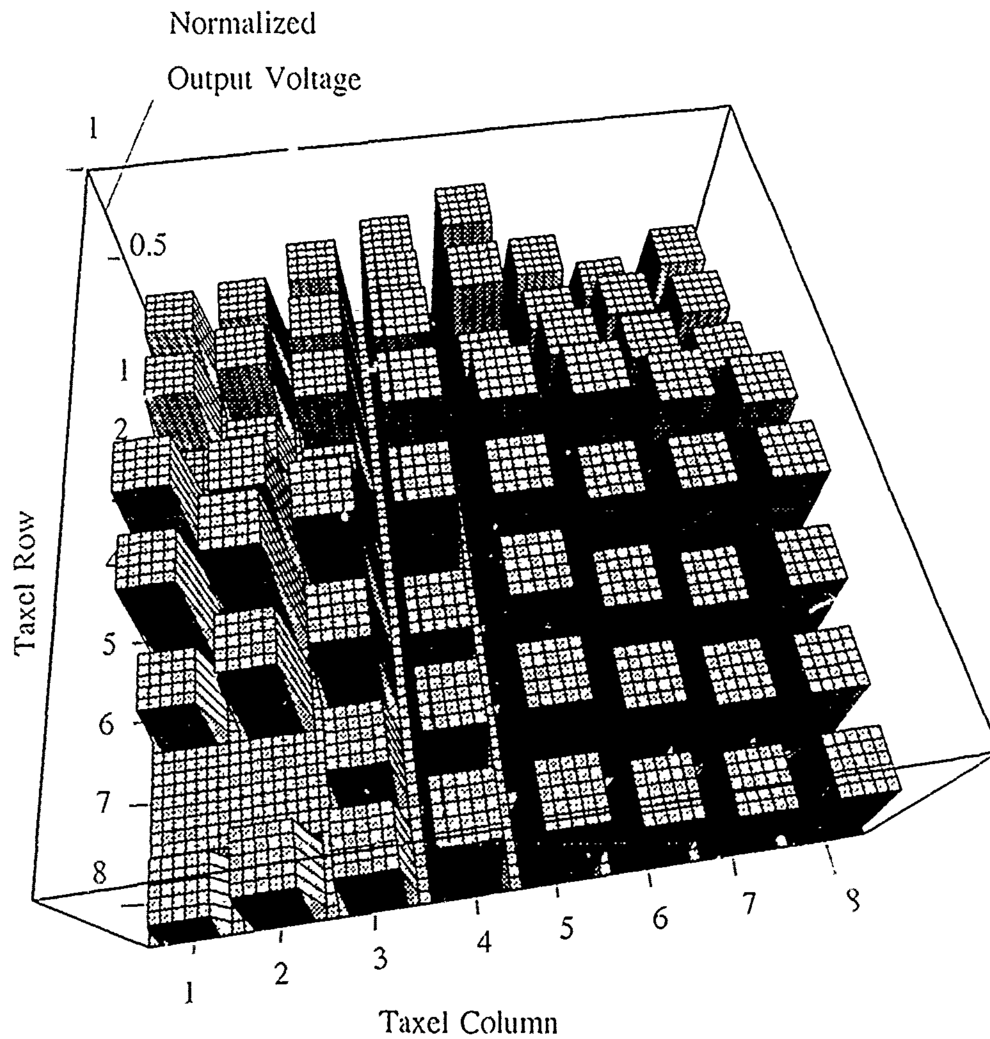

Figure 6.49. Three-Dimensional Representation Of A Large Solid Circularly Shaped Load Applied To The Surface Of The Electrode Array. The z-Axis Corresponds To The Normalized Difference Between The Sensor's Loaded And Unloaded States. And The x- And y-Axes Correspond To The Electrode Columns And Rows, Respectively.

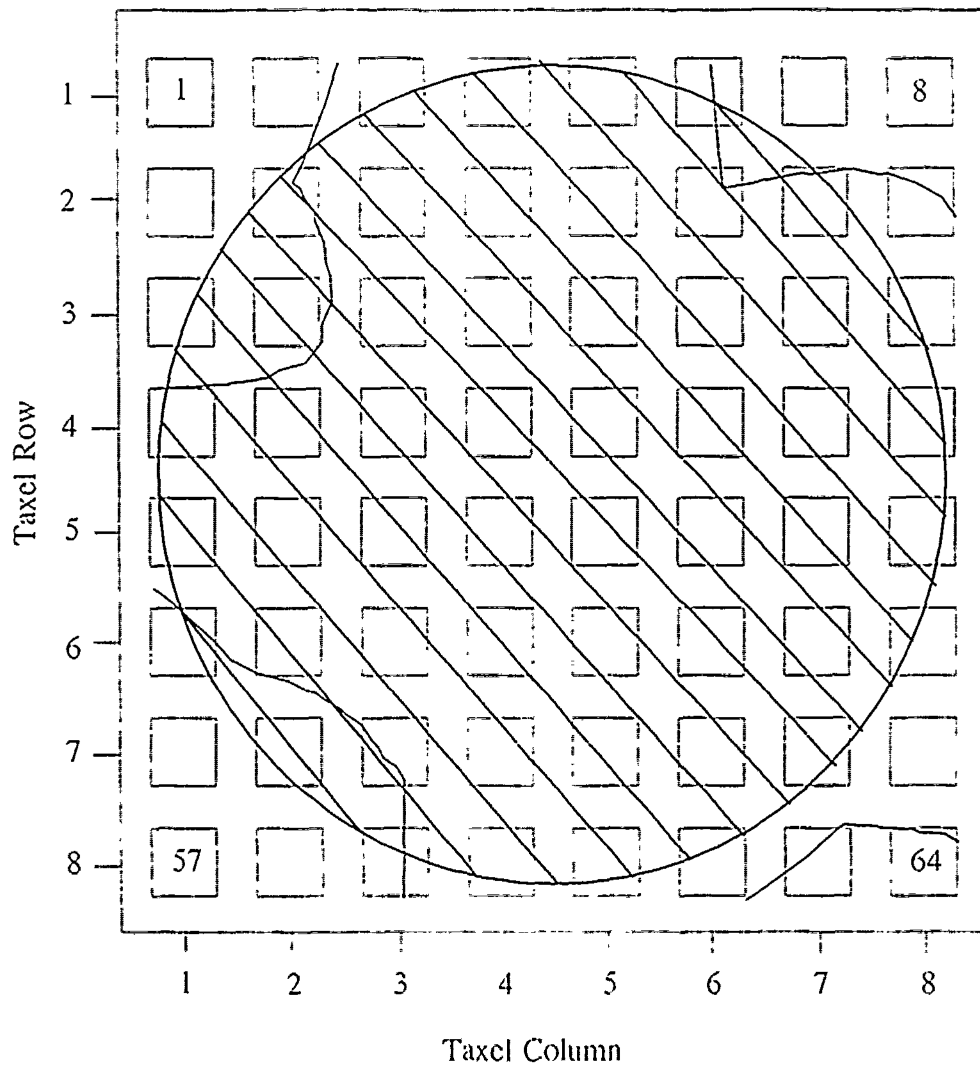

Figure 6.50. 0.5-V Equipotential Contour Plot For A 100 g Large Solid Circularly Shaped Load Applied To The Surface Of The Electrode Array.

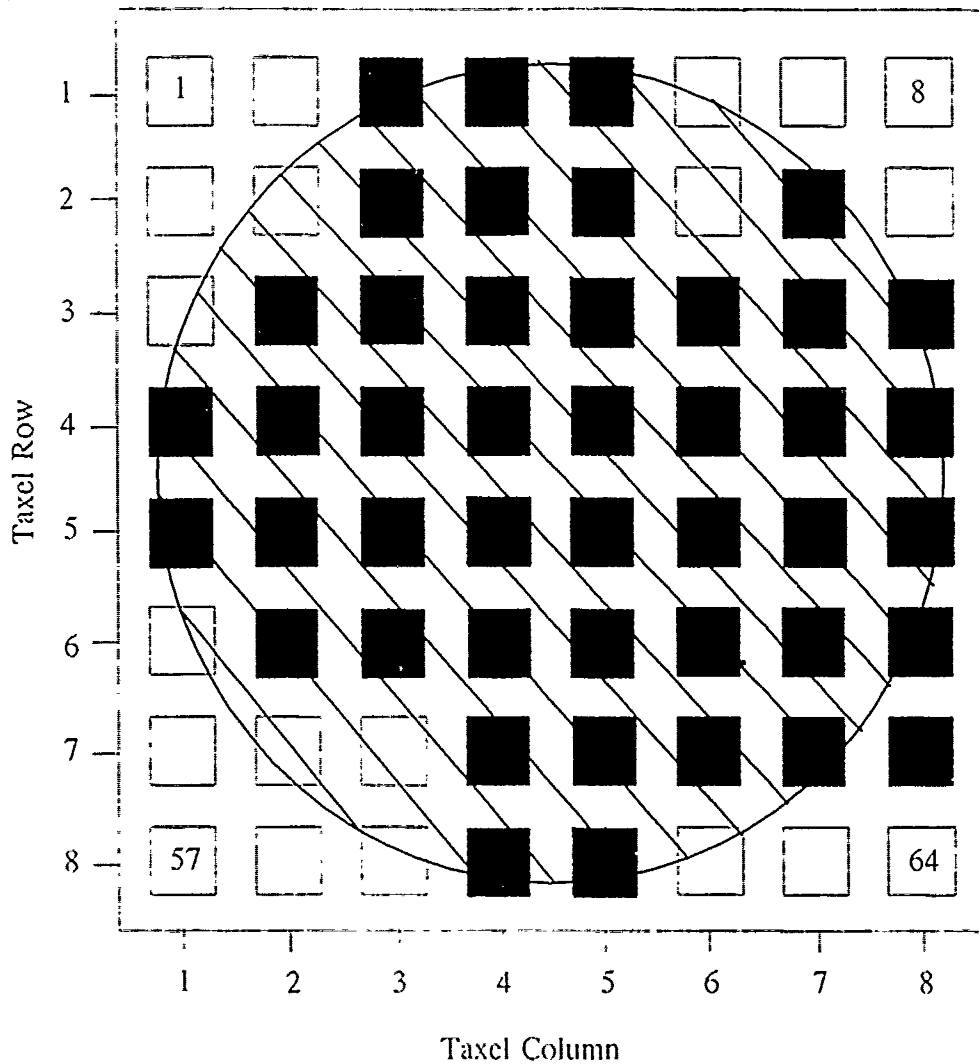

Figure 6.51. 0.5-V Threshold Plot Of A 100 g Large Solid Circularly Shaped Load – Taxeis With An Output Level Above This Threshold Level Are Displayed As Black And Taxels With An Output Level Below This Threshold Level Are Displayed As White.

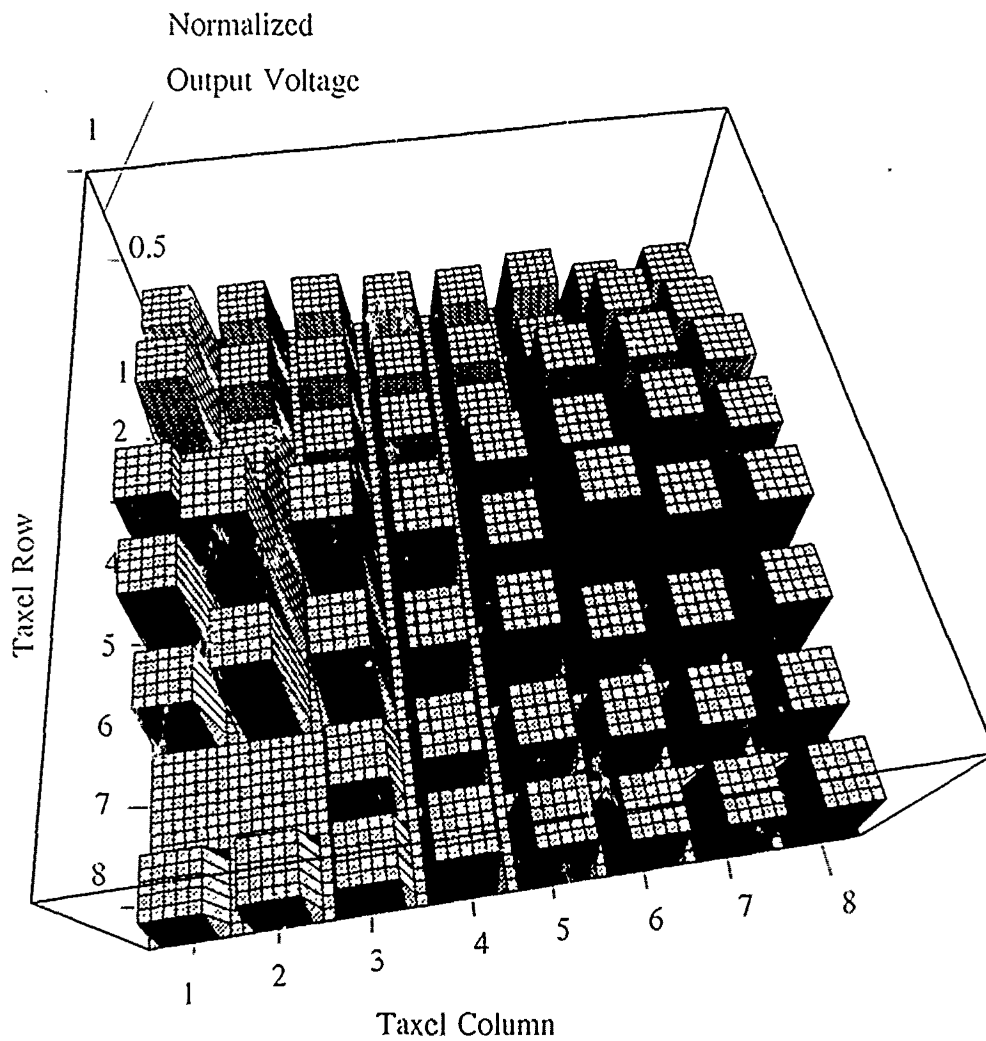

Figure 6.52. Three-Dimensional Representation Of A Toroid Shaped Load Applied To The Surface Of The Electrode Array. The z-Axis Corresponds To The Normalized Difference Between The Sensor's Loaded And Unloaded States, And The x- And y-Axes Correspond To The Electrode Columns And Rows, Respectively.

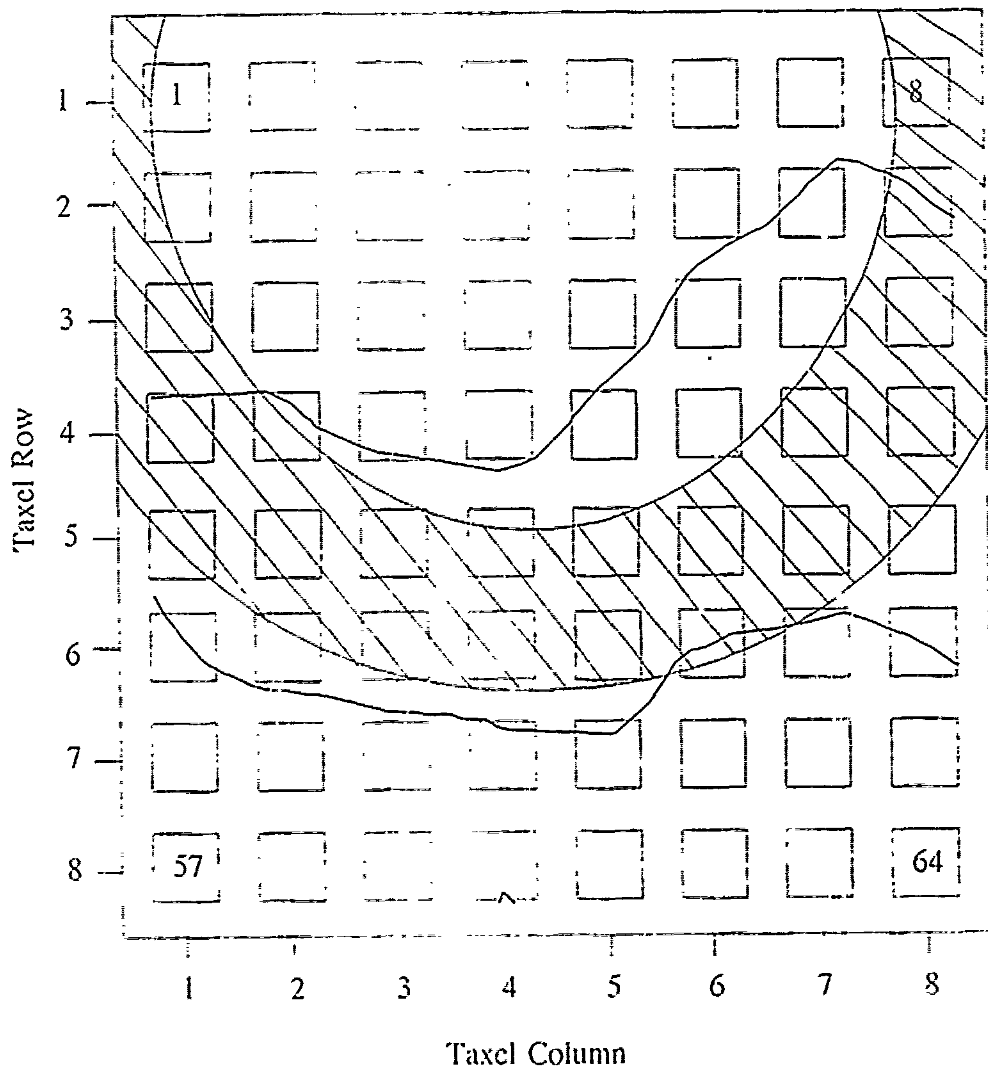

Figure 6.53. 0.5-V Equipotential Contour Plot For A 100 g Toroid Shaped Load Applied To The Surface Of The Electrode Array.

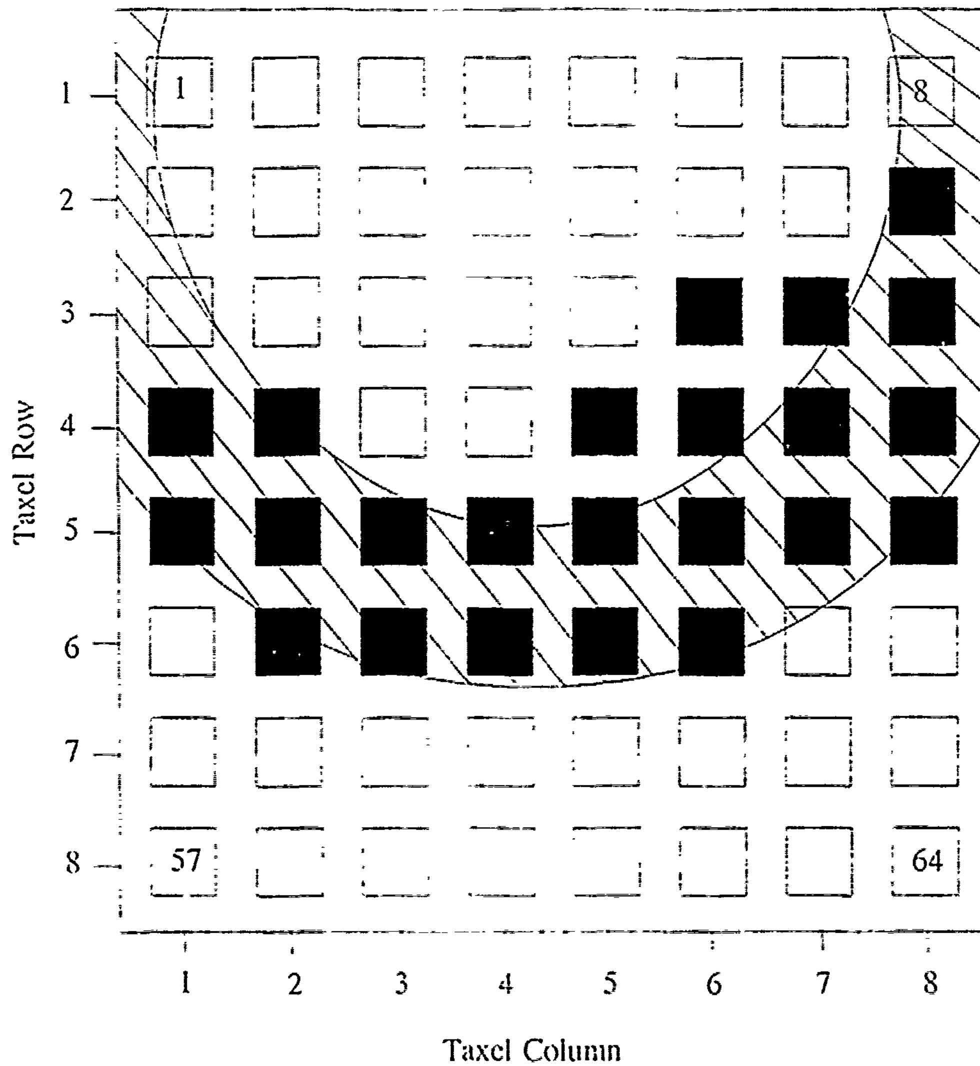

Figure 6.54. 0.5-V Threshold Plot Of A 100 g Toroid Shaped Load - Taxels With An Output Level Above This Threshold Level Are Displayed As Black And Taxels With An Output Level Below This Threshold Level Are Displayed As White.

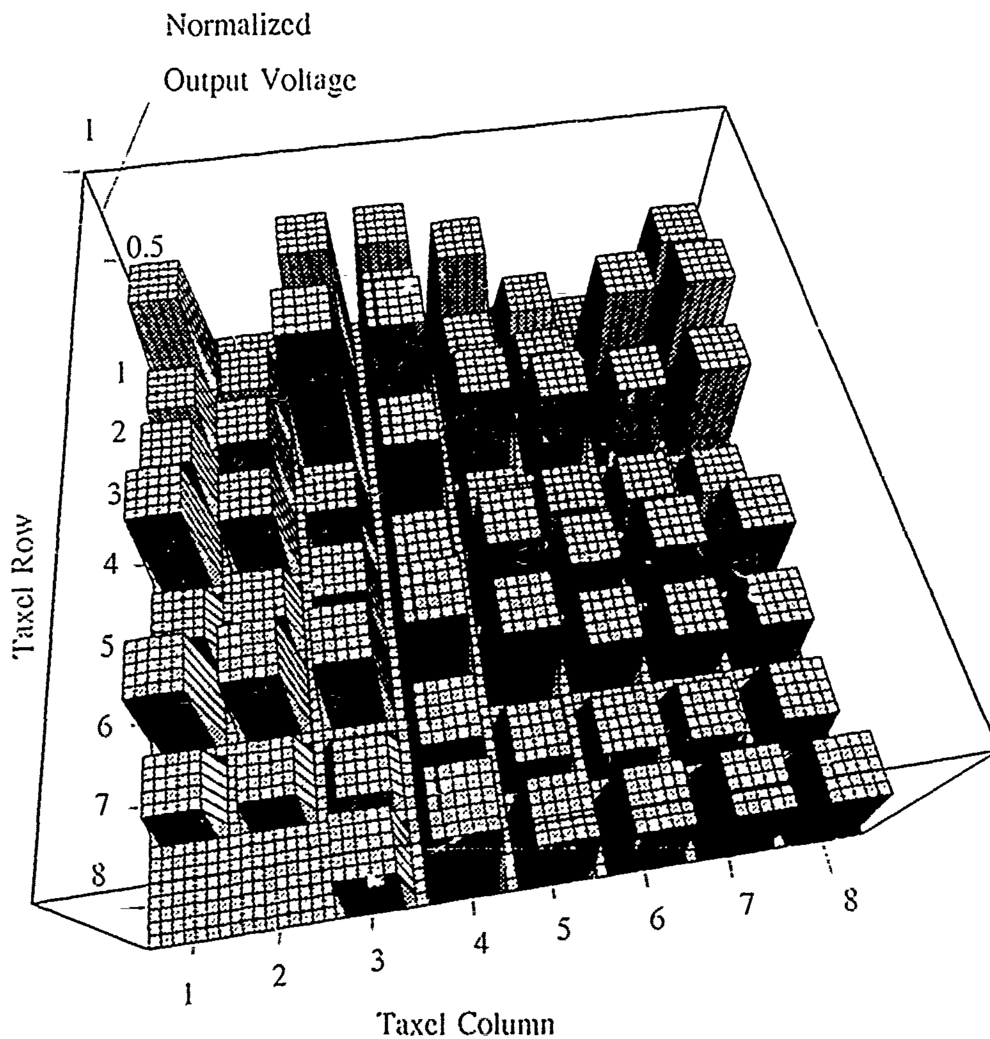

Figure 6.55. Three-Dimensional Representation Of A Sharp Edge Shaped Load Applied To The Surface Of The Electrode Array. The z-Axis Corresponds To The Normalized Difference Between The Sensor's Loaded And Unloaded States. And The x- And y-Axes Correspond To The Electrode Columns And Rows, Respectively - The Sensor Was Fabricated Using A Polyimide Adhesive.

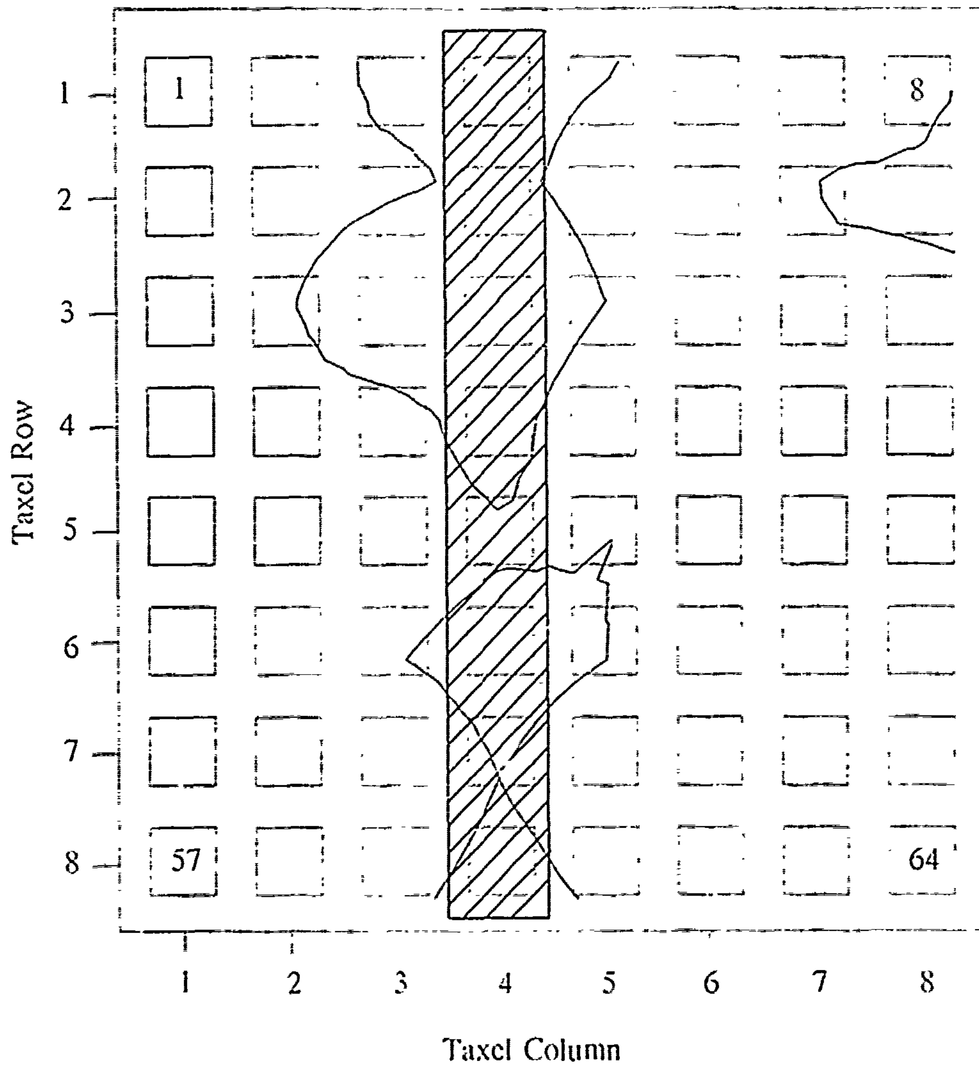

Figure 6.56. 0.58-V Equipotential Contour Plot For A 100 g Sharp Edge Shaped Load Applied To The Surface Of The Electrode Array - The Sensor Was Fabricated Using A Polyimide Adhesive.

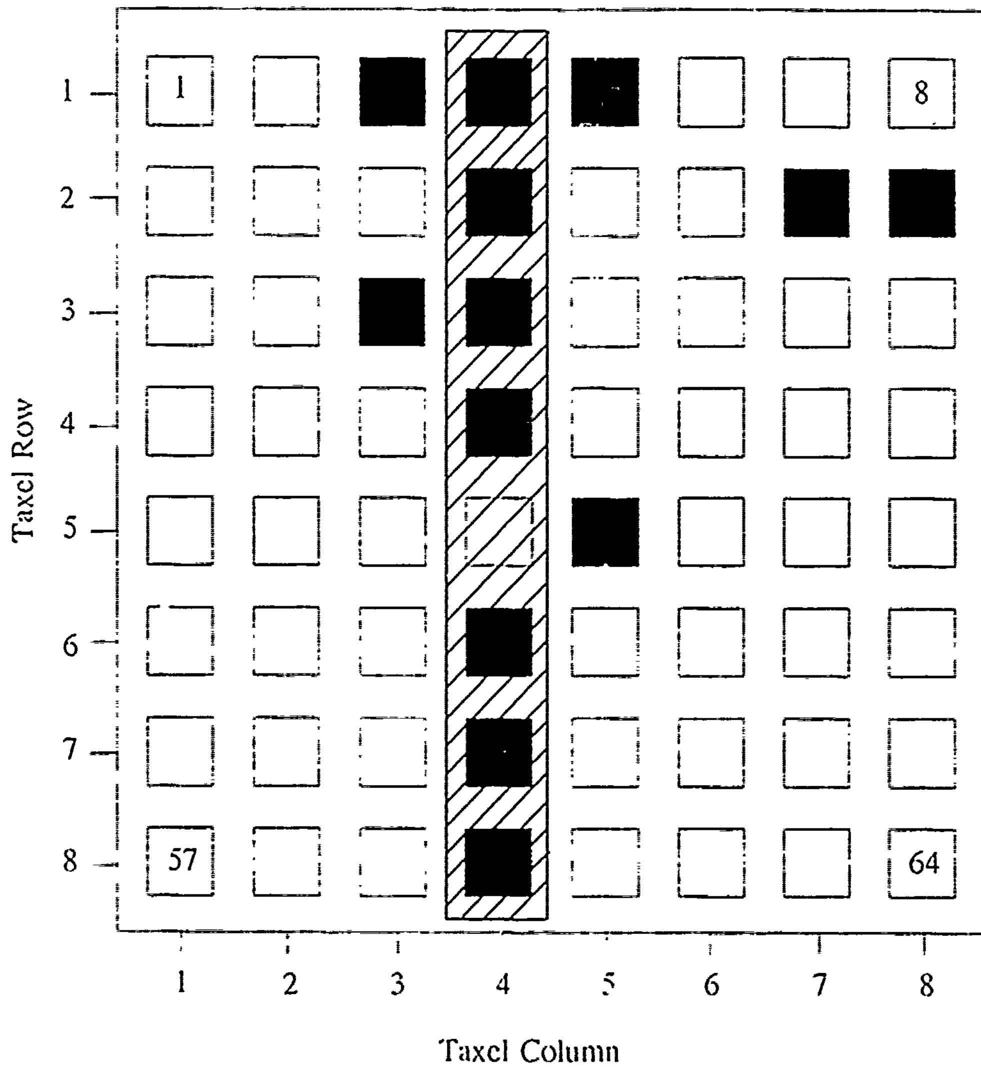

Figure 6.57. 0.58-V Threshold Plot Of A 100 g Sharp Edge Shaped Load - Taxels With An Output Level Above This Threshold Level Are Displayed As Black And Taxels With An Output Level Below This Threshold Level Are Displayed As White - The Sensor Was Fabricated Using A Polyimide Adhesive.

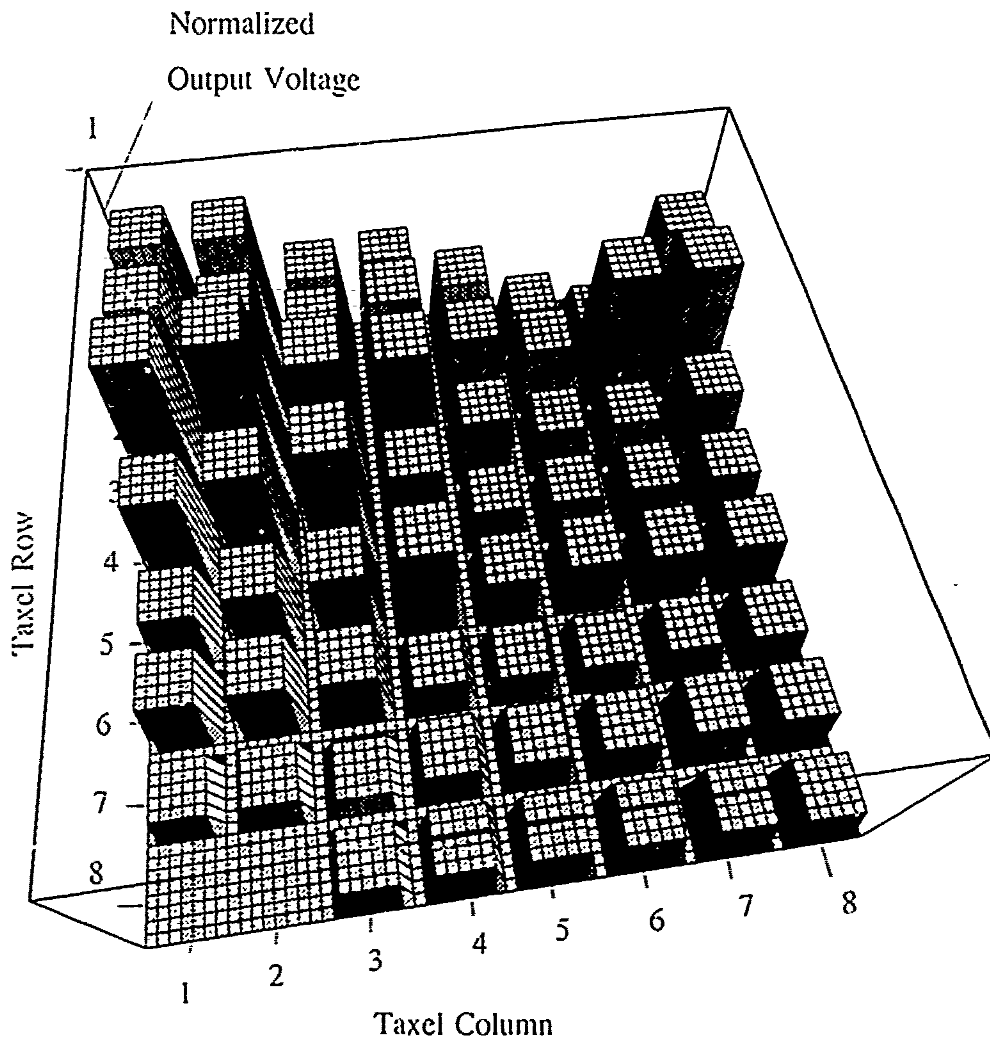

Figure 6.58. Three-Dimensional Representation Of A Small Square Shaped Load Applied To The Surface Of The Electrode Array. The z-Axis Corresponds To The Normalized Difference Between The Sensor's Loaded And Unloaded States. And The x- And y-Axes Correspond To The Electrode Columns And Rows, Respectively - The Sensor Was Fabricated Using A Polyimide Adhesive.

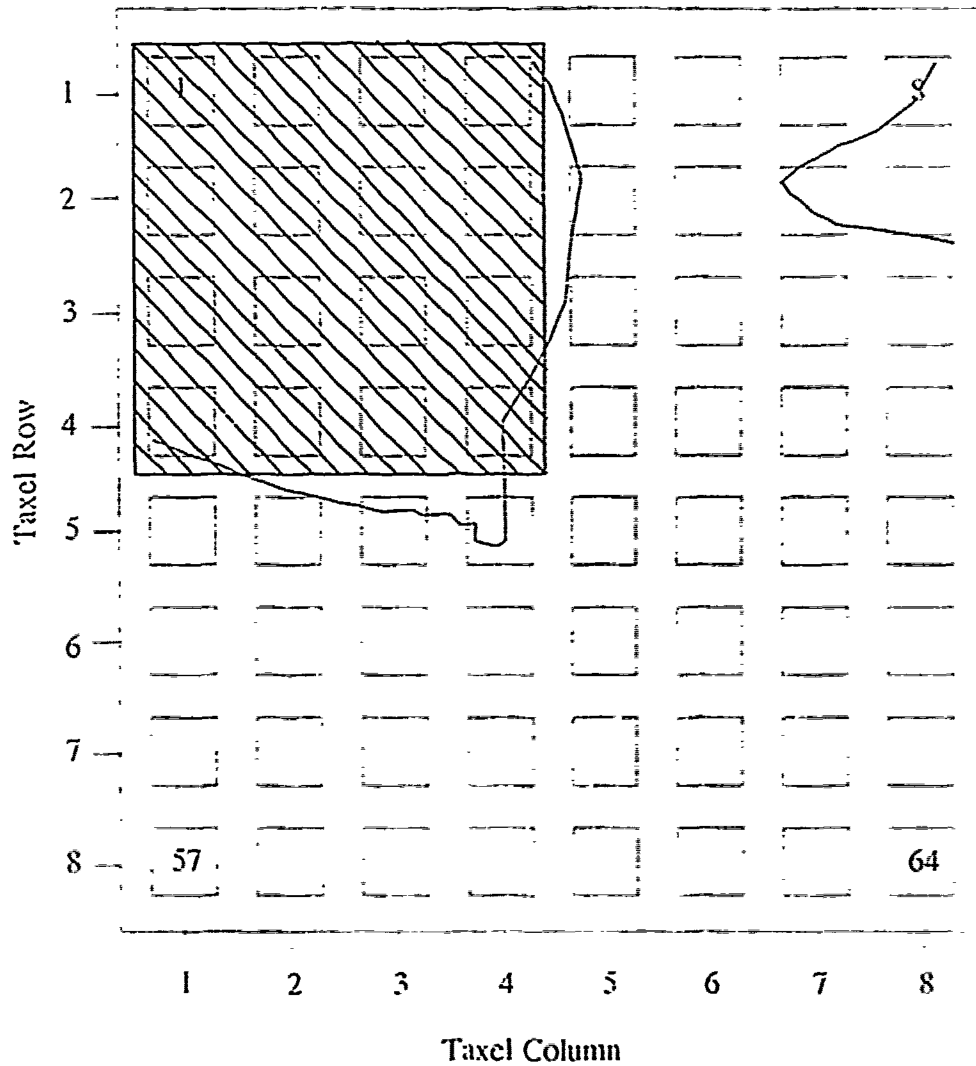

Figure 6.59. 0.55-V Equipotential Contour Plot For A 100 g Small Square Shaped Load Applied To The Surface Of The Electrode Array - The Sensor Was Fabricated Using A Polyimide Adhesive.

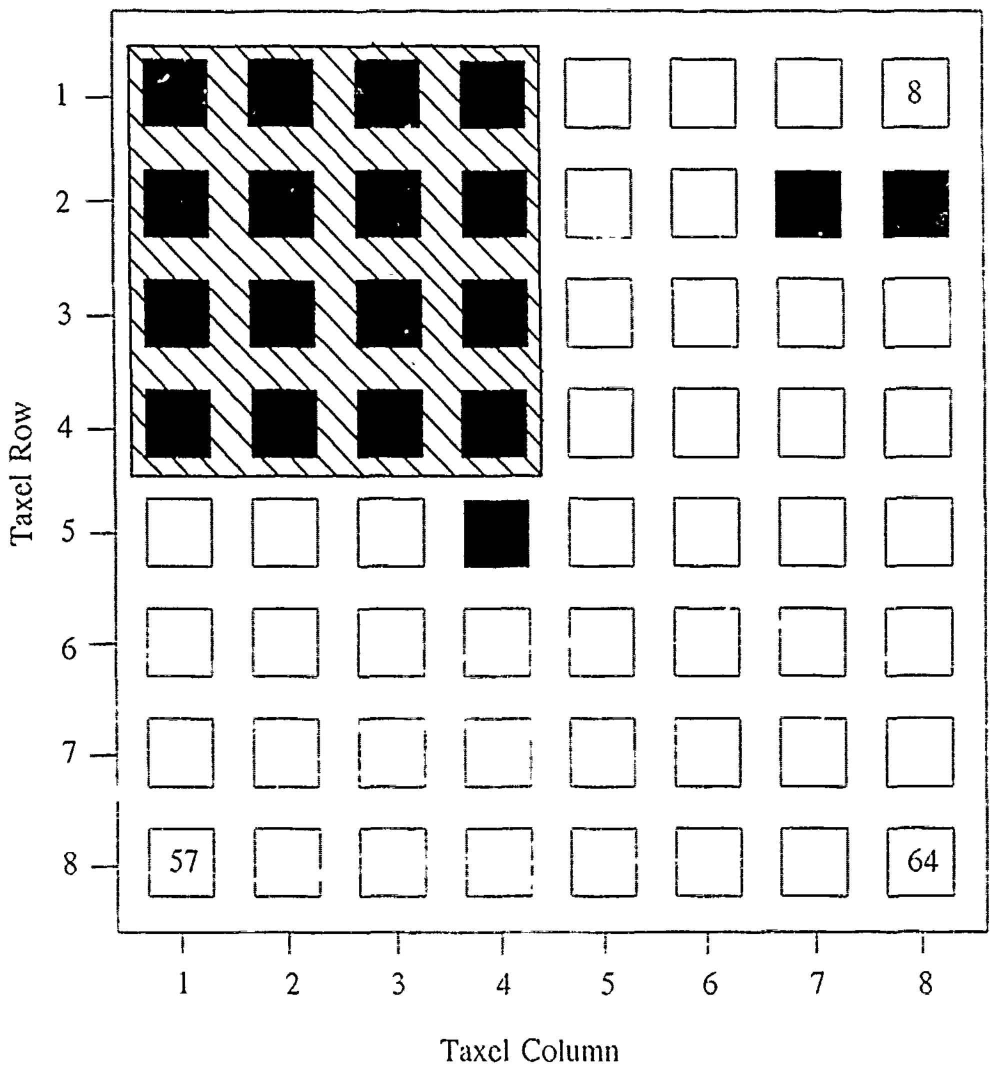

Figure 6.60. 0.55-V Threshold Plot Of A 100 g Small Square Shaped Load – Taxels With An Output Level Above This Threshold Level Are Displayed As Black And Taxels With An Output Level Below This Threshold Level Are Displayed As White – The Sensor Was Fabricated Using A Polyimide Adhesive.

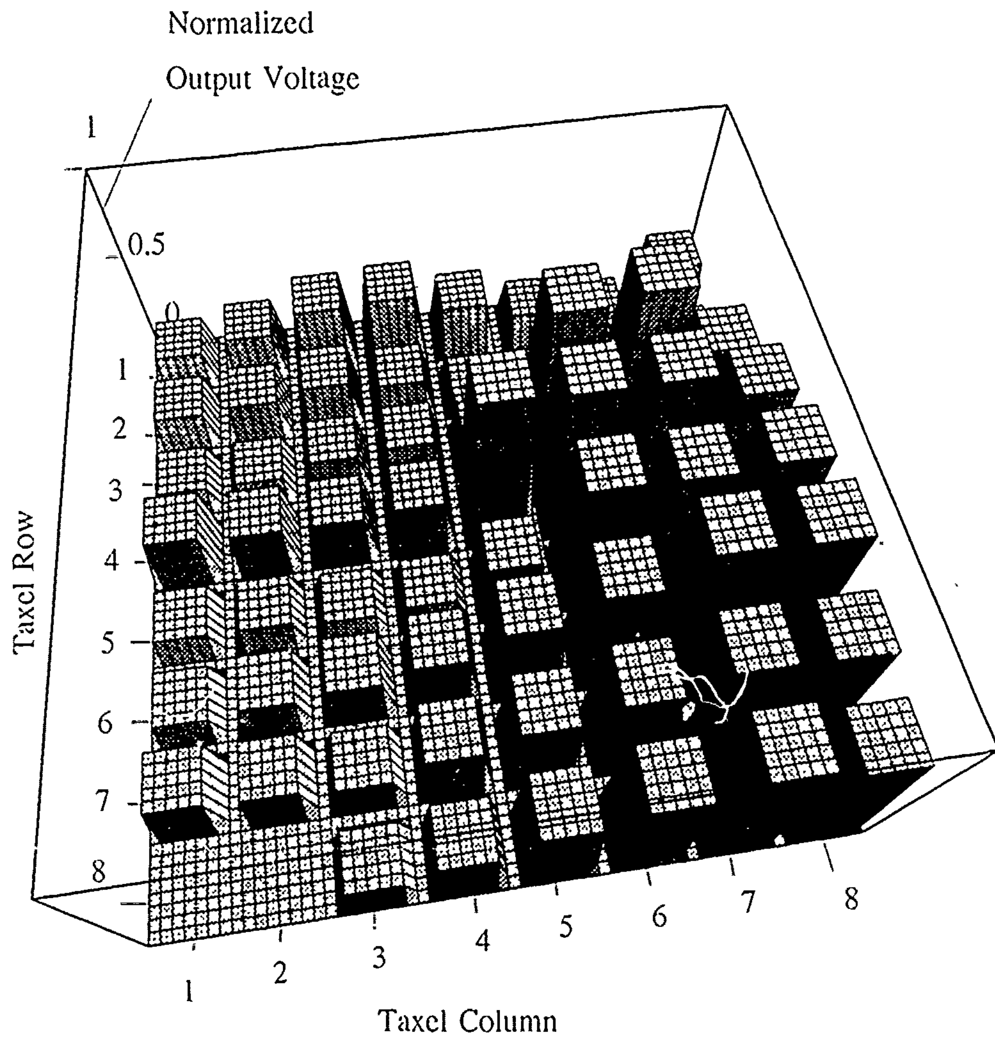

Figure 6.61. Three-Dimensional Representation Of A Small Circularly Shaped Load Applied To The Surface Of The Electrode Array. The z-Axis Corresponds To The Normalized Difference Between The Sensor's Loaded And Unloaded States, And The x- And y-Axes Correspond To The Electrode Columns And Rows, Respectively - The Sensor Was Fabricated Using A Polyimide Adhesive.

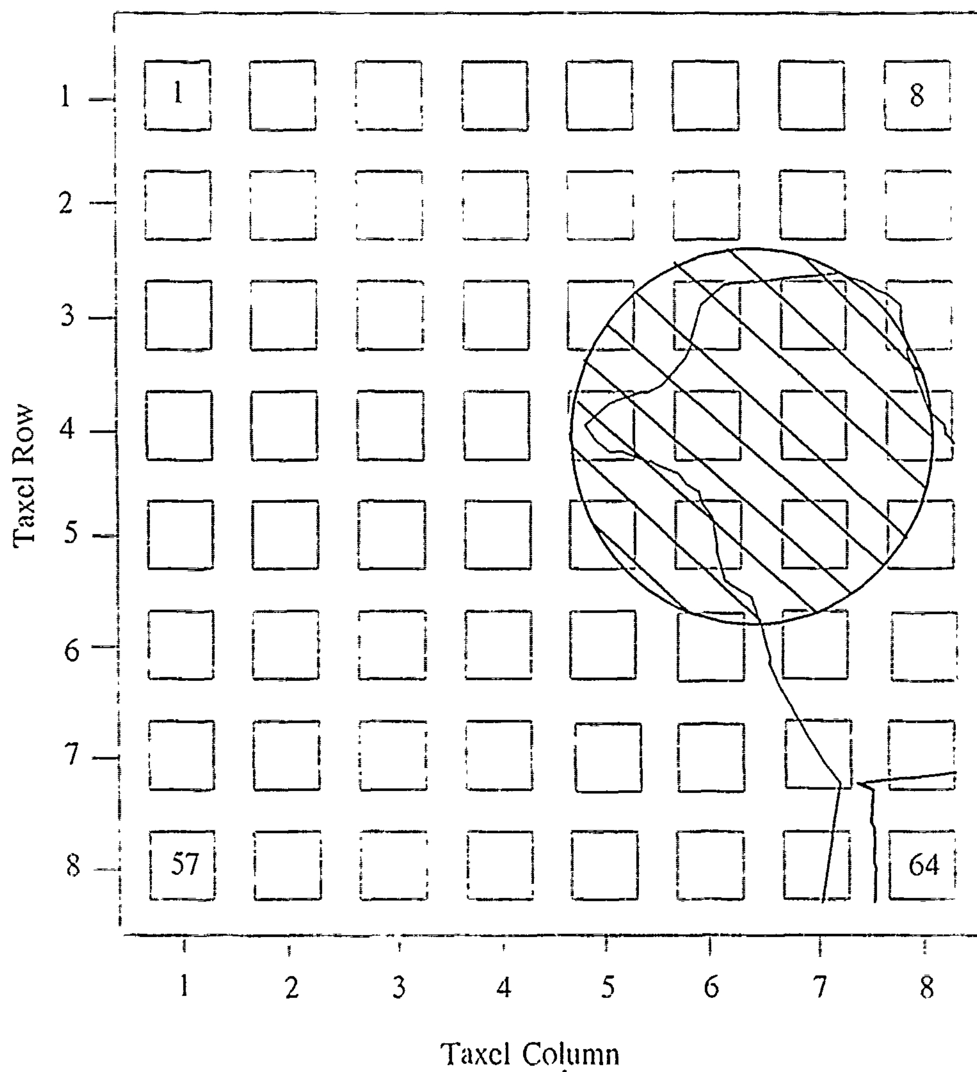

Figure 6.62. 0.8-V Equipotential Contour Plot For A 100 g Small Circularly Shaped Load Applied To The Surface Of The Electrode Array - The Sensor Was Fabricated Using A Polyimide Adhesive.

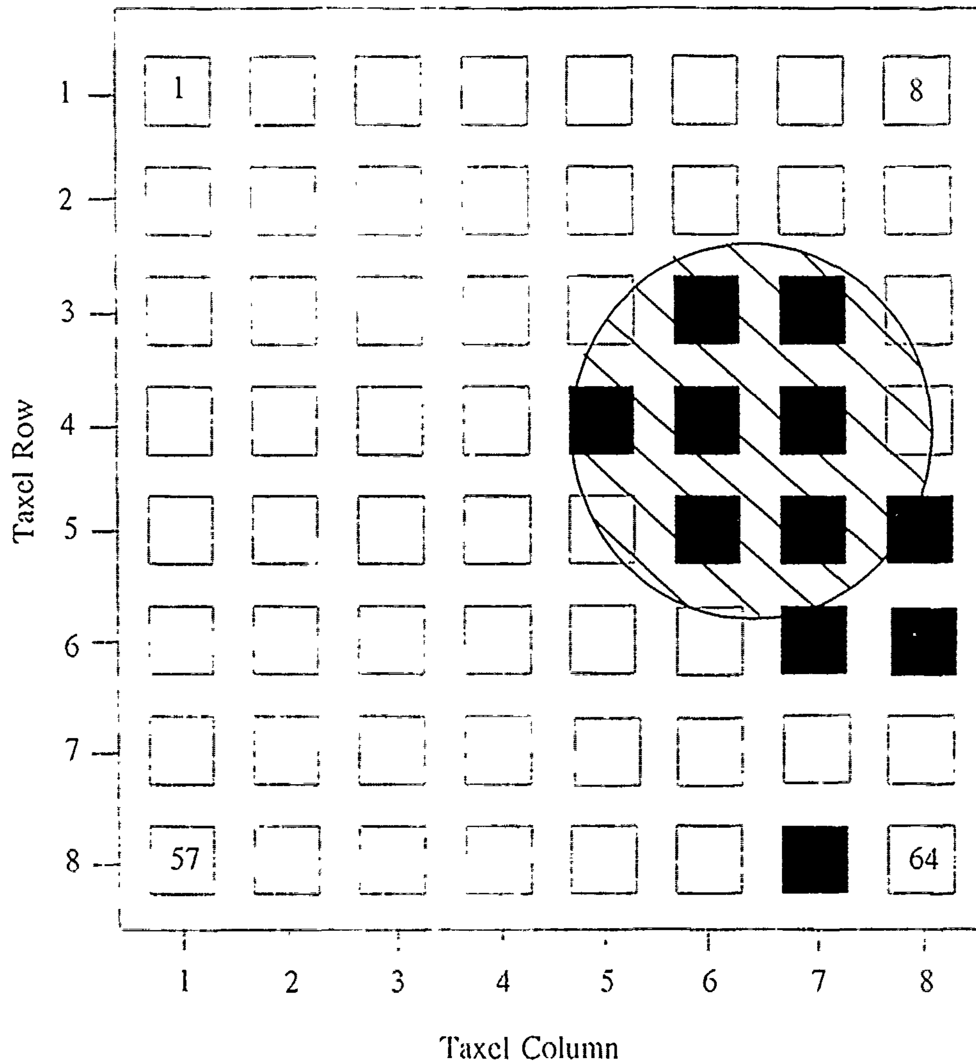

Figure 6.63. 0.8-V Threshold Plot Of A 100 g Small Circularly Shaped Load - Taxels With An Output Level Above This Threshold Level Are Displayed As Black And Taxels With An Output Level Below This Threshold Level Are Displayed As White - The Sensor Was Fabricated Using A Polyimide Adhesive.

Conclusion

This chapter compiled the results of the tactile sensor research effort and presented them in a chronological format beginning with the components of the system, and progressing to the final tactile sensor test configuration. The analysis indicates how each component's performance affected the overall tactile sensor's performance. The progression of testing resulted in the establishment of successful operation of the bias switch circuit, and the ability to establish an operating point for the multiplexer at 1.28 kHz. Initial IC performance tests indicated that the amplifier possessed a gain of 0.98, slightly less than expected SPICE analysis indicated; however, a large linear region resulting from the power supply voltage used was desired. Crosstalk effects inherent in the electrode array IC were discovered and indicated nearest-neighbor taxel responses which span 20% to 67% of the active taxel's voltage magnitude. The adhesive study revealed that fast curing adhesives do not possess the proper characteristics for fabricating a tactile sensor piezoelectric PVDF film on a silicon IC. Tactile sensor electrode tests indicated a linear load versus voltage slope (gradient) of 2 mV/g, a weight resolution of 20 g, and a maximum bandwidth of 25 Hz. They also indicate a 10% enhancement of the crosstalk effects using a urethane adhesive, and an increase of 15% using the polyimide adhesive. Finally, after using a shape detection algorithm, the taxel array tests conclusively show that the shape of the load in contact with the surface of the sensor was detected with a maximum resolution of 700 μm.

VII. Conclusions and Recommendations

Conclusions

The goal of this research effort was to design, fabricate, and characterize a tactile sensor system consisting of a tactile sensor IC, an external high impedance switch circuit, and an external multiplexing circuit. In order to accomplish this objective, a hardware design and fabrication process was implemented along with a logical test methodology. The hardware included an electrode array IC containing an 8 x 8 array of equally spaced aluminum electrodes, and 64 high impedance input MOSFET amplifiers. Also included were supporting component hardware consisting of a high impedance reed switch network and a multiplexer circuit both realized from commercially available components. The test methodology developed ensured that any problems associated with either the supporting component hardware or the integrated circuit could be identified early in the testing phase, and their effects could be accounted for.

This research was successful in designing, fabricating, and characterizing the performance of the entire tactile sensor system. The fabricated IC included *in situ* charge signal amplifiers which possessed a gain of 0.98 and a linear region from 2.5-V to 7-V. Also, charge leakage between input and output pads was not detected. Pyroelectric effects on the piezoelectric PVDF film were investigated; however, the Pyroelectric Minimization Chamber did not reduce variations in temperature. An external high impedance (10^{13} Ω) switch network resulted in the ability to bias the entire electrode array structure and attached piezoelectric PVDF film to a uniform initial condition. Additionally, the external multiplexer circuit enabled sampling of the array without degradation of any taxel charge signal. The response of the tactile sensor fabricated using a 40 μm thick square piece of the piezoelectric PVDF film indicated linearity between 0.8 g and 135 g, an incremental weight resolution of 20 g, and maximum bandwidth of 25 Hz. Using a shape detection procedure consisting of a mathematical manipulation of pre-load, load, and post-load measurements of the tactile sensor electrode array, the tactile sensor could detect the shape of the load in contact with the surface of the tactile sensor IC with a resolution on the order of 700 μm.

The considerable crosstalk (between 35% and 75% resulting from the IC layout design combined with coupling effects due to adhesives used for fabricating the tactile sensor) slightly affected the operation of the sensor; however, shape information could still be retrieved. Unfortunately, the charge signal amplifiers exhibited breakdown over time due to the excessive operating power supply voltage used to achieve the desired operating characteristics of the amplifier. A reduction in V_{dd} to a voltage below 12-V should solve this problem.

The adhesive study revealed that the urethane adhesive possessed the best electrical and physical characteristics when compared to either the polyimide or the *Loctite* materials. The *Loctite* adhesive tended to cure too quickly, resulting in poor adhesion and questionable physical coupling to the electrode array. While the polyimide possessed bonding characteristics similar to the urethane adhesive, its electrical characteristics exhibited an increase in taxel crosstalk larger than the urethane adhesive.

Recommendations

While this effort successfully designed, realized and characterized a fully functional tactile sensor, there are still advances and changes which should be implemented to facilitate attachment of a piezoelectric tactile sensor to a robotic manipulator. Five areas should be considered:

1. Taxel crosstalk inherent in the electrode array should be investigated. In order to fully investigate the source of this crosstalk, a design similar to the one utilized in this thesis effort should possess two distinct characteristics. One half of the electrode array should route the input metal lines in such a manner to ensure that nearest-neighbor electrode lines routed from the electrode to their corresponding amplifier do not lie next to each other. On other half of the array, the electrode input signal lines routed from the input bond pad to the gate of the amplifier should not lie within 25 μm of each other (the metal lines in this effort were 10 μm apart). A design incorporating these changes could help detemine the source of the crosstalk problem.

2. The incorporation of an *in situ* multiplexer. A functional resident multiplexer would relieve the pin count limitations on the number of aluminum electrodes used, which would further improve the sensor image resolution while also

enhancing the reliability of the IC. This feature would limit the number of bond wires exposed; thus, reducing the potential for destroying input or output paths. Appendix M provides the design and test approach for a potential candidate for a future *in situ* multiplexer.

3. A new charge signal amplifier should be designed which possesses a compromise between a large linear operating region and a large gain to facilitate an increased load weight response resolution. The design should incorporate an operating supply voltage of less than 13-V, to inhibit MOSFET destruction.

4. A modified test load application fixture is required. A modification of the load application device to incorporate micrometer adjustment screws would facilitate adjustment of the test load shape and facilitate intimate contact between the surface of the tactile sensor IC and the test load shape. This modification would facilitate full characterization of the tactile sensor relative to the test load shapes (Figure 7.1).

5. An investigation into the pyroelectric effects should be undertaken. These effects should be minimized to ensure proper characterization of the tactile sensor is performed.

These recommendations should provide significant improvement in the tactile sensor system, and they could potentially facilitate incorporating the tactile sensor IC onto a robotic manipulator.

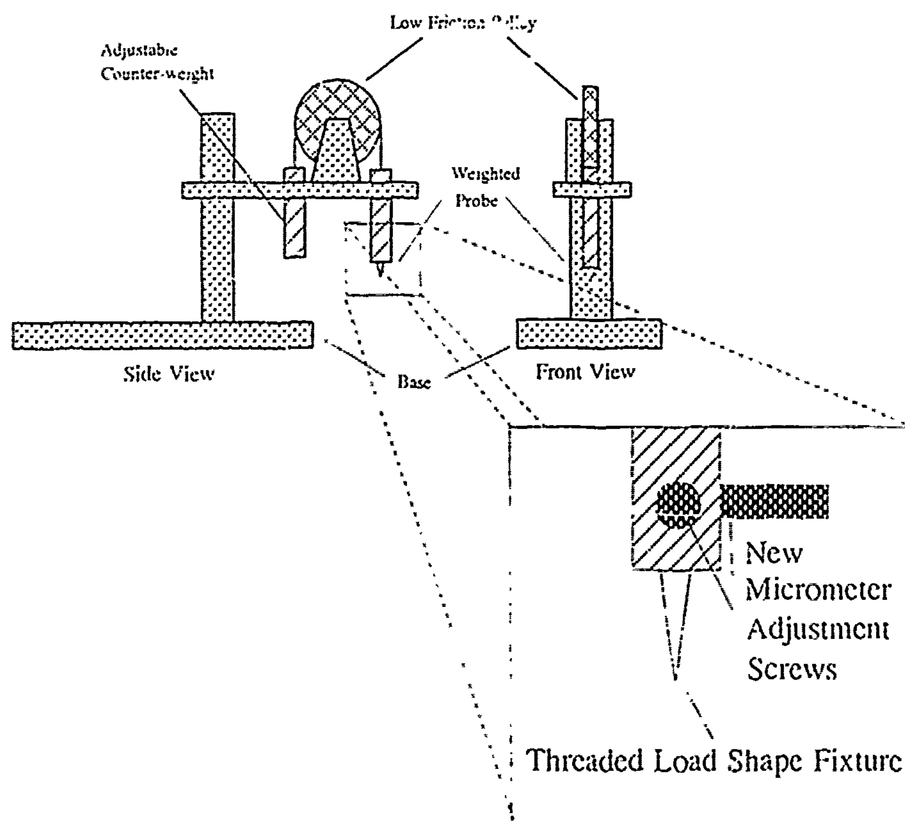

Figure 7.1. Modification Of The Fixture For Applying The Test Load Shapes Incorporating Micrometer Adjustment Screws.

Appendix A. *Materials and Equipment*

The following table summarizes the materials used and equipment utilized in this research effort.

Table A.1. Materials And Equipment.

Materials and Equipment
Solef Polyvinylidene Fluoride Film - 40 μm thick The Solvay America Corporation 609 5th Ave. New York, NY 10017
Metal-oxide-semiconductor Implementation System (MOSIS) Circuits University of Southern California Information Sciences Institute 4676 Admiralty Way Marina Del Rey, CA 90292
Urethane (MS-470/22), Miller-Stephenson Chemical Co. George Washington Highway Danbury, CT 06810
Ultradel Polyimide Dielectric and Adhesion Promoter AMOCO Chemical Co. 200 E. Randolph Dr. Chicago, IL 60601
Plastic Dielectric - Loctite Tak Pak (No. 7586A21) Loctite Corporation Newington, CT 06111
MAX328 Multiplexer Chips Maxim Integrated Products 120 San Gabriel Dr. Sunnyvale, CA 94086
High Impedance Reed Switches Potter and Brumfield Relay Specialties, Inc. 17 Raritan Rd. Oakland, NJ 07436

Keithley Electometer, model 617 Keithley Instruments 28775 Aurora Rd. Cleveland, OH 44139
LeCroy Model 9400A Digital Oscilloscope LeCroy Corporation 700 Chestnut Ridge Rd. Chestnut Ridge. NY 10977
HP 54100A Digital Storage Oscilloscope Hewlett-Packard Co. 3155 Porter Dr. Palo Alto, CA 94304
Fluke 77/AN Multimeter John Fluke Manufacturing Co. Everett, WA 99100
Zenith Z-248 Personal Computer (with IEEE-488 Interface) Zenith Data Systems Hilltop Rd. St Joseph, MI 49085
IEEE-488 Buses
Micromanipulator Model 6200 Microprobe Station The Micromanipulator Company, Inc. 2801 Arrowhead Dr. Carson City, NV 89701
Micromanipulator Model 450/360 VM Manipulators (3) The Micromanipulator Company, Inc. 2801 Arrowhead Dr. Carson City, NV 89701
HP6205B Power Supply Hewlett-Packard Co. 3155 Porter Dr. Palo Alto, CA 94301
Pyroelectric Minimization Chamber
Test Probe Fixture and Weights
Sensor Protoboard

HP3314 Function Generator Hewlett-Packard Co. 3155 Porter Dr. Palo Alto, CA 94304
Elite-1 Circuit Design System E & L Instruments, Inc. 70 Fulton Terrace New Haven, CT 06512
Decade Voltage Divider, Type 654-A General Radio Company Cambridge, MA 01854
SPI Sputter Coater SPI Supplies P. O. Box 342 West Chester, PA 19380
SPI Plasma Prep II SPI Supplies P. O. Box 342 West Chester, PA 19380
VLSI Computer Aided Design (CAD) Tools Magic Integrated Circuit Layout Editor Simulation Programs, Integrated Circuit Emphasis (SPICE)
De-ionized Water
Glass Microscope Slides
Isopropyl Alcohol
Concentrated (37%) HCl
Ferric Chloride
Acetone
Silicone Oil
Silver Conductive Epoxy
Scalpel
Syringe (3 cc)
Heat Source
Aluminum
Gold
Conductive Copper Tape
1-mil Diameter Wire
Nitrogen Gas
Battery

Appendix B. *Test Load Shape Designs*

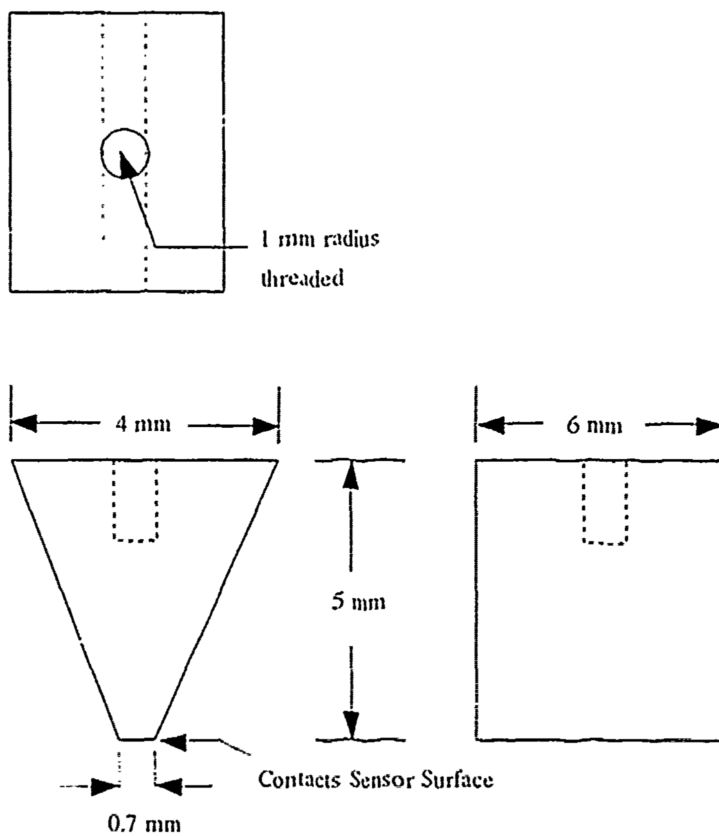

Figure B.1. Sharp-Edge Test Load Shape.

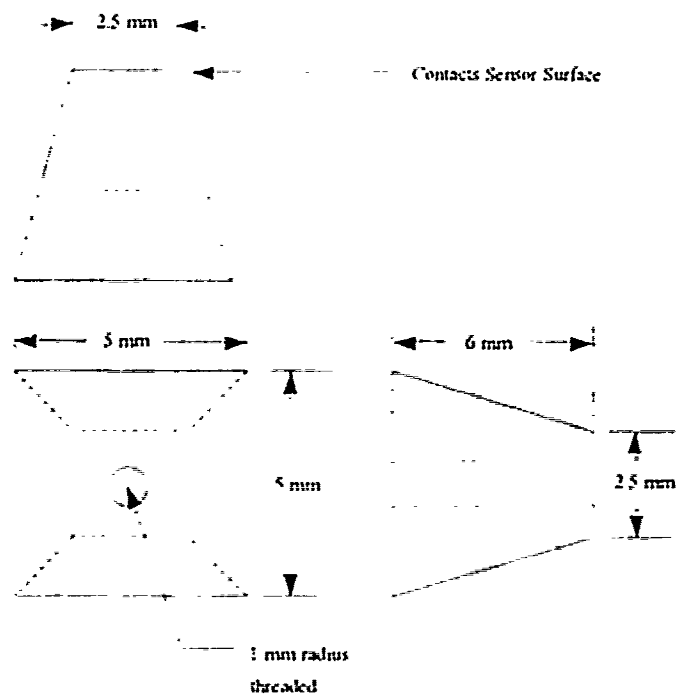

Figure B.2. Square Shaped Test Load.

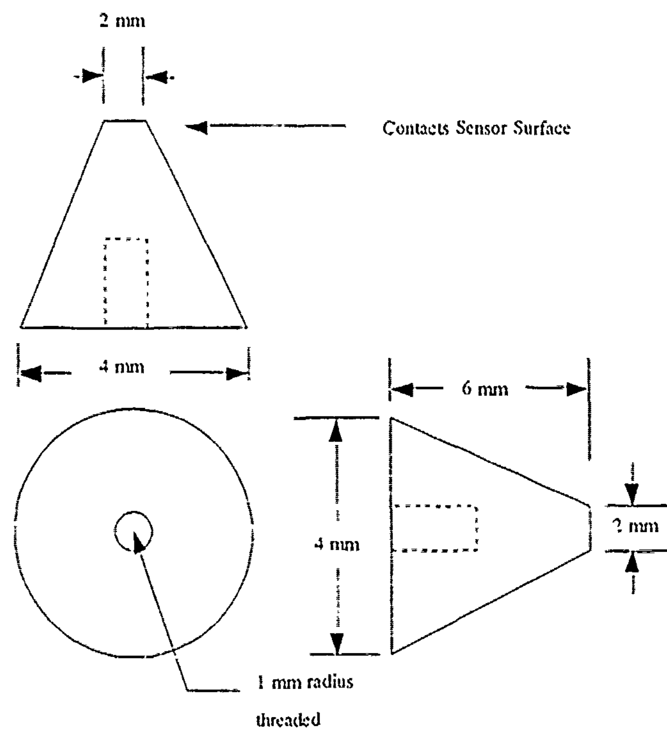

Figure B.3. Solid Circle Test Load Shape.

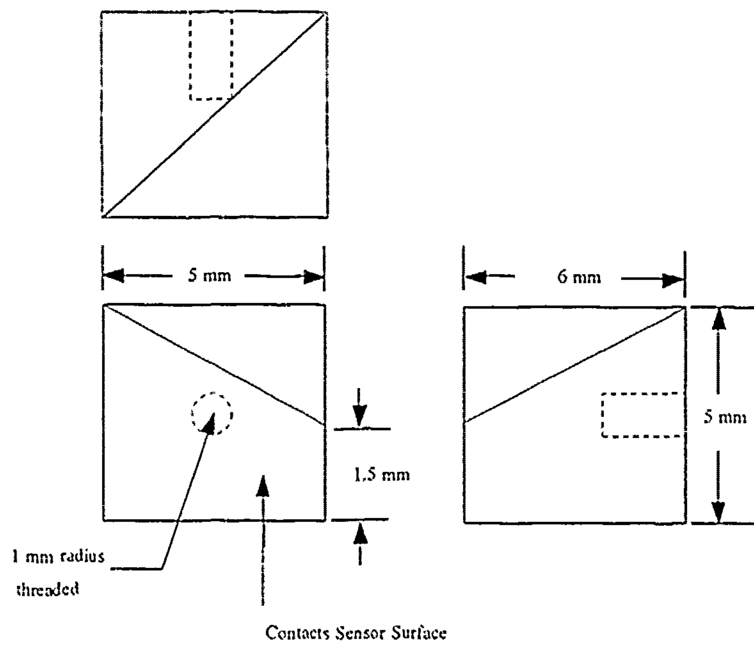

Figure B.4. Polygon Shaped Test Load.

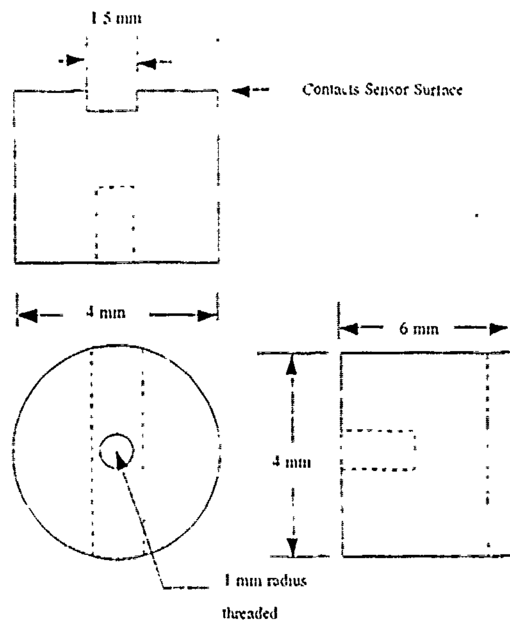

Figure B.5. Slotted Screw Test Load Shape.

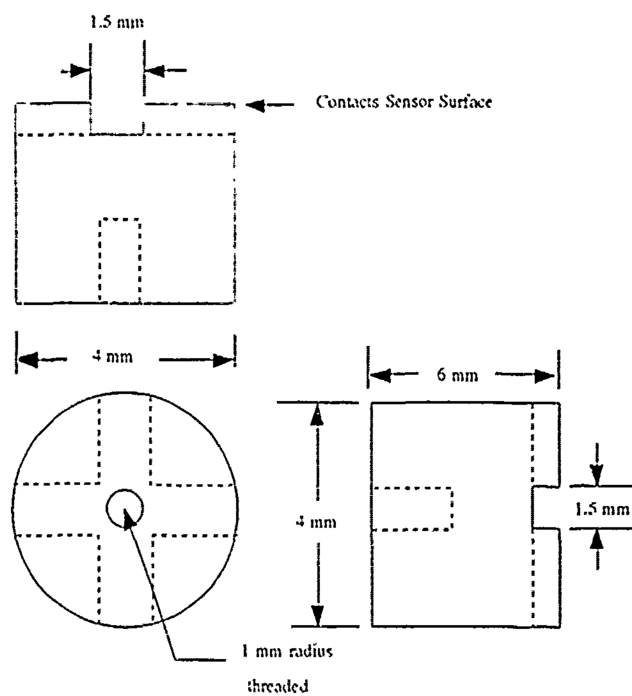

Figure B.6. Cross-slot Screw Test Load Shape.

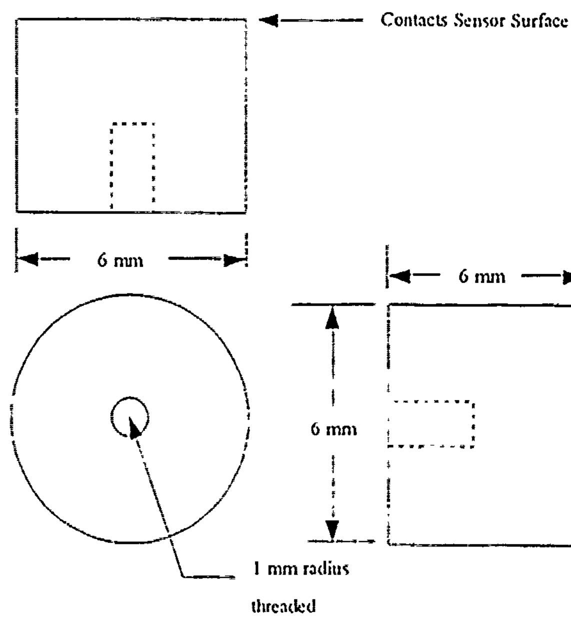

Figure B.7. Large Solid Circle Test Load Shape.

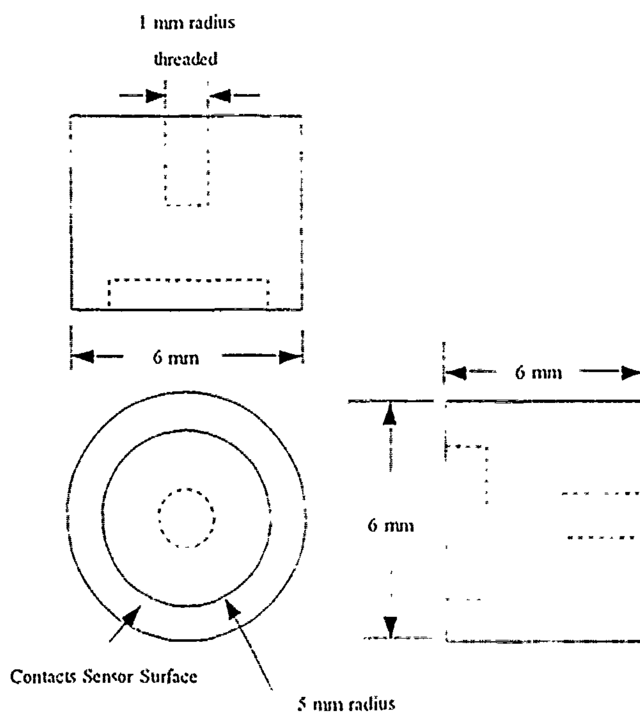

Figure B.8. Toroid Test Load Shape.

Appendix C. *SPICE Deck Files*

The following data includes the tactile sensor charge amplifier SPICE deck and the SPICE model parameters.

Charge Amplifier SPICE Deck

```
**************************************************************
*
* Power Supply and Input Voltages
*
Vdd 1 0 dc 15v
vin 3 0 dc 1.8v $sin(1.8 7.5 1khz) ac 2,0
* Circuit Being Analyzed - Charge Amplifiers
* 2 Inverters In Series with Resistive Loads
.param resistor=1
*.param width=1
*.param length=1
mn1 2 3 0 0 n w=5u l=2u ad=25p as=25p
r1 1 2  7k$'resistor*280'
mn2 4 2 0 0 n w=3u l=2u ad=19p as=19p
r2 1 4  5k$'resistor*200'

.dc vin 0 15 0.2 sweep resistor poi 7 20 22 24 25 26 28 30
*.ac dec 10 1 1e7
*.tran 1e-5 1e-3

*.print dc v(4)

*.plot ac vdb(4,3)
*.plot ac vp(4)
*.plot tran v(4),v(3)
*.plot dc v(4)

*.graph ac MODEL=output vdb(4,3)
*.graph ac MODEL=output vp(4)
*.graph tran v(4),v(3)
.graph dc v(4)

*.model output plot xscal=2

.options nomod
.protect $suppresses the model information
.include /auto/cad/chiplib/spicemodels/vti_hspice.lvl13
.end
```

```
******************************************************************
*
*PROCESS=vti
*RUN=n0al
*WAFER=5
*Gate-oxide thickness= 389.0 angstroms
*Geometries (W-drawn/L-drawn, units are um/um) of transistors
*   measured were:
* 3.0/2.0, 6.0/2.0, 18.0/2.0, 18.0/5.0, 18.0/25.0
*Bias range to perform the extraction (Vdd)=5 volts
*DATE=01-15-91
*
*NMOS PARAMETERS
*
.MODEL N NMOS LEVEL=13 VFB0=
+ -8.26023E-01,-5.61593E-02,-1.67910E-01
+  7.62682E-01, 1.93912E-24, 0.00000E+00
+  1.00898E+00, 1.21488E-01, 5.05816E-01
+  1.14611E-01, 1.69798E-01,-3.90522E-02
+ -9.35442E-03, 2.63766E-02,-5.51985E-03
+  5.59640E+02,6.26337E-001,-2.80950E-001
+  5.14904E-02, 5.52767E-02,-5.37042E-02
+  6.72559E-02, 7.20491E-01,-4.74495E-01
+  7.39485E+00,-8.04217E+00, 4.52431E+01
+ -2.89978E-04,-1.18484E-02,-5.85445E-03
+  1.19460E-03,-8.92090E-04,-1.02105E-02
+  1.06569E-03,-9.12039E-04, 1.40155E-02
+ -1.98398E-02, 3.02754E-02, 7.64969E-02
+  6.41883E+02, 4.40279E+02, 6.05329E+01
+ -1.33791E+01, 3.58763E+01, 1.29922E+02
+  3.71054E+00, 7.68605E+01,-2.72986E+01
+  9.66103E-03, 7.28719E-02,-5.33735E-02
+ 3.89000E-002, 2.70000E+01, 5.00000E+00
+ 4.16998E-010,4.16998E-010,5.96190E-010
+ 1.00000E+000,0.00000E+000,0.00000E+000
+ 1.00000E+000,0.00000E+000,0.00000E+000
+ 0.00000E+000,0.00000E+000,0.00000E+000
+ 0.00000E+000,0.00000E+000,0.00000E+000
+ 19.48,     1.020500e-04,     5.524300e-10,     0,     0.8
+ 0.8,     0.6744,     0.2857,     0,     0
*
* Gate Oxide Thickness is 388 Angstroms
*
*PMOS PARAMETERS
*
.MODEL P PMOS LEVEL=13 VFB0=
+ -4.34134E-01, 6.75224E-02,-2.59323E-03
+  6.85623E-01, 0.00000E+00, 0.00000E+00
+  6.17278E-01,-1.14679E-01, 8.83531E-02
```

```
+  2.52232E-02, 2.70778E-02,-1.84284E-02
+ -9.68790E-03, 4.89835E-02,-5.69373E-03
+  2.30201E+02,4.65059E-001,-3.64377E-001
+  1.20355E-01, 5.44177E-02,-1.02850E-01
+  7.01132E-03, 2.61359E-01,-1.91130E-02
+  9.74288E+00,-5.44796E+00, 5.47627E+00
+ -8.19796E-04,-2.75987E-03,-1.65286E-03
+  1.14756E-03,-3.39669E-03,-3.44013E-03
+  6.39469E-03,-4.55227E-03, 6.15819E-05
+ -1.74819E-03, 7.53192E-03, 9.75447E-03
+  2.32150E+02, 1.22066E+02, 4.63450E+01
+  8.37573E+00, 9.15603E-01, 1.13261E+01
+ -1.05253E+00, 1.07120E+01, 4.41416E+00
+ -1.63221E-02,-2.64327E-03, 2.09036E-02
+ 3.89000E-002, 2.70000E+01, 5.00000E+00
+ 3.09624E-010,3.09624E-010,5.75636E-010
+ 1.00000E+000,0.00000E+000,0.00000E+000
+ 1.00000E+000,0.00000E+000,0.00000E+000
+ 0.00000E+000,0.00000E+000,0.00000E+000
+ 0.00000E+000,0.00000E+000,0.00000E+000
+ 102.6,    2.553000e-04,    3.147200e-10,    0,    0.8
+ 0.8,    0.5533,    0.3306,    0,    0
*
*N+ diffusion::
*
.MODEL PC1_DU1 R
+ RSH=19.5 COX=0.000102 CAPSW=5.52e-10 W=0 DW=0
*
*P+ diffusion::
*
.MODEL PC1_DU2 R
+ RSH=103 COX=0.000255 CAPSW=3.15e-10 W=0 DW=0
*
*METAL LAYER -- 1
*
.MODEL PC1_ML1 R
+ RSH=0.106 COX=0 CAPSW=0 W=0 DW=0
*
*METAL LAYER -- 2
*
.MODEL PC1_ML2 R
+ RSH=0.04 COX=0 CAPSW=0 W=0 DW=0
```

Multiplexer Inverter SPICE Deck

```
*************************************************************
*
* POWER SUPPLY AND INPUT VOLTAGES
*
VDD   1 0 DC 15V
VIN1  2 0 PULSE(0 15 25NS 1NS 1NS 25NS 50NS)
*VIN2 3 0 PULSE(0 5 50NS 1NS 1NS 50NS 100NS)
*VININV 2 0 DC 5V

* CIRCUIT BEING ANALYZED - INVERTER
X2 2  3 1 INVERTER
C2 3  0 149FF
*LOAD CAPACITANCE - 8 GATES

.SUBCKT INVERTER 2 3 1
M1 1  2 3  1 P W=15U L=2U AD=75P AS=75P
M2 3  2 0  0 N W=8U L=2U AD=40P AS=40P
.ENDS INVERTER

*.dc  vininv 0 15 0.2
.tran 1ns  100ns
**.plot dc v(3)

*.graph dc v(3)
.plot tran v(3)
.protect  suppresses the model information
.include /auto/cad/chiplib/spicemodels/vti_.spice.lvl13

.END
```

Appendix D. *Piezoelectric PVDF Film Characterization Procedure*

Concurrent with the IC fabrication process, the piezoelectric PVDF film was characterized to determine its polarization (68:29). The surface of the film which developed a positive charge when the film was compressed was identified as the surface which was attached to the electrode array. This surface was not be metallized. The film polarization detection and pyroelectric effect procedure was implemented as follows:

1. A 6 mm by 6 mm piece of the piezoelectric PVDF film was cut from a larger sheet (8 x 11 in) (one side of the large sheet was marked in one corner with indelible ink for orientation purposes: the same side of the smaller piece of film was similarly marked).

2. A metallization process (either thermal evaporation or sputtering) was used to partially cover a glass microscope slide to create the electrode configuration shown in Figure D.1. One strip of the conductive copper tape was then attached to the electrode.

3. The piece of the piezoelectric PVDF film was attached to the glass microscope slide with the urethane adhesive.

4. A second piece of copper tape was then attached to the unmetallized portion of the glass microscope slide, and a 1-mil diameter wire was attached from the copper tape to the top surface (metallized) of the piezoelectric PVDF film using conductive silver paint.

5. A bias voltage from an electrometer (Keithley Instruments, model 617, Cleveland, OH 44139) was connected across the film.

6. The input probes of the electrometer were connected across the film. To ground this configuration, the ground leads from both the bias voltage, and the input probes were connected together.

7. To observe any pyroelectric effects, a heat source was brought close to the surface of the film, and any voltage detected by the electrometer was recorded. An IEEE-488 bus was used to transmit the data to a personal computer (Zenith Data Systems, model Z-248, St Joseph, MI 49085) where it was stored on floppy disks. A BASIC computer program, listed in Appendix E was used to process this data.

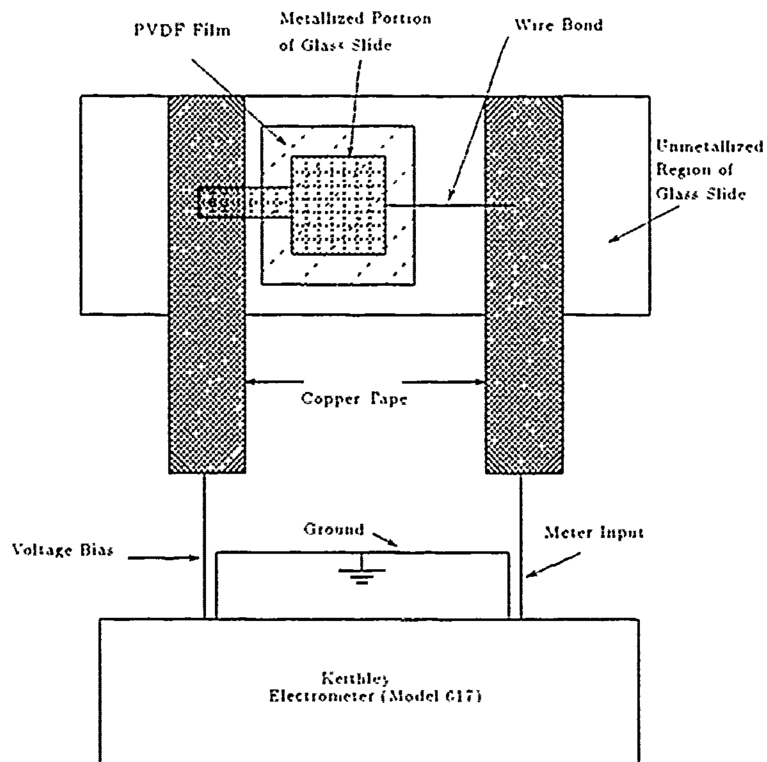

Figure D.1. Bulk Piezoelectric PVDF Film Characterization Scheme Using A Glass Microscope Slide Substrate.

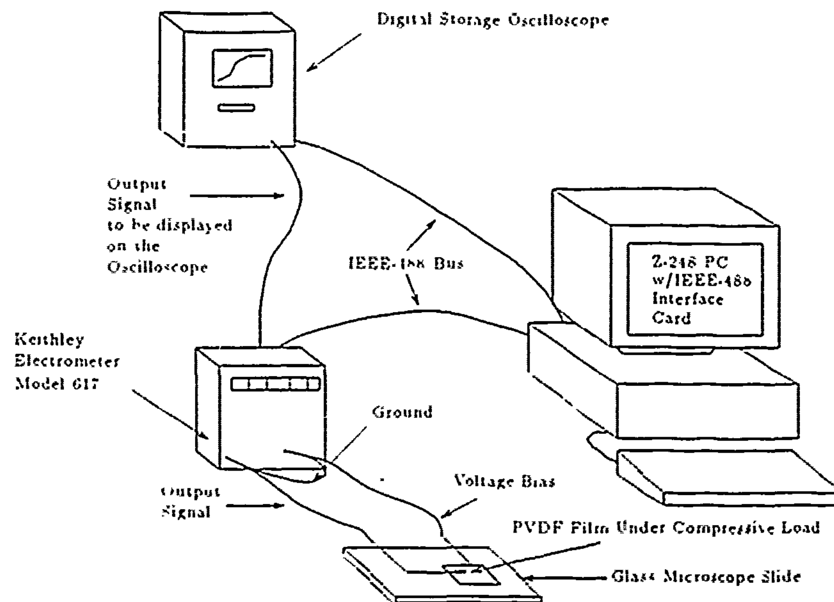

Figure D.2. Piezoelectric PVDF Film Characterization Instrumentation Configuration.

8. A fixed load was then applied to the film, and personal computer. The test configuration is illustrated in Figure D.2. Also, pyroelectric effects was evaluated by placing a heat source close to the piezoelectric PVDF film while it was under a loaded condition. An IEEE-488 bus was used to transmit the data to the Zenith Z-248 personal computer where it was stored on a floppy disk. A BASIC computer program, provided in Appendix E was used to process this data.

a. If the response signal was positive, then the top surface of the film was marked to indicate that the metal on that surface was to be removed with a wet chemical etchant (ferric chloride).

b. If the response signal detected was negative, the film's orientation was reversed, and the load was reapplied. The electrometer should then detect a positive response signal. The newly oriented film's surface was marked for the subsequent etch process as described in the next step.

9. The proper side of a large sheet of the piezoelectric PVDF film was etched with ferric chloride, rinsed in deionized water, and dried with nitrogen. Then, 6

mm by 6 mm pieces were cut from the sheet and stored for preparation of the tactile sensor fabrication step.

Appendix E. *BASIC Data Acquisition Programs*

The following BASIC programs were utilized to retrieve the data from the test equipment.

Keithley Model 617 Electrometer Data Acquisition Program

Reed Switch Impedance Measurements

```
'
'*******************************************************************
'
' ELECTROR.TXT
'
' Configures and runs the Keithley Electro. eter Model 617 in remote
' control using Qu'ckBASIC.  This particular program is designed to
' retrieve data f . . the reed switch impedance evaluation.
'
CLS
LOCATE 1, 1
PRINT "The Acquisition Program For Reed Switches Is Running....."
' Establish communications with device driver
OPEN "$DV488" FOR OUTPUT AS #1    'directives sent
PRINT #1, "BUFFERCLEAR"
OPEN "$DV488" FOR INPUT AS #2    'input from the devices
ON ERROR GOTO 1540
' Initialize MBC-488 board using "SYSCON" command
LOCATE 3, 1
PRINT "Initiallizing GP-IB Card..."
PRINT #1, "SYSCON MAD1=3 CIC1=1 BA1=&H300"
DEV2% = 27
' Set TIMEOUT (timeout time=0.056 x A%)
550  PRINT #1, "REMOTE 27"
LOCATE 5, 1
INPUT "Filename for the data: ", DFILES$
OPEN DFILES$ FOR OUTPUT AS #3
LOCATE 7, 1
INPUT "To configure the Electrometer, hit return", NULL$
     CMD$ = "F1X"
     PRINT #1, "OUTPUT ", DEV2%, " $ +", CMD$
     CMD$ = "COXZO"
     PRINT #1, "OUTPUT ", DEV2%, " $ +", CMD$
     CMD$ = "V70X"
     PRINT #1, "OUTPUT ", DEV2%, " $ +", CMD$
     CMD$ = "Q6X"
     PRINT #1, "OUTPUT ", DEV2%, " $ +", CMD$
     CMD$ = "G1X"
```

```
     PRINT #1, "OUTPUT ", DEV2%, " $ +", CMD$
CLS
LOCATE 2, 1
PRINT "Configured and ready to go....."
LOCATE 4, 1
PRINT "Use the TRIG button to retreive and store the data"
LOCATE 6, 1
INPUT "When ready, hit return to retrieve data ", NULL$
PRINT #1, "OUTPUT ", DEV2%, " $ + OOX"
PRINT #1, "OUTPUT ", DEV2%, " $ + Q7X"
VRD$ = SPACE$(12)
LOCATE 6, 1
PRINT "Retrieving data....."
T = 0
630     PRINT #1, "OUTPUT ", DEV2%, " $ + B1X"
PRINT #1, "ENTER 27 $ +"
INPUT #2, VRD$
T = T + 1
VRD = VAL(VRD$)
PRINT #3, T, VRD
PRINT T, VRD
IF T <= 63 THEN 630
PRINT #1, "LOCAL 27"
CLOSE
STOP
1540 IF (ERR <> 68) AND (ERR <> 57) THEN
 PRINT "BASIC ERROR # "; ERR; " in line "; ERL:
STOP
INPUT #2, E$
PRINT E$
INPUT #2, E$
PRINT E$
END
```

```
'
'*********************************************************************
'
' ELECTROM.TXT
'
' Configures and runs the Keithley Electrometer Model 617 in remote
' control using QuickBASIC.  This particular program is designed to
' retrieve the data from the PVDF film's characterization evaluation.
'
CLS
LOCATE 1, 1
PRINT "The PVDF Film Data Acquisition Program Is Running....."
' Establish communications with device driver
OPEN "$DV488" FOR OUTPUT AS #1    'directives sent
PRINT #1, "BUFFERCLEAR"
OPEN "$DV488" FOR INPUT AS #2     'input from the devices
ON ERROR GOTO 1540
' Initialize MBC-488 board using "SYSCON" command
LOCATE 3, 1
PRINT "Initiallizing GP-IB Card..."
PRINT #1, "SYSCON MAD1=3 CIC1=1 BA1=&H300"
DEV2% = 27
550  PRINT #1, "REMOTE 27"
LOCATE 5, 1
INPUT "Filename for the data: ", DFILES$
OPEN DFILES$ FOR OUTPUT AS #3
LOCATE 7, 1
INPUT "To configure the Electrometer, hit return", NULL$
     CMD$ = "C1XZ1XC0X"
     PRINT #1, "OUTPUT ", DEV2%, " $ +", CMD$
     CMD$ = "V2X"
     PRINT #1, "OUTPUT ", DEV2%, " $ +", CMD$
     CMD$ = "F0X"
     PRINT #1, "OUTPUT ", DEV2%, " $ +", CMD$
     CMD$ = "R0X"
     PRINT #1, "OUTPUT ", DEV2%, " $ +", CMD$
     CMD$ = "Q7X"
     CMD$ = "G1X"
     PRINT #1, "OUTPUT ", DEV2%, " $ +", CMD$
     CLS
LOCATE 1, 1
PRINT "Configured and ready to go!"
LOCATE 3, 1
INPUT "When ready, hit return to begin the test ", NULL$
LOCATE 3, 1
PRINT "Running....."
TI = TIMER
VRD$ = SPACE$(12)
500   CMD$ = "B0X"
```

```
        PRINT #1, "OUTPUT "; DEV2%, " $ +", CMD$
        PRINT #1, "ENTER ", DEV2%, " $ +"
        INPUT #2, VRD$
        VRD = VAL(VRD$)
        T = TIMER - TI
        PRINT T, VRD
        PRINT #3, T, VRD
        IF T < 60 THEN 500
PRINT #1, "OUTPUT ", DEV2%, " $ + OOX"
PRINT #1, "LOCAL ", DEV2%
CLOSE
STOP
1540 IF (ERR <> 68) AND (ERR <> 57) THEN
     PRINT "BASIC ERROR # "; ERR; " in line "; ERL: STOP
INPUT #2, E$
PRINT E$
INPUT #2, E$
PRINT E$
END
```

```
'
'******************************************************************
'
' ELECAMP.TXT
'
' Configures and runs the Keithley Electrometer Model 617 in remote
' control using QuickBASIC.  This particular program is designed to
' retrieve the amplifier characteristic curve data of the tactile
' sensor integrated circuit.
'
CLS
LOCATE 1, 1
PRINT "The Amplifier Data Acquisition Program Is Running....."
' Establish communications with device driver
OPEN "$DV488" FOR OUTPUT AS #1     'directives sent to
PRINT #1, "BUFFERCLEAR"
OPEN "$DV488" FOR INPUT AS #2      'input from the devices
ON ERROR GOTO 1540
' Initialize MBC-488 board using "SYSCON" command
LOCATE 3, 1
PRINT "Initiallizing GP-IB Card..."
PRINT #1, "SYSCON MAD1=3 CIC1=1 BA1=&H300"
DEV2% = 27
550  PRINT #1, "REMOTE 27"
LOCATE 5, 1
INPUT "Filename for the data: ", DFILES$
OPEN DFILES$ FOR OUTPUT AS #3
LOCATE 7, 1
INPUT "To configure the Electrometer, hit return", NULL$
     CMD$ = "C1XZ1XCOX"
     PRINT #1, "OUTPUT ", DEV2%, " $ +", CMD$
     CMD$ = "V2X"
     PRINT #1, "OUTPUT ", DEV2%, " $ +", CMD$
     CMD$ = "ROX"
     PRINT #1, "OUTPUT ", DEV2%, " $ +", CMD$
     CMD$ = "Q7X"
     CMD$ = "G1X"
     PRINT #1, "OUTPUT ", DEV2%, " $ +", CMD$
     CLS
LOCATE 1, 1
PRINT "Configured and ready to go!"
LOCATE 3, 1
VRD$ = SPACE$(12)
LOCATE 3, 1
PRINT "Running....."
FOR VIN = 0 TO 20.5 STEP .5
VIN$ = "V" + RIGHT$(STR$(VIN), LEN(STR$(VIN)) - 1)
CMD$ = VIN$ + "X"
PRINT #1, "OUTPUT ", DEV2%, " $ +", CMD$
```

```
CMD$ = "O1X"
PRINT #1, "OUTPUT ", DEV2%, " $ +", CMD$
VS$ = SPACE$(12)
FOR Q = 1 TO 400: NEXT Q
PRINT #1, "OUTPUT ", DEV2%, " $ + B4X"
        FOR Q = 1 TO 800: NEXT Q
PRINT #1, "ENTER ", DEV2%, " $ +"
INPUT #2, VS$
VS = VAL(VS$)
CMD$ = "BOX"
PRINT #1, "OUTPUT ", DEV2%, " $ +", CMD$
VOUT$ = SPACE$(12)
FOR Q = 1 TO 800: NEXT Q
PRINT #1, "ENTER ", DEV2%, " $ +"
INPUT #2, VOUT$
VOUT = VAL(VOUT$)
PRINT #3, VS, VOUT
        PRINT VS, VOUT
NEXT VIN
PRINT #1, "OUTPUT ", DEV2%, " $ + OOX"
PRINT #1, "LOCAL ", DEV2%
CLOSE
STOP
1540 IF (ERR <> 68) AND (ERR <> 57) THEN
PRINT "BASIC ERROR # "; ERR; " in line "; ERL: STOP
INPUT #2, E$
PRINT E$; D
INPUT #2, E$
PRINT E$
END
```

LeCroy Model 9400A Digital Storage Oscilloscope Data Acquisition Program

Single Trace Data Acquisition

```
'
'*******************************************************************
'
' LECROY.TXT
'
' Configures and runs the LeCroy Model 9400A Oscilloscope in remote
' control using QuickBASIC.  This program is designed to retrieve a
' single oscilloscope trace when the time per division is less than
' .5 seconds per division.  This program was used during the
' multiplexer, bias circuit, and system integration tests.
'
CLS
LOCATE 1, 1
PRINT "The LeCroy Data Acquisition Program Is Running....."
DIM TIME(1024), V(1024), P(1024), Y$(50)
TRUE = 1: FALSE = 0
OPEN "$DV488" FOR OUTPUT AS #1
PRINT #1, "BUFFERCLEAR"
OPEN "$DV488" FOR INPUT AS #2
ON ERROR GOTO 1210
PRINT #1, "SYSCON MAD1=3 CIC1=1 BA1=&H300"
DEV1% = 6
DEV2% = 7
' Put Scope into REMOTE mode
PRINT #1, "REMOTE ", DEV1%
' Set up 'scope configuration
PRINT "Hit return when ready to begin the test", NULL$
PRINT "Configuring O'scope.....                    "
PRINT #1, "OUTPUT 6 $ + REC 8"
PRINT #1, "OUTPUT 6 $ + TRC1 ON;C1VD .2"
PRINT #1, "OUTPUT 6 $ + C1OF 0.0;C1AT 1;C1CP D1M;"
PRINT #1, "OUTPUT 6 $ + TRC2 OFF"
PRINT #1, "OUTPUT 6 $ + TRP PO;TRL .8"
PRINT #1, "OUTPUT 6 $ + TD .2mS;TRD 0.0"
PRINT #1, "OUTPUT 6 $ + STO C1,MC"
' Set up 'scope interface options
PRINT #1, "OUTPUT 6 $ + CHLP PPO"
PRINT #1, "OUTPUT 6 $ + CTRL OFF"
PRINT #1, "OUTPUT 6 $ + CPRM "; CHR$(34); "%"; CHR$(34)
'  Use ASCII data transfer with <CRLF> between each datum
PRINT #1, "OUTPUT 6 $ + CFMT,L,BYTE,UNSIGNED_SHORT,CRLF"
' Request data be sent
LOCATE 5, 1
INPUT "Type the name of the data file: " DATAF$
OPEN DATAF$ FOR OUTPUT AS #3
CYCLE = TRUE: CYCLE2 = TRUE
i = 0: i1 = 0
```

```
i2 = 0: J = 0
LOCATE 7, 1
PRINT "Reading O'scope's settings and waveform....."
PRINT #1, "OUTPUT 6 $ + READ C1.DE"
CYCLE = TRUE
WHILE CYCLE
loop1:
   PRINT #1, "ENTER 6 $ +"
   PRINT #2, Y$
   IF J = 2 THEN x$ = Y$
   IF J = 11 THEN s$ = Y$
   J = J + 1
   IF (Y$ = "%") THEN GOTO loop1
   IF (INSTR(Y$, "#L") <> 0) THEN
      PRINT #1, "ENTER 6 $ +"
      INPUT #2, Y$
      i2 = i2 + VAL(Y$)
      GOTO loop1
   END IF
   IF (INSTR(Y$, "#I") <> 0) THEN
      CYCLE = FALSE
   END IF
WEND
LOCATE 9, 1
PRINT "Number of O'scope setup data points:"; i2
PRINT "Time base code = "; s$, "Voltage base code = "; x$
'Determine the voltage/div and time/div scales
x = VAL(x$)
IF x = 22 THEN V = .005
ELSEIF x = 23 THEN V = .01
ELSEIF x = 24 THEN V = .02
ELSEIF x = 25 THEN V = .05
ELSEIF x = 26 THEN V = .1
ELSEIF x = 27 THEN V = .2
ELSEIF x = 28 THEN V = .5
ELSEIF x = 29 THEN V = 1
ELSEIF x = 30 THEN V = 2
ELSEIF x = 31 THEN V = 5
END IF
z = VAL(s$)
IF z = 4 THEN t = 2E-09
ELSEIF z = 5 THEN t = 5E-09
ELSEIF z = 6 THEN t = 1E-08
ELSEIF z = 7 THEN t = 2E-08
ELSEIF z = 8 THEN t = 5E-08
ELSEIF z = 9 THEN t = .0000001
ELSEIF z = 10 THEN t = .0000002
ELSEIF z = 11 THEN t = .0000005
ELSEIF z = 12 THEN t = .000001
ELSEIF z = 13 THEN t = .000002
ELSEIF z = 14 THEN t = .000005
```

```
ELSEIF z = 15 THEN t = .00001
ELSEIF z = 16 THEN t = .00002
ELSEIF z = 17 THEN t = .00005
ELSEIF z = 18 THEN t = .0001
ELSEIF z = 19 THEN t = .0002
ELSEIF z = 20 THEN t = .0005
ELSEIF z = 21 THEN t = .001
ELSEIF z = 22 THEN t = .002
ELSEIF z = 23 THEN t = .005
ELSEIF z = 24 THEN t = .01
ELSEIF z = 25 THEN t = .02
ELSEIF z = 26 THEN t = .05
ELSEIF z = 27 THEN t = .1
ELSEIF z = 28 THEN t = .2
ELSEIF z = 29 THEN t = .5
ELSEIF z = 30 THEN t = 1
ELSEIF z = 31 THEN t = 2
ELSEIF z = 32 THEN t = 5
ELSEIF z = 33 THEN t = 10
ELSEIF z = 34 THEN t = 20
ELSEIF z = 35 THEN t = 50
ELSEIF z = 36 THEN t = 100
END IF
PRINT "The LeCroy is set on "; t; "seconds/div and
                              "; V; "volts/div"
PRINT #1, "OUTPUT 6 $ + READ MC.DA,50,500"
WHILE CYCLE2
loop2:
      PRINT #1, "ENTER 6 $ +"
      INPUT #2, Y$
      IF (Y$ = "%") THEN GOTO loop2
      IF (INSTR(Y$, "#L") <> 0) THEN
 PRINT #1, "ENTER 6 $ +"
 INPUT #2, Y$
 i1 = i1 + VAL(Y$)
 GOTO loop2
      END IF
      IF (INSTR(Y$, "#I") <> 0) THEN
 CYCLE2 = FALSE
      ELSE
 Q = (VAL(Y$) - 128) * V / 32
 IF (ABS(Q) < .001) THEN Q = 0
 TIME = t / 50 * i - t
 PRINT #3, TIME, Q
 i = i + 1
      END IF
   WEND
   PRINT "Number of data points: "; i, i1
PRINT #1, "LOCAL 6"
STOP
```

Oscilloscope Memory Data Acquisition

```
'
'*******************************************************************
'
' LCROYMEM.TXT
'
' Configures and runs the LeCroy Model 9400A Oscilloscope in remote
' control using QuickBASIC.  This program is designed to retrieve the
' signal traces stored into the memory of the oscilloscope.  This
' program was used to record long signal traces during the tactile
' sensor taxel crosstalk evaluation.  This program was used the
' oscilloscope was configured with the time per division greater
' than .5 seconds per division.
'
CLS
LOCATE 1, 1
PRINT "The LeCroy Data Acquisition Program Is Running....."
DIM TIME(1024), v(1024), P(1024), Y$(50)
TRUE = 1: FALSE = 0
OPEN "$DV488" FOR OUTPUT AS #1
PRINT #1, "BUFFERCLEAR"
OPEN "$DV488" FOR INPUT AS #2
' Initialize MBC-488 board using "SYSCON" command
PRINT #1, "SYSCON MAD1=3 CIC1=1 BA1=&H300"
DEV1% = 6
DEV2% = 7
' Put Scope into REMOTE mode
PRINT #1, "REMOTE ", DEV1%
' Set TIMEOUT (timeout time=0.056 x A%)
A% = 100
PRINT #1, "TIMEOUT", A%
' Set up O'scope configuration
LOCATE 2, 1
PRINT "Configuring O'scope.....          "
PRINT #1, "OUTPUT 6 $ + REC 8"
PRINT #1, "OUTPUT 6 $ + TRC1 ON;C1VD .2;C1OF -3.0
PRINT #1, "OUTPUT 6 $ + C1AT 1;C1CP D1M;"
PRINT #1, "OUTPUT 6 $ + TRC2 OFF"
PRINT #1, "OUTPUT 6 $ + TRC DC;TRM NORM;TRS EXT;TRP NEG;TRL 1"
PRINT #1, "OUTPUT 6 $ + TD 5S;TRD 0.0"
' Set up O'scope interface options
PRINT #1, "OUTPUT 6 $ + CHLP PPO"
PRINT #1, "OUTPUT 6 $ + CTRL OFF"
PRINT #1, "OUTPUT 6 $ + CPRM "; CHR$(34); "%"; CHR$(34)
'  Use ASCII data transfer with <CRLF> between each datum
PRINT #1, "OUTPUT 6 $ + CFMT,L,BYTE,UNSIGNED_SHORT,CRLF"
   OPEN "setup.dat" FOR OUTPUT AS #5
   CYCLE = TRUE: CYCLE2 = TRUE: CYCLE3 = TRUE
   i = 0: i1 = 0
   i2 = 0: J = 0
```

```
LOCATE 3, 1
PRINT "Reading O'scope's settings from Memory C....."
PRINT #1, "OUTPUT 6 $ + READ MC.DE"
CYCLE = TRUE
WHILE CYCLE
loop1:
   PRINT #1, "ENTER 6 $ +"
   INPUT #2, Y$
   PRINT #5, Y$
   IF J = 2 THEN x$ = Y$
   IF J = 11 THEN s$ = Y$
   J = J + 1
   IF (Y$ = "%") THEN GOTO loop1
   IF (INSTR(Y$, "#L") <> 0) THEN
      PRINT #1, "ENTER 6 $ +"
      INPUT #2, Y$
      PRINT #5, Y$
      i2 = i2 + VAL(Y$)
      GOTO loop1
   END IF
   IF (INSTR(Y$, "#I") <> 0) THEN
      CYCLE = FALSE
   END IF
WEND
LOCATE 4, 1
PRINT "Number of O'scope setup data points:"; i2
LOCATE 6, 1
PRINT "Time base code = "; s$, "Voltage base code = "; x$
'Determine the voltage/div and time/div scales
 x = VAL(x$)
 IF x = 22 THEN
v = .005
 ELSEIF x = 23 THEN v = .01
 ELSEIF x = 24 THEN v = .02
 ELSEIF x = 25 THEN v = .05
 ELSEIF x = 26 THEN v = .1
 ELSEIF x = 27 THEN v = .2
 ELSEIF x = 28 THEN v = .5
 ELSEIF x = 29 THEN v = 1
 ELSEIF x = 30 THEN v = 2
 ELSEIF x = 31 THEN v = 5
 END IF
 z = VAL(s$)
 IF z = 4 THEN
t = 2E-09
 ELSEIF z = 5 THEN t = 5E-09
 ELSEIF z = 6 THEN t = 1E-08
 ELSEIF z = 7 THEN t = 2E-08
 ELSEIF z = 8 THEN t = 5E-08
 ELSEIF z = 9 THEN t = .0000001
 ELSEIF z = 10 THEN t = .0000002
```

```
ELSEIF z = 11 THEN t = .0000005
ELSEIF z = 12 THEN t = .000001
ELSEIF z = 13 THEN t = .000002
ELSEIF z = 14 THEN t = .000005
ELSEIF z = 15 THEN t = .00001
ELSEIF z = 16 THEN t = .00002
ELSEIF z = 17 THEN t = .00005
ELSEIF z = 18 THEN t = .0001
ELSEIF z = 19 THEN t = .0002
ELSEIF z = 20 THEN t = .0005
ELSEIF z = 21 THEN t = .001
ELSEIF z = 22 THEN t = .002
ELSEIF z = 23 THEN t = .005
ELSEIF z = 24 THEN t = .01
ELSEIF z = 25 THEN t = .02
ELSEIF z = 26 THEN t = .05
ELSEIF z = 27 THEN t = .1
ELSEIF z = 28 THEN t = .2
ELSEIF z = 29 THEN t = .5
ELSEIF z = 30 THEN t = 1
ELSEIF z = 31 THEN t = 2
ELSEIF z = 32 THEN t = 5
ELSEIF z = 33 THEN t = 10
ELSEIF z = 34 THEN t = 20
ELSEIF z = 35 THEN t = 50
ELSEIF z = 36 THEN t = 100
END IF
PRINT "Memory C is set on "; t; "seconds/div and
  "; v; "volts/div"
LOCATE 9, 1
INPUT "Type the name of the data file for Memory C: ", DATAF$
OPEN DATAF$ FOR OUTPUT AS #3          'stores converted data to #3
LOCATE 10, 1
PRINT "Getting data from Memory C....."
PRINT #1, "OUTPUT 6 $ + READ MC.DA,50,500"
WHILE CYCLE2
loop2:
      PRINT #1, "ENTER 6 $ +"
      INPUT #2, Y$
      IF (Y$ = "%") THEN GOTO loop2
      IF (INSTR(Y$, "#L") <> 0) THEN
PRINT #1, "ENTER 6 $ +"
INPUT #2, Y$
i1 = i1 + VAL(Y$)
GOTO loop2
      END IF
      IF (INSTR(Y$, "#I") <> 0) THEN
CYCLE2 = FALSE
ELSE
Q = (VAL(Y$) - 128) * (v / 32) * 10 + 10 * 3 * v
IF (ABS(Q) < .001) THEN Q = 0
```

```
 TIME = t / 50 * i' - t / 2
 PRINT #3, TIME, Q
 i = i + 1
      END IF
   WEND
   PRINT "Number of data points: "; i, i1
LOCATE 13, 1
PRINT "Reading O'scope's settings from Memory D....."
PRINT #1, "OUTPUT 6 $ + READ MD.DE"
CYCLE7 = TRUE: M = 0: i7 = 0
WHILE CYCLE7
loop7:
   PRINT #1, "ENTER 6 $ +"
   INPUT #2, Y$
   PRINT #5, Y$
   IF M = 1 THEN h$ = Y$
   IF M = 11 THEN k$ = Y$
   M = M + 1
   IF (Y$ = "%") THEN GOTO loop7
   IF (INSTR(Y$, "#L") <> 0) THEN
      PRINT #1, "ENTER 6 $ +"
      INPUT #2, Y$
      PRINT #5, Y$
      i7 = i7 + VAL(Y$)
      GOTO loop7
   END IF
   IF (INSTR(Y$, "#I") <> 0) THEN
      CYCLE7 = FALSE
   END IF
WEND
LOCATE 14, 1
PRINT "Number of O'scope setup data points:"; i7
LOCATE 16, 1
PRINT "Time base code = "; k$, "Voltage base code = "; h$
'Determine the voltage/div and time/div scales
 h = VAL(h$)
 IF h = 22 THEN
c = .005
 ELSEIF h = 23 THEN c = .01
 ELSEIF h = 24 THEN c = .02
 ELSEIF h = 25 THEN c = .05
 ELSEIF h = 26 THEN c = .1
 ELSEIF h = 27 THEN c = .2
 ELSEIF h = 28 THEN c = .5
 ELSEIF h = 29 THEN c = 1
 ELSEIF h = 30 THEN c = 2
 ELSEIF h = 31 THEN c = 5
 END IF
 k = VAL(k$)
 IF k = 4 THEN
u = 2E-09
```

```
 ELSEIF k = 5 THEN u = 5E-09
 ELSEIF k = 6 THEN u = 1E-08
 ELSEIF k = 7 THEN u = 2E-08
 ELSEIF k = 8 THEN u = 5E-08
 ELSEIF k = 9 THEN u = .0000001
 ELSEIF k = 10 THEN u = .0000002
 ELSEIF k = 11 THEN u = .0000005
 ELSEIF k = 12 THEN u = .000001
 ELSEIF k = 13 THEN u = .000002
 ELSEIF k = 14 THEN u = .000005
 ELSEIF k = 15 THEN u = .00001
 ELSEIF k = 16 THEN u = .00002
 ELSEIF k = 17 THEN u = .00005
 ELSEIF k = 18 THEN u = .0001
 ELSEIF k = 19 THEN u = .0002
 ELSEIF k = 20 THEN u = .0005
 ELSEIF k = 21 THEN u = .001
 ELSEIF k = 22 THEN u = .002
 ELSEIF k = 23 THEN u = .005
 ELSEIF k = 24 THEN u = .01
 ELSEIF k = 25 THEN u = .02
 ELSEIF k = 26 THEN u = .05
 ELSEIF k = 27 THEN u = .1
 ELSEIF k = 28 THEN u = .2
 ELSEIF k = 29 THEN u = .5
 ELSEIF k = 30 THEN u = 1
 ELSEIF k = 31 THEN u = 2
 ELSEIF k = 32 THEN u = 5
 ELSEIF k = 33 THEN u = 10
 ELSEIF k = 34 THEN u = 20
 ELSEIF k = 35 THEN u = 50
 ELSEIF k = 36 THEN u = 100
 END IF
 PRINT "Memory D is set on "; u; "seconds/div and
   "; c; "volts/div"
LOCATE 19, 1
INPUT "What is the filename of Memory D: ", D$
OPEN D$ FOR OUTPUT AS #6
LOCATE 20, 1
PRINT "Getting data from Memory D....."
i = 0
i1 = 0
PRINT #1, "OUTPUT 6 $ + READ MD.DA,50,500"
WHILE CYCLE3
loop3:
      PRINT #1, "ENTER 6 $ +"
      INPUT #2, Y$
      IF (Y$ = "%") THEN GOTO loop2
      IF (INSTR(Y$, "#L") <> 0) THEN
 PRINT #1, "ENTER 6 $ +"
 INPUT #2, Y$
```

```
 i1 = i1 + VAL(Y$)
 GOTO loop3
      END IF
      IF (INSTR(Y$, "#I") <> 0) THEN
 CYCLE3 = FALSE
      ELSE
 Q = (VAL(Y$) - 128) * (v / 32) * 10 + 30 * v
 IF (ABS(Q) < .001) THEN Q = 0
 TIME = t / 50 * i' - t / 2
 PRINT #6, TIME, Q
 i = i + 1
      END IF
   WEND
   PRINT "Number of data points: "; i, i1
PRINT #1, "LOCAL 6"
STOP
```

```
'
'*******************************************************************
'
' SHAPE.TXT
'
' Configures and runs the LeCroy Model 9400A Oscilloscope in remote
' control in QuickBASIC.  This program is designed to retrieve
' preload, load, and post load measurements from the oscilloscope.
' Then, the program computes the voltage per taxel information, and,
' finally, it computes the shape information, displaying the 8 x 8
' array on the screen.  This program was used during the tactile
' sensor array evaluation.
'
CLS
LOCATE 1, 1
PRINT "The LeCroy Data Acquisition Program Is Running....."
DIM time(1024), V(1024), P(1024), Y$(50)
TRUE = 1: FALSE = 0
OPEN "$DV488" FOR OUTPUT AS #1
PRINT #1, "BUFFERCLEAR"
OPEN "$DV488" FOR INPUT AS #2
' Initialize MBC-488 board using "SYSCON" command
PRINT #1, "SYSCON MAD1=3 CIC1=1 BA1=&H300"
DEV1% = 6
DEV2% = 7
' Put Scope into REMOTE mode
PRINT #1, "REMOTE ", DEV1%
' Set TIMEOUT (timeout time=0.056 x A%)
A% = 100
PRINT #1, "TIMEOUT", A%
' Set up 'scope configuration
LOCATE 2, 1
PRINT "Configuring O'scope.....               "
PRINT #1, "OUTPUT 6 $ + REC 8"
PRINT #1, "OUTPUT 6 $ + TRC1 ON;C1VD .2;C1OF -3.0;C1AT 1;C1CP D1M;"
PRINT #1, "OUTPUT 6 $ + TRC2 OFF"
PRINT #1, "OUTPUT 6 $ + TRC DC;TRM NORM;TRS EXT;TRP NEG;TRL 1"
PRINT #1, "OUTPUT 6 $ + TD 5MS;TRD 0.0"
' PRINT #1, "OUTPUT 6 $ + STO C1,MC"
' Set up 'scope interface options
PRINT #1, "OUTPUT 6 $ + CHLP PPO"
PRINT #1, "OUTPUT 6 $ + CTRL OFF"
PRINT #1, "OUTPUT 6 $ + CPRM "; CHR$(34); "%"; CHR$(34)
'  Use ASCII data transfer with <CRLF> between each datum
PRINT #1, "OUTPUT 6 $ + CFMT,L,BYTE,UNSIGNED_SHORT,CRLF"
OPEN "setup" FOR OUTPUT AS #5   'stores scope's setup data in #5
CYCLE = TRUE: CYCLE2 = TRUE: CYCLE3 = TRUE: CYCLE4 = TRUE
i = 0: i1 = 0: i3 = 0: i4 = 0: i5 = 0: i6 = 0: i2 = 0: J = 0
INPUT "When ready to store the Pre-load condition into
```

```
Mem C, hit return:  ", NULL$
    PRINT #1, "OUTPUT 6 $ + STO C1,MC"
INPUT "When ready to store the Load condition into
Mem D, hit return:  ", NULL$
    PRINT #1, "OUTPUT 6 $ + STO C1,MD"
INPUT "When ready to read the Post-load condition from
the display, hit return:  ", NULL$
OPEN "ppo100o1.pos" FOR OUTPUT AS #10
OPEN "ppo100o1.raw" FOR OUTPUT AS #20
LOCATE 13, 1
PRINT "Reading Post-load condition....."
PRINT #1, "OUTPUT 6 $ + READ C1.DA,39,700"
'Read info from Channel 1
r = 1: avg = 0: taxel = 1: temp = 0
WHILE CYCLE4
loop4:
      PRINT #1, "ENTER 6 $ +"
      INPUT #2, Y$
      IF (Y$ = "%") THEN GOTO loop2
      IF (INSTR(Y$, "#L") <> 0) THEN
 PRINT #1, "ENTER 6 $ +"
 INPUT #2, Y$
 i1 = i1 + VAL(Y$)
 GOTO loop4
      END IF
      IF (INSTR(Y$, "#I") <> 0) THEN
 CYCLE4 = FALSE
      ELSE
 q = (VAL(Y$) - 128) * V / 32 * 10 + 30 * V
 IF r = 10 THEN
      avg = temp / 4
      PRINT #10, taxel, avg
      PRINT #20, avg
      temp = 0: avg = 0: r = 0
      taxel = taxel + 1
 ELSEIF r = 4 THEN
      temp = temp + q
 ELSEIF r = 5 THEN
      temp = temp + q
 ELSEIF r = 6 THEN
      temp = temp + q
 ELSEIF r = 7 THEN
      temp = temp + q
 END IF
 r = r + 1
 i = i + 1
      END IF
   WEND
   PRINT "Number of data points: "; i, i1
OPEN "ppo100p1.pos" FOR OUTPUT AS #11
OPEN "ppo100p1.raw" FOR OUTPUT AS #21
```

```
PRINT "Reading Pre-load Condition....."
PRINT #1, "OUTPUT 6 $ + READ MC.DA,39,700"
'Read info from Memory C
r = 1: avg = 0: taxel = 1: temp = 0
WHILE CYCLE2
loop2:
      PRINT #1, "ENTER 6 $ +"
      INPUT #2, Y$
      IF (Y$ = "%") THEN GOTO loop2
      IF (INSTR(Y$, "#L") <> 0) THEN
 PRINT #1, "ENTER 6 $ +"
 INPUT #2, Y$
 i3 = i3 + VAL(Y$)
 GOTO loop2
      END IF
      IF (INSTR(Y$, "#I") <> 0) THEN
 CYCLE2 = FALSE
      ELSE
 q = (VAL(Y$) - 128) * V / 32 * 10 + 30 * V
 IF (ABS(q) < .001) THEN q = 0
 IF r = 10 THEN
      avg = temp / 4
      PRINT #11, taxel, avg
      PRINT #21, avg
      temp = 0: avg = 0: r = 0
      taxel = taxel + 1
 ELSEIF r = 4 THEN
      temp = temp + q
 ELSEIF r = 5 THEN
      temp = temp + q
 ELSEIF r = 6 THEN
      temp = temp + q
 ELSEIF r = 7 THEN
      temp = temp + q
 END IF
 r = r + 1
 i4 = i4 + 1
   END IF
   WEND
   PRINT "Number of data points: "; i4, i3
OPEN "ppo10011.pos" FOR OUTPUT AS #12
OPEN "ppo10011.raw" FOR OUTPUT AS #22
PRINT "Reading Load condition....."
PRINT #1, "OUTPUT 6 $ + READ MD.DA,39,700"
r = 1: avg = 0: taxel = 1: temp = 0
WHILE CYCLE3
loop3:
      PRINT #1, "ENTER 6 $ +"
      INPUT #2, Y$
      IF (Y$ = "%") THEN GOTO loop2
      IF (INSTR(Y$, "#L") <> 0) THEN
```

```
PRINT #1, "ENTER 6 $ +"
INPUT #2, Y$
i5 = i5 + VAL(Y$)
GOTO loop3
     END IF
     IF (INSTR(Y$, "#I") <> 0) THEN
CYCLE3 = FALSE
     ELSE
q = (VAL(Y$) - 128) * V / 32 * 10 + 30 * V
IF (ABS(q) < .001) THEN q = 0
IF r = 10 THEN
     avg = temp / 4
     PRINT #12, taxel, avg
     PRINT #22, avg
     temp = 0: avg = 0: r = 0
     taxel = taxel + 1
ELSEIF r = 4 THEN
     temp = temp + q
ELSEIF r = 5 THEN
     temp = temp + q
ELSEIF r = 6 THEN
     temp = temp + q
ELSEIF r = 7 THEN
     temp = temp + q
END IF
r = r + 1
i6 = i6 + 1
     END IF
  WEND
  PRINT "Number of data points: "; i5, i6
PRINT #1, "LOCAL 6"
CLOSE #20
CLOSE #21
CLOSE #22
CLOSE #10
CLOSE #11
CLOSE #12
CLOSE #3
CLOSE #4
CLOSE #6
CLOSE #7
OPEN "ppo100p1.raw" FOR INPUT AS #51
OPEN "ppo100l1.raw" FOR INPUT AS #52
OPEN "ppo100o1.raw" FOR INPUT AS #53
OPEN "ppo100s1.pos" FOR OUTPUT AS #50
OPEN "ppo100s1.raw" FOR OUTPUT AS #49
LOCATE 20, 1
PRINT "Calculating the shape information....."
FOR TAX = 1 TO 64
INPUT #51, PRE$
INPUT #52, LOAD$
```

```
INPUT #53, POST$
P = VAL(PRE$)
L = VAL(LOAD$)
O = VAL(POST$)
SHAPE = L - (P + O) / 2
PRINT #49, SHAPE
PRINT #50, TAX, SHAPE
NEXT TAX
CLOSE #49: CLOSE #50: CLOSE #51: CLOSE #52: CLOSE #53
LOCATE 22, 1
INPUT "Threshold voltage value=", VL
1369 OPEN "ppo100s1.raw" FOR INPUT AS #60
SCREEN 2
Y1 = 41
FOR ICOL = 1 TO 8
X1 = 101
FOR IROW = 1 TO 8
INPUT #60, V
X2 = X1 + 24
Y2 = Y1 + 10
IF V >= VL THEN LINE (X1, Y1)-(X2, Y2), 4, BF
ELSE LINE (X1, Y1)-(X2, Y2), 7, B
X1 = X1 + 48
NEXT IROW
Y1 = Y1 + 20
NEXT ICOL
INPUT "Threshold voltage value=", VL
CLS
CLOSE #60
GOTO 1369
STOP
```

Hewlett-Packard Model 54100A Digital Storage Oscilloscope Data Acquisition Program

```
'
'*********************************************************************
'
' SCOPE.TXT
'
' Configures and runs the HP 54100A Digital Storage Oscilloscope in
' remote control.  This program is designed to retrieve the
' oscilloscope's trace using QuickBASIC.
'
CLS
LOCATE 1, 1
PRINT "The HP 54100 Acquisition Program Is Running"
' Establish communications with device driver
OPEN "$DV488" FOR OUTPUT AS #1    'HP Scope
PRINT #1, "BUFFERCLEAR"
OPEN "$DV488" FOR INPUT AS #2    'input from scope
ON ERROR GOTO 1540
' Initialize MBC-488 board using "SYSCON" command
PRINT #1, "SYSCON MAD1=3 CIC1=1 BA1=&H300"
DEV1% = 7
' Set HP Digitizing Oscilloscope into REMOTE
PRINT #1, "REMOTE", DEV1%
' Set TIMEOUT (timeout time=0.056 x A%)
450  'A% = 100
'PRINT #1, "OUTPUT ", DEV1%, " $ + TIMEOUT "; A$
LOCATE 3, 1
PRINT "Configuring the HP O'scope....."
     CMD$ = "STOP"
     PRINT #1, "OUTPUT ", DEV1%, " $ +", CMD$
     CMD$ = "RUN"
     PRINT #1, "OUTPUT ", DEV1%, " $ +", CMD$
     CMD$ = "DISPLAY BRIGHTNESS HIGH"
     PRINT #1, "OUTPUT ", DEV1%, " $ +", CMD$
     CMD$ = "DISPLAY GRAT GRID"
     PRINT #1, "OUTPUT ", DEV1%, " $ +", CMD$
     CMD$ = "CHANNEL 1"
     PRINT #1, "OUTPUT ", DEV1%, " $ +", CMD$
     CMD$ = "CHANNEL 1 SENS 5"
     PRINT #1, "OUTPUT ", DEV1%, " $ +", CMD$
     CMD$ = "CHANNEL 1 PROBE 10"
     PRINT #1, "OUTPUT ", DEV1%, " $ +", CMD$
     CMD$ = "TIMEBASE MODE TRIGGERED"
     PRINT #1, "OUTPUT ", DEV1%, " $ +", CMD$
     CMD$ = "TIMEBASE SENSITIVITY 64e-6"
     PRINT #1, "OUTPUT ", DEV1%, " $ +", CMD$
     CMD$ = "TIMEBASE DELAY 0"
     PRINT #1, "OUTPUT ", DEV1%, " $ +", CMD$
     CMD$ = "TRIGGER MODE EDGE"
```

```
     PRINT #1, "OUTPUT ", DEV1%, " $ +", CMD$
     CMD$ = "TRIGGER SOURCE CHANNEL 2"
     PRINT #1, "OUTPUT ", DEV1%, " $ +", CMD$
     CMD$ = "TRIGGER LEVEL .6"
     PRINT #1, "OUTPUT ", DEV1%, " $ +", CMD$
     CMD$ = "TRIGGER SLOPE NEGATIVE"
     PRINT #1, "OUTPUT ", DEV1%, " $ +", CMD$
LOCATE 5, 1
INPUT "Press (s) to store the data into the scope's Memory 1: ", D1$
IF D$ = "s" THEN GOTO 880 ELSE GOTO 450
880  CMD$ = "STORE CHANNEL 1, MEMORY 1"
     PRINT #1, "OUTPUT ", DEV1%, " $ +", CMD$
IF D$ = "s" THEN GOTO 880 ELSE GOTO 450
980  CMD$ = "STORE CHANNEL 1, MEMORY 3"
     PRINT #1, "OUTPUT ", DEV1%, " $ +", CMD$
LOCATE 7, 1
INPUT "Filename for data from scope's Memory 1: ", DF$
OPEN DF$ FOR OUTPUT AS #3
     CMD$ = "WAVEFORM SOURCE MEMORY 1 FORMAT ASCII"
     PRINT #1, "OUTPUT ", DEV1%, " $ +", CMD$
     R$ = SPACE$(15)
     CMD$ = "POINTS?"
     PRINT #1, "OUTPUT ", DEV1%, " $ +", CMD$
     PRINT #1, "ENTER 07 $ +"
     INPUT #2, R$
     PNTS = VAL(R$)
     LOCATE 9, 1
     PRINT "The number of points is: ", PNTS
     CMD$ = "YREF?"
     PRINT #1, "OUTPUT ", DEV1%, " $ +", CMD$
     PRINT #1, "ENTER 07 $ +"
     INPUT #2, R$
     YREF = VAL(R$)
     CMD$ = "YINC?"
     PRINT #1, "OUTPUT ", DEV1%, " $ +", CMD$
     PRINT #1, "ENTER 07 $ +"
     INPUT #2, R$
     YINC = VAL(R$)
     CMD$ = "YOR?"
     PRINT #1, "OUTPUT ", DEV1%, " $ +", CMD$
     PRINT #1, "ENTER 07 $ +"
     INPUT #2, R$
     YORG = VAL(R$)
     CMD$ = "XINC?"
     PRINT #1, "OUTPUT ", DEV1%, " $ +", CMD$
     PRINT #1, "ENTER 07 $ +"
     INPUT #2, R$
     XINC = VAL(R$)
     CMD$ = "XOR?"
     PRINT #1, "OUTPUT ", DEV1%, " $ +", CMD$
     PRINT #1, "ENTER 07 $ +"
```

```
     INPUT #2, R$
     XORG = VAL(R$)
     CMD$ = "XREF?"
     PRINT #1, "OUTPUT ", DEV1%, " $ +", CMD$
     PRINT #1, "ENTER 07 $ +"
     INPUT #2, R$
     XREF = VAL(R$)
LOCATE 12, 1
PRINT "YINC ="; YINC, "YORG ="; YORG, "YREF ="; YREF
PRINT "XINC ="; XINC, "XORG ="; XORG, "XREF ="; XREF
X$ = SPACE$(15)
Y$ = SPACE$(15)
LOCATE 16, 1
PRINT "Retrieving the data from the scope........"
CMD$ = "DATA?"
PRINT #1, "OUTPUT ", DEV1%, " $ +", CMD$
FOR I = 1 TO PNTS
PRINT #1, "ENTER 07 $ +"
INPUT #2, Y$
X = (I * XINC) + XORG
Y = ((VAL(Y$) - YREF) * YINC) + YORG
WRITE #3, X, Y
NEXT I
CLOSE #3
     CMD$ = "LOCAL"
     PRINT #1, "OUTPUT ", DEV1%, " $ +", CMD$
CLOSE
STOP
1540 IF (ERR <> 68) AND (ERR <> 57) THEN
PRINT "BASIC ERROR # "; ERR; " in line "; ERL: STOP
INPUT #2, E$
PRINT E$
INPUT #2, E$
PRINT E$
END
```

Appendix F. *Procedure for Fabricating the Tactile Sensor*

The physical size of the IC was intentionally confined to an area measuring 7.9 mm by 9.2 mm. The tactile sensor was fabricated using three different adhesives (urethane, polyimide, and *Loctite*) to couple the piezoelectric PVDF film to the surface of the IC.

The fabrication procedure for the tactile sensor follows:

1. The charge on a 6 mm by 6 mm piezoelectric PVDF film sample was neutralized by immersing it in an electrically-grounded solution composed of 200 ml of deionized water and 1 drop of HCl.

2. Nitrogen gas was used to thoroughly dry the PVDF film.

3. One drop of the adhesive dispensed from a 3 cc syringe was placed in the center of the piezoelectric PVDF film. The adhesive was then smoothed with a glass slide and the film was properly centered on the taxel array.

4. A square piece of cellophane was placed over the piezoelectric PVDF film to prevent the square microscope slide from bonding to the top surface of the PVDF film.

5. A square microscope slide was then centered over and placed on the film.

6. To ensure proper bonding of the piezoelectric PVDF film to the taxel array, the IC, PVDF film, glass microscope slide, and a spacer was sandwiched by the compressive force (F) supplied by two paper binder clips. A uniform force applied by the binder clip configuration is critical to the proper attachment of the film. Care must be taken in adjusting the binder clip configuration. The configuration is detailed in Figure F.1.

7. The entire package was then transferred to a vacuum system and exposed to a pressure of 100 microns of mercury for 30 minutes. This cure process was utilized to eliminate trapped gaseous molecules from beneath the piezoelectric PVDF film, and it caused the film to be snugly drawn against the IC's electrode structure.

8. The adhesives were cured at 65°C for one hour.

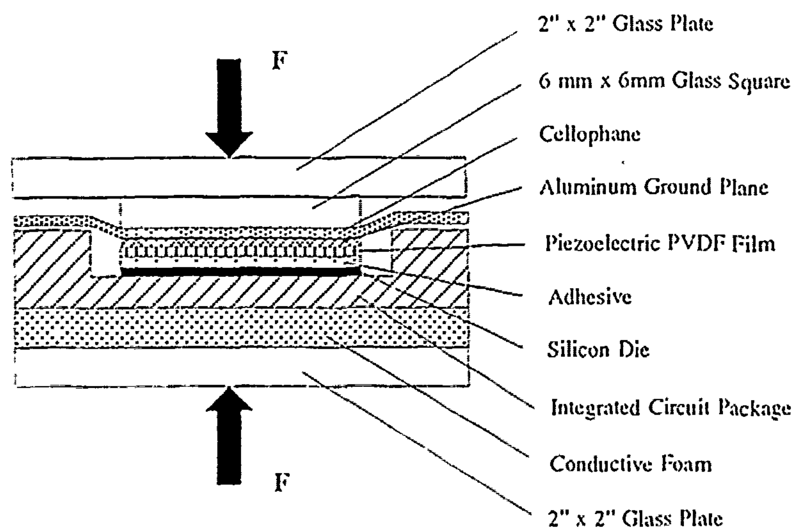

Figure F.1. Fabrication Configuration Of The Tactile Sensor.

9. The ensemble was then visually inspected under an optical microscope to discern the overall quality of the bonded piezoelectric PVDF film.

10. Should the piezoelectric PVDF film not adhere properly, the film was removed, the adhesive was removed with acetone, and the IC was placed in the plasma asher to remove residual acetone. The DC resistance between adjacent gold bond pads was remeasured using the electrometer (Keithley Instruments, model 617, Cleveland, OH 44139). If the DC resistance between adjacent gold bond pads has decreased below $\approx 10^{12}\ \Omega$, the gold bonding pads of this and subsequent ICs were coated with silicone rubber, and the DC resistance was remeasured with the electrometer.

11. When the piezoelectric PVDF film was properly bonded to the surface of the IC, a 1-mil diameter wire was connected from the top surface electrode on the piezoelectric PVDF film to the gold wire bond pad on the IC's ceramic package. Conductive silver epoxy was used to attach the wire to the polymer's top surface electrode. This connection serves to ground the top surface electrode.

Appendix G. *Adhesive Study Photographs*

The following figures document the initial and final photographs of three tactile sensors used in the adhesive evaluation study. No visible degradation of the film's adherence can be discerned; however, a visible difference between the urethane and polyimide adhesive's electrode coverage and the *Loctite* adhesive's electrode coverage is apparent.

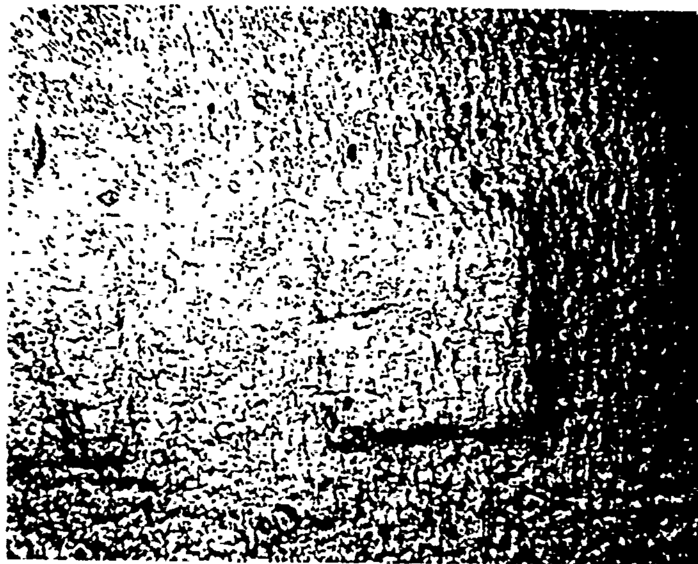

Figure G.1. Electrode Coverage With A 40 μm Thick Piezoelectric PVDF Film Attached With The Urethane Adhesive - Initial Photo (75 ×).

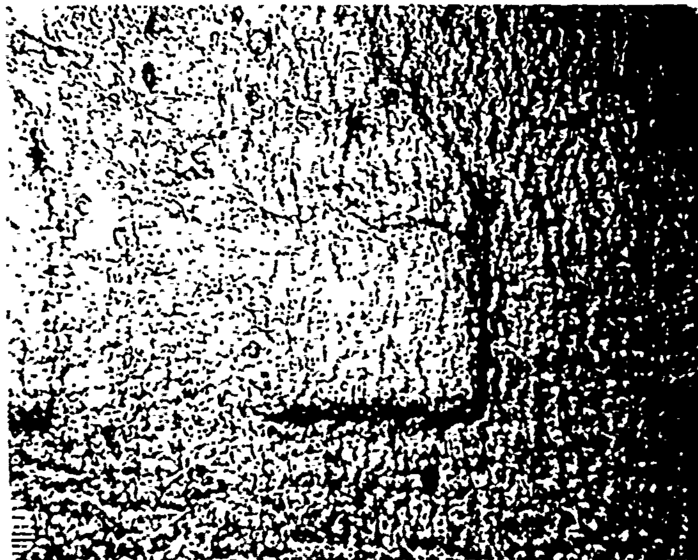

Figure G.2. Electrode Coverage With A 40 μm Thick Piezoelectric PVDF Film Attached With The Urethane Adhesive - Initial Photo (75 ×).

Figure G.3. Corner Of The 40 μm Thick Piezoelectric PVDF Film Attached With The Urethane Adhesive - Initial Photo (75 ×).

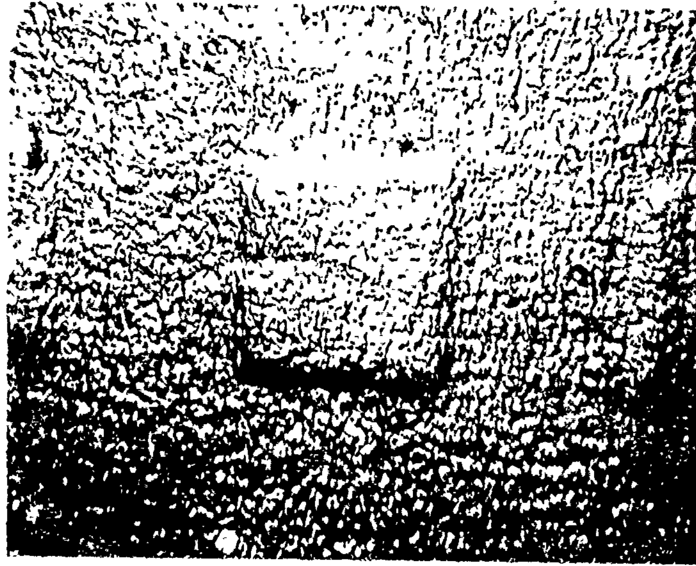

Figure G.4. Electrode Coverage With A 40 μm Thick Piezoelectric PVDF Film Attached With The Urethane Adhesive – Final Photo (75 ×).

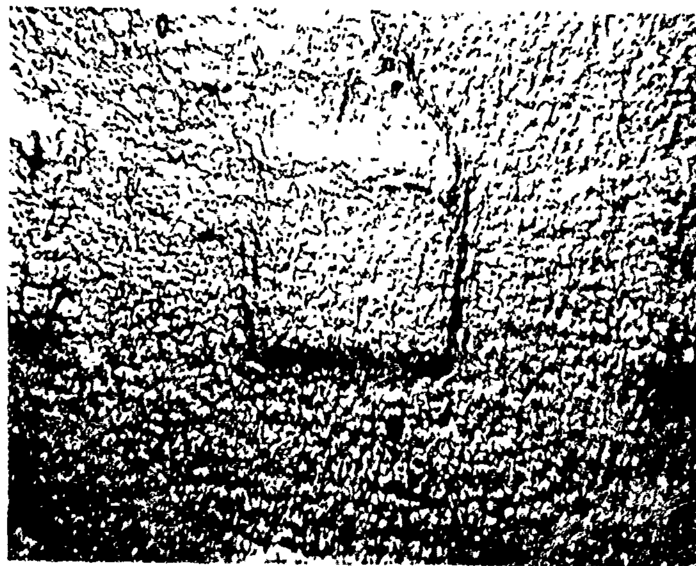

Figure G.5. Electrode Coverage With A 40 μm Thick Piezoelectric PVDF Film Attached With The Urethane Adhesive – Final Photo (75 ×).

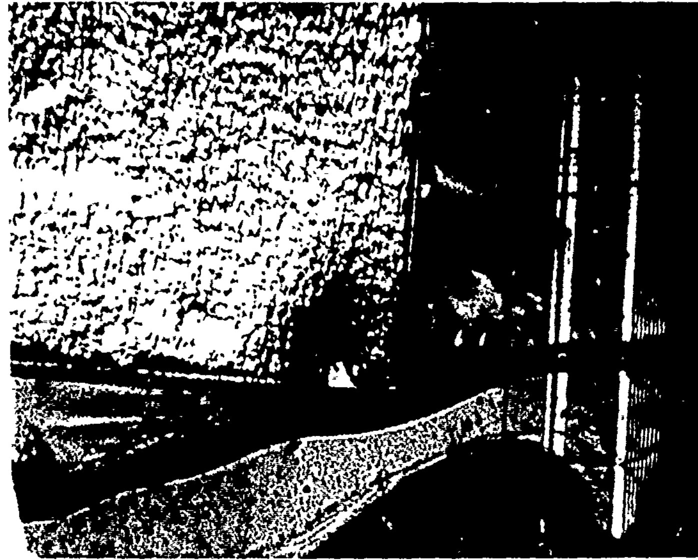

Figure G.6. Corner Of The 40 μm Thick Piezoelectric PVDF Film Attached With The Urethane Adhesive - Final Photo (75 ×).

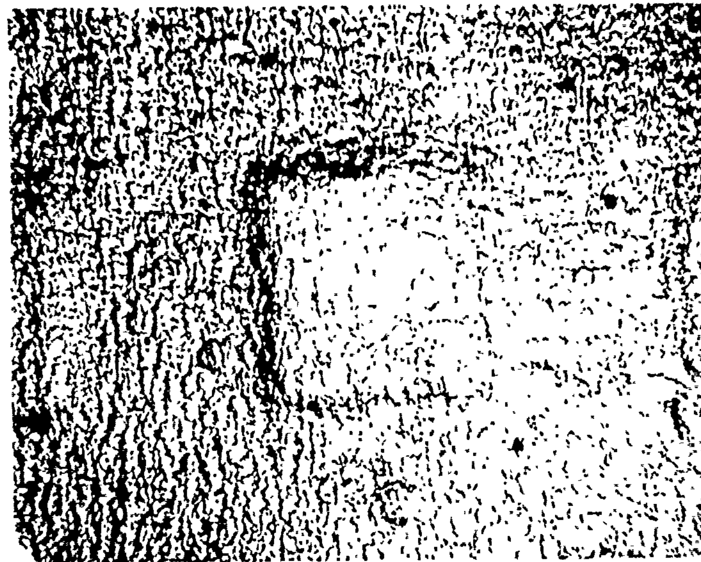

Figure G.7. Electrode Coverage With A 40 μm Thick Piezoelectric PVDF Film Attached With The Polyimide Adhesive - Initial Photo (75 ×).

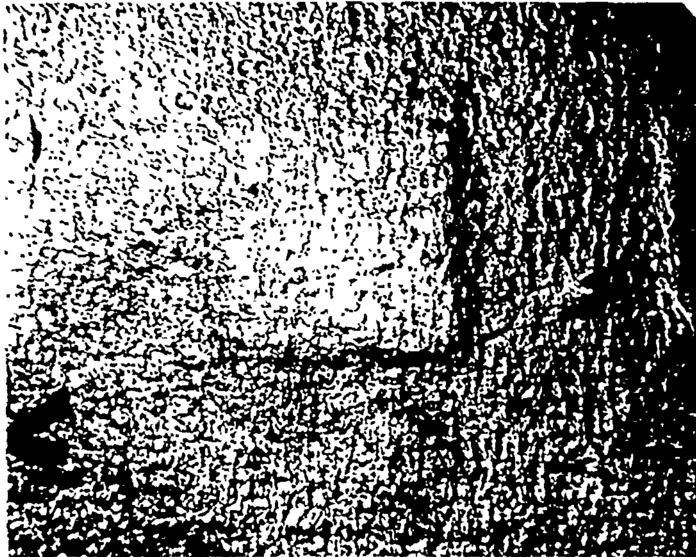

Figure G.8. Electrode Coverage With A 40 μm Thick Piezoelectric PVDF Film Attached With The Polyimide Adhesive - Initial Photo (75 ×).

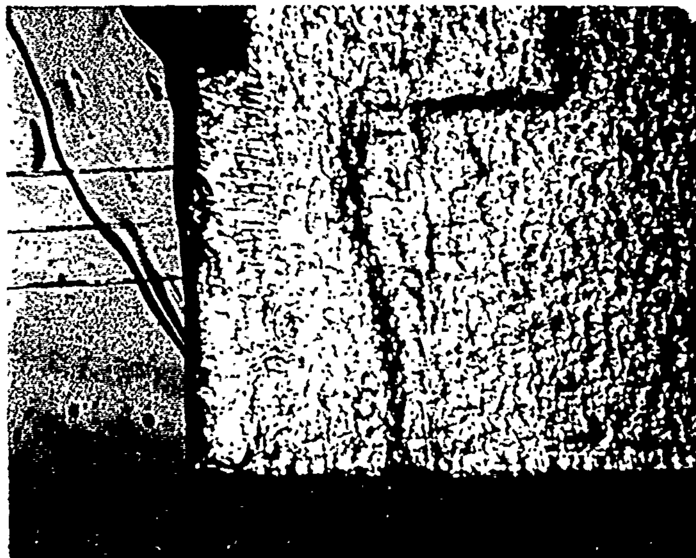

Figure G.9. Corner Of The 40 μm Thick Piezoelectric PVDF Film Attached With The Polyimide Adhesive - Initial Photo (75 ×).

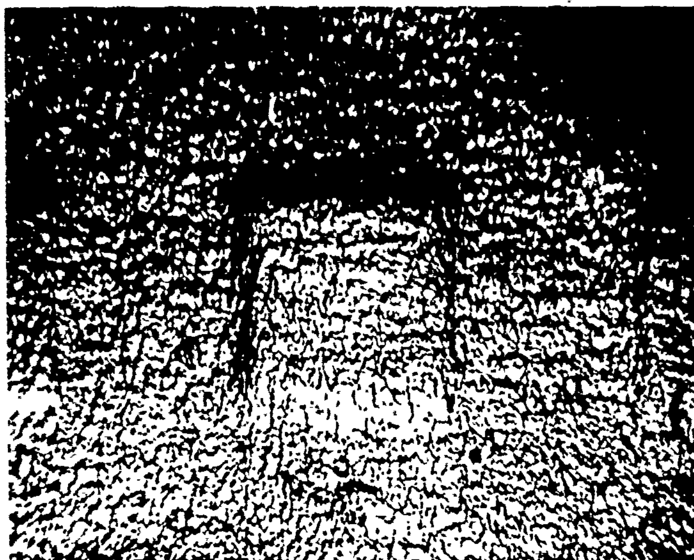

Figure G.10. Electrode Coverage With A 40 μm Thick Piezoelectric PVDF Film Attached With The Polyimide Adhesive - Final Photo (75 ×).

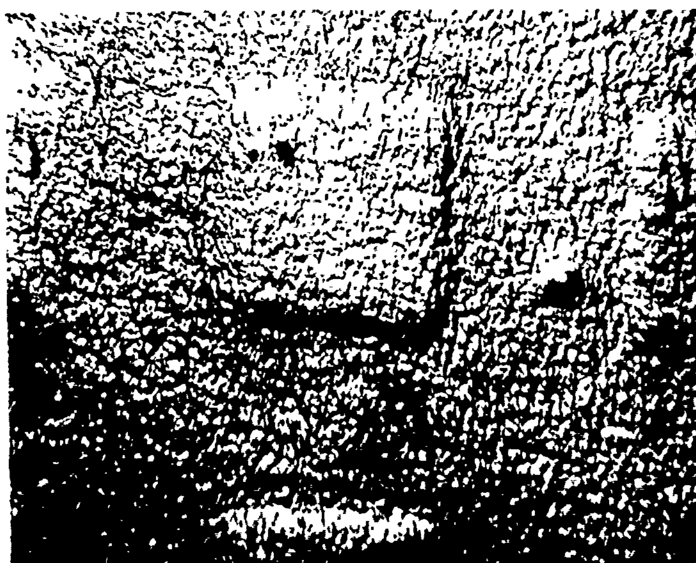

Figure G.11. Electrode Coverage With A 40 μm Thick Piezoelectric PVDF Film Attached With The Polyimide Adhesive - Final Photo (75 ×).

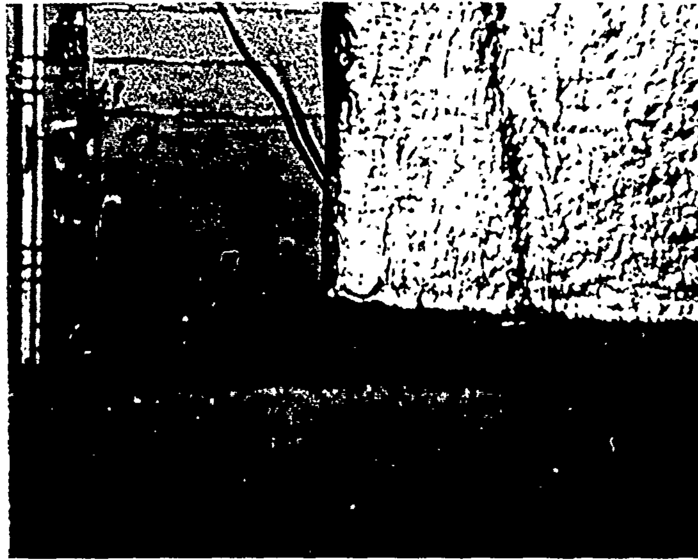

Figure G.12. Corner Of The 40 μm Thick Piezoelectric PVDF Film Attached With The Polyimide Adhesive - Final Photo (75 ×).

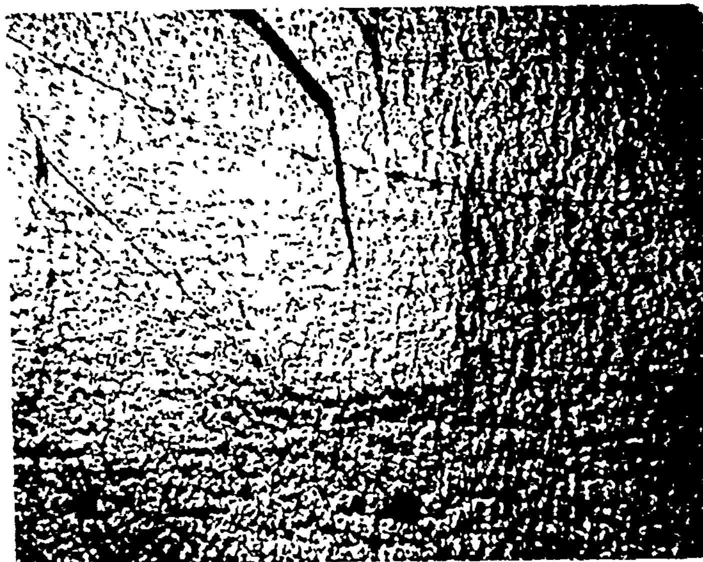

Figure G.13. Electrode Coverage With A 40 μm Thick Piezoelectric PVDF Film Attached With The *Loctite* Adhesive- Initial Photo (75 ×).

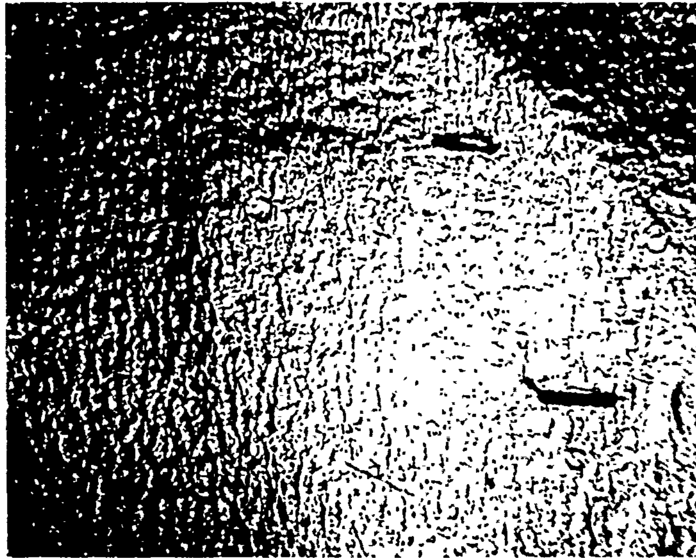

Figure G.14. Electrode Coverage With A 40 μm Thick Piezoelectric PVDF Film Attached With The *Loctite* Adhesive - Initial Photo (75 ×).

Figure G.15. Corner Of The 40 μm Thick Piezoelectric PVDF Film Attached With The *Loctite* Adhesive - Initial Photo (75 ×).

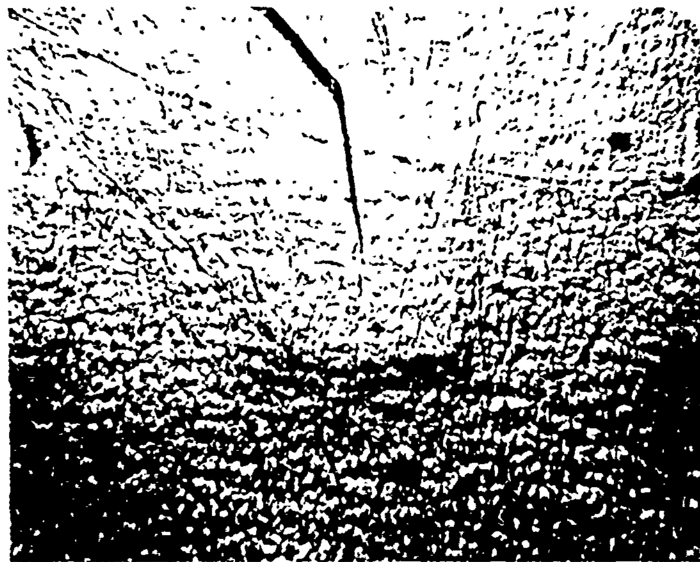

Figure G.16. Electrode Coverage With A 40 μm Thick Piezoelectric PVDF Film Attached With The *Loctite* Adhesive - Final Photo (75 ×).

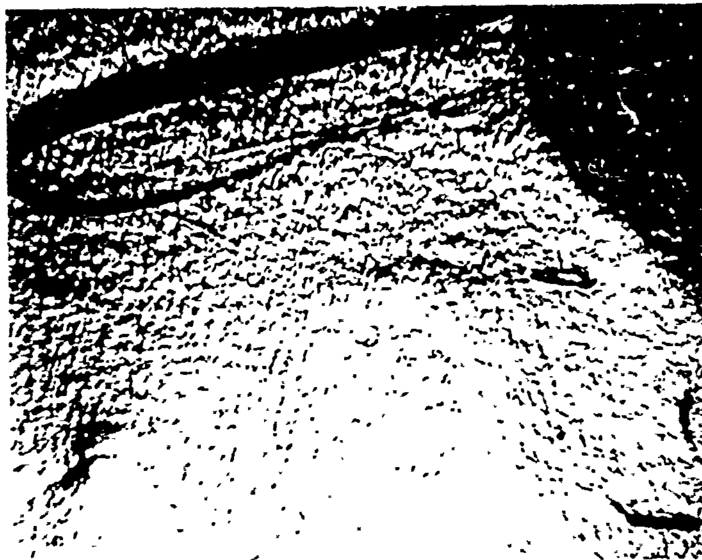

Figure G.17. Electrode Coverage With A 40 μm Thick Piezoelectric PVDF Film Attached With The *Loctite* Adhesive - Final Photo (75 ×).

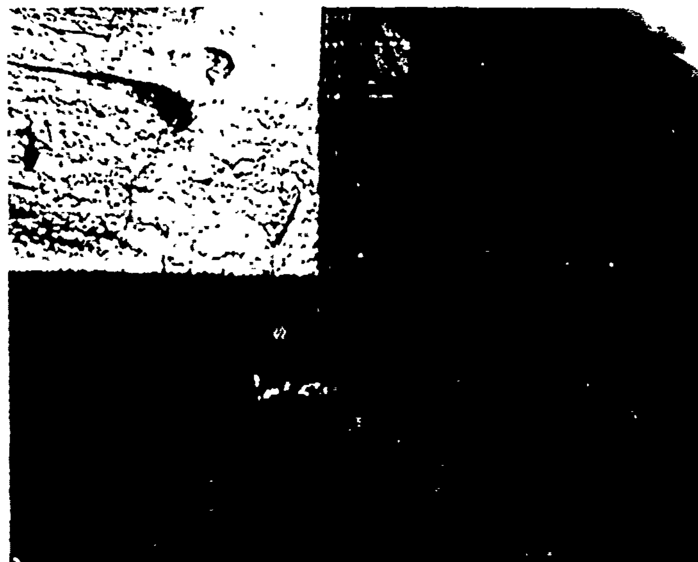

Figure G.18. Corner Of The 40 μm Thick Piezoelectric PVDF Film Attached With The *Loctite* Adhesive - Final Photo (75 ×).

Appendix H. *Tactile Sensor Evaluation Procedures*

The complete tactile sensor system was configured according to Figure H.1 and tested using the following procedures:

1. The multiplexer circuit was clocked at various frequencies spanning 500 Hz to 100 kHz, using a function generator (Hewlett-Packard, model 3314, Palo Alto, CA 94304).

2. The bias circuit was switched-on for a sufficient length of time to facilitate achieving a uniform charge state throughout the tactile sensor's electrodes.

3. The digital storage oscilloscope (either the Hewlett-Packard, model 54100, Palo Alto, CA 94304 or the LeCroy Corporation, model 9400, Chestnut Ridge, NY 10977) was used to display the output of the multiplexer. The pre-load condition was measured and recorded, and an IEEE-488 bus was used to route the data to the personal computer (Zenith Data Systems, model Z-248, St Joseph, MI 49085) for storage and subsequent processing.

4. The test probe was configured with various load shapes (for example, a sharp edge, small square, small solid circle, slotted screw, cross-slotted screw, large solid circle, and toroid). The load was applied to the array.

5. The load condition was measured and recorded with the digital storage oscilloscope. An IEEE-488 bus was used to transfer the data to a Z-248 personal computer for storage and subsequent processing.

6. The load was removed.

7. The post-load condition was measured and recorded by the digital storage oscilloscope. An IEEE-488 bus was used to transfer the data to a Z-248 personal computer for storage and subsequent processing.

8. Steps 2 through 7 were repeated for several different load shapes.

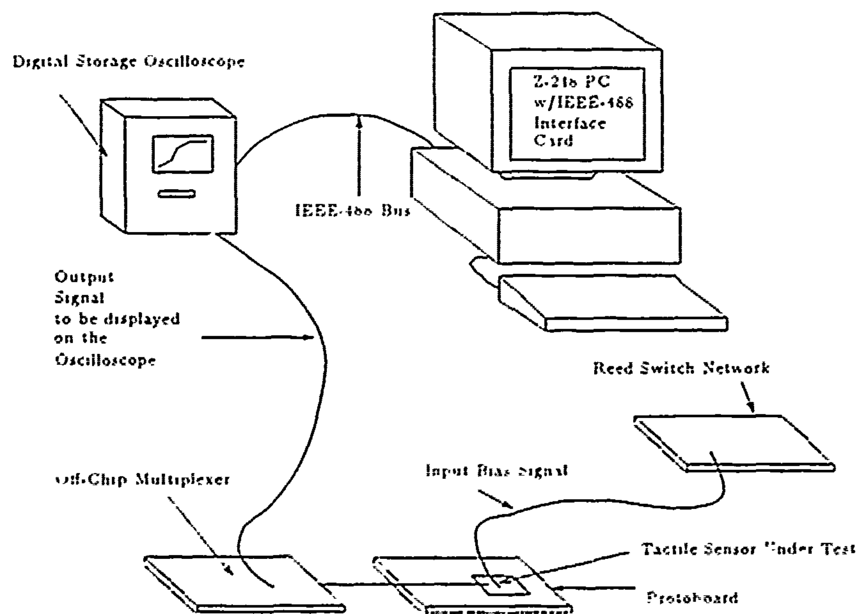

Figure H.1. Tactile Sensor Array Performance Evaluation Instrumentation Configuration.

Appendix I. *Three-dimensional Tactile Sensor Shape Information*

The three-dimensional plots produced in this thesis were generated using a software program called *Mathematica* (Wolfram Research, Inc., *Mathematica*, Version 2.0, Champaign, IL 61826). The program inputs the 64 taxel output voltage difference values (designated by "filename" in the program listing below), and then it generates a normalized output response based upon the largest voltage difference value. It assigns each taxel voltage value to 36 points arranged in a fashion to immitate the taxel dimensions and location. Between each of the simulated taxel locations, a 0-V value is displayed corresponding to the voltage measured between taxels. A sample data file for an edge shaped load in contact with one row of the tactile sensor is listed. The file contains 64 taxel output voltage difference values. The *Mathematica* program which processes the data is also provided.

```
**********************************************************************
A Sample Data File For An Edge Shaped Load Applied To One Row Of
The Tactile Sensor:
-.1015625
-.1328125
-.1640625
-.1875
-.1328125
-.140625
-.0546875
-.0859375
-.1171875
-.1171875
-.1328125
-.1328125
-.1328125
-.0859375
-.1171875
-.0703125
 .015625
-.0625
-.1328125
-.109375
-.1328125
-.09375
-.109375
```

-.1171875
.15625
.03125
-.015625
-.1796875
.078125
0
-.0390625
-.0703125
.4296875
.4921875
.453125
.3828125
.1796875
.34375
.3203125
.265625
.171875
.40625
.359375
-.0625
.0625
-.09375
0
.15625
.0078125
.0234375
-.078125
-.0390625
-.03125
-.0703125
-.0546875
-.046875
.0546875
-.0546875
-.0703125
.046875
-.0390625
-.078125
-.0625
-.0390625

```
*****************************************************************************
q=ReadList["filename"]
s=Max[q]
OpenRead["filename"]
Do[f[j,i]=Read["filename"], {i, 8}, {j, 8}]
Close["filename"]
Do[x[j,i]=f[j,i]/s, {i, 8}, {j, 8}]
Do[z[8j-7, 8i-7]=0, {i, 8}, {j,8}]
Do[z[8j-6, 8i-7]=0, {i, 8}, {j,8}]
Do[z[8j-5, 8i-7]=0, {i, 8}, {j,8}]
Do[z[8j-4, 8i-7]=0, {i, 8}, {j,8}]
Do[z[8j-3, 8i-7]=0, {i, 8}, {j,8}]
Do[z[8j-2, 8i-7]=0, {i, 8}, {j,8}]
Do[z[8j-1, 8i-7]=0, {i, 8}, {j,8}]
Do[z[8j, 8i-7]=0, {i, 8}, {j,8}]
Do[z[8j-7, 8i-6]=0, {i, 8}, {j,8}]
Do[z[8j-6, 8i-6]=x[j,i], {i, 8}, {j,8}]
Do[z[8j-5, 8i-6]=x[j,i], {i, 8}, {j,8}]
Do[z[8j-4, 8i-6]=x[j,i], {i, 8}, {j,8}]
Do[z[8j-3, 8i-6]=x[j,i], {i, 8}, {j,8}]
Do[z[8j-2, 8i-6]=x[j,i], {i, 8}, {j,8}]
Do[z[8j-1, 8i-6]=x[j,i], {i, 8}, {j,8}]
Do[z[8j, 8i-6]=0, {i, 8}, {j,8}]
Do[z[8j-7, 8i-5]=0, {i, 8}, {j,8}]
Do[z[8j-6, 8i-5]=x[j,i], {i, 8}, {j,8}]
Do[z[8j-5, 8i-5]=x[j,i], {i, 8}, {j,8}]
Do[z[8j-4, 8i-5]=x[j,i], {i, 8}, {j,8}]
Do[z[8j-3, 8i-5]=x[j,i], {i, 8}, {j,8}]
Do[z[8j-2, 8i-5]=x[j,i], {i, 8}, {j,8}]
Do[z[8j-1, 8i-5]=x[j,i], {i, 8}, {j,8}]
Do[z[8j, 8i-5]=0, {i, 8}, {j,8}]
Do[z[8j-7, 8i-4]=0, {i, 8}, {j,8}]
Do[z[8j-6, 8i-4]=x[j,i], {i, 8}, {j,8}]
Do[z[8j-5, 8i-4]=x[j,i], {i, 8}, {j,8}]
Do[z[8j-4, 8i-4]=x[j,i], {i, 8}, {j,8}]
Do[z[8j-3, 8i-4]=x[j,i], {i, 8}, {j,8}]
Do[z[8j-2, 8i-4]=x[j,i], {i, 8}, {j,8}]
Do[z[8j-1, 8i-4]=x[j,i], {i, 8}, {j,8}]
Do[z[8j, 8i-4]=0, {i, 8}, {j,8}]
Do[z[8j-7, 8i-3]=0, {i, 8}, {j,8}]
Do[z[8j-6, 8i-3]=x[j,i], {i, 8}, {j,8}]
Do[z[8j-5, 8i-3]=x[j,i], {i, 8}, {j,8}]
Do[z[8j-4, 8i-3]=x[j,i], {i, 8}, {j,8}]
Do[z[8j-3, 8i-3]=x[j,i], {i, 8}, {j,8}]
Do[z[8j-2, 8i-3]=x[j,i], {i, 8}, {j,8}]
Do[z[8j-1, 8i-3]=x[j,i], {i, 8}, {j,8}]
Do[z[8j, 8i-3]=0, {i, 8}, {j,8}]
Do[z[8j-7, 8i-2]=0, {i, 8}, {j,8}]
Do[z[8j-6, 8i-2]=x[j,i], {i, 8}, {j,8}]
Do[z[8j-5, 8i-2]=x[j,i], {i, 8}, {j,8}]
Do[z[8j-4, 8i-2]=x[j,i], {i, 8}, {j,8}]
```

```
Do[z[8j-3, 8i-2]=x[j,i], {i, 8}, {j,8}]
Do[z[8j-2, 8i-2]=x[j,i], {i, 8}, {j,8}]
Do[z[8j-1, 8i-2]=x[j,i], {i, 8}, {j,8}]
Do[z[8j, 8i-2]=0, {i, 8}, {j,8}]
Do[z[8j-7, 8i-1]=0, {i, 8}, {j,8}]
Do[z[8j-6, 8i-1]=x[j,i], {i, 8}, {j,8}]
Do[z[8j-5, 8i-1]=x[j,i], {i, 8}, {j,8}]
Do[z[8j-4, 8i-1]=x[j,i], {i, 8}, {j,8}]
Do[z[8j-3, 8i-1]=x[j,i], {i, 8}, {j,8}]
Do[z[8j-2, 8i-1]=x[j,i], {i, 8}, {j,8}]
Do[z[8j-1, 8i-1]=x[j,i], {i, 8}, {j,8}]
Do[z[8j, 8i-1]=0, {i, 8}, {j,8}]
Do[z[8j-7, 8i]=0, {i, 8}, {j,8}]
Do[z[8j-6, 8i]=0, {i, 8}, {j,8}]
Do[z[8j-5, 8i]=0, {i, 8}, {j,8}]
Do[z[8j-4, 8i]=0, {i, 8}, {j,8}]
Do[z[8j-3, 8i]=0, {i, 8}, {j,8}]
Do[z[8j-2, 8i]=0, {i, 8}, {j,8}]
Do[z[8j-1, 8i]=0, {i, 8}, {j,8}]
Do[z[8j, 8i]=0, {i, 8}, {j,8}]
t3=Table[z[i,j], {i,64}, {j,64}]
ListPlot3D[t3, ViewPoint -> {.7,-.1,1.2}, PlotRange -> {0, 1},
Ticks -> None]
```

Appendix J. *Contour and Threshold Plots*

The figures contained within this appendix are provided as support for the set of figures presented in Chapter VI. For each shape presented, the first two plots are for one equipotential level below the "best-fit" equipotential, containing the contour plot and the taxel threshold level plot. The next two are for one equipotential contour above the "best-fit" equipotential. The following plots were obtained from a tactile sensor fabricated using urethane, and they include the sharp edge, small square small circle, polygon, slotted screw, cross-slotted screw, large solid circle, toroid. Also included are supporting plots for the data obtained from a sensor fabricated with polyimide for the sharp edge, small square, and small circle shaped loads.

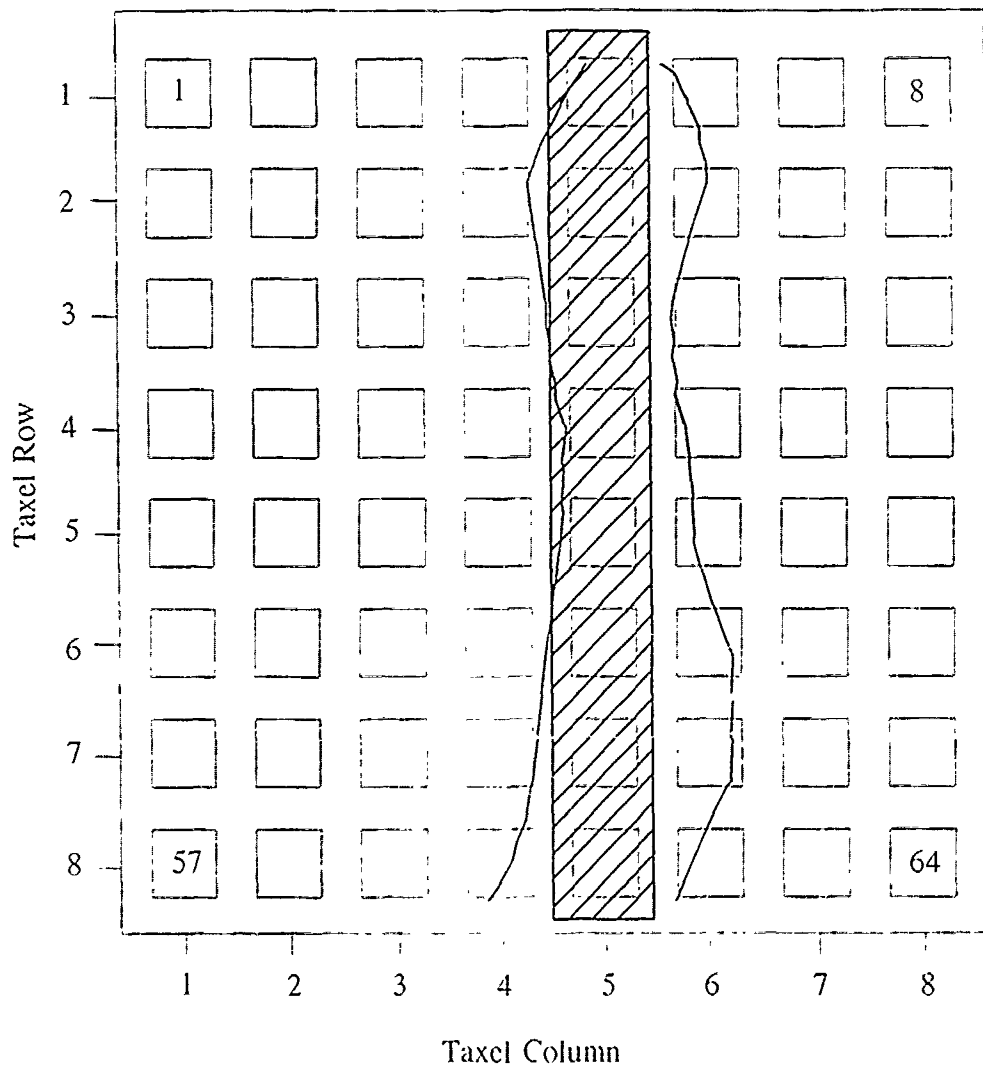

Figure J.1. 0.3-V Equipotential Contour Plot For A 100 g Sharp Edge Shaped Load Applied To The Surface Of The Electrode Array.

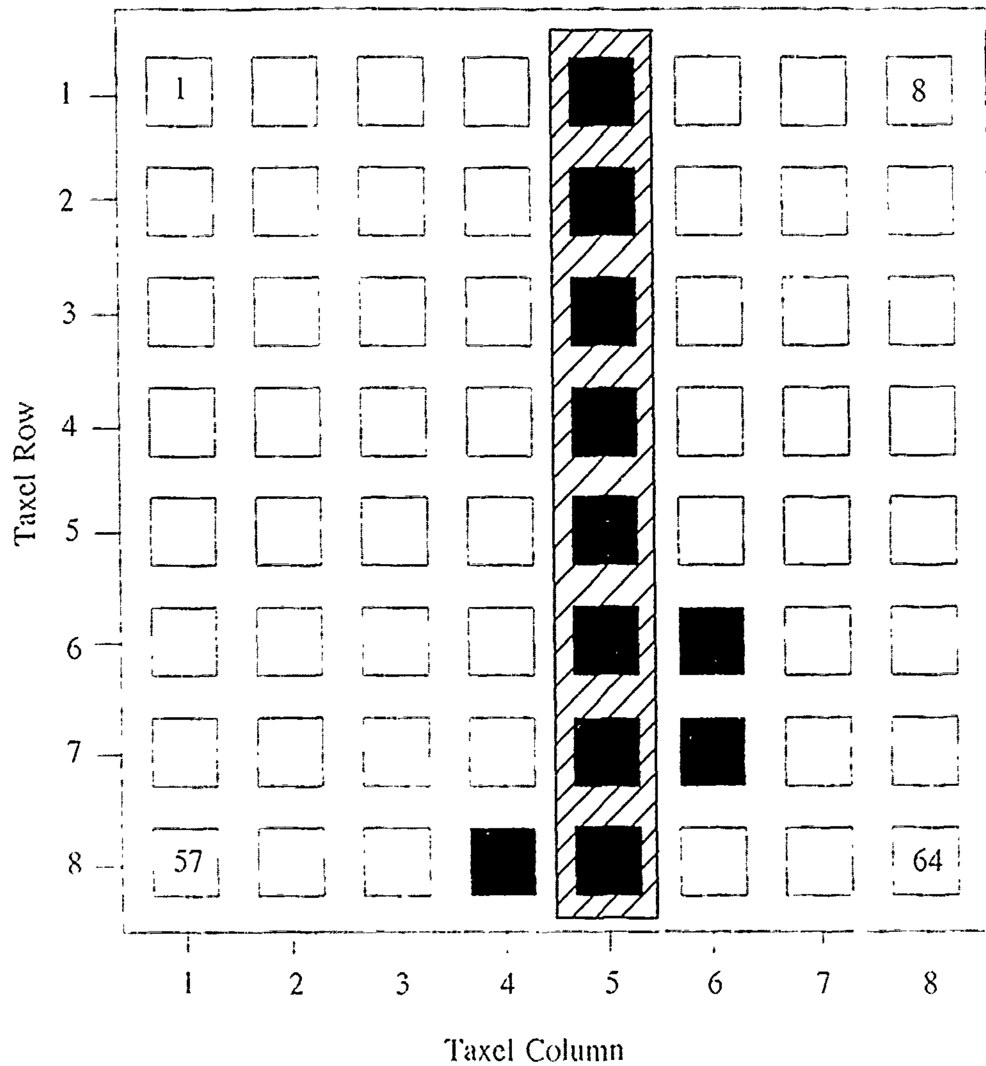

Figure J.2. 0.3-V Threshold Plot Of A 100 g Sharp Edge Shaped Load – Taxels With An Output Level Above This Threshold Level Are Displayed As Black And Taxels With An Output Level Below This Threshold Level Are Displayed As White.

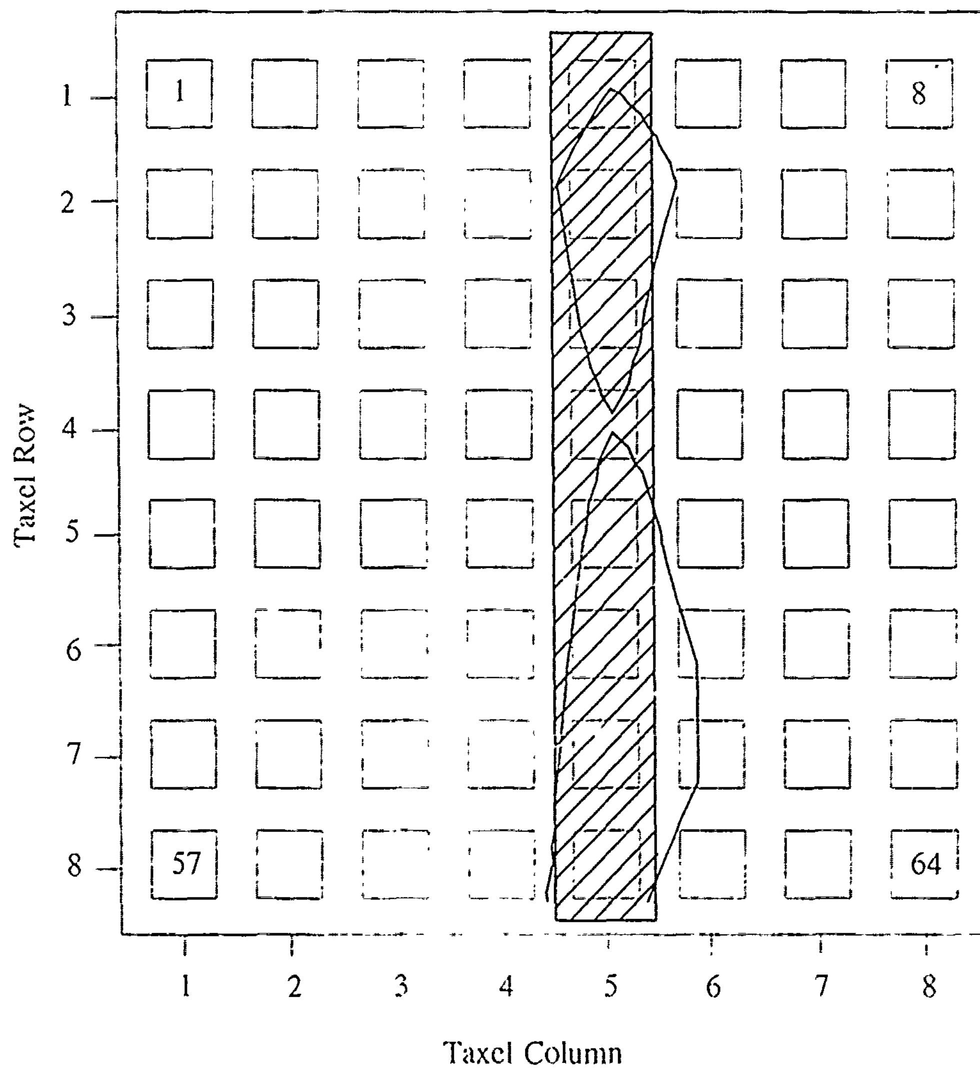

Figure J.3. 0.5-V Equipotential Contour Plot For A 100 g Sharp Edge Shaped Load Applied To The Surface Of The Electrode Array.

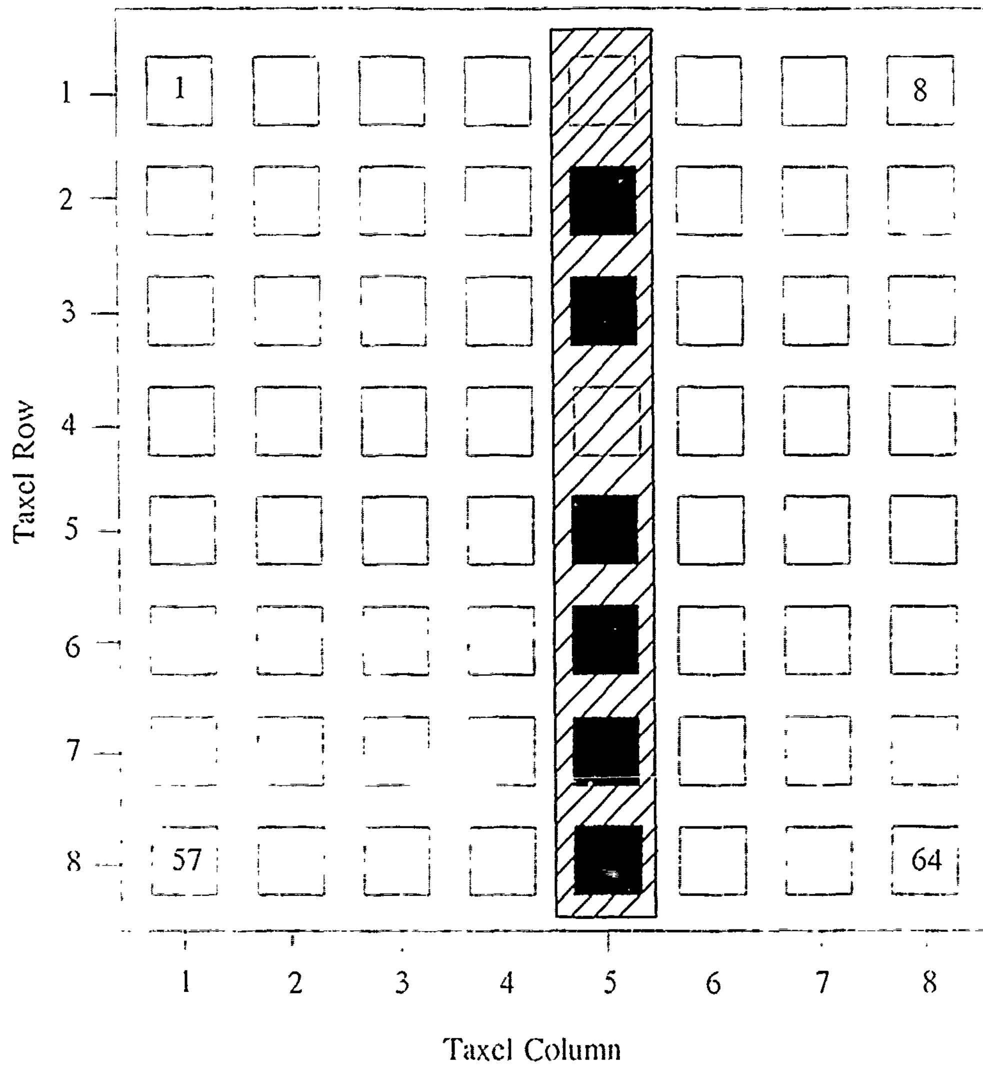

Figure J.4. 0.5-V Threshold Plot Of A 100 g Sharp Edge Shaped Load - Taxels With An Output Level Above This Threshold Level Are Displayed As Black And Taxels With An Output Level Below This Threshold Level Are Displayed As White.

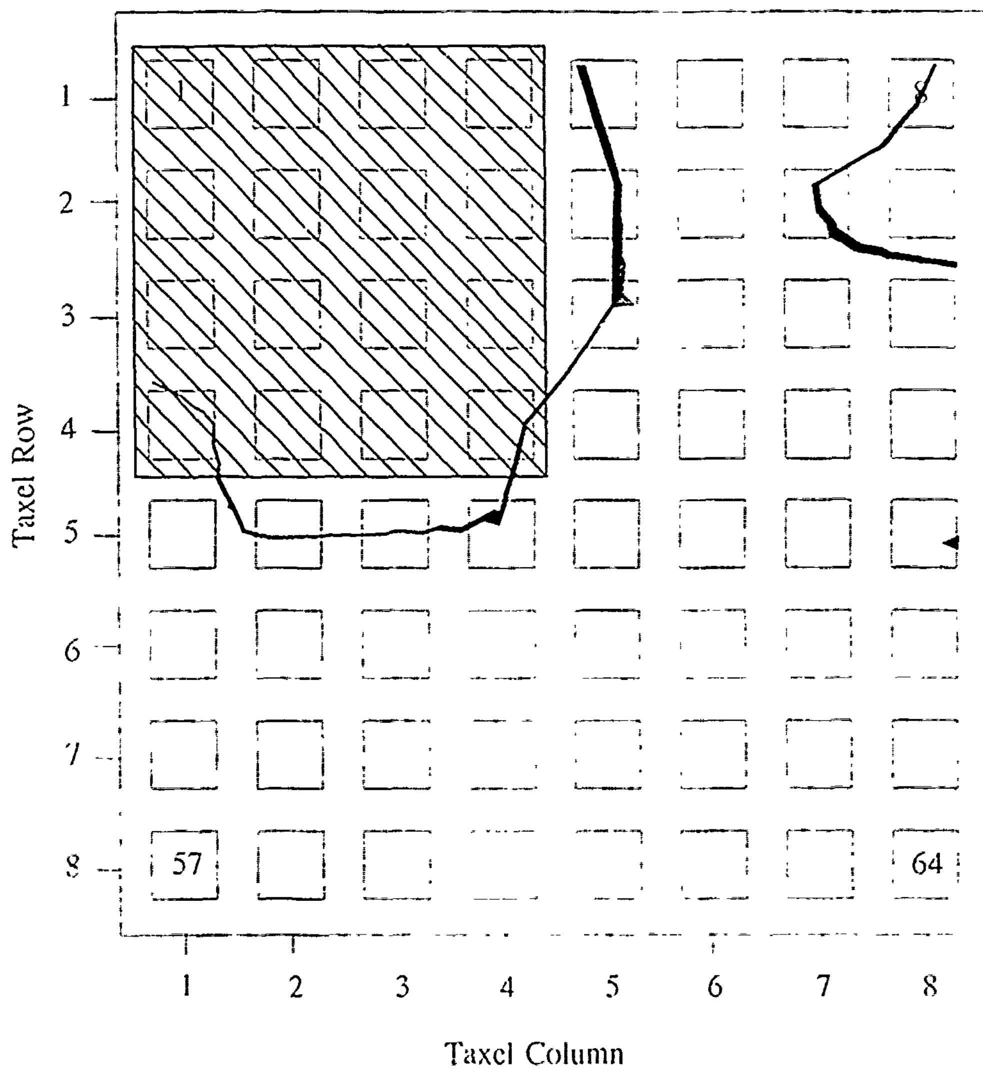

Figure J.5. 0.3-V Equipotential Contour Plot For A 100 g Small Square Shaped Load Applied To The Surface Of The Electrode Array.

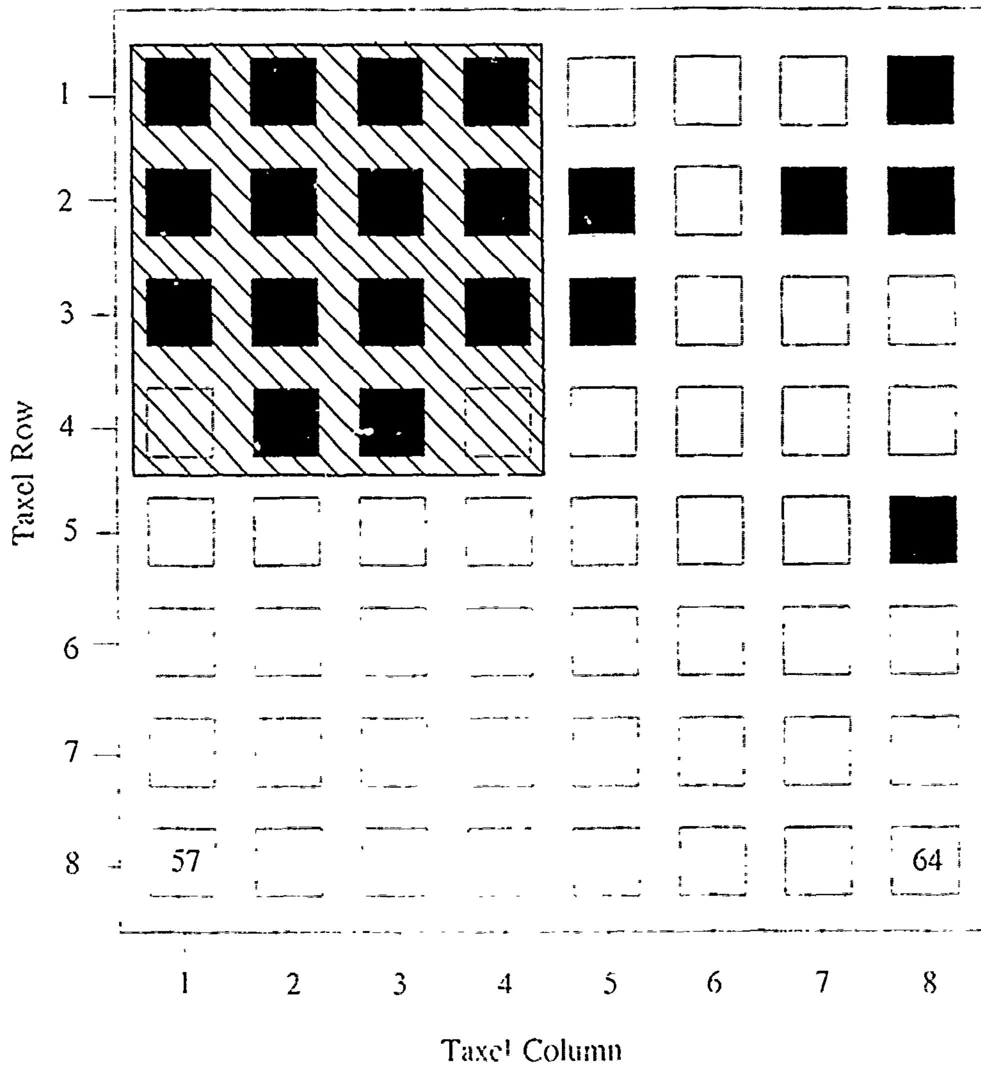

Figure J.6. 0.3-V Threshold Plot Of A 100 g Small Square Shaped Load - Taxels With An Output Level Above This Threshold Level Are Displayed As Black And Taxels With An Output Level Below This Threshold Level Are Displayed As White.

Figure J.7. 0.4-V Equipotential Contour Plot For A 100 g Small Square Shaped Load Applied To The Surface Of The Electrode Array.

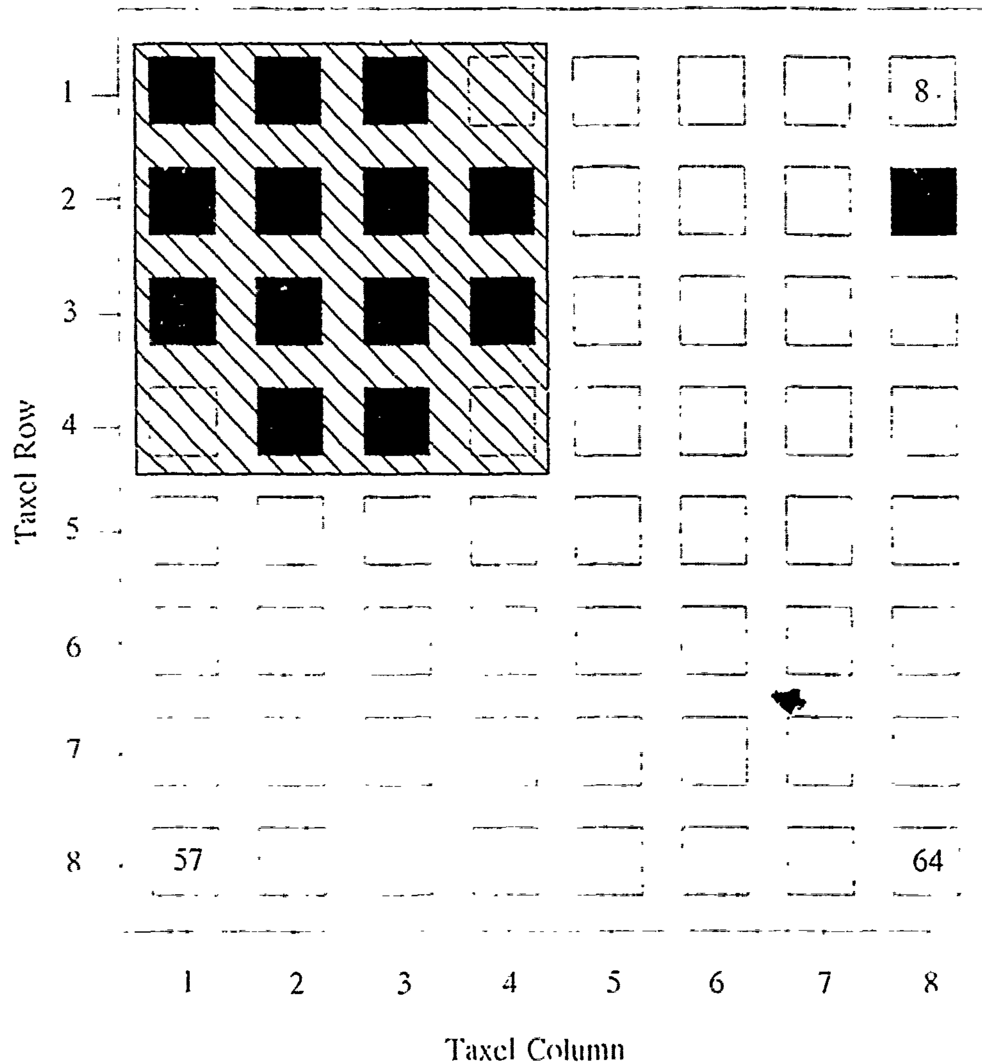

Figure J.8. 0.4-V Threshold Plot Of A 100 g Small Square Shaped Load - Taxels With An Output Level Above This Threshold Level Are Displayed As Black And Taxels With An Output Level Below This Threshold Level Are Displayed As White.

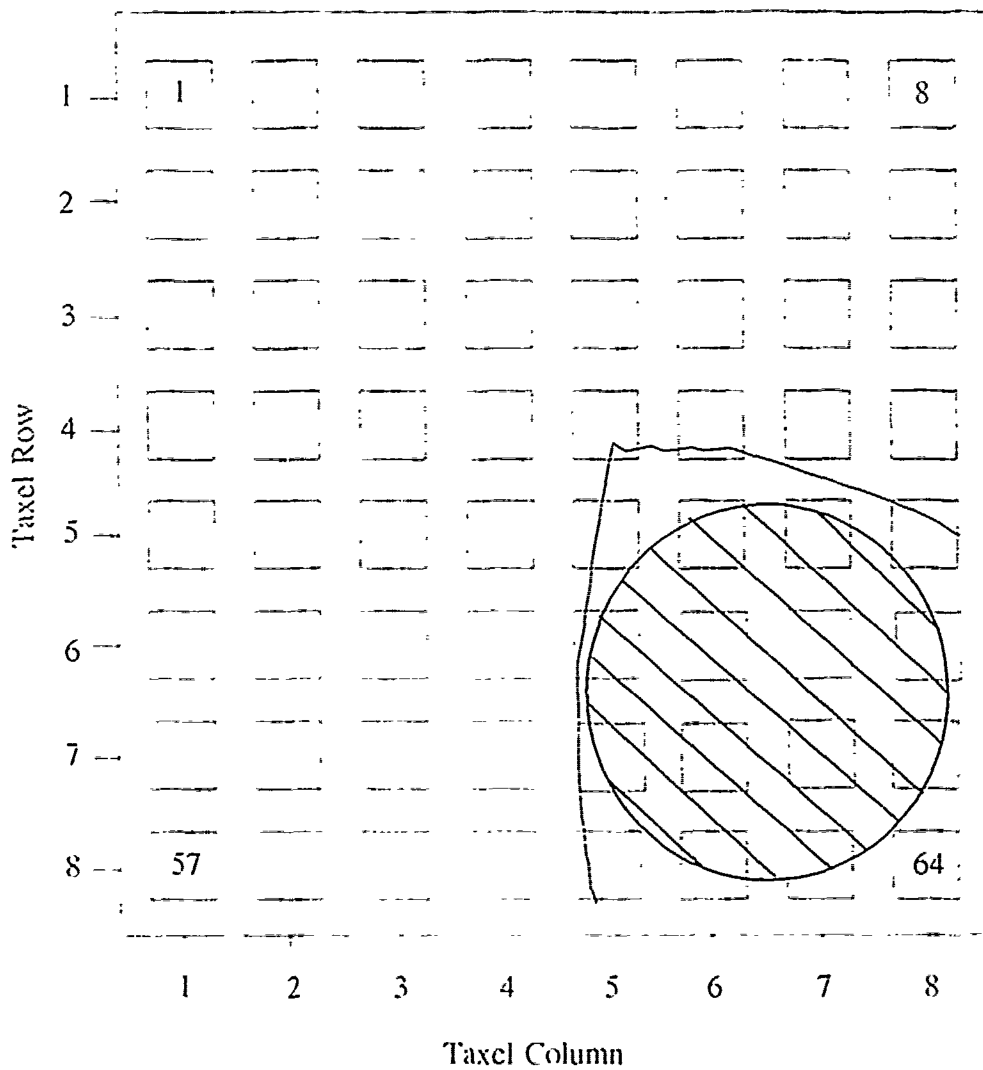

Figure J.9. 0.6-V Equipotential Contour Plot For A 100 g Small Circularly Shaped Load Applied To The Surface Of The Electrode Array.

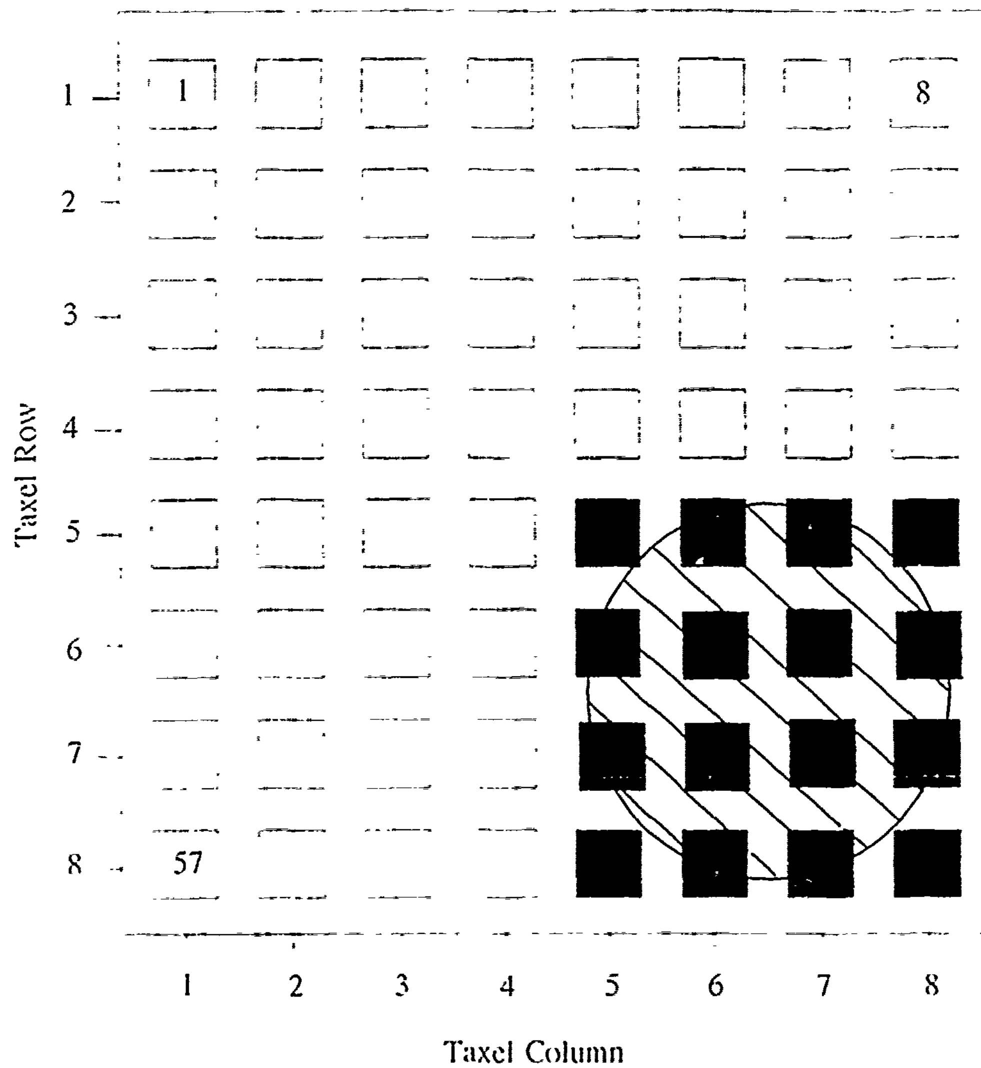

Figure J.10. 0.6-V Threshold Plot Of A 100 g Small Circularly Shaped Load - Taxels With An Output Level Above This Threshold Level Are Displayed As Black And Taxels With An Output Level Below This Threshold Level Are Displayed As White.

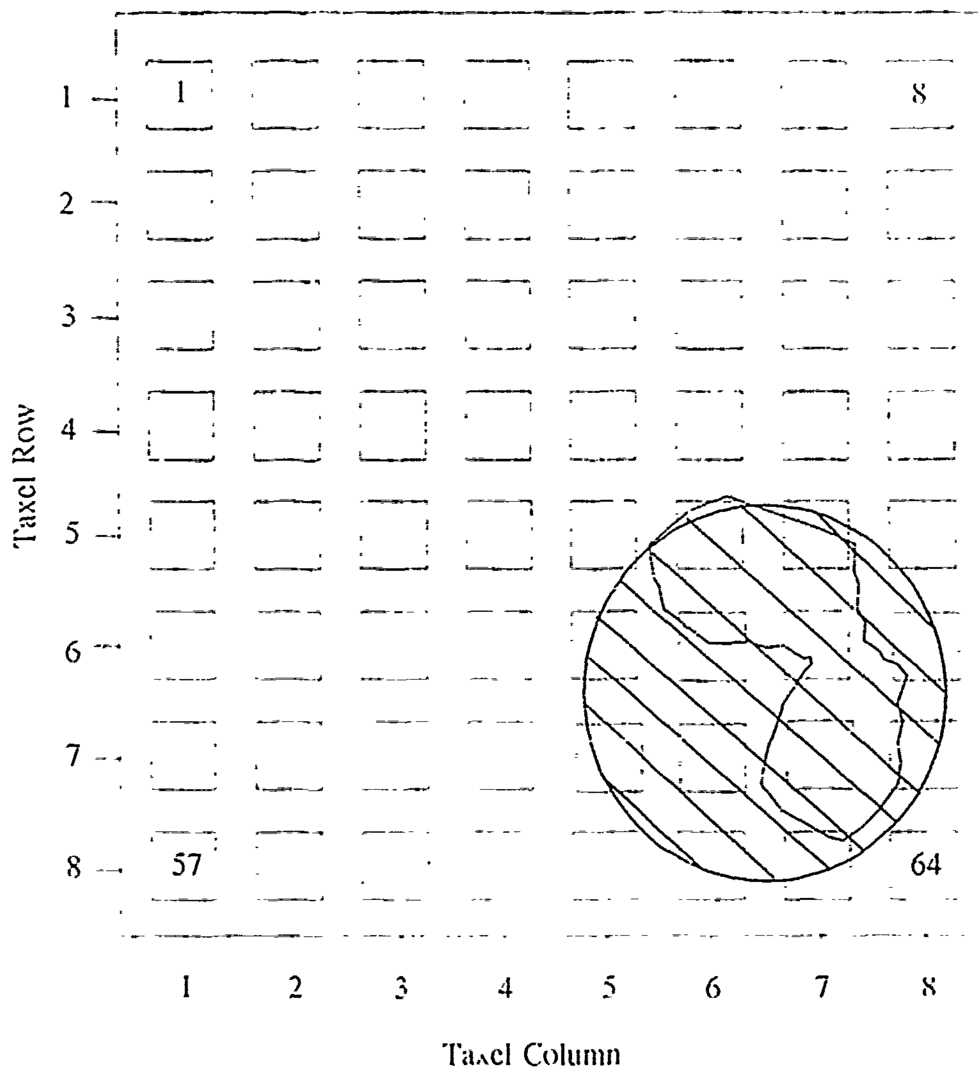

Figure J.11. 0.8-V Equipotential Contour Plot For A 100 g Small Circularly Shaped Load Applied To The Surface Of The Electrode Array.

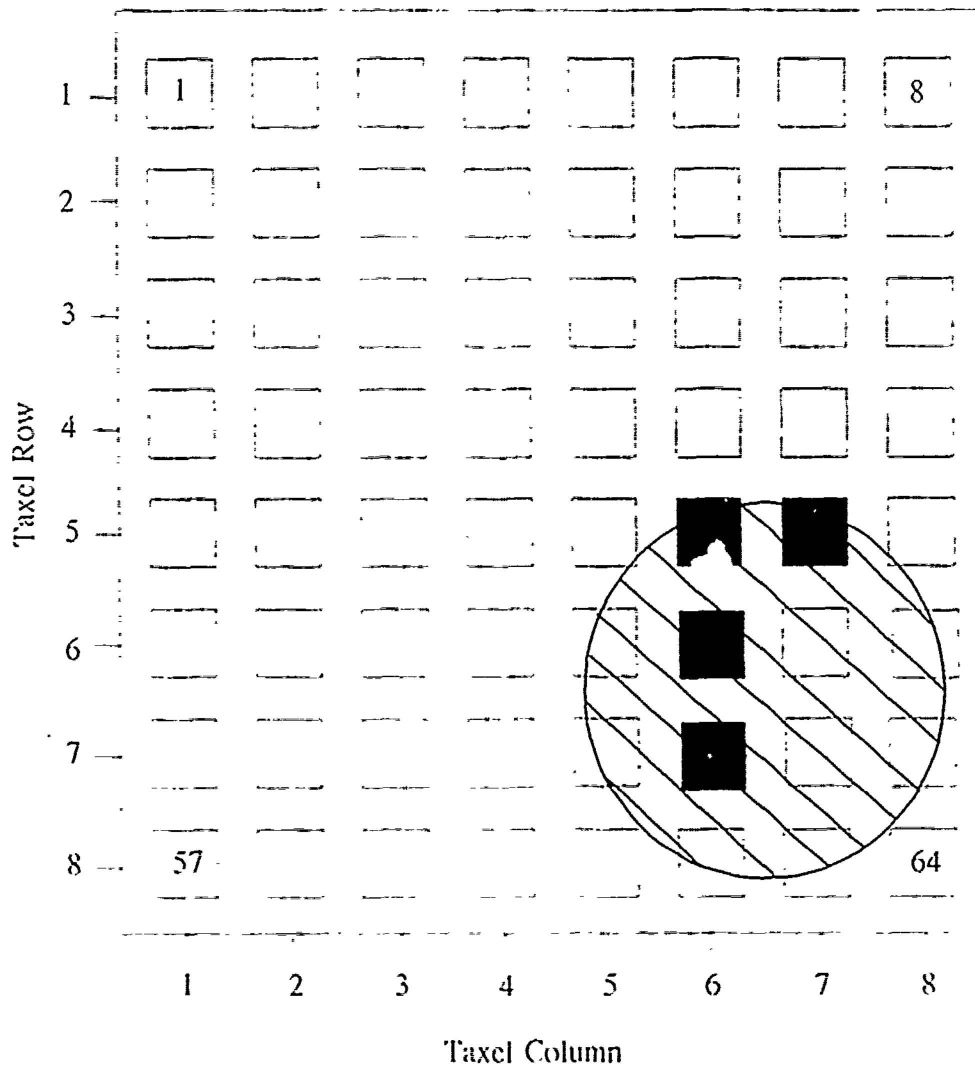

Figure J.12. 0.8-V Threshold Plot Of A 100 g Small Circularly Shaped Load - Taxels With An Output Level Above This Threshold Level Are Displayed As Black And Taxels With An Output Level Below This Threshold Level Are Displayed As White.

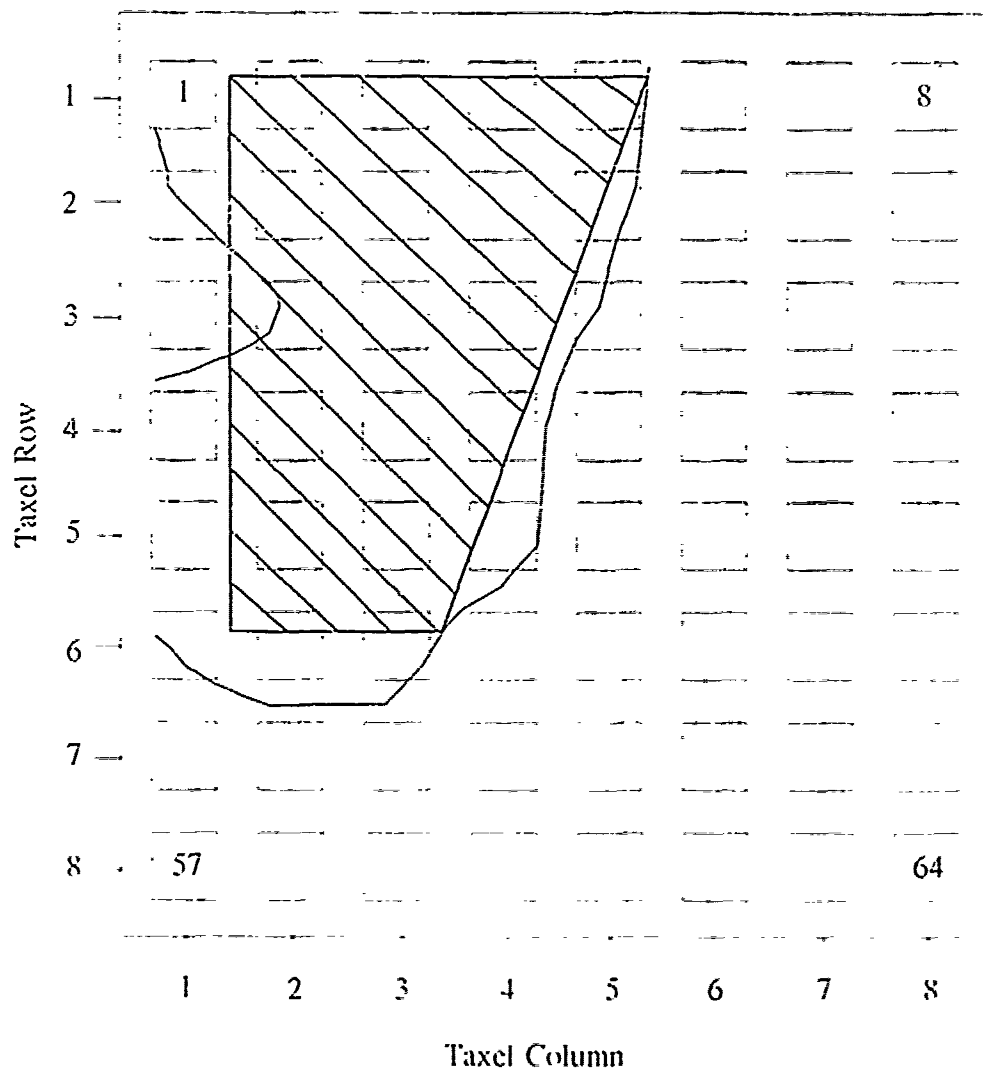

Figure J.13. 0.3-V Equipotential Contour Plot For A 100 g Polygon Shaped Load Applied To The Surface Of The Electrode Array.

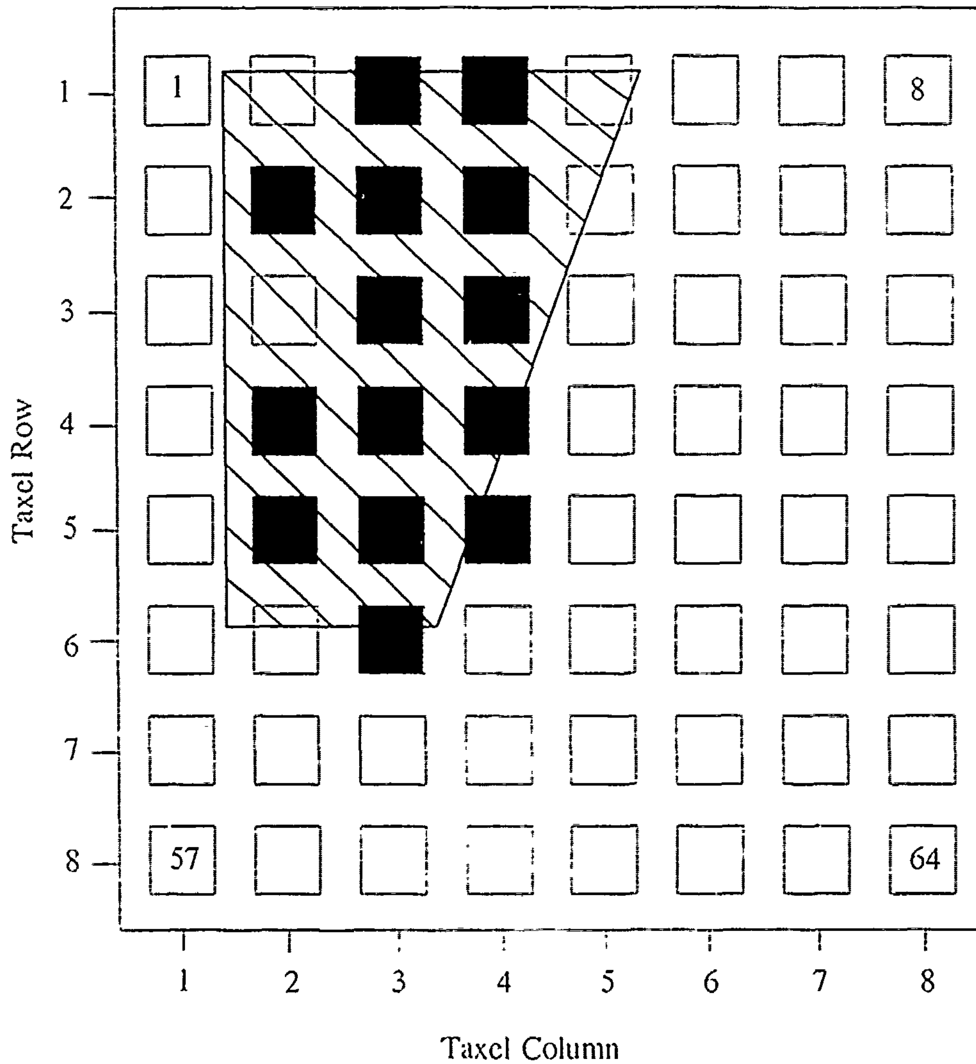

Figure J.16. 0.5-V Threshold Plot Of A 100 g Polygon Shaped Load - Taxels With An Output Level Above This Threshold Level Are Displayed As Black And Taxels With An Output Level Below This Threshold Level Are Displayed As White.

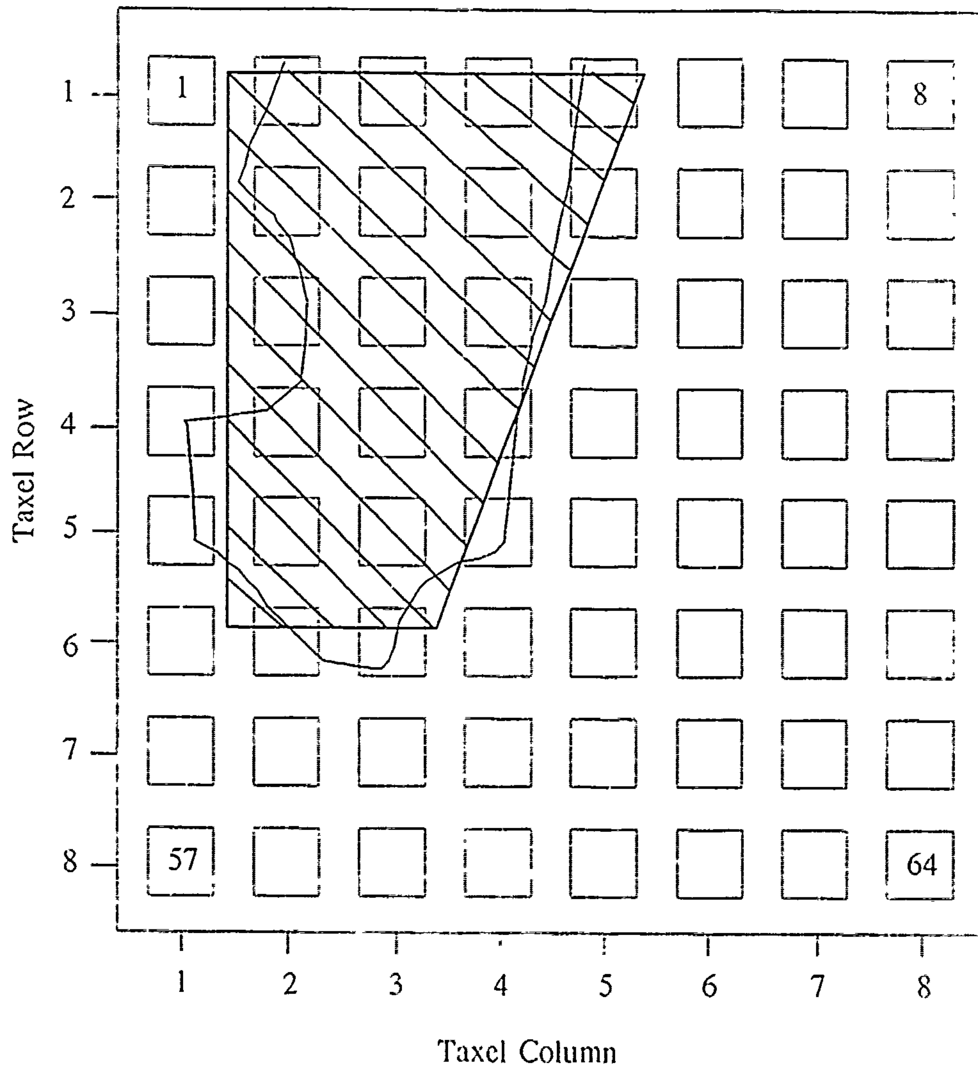

Figure J.15. 0.5-V Equipotential Contour Plot For A 100 g Polygon Shaped Load Applied To The Surface Of The Electrode Array.

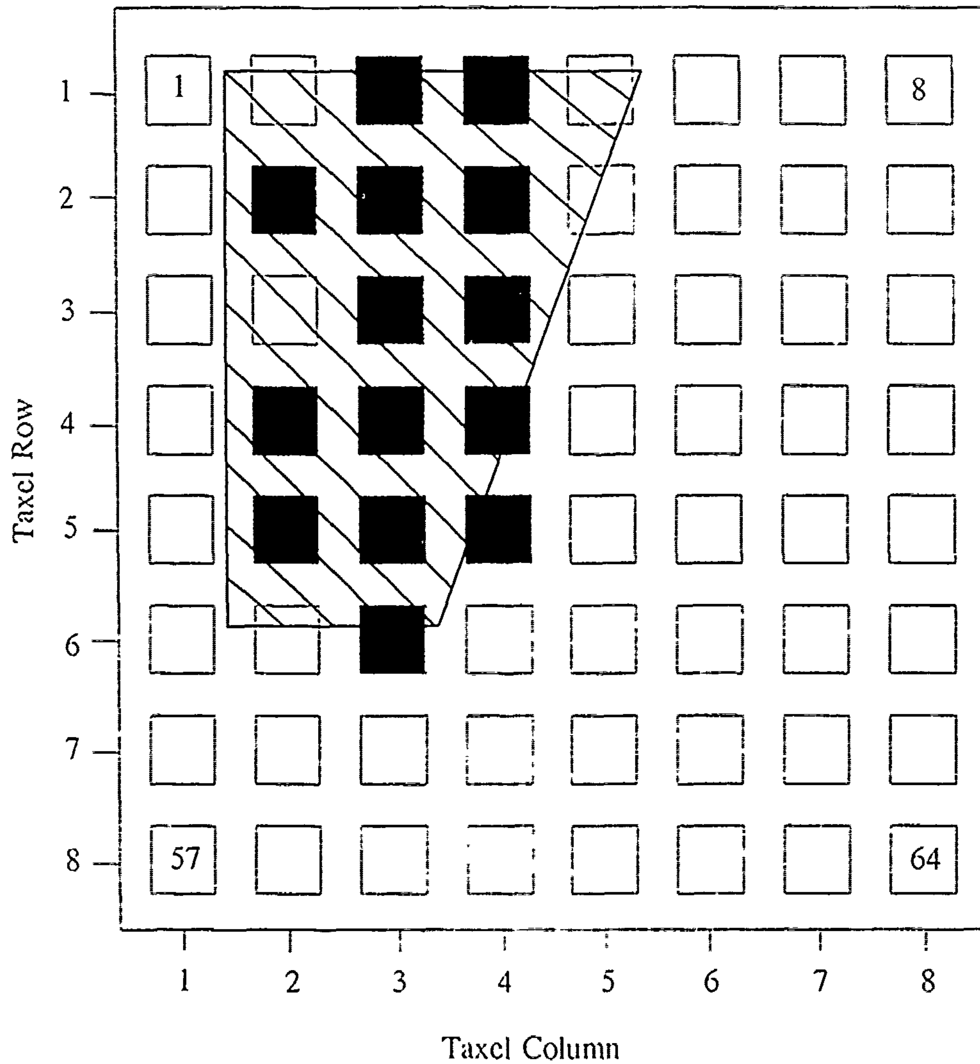

Figure J.16. 0.5-V Threshold Plot Of A 100 g Polygon Shaped Load – Taxels With An Output Level Above This Threshold Level Are Displayed As Black And Taxels With An Output Level Below This Threshold Level Are Displayed As White.

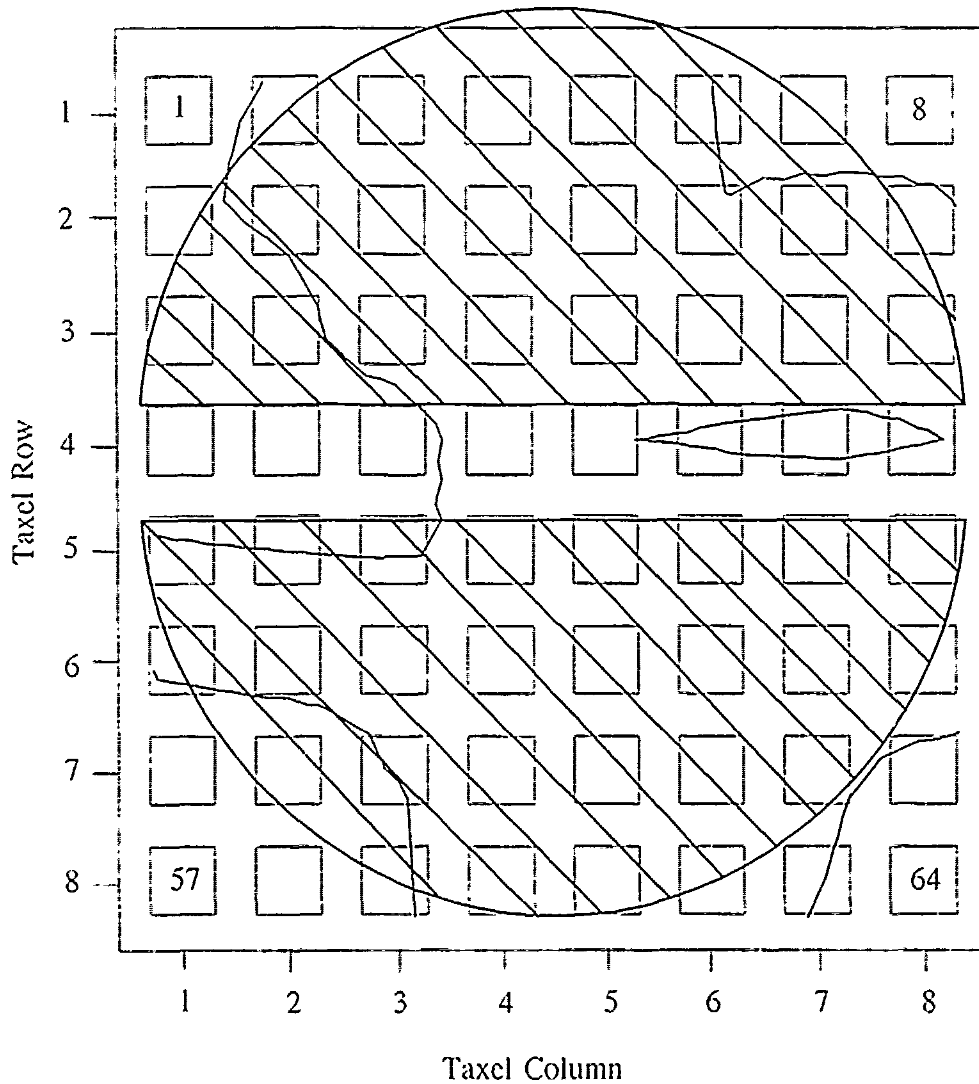

Figure J.17. 0.5-V Equipotential Contour Plot For A 100 g Slotted Screw Shaped Load Applied To The Surface Of The Electrode Array.

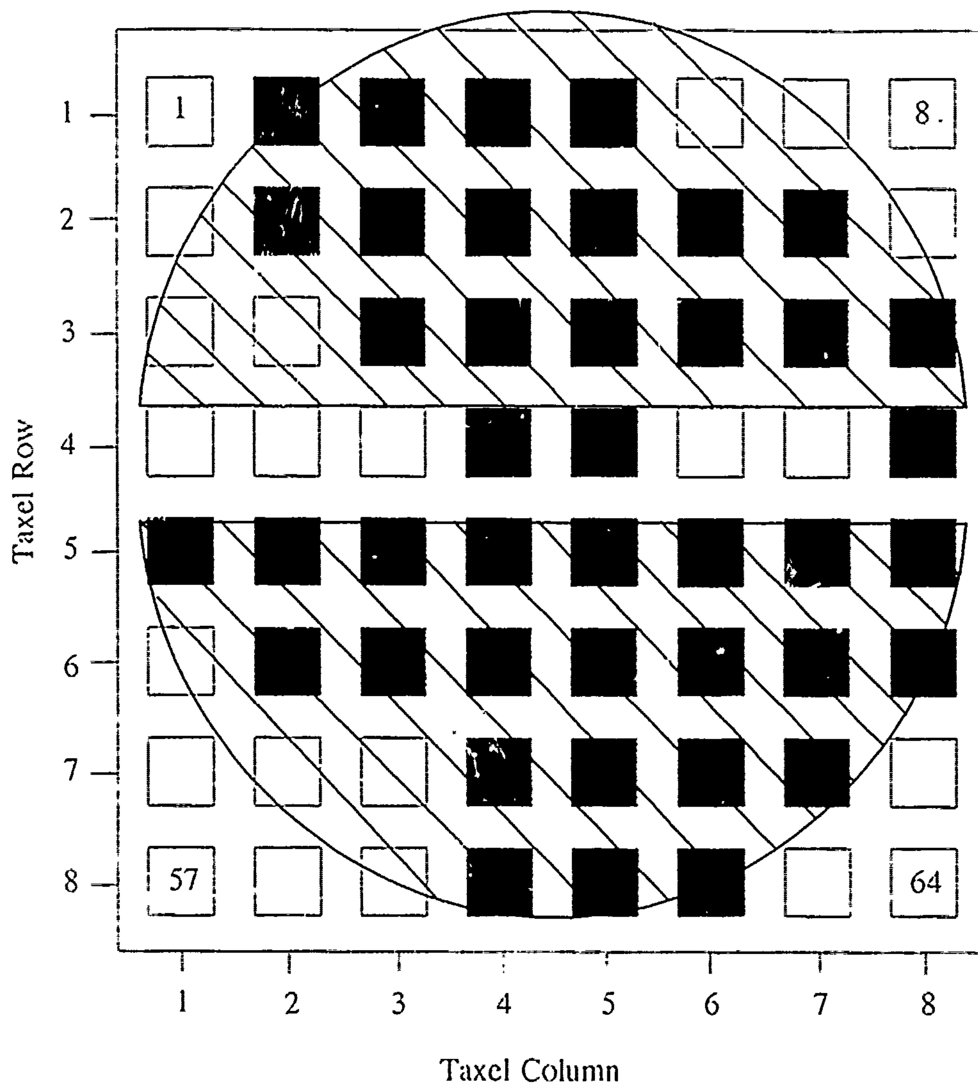

Figure J.18. 0.5-V Threshold Plot Of A 100 g Slotted Screw Shaped Load - Taxels With An Output Level Above This Threshold Level Are Displayed As Black And Taxels With An Output Level Below This Threshold Level Are Displayed As White.

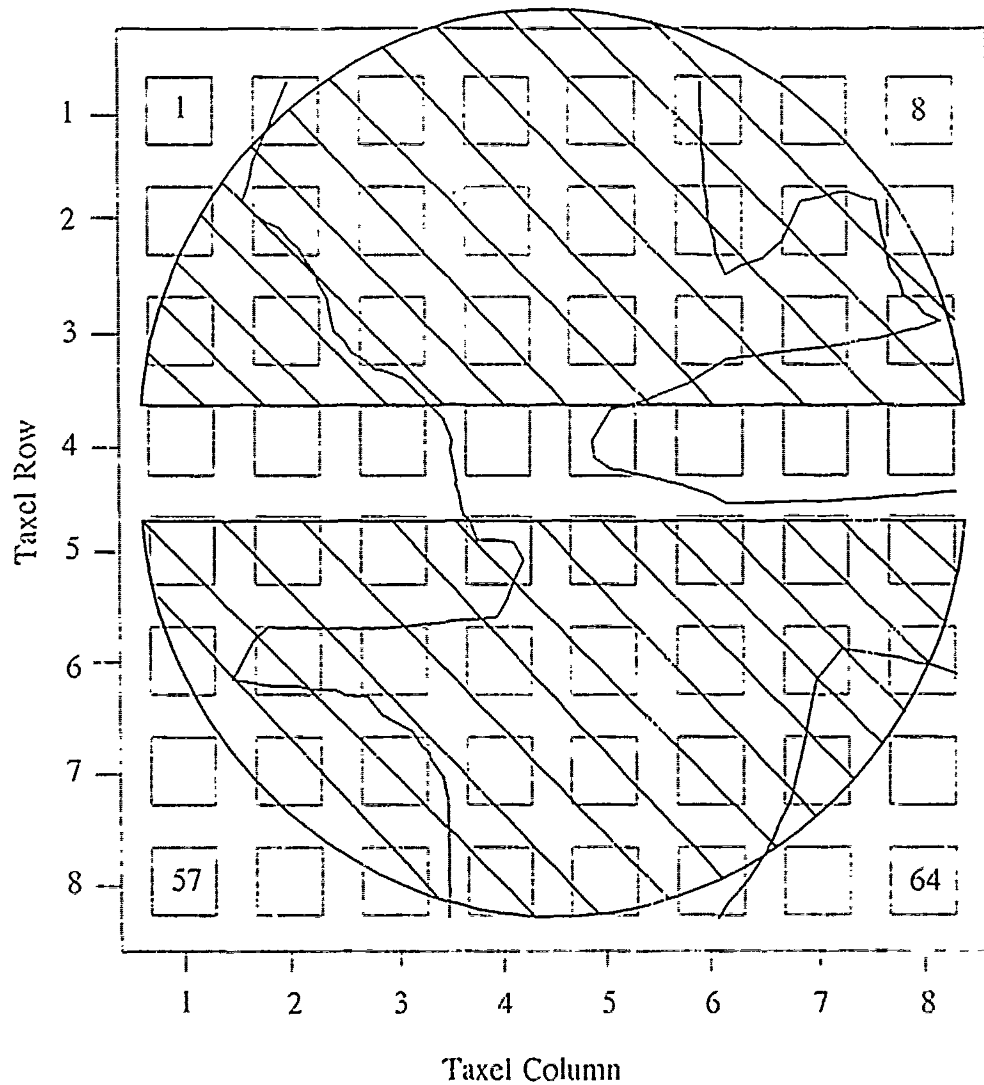

Figure J.19. 0.56-V Equipotential Contour Plot For A 100 g Slotted Screw Shaped Load Applied To The Surface Of The Electrode Array.

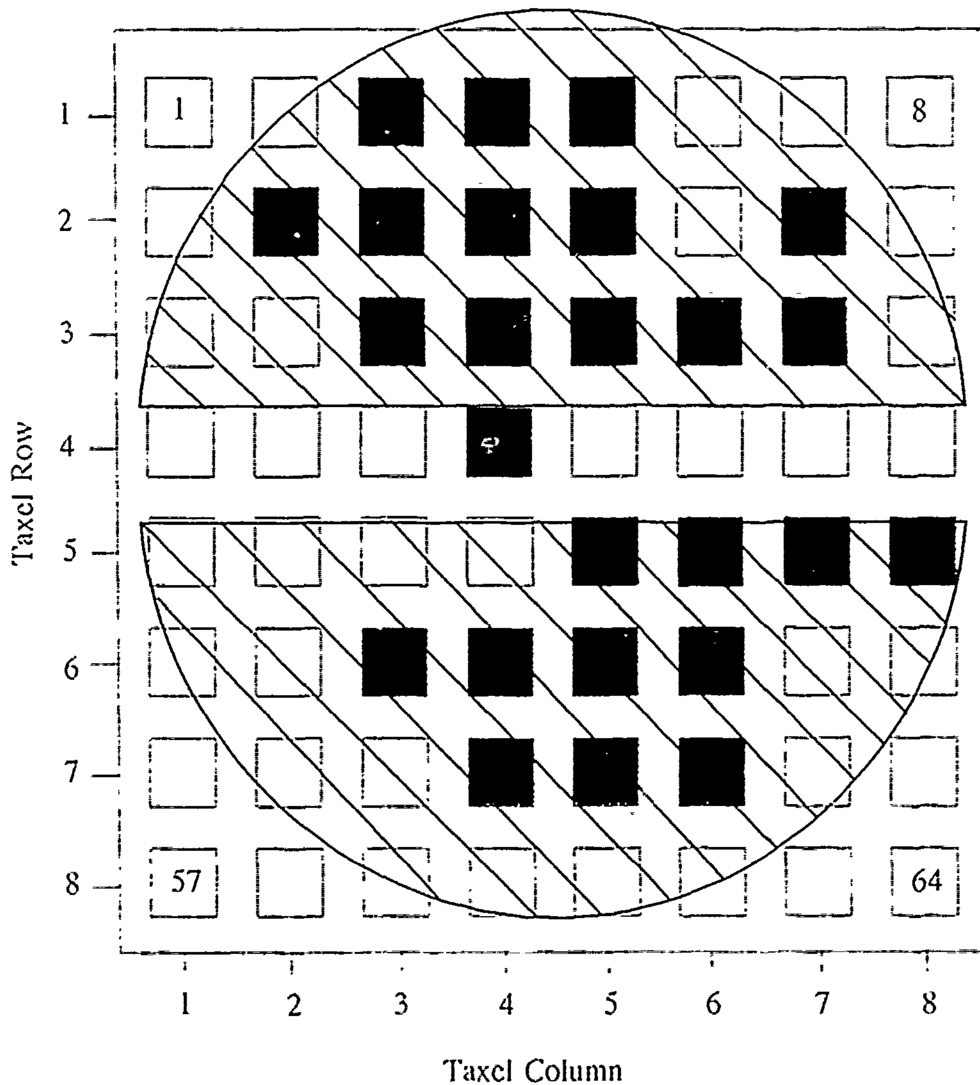

Figure J.20. 0.56-V Threshold Plot Of A 100 g Slotted Screw Shaped Load - Taxels With An Output Level Above This Threshold Level Are Displayed As Black And Taxels With An Output Level Below This Threshold Level Are Displayed As White.

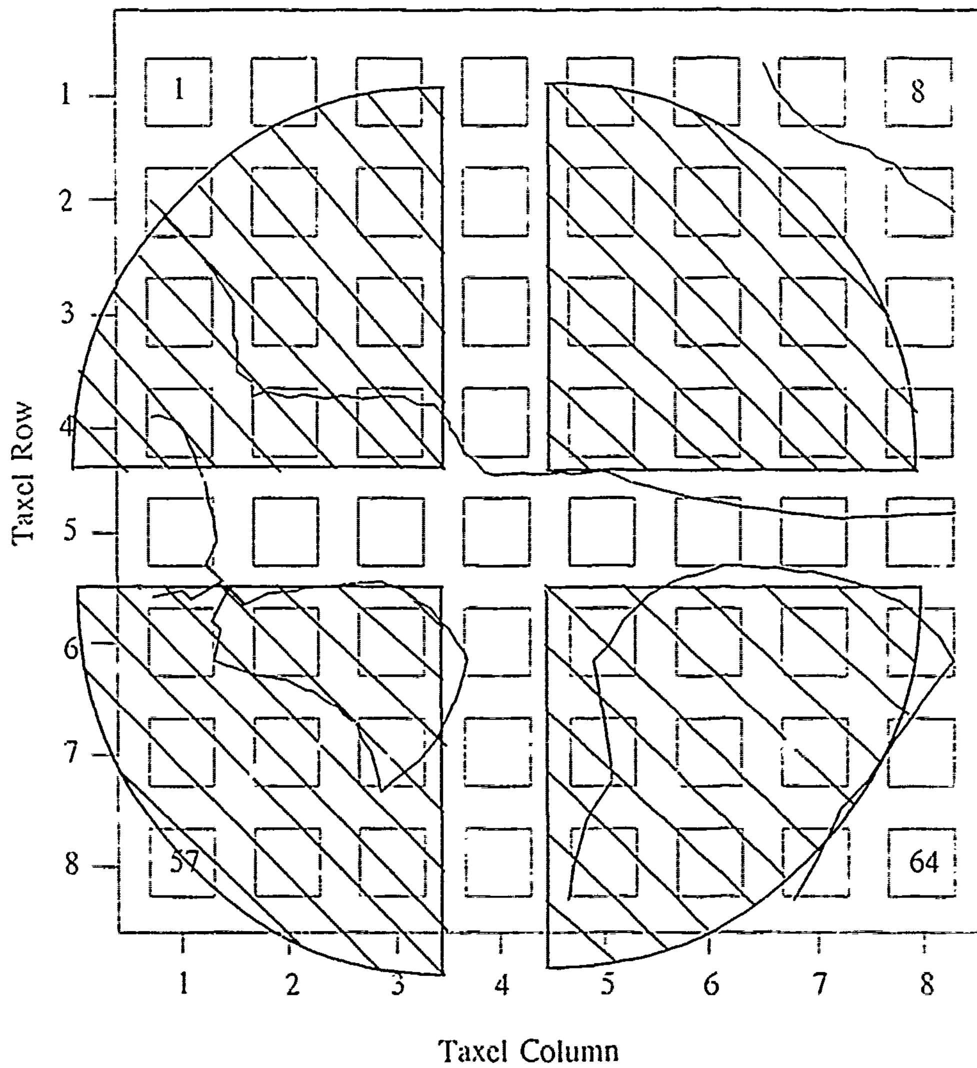

Figure J.21. 0.4-V Equipotential Contour Plot For A 100 g Cross-Slotted Screw Shaped Load Applied To The Surface Of The Electrode Array.

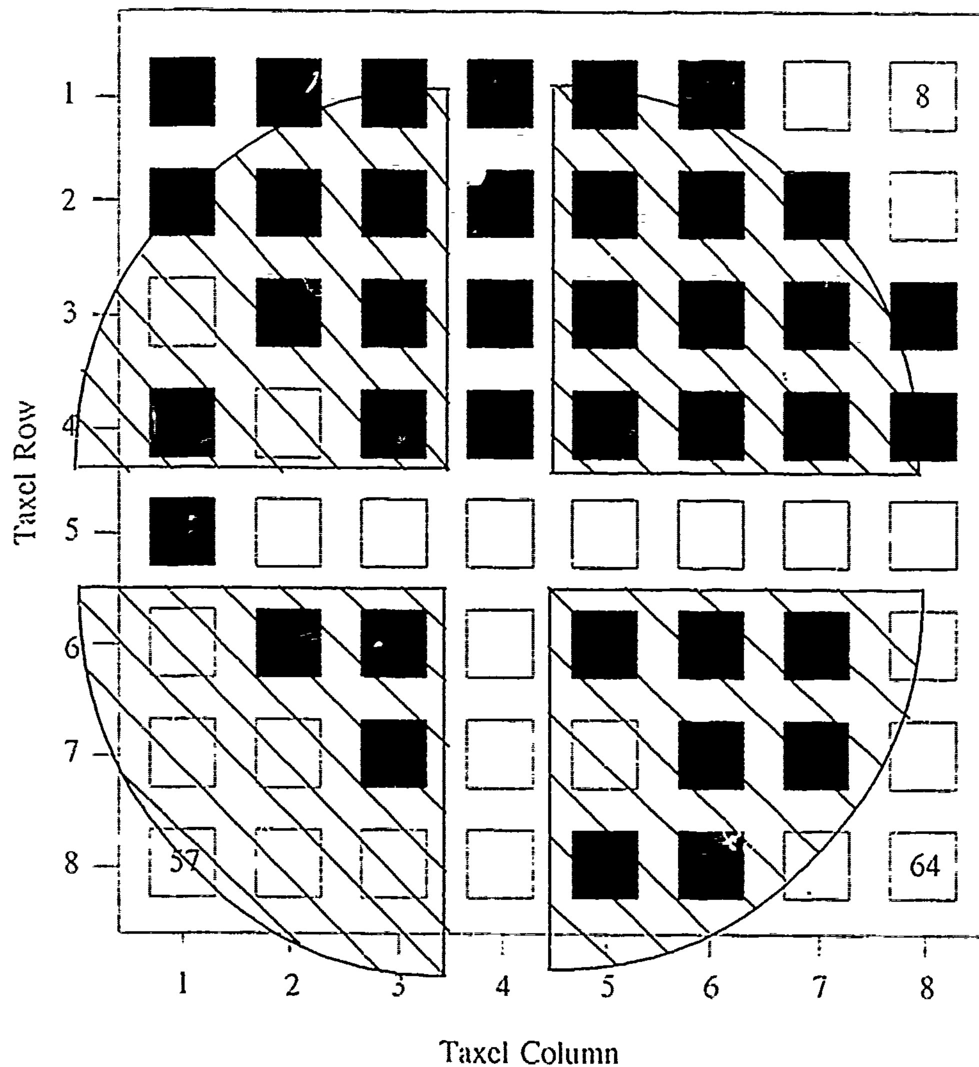

Figure J.22. 0.4-V Threshold Plot Of A 100 g Cross-Slotted Screw Shaped Load - Taxels With An Output Level Above This Threshold Level Are Displayed As Black And Taxels With An Output Level Below This Threshold Level Are Displayed As White.

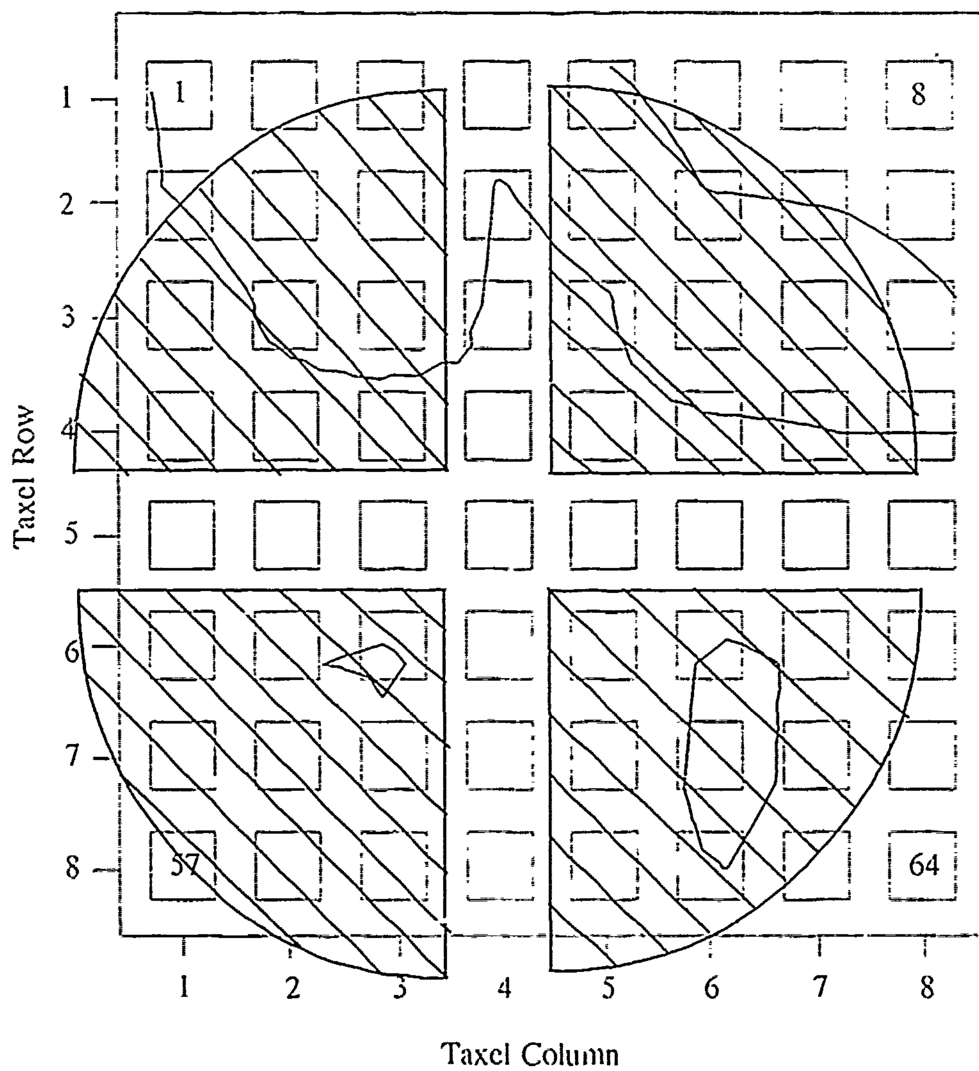

Figure J.23. 0.5-V Equipotential Contour Plot For A 100 g Cross-Slotted Screw Shaped Load Applied To The Surface Of The Electrode Array.

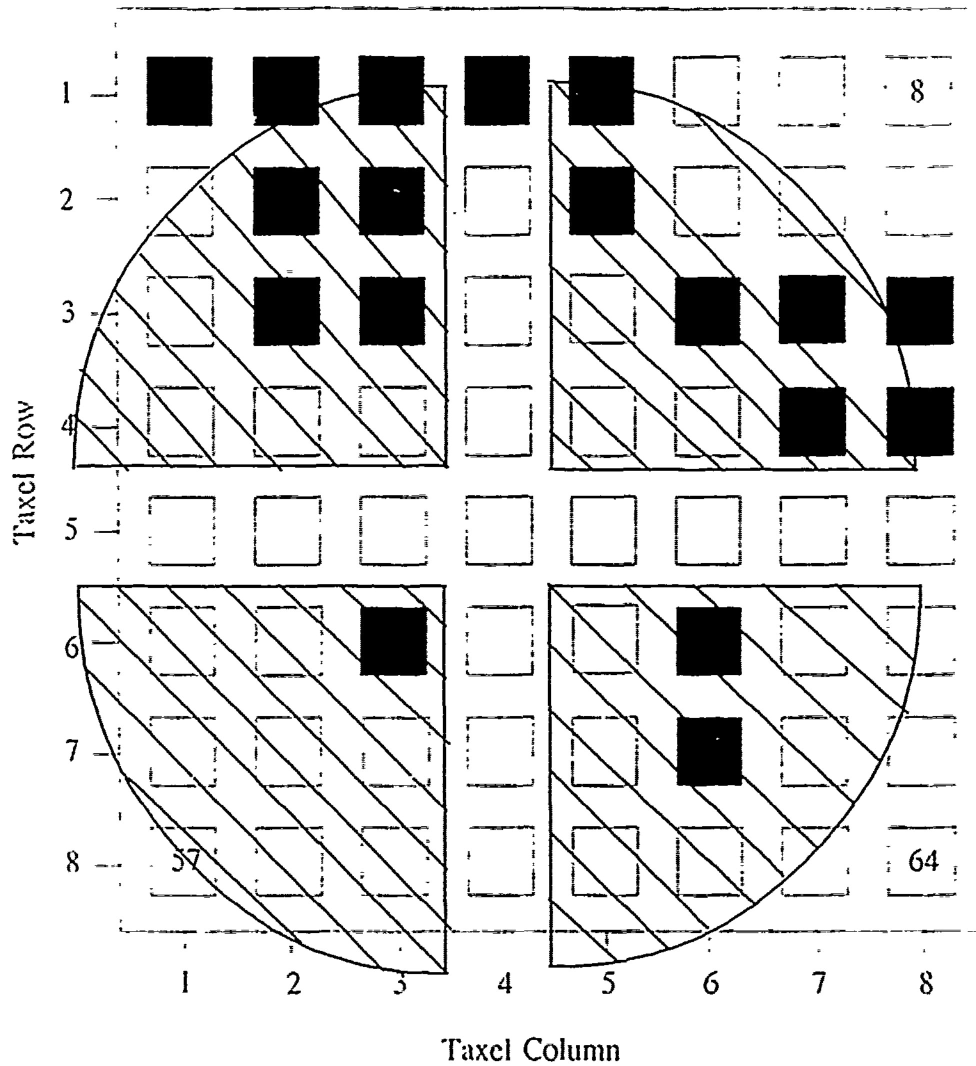

Figure J.24. 0.5-V Threshold Plot Of A 100 g Cross-Slotted Screw Shaped Load - Taxels With An Output Level Above This Threshold Level Are Displayed As Black And Taxels With An Output Level Below This Threshold Level Are Displayed As White.

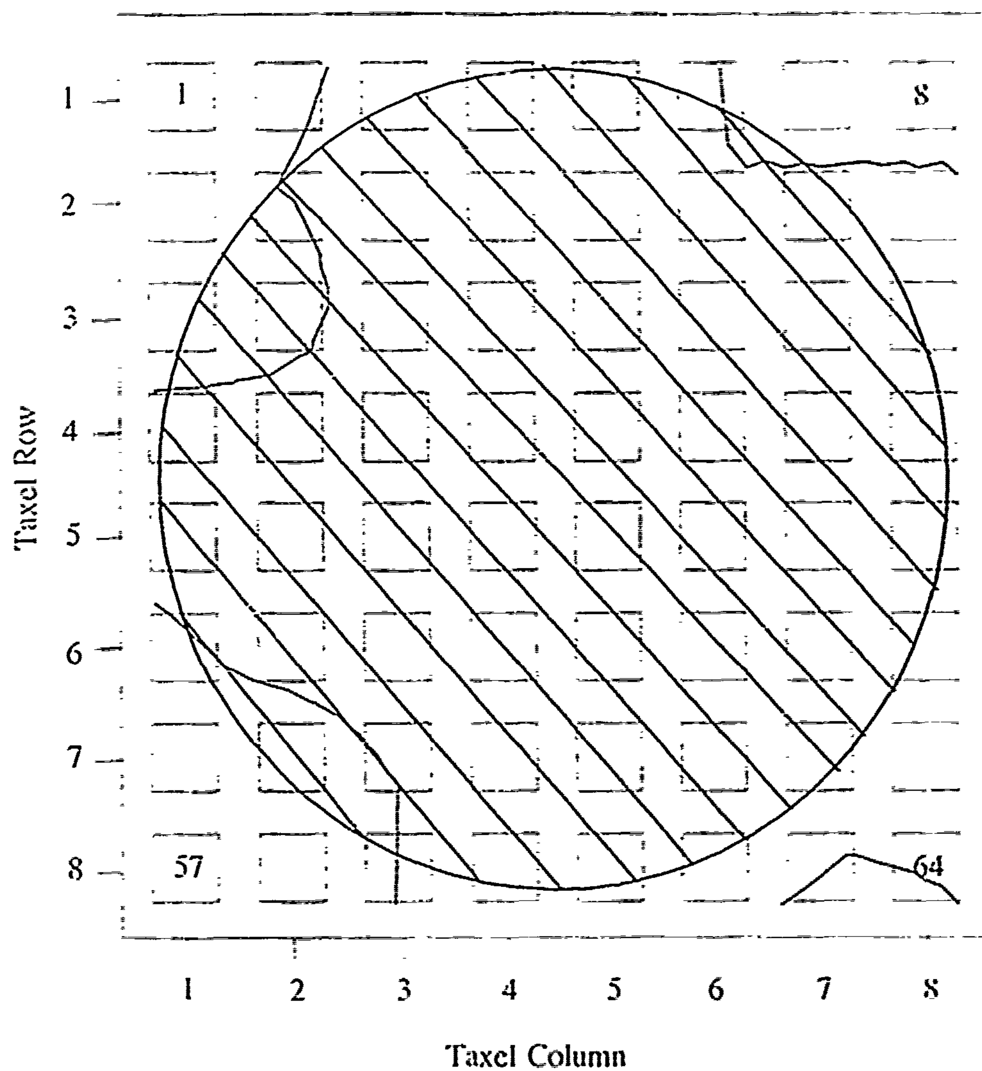

Figure J.25. 0.48-V Equipotential Contour Plot For A 100 g Large Solid Circularly Shaped Load Applied To The Surface Of The Electrode Array.

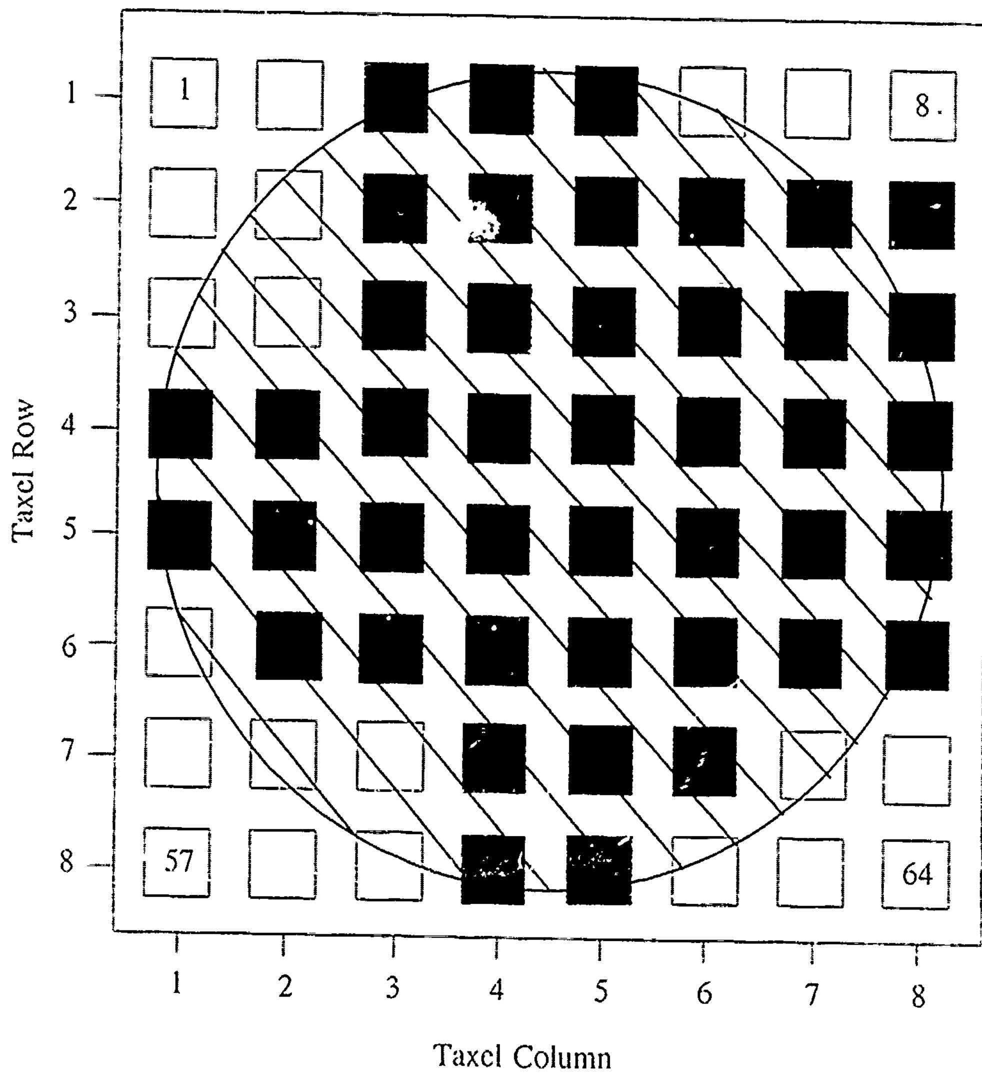

Figure J.26. 0.48-V Threshold Plot Of A 100 g Large Solid Circularly Shaped Load - Taxels With An Output Level Above This Threshold Level Are Displayed As Black And Taxels With An Output Level Below This Threshold Level Are Displayed As White.

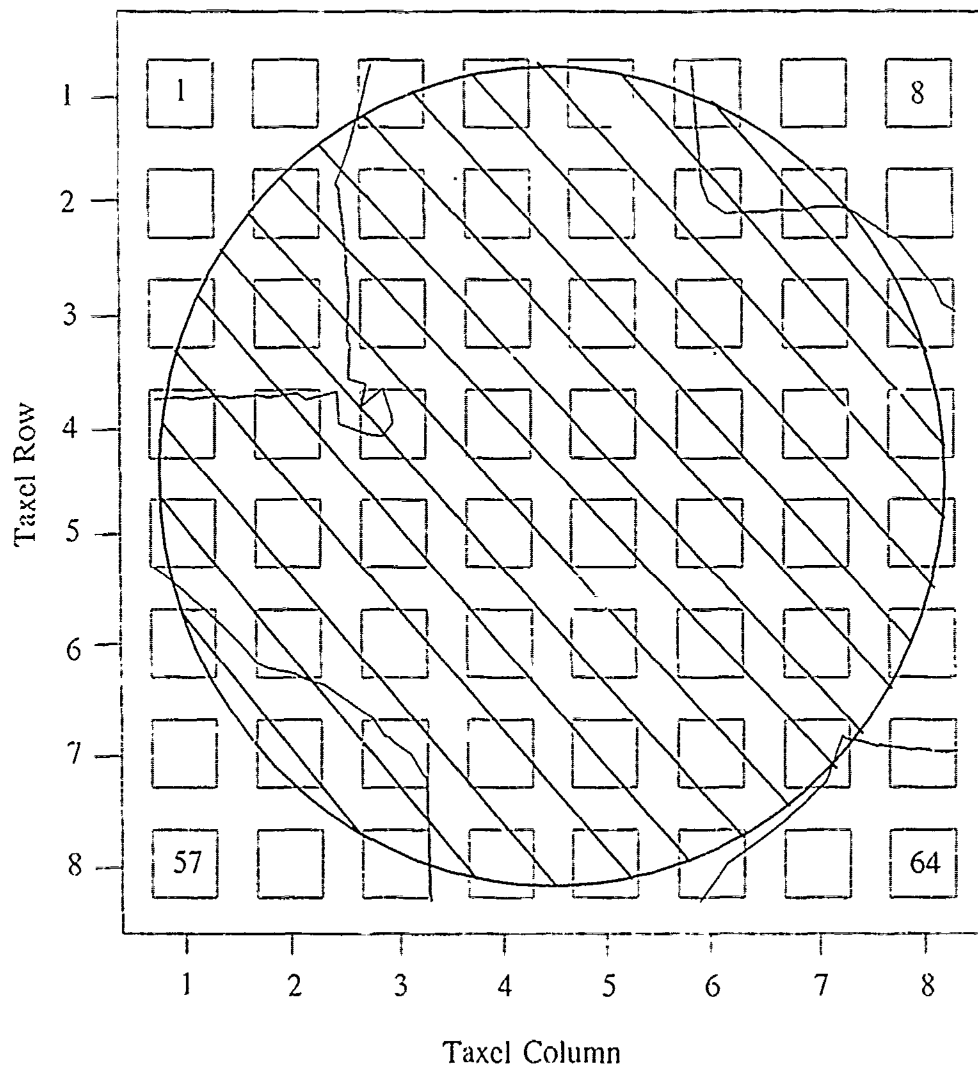

Figure J.27. 0.55-V Equipotential Contour Plot For A 100 g Large Solid Circularly Shaped Load Applied To The Surface Of The Electrode Array.

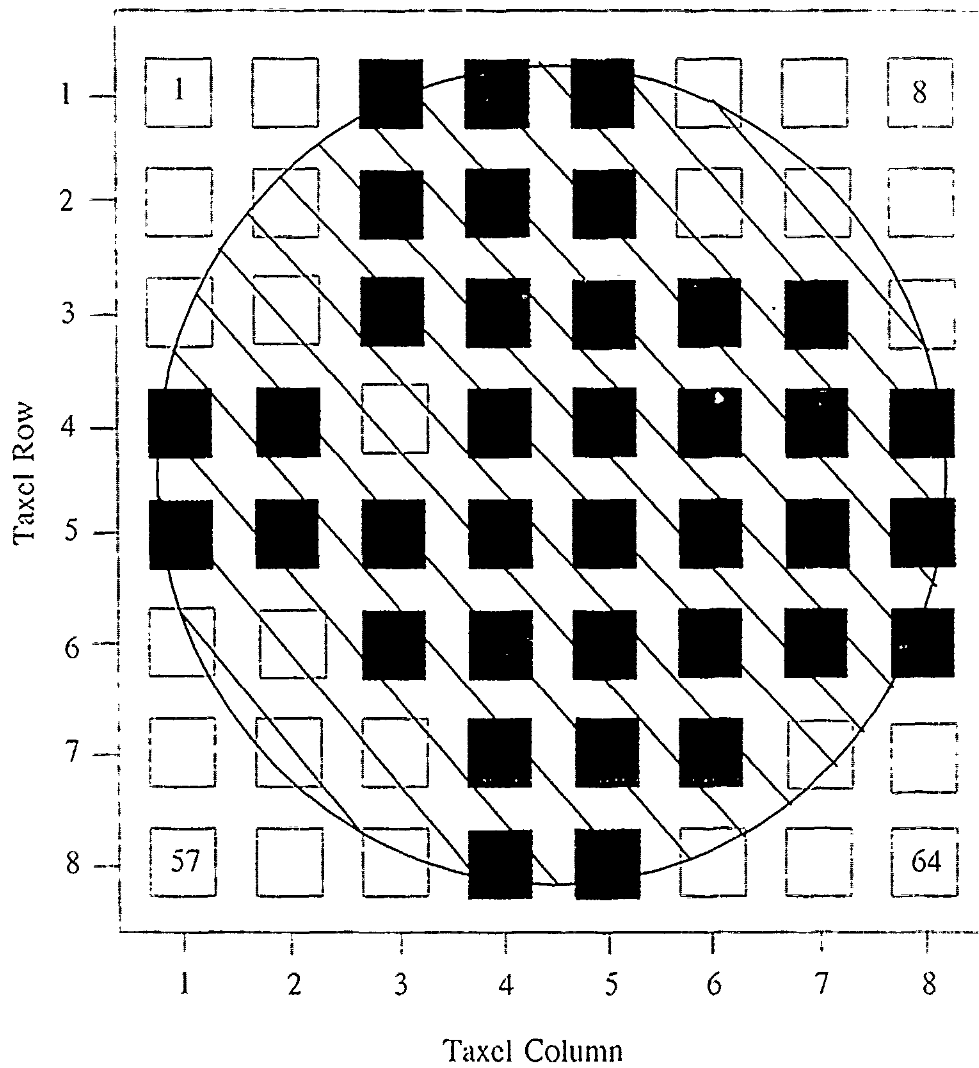

Figure J.28. 0.55-V Threshold Plot Of A 100 g Large Solid Circularly Shaped Load - Taxels With An Output Level Above This Threshold Level Are Displayed As Black And Taxels With An Output Level Below This Threshold Level Are Displayed As White.

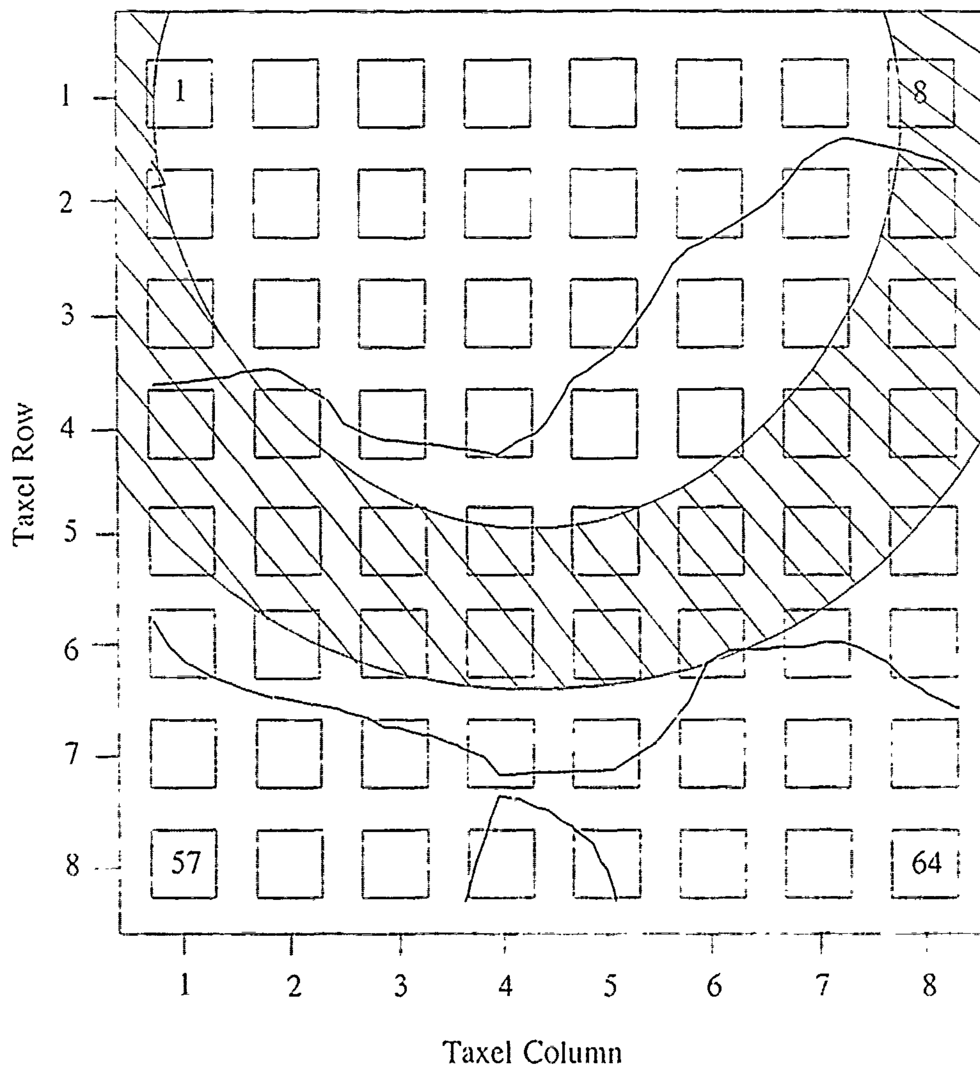

Figure J.29. 0.45-V Equipotential Contour Plot For A 100 g Toroid Shaped Load Applied To The Surface Of The Electrode Array.

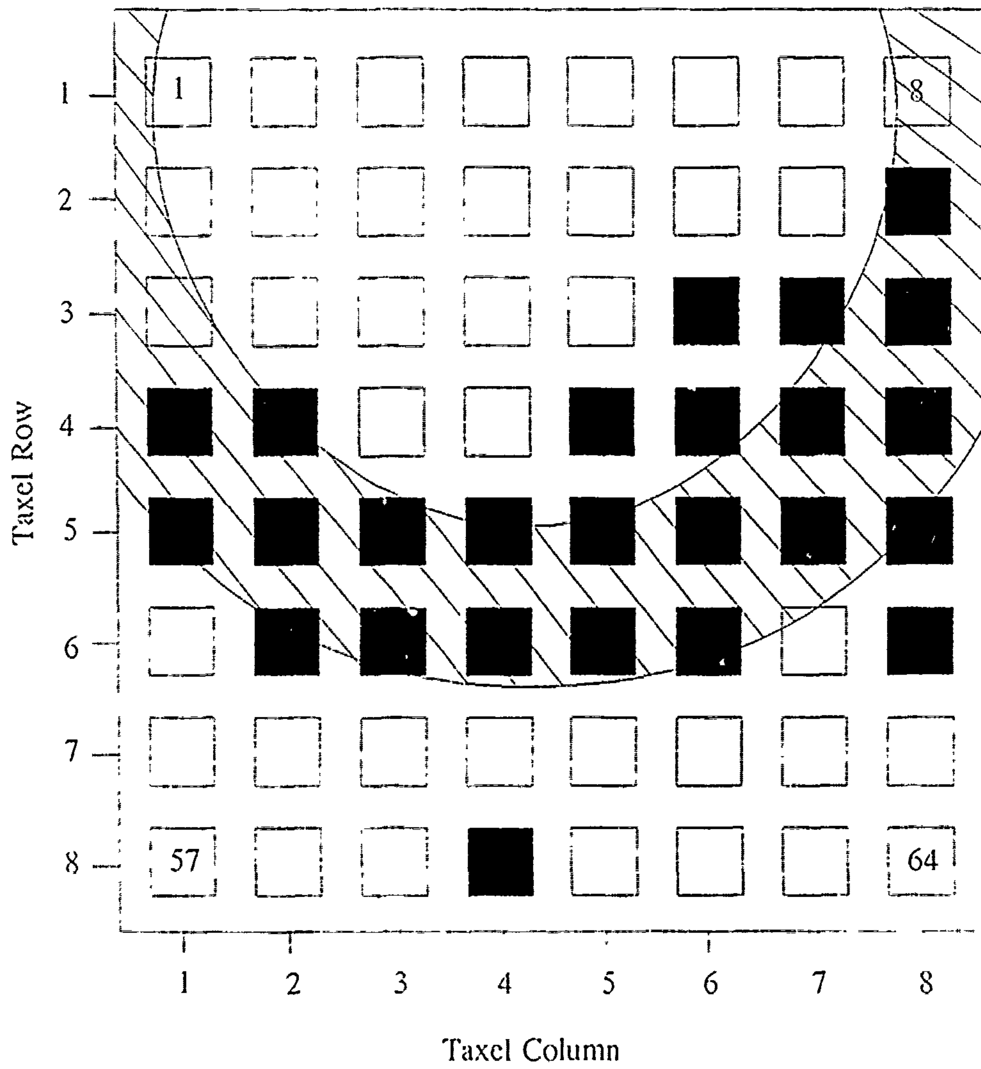

Figure J.30. 0.45-V Threshold Plot Of A 100 g Toroid Shaped Load - Taxels With An Output Level Above This Threshold Level Are Displayed As Black And Taxels With An Output Level Below This Threshold Level Are Displayed As White.

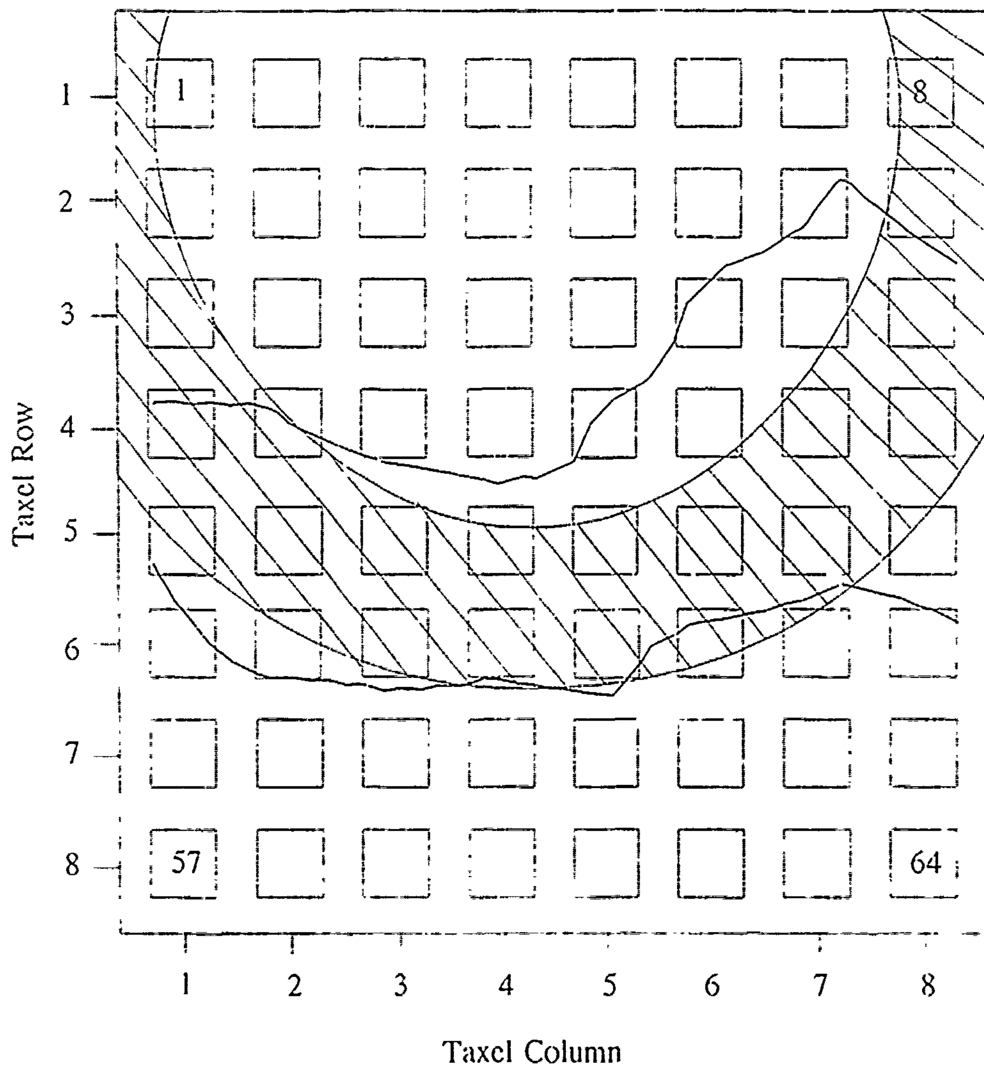

Figure J.31. 0.55-V Equipotential Contour Plot For A 100 g Toroid Shaped Load Applied To The Surface Of The Electrode Array.

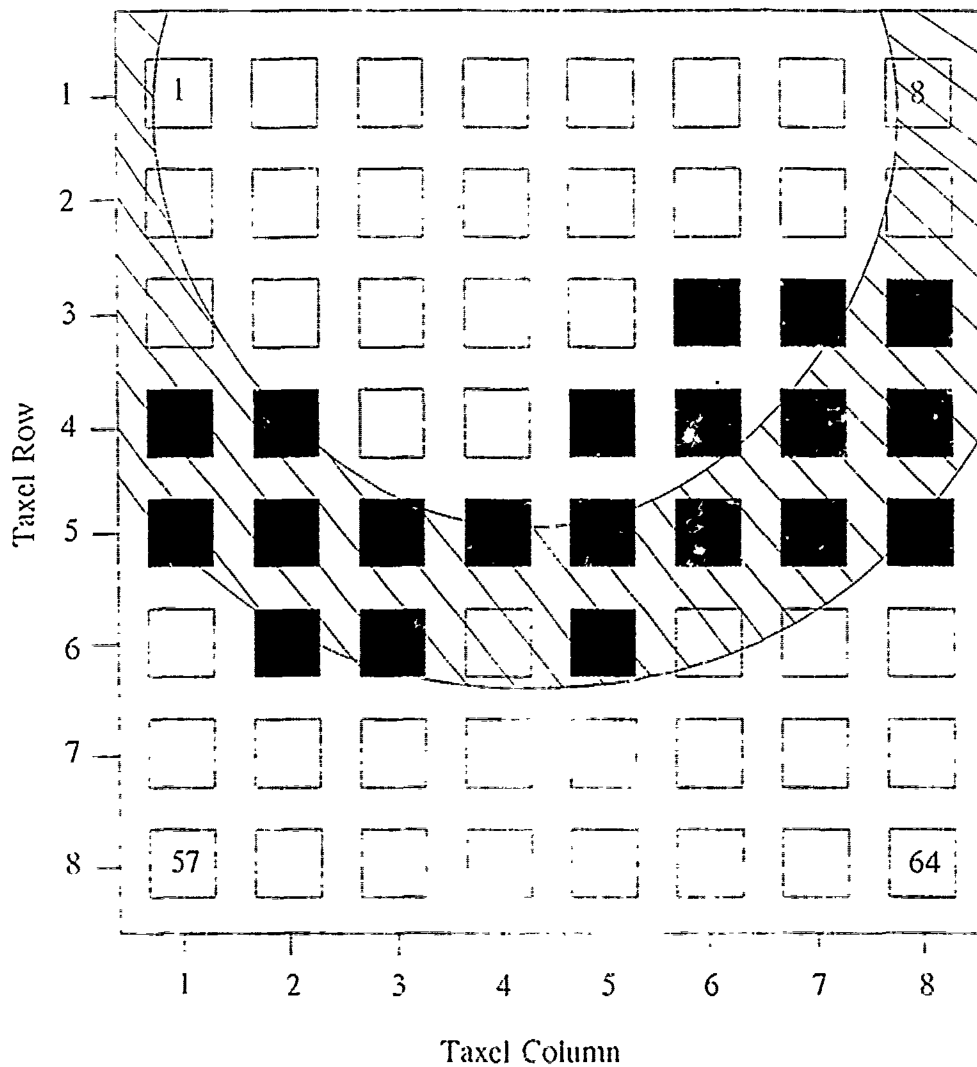

Figure J.32. 0.55-V Threshold Plot Of A 100 g Toroid Shaped Load - Taxels With An Output Level Above This Threshold Level Are Displayed As Black And Taxels With An Output Level Below This Threshold Level Are Displayed As White.

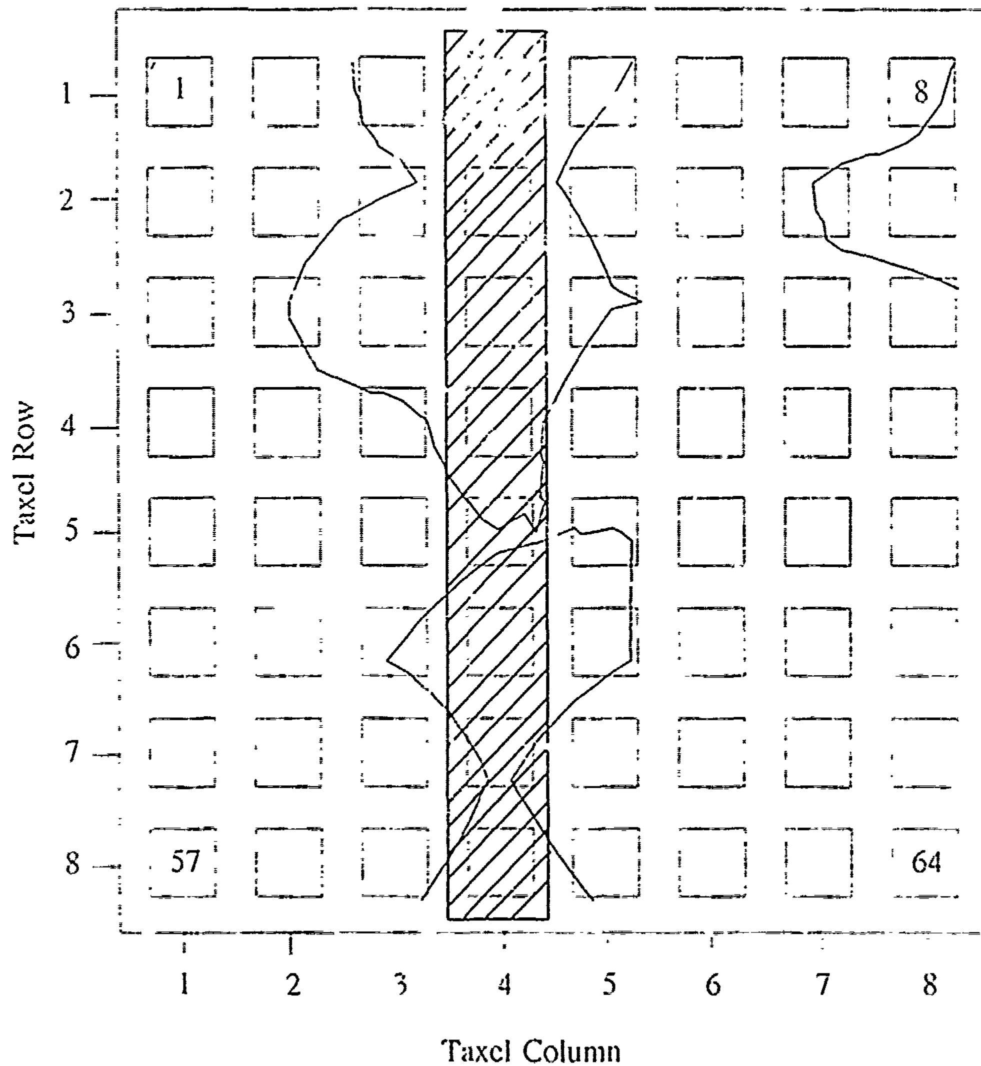

Figure J.33. 0.54-V Equipotential Contour Plot For A 100 g Sharp Edge Shaped Load Applied To The Surface Of The Electrode Array - The Sensor Was Fabricated Using A Polyimide Adhesive.

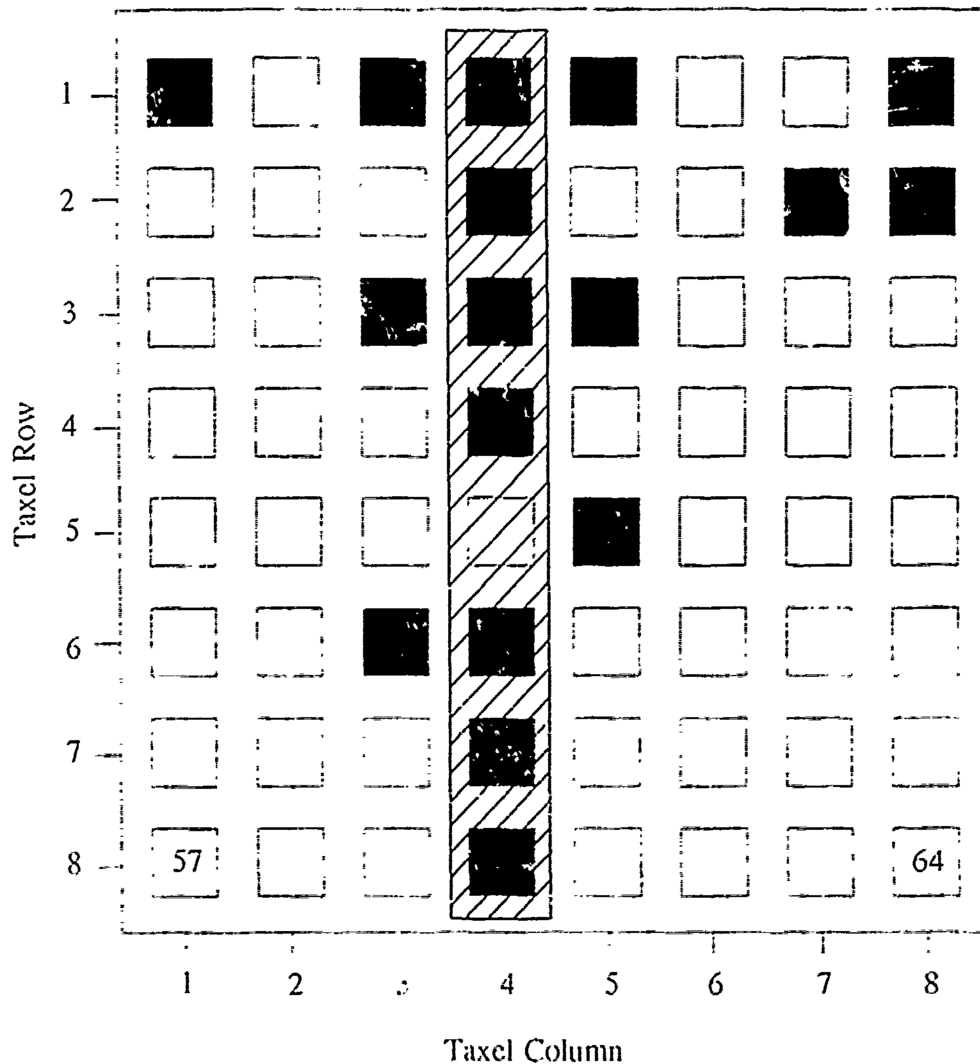

Figure J.34. 0.54-V Threshold Plot Of A 100 g Sharp Edge Shaped Load - Taxels With An Output Level Above This Threshold Level Are Displayed As Black And Taxels With An Output Level Below This Threshold Level Are Displayed As White - The Sensor Was Fabricated Using A Polyimide Adhesive.

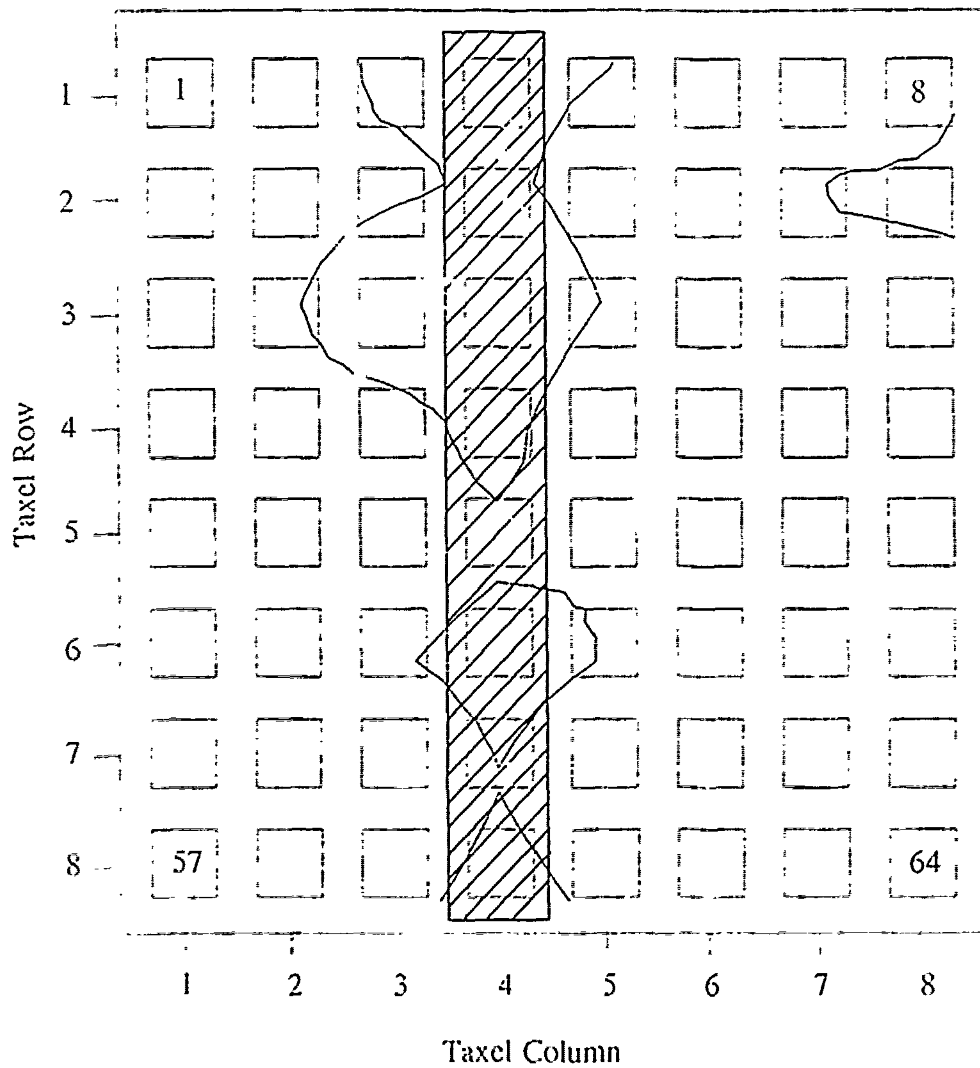

Figure J.35. 0.6-V Equipotential Contour Plot For A 100 g Sharp Edge Shaped Load Applied To The Surface Of The Electrode Array - The Sensor Was Fabricated Using A Polyimide Adhesive.

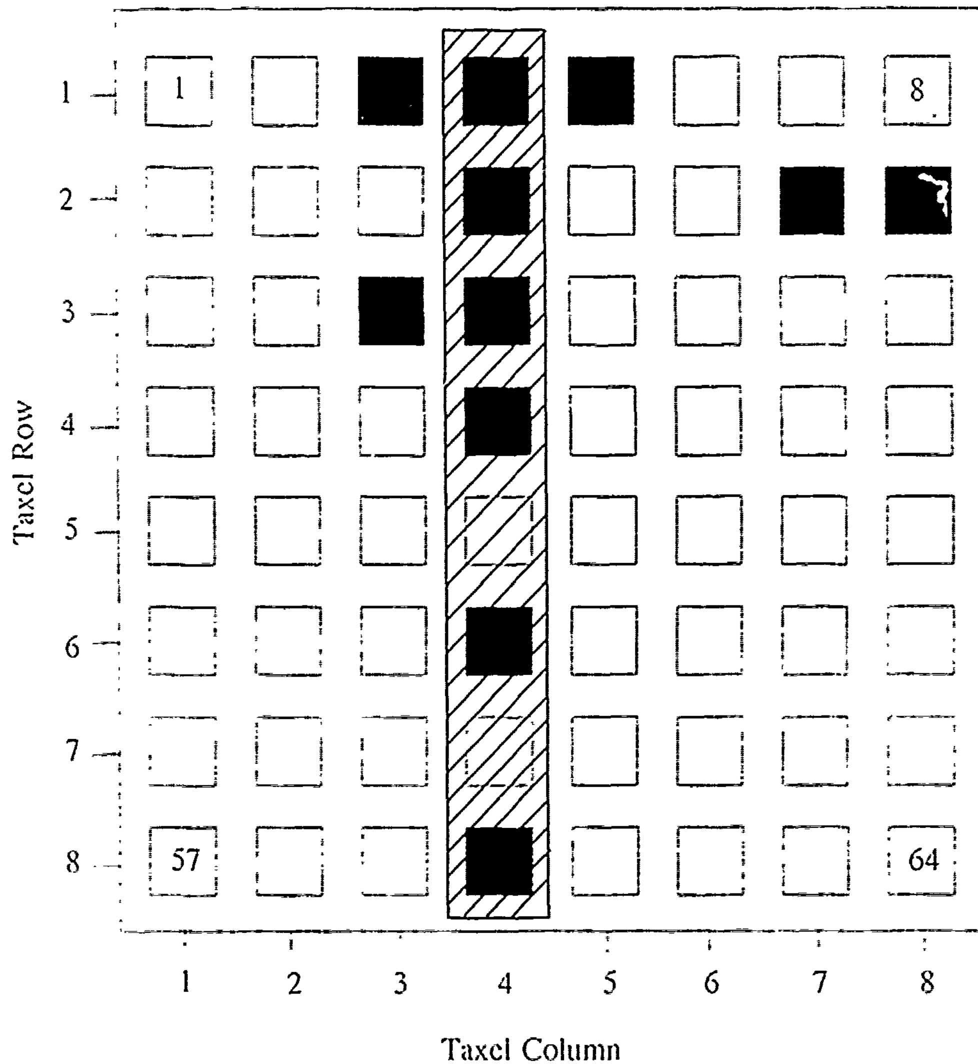

Figure J.36. 0.6-V Threshold Plot Of A 100 g Sharp Edge Shaped Load – Taxels With An Output Level Above This Threshold Level Are Displayed As Black And Taxels With An Output Level Below This Threshold Level Are Displayed As White – The Sensor Was Fabricated Using A Polyimide Adhesive.

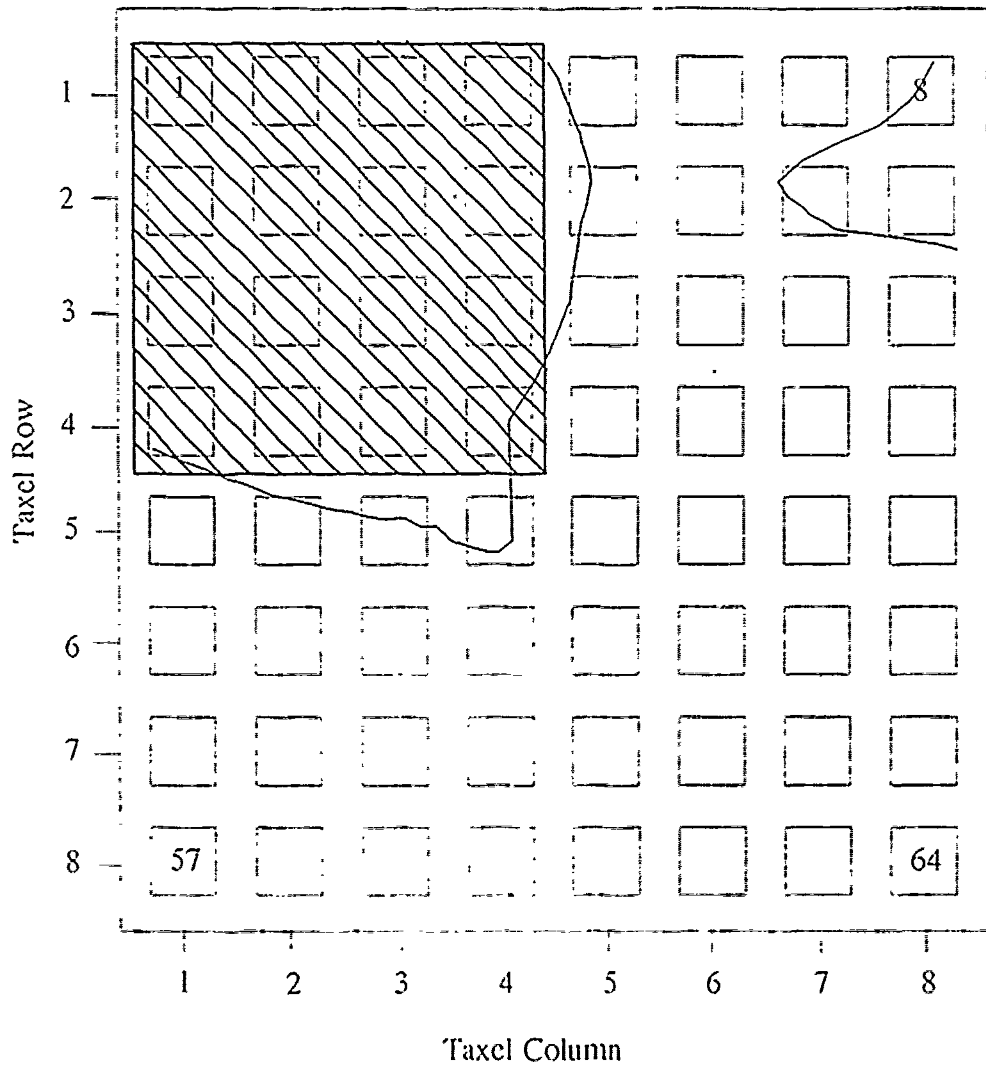

Figure J.37. 0.55-V Equipotential Contour Plot For A 100 g Small Square Shaped Load Applied To The Surface Of The Electrode Array - The Sensor Was Fabricated Using A Polyimide Adhesive.

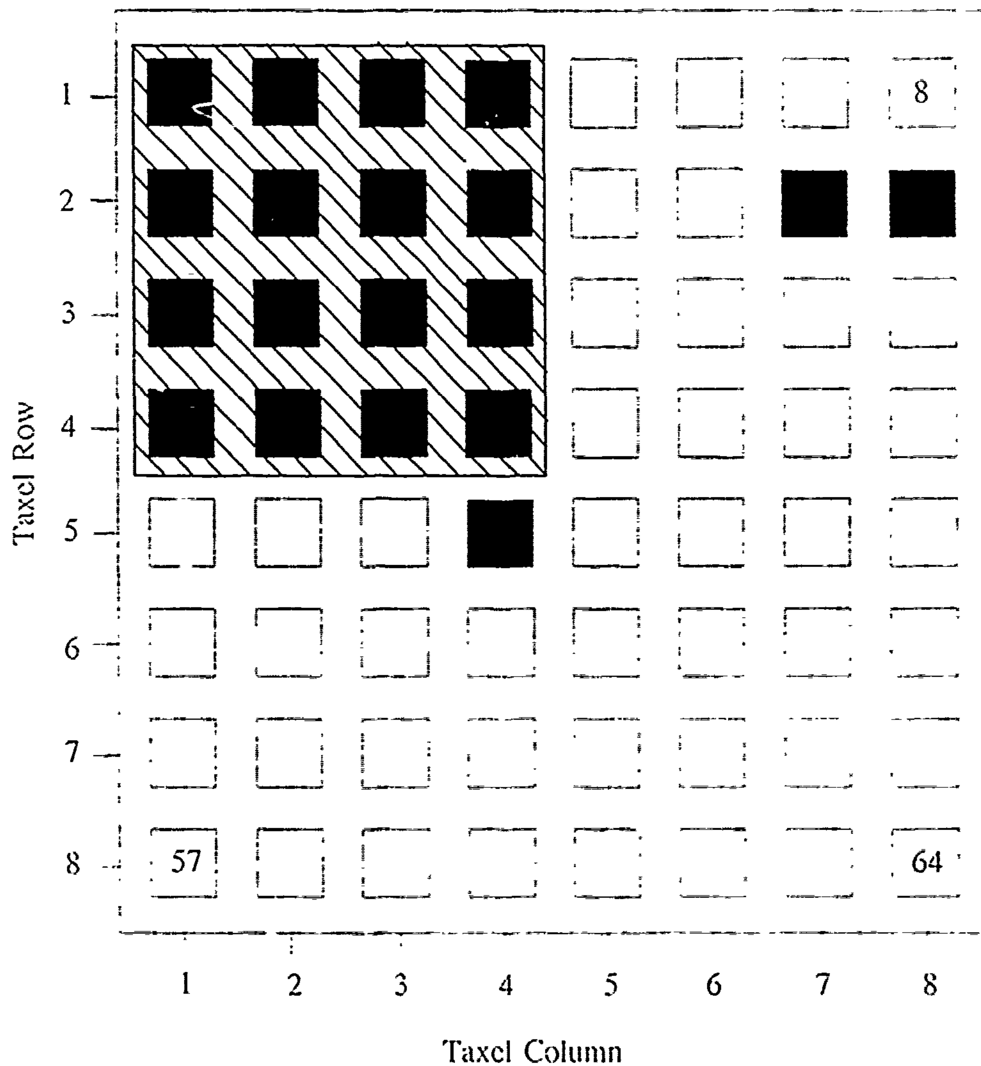

Figure J.38. 0.55-V Threshold Plot Of A 100 g Small Square Shaped Load. Taxels With An Output Level Above This Threshold Level Are Displayed As Black And Taxels With An Output Level Below This Threshold Level Are Displayed As White - The Sensor Was Fabricated Using A Polyimide Adhesive.

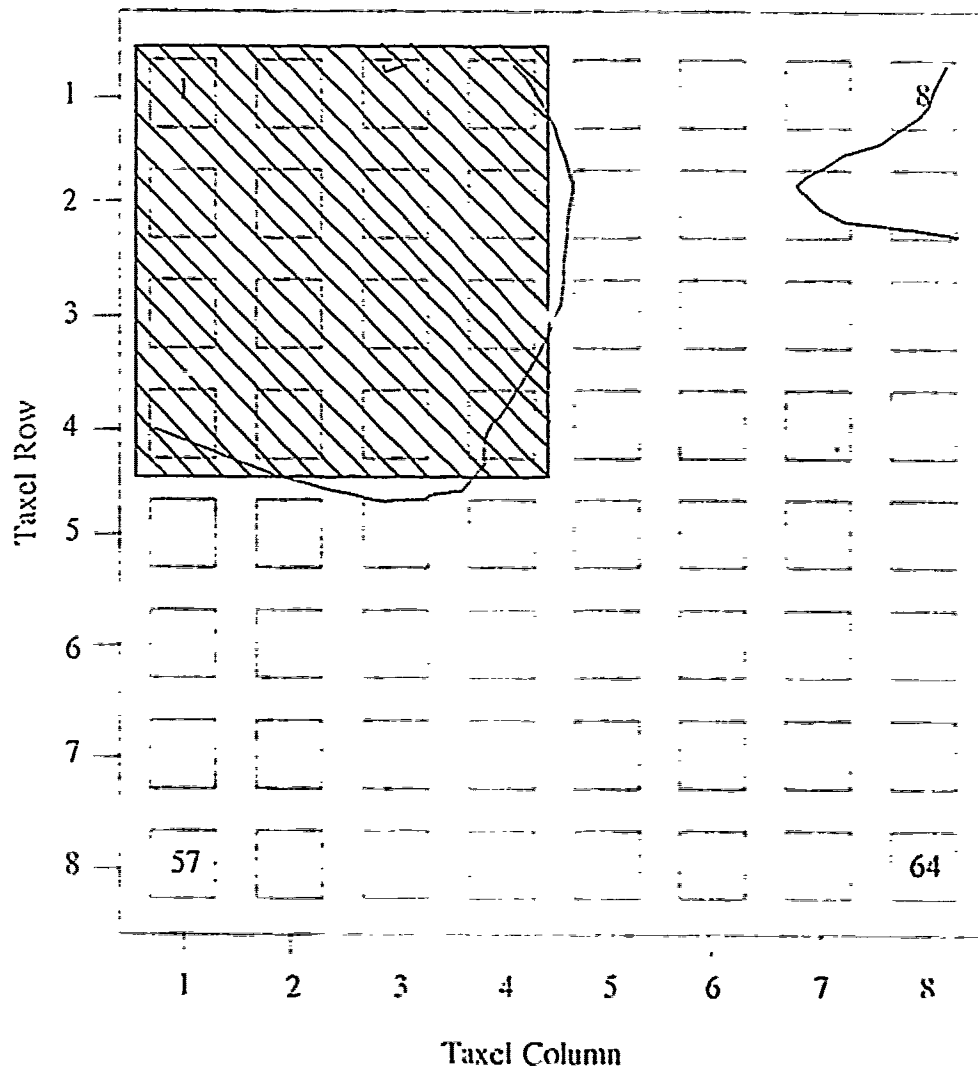

Figure J.39. 0.58-V Equipotential Contour Plot For A 100 g Small Square Shaped Load Applied To The Surface Of The Electrode Array - The Sensor Was Fabricated Using A Polyimide Adhesive.

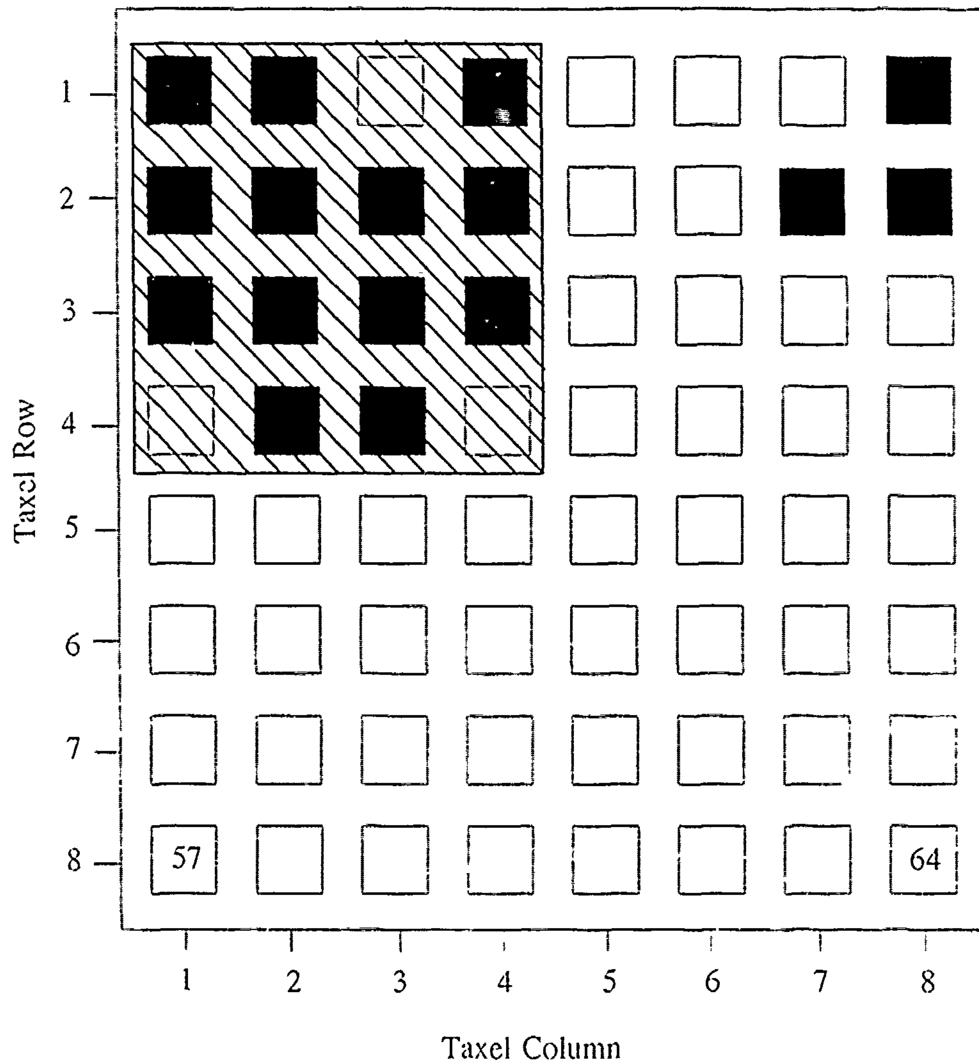

Figure J.40. 0.58-V Threshold Plot Of A 100 g Small Square Shaped Load - Taxels With An Output Level Above This Threshold Level Are Displayed As Black And Taxels With An Output Level Below This Threshold Level Are Displayed As White - The Sensor Was Fabricated Using A Polyimide Adhesive.

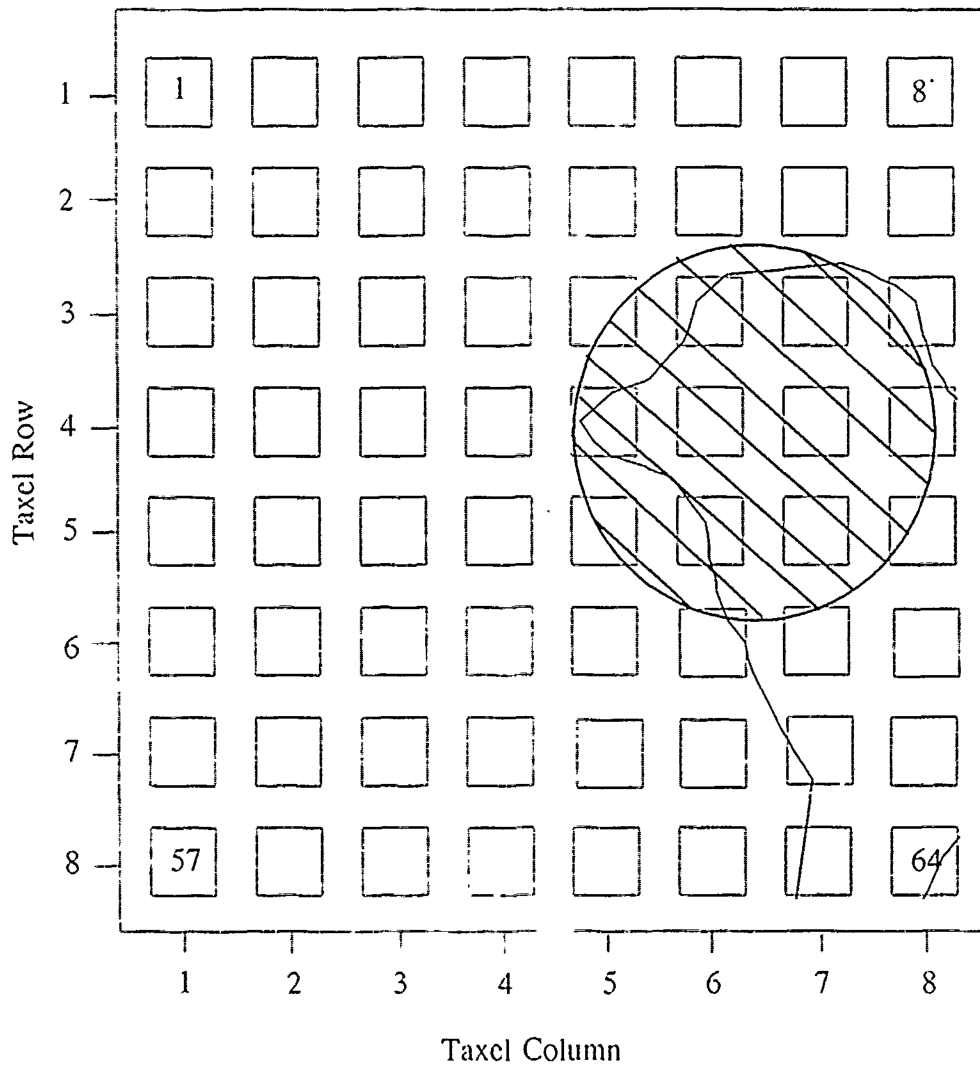

Figure J.41. 0.76-V Equipotential Contour Plot For A 100 g Small Circularly Shaped Load Applied To The Surface Of The Electrode Array - The Sensor Was Fabricated Using A Polyimide Adhesive.

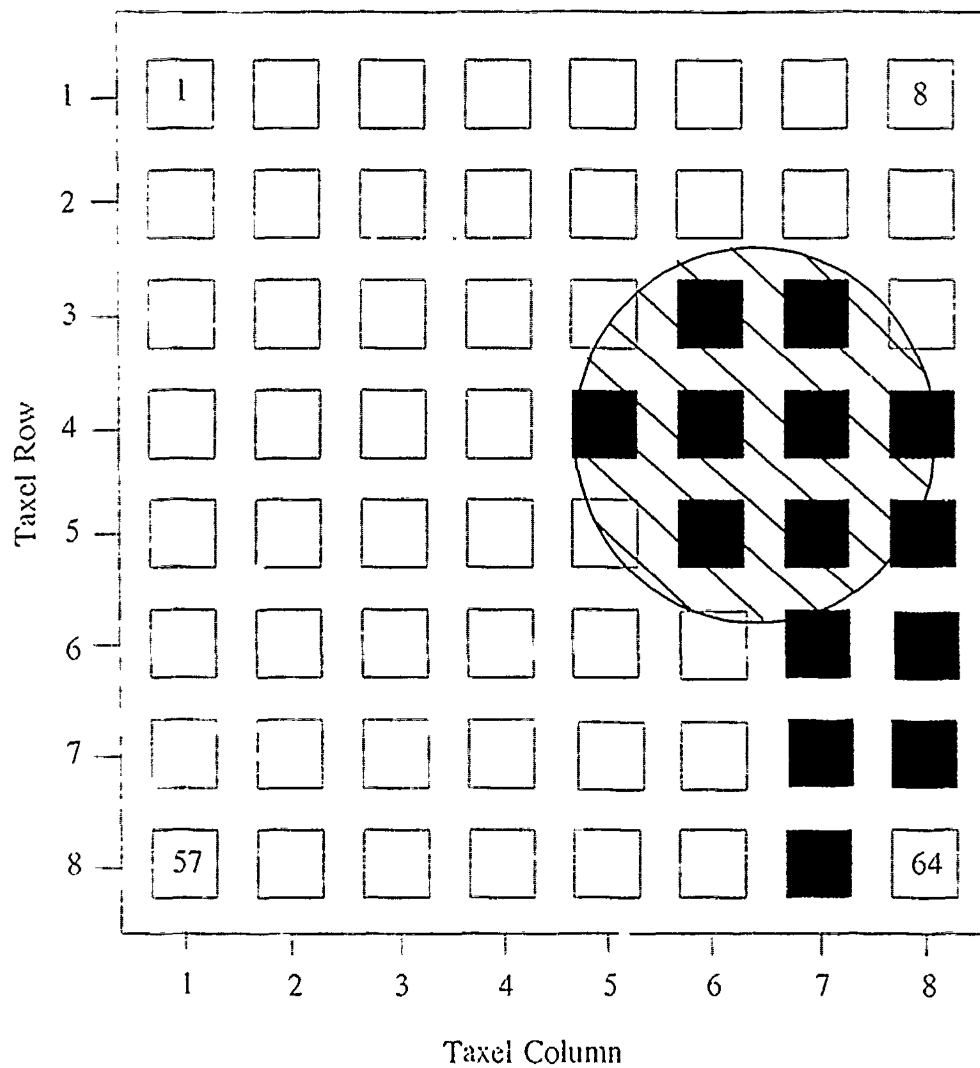

Figure J.42. 0.76-V Threshold Plot Of A 100 g Small Circularly Shaped Load - Taxels With An Output Level Above This Threshold Level Are Displayed As Black And Taxels With An Output Level Below This Threshold Level Are Displayed As White - The Sensor Was Fabricated Using A Polyimide Adhesive.

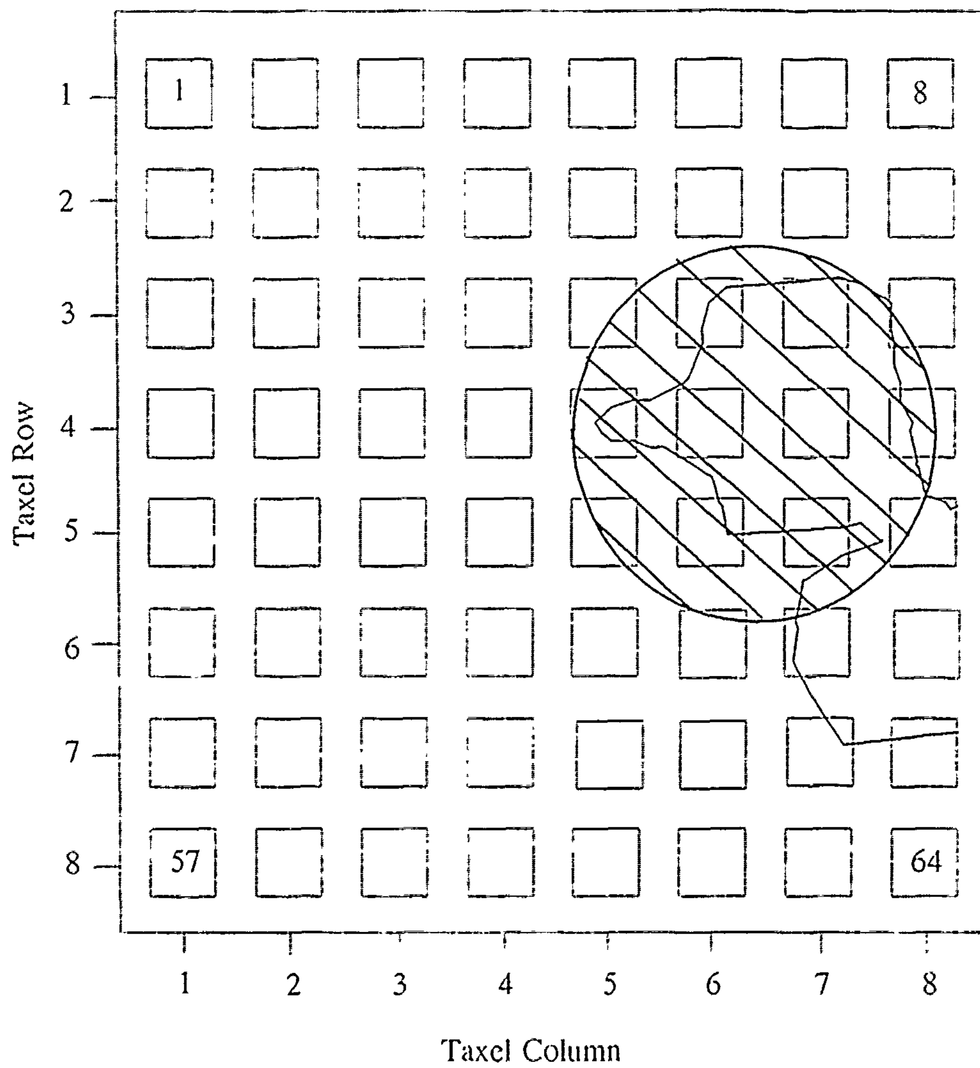

Figure J.43. 0.84-V Equipotential Contour Plot For A 100 g Small Circularly Shaped Load Applied To The Surface Of The Electrode Array - The Sensor Was Fabricated Using A Polyimide Adhesive.

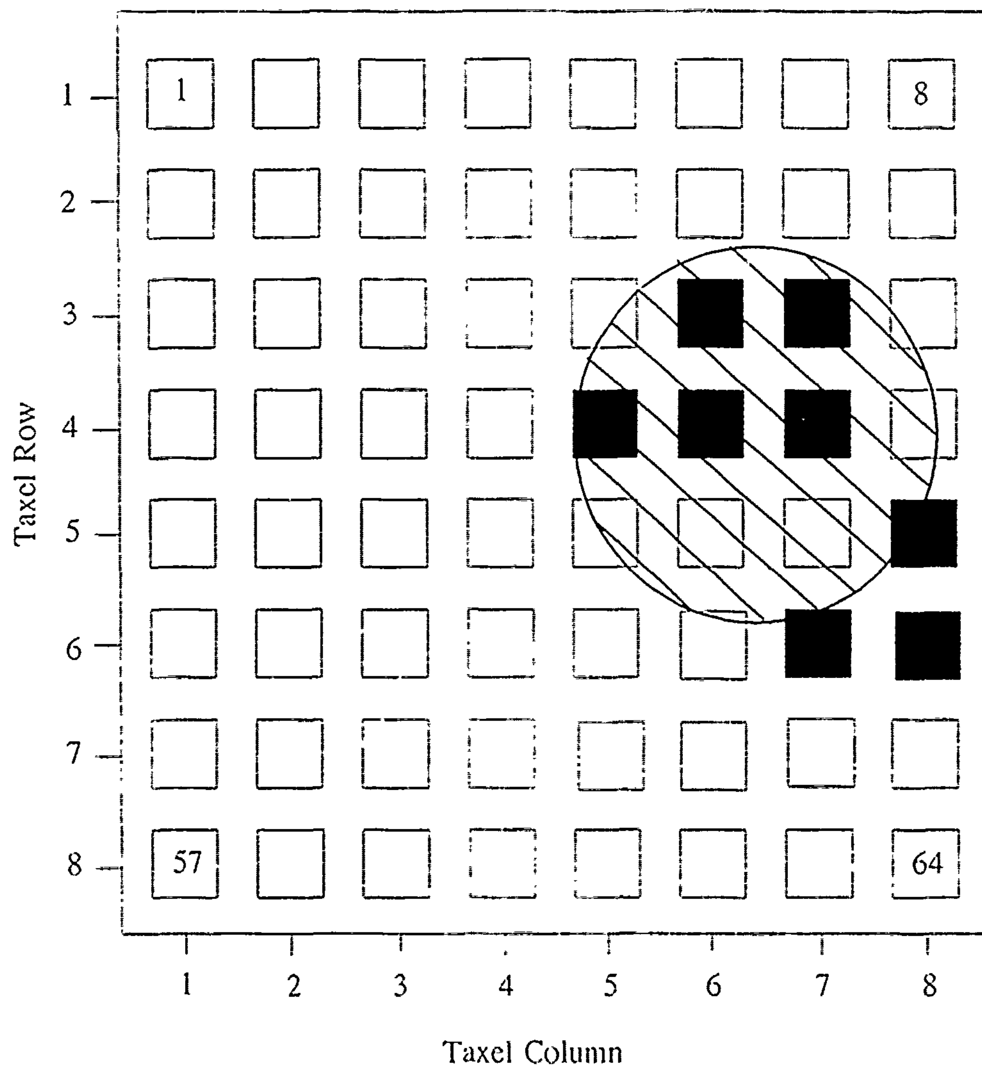

Figure J.44. 0.84-V Threshold Plot Of A 100 g Small Circularly Shaped Load - Taxels With An Output Level Above This Threshold Level Are Displayed As Black And Taxels With An Output Level Below This Threshold Level Are Displayed As White - The Sensor Was Fabricated Using A Polyimide Adhesive.

Appendix K. *Response of the Sensor to Several Different Weights*

The following pages illustrate the sensor's ability to sense the shape of the load applied to the surface of the tactile sensor IC for several different load weights. The figures provided include one set of plots for 75 g, 50 g, and 10 g loac' for the sharp edge, small square, and small circle. The position of the load is the same as the position of the load presented in Chapter VI.

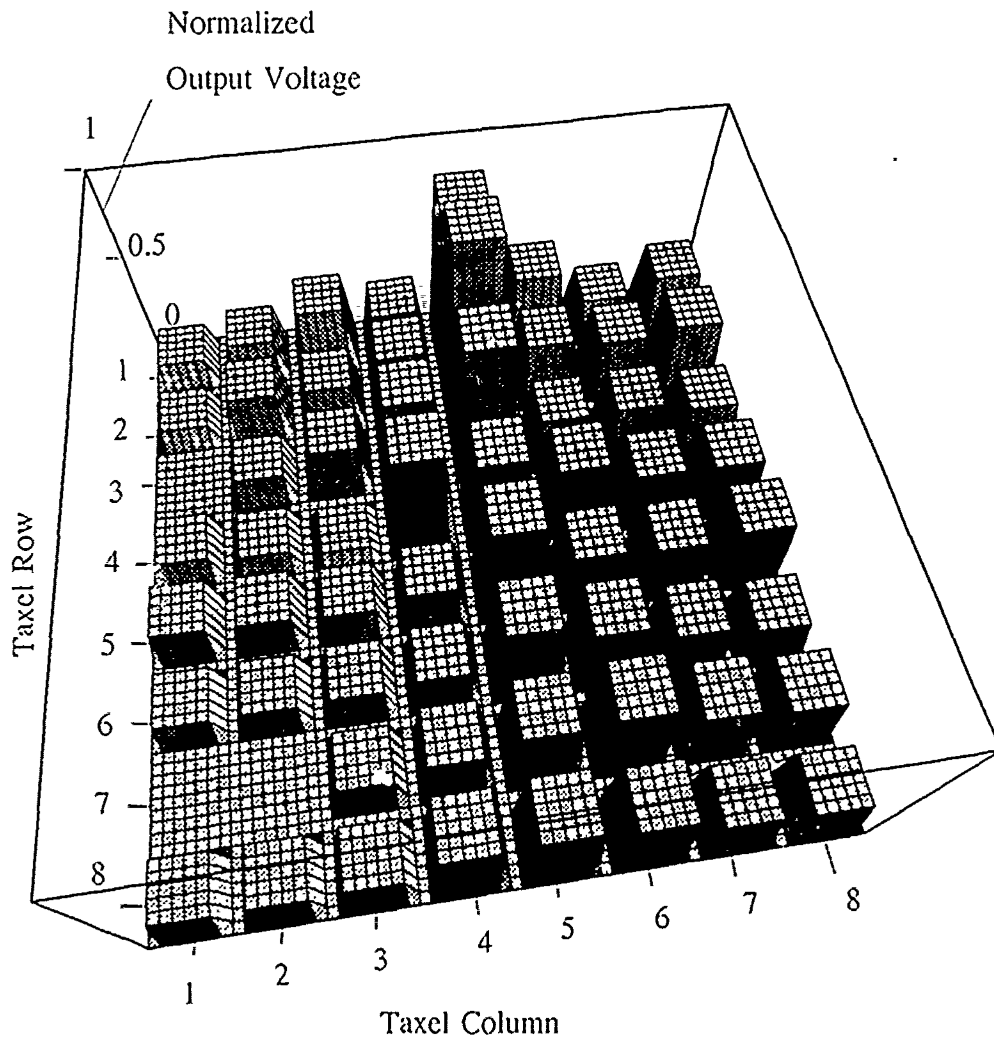

Figure K.1. Three-Dimensional Representation Of A Sharp Edge Shaped Load Applied To The Surface Of The Electrode Array. The z-Axis Corresponds To The Normalized Difference Between The Sensor's Loaded And Unloaded States. And The x- And y-Axes Correspond To the Electrode Columns And Rows, Respectively.

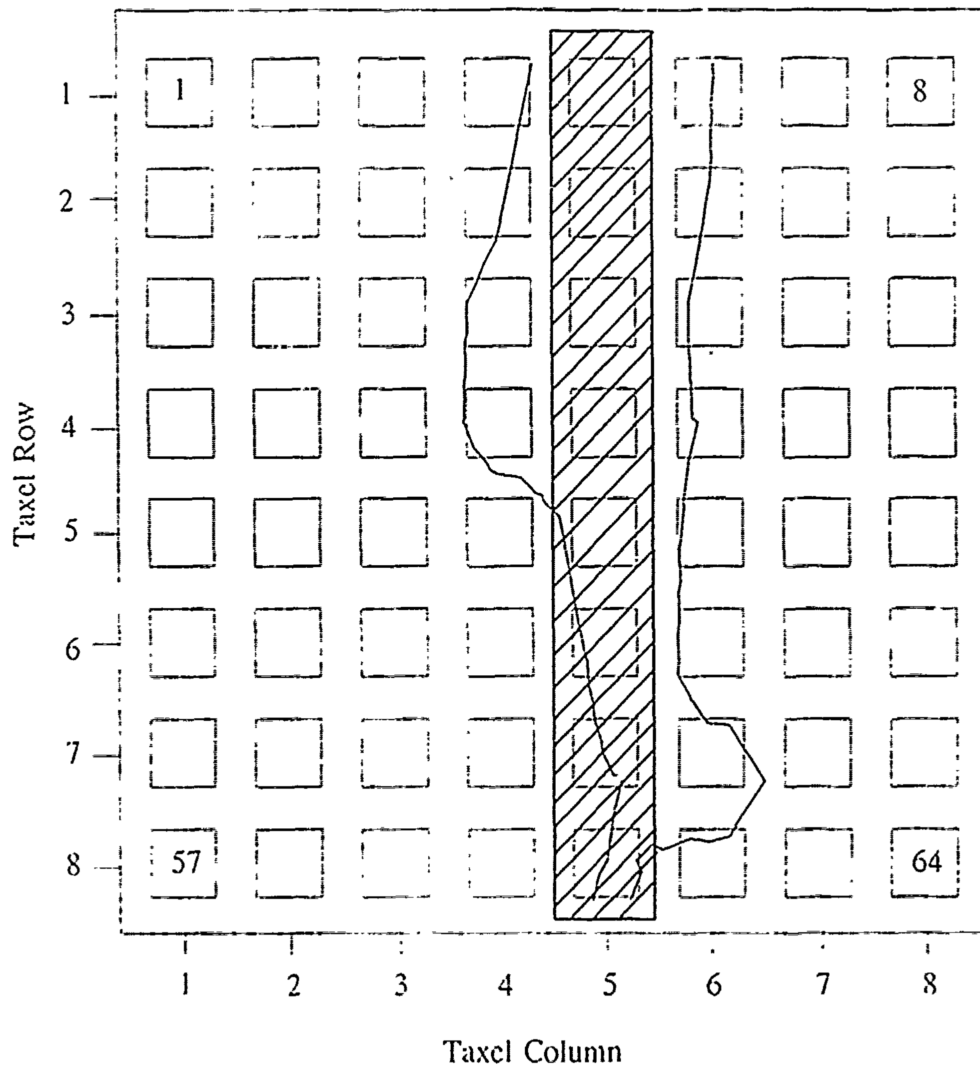

Figure K.2. 0.47-V Equipotential Contour Plot For A 75 g Sharp Edge Shaped Load Applied To The Surface Of The Electrode Array.

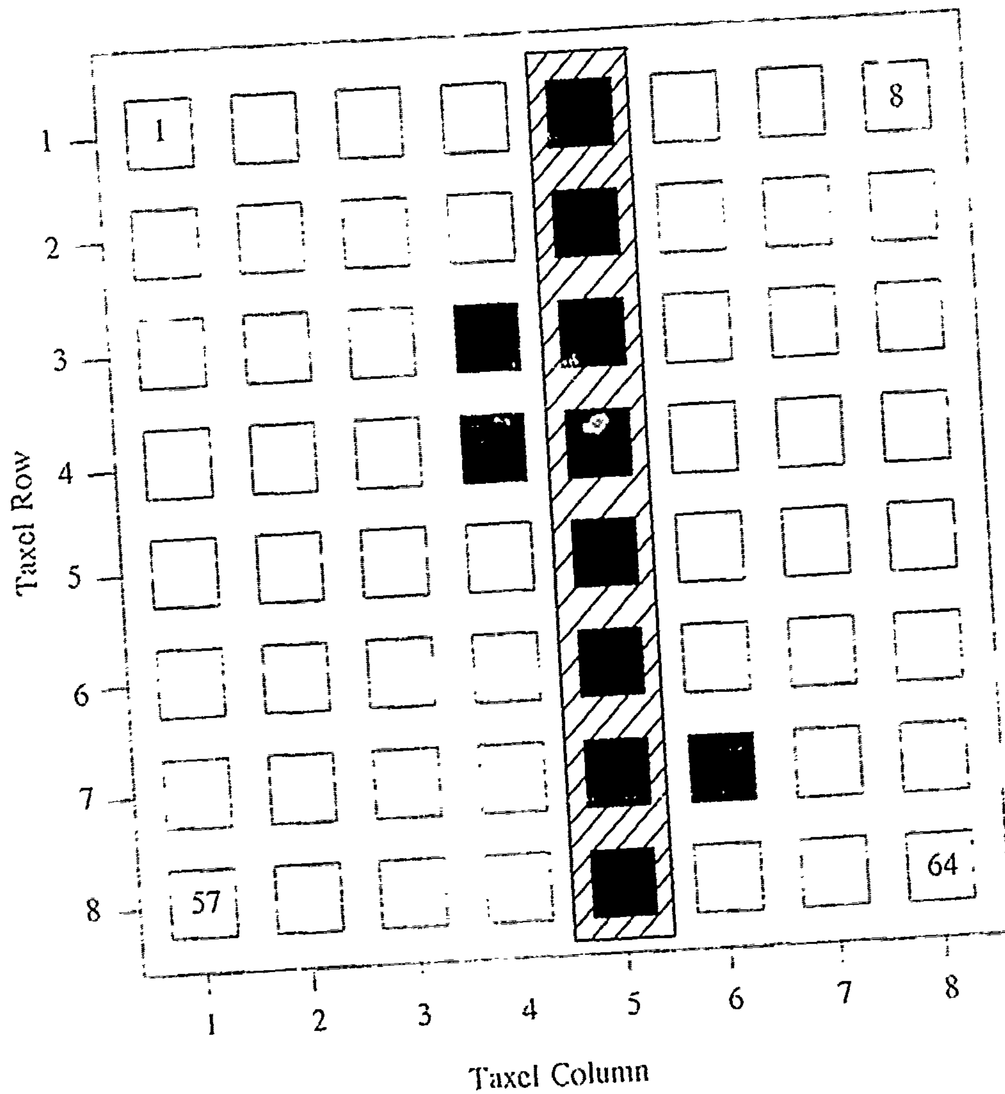

Figure K.3. 0.47-V Threshold Plot Of A 75 g Sharp Edge Shaped Load – Taxels With An Output Level Above This Threshold Level Are Displayed As Black And Taxels With An Output Level Below This Threshold Level Are Displayed As White.

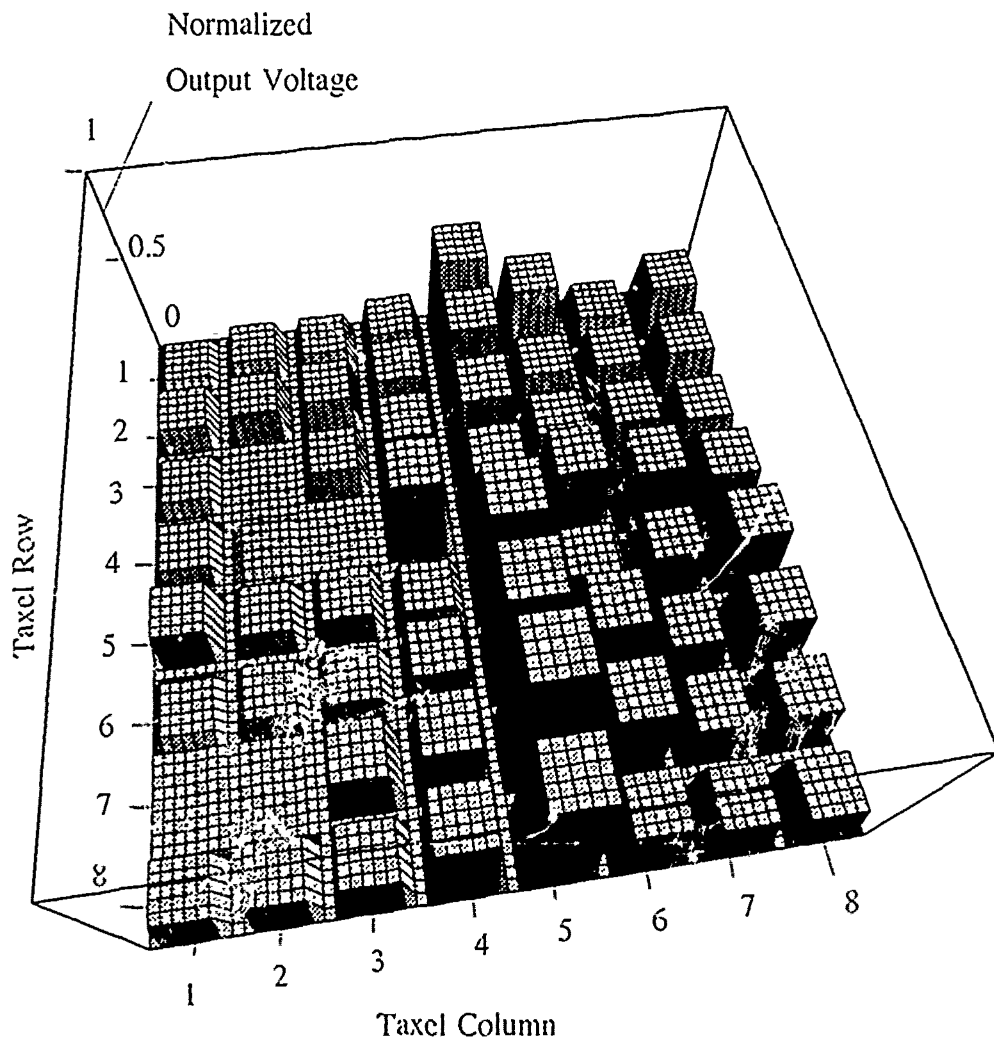

Figure K.4. Three-Dimensional Representation Of A Sharp Edge Shaped Load Applied To The Surface Of The Electrode Array. The z-Axis Corresponds To The Normalized Difference Between The Sensor's Loaded And Unloaded States. And The x- And y-Axes Correspond To the Electrode Columns And Rows, Respectively.

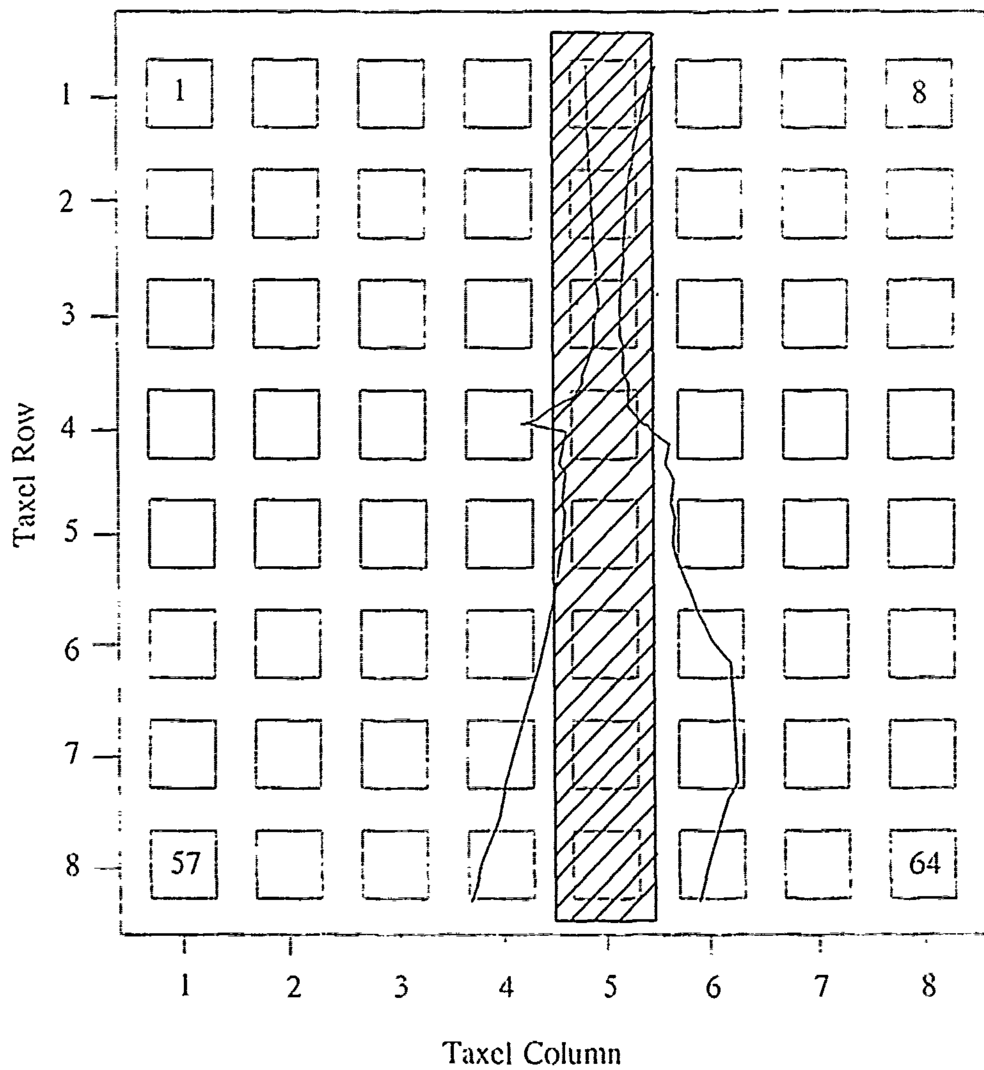

Figure K.5. 0.52-V Equipotential Contour Plot For A 50 g Sharp Edge Shaped Load Applied To The Surface Of The Electrode Array.

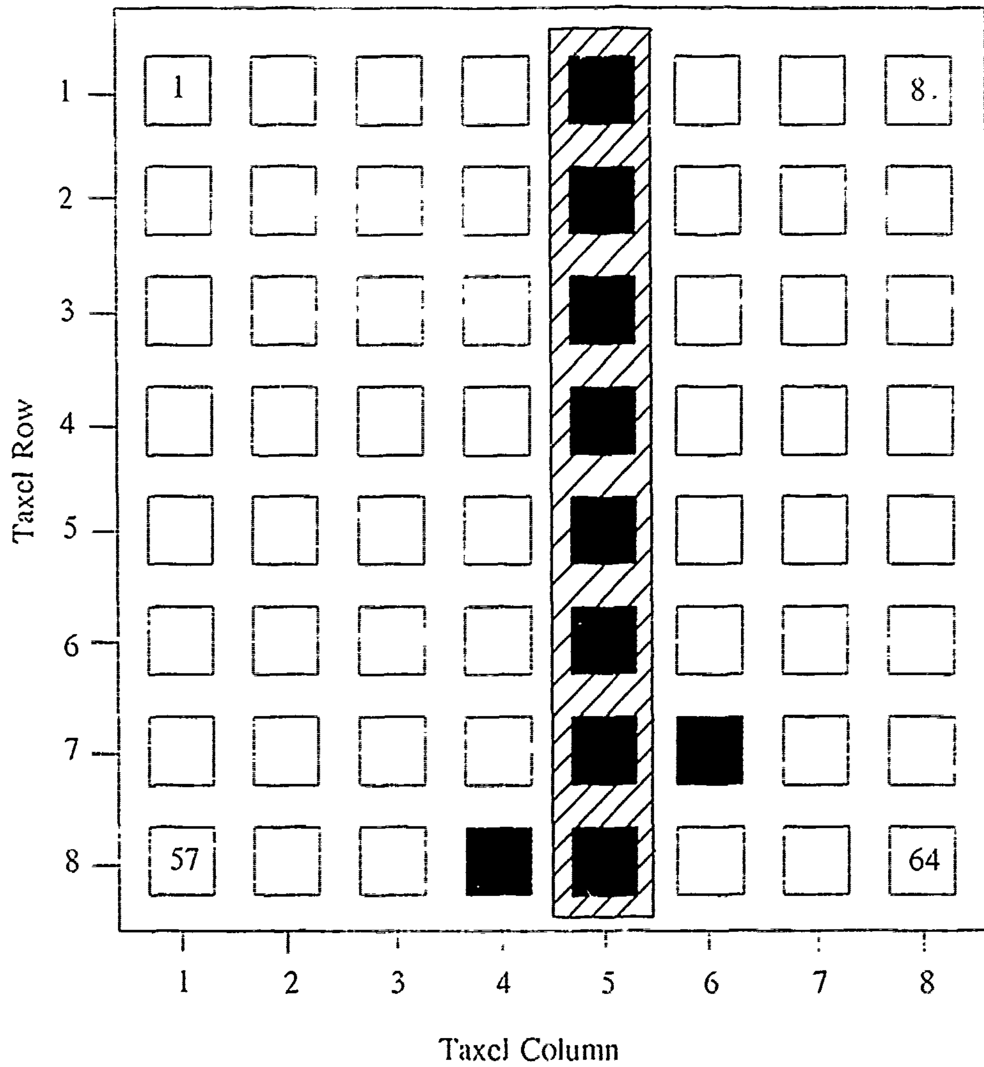

Figure K.6. 0.52-V Threshold Plot Of A 50 g Sharp Edge Shaped Load - Taxels With An Output Level Above This Threshold Level Are Displayed As Black And Taxels With An Output Level Below This Threshold Level Are Displayed As White.

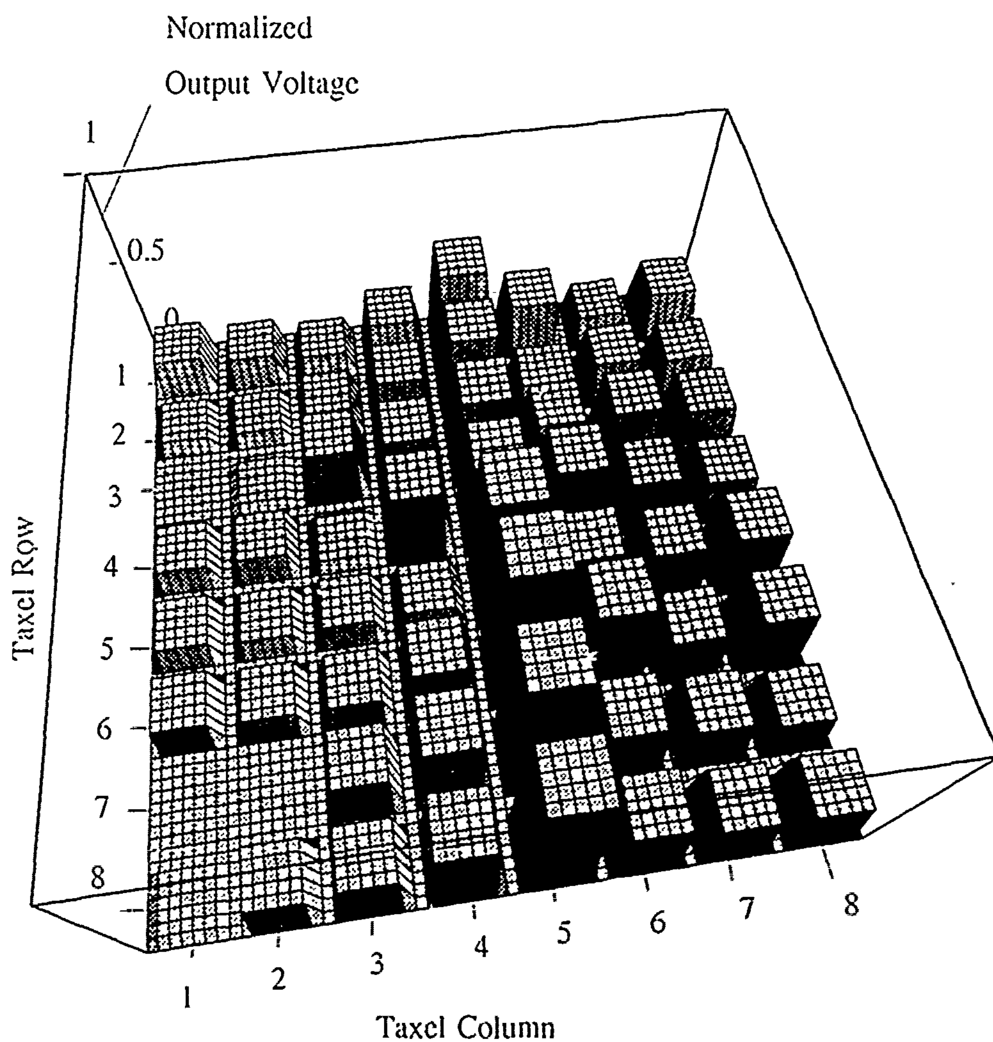

Figure K.7. Three-Dimensional Representation Of A Sharp Edge Shaped Load Applied To The Surface Of The Electrode Array. The z-Axis Corresponds To The Normalized Difference Between The Sensor's Loaded And Unloaded States. And The x- And y-Axes Correspond To the Electrode Columns And Rows, Respectively.

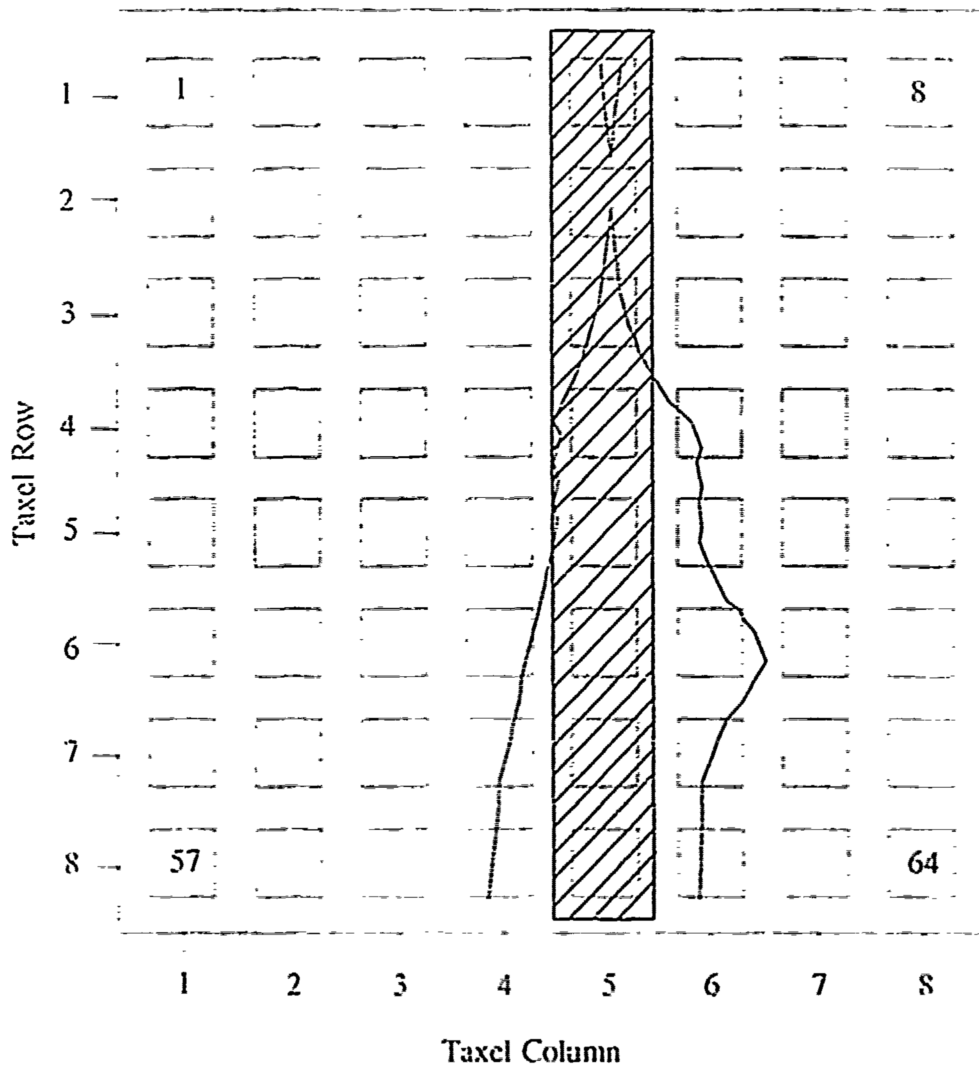

Figure K.8. 0.5-V Equipotential Contour Plot For A 10 g Sharp Edge Shaped Load Applied To The Surface Of The Electrode Array.

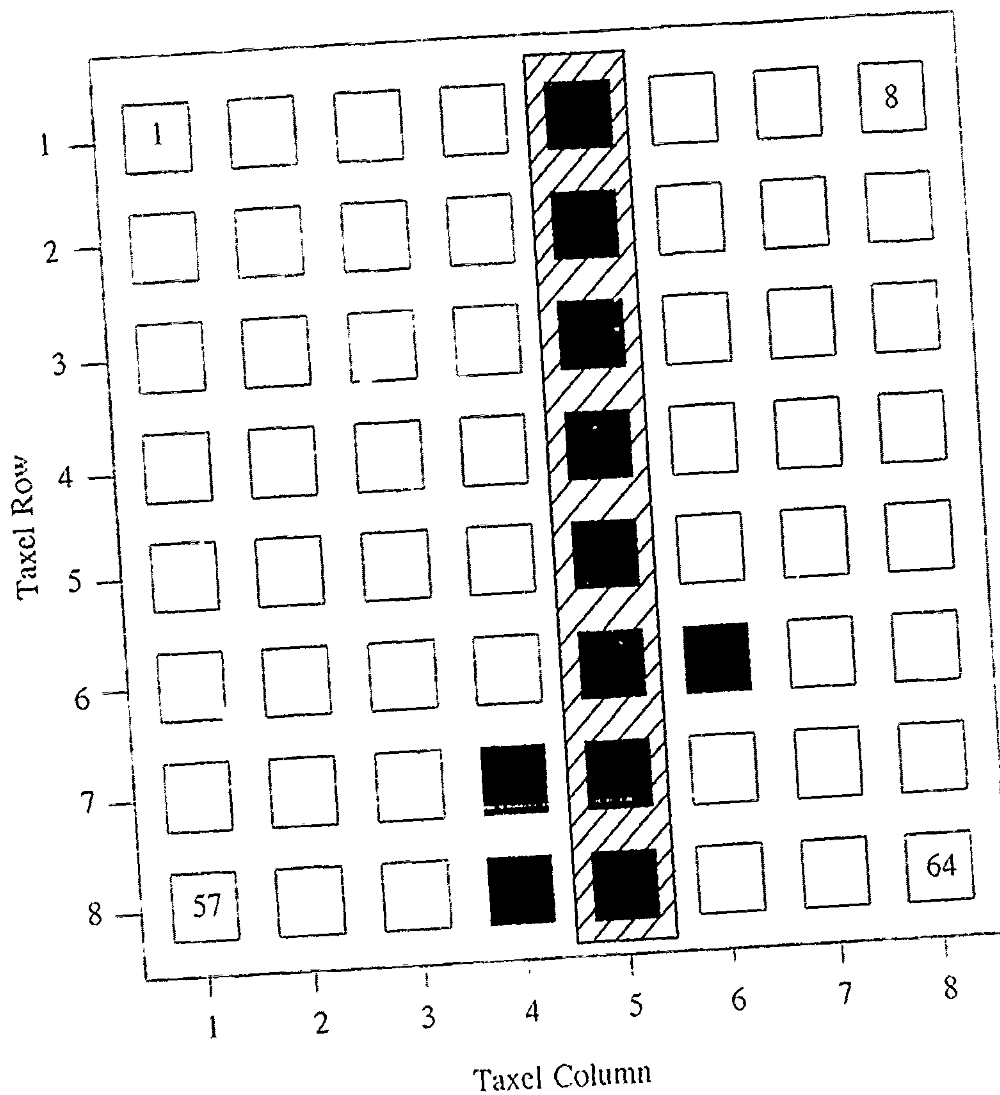

Figure K.9. 0.5-V Threshold Plot Of A 10 g Sharp Edge Shaped Load – Taxels With An Output Level Above This Threshold Level Are Displayed As Black And Taxels With An Output Level Below This Threshold Level Are Displayed As White.

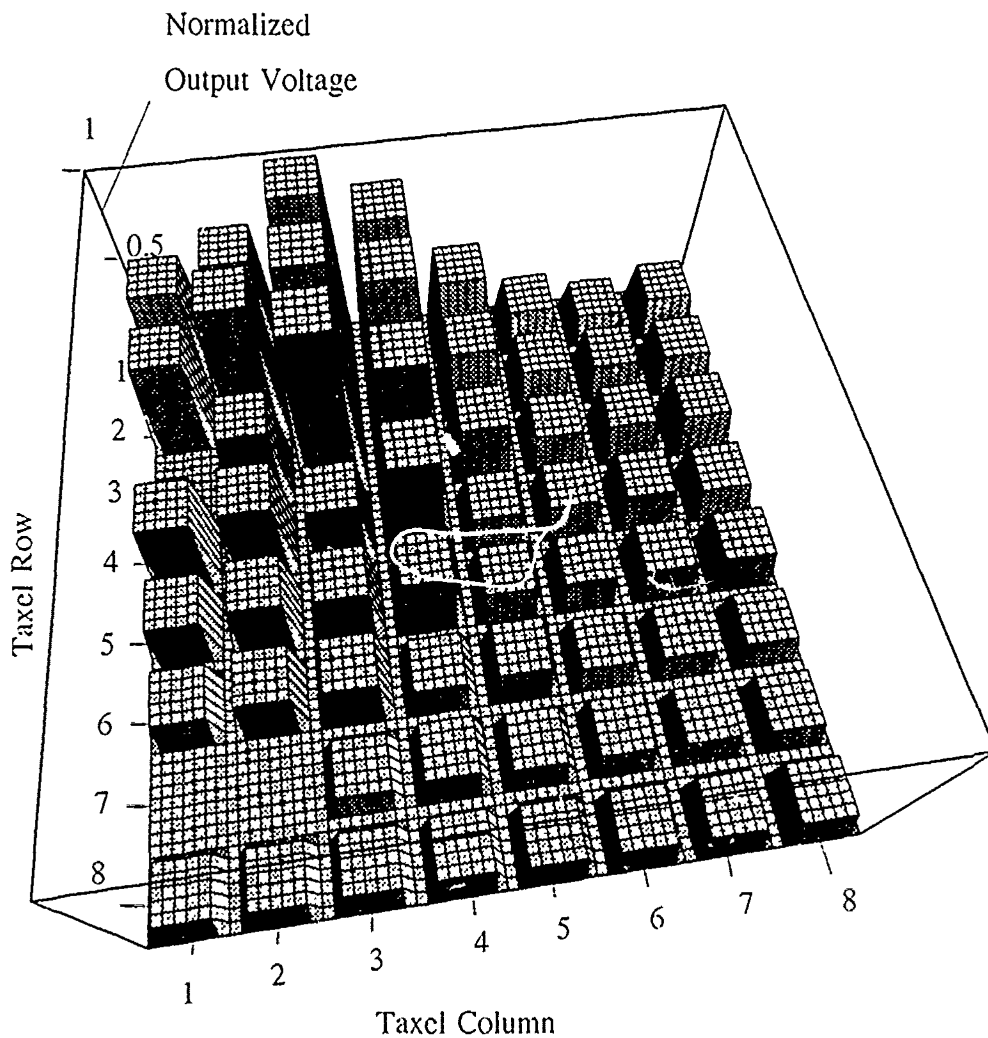

Figure K.10. Three-Dimensional Representation Between A Small Square Shaped Load Applied To The Surface Of The Electrode Array. The z-Axis Corresponds To The Normalized Difference Between The Sensor's Loaded And Unloaded States, And The x- And y-Axes Correspond To the Electrode Columns And Rows, Respectively.

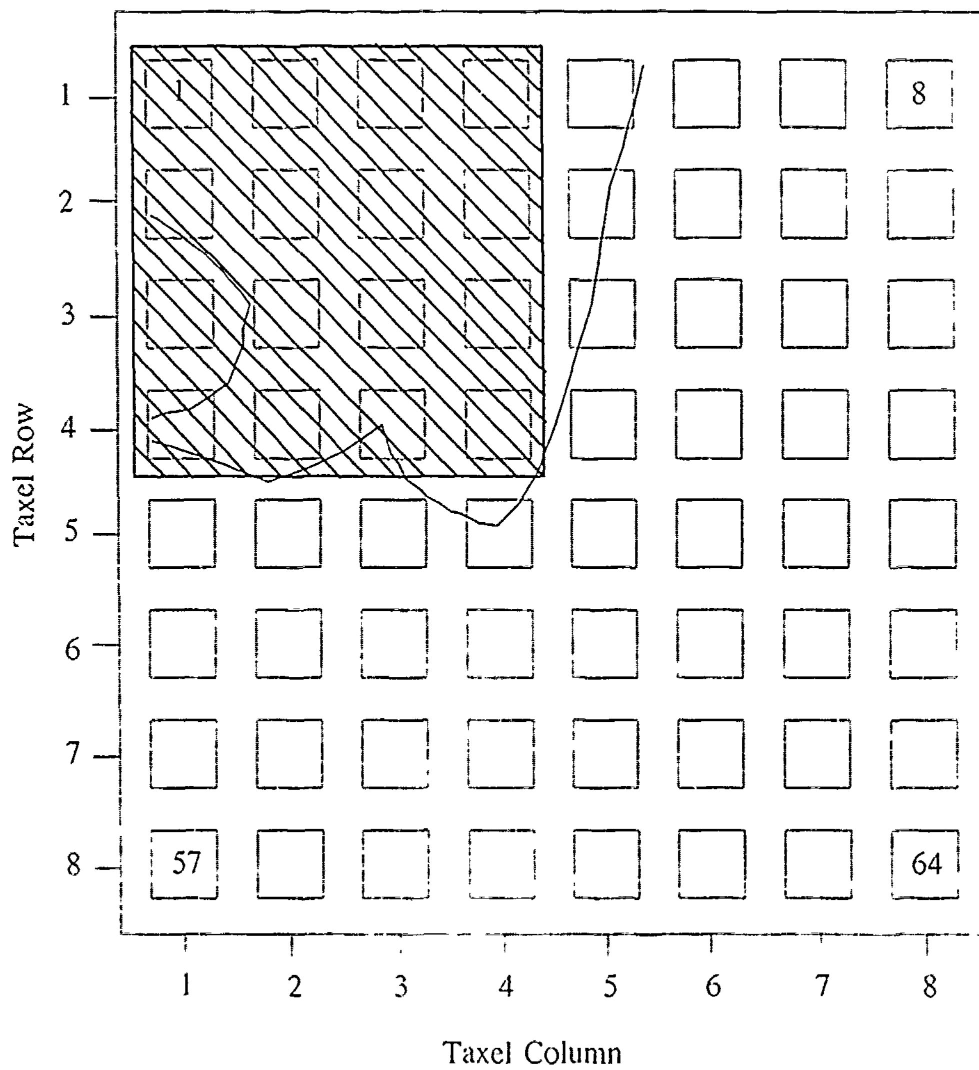

Figure K.11. 0.39-V Equipotential Contour Plot For A 75 g Small Square Shaped Load Applied To The Surface Of The Electrode Array.

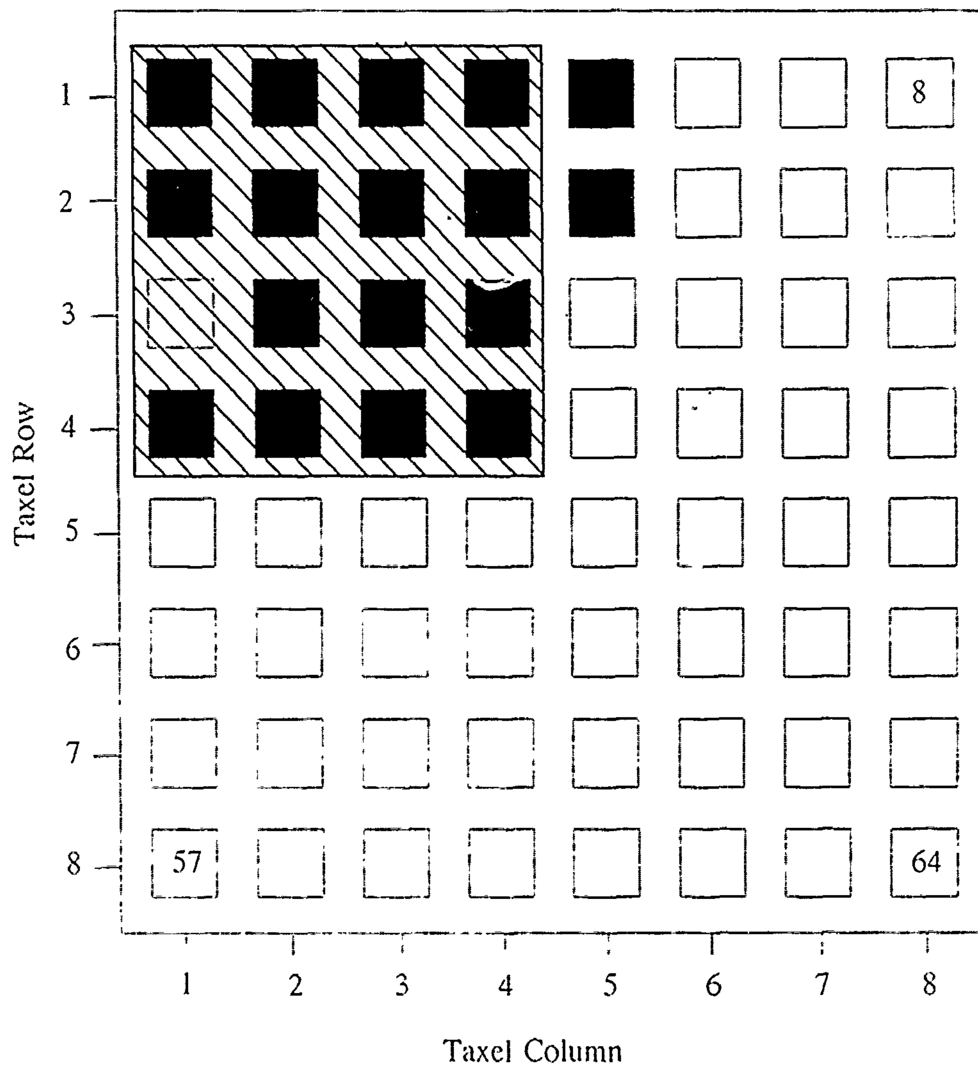

Figure K.12. 0.39-V Threshold Plot Of A 75 g Small Square Shaped Load - Taxels With An Output Level Above This Threshold Level Are Displayed As Black And Taxels With An Output Level Below This Threshold Level Are Displayed As White.

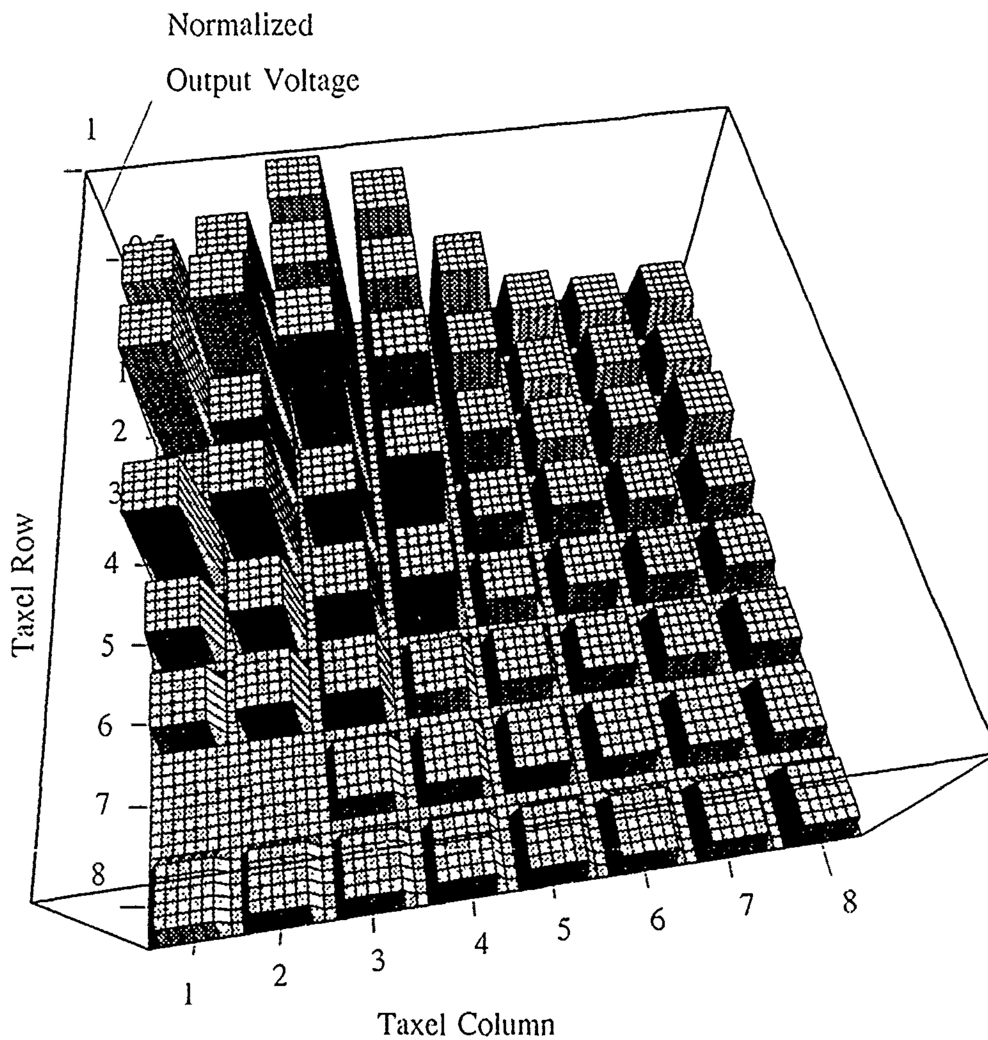

Figure K.13. Three-Dimensional Representation Between A Small Square Shaped Load Applied To The Surface Of The Electrode Array. The z-Axis Corresponds To The Normalized Difference Between The Sensor's Loaded And Unloaded States. And The x- And y-Axes Correspond To the Electrode Columns And Rows, Respectively.

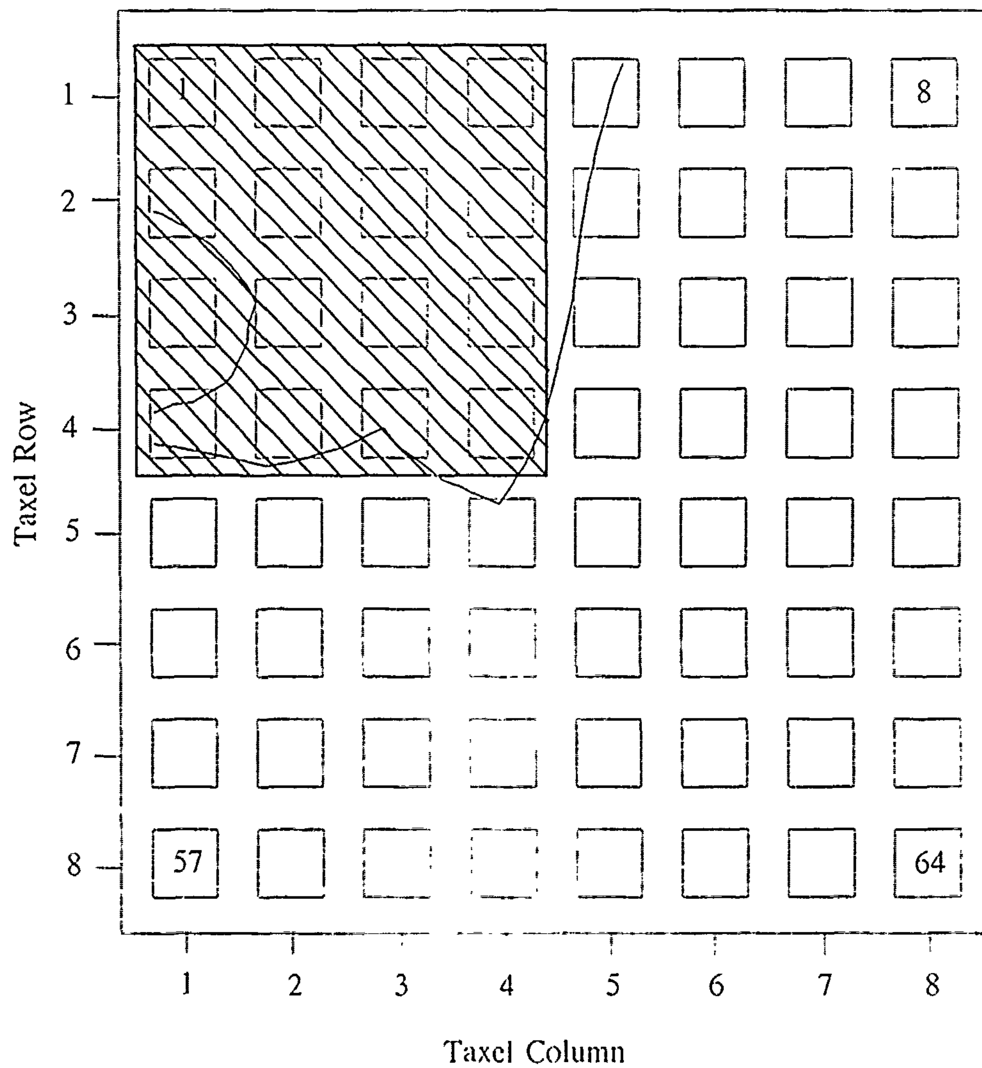

Figure K.14. 0.51-V Equipotential Contour Plot For A 50 g Small Square Shaped Load Applied To The Surface Of The Electrode Array.

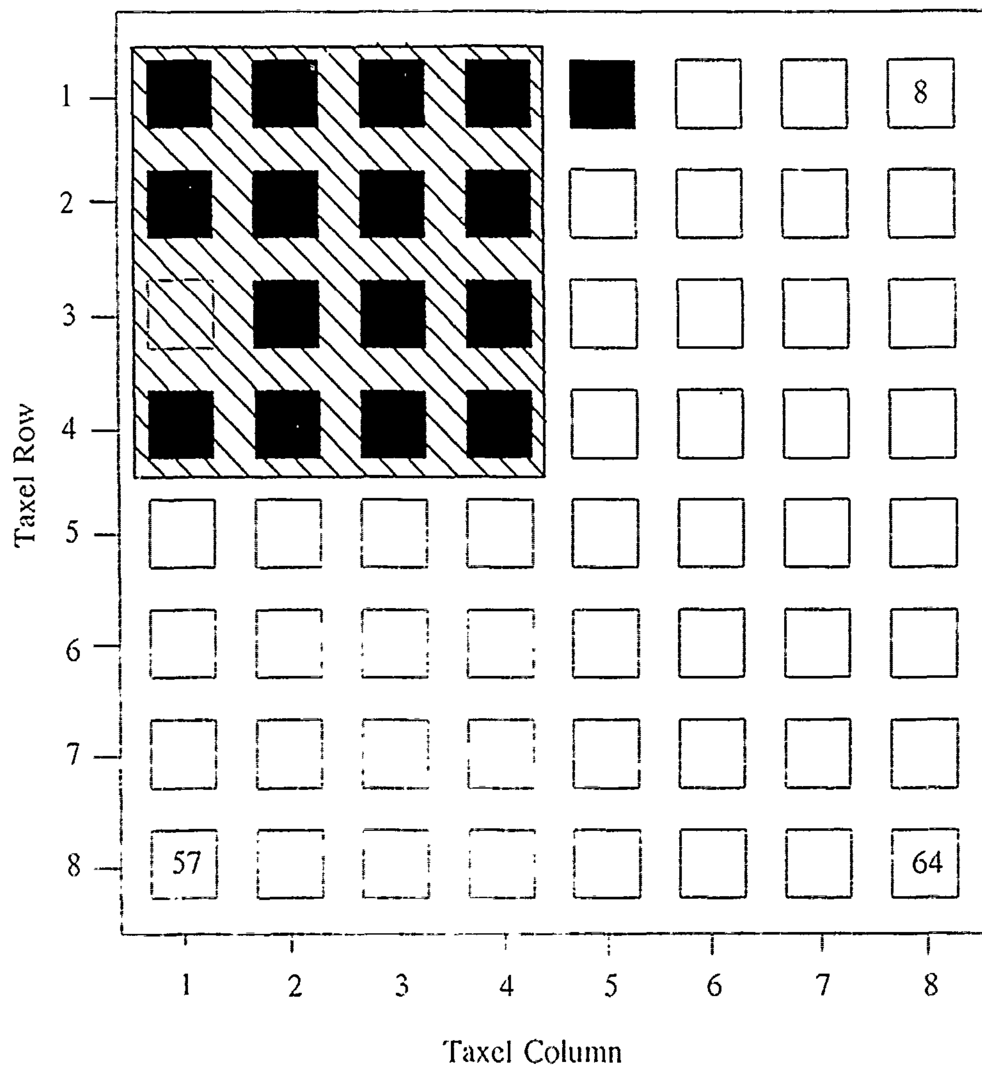

Figure K.15. 0.51-V Threshold Plot Of A 50 g Small Square Shaped Load - Taxels With An Output Level Above This Threshold Level Are Displayed As Black And Taxels With An Output Level Below This Threshold Level Are Displayed As White.

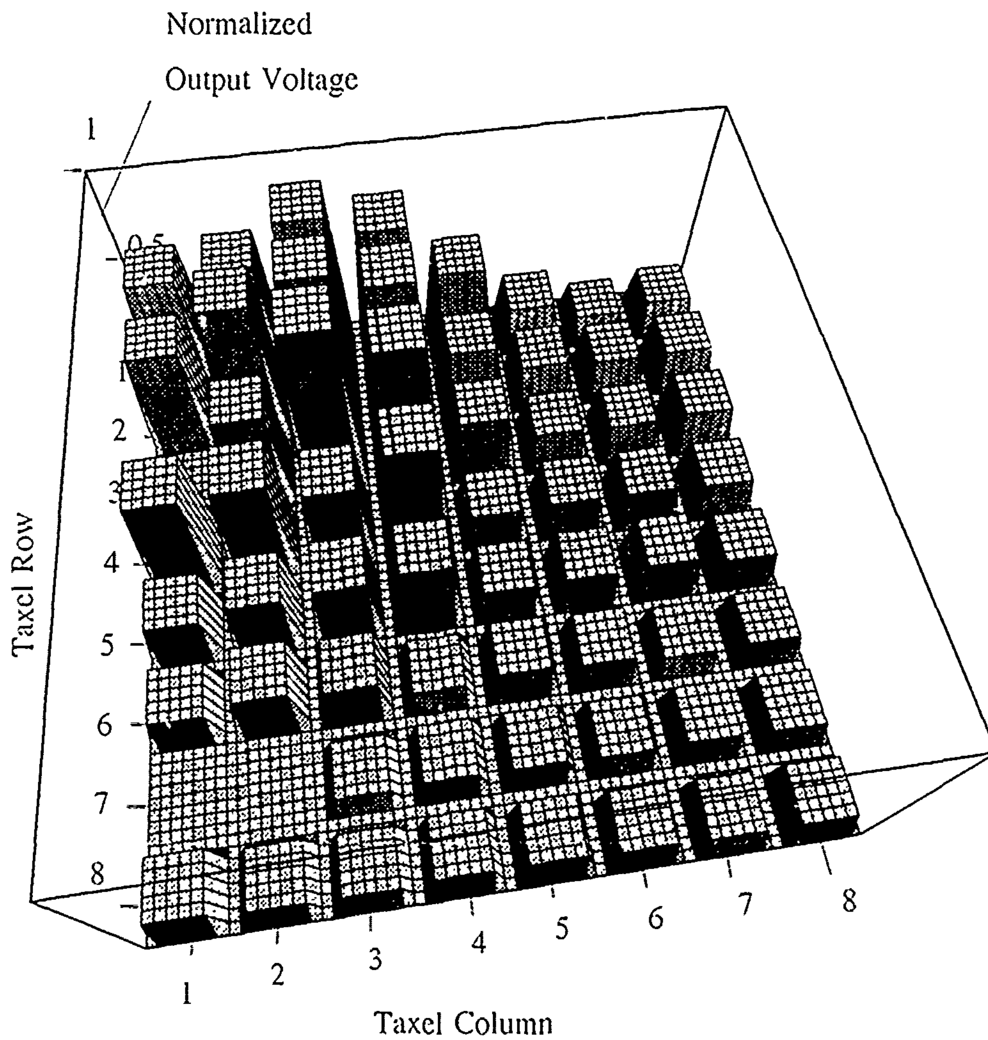

Figure K.16. Three-Dimensional Representation Between A Small Square Shaped Load Applied To The Surface Of The Electrode Array. The z-Axis Corresponds To The Normalized Difference Between The Sensor's Loaded And Unloaded States, And The x- And y-Axes Correspond To the Electrode Columns And Rows, Respectively.

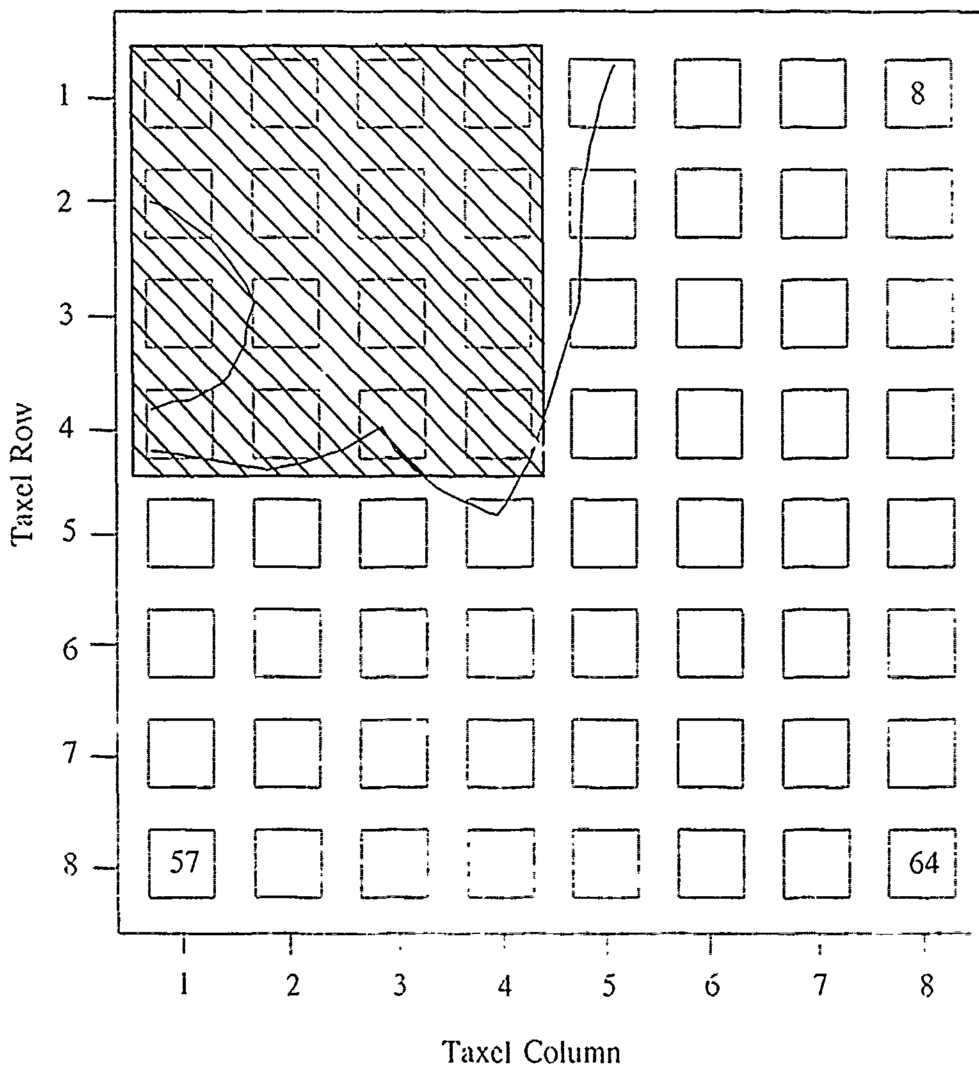

Figure K.17. 0.5-V Equipotential Contour Plot For A 10 g Small Square Shaped Load Applied To The Surface Of The Electrode Array.

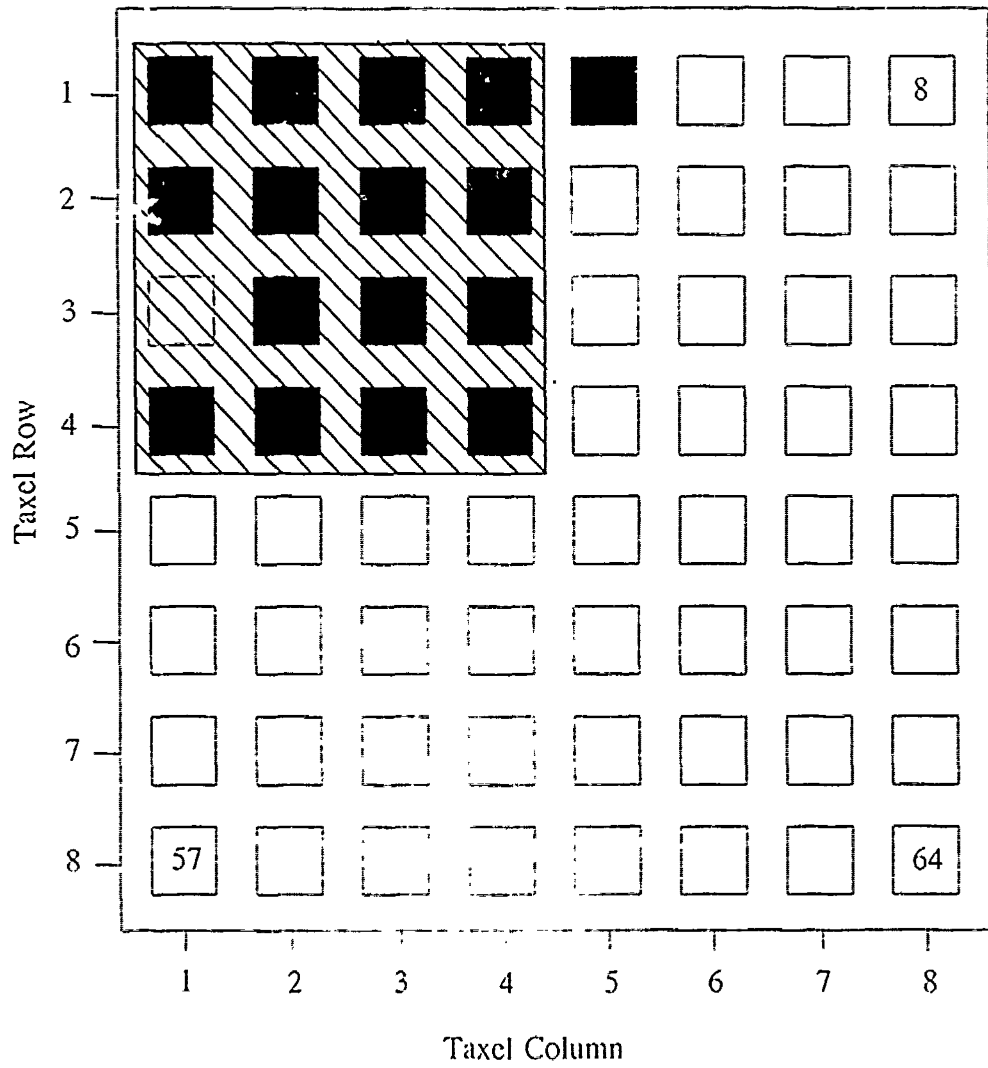

Figure K.18. 0.5-V Threshold Plot Of A 10 g Small Square Shaped Load - Taxels With An Output Level Above This Threshold Level Are Displayed As Black And Taxels With An Output Level Below This Threshold Level Are Displayed As White.

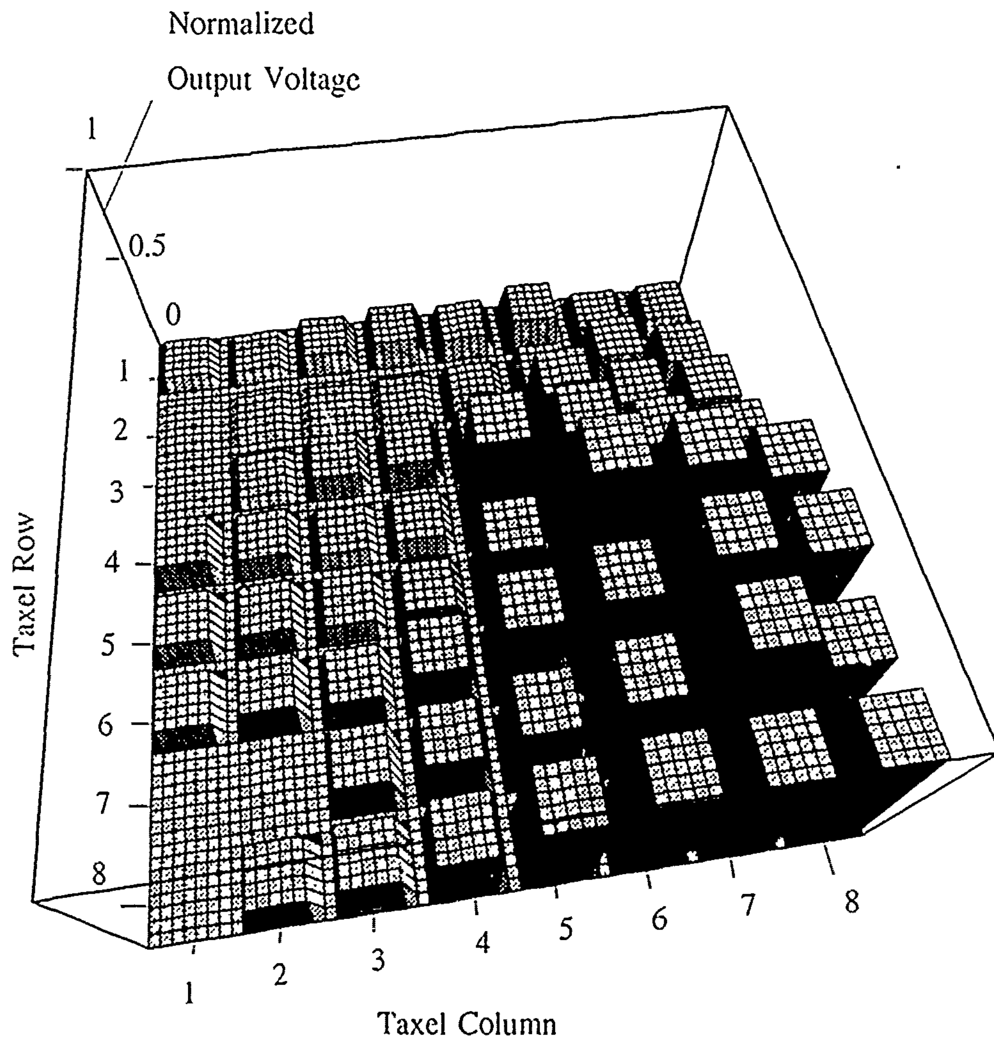

Figure K.19. Three-Dimensional Representation Of A Small Circularly Shaped Load Applied To The Surface Of The Electrode Array. The z-Axis Corresponds To The Normalized Difference Between The Sensor's Loaded And Unloaded States, And The x- And y-Axes Correspond To the Electrode Columns And Rows, Respectively.

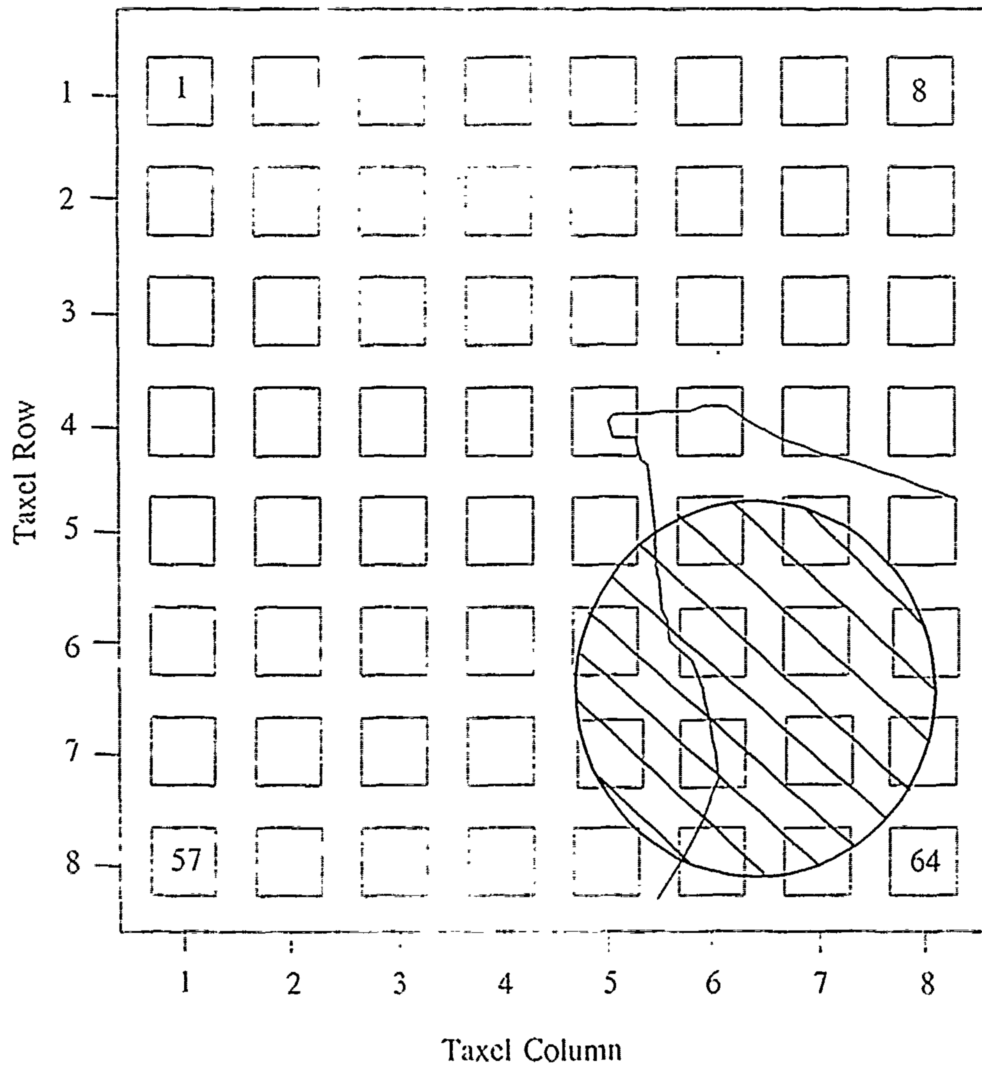

Figure K.20. 0.68-V Equipotential Contour Plot For A 75 g Small Circularly Shaped Load Applied To The Surface Of The Electrode Array.

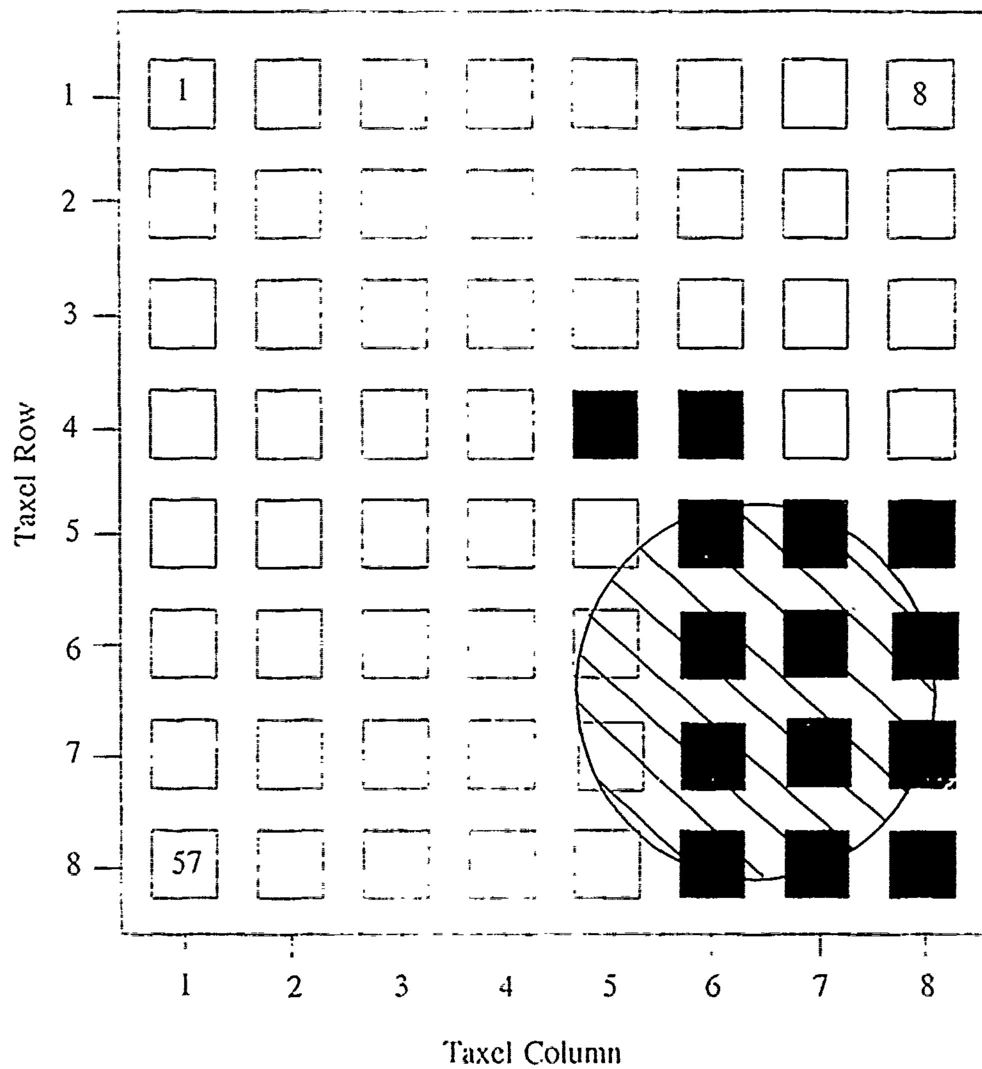

Figure K.21. 0.68-V Threshold Plot Of A 75 g Small Circularly Shaped Load - Taxels With An Output Level Above This Threshold Level Are Displayed As Black And Taxels With An Output Level Below This Threshold Level Are Displayed As White.

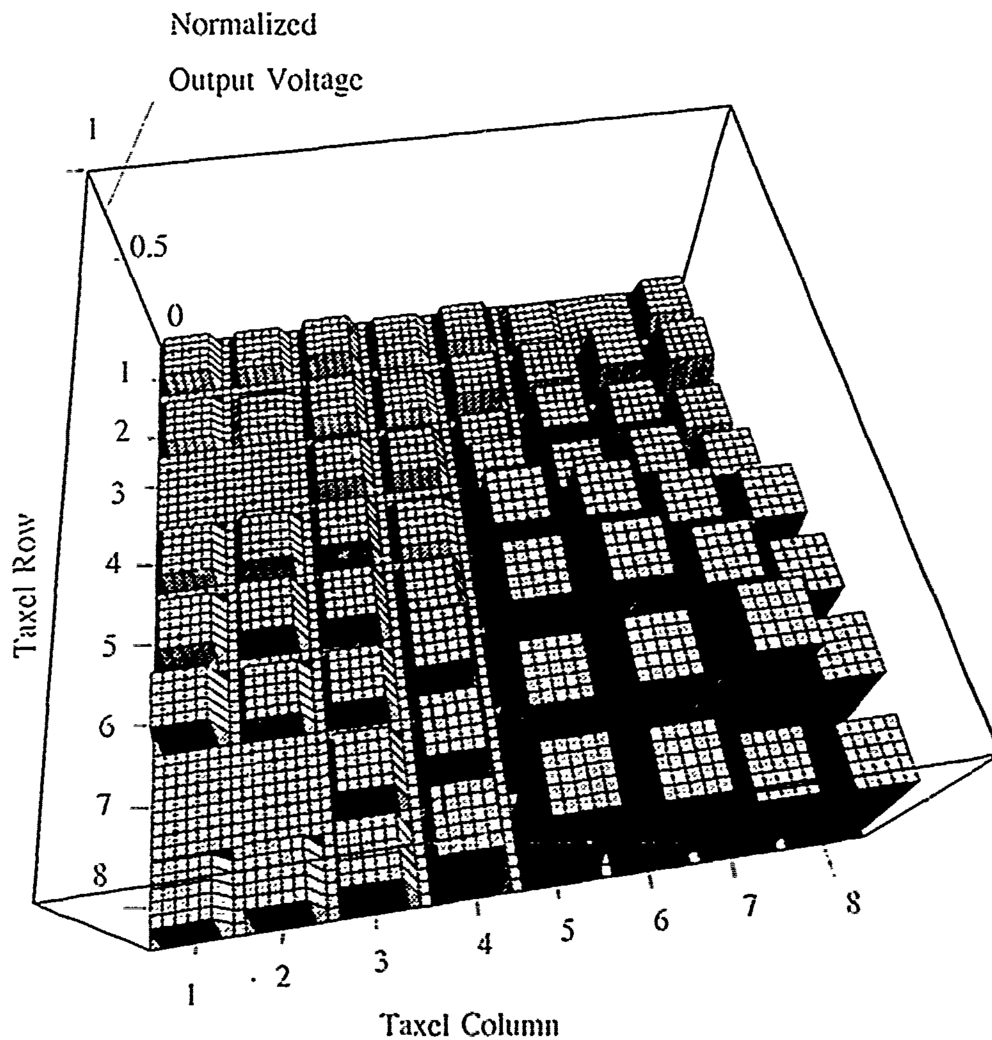

Figure K.22. Three-Dimensional Representation Of A Small Circularly Shaped Load Applied To The Surface Of The Electrode Array. The z-Axis Corresponds To The Normalized Difference Between The Sensor's Loaded And Unloaded States. And The x- And y-Axes Correspond To the Electrode Columns And Rows. Respectively.

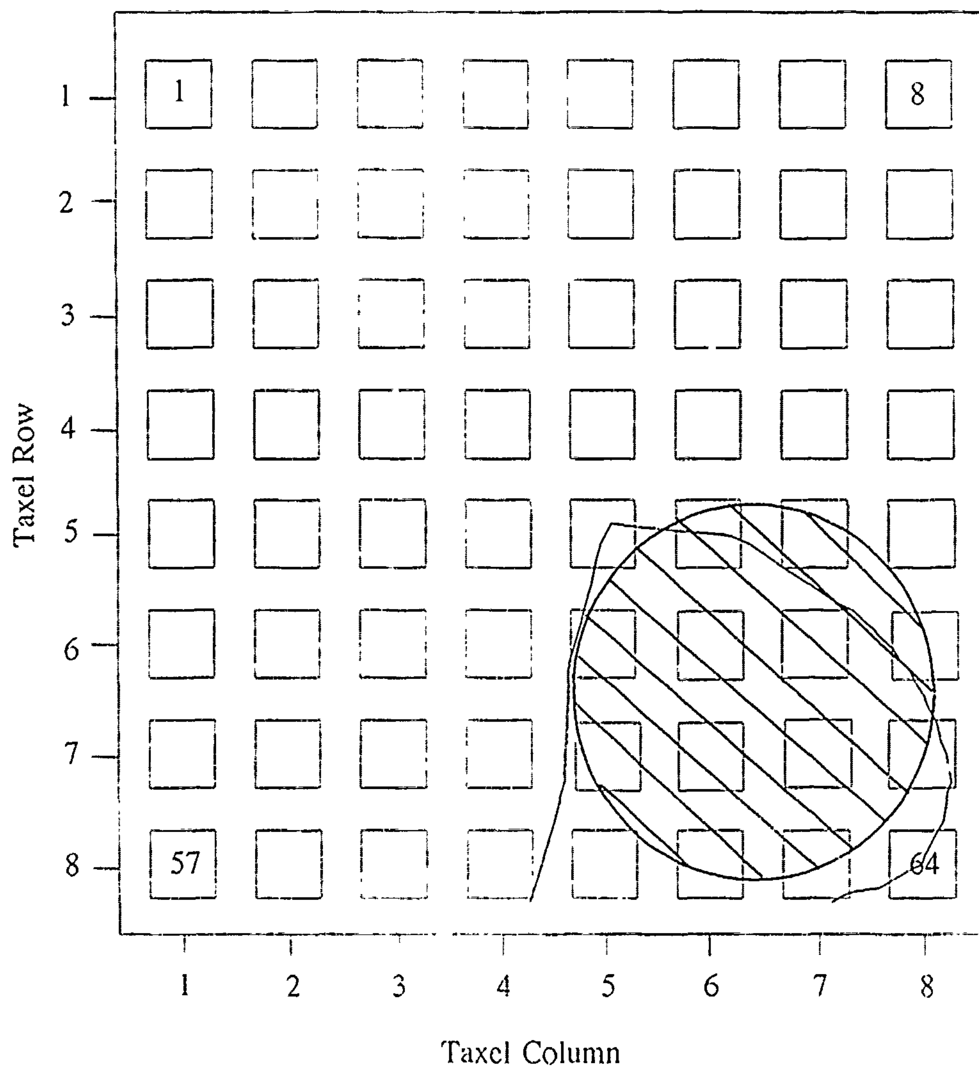

Figure K.23. 0.67-V Equipotential Contour Plot For A 50 g Small Circularly Shaped Load Applied To The Surface Of The Electrode Array.

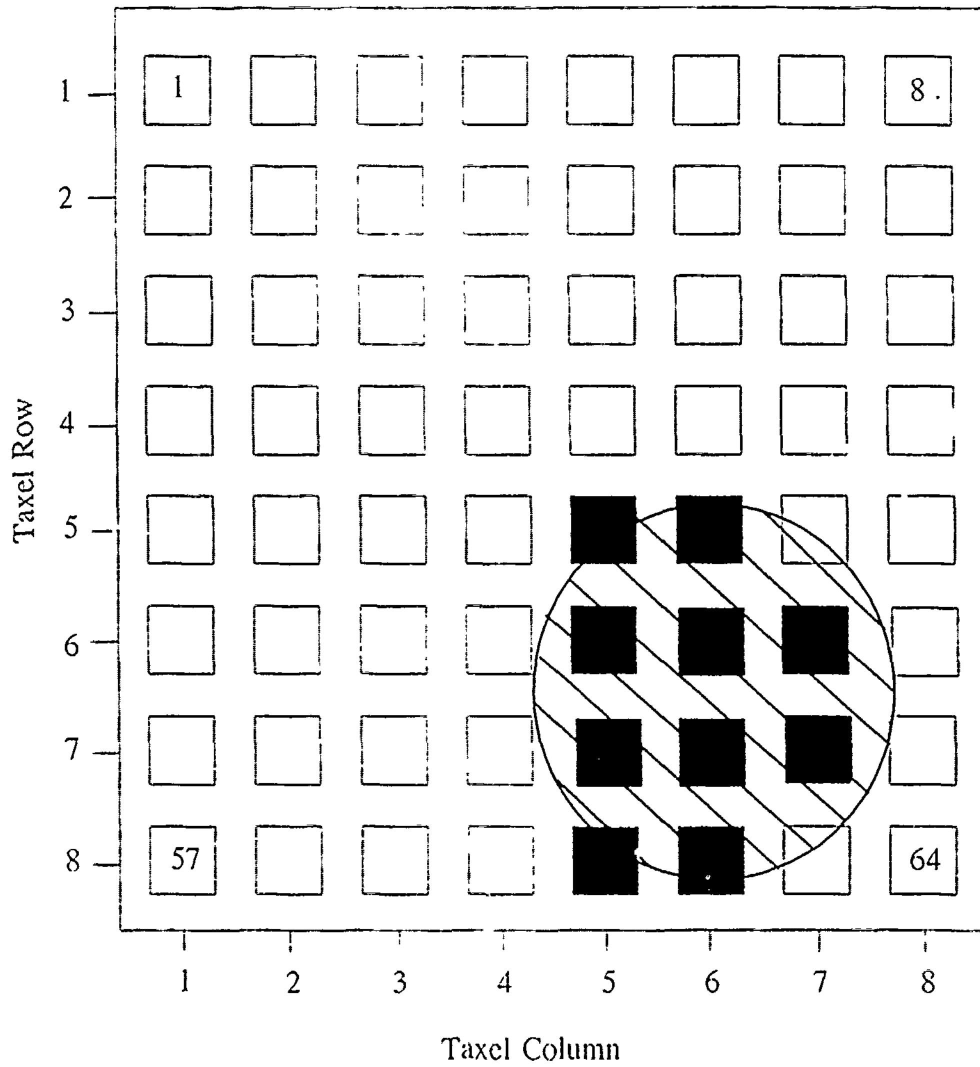

Figure K.24. 0.67-V Threshold Plot Of A 50 g Small Circularly Shaped Load - Taxels With An Output Level Above This Threshold Level Are Displayed As Black And Taxels With An Output Level Below This Threshold Level Are Displayed As White.

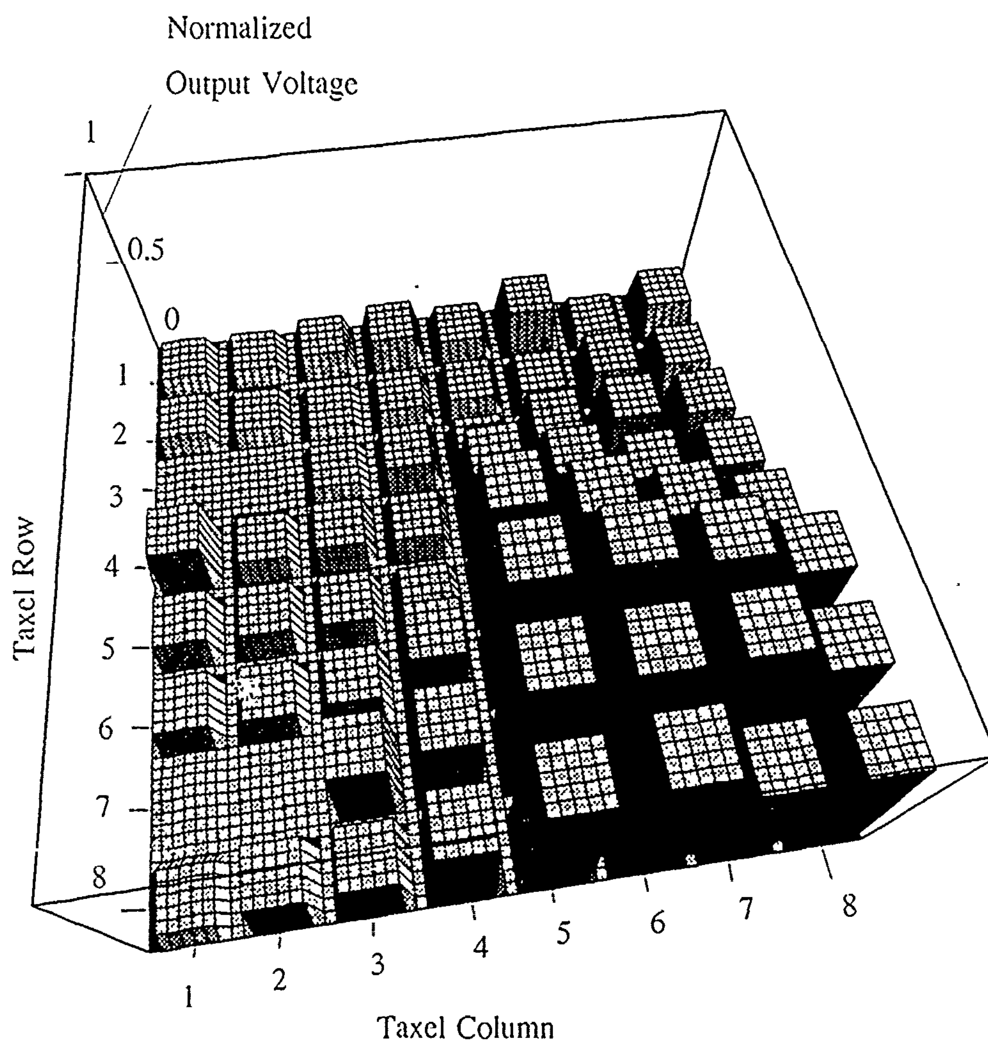

Figure K.25. Three-Dimensional Representation Of A Small Circularly Shaped Load Applied To The Surface Of The Electrode Array. The z-Axis Corresponds To The Normalized Difference Between The Sensor's Loaded And Unloaded States. And The x- And y-Axes Correspond To the Electrode Columns And Rows, Respectively.

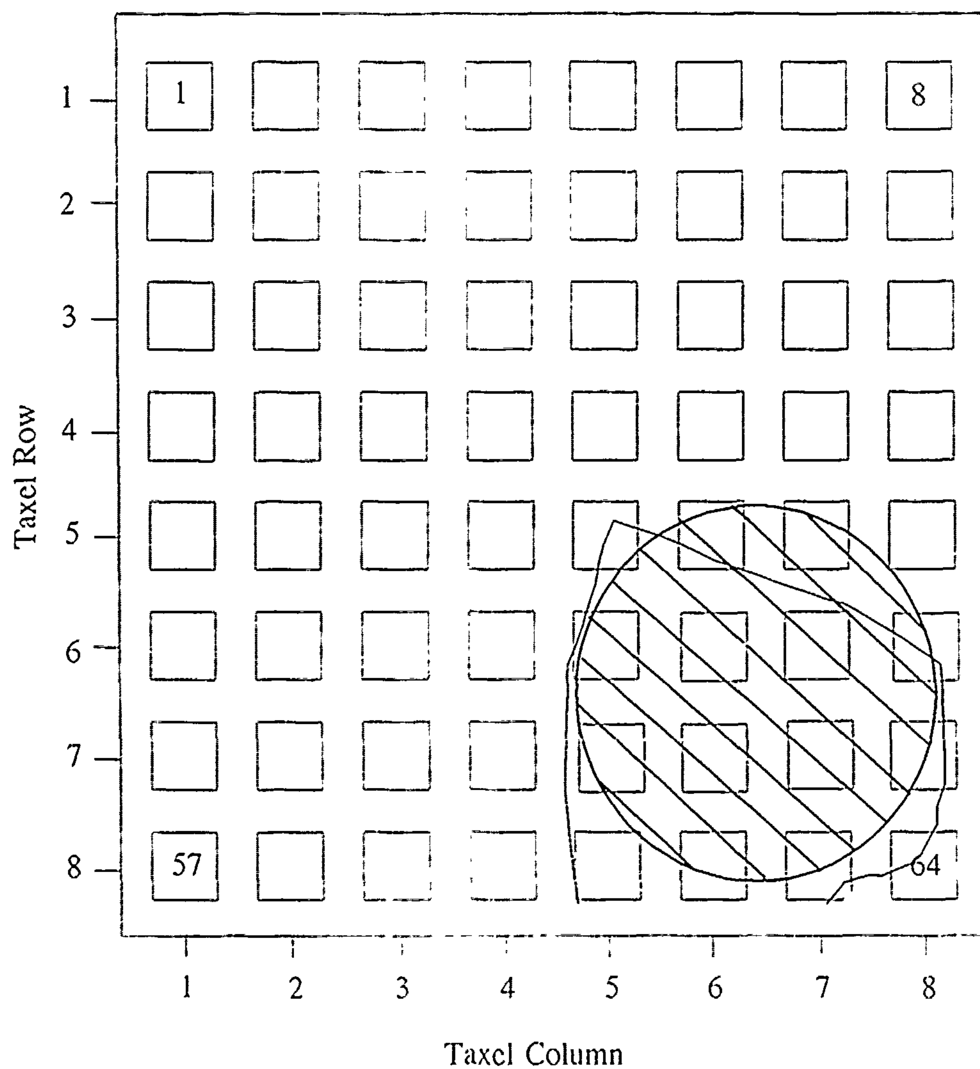

Figure K.26. 0.78-V Equipotential Contour Plot For A 10 g Small Circularly Shaped Load Applied To The Surface Of The Electrode Array.

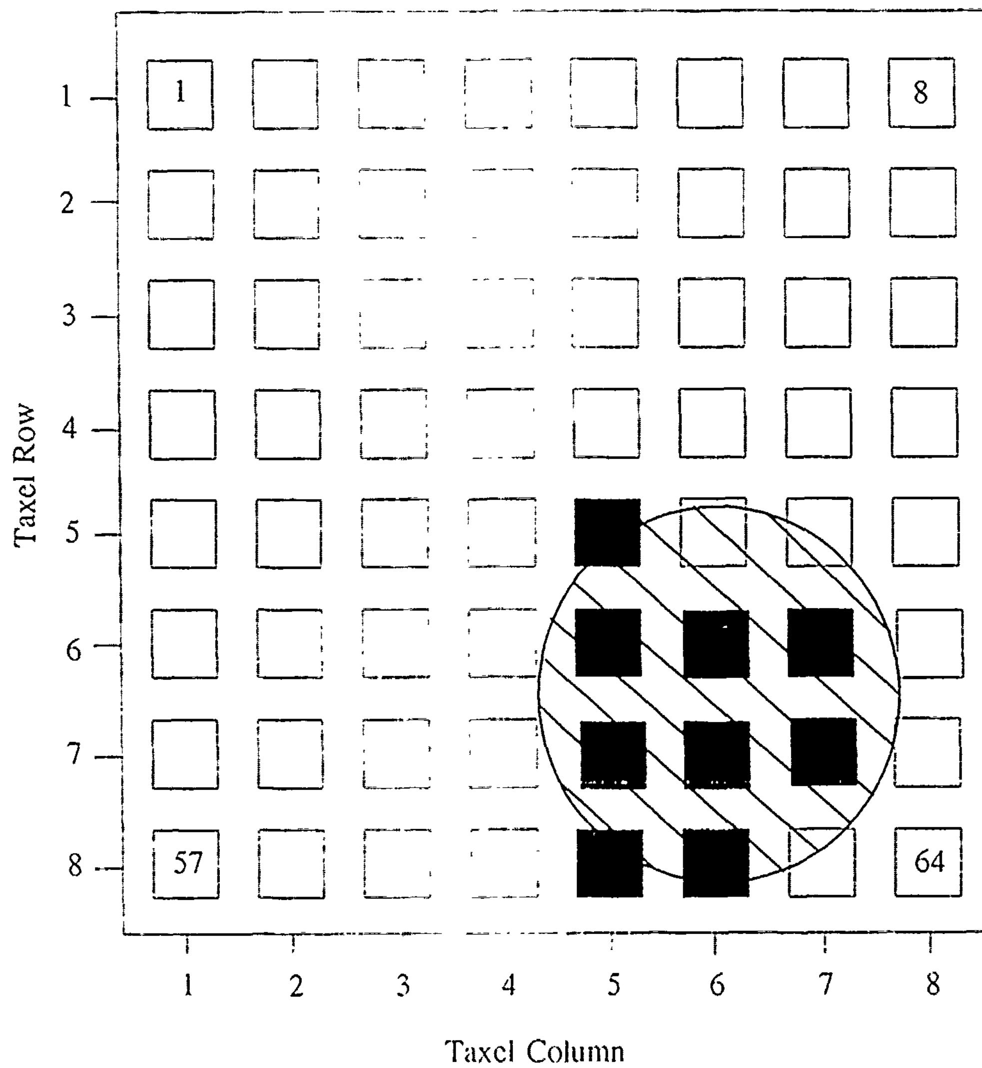

Figure K.27. 0.78-V Threshold Plot Of A 10 g Small Circularly Shaped Load - Taxels With An Output Level Above This Threshold Level Are Displayed As Black And Taxels With An Output Level Below This Threshold Level Are Displayed As White.

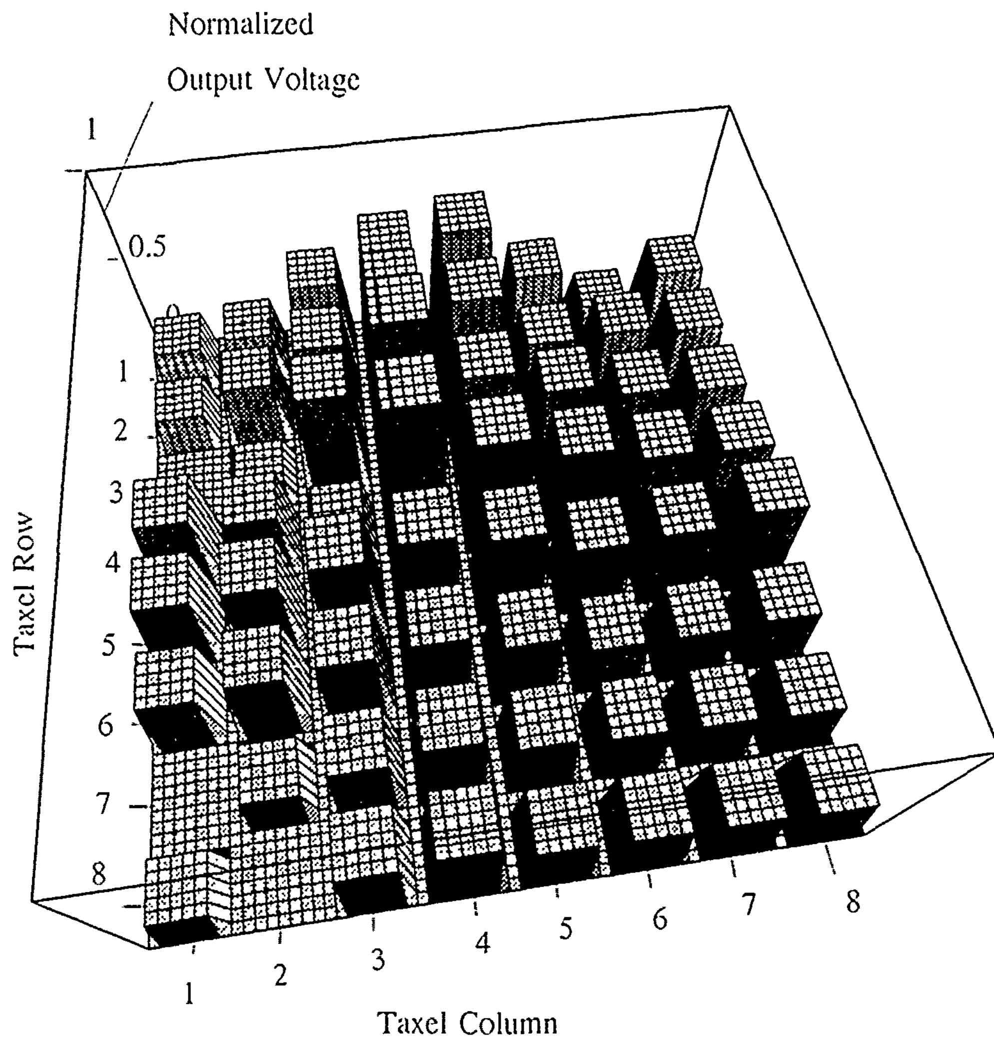

Figure K.28. Three-Dimensional Representation Of A Polygon Shaped Load Applied To The Surface Of The Electrode Array. The z-Axis Corresponds To The Normalized Difference Between The Sensor's Loaded And Unloaded States. And The x- And y-Axes Correspond To the Electrode Columns And Rows, Respectively.

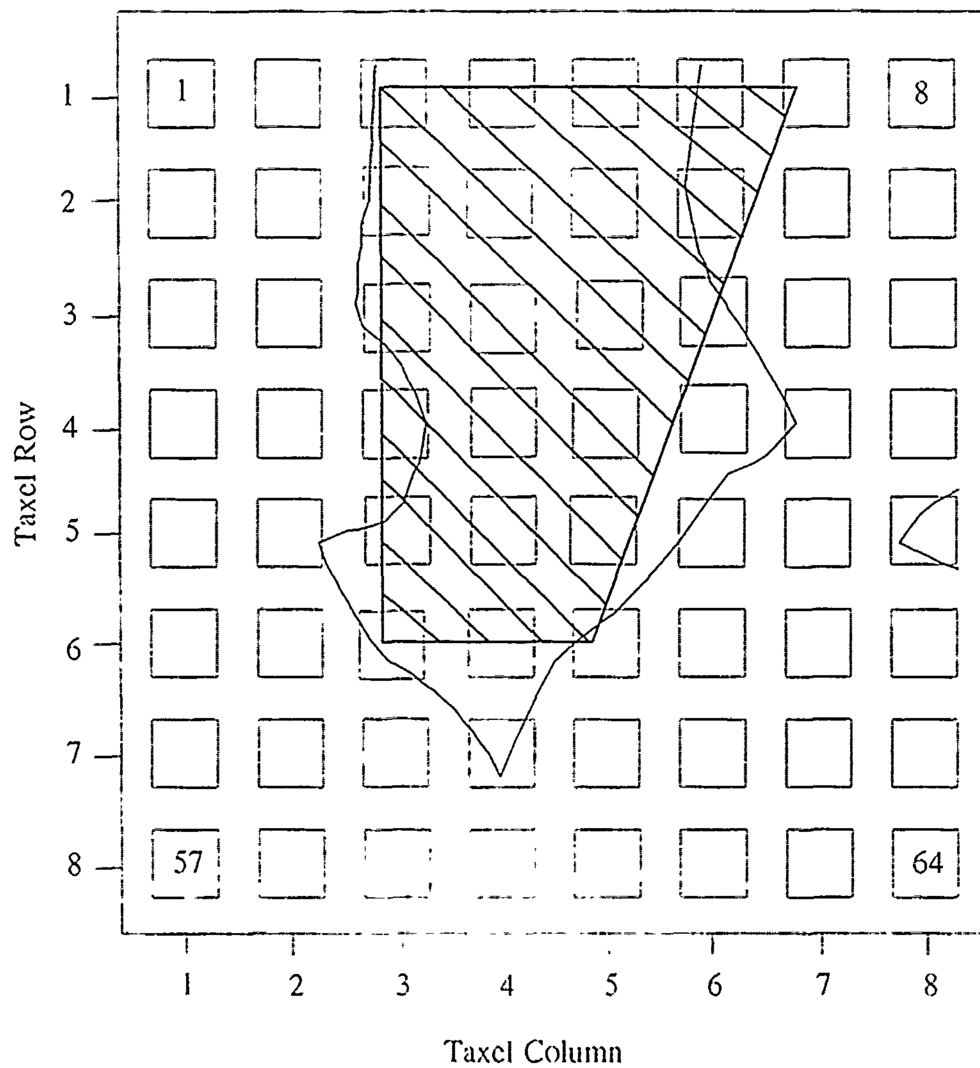

Figure K.29. 0.51-V Equipotential Contour Plot For A 75 g Polygon Shaped Load Applied To The Surface Of The Electrode Array.

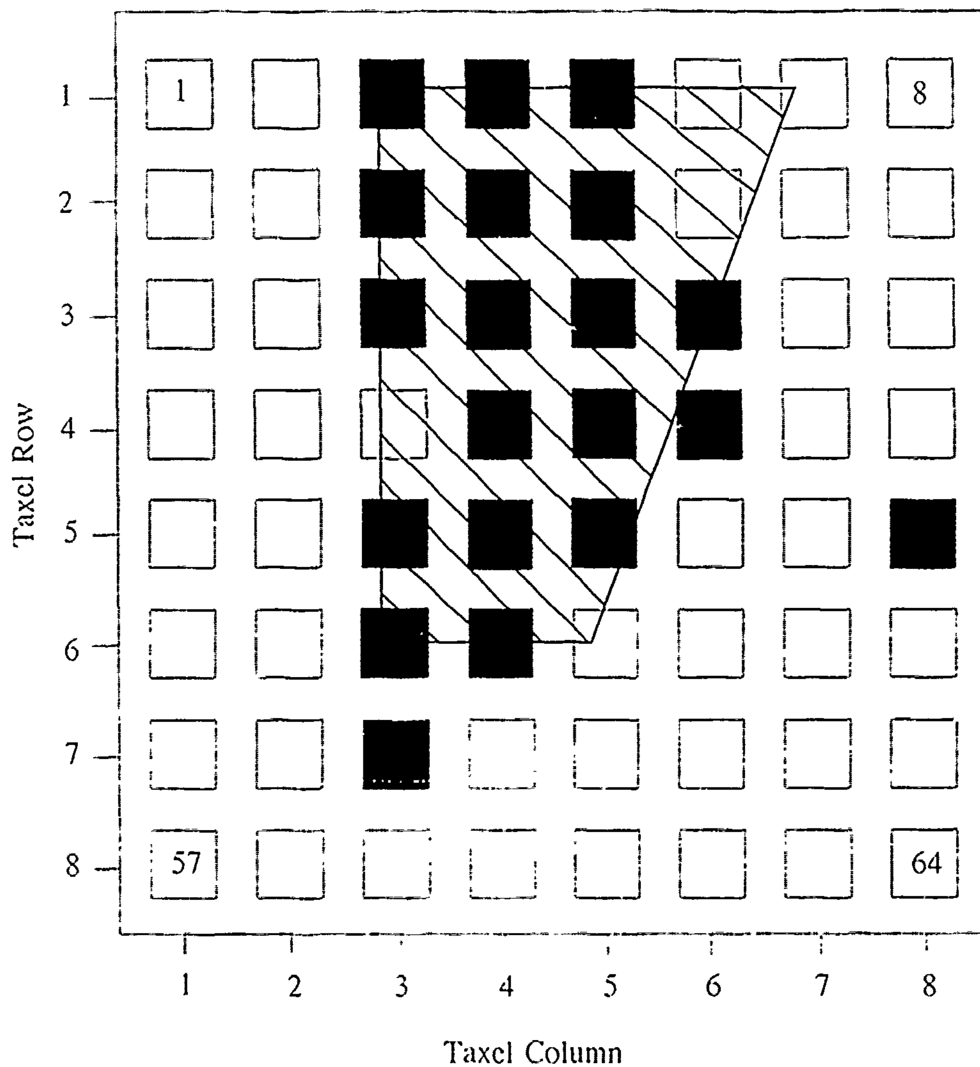

Figure K.30. 0.51-V Threshold Plot Of A 75 g Polygon Shaped Load - Taxels With An Output Level Above This Threshold Level Are Displayed As Black And Taxels With An Output Level Below This Threshold Level Are Displayed As White.

Figure K.31. Three-Dimensional Representation Of A Polygon Shaped Load Applied To The Surface Of The Electrode Array. The z-Axis Corresponds To The Normalized Difference Between The Sensor's Loaded And Unloaded States, And The x- And y-Axes Correspond To the Electrode Columns And Rows, Respectively.

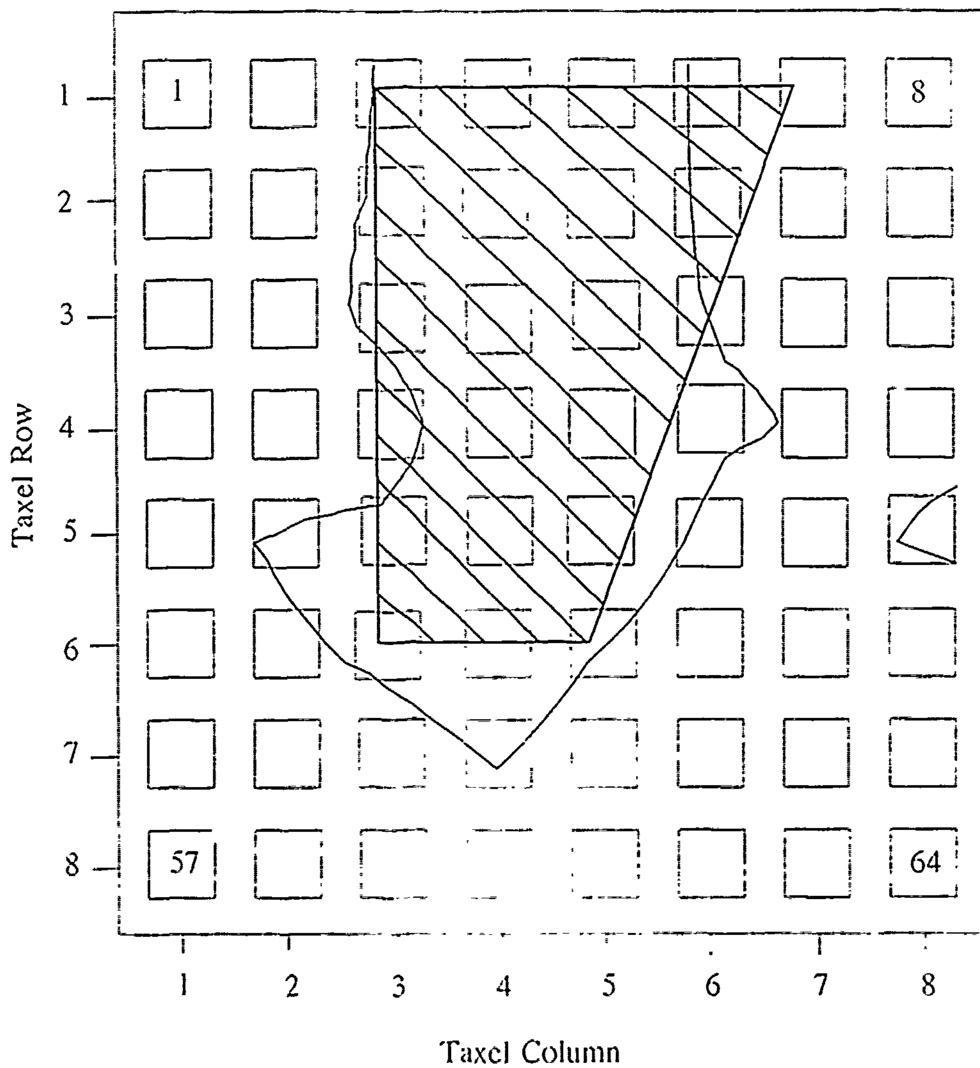

Figure K.32. 0.5-V Equipotential Contour Plot For A 50 g Polygon Shaped Load Applied To The Surface Of The Electrode Array.

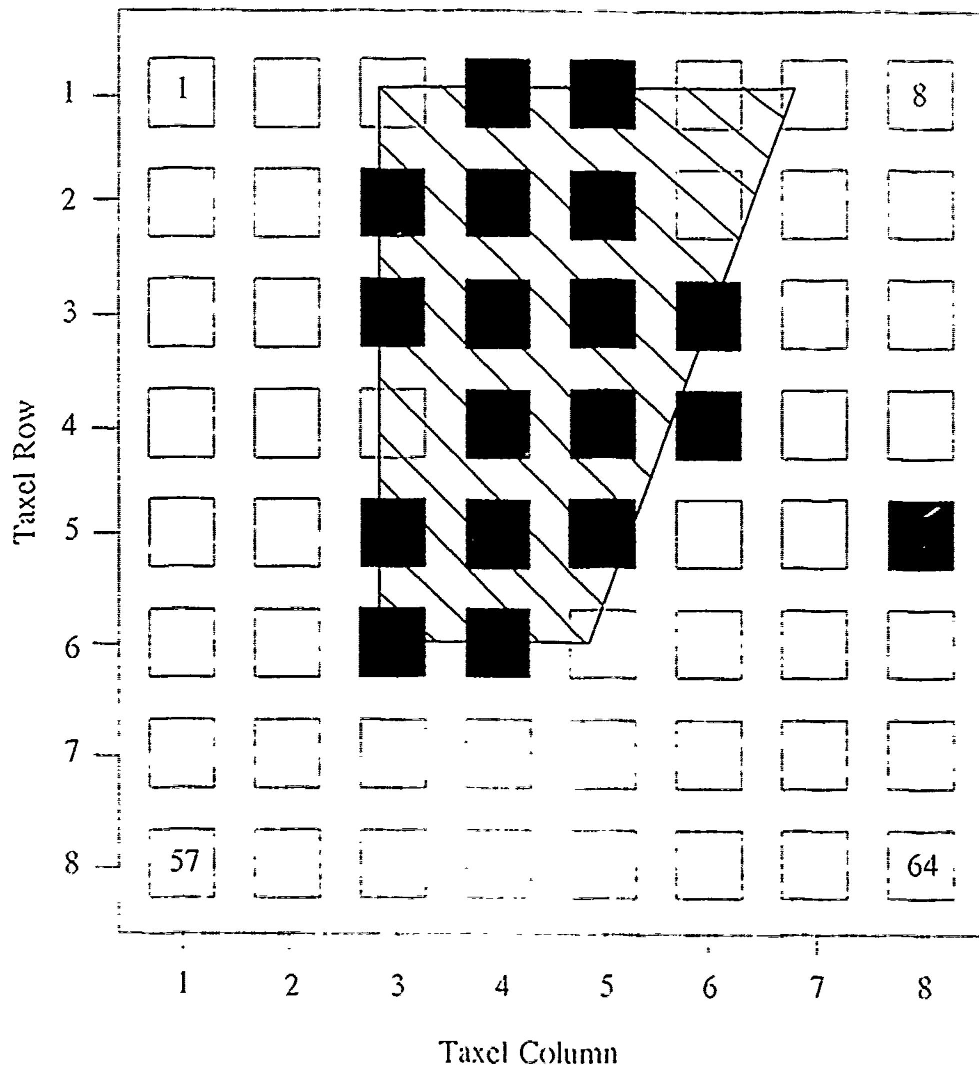

Figure K.33. 0.5-V Threshold Plot Of A 50 g Polygon Shaped Load - Taxels With An Output Level Above This Threshold Level Are Displayed As Black And Taxels With An Output Level Below This Threshold Level Are Displayed As White.

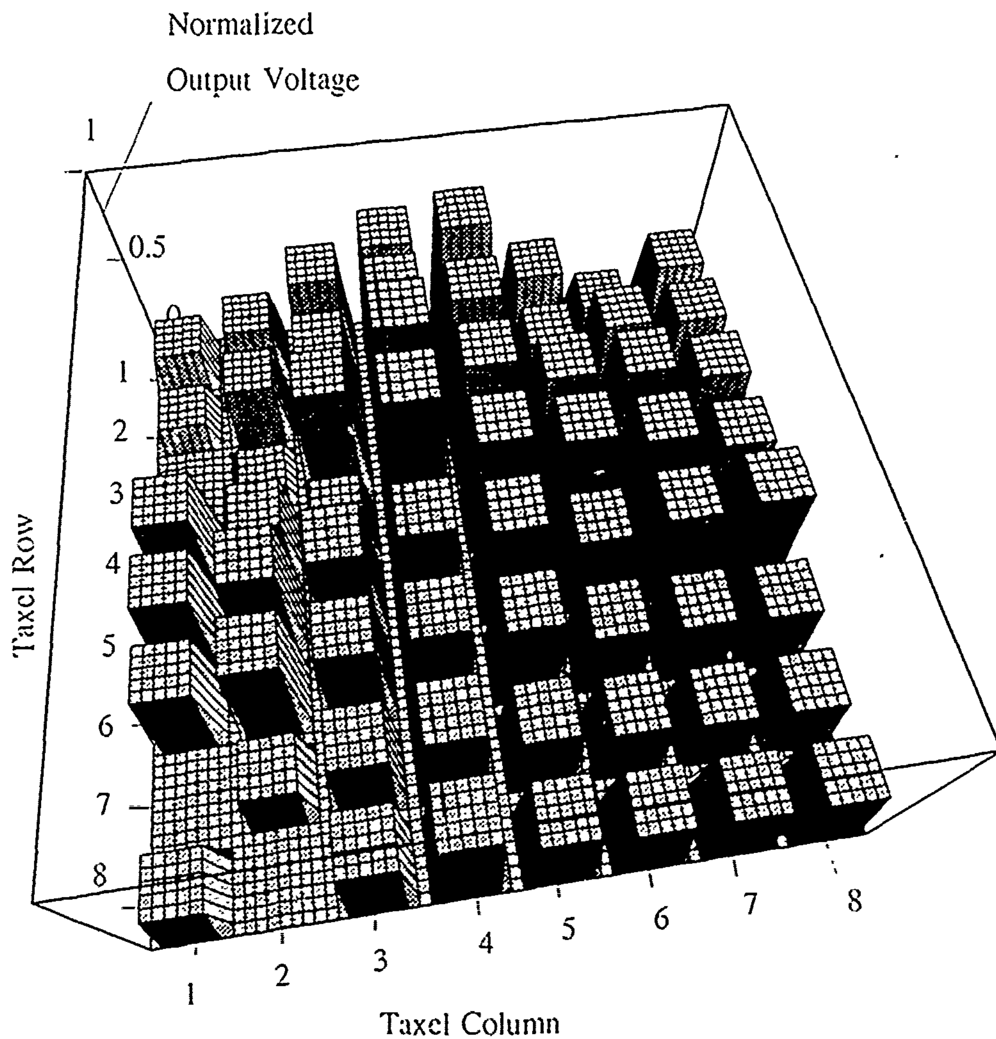

Figure K.34. Three-Dimensional Representation Of A Polygon Shaped Load Applied To The Surface Of The Electrode Array. The z-Axis Corresponds To The Normalized Difference Between The Sensor's Loaded And Unloaded States, And The x- And y-Axes Correspond To the Electrode Columns And Rows, Respectively.

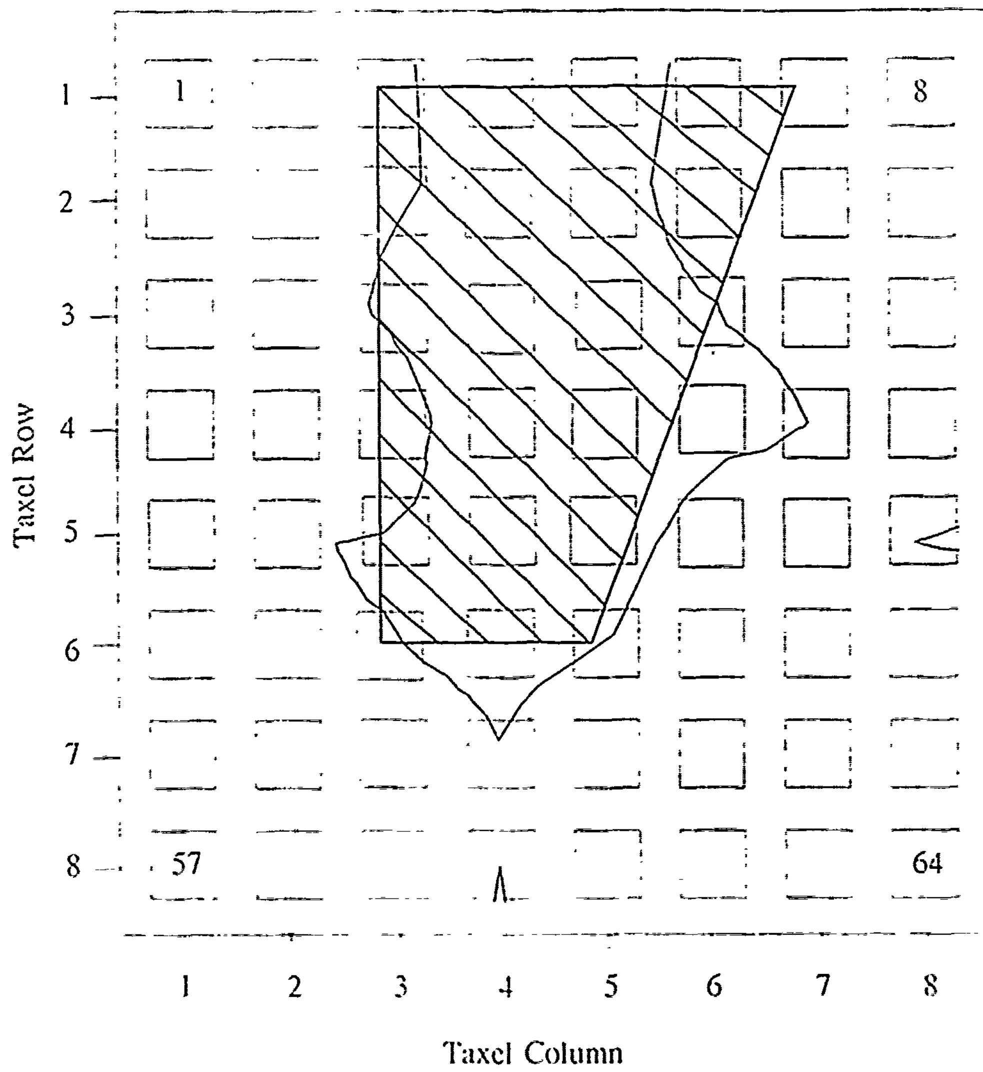

Figure K.35. 0.6-V Equipotential Contour Plot For A 10 g Polygon Shaped Load Applied To The Surface Of The Electrode Array.

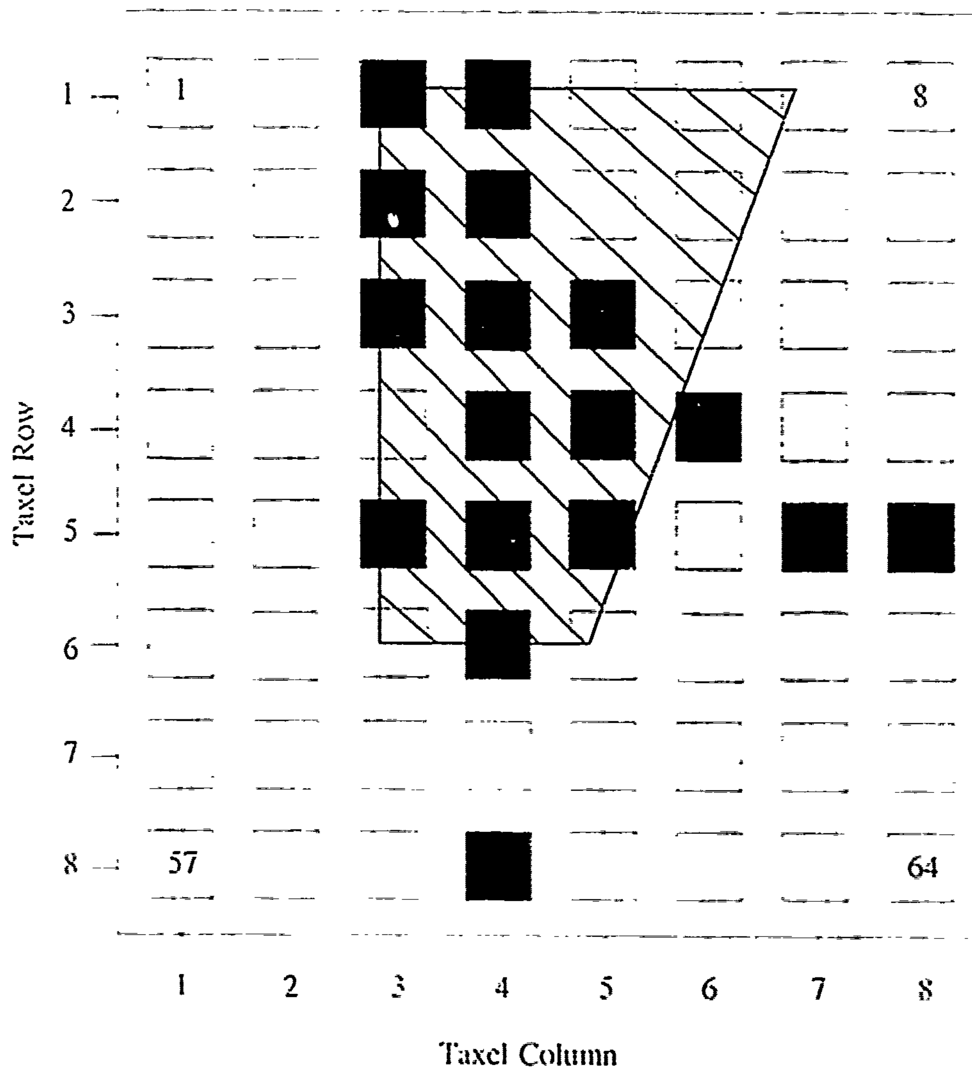

Figure K.36. 0.6-V Threshold Plot Of A 10 g Polygon Shaped Load Taxels With An Output Level Above This Threshold Level Are Displayed As Black And Taxels With An Output Level Below This Threshold Level Are Displayed As White.

Appendix L. *Tactile Sensor Shape Plots in Several Different Locations*

The plots presented in this appendix illustrate the tactile sensor's ability to detect the same shape in several different locations on its surface. The sharp edge, small square, and small circular shapes were applied in several locations on the sensor surface; each application resulted in the development of three plots: a three-dimensional plot of the normalized voltage output for each taxel, a contour plot of the "best-fit" threshold level, and the taxel outputs which are above and below that threshold level.

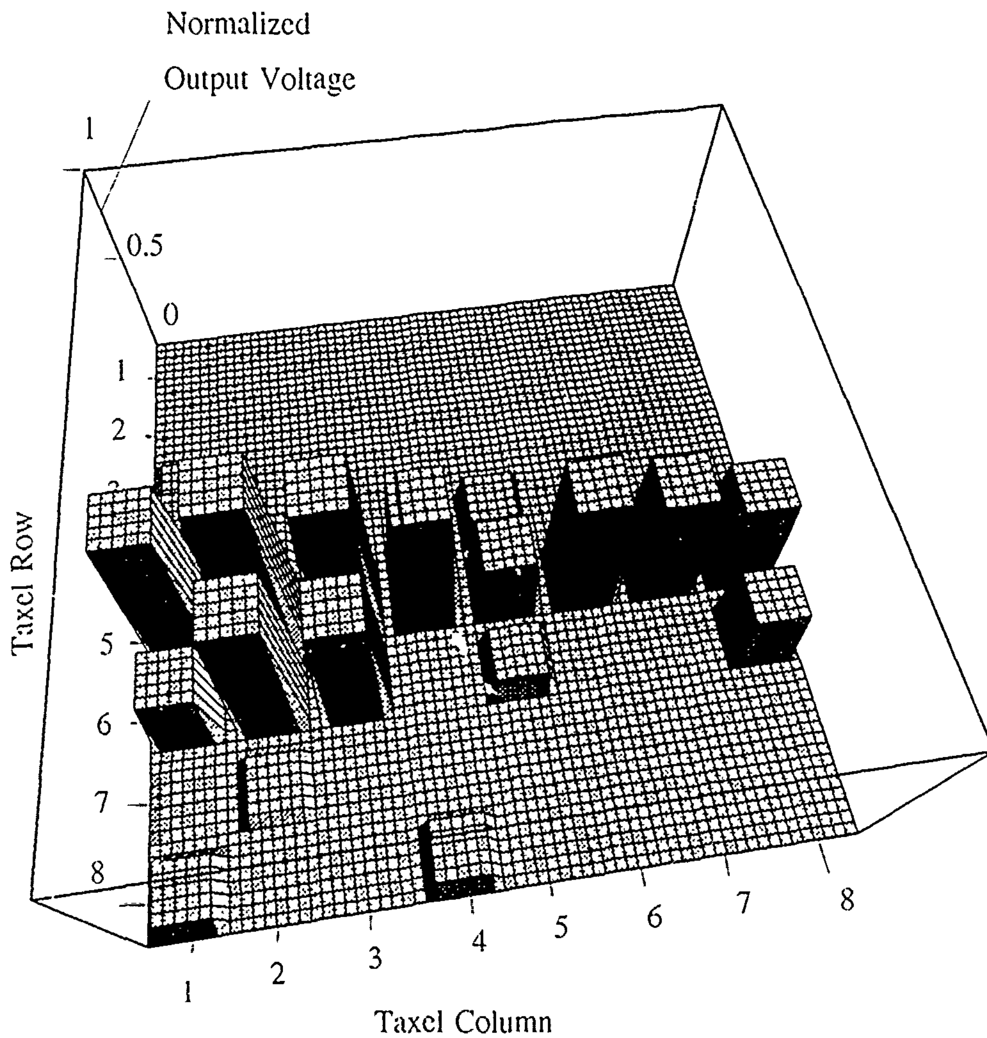

Figure L.1. Three-Dimensional Representation Of A 100 g Sharp Edge Shaped Load Applied To The Surface Of The Electrode Array. The z-Axis Corresponds To The Normalized Difference Between The Sensor's Loaded And Unloaded States, And The x- And y-Axes Correspond To The Electrode Columns And Rows, Respectively.

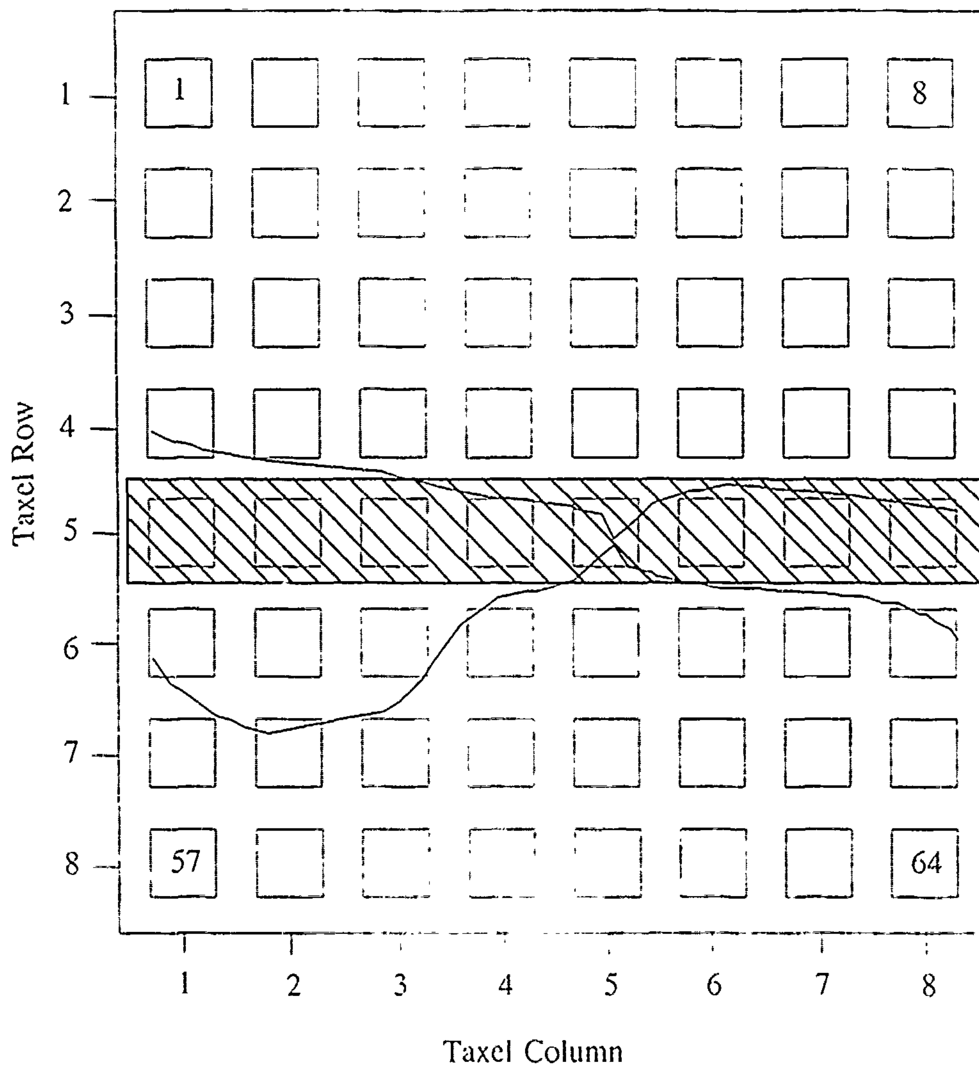

Figure L.2. 0.36-V Equipotential Contour Plot For A 100 g Sharp Edge Shaped Load Applied To The Surface Of The Electrode Array.

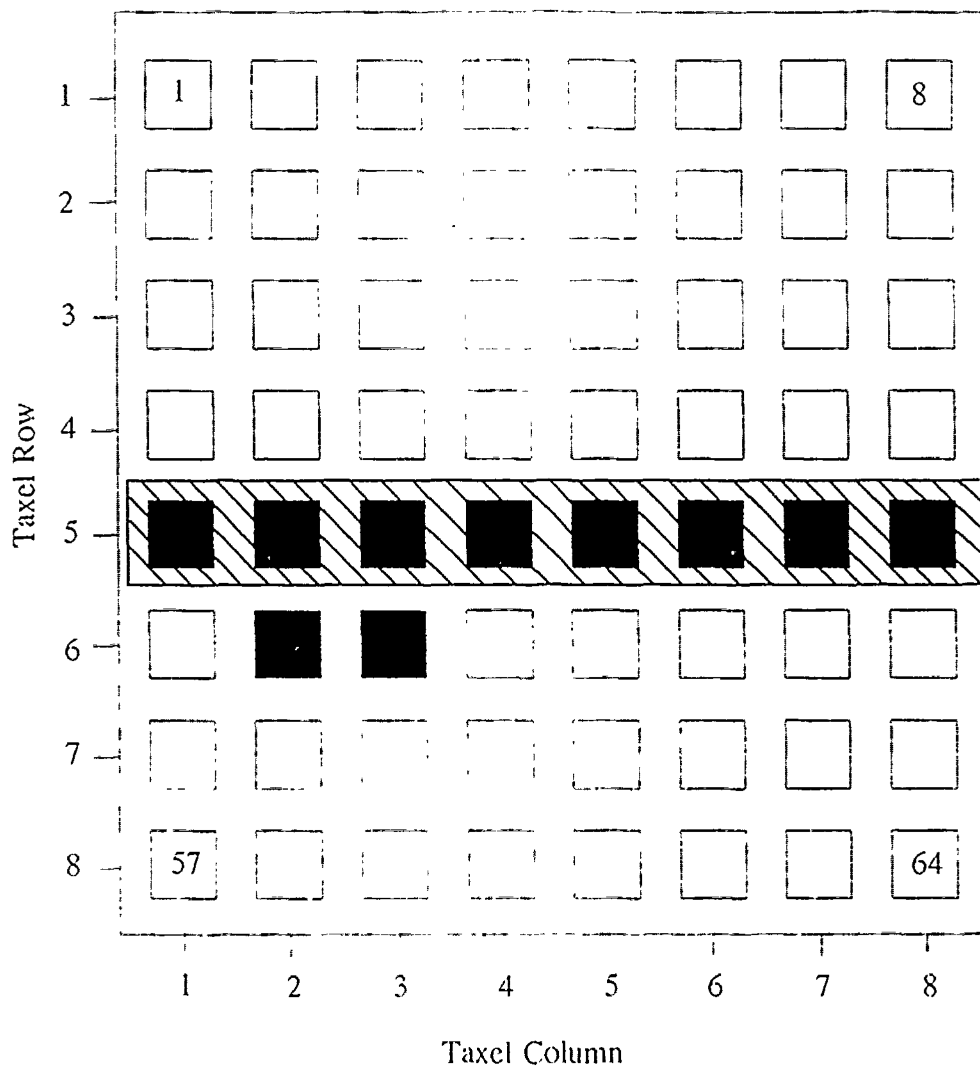

Figure L.3. 0.37-V Threshold Plot Of A 100 g Sharp Edge Shaped Load – Taxels With An Output Level Above This Threshold Level Are Displayed As Black And Taxels With An Output Level Below This Threshold Level Are Displayed As White.

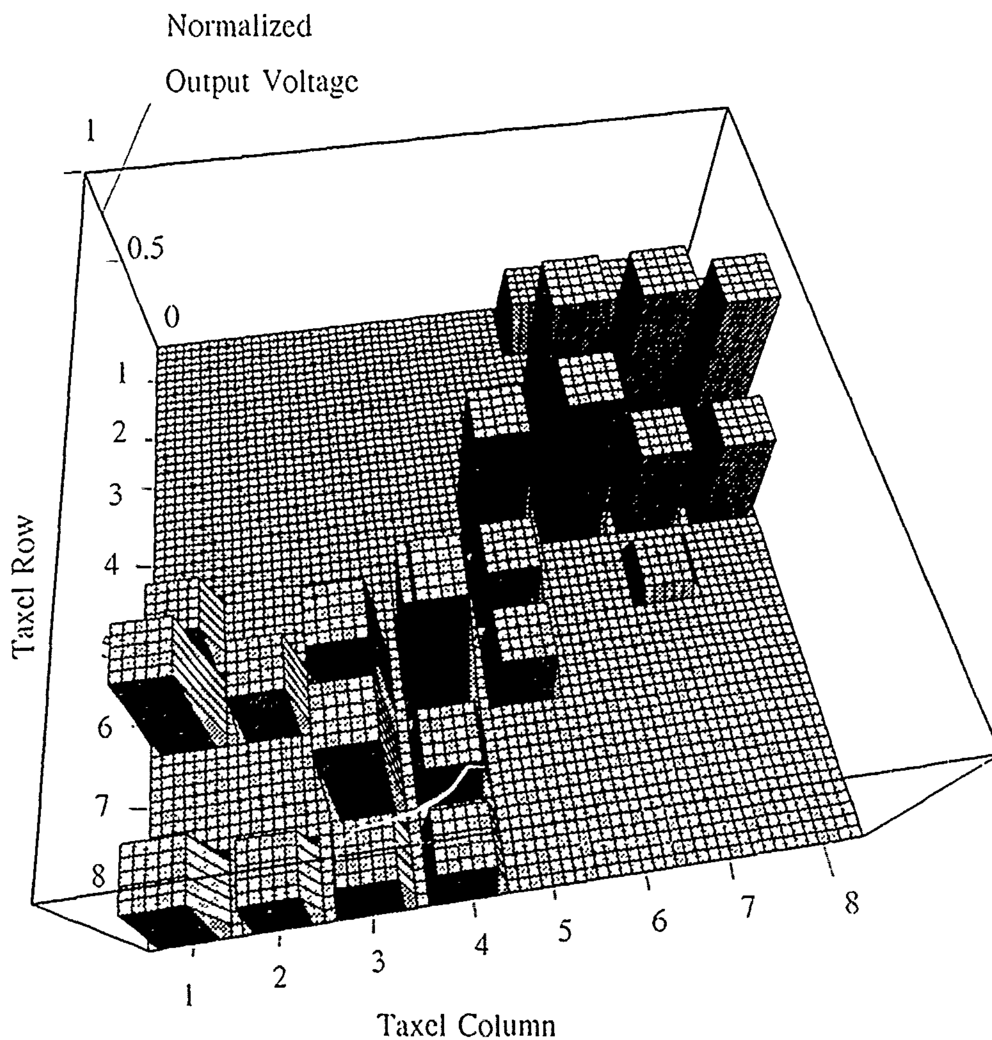

Figure L.4. Three-Dimensional Representation Of A 100 g Sharp Edge Shaped Load Applied To The Surface Of The Electrode Array. The z-Axis Corresponds To The Normalized Difference Between The Sensor's Loaded And Unloaded States, And The x- And y-Axes Correspond To The Electrode Columns And Rows, Respectively

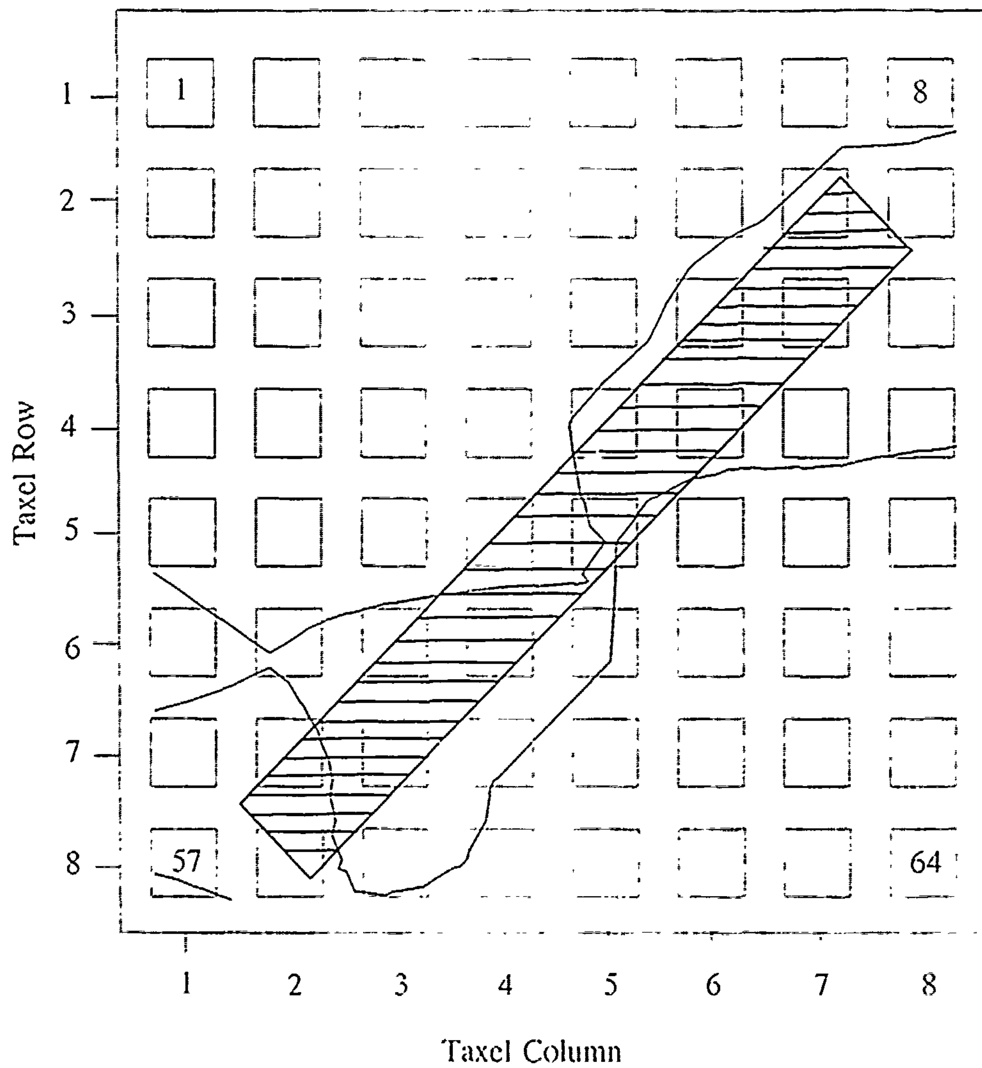

Figure L.5. 0.35-V Equipotential Contour Plot For A 100 g Sharp Edge Shaped Load Applied To The Surface Of The Electrode Array.

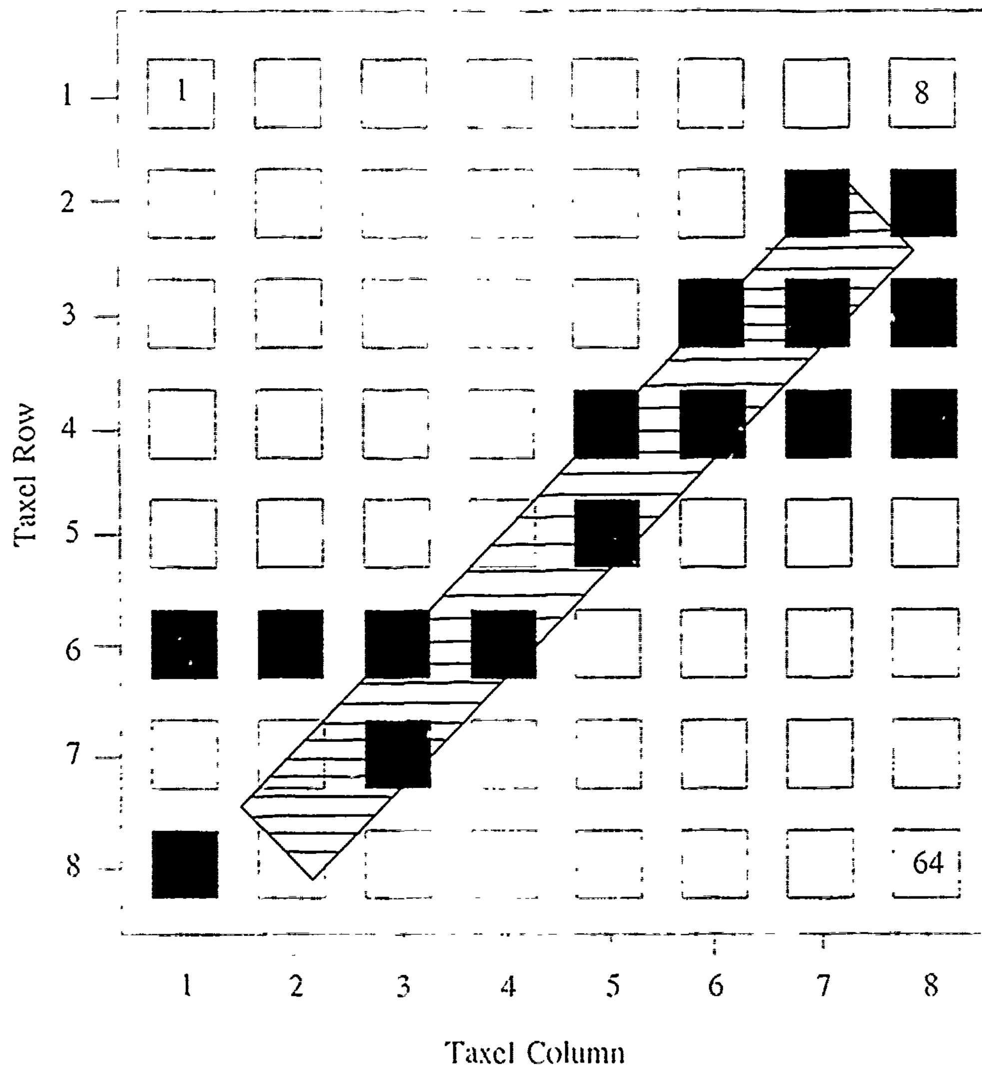

Figure L.6. 0.35-V Threshold Plot Of A 100 g Sharp Edge Shaped Load - Taxels With An Output Level Above This Threshold Level Are Displayed As Black And Taxels With An Output Level Below This Threshold Level Are Displayed As White.

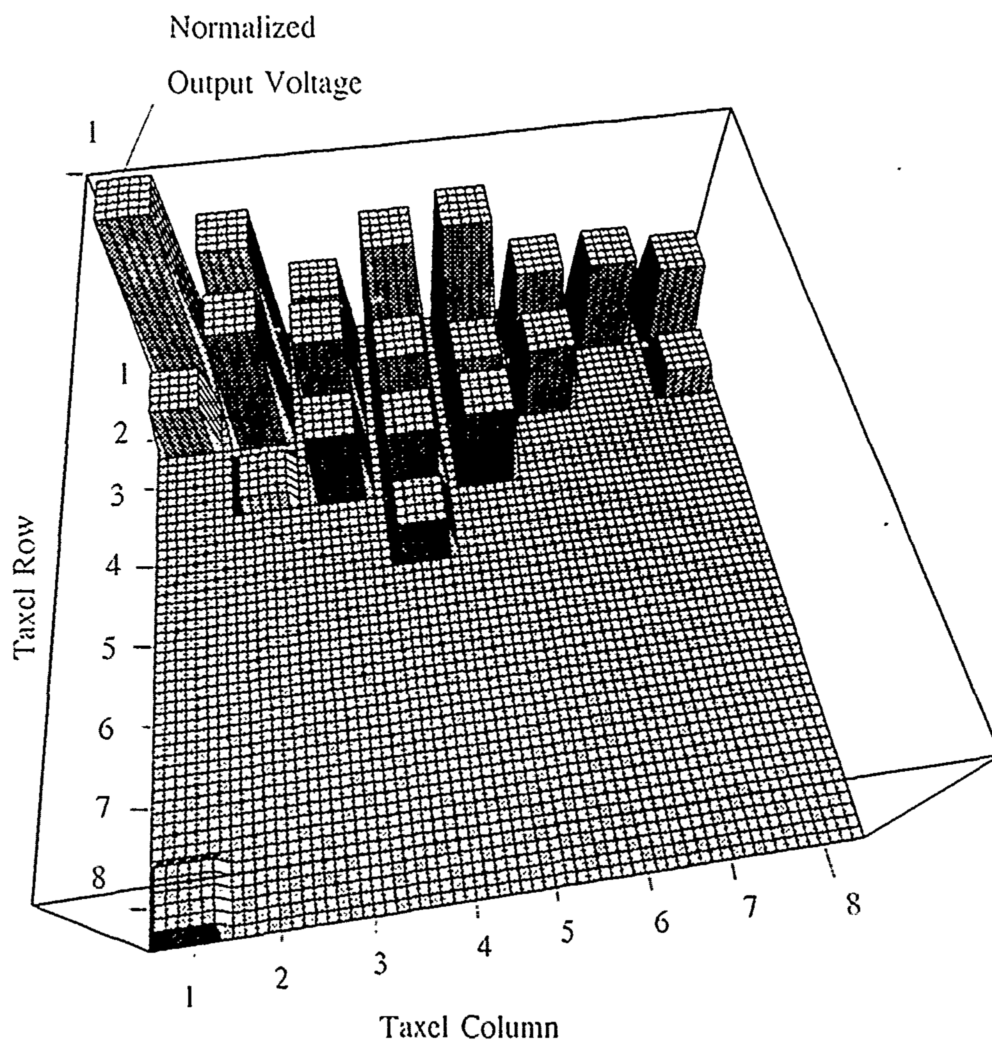

Figure L.7. Three-Dimensional Representation Of A 100 g Sharp Edge Shaped Load Applied To The Surface Of The Electrode Array. The z-Axis Corresponds To The Normalized Difference Between The Sensor's Loaded And Unloaded States, And The x- And y-Axes Correspond To The Electrode Columns And Rows, Respectively.

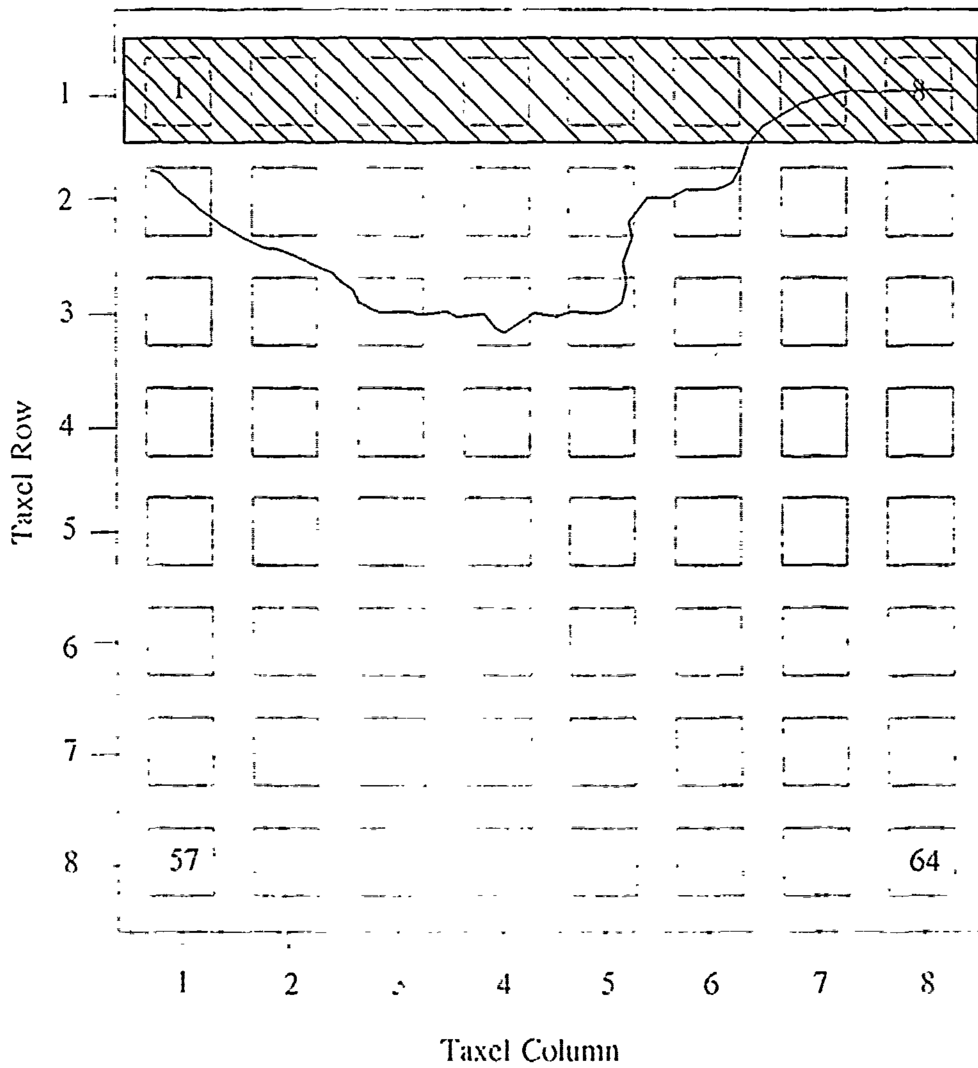

Figure L.8. 0.35-V Equipotential Contour Plot For A 100 g Sharp Edge Shaped Load Applied To The Surface Of The Electrode Array.

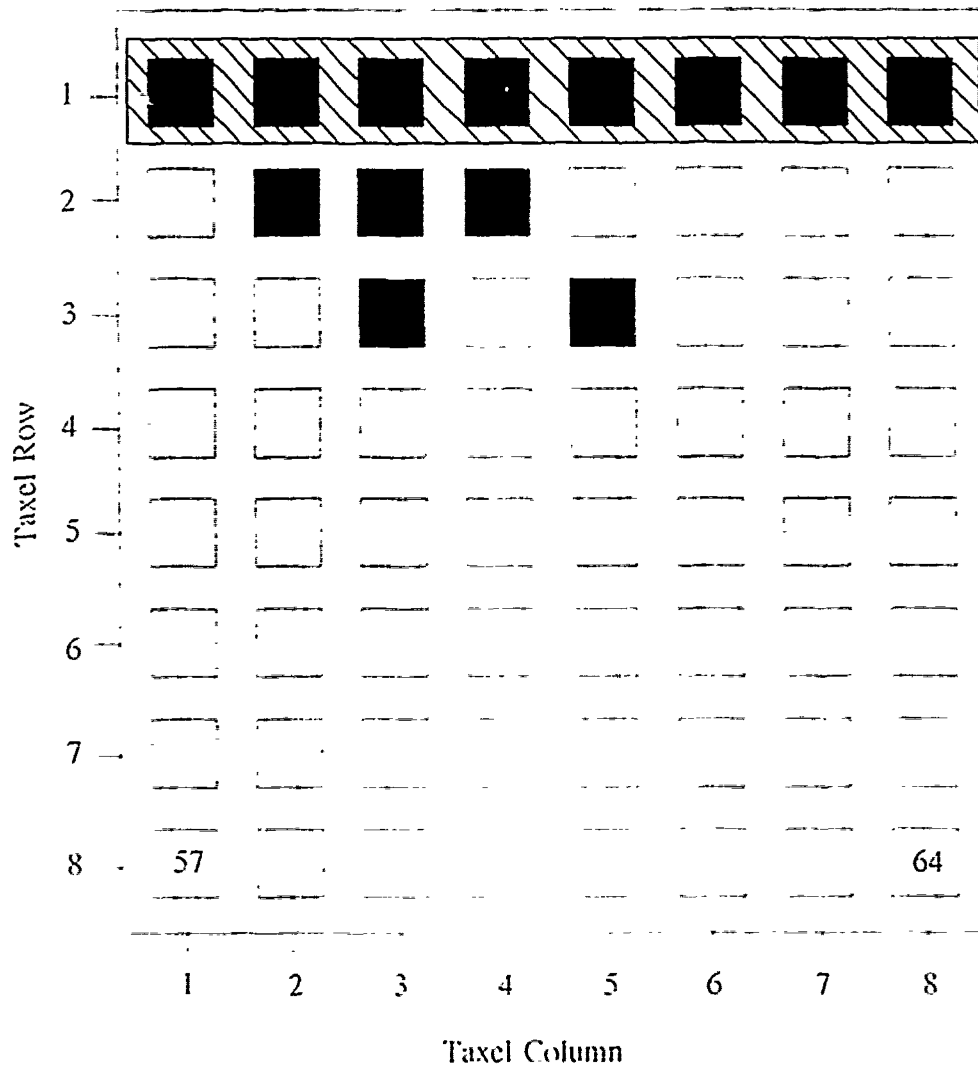

Figure L.9. 0.35-V Threshold Plot Of A 100 g Sharp Edge Shaped Load – Taxels With An Output Level Above This Threshold Level Are Displayed As Black And Taxels With An Output Level Below This Threshold Level Are Displayed As White.

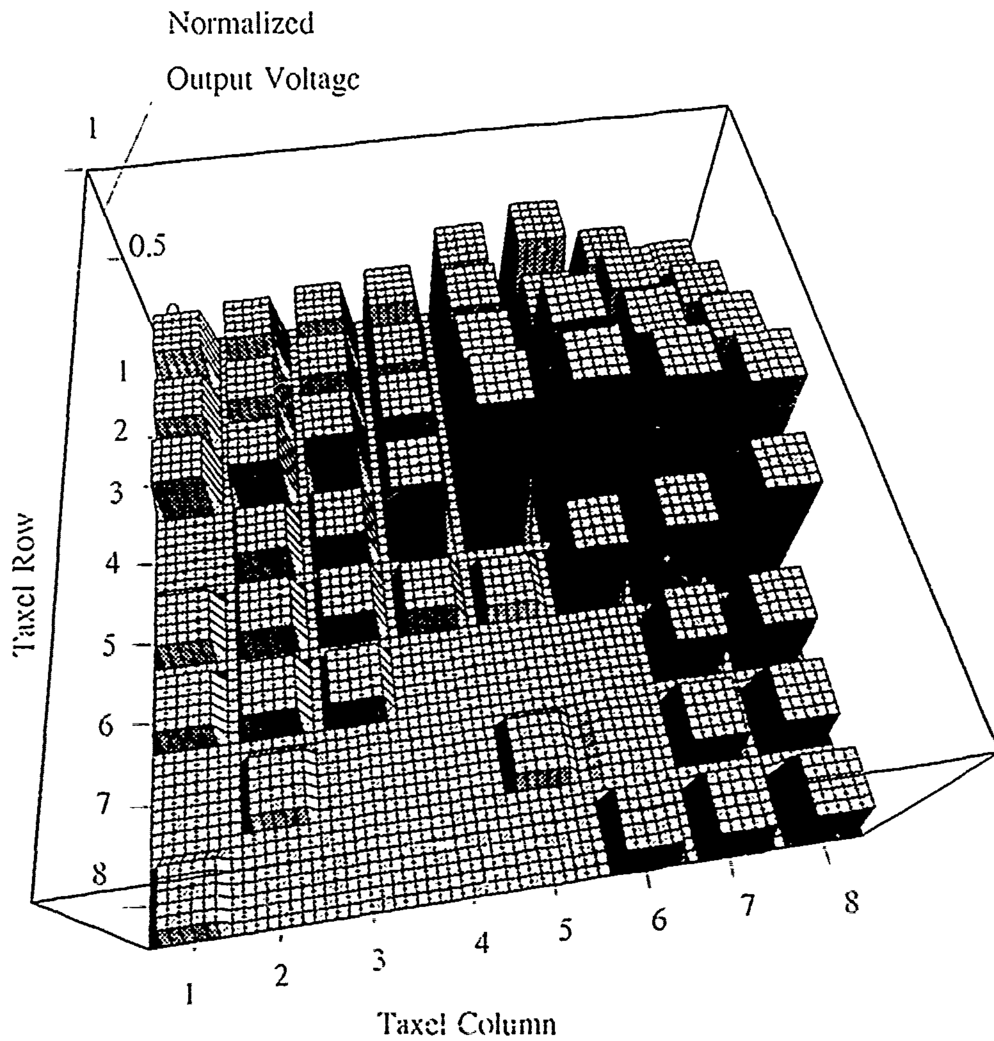

Figure L.10. Three Dimensional Representation Of A 100 g Small Square Shaped Load Applied To The Surface Of The Electrode Array. The z-Axis Corresponds To The Normalized Difference Between The Sensor's Loaded And Unloaded States, And The x- And y-Axes Correspond To The Electrode Columns And Rows, Respectively.

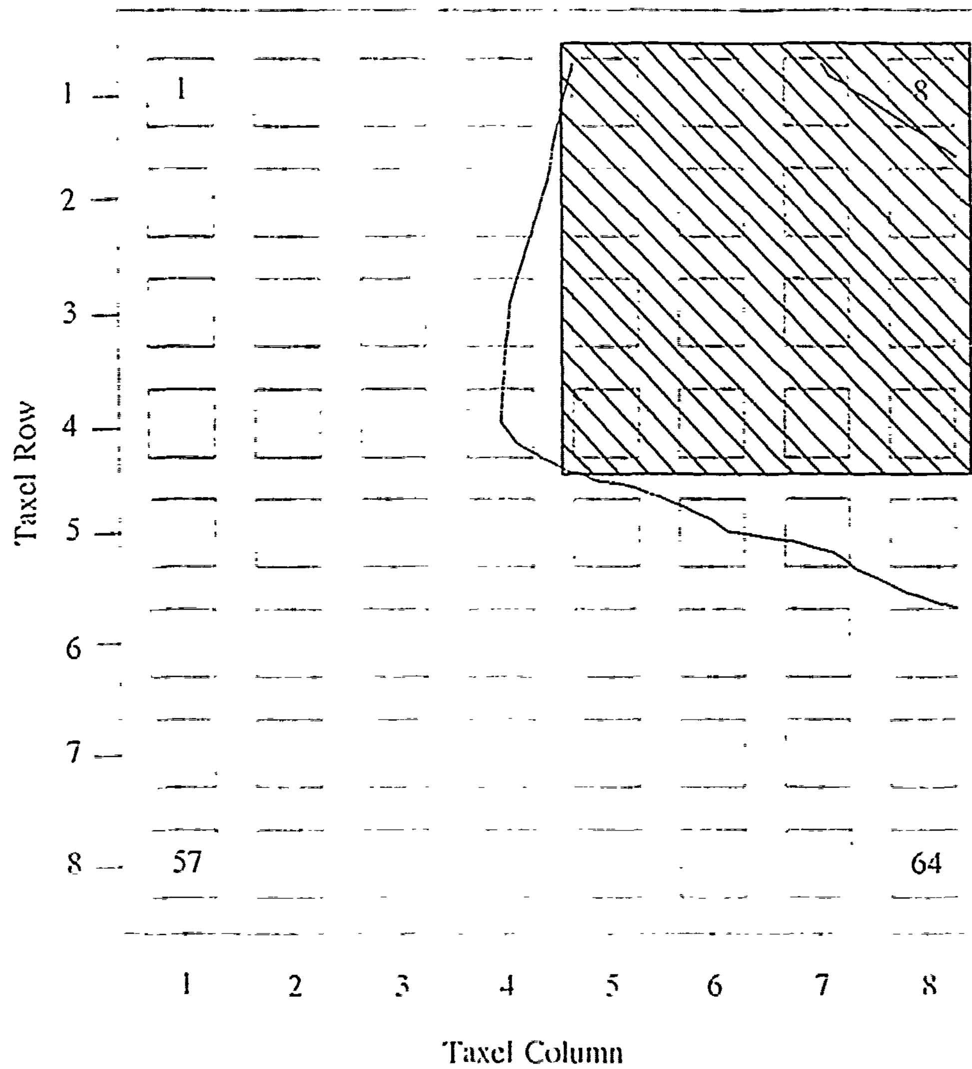

Figure L.11. 0.5-V Equipotential Contour Plot For A 100 g Small Square Shaped Load Applied To The Surface Of The Electrode Array.

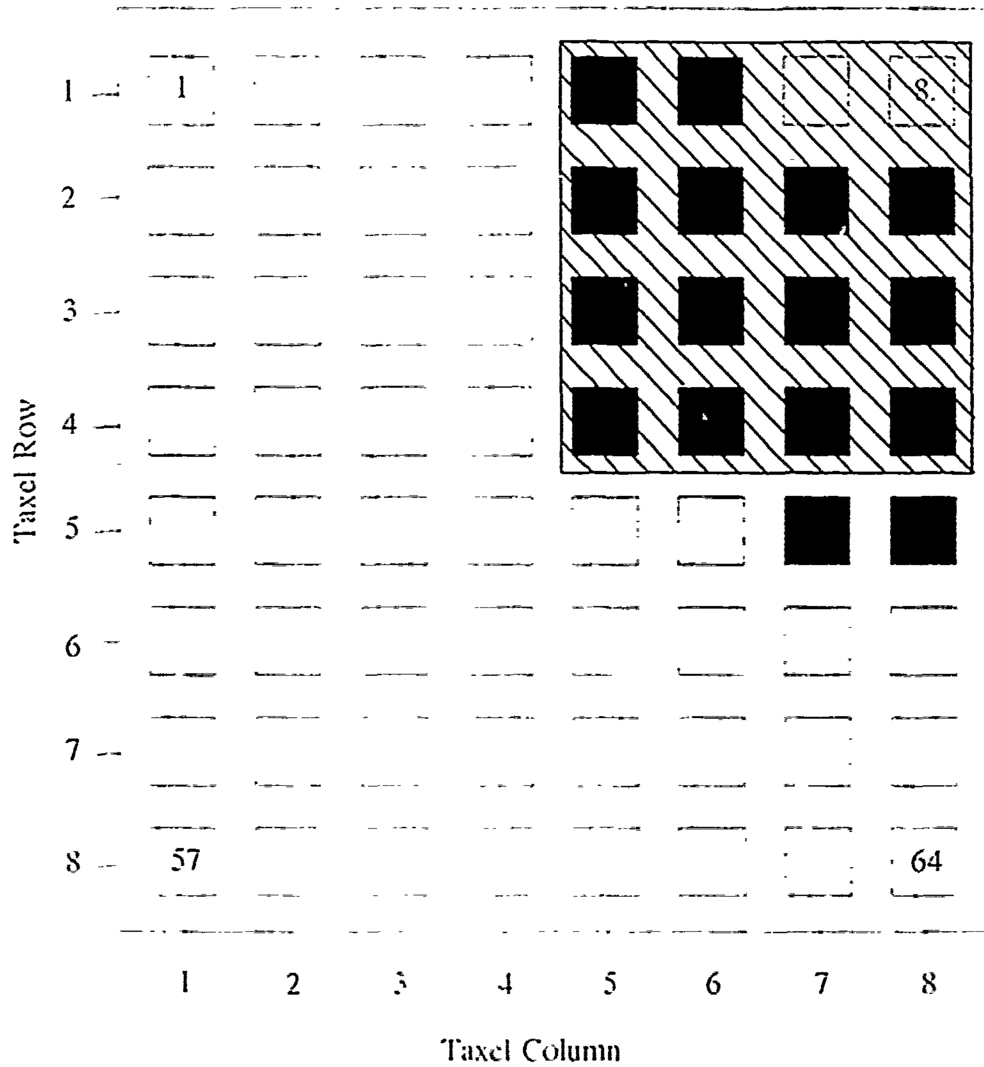

Figure L.12. 0.5-V Threshold Plot Of A 100 g Small Square Shaped Load - Taxels With An Output Level Above This Threshold Level Are Displayed As Black And Taxels With An Output Level Below This Threshold Level Are Displayed As White.

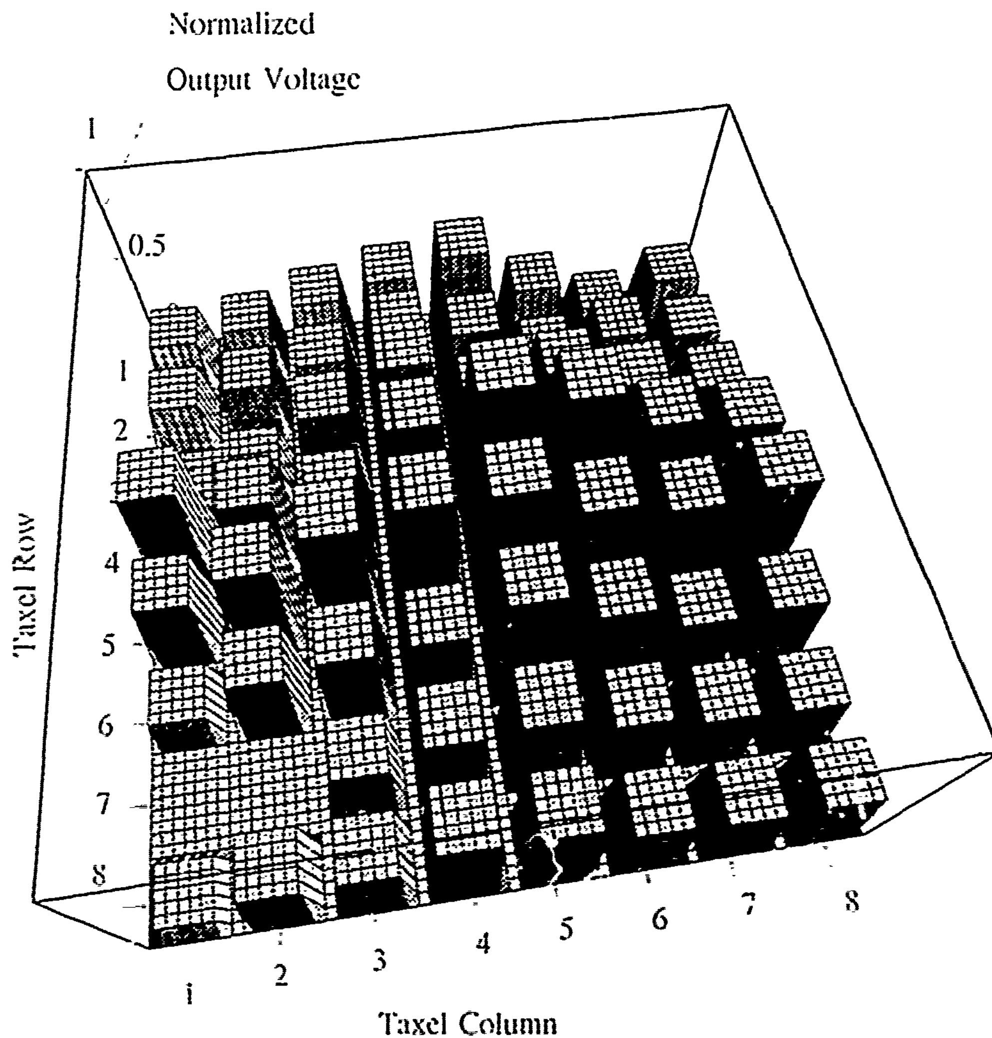

Figure L.13. Three-Dimensional Representation Of A 100 g Small Square Shaped Load Applied To The Surface Of The Electrode Array. The z-Axis Corresponds To The Normalized Difference Between The Sensor's Loaded And Unloaded States, And The x- And y-Axes Correspond To The Electrode Columns And Rows, Respectively.

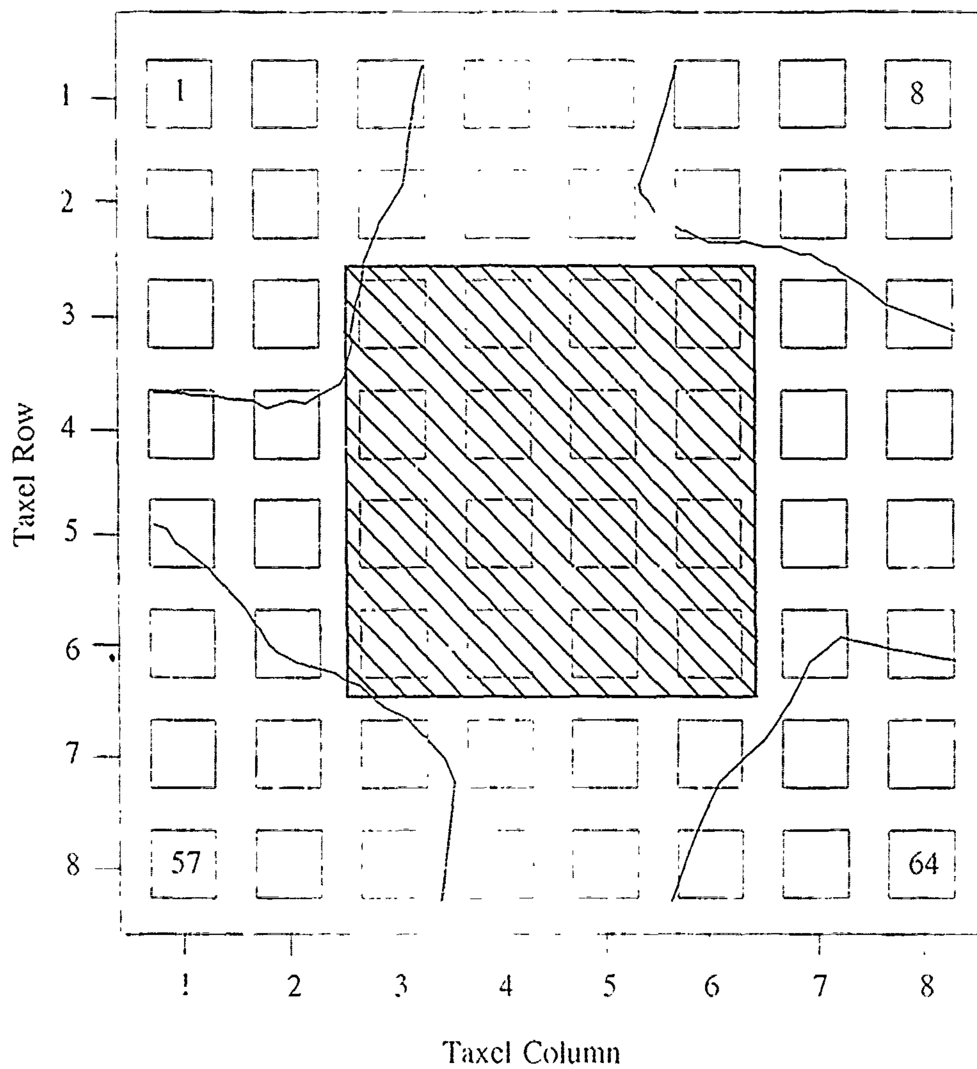

Figure L.14. 0.46-V Equipotential Contour Plot For A 100 g Small Square Shaped Load Applied To The Surface Of The Electrode Array.

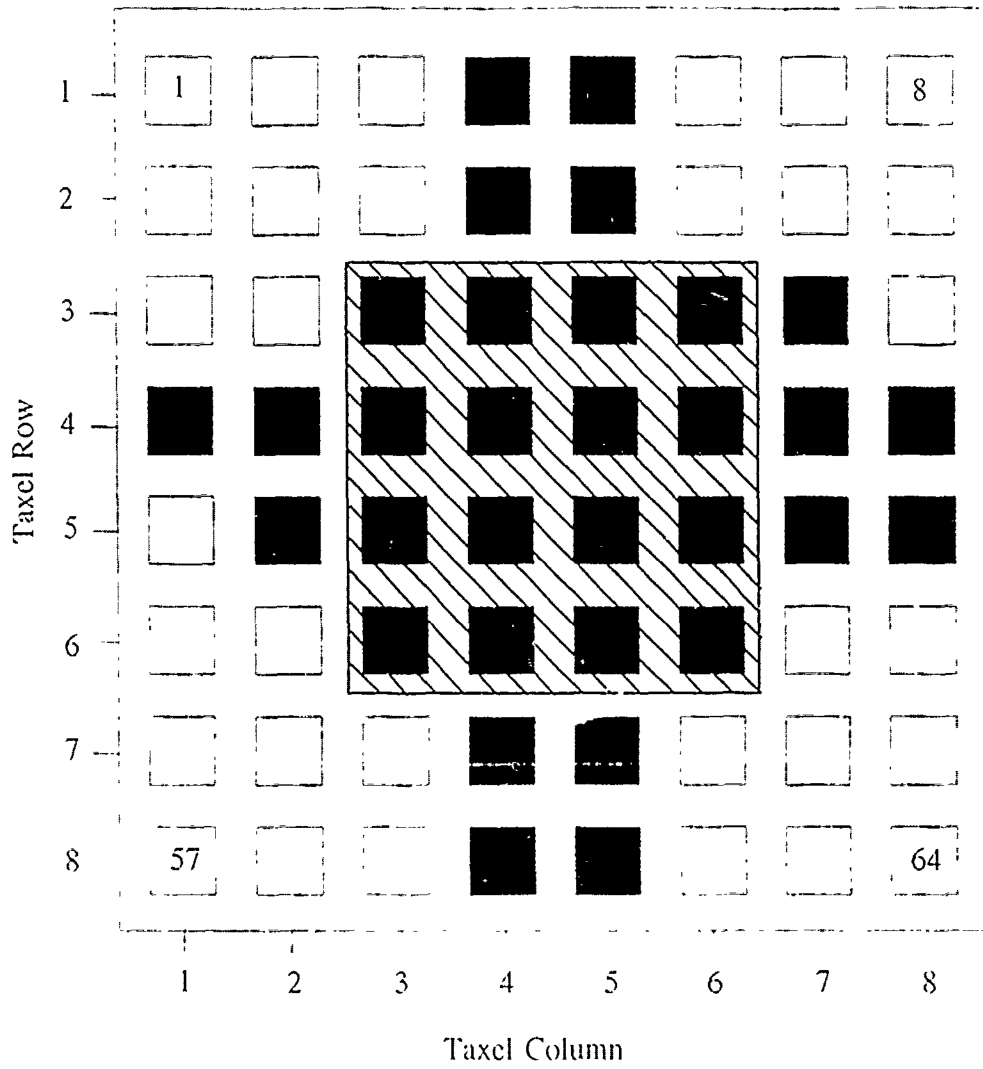

Figure L.15. 0.46-V Threshold Plot Of A 100 g Small Square Shaped Load - Taxels With An Output Level Above This Threshold Level Are Displayed As Black And Taxels With An Output Level Below This Threshold Level Are Displayed As White.

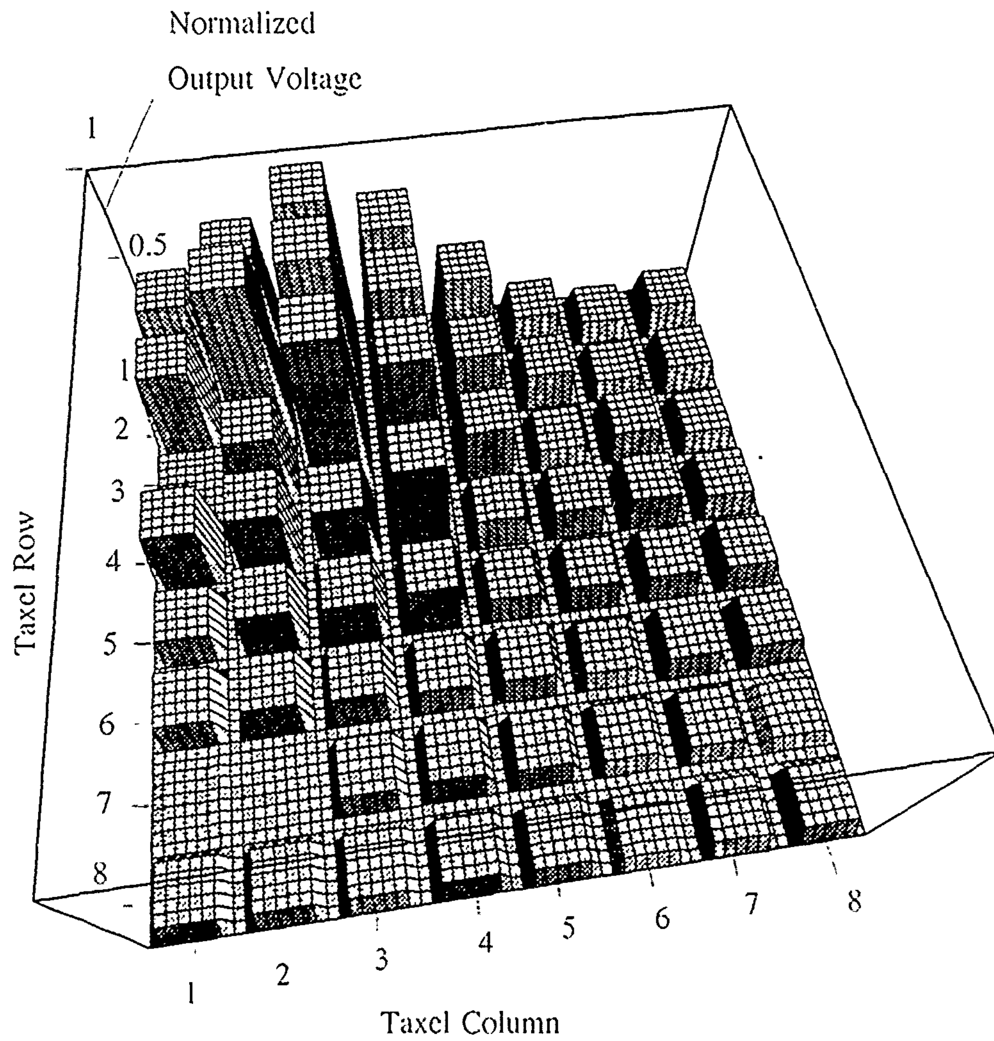

Figure L.16. Three-Dimensional Representation Of A 100 g Small Circularly Shaped Load Applied To The Surface Of The Electrode Array. The z-Axis Corresponds To The Normalized Difference Between The Sensor's Loaded And Unloaded States, And The x- And y-Axes Correspond To The Electrode Columns And Rows, Respectively.

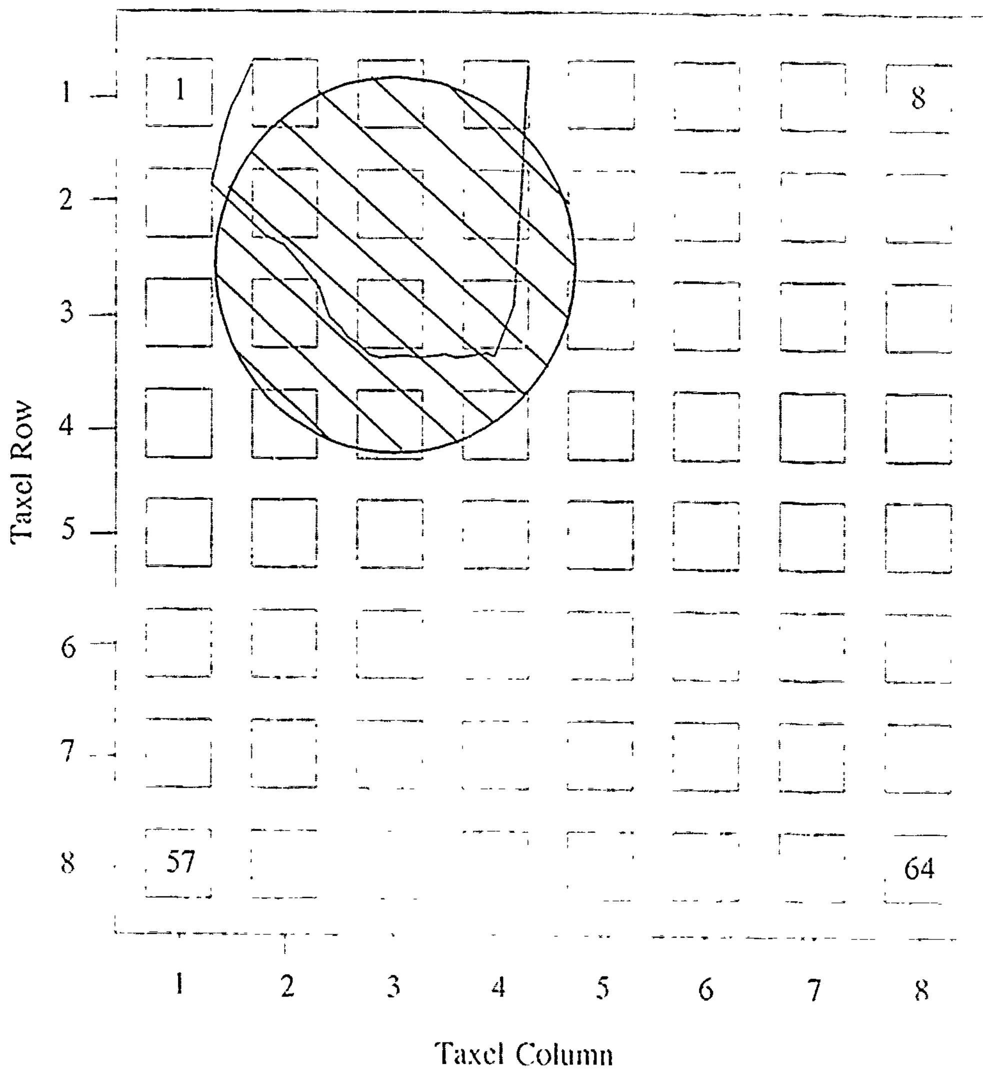

Figure L.17. 0.7-V Equipotential Contour Plot For A 100 g Small Circularly Shaped Load Applied To The Surface Of The Electrode Array.

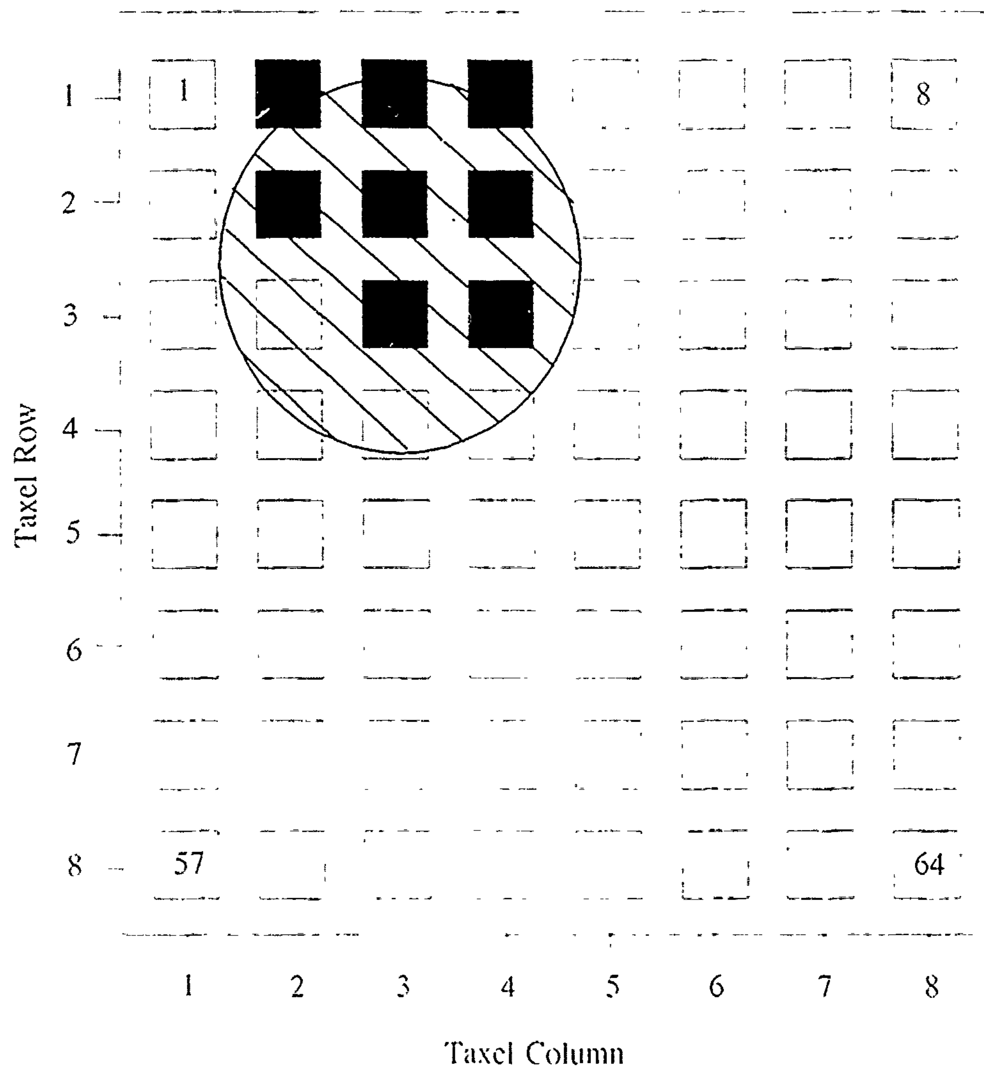

Figure L.18. 0.7-V Threshold Plot Of A 100 g Small Circularly Shaped Load - Taxels With An Output Level Above This Threshold Level Are Displayed As Black And Taxels With An Output Level Below This Threshold Level Are Displayed As White.

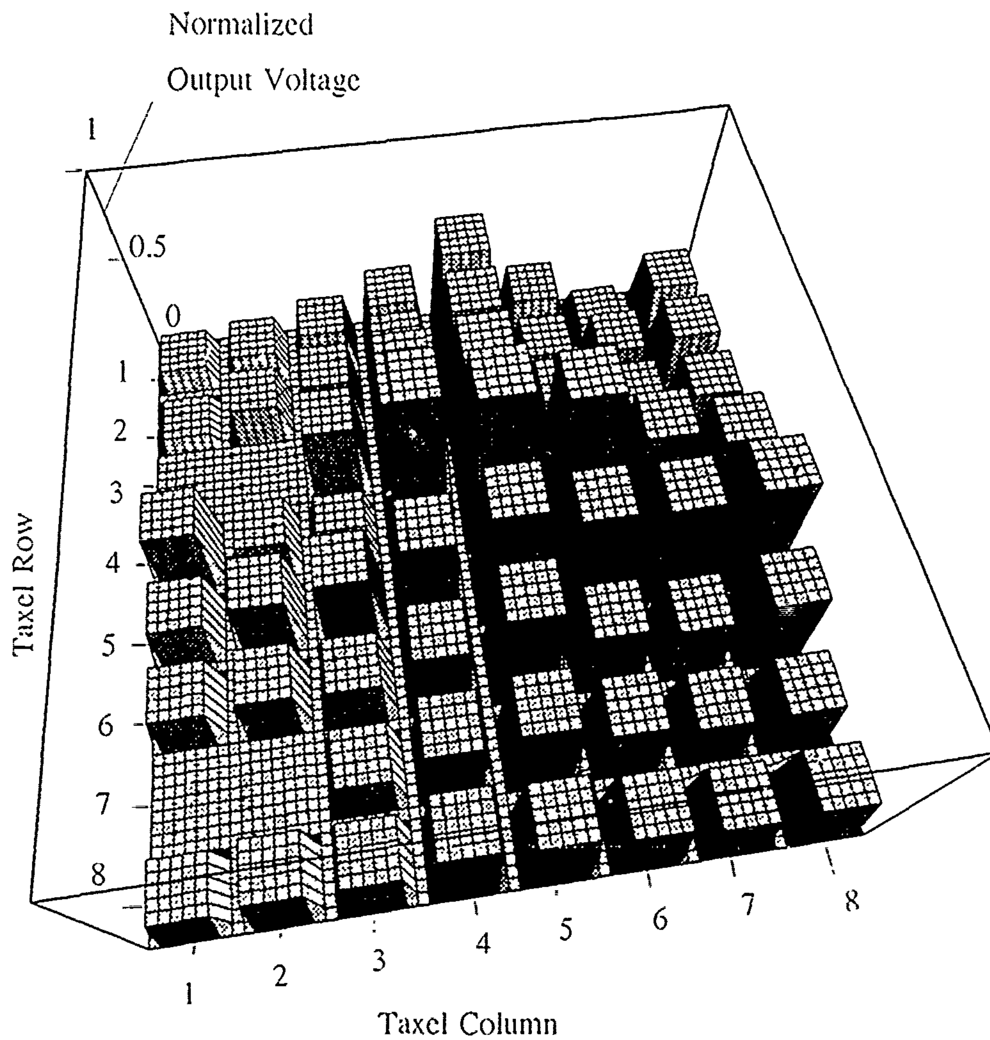

Figure L.19. Three-Dimensional Representation Of A 100 g Small Circularly Shaped Load Applied To The Surface Of The Electrode Array. The z-Axis Corresponds To The Normalized Difference Between The Sensor's Loaded And Unloaded States, And The x- And y-Axes Correspond To The Electrode Columns And Rows, Respectively.

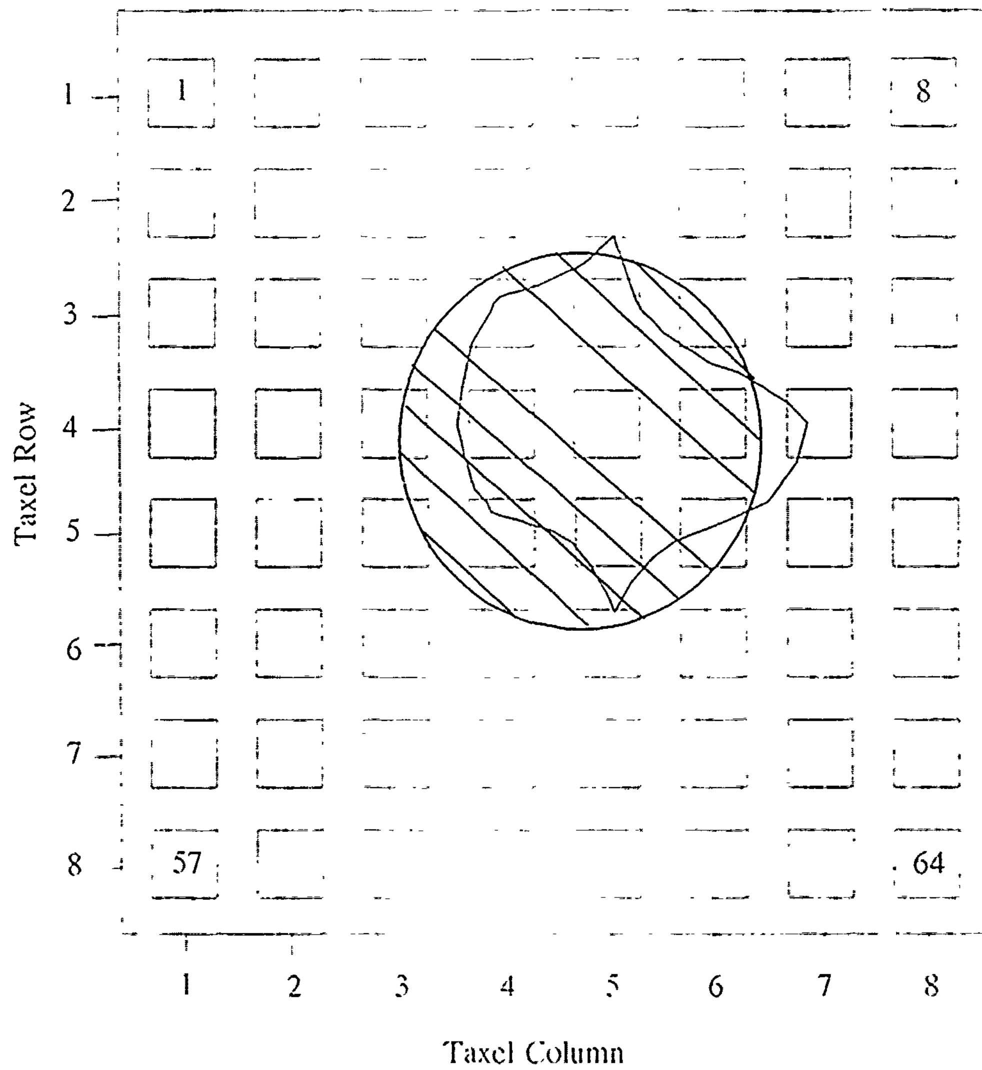

Figure L.20. 0.7-V Equipotential Contour Plot For A 100 g Small Circularly Shaped Load Applied To The Surface Of The Electrode Array.

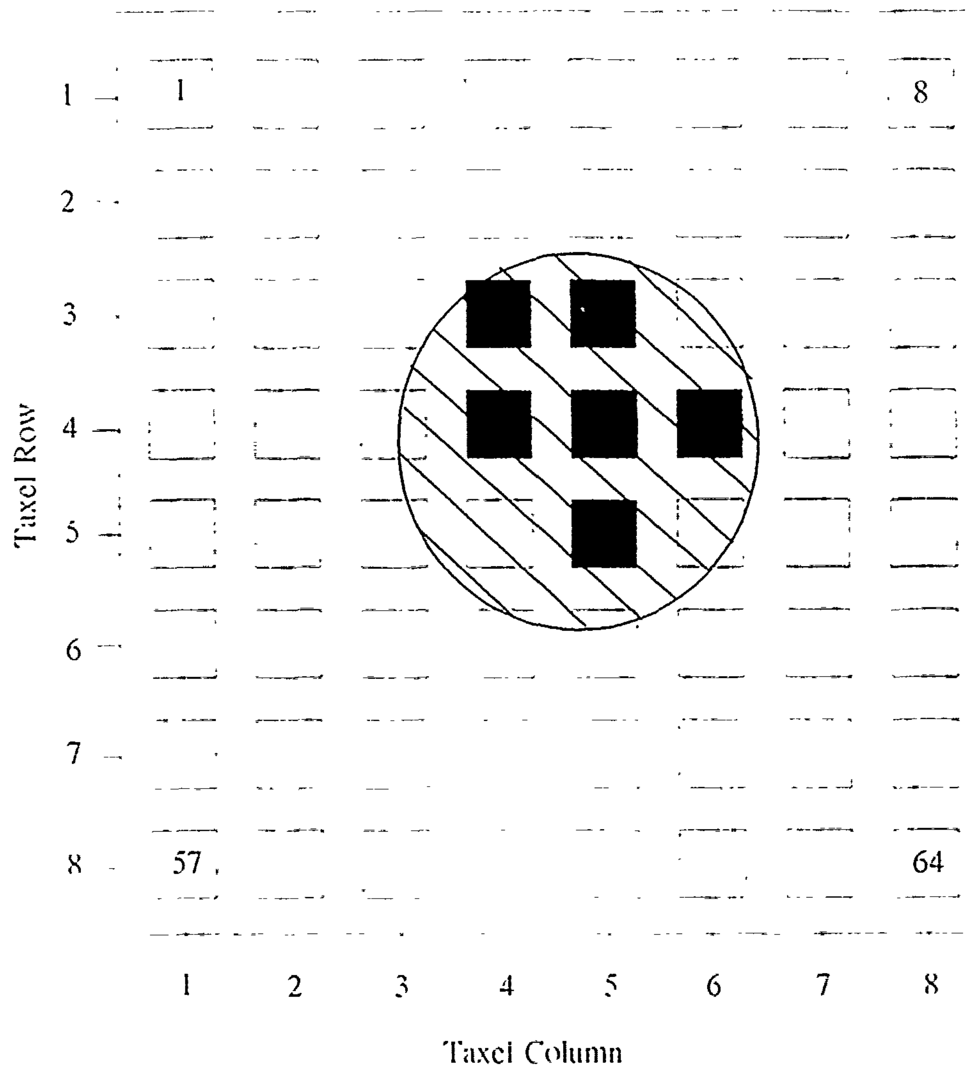

Figure L.21. 0.7-V Threshold Plot Of A 100 g Small Circularly Shaped Load – Taxels With An Output Level Above This Threshold Level Are Displayed As Black And Taxels With An Output Level Below This Threshold Level Are Displayed As White.

Appendix M. *Potential T-Gate Multiplexer Design*

In the previous research, charge leakage due to interface problems with an *in situ* multiplexer compromised the operation of the tactile sensor integrated circuit (45:6-1; 46:VI-1). In this research effort, a commercial multiplexer IC was used; however, an *in situ* multiplexer for future research efforts is still desired. To evaluate the functionality of an *in situ* T-gate multiplexer (a design used by Capt Fitch in his tactile sensor integrated circuit research), a 16-to-1 T-gate multiplexer was fabricated using the *tiny-chip* format offered by MOSIS. The T-gate multiplexer included a plethora of test probe pads to facilitate characterizing of each node in a given signal path.

T-Gate Array Design A 16-to-1 multiplexer was designed using CMOS T-gates arranged in a 4 x 4 array. The T-gate transistor sizing and optimizing process was completed by Capt Fitch when the multiplexer design was incorporated as an *in situ* element in the tactile integrated circuit sensor; the final design was a 19-to-1 multiplexer. The multiplexer designed in this research effort used the same Magic CAD CIF file, but it removed 16 T-gates, leaving a 16-to-1 multiplexer (Figure M.1). A 16-input design was chosen because it corresponds to one fourth of the actual tactile sensor array configuration, and it could also be easily integrated into the control scheme of the commercial multiplexer control circuit. Should this multiplexer function properly, four of these multiplexers could be used as an off-chip multiplexer for the tactile sensor. Each T-gate in the multiplexing array is selected using a control scheme which selects one column of the array, and it also simultaneously selects one row of the array, and thus, one input to the multiplexer is passed to the output.

Various test probe pads were incorporated in the layout of the multiplexer circuit. The test probe pads provide the ability to verify the T-gate select line voltages across the IC, the input signal voltages, and the signal voltages passed through the selected T-gates (Figure M.2). Four horizontally selected T-gates possess four test probe pads each. This configuration facilitates evaluation of the select/control line voltage drops across the IC. The associated input signal corresponding to each of these four T-gates can be traced across the IC by placing probe pads on any subsequent T-gate in its path.

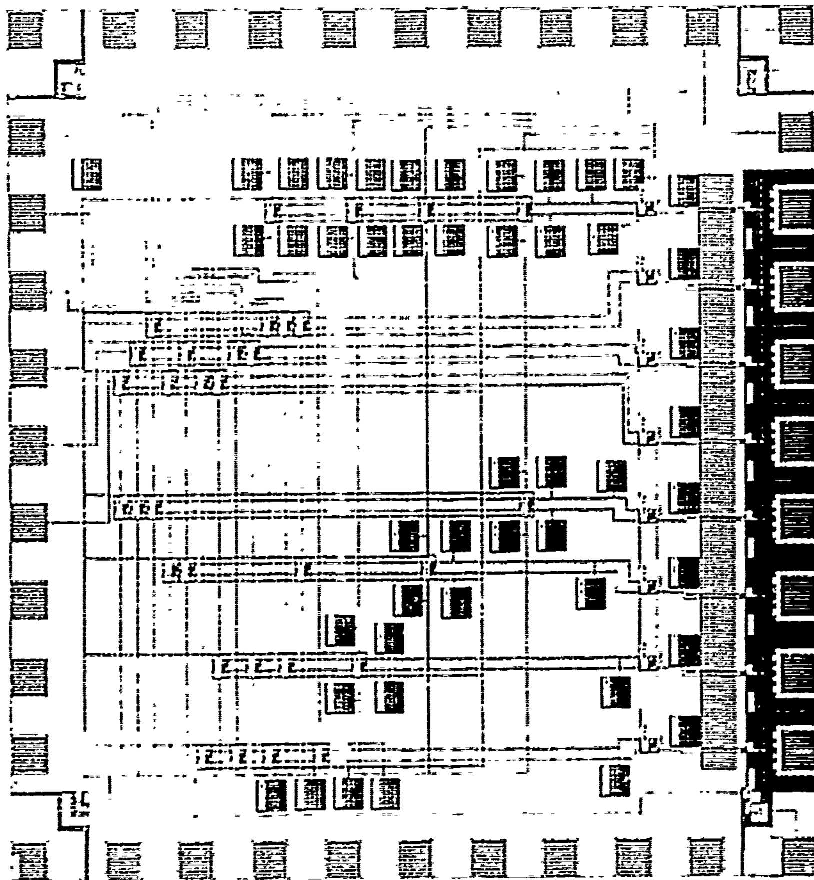

Figure M.1. T-gate Multiplexer Caltech Intermediate Format (CIF) File (40×).

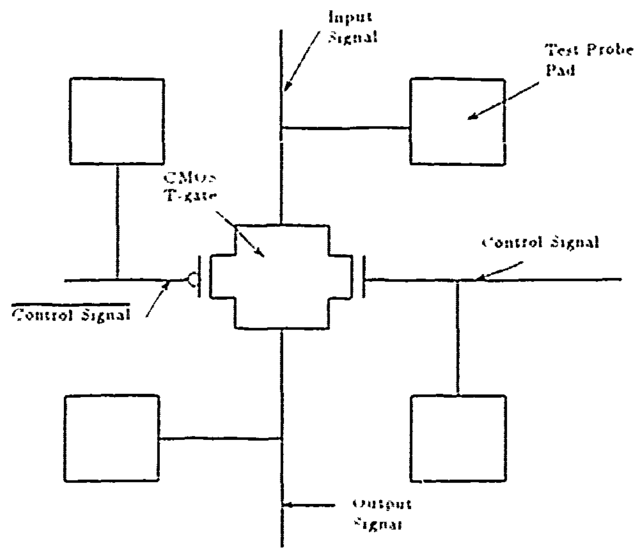

Figure M.2. Schematic Diagram Of The Test Probe Pad Locations In One Element Of The 16-to-1 Multiplexer T-gate.

Control Scheme To select the T-gates in sequence, a ring counter was used in the *in situ* version of the T-gate multiplexer designed by Capt Fitch; however, after evaluation of the individual circuits, Capt Fitch discovered that the ring counter output did not correspond with the theoretical output predicted by SPICE (45:5-10). Therefore, in this effort, the ring counter function will be realized off-chip, and only the T-gate performance will be evaluated. The control of each T-gate requires that the control signal and its complement, and as a consequence, eight inverters were included to complement the input control signals. The control signal inverters possess probe pads on all inputs and outputs to evaluate their signal conversion capability. Additionally, diode protection is included on the inputs to the control signal line to protect the gates of these inverters. Appendix C contains the SPICE deck used to evaluate the operation of the inverter.

Suggested T-Gate Multiplexer Evaluation The T-gate multiplexer IC should be evaluated to determine the feasibility of incorporating the design into a multiplexer on a future generation tactile sensor IC. To properly evaluate the multiplexer's design, each component within it should be evaluated, and then the entire circuit's performance should be measured.

The IC should be placed into an Elite-1 Circuit Design System Protoboard and configured with input signals, bias supply voltage (V_{dd}), and ground. This ensemble could then be positioned beneath the Micromanipulator probe station where pin-point probes can be used to access the test probe pads on the IC. Voltage readings across the IC should be measured using a digital multimeter; they include: those at the inverter, V_{dd}, and the input signal lines. Next, the control lines of the multiplexer should be configured to route one of the input lines to the output pin. The voltage readings associated with this signal should then be measured with a digital multimeter and recorded along the signal path. Finally, the control signals used to control the multiplexer could be clocked at frequencies spanning 500 Hz to 100 kHz, and the output response should be displayed on the digital storage oscilloscope. Various input voltages spanning 0 V to 15 V should be supplied by a battery connected to the multiplexer. The output response should then be displayed on the digital storage oscilloscope, recorded, and stored on a floppy diskette via the Z-248 personal computer and a BASIC program listed in Appendix E.

Bibliography

1. Allen. H. V. and others. "A Sub-miniature Load Cell Configurable for Multiplexed Tactile Arrays." *Proceeding of the 4th International Conference on Solid-state Sensors and Actuators (Transducers '87).* Tokyo. Japan. 2-5 June 1987. 448-450.

2. Allen, P. "Surface Descriptions from Vision and Touch," *International Conference on Robotics.* Atlanta. Georgia. U.S.A., 13-15 March 1984. 394-396.

3. Allen. P. "Current Research in Robotics and Automation," *Computer. 22:* 3. 50-52 (March 1989).

4. Arbib. M. A. and others. "Perceptual Systems for Robots." *Interdisciplinary Science Reviews. 9:* 1. 31-46 (1984).

5. Arges. K. P. and A. E. Palmer. *Mechanics of Materials.* New York: McGraw-Hill. Inc.. 1963.

6. Assente. R. and others. "Distributed Multiplexing Architecture for PVDF Multitransducer Platform Scanning: A Theoretical and Practical Approach." *Proceedings of the 5th International Symposium on Electrets.* Heidelberg. FRG. 1985. 795-801.

7. Bardelli. R. and others. "Piezo- and P oelectric Polymers Skin Like Tactile Sensor for Robots and Protheses." *Proceedings of the 13th International Symposium On Industrial Robots:* 18-15 - 18-55 (April 1983).

8. Barsky. M. F. and others. "Robot Gripper Control System Demonstrating PVDF Piezoelectric Sensors." *Proceedings of the IEEE Ultrasonics Symposium.* Williamsburg. VA. U.S.A.. 17-19 November 1986. 545-548.

9. Barth. P. W. "Sensor Applications in Robotics." *Robotics Engineering:* 17-20 (September 1986).

10. Begej. S. "An Optical Tactile Array Sensor." *SPIE Intelligent Robots and Computer Vision. 521:* 271-280 (1984).

11. Begej. S. "Planar and Finger-shaped Optical Tactile Sensors for Robotic Applications." *IEEE Journal of Robotics and Automation. 4:* 472-484 (October 1988).

12. Ben'kova. L. F. and others. "Piezoelectric Sensor Made from Polyvinylidene Fluoride." *Pribory I Teknika Eksperimenta. 83:* 4. 220-221 (August 1982).

13. Boie. R. A. "Capacitive Impedance Readout Tactile Image Sensor." *International Conference on Robotics.* Atlanta. Georgia. U.S.A.. 13-15 March 1984. 370-378.

14. Boie, R. A. "Conformable Tactile Sensor." U. S. Patent 4,526,043, July 2, 1985.

15. Borenstein, J. and Y. Koren. "Obstacle Avoidance with Ultrasonic Sensors." *IEEE Journal of Robotics and Automation, 4:* 2, 213–218 (April 1988).

16. Brady, M. *Robotics and Artificial Intelligence.* New York: Springer-Verlag, 1984.

17. Broadhurst, M. G. "Physical Basis for Piezoelectricity in PVDF." *Ferroelectrics, 60:* 1, 3-13 (1984).

18. Brown, M. K. "Feature Extraction Techniques for Recognizing Solid Objects with an Ultrasonic Range Sensor." *IEEE Journal of Robotics and Automation, RA-1:* 4, 191-205 (December 1985).

19. Brown, R. "Piezo Film for Monitoring Vibration." *Sensors, 5:* 20-26 (January 1988).

20. Cady, W. G. *Piezoelectricity, An Introduction to the Theory and Application of Electromechanical Phenomena in Crystals*, Volumes I and II. New York: Dover Publications, 1964.

21. Chatigny, J. V. and L. E. Robb. "Piezo Film Sensors." *Sensors, 3:* 50-56 (1986).

22. Checinski, S. S. "Magnetoelastic Tactile Sensor." *Robot Sensors, Tactile and Non-Vision*, Volume 2, edited by Alan Pugh. New York: Springer-Verlag, 1986, 229–233.

23. Chen, Y. and L. Wang. "A Piezopolymer Finger Pulse and Breathing Wave Sensor." *Sensors and Actuators, 23:* 879-882 (1990).

24. Clark, J. J. "A Magnetic Field Based Compliance Matching Sensor for High Resolution, High Compliance Tactile Sensing." *Proceeding of the IEEE International Conference on Robotics and Automation, 2:* 760-764 (1988).

25. Chun, K. J. and K. D. Wise. "A Capacitive Silicon Tactile Imaging Array." *Proceedings of the 3rd International Conference on Solid-State Sensors and Actuators (Transducers '85)*, Philadelphia, PA, U.S.A., 11-14 June 1985, 22-25.

26. Coiffet, P. *Interaction with the Environment.* Englewood Cliffs, New Jersey: Prentice Hall, Inc., 1983.

27. Dario, P. "Tactile Sensing: Technology and Applications." *Sensors and Actuators, 27:* 251–256 (1991).

28. Dario, P. and D. De Rossi. "Tactile Sensors and the Gripping Challenge." *IEEE Spectrum, 22:* 46–52 (1985).

29. Dario, P. and others. "Ferroelectric Polymer Tactile Sensors with Anthropomorphic Features," *Proceedings of the IEEE Conference on Robotics*. Atlanta, GA, U.S.A., 5-7 March 1984, 332-340.

30. Dario, P. and others. "Multiple Sensing Fingertip for Robot Active Touch." *Proceeding of the 3rd ICAR*. Versaille. France. 1987, 347-358.

31. Dario, P. and G. Buttazzo. "An Anthropomorphic Robot Finger for Investigating Artificial Tactile Perception." *Journal of Robotics Research. 6:* 3, 25-48, (1987).

32. Davis, G. T. "Structure, Morphology, and Models of Polymer Ferroelectrics." *The Application of Ferroelectric Polymers*, edited by T. T. Wang. New York: Chapman and Hall, 1988, 37-65.

33. De Rossi, D. and P. Dario. "Multiple Sensing Polymeric Transducers for Object Recognition Through Active Touch Exploration." *Proceedings Robotics Research: The Next Five Years and Beyond*. MS84-492. Society of Manufacturing Engineers, Dearborn, MI, U.S.A., 14-16 August 1984, 1-13.

34. De Rossi, D. and others. "Biomimetic Tactile Sensor with Stress-Component Discrimination Capability," *Journal of Molecular Electronics, 3:* 173-181 (1987).

35. Durelli, A. J. *Introduction to the Theoretical and Experimental Analysis of Stress and Strain*. New York: McGraw-Hill, Inc., 1958.

36. Eckerle, J. S. and P. M. Newgard. "Arterial Tonometry: The Development of a New Medical Sensor," *Sensors. 8:* 11-16 (May 1991).

37. Emge, S. R. and C. Chen. "Two-dimensional Contour Imaging with a Fiber Optic Microbend Tactile Sensor Array." *Sensors and Actuators, 3:* 31-42 (1991).

38. Ermert, H. and others. "An Adaptive Ultrasonic Sensor for Object Identification." *Proceedings of the IEEE Ultrasonics Symposium*, Williamsburg, VA, U.S.A., 17-19 November 1986, 555-558.

39. Fearing, R. S. "Tactile Sensing Mechanisms," *The International Journal of Robotics Research. 9:* 3-23 (June 1990).

40. Fearing, R. S. and John M. Hollerbach. "Basic Solid Mechanics for Tactile Sensing," *International Journal of Robotics Research. 4:* 3, 40-54 (1985).

41. Fearing, R. S. and T. O. Binford. "Using a Cylindrical Tactile Sensor for Determining Curvature," *Proceedings of the IEEE International Conference on Robotics and Automation*. Philadelphia, PA, U.S.A., 24-29 April 1988, 765-771.

42. Fielding, P. J. "Evaluation of a Robotic Tactile Sensing System." *Sensors. 3:* 35-46 (1986).

43. Finch, J. W. and others. "Control Aspects of an Integrated Sensor Based Robot System with Novel Tactile Pads," *Robot Control 1988 (SYROCO '88)*. edited by U. Rembold, New York: Pergamon Press, 1989, 305–309.

44. Fiorillo, A. S. and others. "A P(VDF-TrFE)-based Integrated Ultrasonic Transducer." *Sensors and Actuators. 21:* 719–725 (1990).

45. Fitch, R. C. *A Robotic Tactile Sensor Incorporating Silicon Planar Technology, a Piezoelectric Polyvinylidene Fluoride Film. and On-chip Signal Processing.* MS Thesis, AFIT/GE/ENG/90D-21. School of Engineering, Air Force Institute of Technology (AU), Wright Patterson AFB, OH, December 1990.

46. Ford, D. G. *Multiplexed Robotic Tactile Sensor Fabricated From Polyvinylidene Fluoride Films.* MS Thesis, AFIT/GE/ENG/89D-13. School of Engineering. Air Force Institute of Technology (AU), Wright Patterson AFB. OH, December 1989.

47. Gao, G. and others. "A PVDF Film Sensor for Material Identification," *Sensors and Actuators, 21:* 886–889 (1990).

48. Garner, G. M. "Microphones, Headphones, and Tone Generators," *The Application of Ferroelectric Polymers*, edited by T. T. Wang. New York: Chapman and Hall, 1988, 190-208.

49. Gehlbach, S. M. and R. E. Alvarez. "Digital Ultrasound Imaging Techniques Using Vector Sampling and Raster Line Reconstruction," *Ultrasonic Imaging. 3:* 83–107 (1981).

50. Gerliczy, G. and R. Betz. "SOLEF PVDF Biaxially Oriented Piezo- and Pyroelectric Films for Transducers." *Sensors and Actuators. 12:* 207–223 (1987).

51. Glass. A. M. "An Introduction," *The Application of Ferroelectric Polymers*, edited by T. T. Wang. New York: Chapman and Hall, 1988, 1–5.

52. Grahn, A. and L. Astle. "Robotic Ultrasonic Force Sensor Arrays," *Conference Proceedings of Robots.* Society of Manufacturing Engineers. Dearborn. MI, U.S.A., Volume 8, 1984. 21-1–21-18.

53. Greeneich, E. W. and R. S. Muller. "Theoretical Transducer Properties of Piezoelectric Insulator FET Transducers." *Journal of Applied Physics. 46:* 11. 4631-4640 (November 1975).

54. Hackwood, S., G. Beni, and T. J. Nelson. "Torque-sensitive Tactile Array for Robotics. *Robot Sensors, Tactile and Non-Vision,* Volume 2, edited by Alan Pugh. New York: Springer-Verlag, 1986, 123–132.

55. Harmon, L. D. "Automated Tactile Sensing." *International Journal of Robotics Research, 1:* 3–32 (1982).

56. Harmon, L. D. "A Sense of Touch Begins to Gather Momentum," *Sensor Review, 1:* 82-88 (1981).

57. Harmon, L. D. "Robotic Taction for Industrial Assembly," *International Journal of Robotics Research. 3:* 72–76 (1983).

58. Herbert, J. M. *Ferroelectric Transducers and Sensors.* New York: Gordon and Breach Science Publishers. 1982.

59. Higuchi, K. and others. "Ultrasonic Phased Array Transducer for Acoustic Imaging in Air," *Proceedings of the IEEE Ultrasonics Symposium.* Williamsburg, VA, U.S.A., 17–19 November 1986, 559–562.

60. Hillis. D. W. "A High-Resolution Imaging Touch Sensor," *International Journal of Robotics Research. 1:* 2, 33–44 (1982).

61. Jenstrom, D. T. and C. Chen. "A Fiber Optic Microbend Tactile Sensor Array," *Sensors and Actuators. 20:* 239–248 (1989).

62. Kanade, T. and T. Sommer. "An Optical Proximity Sensor for Measuring Surface Position and Orientation for Robot Manipulation," *Robotics Research, The First International Symposium.* edited by Michael Brady and Richard Paul. Cambridge, MA: The MIT Press, 1984, 547–563.

63. Kolesar, E. S. and others. "Object Imaging With A Multiplexed Piezoelectric Polymer Tactile Sensor," *IEEE International Conference on Systems Engineering,* Fairborn, OH, U.S.A., 1–3 August 1991, 280–283.

64. Kleinschmidt, P. and V. Magori. "Ultrasonic Robotic-sensors for Exact Short Range Distance Measurement and Object Identification," *Proceedings of the IEEE Ultrasonics Symposium.* San Fransisco, CA. U.S.A., 16–18 October 1985, 457–462.

65. Knittel, J. and T. C. Hsia. "Design of a Robot Force Sensor System," *Advances in Robotics and Automation.* 1-5 (1984).

66. Kraus. J. D. *Electromagnetics.* New York: McGraw-Hill, Inc., 1984.

67. Kuroda, S. and others. "Ultrasonic Imaging Systems for Robots Using an Electronic Scanning Method," *Robotica. 2:* 47–53 (1984).

68. KYNAR Piezo Film Department. *Kynar Piezo Film Technical Manual.* Manual 10-M-11-83-M. Pennwalt Corporation. King of Prussia. PA, 1983.

69. Lerch, R. "Electroacoustic Transducers Using Piezoelectric Polyvinylidene Fluoride Films," *Journal of the Acoustical Society of America, 66:* 4, 952–954. (October 1979).

70. Luo. R. C., F. Wang, and Y. Liu. "An Imaging Tactile Sensor with Magnetostrictive Transduction," *Robot Sensors, Tactile and Non-Vision.* Volume 2. edited by Alan Pugh. New York: Springer-Verlag, 1986, 113–122.

71. Mader, G. and H. Meixner. "Pyroelectric Infrared Sensor Arrays Based on the Polymer PVDF," *Sensors and Actuators, 21:* 503–507 (1990).

72. Marcus, M. A. "Orientation Effects on Dielectric and Piezoelectric Properties of Polyvinylidene Fluoride Films," *Proceedings of the 5th International Symposium on Electrets, Heidelberg:* 894–899 (1985).

73. Marcus, M. A. "Applications of Polyvinylidene Fluoride Films," *Proceedings of the 5th International Symposium on Electrets, Heidelberg:* 724–731 (1985).

74. Marsh, K. A. "Acoustic Imaging in Robotics Using a Small Set of Transducers," *Proceedings of the 4th International Conference on Robot Vision and Sensory Controls,* London, U.K. 31 October 1984, 261–266.

75. Mason, W. P. *Piezoelectric Crystals and Their Application to Ultrasonics.* New York: D. Van Nostrand Co., 1950.

76. Megaw, H. D. *Ferroelectricity In Crystals.* London: Methuen and Co., 1957.

77. Meixner, H. and others. "Infrared Sensors Based on the Pyroelectric Polymer Polyvinylidene Fluoride (PVDF)," *Siemens Forsch-u. Entwickl.-Ber.. 15:* 105–113 (1986).

78. Miller, G. L. and others. "Active Damping of Ultrasonic Transducers for Robotic Applications," *International Conference on Robotics,* Atlanta, GA, U.S.A., 13–15 March 1984, 379–384.

79. Moravec, H. P. and A. Elfes. "High Resolution Maps from Wide Angle Sonar," *Proceedings of the International Conference on Robotics and Automation.* St. Louis, MO, U.S.A.. March 1985, 116-121.

80. Mott, D. H. and others. "An Experimental Very High Resolution Tactile Sensor Array," *Proceedings of the 4th International Conference on Robot Vision and Sensory Controls.* London. U.K. October 1984, 251-260.

81. Muller. R. S. "Integrated Circuit Sensor." U. S. Patent 4,674,319, June 23. 1987.

82. Muller. R. S. and others. "Piezoelectric-Semiconductor, Electromechanical Transducer," U.S. Patent 3,351,786, 7 November 1967.

83. Muller. R. S. "Stress-Strain Transducer Charge Coupled to a Piezoelectric Material," U.S. Patent 3,585,415. 15 June 1971.

84. Muller, R. S. and others. "Integrated Pyroelectric Sensor and Method," U.S. Patent 4,608,865, 2 September 1986.

85. Münch, W. V. and U. Thiemann. "Pyroelectric Detector Array with PVDF on Silicon Integrated Circuit," *Sensors and Actuators, 27:* 167–172 (1991).

86. Park, K. and others. "A PVDF Tactile Sensor for Industrial Robots," *Conference of Robots,* Society of Manufacturing Engineers, Dearborn, MI. U.S.A., Volume 10. April 1986. 4/47–4/72.

87. Patterson, R. W. and G. E. Neville, Jr. "The Induced Vibration Touch Sensor - A New Dynamic Touch Sensing System," *Robotica, 4:* 27–31 (1986).

88. Paul, C. R. and S. A. Nasar. *Introduction To Electromagnetic Fields.* New York: McGraw-Hill, Inc., 1987.

89. Pedotti, A. and others. "Multisensor Piezoelectric Polymer Insole for Pedobarography," *Ferroelectrics, 60:* 163–174 (1984).

90. Pennywitt, K. E. "Robotic Tactile Sensing," *Byte, 11:* 177–200 (January 1986).

91. Pirolo, D. G. *Piezoelectric Polymer Tactile Sensor Arrays for Robotics.* MS Thesis, AFIT/GE/ENG/87D-52. School of Engineering, Air Force Institute of Technology (AU), Wright Patterson AFB, OH, December 1987.

92. Podoloff, R. M. and M. Benjamin. "A Tactile Sensor for Analyzing Dental Occlusion," *Sensors*, 41–47 (March 1989).

93. Podoloff, R. M. "A Pressure Mapping System for Gait Analysis," *Sensors*, 21–25 (May 1991).

94. Polla, D. L. and others. "Integrated Zinc Oxide-on-Silicon Tactile Sensor Array," *IEEE International Electron Devices Meetings (IEDM)*, Washinton, D.C., U.S.A., 1–4 December 1985, 133–136 .

95. Powers, J. M. "Long Range Hydrophones," *The Application of Ferroelectric Polymers*, edited by T. T. Wang. New York: Chapman and Hall, 1988, 118–161.

96. Rebman, J. and K. A. Morris. "A Tactile Sensor with Electrooptical Transduction," *Proceedings of the 3rd International Conference on Robot Vision and Sensory Controls*, Cambridge, MA, U.S.A., November 1983, 210–216.

97. Regtien, P. P. L. "Sensor Systems for Robot Control," *Sensors and Actuators, 17:* 91–101 (1989).

98. Regtien, P. P. L. and R. F. Wolffenbuttel. "A Novel Solid-state Colour Sensor Suitable for Robotic Applications," *Proceedings of the 5th International Conference on Robot Vision and Sensory Controls,* Amsterdam, The Netherlands, October 1985, 259–266.

99. Regtien, P. P. L. and H. C. Hakkesteegt. "A Low-cost Sonar System for Object Identification," *Proceedings of the 18th International Symposium on Industrial Robots,* Lausanne, Switzerland, 1988, 201–210.

100. Reston, R. R. *Robotic Tactile Sensor Fabricated from Piezoelectric Polyvinylidene Fluoride Films.* MS Thesis, AFIT/GE/ENG/88D-41. School of Engineering, Air Force Institute of Technology (AU), Wright Patterson AFB, OH, December 1988.

101. Reston, R. R. and E. S. Kolesar. "Pressure-Sensitive Field-Effect Transistor Sensor Array Fabricated from a Piezoelectric Polyvinylidene Fluoride Film," *Proceedings of the Annual International Conference of the IEEE Engineering in Medicine and Biology Society,* Seattle, WA, 9–12 November 1989, 918–919.

102. Roberston, B. E. "Tactile Sensor System for Robotics," *Robot Sensors. Tactile and Non-Vision,* Volume 2, edited by Alan Pugh. New York: Springer-Verlag, 1986, 89–98.

103. Rooks, B. "Tactile Sensing Should Not Be Forgotten," *Sensor Review, 3:* 2 (1983).

104. Russell, R. A. *Robot Tactile Sensing.* Englewood Cliffs, New Jersey: Prentice Hall, 1990.

105. Schneiter, J. L. and T. B. Sheridan. "An Optical Tactile Sensor for Manipulat)rs," *Robotics and Computer-Integrated Manufacturing, 1:* 1 65–71 (1984).

106. Schoenwald, J. S. and others. "A Novel Fiber Optic Tactile Array Sensor," *Proceedings of SPIE Fiber Optic and Laser Sensors IV, 718:* Cambridge, MA, 22–24 September 1986, 148–152.

107. Schoenwald, J. S. and J. F. Martin. "PVF_2 Transducers for Acoustic Ranging an Imaging in Air," *Proceedings of the IEEE Ultrasonics Symposium,* Atlanta, GA, U.S.A, 31 October–2 November 1983, 577–580.

108. Schoenwald, J. S. "Strategies for Robotic Sensing Using Acoustics," *Proceedings of the IEEE Ultrasonics Symposium.* San Fransisco, CA, U.S.A., 16–18 October 1985, 457–462.

109. Seekircher, J. and B. Hoffmann. "Improved Tactile Sensors," *Proceedings of the 2nd IFAC Symposium (SYROCO '88),* Karlsrule, FRG, 5–7 October 1988, 317–322.

110. Sessler, G. M. "Piezoelectricity in Polyvinylidene Fluoride," *Journal of Acoustical Society of America, 70:* 6, 1586–1608 (December 1981).

111. Severwright, J. "Tactile Sensor Arrays - The Other Option." *Sensor Review. 3:* 27–29 (1983).

112. Solef Piezo Film. *Principle of Piezoelectric Film Number 016/212/314/007.* Solvay and Co. Brussels. Belgium. 1 (March 1987).

113. Squire, P. L. "Piezoelectric PVDF Ultrasonic Transducers," *Sensors. 3* 12–16 (July 1986).

114. Staugaard, A. C., Jr. *Robotics and AI: An Introduction to Applied Machine Intelligence.* Englewood Cliffs, New Jersey: Prentice Hall, Inc., 1987.

115. Sugiyama, S. and others. "Tactile Image Detection Using a 1k-element Silicon Pressure Sensor Array," *Sensors and Actuators. 21* 397–400 (1990).

116. Suzuki, K. and others. "A 1024-Element High Performance Silicon Tactile Imager," *IEEE Electron Devices Meeting*, San Fransisco, California, U.S.A. 11–14 December 1988, 674–677.

117 Suzuki, K. and others. "Process Alternatives and Scaling Limits for High-Density Silicon Tactile Imagers," *Sensors and Actuators, 21* 915–918 (1990).

118. Swartz, R. G. and J. D. Plummer. "Integrated Silicon-PVDF Acoustic Transducer Arrays," *IEEE Transactions on Electron Devices, ED-26:* 12, 1921–1931 (December 1979).

119. Tanie, K. and others. "A High Resolution Tactile Sensor," *Proceedings of the 4th International Conference on Robot Vision and Sensory Controls*, London. U.K. October 1984, 251–260.

120. Tise, B. "A Compact High Resolution Piezoresistive Digital Tactile Sensor," *Proceeding of the IEEE International Conference on Robotics and Automation. 2:* 760–764 (1988).

121. Togai, M., P. P. Wang, and J. Rebman. "Design Criteria and Recognition Schemes for an Arrayed Touch Sensor," *International Conference on Robotics*, Atlanta, Georgia, U.S.A., 13–15 March 1984, 370–378.

122. Tone, M. and others. "High-Frequency Ultrasonic Transducer Operating in Air," *Japanese Journal of Applied Physics, 23:* 6, L436–L438 (June 1984).

123. Trietley, H. L. *Transducers in Mechanical and Electronic Design.* New York: Marcel Dekker. 1986.

124. Tsujimura, T. and T. Yabuta. "Object Detection by Tactile Sensing Method Employing Force/Torque Information," *IEEE Transactions on Robotics and Automation. 5:* 4, 444–450 (August 1989).

125. Tsujimura, T. and others. "Three-Dimensional Shape Recognition Method Using Ultrasonics for Manipulator Control System," *Journal of Robotic Systems. 3:* 2, 205–216 (1986).

126. Tzou, H. S. and S. Pandita. "A Multi-Purpose Dynamic and Tactile Sensor for Robot Manipulators," *Journal of Robotic Systems, 4:* 6, 719–741 (1987).

127 Ueda, M. "Spectrum of Echo Scattered by Simple Object Placed at Focal Plane of Ultrasonic Transducer." *Proceedings of the 13th International Symposium on Acoustical Imaging*, Minneapolis, MN, U.S.A., October 1983, 149–162.

128. Voorthuyzen, J. A. and P. Bergveld. "The PRESSFET: An Integrated Electret-MOSFET Based Pressure Sensor." *Sensors and Actuators. 14:* 349–360 (1988).

REPORT DOCUMENTATION PAGE

Form Approved
OMB No. 0704-0188

Public reporting burden for this collection of information is estimated to average 1 hour per response, including the time for reviewing instructions, searching existing data sources, gathering and maintaining the data needed, and completing and reviewing the collection of information. Send comments regarding this burden estimate or any other aspect of this collection of information, including suggestions for reducing this burden, to Washington Headquarters Services, Directorate for Information Operations and Reports, 1215 Jefferson Davis Highway, Suite 1204, Arlington, VA 22202-4302, and to the Office of Management and Budget, Paperwork Reduction Project (0704-0188), Washington, DC 20503

1. AGENCY USE ONLY (Leave blank)

2. REPORT DATE
December 1991

3. REPORT TYPE AND DATES COVERED
Master's Thesis

4. TITLE AND SUBTITLE
ROBOTIC TACTILE SENSOR FABRICATED FROM A MONOLITHIC SILICON INTEGRATED CIRCUIT AND A PIEZOELECTRIC POLYVINYLIDINE FLUORIDE THIN FILM

5. FUNDING NUMBERS

6. AUTHOR(S)
Craig S. Dyson, Captain, USAF

7. PERFORMING ORGANIZATION NAME(S) AND ADDRESS(ES)
Air Force Institute of Technology, WPAFB OH 45433-6583

8. PERFORMING ORGANIZATION REPORT NUMBER
AFIT/GE/ENG/91D-16

9. SPONSORING/MONITORING AGENCY NAME(S) AND ADDRESS(ES)
Capt Ron Julian
AL/CFBA
WPAFB, OH 45433

10. SPONSORING/MONITORING AGENCY REPORT NUMBER

11. SUPPLEMENTARY NOTES

12a. DISTRIBUTION/AVAILABILITY STATEMENT
Approved for public release; distribution unlimited

12b. DISTRIBUTION CODE

13. ABSTRACT (Maximum 200 words)
The purpose of this research effort was to design, fabricate, and test a tactile sensor system consisting of an external high impedance switch circuit, an external multiplexing circuit, and a tactile sensor IC. In order to accomplish this objective, a hardware design and selection process was implemented along with a logical test methodology. An external multiplexer circuit samples all of the array elements in 50 ms. The current prototype sensor has linearity spanning loads of 0.8 g to 135 g, a load resolution of 20 g, and a maximum bandwidth of 25 Hz. Using an elementary shape recognition algorithm the sensor can recognize the shape of a contact load with a spatial resolution on the order of 700 μm. A comparison of three different adhesives used to bond the piezoelectric PVDF film to the surface of the electrode array was made and a urethane adhesive was selected for its superior electrical and physical properties.

14. SUBJECT TERMS
Tactile Sensing, Robotic Sensors, Piezoelectric Materials, Piezoelectric Transducers

15. NUMBER OF PAGES
390

16. PRICE CODE

17. SECURITY CLASSIFICATION OF REPORT	18. SECURITY CLASSIFICATION OF THIS PAGE	19. SECURITY CLASSIFICATION OF ABSTRACT	20. LIMITATION OF ABSTRACT
Unclassified	Unclassified	Unclassified	UL